An Experimental Study Of Two-Phase Flow In Idealised Tube Bundles

Azmahani Sadikin

Submitted for the degree of Doctor of Philosophy

Heriot-Watt University

School of Engineering and Physical Sciences

August 2013

ABSTRACT

This thesis reports on an experimental study of air-water mixtures flowing through idealized shell and tube, in-line and staggered heat exchangers. The measured void fractions in the maximum and minimum gaps between the tubes are reported at near atmospheric conditions, to give local variations for different tube diameters and tube bundle arrangements. The void fraction measurements were made using a gamma-ray densitometer. The pressure drops in the tube bundles are also reported. These data are compared with the correlations available in the open literatures to investigate the void fraction and pressure drop prediction methods for these heat exchangers. The in-line 38 mm tube bundle is shown to provide no significant effect on void fraction or drag force when compared with the 20 mm tube diameter bundle. A new void fraction model is therefore proposed by modifying the characteristic length of an existing slip ratio method. A new pressure drop model is presented. The acceleration pressure drop between the tubes from the separation to re-attachment is shown to be responsible for some of the frictional pressure drop with a liquid film on the tubes responsible for the remainder. The staggered bundle shows the bundle arrangement gives different void fraction and different pressure drop data when compared to the in-line bundle.

To my children

Iman and Marissa

ACKNOWLEDGEMENTS

I am indebted to Dr. David A. McNeil who had given a big assistant, support, expertise, motivation and a great patience.

I am also grateful to all the staff and technicians of the School of Engineering and Physical Sciences, especially Mr. Richard Kinsella and Mr. Kenny W. Carruthers for the tube bundles construction.

I am thankful to my own family, especially my husband for a constant source of inspiration and my parent for always believe in me.

Finally, thanks to the Ministry of Higher Education of Malaysia for funding my study in Heriot-Watt University, Edinburgh, UK.

ACADEMIC REGISTRY
Research Thesis Submission

Name*:*	AZMAHANI SADIKIN		
School/PGI:	EPS/IMPEE		
Version: *(i.e. First, Resubmission, Final)*	FINAL	Degree Sought (Award **and** Subject area)	PhD MECHANICAL ENGINEERING

Declaration

In accordance with the appropriate regulations I hereby submit my thesis and I declare that:

1) the thesis embodies the results of my own work and has been composed by myself
2) where appropriate, I have made acknowledgement of the work of others and have made reference to work carried out in collaboration with other persons
3) the thesis is the correct version of the thesis for submission and is the same version as any electronic versions submitted*.
4) my thesis for the award referred to, deposited in the Heriot-Watt University Library, should be made available for loan or photocopying and be available via the Institutional Repository, subject to such conditions as the Librarian may require
5) I understand that as a student of the University I am required to abide by the Regulations of the University and to conform to its discipline.

* *Please note that it is the responsibility of the candidate to ensure that the correct version of the thesis is submitted.*

Signature of Candidate*:*	[signature]	Date:	19 AUGUST 2013

Submission

Submitted By *(name in capitals):*	
Signature of Individual Submitting:	
Date Submitted:	

For Completion in the Student Service Centre (SSC)

Received in the SSC by *(name in capitals):*			
Method of Submission *(Handed in to SSC; posted through internal/external mail):*			
*E-thesis Submitted (**mandatory for final theses)***			
Signature:		Date:	

Please note this form should bound into the submitted thesis.

Updated February 2008, November 2008, February 2009, January 2011

TABLE OF CONTENTS

LIST OF TABLES

LIST OF FIGURES

GLOSSARY

Nomenclature

a	gap between tubes (m)
A_{he}	area of heat exchanger (m^2)
A_t	area of orifice throat (m^2)
b	constant
c	constant
C	constant
Ca	Capillary number
C_d	discharged coefficient
C_D	drag coefficient
C_{D_u}	upper region of drag coefficient
C_{D_l}	lower region of drag coefficient
C_d	drag coefficient of upper and lower region
C_L	pressure loss coefficients
c_m	momentum correction factor
D	tube diameter (m)
D_p	bubble diameter (m)
D_G	drag group (N)
E	constants for C_d calculations
e	base of the natural logarithm
f_1	single-phase loss coefficient
Fr	Froude number
G	mass flux (kg/m^{2}s)
g	gravity acceleration (m^2/s)
h	height of the water (m)

I	electrical current, (Ampere)
I_B	background readings
I_G	the air-only gamma-ray intensity
I_L	the water-only gamma-ray intensity
$I_{2\theta}$	two phase mixture gamma-ray intensity
j	superficial velocity (m/s)
j_g^*	dimensionless gas velocity (m/s)
k	slip ratio
M	mass flow rate (kg/s)
$N_{t,}$	number of bubbles that hit the sensor
P	tube pitch (m)
p_{abs}	absolute pressure
$P_{transducer}$	transducer pressure (pa)
P_{head}	pressure head (pa)
Q	liquid flow rate (kg/s)
Re	Reynolds number
Ri	Richardson number
S	slip ratio
t_G	the total duration of the probe detects vapour
T	temperature (K)
T_{UR}	upstream signal
T_{DR}	downstream signal
$\bar{u}_g$	average gas velocity (m/s)
u	velocity (m/s)
V	voltage (V)
v	specific volume (m^3/kg)
v_r	relative velocity of the bubble (m/s)

V_{db}	noise (Hz)
x	quality
x_{tt}	Martinelli parameter

Greek symbols

α	void fraction
β	constants for C_d calculations
ε	volume fraction
Δp	pressure drop
Δs	distance between the two tips of the double-sensor probe (m)
Δt	total sampling time (s)
η	constants for C_d calculations
ρ_{tp}	two-phase density (kg/m^3)
ρ	density (kg/m^3)
δ	product of the porosity
σ	surface tension (N/m)
μ	dynamic viscosity (kg/m.s)
φ	porosity
ϕ_l^2	two-phase frictional multiplier
ϕ_{LE}^2	measured two-phase multiplier
θ_R	reattachment angle (°)
θ_S	separation angle (°)
γ	gamma-ray

Subscripts

avg	average

A	acceleration
F	frictional
G	gravitational
g	gas
H	homogenous
l	liquid
LF	liquid friction
max	maximum
min	minimum
n	number
S	separation
R	re-attachment
tp	two-phase
v	vertical

Abbreviations

1-D	One-dimensional
2-D	Two-dimensional
HEM	Homogenous equilibrium model
ID	Internal diameter
LRV	Lower range value
P/D	Pitch to diameter ration
R11	Refrigerant-11
R113	Refrigerant-113
URV	Upper range value
PC	personal computer
Re	Reynolds Number
RMS	Root Mean Square

LIST OF PUBLICATIONS

David A. McNeil, Azmahani Sadikin, Khalid H. Bamardouf, 2012, *A mechanistic analysis of shell-side two-phase flow in an idealised in-line tube bundle*, International Journal of Multiphase Flow 45, 53–69.

Azmahani Sadikin, David A. McNeil, Khalid H. Bamardouf, 2010, *Two-Phase Flow on the Shell Side of a Shell and Tube Heat Exchanger*, Proceedings of the International Heat Transfer Conference, IHTC14, August 8-13, Washington, DC, USA.

CHAPTER 1- INTRODUCTION

Shell and tube heat exchangers are commonly used in the process industry to boil liquids. The most common one is the kettle reboiler, which consists of a horizontal tube bundle placed in a shell. The heating fluid flows inside the tubes while the heated fluid boils outside the tubes, in a pool. The flow is natural circulation because of the density difference between the two-phase mixture flowing in the tube bundle and the liquid flowing between the tube bundle and the shell wall.

The design of this heat exchanger has been extensively studied in the past. However, there are few studies on the local two-phase flow conditions on the shell-side of the tube bundle. Current design is based on one-dimensional modeling of the mass, momentum and energy equations. There are many empirical correlations for predicting void fractions, e.g. Schrage et al. [1], Dowlati et al. [2] and Feenstra et al. [3]. Meanwhile, Ishihara et al. [4] and Xu et al. [5] have proposed methods for frictional pressure drop. The void fraction and pressure drop methods proposed by these researchers are based on bundle or pitch average measurements of void fraction. The pressure drop correlations were based on the flow process in a pipe without any reference to the flow phenomena on the shell-side of heat exchangers and the flow between the tube passages. The work of Ishihara et al. [4], for example, produced a two-phase friction multiplier which is extensively used. However, this correlation assumes a similarity with frictional pressure drop in a pipe. Shell-side pressure drops are different. The pressure drops in a pipe are due to wall friction whereas the shell-side values are due to separation and re-attachment of the fluid as it passes around the tubes. These correlations are also based on data from tube bundles with tubes less than 20 mm in diameter. The present work addresses the important parameters of two-phase flow in vertical cross-flows in tube bundles using air-water mixtures at adiabatic conditions, by measuring the void fraction and pressure drop, and investigating the effect of tube bundle geometry on these parameters. This was achieved by modifying a purpose built test facility. Therefore, the objective of this research is to measure the local void fractions in the gaps between the tubes in tube bundles, so the local void fraction variations with position can be found. In addition, the measurement of pressure drops on the shell-side of shell and tube bundles are obtained. The drag force by the tubes is deduced from the local void fractions and pressure drop measurements to produce drag coefficients required by the two-fluid model. Additionally, new correlations are proposed to predict the void fraction and frictional pressure drop in a heat exchanger.

The experimental investigation consists of two separate experiments. First, the local void fractions measurements were made at the maximum and minimum gaps between the tubes. These measurements were made using a single-beam, gamma-ray densitometer. The densitometer's isotope was Americium (Am) 241. This collimated low-energy source projected a beam 10 mm in diameter through the flow, parallel to the tubes, onto a photomultiplier tube. A PC card-based, electronically controlled pulse counter was used to measure the radiation incident on the photomultiplier. Second, the pressure drop measurements were made between the rows in the bundles at the pressure taps located between the rows. The pressure drop measurements were collected through a data logger connected to a PC and controlled by LabVIEW software.

The experimental works were conducted on three tube bundles. Two of the bundles are in-line bundles, and one is a staggered bundle. One in-line bundle has 19 mm diameter tubes and the other 38 mm diameter tubes. The staggered bundle has 19 mm diameter tubes. The pitch to diameter ratio is 1.32 for all tube bundles. The rod tubes and the plates were all made of Perspex sheet that was 12 mm thick and joined together by bolts to provide a transparent view of the flow. These bundles are used to give reasonable geometric variation to the measured parameters.

This thesis consists of 11 chapters. In Chapter 2, the studies of the flow in a heat exchanger are critically reviewed. The output of the review was the basis of this research. Chapter 3 provides a detailed description of the experimental rig design, fabrication and instrumentation. The corresponding experimental conditions, procedures and commissioning of the test facility are described in Chapter 4. In Chapter 5, which is a stand-alone chapter where the reviews, methodology and design of a conductive probe are presented. The conductivity probe and the gamma-ray densitometer were used to measure the void fraction. However, the results of the measurements of void fraction from the conductivity probe did not agreed with the measured void fractions from the gamma-ray densitometer. Therefore, the more established gamma-ray densitometer method was chosen. The local void fractions measurements obtained were analyzed in Chapter 6 by comparing the measurements with the existing correlations by Schrage et al. [1], Feenstra et al. [3] and Dowlati et al. [2]. The measured pressure drops are discussed in Chapter 7 and the measured frictional pressure drop are compared with two-phase friction multiplier of Ishihara et al. [4] and Xu et al. [5]. The drag force for modeling the two-fluid model of the flow in a heat exchanger is presented in Chapter 8. The results were compared with models taken from the literature, which were Rahman et al. [6] and Simovic et al. [7]. In Chapter 9, CFD simulations provide a better understanding of the flow path through the heat exchanger for both bundle arrangements. The separation and re-attachment flow phenomena that occur in the tube bundles are described. The CFD simulations, coupled to the measurements of local void fraction and pressure drop, give a greater understanding of the flow in a heat exchanger. A new model of a heat exchanger is introduced in Chapter 10, where the new correlations of void fractions and frictional pressure drops are proposed. Final conclusions and recommendations are made in Chapter 11.

The evaluation of the experimental data, and the correlations produced, allowed a new design model to be produced. This model is in its infancy but is based on the actual processes that occur in a heat exchanger. This research gives a better understanding of the flow on the shell-side of a heat exchanger and add valuable data to the literature that will help improve the design of heat exchangers.

CHAPTER 2 - LITERATURE REVIEW

2.1 Kettle reboilers

This study was initiated to support previous studies of kettle reboilers [1-23]. Reboilers are widely used in the process industry for vapour generation. Some developments of horizontal steam generators for nuclear power plants are based on the kettle reboiler design.

The kettle reboiler is a shell and tube type heat exchanger usually consisting of a tube bundle arranged on a square-in-line pitch enclosed in a shell for easy cleaning. It also contains a vertical oriented weir of sufficient height to ensure liquid covers the bundle. The heating medium, usually steam, flows in the tubes while the liquid to be partially vapourised is on the shell side. The liquid is usually below the boiling temperature at the bottom-most portion of the bundle. It is heated by natural convection and then by subcooled and saturated boiling as it moves from the bottom to the top. The extent of each regime depends upon the composition of fluid as well as parameters affecting performance, such as type and volume of liquid, operating pressure, heat flux and geometrical parameters. From the bottom to the bundle the temperature of the liquid increases, until the saturation temperature is reached, and then vapour bubble formation on the tube surface takes place, leading to a two-phase liquid and vapour mixture. This phenomenon continues and the vapour fraction in the mixture rises until the bundle top is reached. The difference in density between the two-phase mixture flowing in the bundle and the liquid flowing between the bundle and the shell wall causes natural circulation to occur. The recirculated liquid joins the fresh liquid entering the reboiler. The combined (fresh and recirculating) liquid attains a velocity dependent upon physico-thermal properties, the quantity of liquid, the reboiler geometry and other parameters. Heat transfer in this region is by convective boiling due to the velocity induced by the recirculation of liquid. Many flow regimes are observed in the tube bundle, depending on the velocity of liquid, the heat flux, operating pressure, diameter of tubes and spacing between them. Void fractions and two-phase pressure drop are both hydrodynamics parameters needed for analysis of tube bundle performance because these parameters affect the overall heat transfer performance. Thus, they are central to good design.

2.2 One-Fluid Model

The one-dimensional (1-D) model is the simplest approach available for designing kettle reboilers. It assumes that recirculating liquid enters the bundle at the bottom and flows vertically upwards through the tubes, until it reaches the free surface, where the vapour separates from the liquid and the liquid returns to the bottom of the bundle.

The recirculating liquid flow rate is determined by assuming that the two-phase pressure drop in the tube bundle consists of frictional, acceleration and gravitational components and that their sum is equal to the static pressure drop of the liquid outside the bundle. The frictional and accelerational pressure drops in the shell side are assumed to be zero. The fountain effect at the free surface is due to high vapour velocity at the bundle exit and is normally neglected, with the liquid flow assumed to flow horizontally at the top of the bundle. This model was widely used in the literature [24-28].

Jensen [28] modified the (1-D) model by including the effect of frictional and accelerational pressure drop in the shell side of their model. The recirculating flow predicted by these models showed that it initially increased as the heat flux increased before decreasing with further increases in heat flux. It also depended on the weir height and increased when the weir height increased. The effect of weir height was small at low heat fluxes when the liquid hydrostatic pressure dominated. He also found that the effect of frictional and acceleration pressure drop at the shell side was negligible. Since the two-phase pressure drop has gravity, acceleration and friction components, the void fraction and a two-phase friction multiplier are required to complete the model. Several investigators have proposed void fraction correlations, e.g. Schrage et al. [1], Dowlati et al. [2] and Feenstra et al. [3]. For the two-phase multiplier, various investigators have applied the Lockhart and Martinelli [29] method, used by Ishihara et al. [4] and Xu et al. [5]. Barmardouf and McNeil, [30], studied a range of available experimental data, mostly for pure fluids at atmospheric pressure, and concluded that the Feenstra et al. [3] void fraction correlation and the Ishihara et al. [4] two-phase multiplier correlation provided the best empirical information for the range of conditions likely to occur in a kettle reboiler. Sadikin et al. [31] reported that Dowlati et al. [2] void fraction correlation and Ishihara et al. [4] two-phase multiplier correlation give the best prediction on air-water test in 38 mm in-line tube bundle at near atmospheric pressure.

McNeil et al. [32] developed two one-point-five-dimensional models, one to aid the investigation of static liquid distribution surrounds the tube bundle, by allowing two-dimensional model effects to be added, and another to aid the investigation of the cause of the change from reasonably constant to continually declining row pressure drop. The data and the analysis showed that the flow within the tube bundle was always two-dimensional and that the flow pattern was dominated by the static liquid at the tube bundle edge when the heat flux was less than 10 kW/m^2, and the flow regime is bubbly flow. At larger heat flux, the flow regime changed to intermittent flow. McNeil et al. [32] has concluded that one-dimensional flows never occur and the flow is two-dimensional with heat-flux dependent boundary conditions.

2.3 Two-Fluid Model

The two-fluid model is a more advanced approach to modelling two-phase flow in a complex geometries. The model assumes that the flow contains two or more fluids, each having its own thermophysical properties and each moving with its own velocity, and each phase has its own conservation equations for mass, momentum and energy. These are solved together with closure equations used to define the interaction between them and other materials. The interfacial drag force and the force on the fluid by the tubes are the most important forces that require closure equations because they strongly affect the void fraction and the pressure drop. The accuracy of the two-fluid model depends mainly on the accuracy of these forces which are not well developed for the flow across tube bundles.

Attempts to model the two-dimensional flow in the kettle reboiler have been made using the algebraic slip model and the two-fluid model. The algebraic model assumes that the two phases move in the same direction but with different velocities and was used by Burnside [26] to simulate the kettle reboiler used by Cornwell et al. [33]. The model was constructed with a rectangular tube bundle of 17 rows and 9 columns and a symmetry plane, as shown in the Figure 2.1.

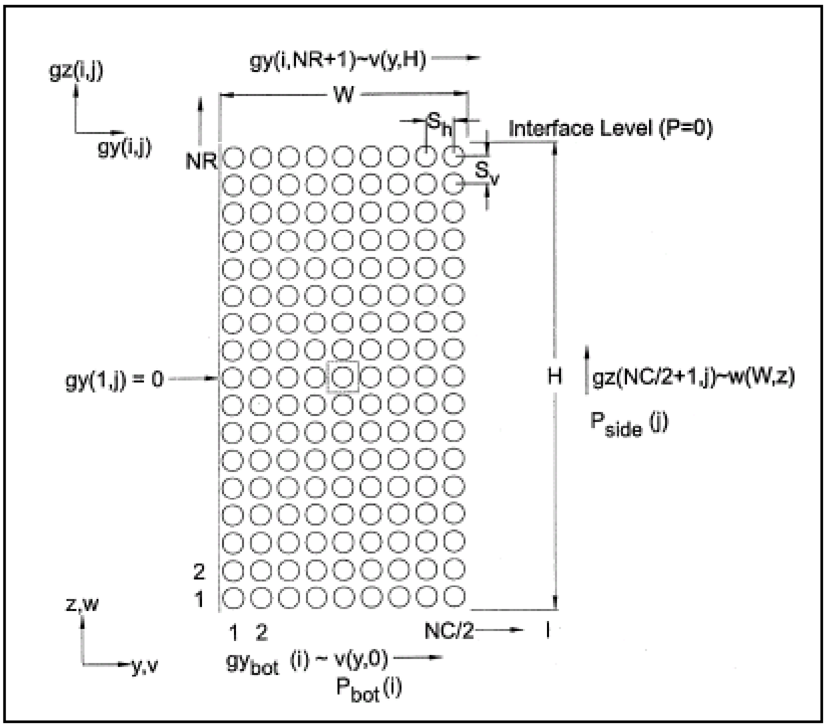

Figure 2.1: 2-D kettle reboiler model designed by Burnside [26]

The model was restricted to the tube bundle with an all-liquid variation in static pressure applied to the side. The author concluded that the flow outside the bundle had a negligible effect on the flow distribution inside the tube bundle.

Edwards and Jensen [34] produced a 2-D model for the kettle reboiler using the two-fluid approach. However, due to the absence of information on the interfacial momentum force at that time, the authors assumed a constant drag coefficient for the whole flow field. The value used allowed the experimental void fraction results to be approached, but convergence problems appeared when they got within 30% of the experimental values.

Rahman et al. [6] were the first to model the interfacial drag coefficient for vertical two phase flow across a horizontal tube bundle. The drag coefficient was developed from experimental data obtained by Schrage et al. [1] and Dowlati [12], with the assumption of negligible resistance between the tube walls and the gas or vapour flow, arguing that only the liquid phase was in contact with the tubes in the bundle. It was based on a Reynolds number defined as

$$\mathrm{Re} = \frac{\rho_{tp} v_r \delta}{\mu_l} \tag{2.1}$$

where ρ_{tp}, v_r, δ, μ_l are the two-phase mixture density, the relative velocity of the bubble, the product of the porosity and the transverse pitch and the dynamic viscosity of the liquid phase respectively. The variation of interfacial drag coefficient with Reynolds number is shown in Figure 2.2.

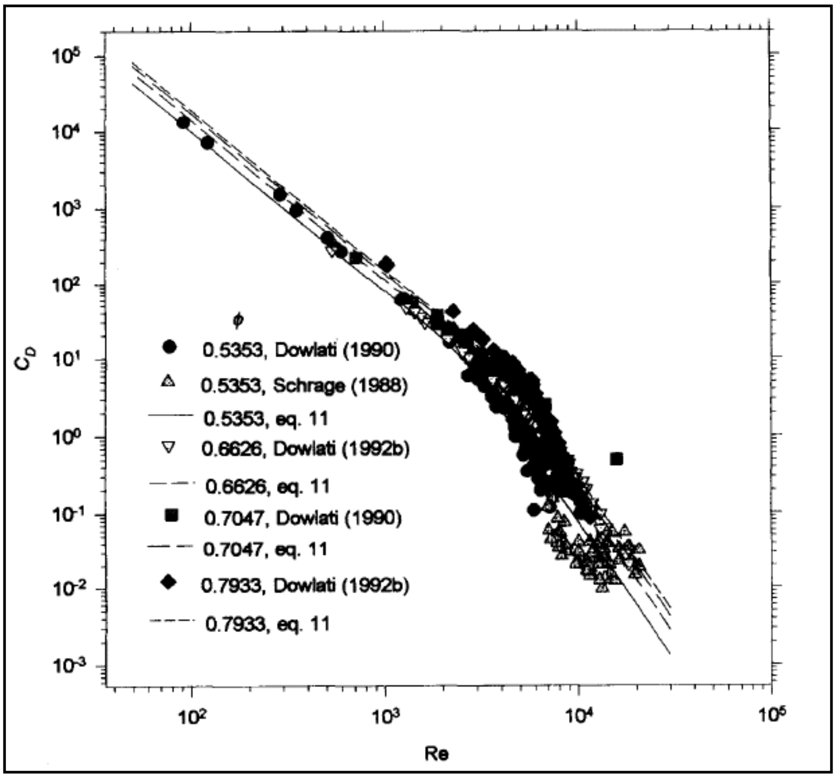

Figure 2.2: Drag coefficient by Rahman et al. [6]

They separated the outcome into two regions based on the slope: the upper region and the lower region. The upper region, which had a drag coefficient of more than 4, was interpreted as applying to flow patterns of churn and spray/annular flow, since the mass flows and density were low, causing the Reynolds number to be low. The lower region was interpreted as applying to bubbly and slug flows because the liquid mass flow and the mixture density were high or moderate, so that the Reynolds number was high. The final form of the drag coefficient was

$$C_D = (C_{D_u}^{-4} + C_{D_l}^{-4})^{-0.25} \tag{2.2}$$

where C_{D_u} and C_{D_l} represents lower and upper region value that, both of which were calculated from the following equation

$$C_d = e^E \varphi^\beta \operatorname{Re}^\eta \tag{2.3}$$

where φ is a porosity, E, β and η are constants given different values depending on the tube bundle geometry, as shown in Table 2.1.

Table 2.1: Rahman et al. [6] correlation for constant

	E	β	η
In-line/ Upper	19.91	1.63	-2.1
In-line/ Lower	33.49	3.49	-3.68
Staggered/Upper	20.17	0.31	-2.2
Staggered/Lower	31.97	0.53	-3.72

The author used the 2-D two-fluid model to test the new drag coefficient model which predicted void fraction better than previous studies as shown in Figure 2.3.

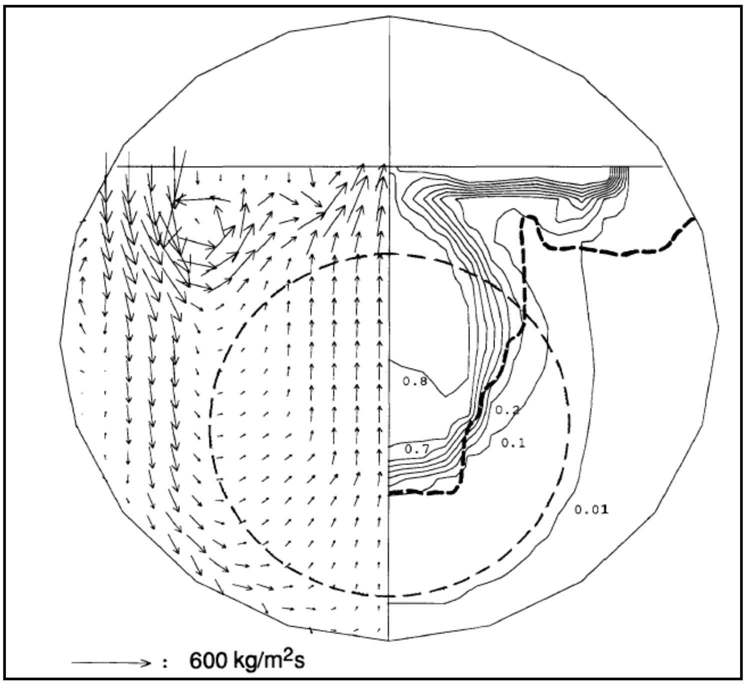

Figure 2.3: Void fraction contour plot and total mass flux vector plot obtained at a constant wall heat flux of 20 kW/m^2 using the interfacial friction correlation [6]

Stosic and Stevanovic [35], Stevanovic et al. [36], Stevanovic et al. [37] and Pezo et al. [8] proposed two correlations for interfacial drag coefficient for vertical flow across horizontal tube bundles; one for bubbly and the other for churn flow.

For bubbly flow,

$$C_D = 0.267 D_p \left(\frac{g \Delta \rho}{\sigma} \right)^{0.5} \left(\frac{1 + 17.67 (1-\alpha)^{9/7}}{18.67 (1-\alpha)^{3/2}} \right)^2 \tag{2.4}$$

For churn flow,

$$C_D = 1.487 D_p \left(\frac{g \Delta \rho}{\sigma} \right)^{0.5} (1-\alpha)^3 (1 - 0.75\alpha)^2 \tag{2.5}$$

where D_p is a bubble diameter, g is gravity acceleration, σ is surface tension, and α is a void fraction.

The bubbly flow model was adapted from Ishii and Zuber [38] by multiplying by 0.4. This reduction was attributed to the tubes in the bundle changing the shape of the bubbles to reduce the drag coefficient by Simovic et al. [7]. These coefficients were derived from the air-water void fraction data of Dowlati et al. [39] so that they were in very good agreement with them, as shown in Figure 2.4.

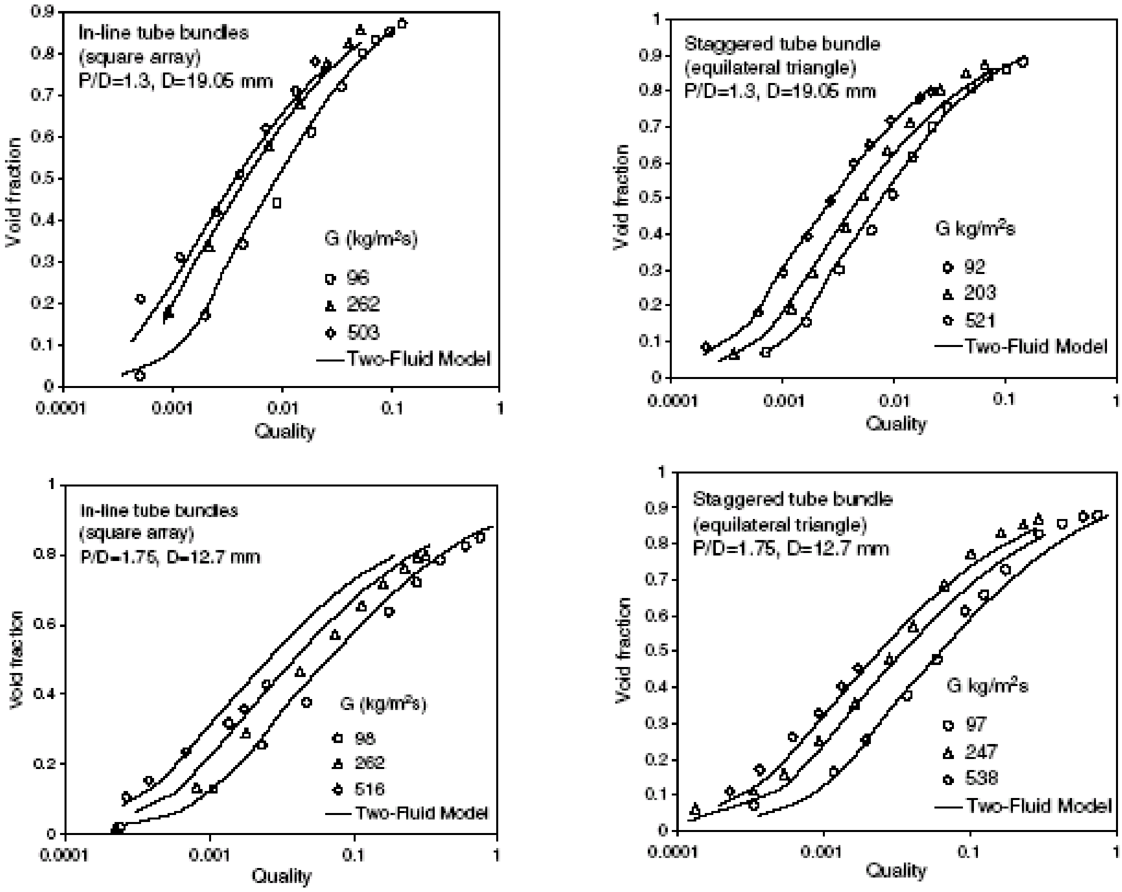

Figure 2.4: Predicted void fraction by Stevanovic et al. [36]

The two correlations were not tested against refrigerant R113 data used in the experimental kettle reboilers. They were used in a 2-D two-fluid model developed to model flow in horizontal steam generators and kettle reboilers. The kettle reboiler model, reported in Pezo et al. [8], was implemented with two different kinds of boundary conditions at the free surface. The first was similar to that used by Edwards and Jensen [34] and Burnside [26], where constant pressure at the free surface was adopted. The second boundary condition suggested assumed that the recirculating liquid had a zero vertical velocity gradient. There was no change of horizontal liquid velocity component in the vertical direction. The vapour velocity was assumed not to change on the liquid side of the swell level.

Bamardouf and McNeil [30] compared the predictions of the two-fluid model with one-dimensional flows and found it wanting because the model assumed a wall force model and a drag coefficient that was not sufficiently accurate. McNeil et al. [32] has shown that the static liquid boundary condition is not always appropriate. McNeil et al. [40] used the one-fluid model to simulate two-dimensional, two-phase flow in a kettle reboiler with a more realistic tube bundle geometry, which was an octagonal shape. Burnside [26] used a rectangular shape. The model uses boundary conditions that allowed for a change in flow pattern from bubbly to intermittent flow at a critical superficial gas velocity which was observed experimentally. The model is based on information for void fraction and tube wall force that has been established by many investigators. The model only use one tube bundle and two fluids, pentane and R113, therefore it is not universal for other geometries or working fluids. However, the model can predict the observed phenomenon in the kettle reboiler.

2.4 Void Fraction

Many correlations have been proposed for void fraction correlations, e.g. Dowlati et al. [2], Schrage et al. [1] and Feenstra et al. [3]. These three correlations were widely used for shell side void fraction predictions. The homogenous equilibrium model (HEM) is also widely used.

The HEM is also known as the friction factor model, it describes a two-phase flow as a single-phase flow, with pseudo properties arrived at by suitable weighting of the properties of the individual phases. The basic assumption upon which the model is based is that the velocities of the gas and liquid phases, which are in thermodynamic equilibrium, are equal. Therefore, the homogenous model assumes a slip ratio of unity or $k = 1$. This is the simplest way of predicting void fraction. Although it is unlikely to predict a complex flow that occurs in a tube bank, the homogenous assumption represents a good starting point for a void fraction investigation.

Schrage et al. [1] obtained void fraction and two-phase friction multiplier data for an adiabatic, vertical, air-water cross-flow at a variety of flow vapour qualities using quick-closing plate valves. The bundle consisted of 27 rows and 5 columns of tubes with a diameter of 7.94 mm. These tubes were arranged in an in-line square array with a pitch-to-diameter ratio of 1.3. The measured values were compared to those estimated from the homogenous model. Although the data showed the same general trend as the homogenous model, the homogenous model considerably over predicted the void fraction data for all quality and mass velocity levels. This poor agreement indicated that the homogenous flow model is not applicable to tube bundles. The data also showed that there is a dependency of void fraction on mass velocity. They noted that the flow behaved homogenously when the quality approached 0 and 1, and at large mass velocity.

Two experiments were conducted by Schrage et al. [1], one using diabatic flow of R-113 (G ranging from 54 to 683 kg/m^{2}s) and one with adiabatic air-water (G ranging from 50 to 675 kg/m^{2}s) as the working fluids.

The void fraction correlation produced by Schrage et al. [1] was;

$$\frac{\alpha}{\alpha_h} = \left[1 + 0.123 Fr^{-0.191} \ln x\right] \tag{2.6}$$

where α is a void fraction, α_h is the homogenous void fraction and Fr is the Froude number (non-dimensional mass velocity), defined as

$$Fr = \frac{G_{\max}}{\rho_l \sqrt{gD}} \tag{2.7}$$

where G_{max} is a mass flux based on maximum area of flow, ρ_l is liquid density, and D is the tube diameter. The void fraction correlation was not tested against other data. A refinement to the model restricted the ratio in Equation (2.6) to be not less than 0.1. The quality should be greater than 0.02.

Xu et al. [11] confirmed the observations of Schrage et al. [1] that void fractions are much lower than those predicted by the homogenous model. They conducted an experimental investigation into two-phase void fraction and pressure drop in horizontal cross-flow over a tube bundle with air-water and air-oil flow using quick-closing valves to measure the volumetric average void fraction. They also noted that a strong mass velocity effect was present for vapour qualities less than 0.1, where void fraction increased and approached the homogenous prediction with increasing mass velocity. At vapour quality greater than 0.1, the data showed that the effect of mass velocity was reduced.

A few articles have been published on the prediction of void fraction in vertical upward flow through tube bundles. Dowlati [9], Dowlati et al. [2] and Dowlati et al. [12] measured void fraction with a gamma-ray densitometer in air-water cross-flow experiments on horizontal tube bundles. Square and triangular patterns of tubes with pitch-to-diameter (P/D) ratios of 1.3 and 1.75 were used. They found that the HEM significantly over-predicted the void fraction when compared to their gamma-ray densitometer measurements. They developed a model to predict void fraction that was based upon the dimensionless superficial gas velocity, which they argued was an appropriate scaling parameter for vertical upward two-phase flows. Their model agreed well with their own void fraction measurements but was not thoroughly tested on other appropriate data.

Dowlati et al. [13] measured void fraction of mixtures of air and water using a gamma ray densitometer with a beam of 24 mm high x 50 mm wide in a horizontal in-line 5x10 tube bundle. This allowed a pitch average void fraction measurements to be taken. The measured void fraction was used to determine the gravitational pressure drop which was subtracted from the measured total pressured drop through the bundle to obtain the two-phase frictional pressure drop. The acceleration pressure drop was neglected in the study. The void fraction, α was calculated from the following equation;

$$\alpha = \frac{\ln(I - I_B) - \ln(I_L - I_B)}{\ln(I_G - I_B) - \ln(I_L - I_B)} \tag{2.8}$$

where I is two-phase reading, I_B is the background reading, I_L is the water-only reading and I_G is the air-only readings.

They observed that for a given quality, void fraction increased as mass flux increased. At high mass flux, the degree of mixing increases due to high turbulence which led to a more homogenous mixture. On the other hand, at low mass flux and low qualities, the air bubbles tended to flow as a jet in the vertical column between the tubes because of the significant effect of buoyancy. Dowlati et al. [13] used the dimensionless gas velocity developed by Wallis [14] to compare their experimental results with Schrage et al. [1] and found disagreement when the mass flux was less than 350 and more than 530 kg/m^{2}s.

The Dowlati et al. [2] void fraction correlation is

$$\alpha = 1 - \frac{1}{(1 + C_1 j_g^* + C_2 j_g^{*2})^{1/2}} \tag{2.9}$$

where j_g^* is a dimensional gas velocity. For $j_g^* < 0.2$, C_1 = 34 and C_2 = 1 and the average deviation with the data is 10%. For $j_g^* \geq 0.2$, they proposed C_2 = 30. The effect on void fraction of pitch-to-diameter ratio (1.3 and 1.75) was negligible.

Dowlati et al. [9] used the drift flux model to predict void fraction for two-phase crossflow in tube bundles with air-water. Data was taken from six test bundles of horizontal tubes with 5 columns and 20 rows. A gamma-ray densitometer was used to measure the void fraction and the following equations was obtained from a linear regression

$$\bar{u}_g = 1.1035[j] + 0.33 = \frac{j_g}{\alpha} \tag{2.10}$$

where the average gas velocity $\bar{u}_g$ is evaluated at the minimum flow area and $j = j_l + j_g$, with j is the mixture superficial velocity, j_l is the liquid superficial velocity and j_g is the gas superficial velocity. This correlation was used to find the average void fraction which, when compared to the experimental results, gave an 11.1 % average deviation.

Feenstra et. al [3] used the slip ratio k as the fundamental unknown parameter on which to predict void fraction in vertical cross-flow on horizontal tube bundles. The functional dependency of the slip ratio on a set of physical properties and parameters were defined before the Buckingham Pi theorem was applied to reduce the number of variables to a small number of dimensionless groups.

The non-dimensional, implicit expression that best fitted their R11 experimental data was

$$k = 1 + 25.7\,(RiCa)^{0.5}\,(P/D)^{-1} \tag{2.11}$$

where *Ca* is the Capillary number, given by

$$Ca = \frac{\mu_l u_g}{\sigma} \tag{2.12}$$

where μ_l is the dynamic viscosity of the liquid phase, u_g is the velocity of the gas phase and *Ri* is the Richardson number, found from

$$Ri = \frac{(\rho_l - \rho_g)^2 (P - D) g}{G_{\max}{}^2} \tag{2.13}$$

in which (*P-D*) is the gap between the tubes and ρ_g and ρ_l are the densities of the gas and vapour phases respectively. The Feenstra et al. [3] model requires an iterative procedure because the capillary number includes the gas phase velocity, u_g, where

$$u_g = \frac{xG_{\max}}{\alpha\,\rho_g} \tag{2.14}$$

and *x* is the quality, G_{max} is the mass flux based on minimum area of flow, and α is the void fraction which in turn is a function of the void fraction, and thus of *k*.

The correlation was compared to other data obtained by Axisa et al. [15], Shrage et al. [1], Dowlati et al. [9] and Noghrehkar [16]. These included many working fluids, including air-water, R113 and steam-water at different *P/D* (1.3-1.75), different geometries and a wide range of mass velocities. All of the data agreed well except that of Schrage et al. [1].

Chan and Shoukri [17] obtained void distributions using gamma ray flux measurements with a working fluid of R113 under pool boiling conditions in a 3x3 and 3x9 tube bundle. In the 3x3 tube bundle, all tubes were heated in the 3x9 bundle only tubes in the center column were heated. The bundles were designed with an outside tube diameter of 19.05

mm and a heated length of 520 mm, arranged in a rectangular array with a vertical pitch of 23.8 mm and a horizontal pitch of 31.75 mm. They boiled refrigerant R113 at two different liquid pool heights at a heat flux of 15 kW/m^2. Visual observations showed that there was a large liquid recirculation flow around the bundle, Figure 2.5. In the smaller bundle, the void fraction increased in the columns and became slightly less near the top of the bundle for a short distance, before rising again near the free surface. Meanwhile, for the bigger bundle, there was no decrease in void fraction at the top of the bundle. At higher heat flux, the void fraction was seen to decline in two areas, one just above the bundle and the other near the free surface.

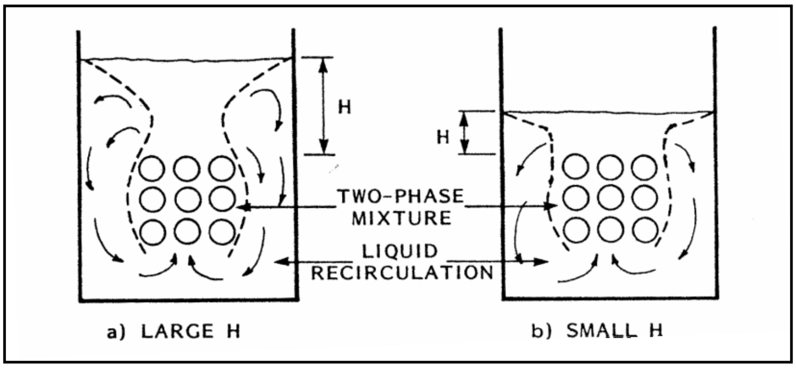

Figure 2.5: Flow pattern at low and high liquid pool level [17]

Kondo and Nakajima [18] made indirect void fraction measurements in vertical cross-flow in a bundle. Their experiments were performed at very low flow rates, (G < 5 kg/m^{2}s). They noted that the void fraction was dependent on the superficial gas velocity and not on the liquid velocity. They also studied the effect of pitch-to-diameter ratios and observed it to have little effect on the void fraction.

Fair and Klip [19], Palen and Yang [20], and Payvar [21] have presented circulation boiling models to predict the thermo-hydraulic performance of shell and tube boilers. The lack of a suitable void fraction model led them to use correlations that were originally developed for internal pipe flows. Other researchers, such as Whalley and Butterworth [22] and Leong and Cornwell [23], used the HEM i.e. k = 1 to predict void fraction, but this model neglects the effect of the velocity ratio altogether. The applicability of these models to shell-side cross-flow in a tube bundle seems difficult to justify.

2.5 Frictional pressure drop

The two-phase pressure gradient, *dp/dz*, contain three components, the acceleration component, $(dp/dz)_A$, the gravitational component, $(dp/dz)_G$, and the frictional component, $(dp/dz)_F$, thus

$$\frac{dp}{dz} = \left(\frac{dp}{dz}\right)_A + \left(\frac{dp}{dz}\right)_G + \left(\frac{dp}{dz}\right)_F \tag{2.15}$$

In tube bundles only the latter two are important. The gravitational pressure gradient is given by

$$\left(\frac{dp}{dz}\right)_G = -\rho_{tp}\, g \tag{2.16}$$

where g is the acceleration due to gravity and ρ_{tp} is the two-phase density, which can be determined from

$$\rho_{tp} = \alpha \rho_g + (1-\alpha)\rho_l \tag{2.17}$$

in which ρ_g and ρ_l are the densities of the gas and vapour phases respectively.

The two-phase frictional pressure drop is often expressed in terms of a two-phase frictional multiplier ϕ_l^2 i.e. the ratio of the two-phase friction pressure drop to the pressure drop that would occur if the flow were to consist of liquid only. For a turbulent flow of a homogenous mixture in a smooth pipe, ϕ_l^2 can be expressed as (see for example, Collier and Thome [41]),

$$\phi_l^2 = \left[1 + x\left(\frac{\rho_l}{\rho_g} - 1\right)\right]\left[1 + x\left(\frac{\mu_l}{\mu_g} - 1\right)\right]^{-1/4} \tag{2.18}$$

According to Owen [42] an appropriate value for the two-phase frictional multiplier may be estimated from the following simple relationship

$$\phi_l^2 = \left[1 + x\left(\frac{\rho_l}{\rho_g} - 1\right)\right] \qquad (2.19)$$

Lockhart and Martinelli [29] and Martinelli and Nelson [43] developed expressions for the two-phase frictional multiplier ϕ_l^2 and the void fraction, α, in terms of independent flow variables. For turbulent, forced convection boiling of water, Martinelli and Nelson [43] presented their calculated values of ϕ_l^2 and void fraction as functions of the flow quality and system pressure. The Martinelli-Nelson correlation provided more accurate pressured drop estimates in the low mass-flux range (i.e. G < 1360 kg/m^{2}s); the homogenous model gave better agreement at higher mass flux (i.e. G > 2000 kg/m^{2}s). The void fraction, α has also been shown to be a function of mass flux, G, with void fraction, α decreasing with a reduction in mass flux, G.

The frictional pressure drop or wall shear stress of the two phases has been widely determined from the separated flow model. Ishihara et al. [4] plotted a large data set for shell-side tube bundle pressure drop and proposed the following equation

$$\phi_l^2 = 1 + \frac{C}{x_{tt}} + \frac{1}{x_{tt}^2} \qquad (2.20)$$

where Martinelli parameter, x_{tt} is obtained from

$$x_{tt} = \left(\frac{1-x}{x}\right)^{2-m}\left(\frac{\rho_g}{\rho_l}\right)\left(\frac{\mu_l}{\mu_g}\right)^m \qquad (2.21)$$

Ishihara et al. [4] found the correlation was optimised when C = 8 and m = 0.1. A large scatter existed when x_{tt} was less than 0.2. The void fraction model used to deduce the two-phase friction pressure drop from the total pressure drop was not given. Schrage et al. [1] and Dowlati et al. [2] also used a Martinelli-type model to represent the two-phase friction multiplier data and confirmed the correlation proposed by Ishihara et al. [4].

Schrage et al. [1] plotted the two phase friction multiplier against the Martinelli parameter with a fixed value of m = 0.2. They observed that the mass velocity strongly affected the values of the two-phase friction multiplier as shown in Figure 2.6. It can be seen that ϕ_l^2 increased as the mass velocity increases for x_{tt} less than 0.9. However, ϕ_l^2 decreased with the increase in mass velocity when x_{tt} was more than 0.9. They noted that the C factor of 8 proposed by Ishihara et al. [4] over predicted their data by 17%.

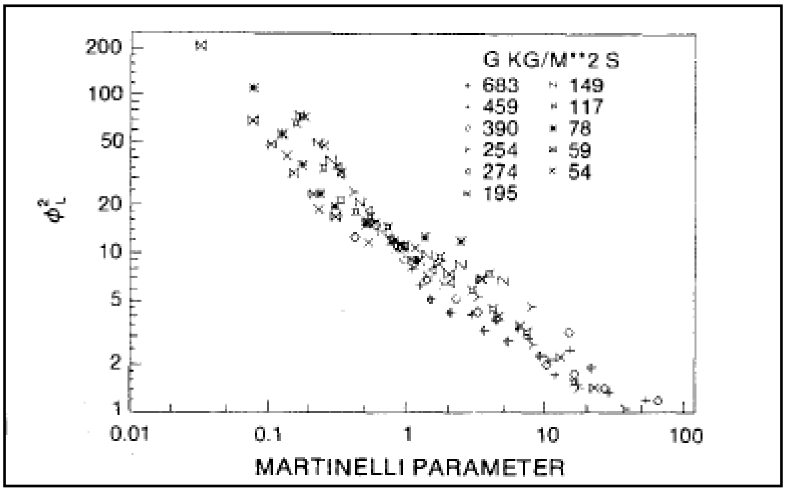

Figure 2.6: Two-phase friction multiplier for liquid-only data [1])

Xu et al. [5] plotted the two-phase friction multiplier data against the Martinelli parameter as shown in Figure 2.7. It was observed that a strong mass velocity effect when $x_{tt} > 0.2$, and the value of ϕ_l^2 increases with decreasing mass flux at a given value of x_{tt}, but the mass flux effect is not obvious when $x_{tt} < 0.2$, which is consistent with Dowlati et al. [2] results.

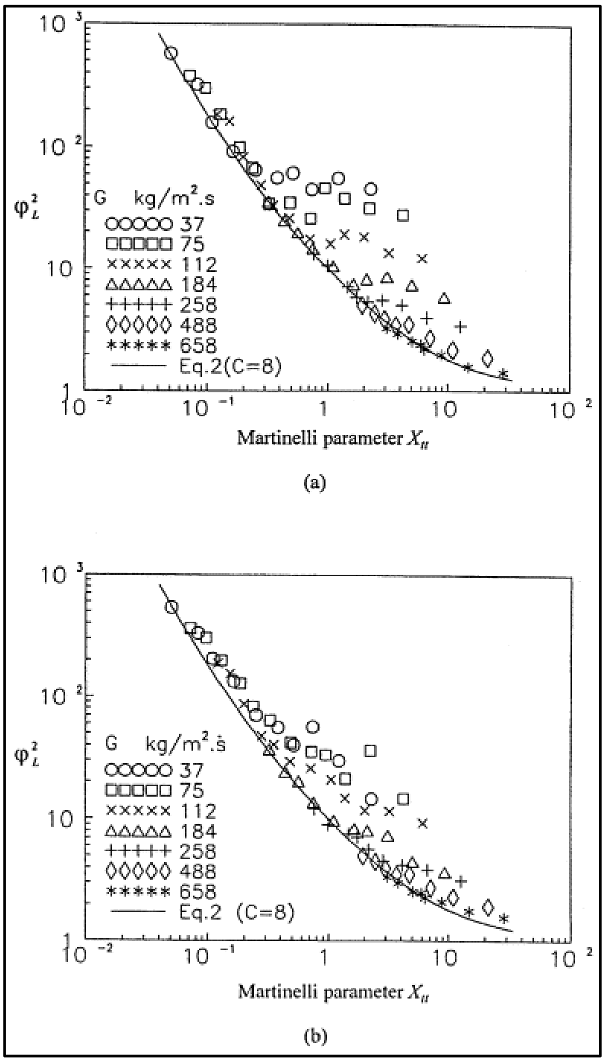

Figure 2.7: Liquid-only two-phase friction multiplier data and Martinelli parameter: (a) vertical down-flow; and (b) vertical up-flow [5]

The use of C = 8 as suggested by Ishihara et al [4] did not result in good representation of the data, as shown by the value lying above C = 8 curve in Figure 2.7. Therefore, Xu et al. [5] suggested that the constant C deduced on the dimensionless gas velocity, u_g, the Martineli parameter, x_{tt} and the quality ratio, x / (1 - x). The new correlations for the constant C for up-flow in in-line bundles was given as

$$C = 24.45 u_g^{-0.654} \left(\frac{x}{1-x} \right)^{0.336} \tag{2.22}$$

and the constant C for down-flow in in-line bundles was given as

$$C = 22.5 u_g^{-0.723} \left(\frac{x}{1-x} \right)^{0.340} \tag{2.23}$$

where the dimensionless gas velocity, u_g is expressed as

$$u_g = \frac{G_{\max} x}{\sqrt{\rho_g g D(\rho_l - \rho_g)}} \tag{2.24}$$

The two-phase friction multiplier data could be correlated well in terms of Martinelli parameter when using the proposed *C* factor. The equations are able to correlate the corresponding sets of data with an average absolute deviation of 12.5% in up-flow, and 14.8%. Figure 2.8 shows the ratio of the experimental two-phase friction multiplier to the predicted two-phase friction multiplier.

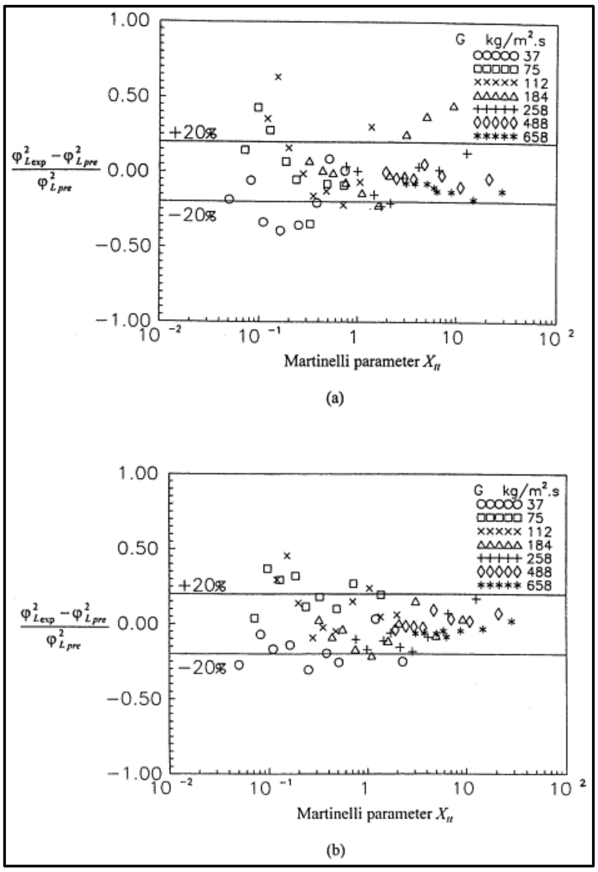

Figure 2.8: Predicted and experimental liquid-only two phase friction multiplier data; (a) vertical down-flow; and (b) vertical up-flow [5]

2.6 Flow pattern

Two-phase flow is characterized by the existence of an interface between the phases and discontinuities in properties associated with them. The internal structures of two-phase flows are identified by two-phase flow regimes. The basic structure of flow can be characterized by two fundamental geometrical parameters. These are the void fraction and the interfacial area concentration. The void fraction expresses the phase distribution whereas the interfacial area describes the available area for the interfacial transfer of mass, momentum and energy. Therefore, an accurate knowledge of these parameters is necessary for any two-phase flow analysis.

Two-phase flow has different flow regimes that depend upon the concentration of gas, fluid properties and the mass flow rate of the phases. The two-phase flow pattern characteristics result in different frictional pressure drop and heat transfer modes. Many studies have been carried out, experimentally and numerically, to investigate the flow pattern, i.e. flow maps, in tube bundles.

Kondo and Nakajima [18] observed the flow regime of vertical adiabatic two-phase flow of air-water in a staggered horizontal tube bundle by visual observation and a photographic technique. The bundles had different pitch to diameter ratios of 1.4, 1.28 and 1.08. The range of the experimental superficial velocities of water and air were 0.00032- 0.0032 and 0.015-0.5 m/s respectively. They identified four flow regimes, bubbly, slug, froth and spray. The flow pattern was observed to change quickly from bubbly to froth for a pitch to diameter ratio of 1.08. The effect of water flow rate on the flow regime was negligible.

Cornwell et al. [33] studied the flow pattern of refrigerant R113 in a 241-tube kettle reboiler using a high speed video camera. They pointed out that the flow pattern in a tube bundle is different from that inside a tube. In tube bundles, the complex flow of fluid between tubes makes slug and annular flow difficult to form so that bubbly and the spray flows are more likely at various heat fluxes. The local inter-tube flow pattern, Figure 2.9, showed that the lower tubes did not produce boiling as it was subcooled so that the fluid behaved as single phase, Figure 2.9a. However the upper region contained a high voidage, high velocity flow concentrated in the vertical channel between the tubes while liquid dominated in the horizontal channels between the upper and lower tubes, Figure 2.9b.

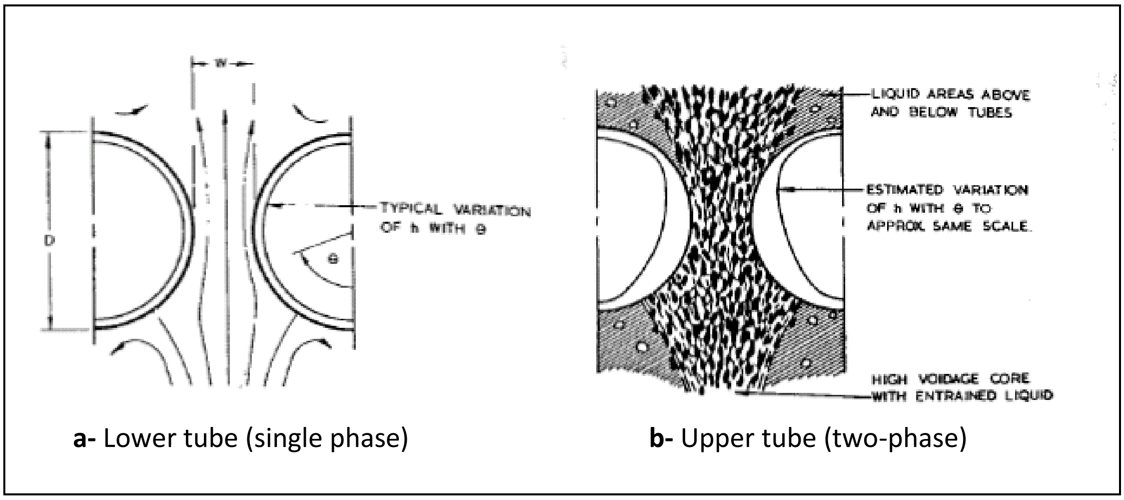

Figure 2.9: Sketch of flow pattern at (a) lower tube and (b) upper tube [33]

Many researchers have constructed flow regime maps to improve the design of shell and tube heat exchangers. Most of these maps were based on visual observations and they were constructed using the maximum superficial gas velocity on the *x*-axis and the maximum superficial liquid velocity on the *y*-axis. Some were constructed using more objective methods, e.g. void fraction transients. Tong et al. [44] presented a flow patterns for upward two-phase flow in a vertical tube as shown in Figure 2.10.

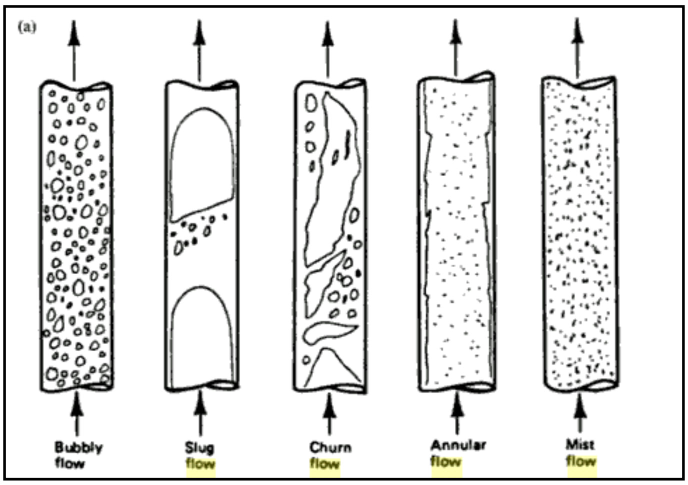

Figure 2.10: Flow pattern in vertical upward flow in a tube by Tong et al. [44]

Grant and Chisholm [45] used visual observations to study the flow regimes of vertical air-water flow across horizontal tube bundles. The bundle, shown in Figure 2.11, is a segmental baffled heat exchanger consisting of 39 tubes, 19 mm in outside diameter, arranged in an in-line configuration with a pitch to diameter ratio of 1.25. Upward flow could be described as either bubbly, intermittent, or spray flow, whereas downward flow could be described as bubbly, stratified and stratified-spray or spray flow. They presented the flow map as shown in Figure 2.12.

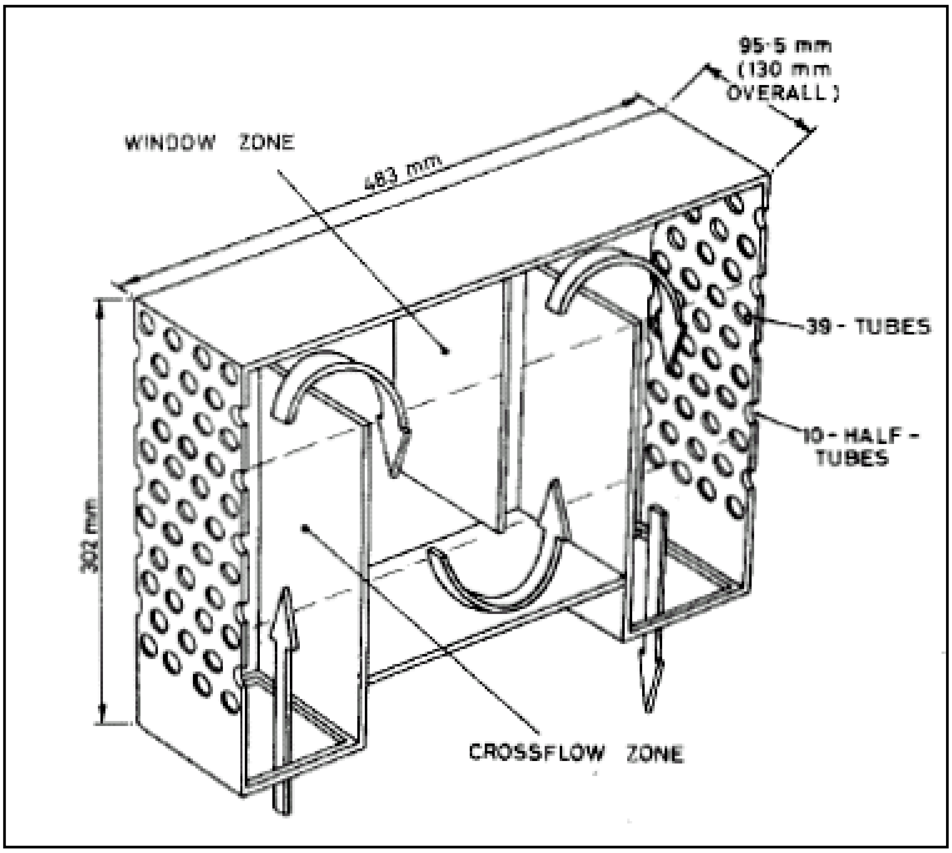

Figure 2.11: Test section by Grant and Chisholm [45]

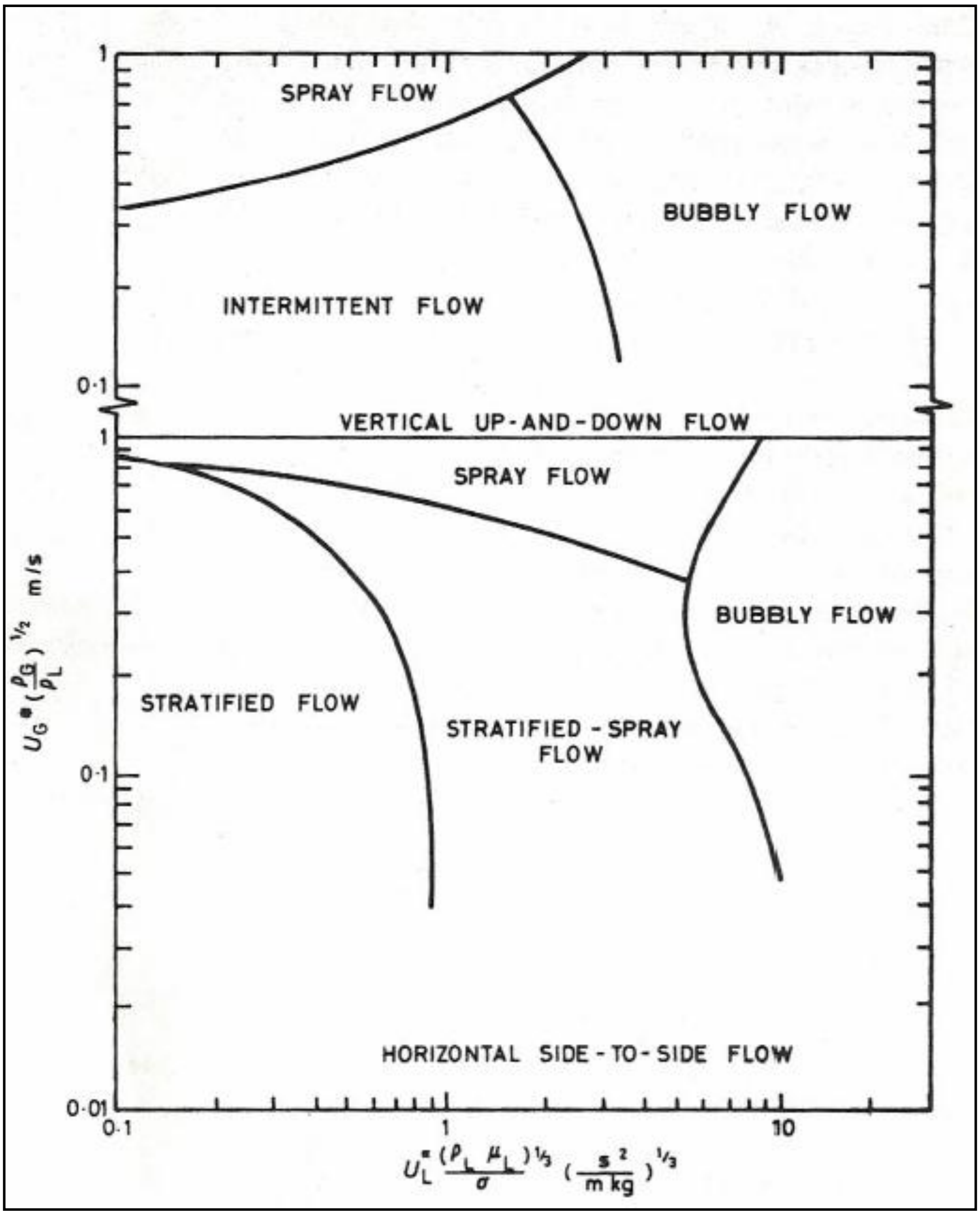

Figure 2.12: Shell side flow pattern map [45]

Ulbrich and Mewes [46] identified the flow regimes by visual observation and a photographic technique and found that the regimes were bubbly, intermittent, annular intermittent and annular dispersed flow. The flows where observed in vertical air-water flows across a horizontal tube bundle, consisting of 10 rows and 5 columns. The tubes were 20 mm in outside diameter and 200 mm in length and arranged in a square in-line configuration with a pitch to diameter ratio of 1.5. The superficial gas velocity was the primary criterion for changing flow pattern. Time traces of pressure drop were used as an objective method to aid the analysis. The gas superficial velocities ranged from 0.047 to

9.3 m/s and the liquid values from 0.001 to 0.65 m/s. They proposed the flow pattern map in Figure 2.13, which shows the bubble, intermittent and dispersed flow.

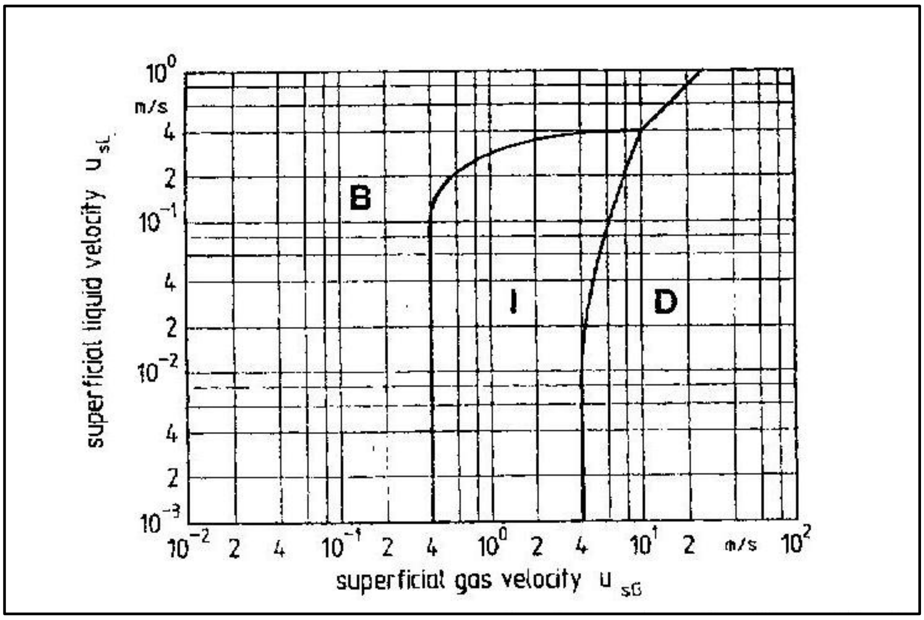

Figure 2.13: Generalized flow pattern map (B - bubble, I – intermittent, D – dispersed flows [46]

Xu et al. [5] investigated the flow regimes of vertical up and down flow across a horizontal tube bundle consisting of 20 rows of tubes 9.79 mm in outside diameter on a pitch to diameter ratio of 1.28. Visual observation was used to identify the flow regimes. Figure 2.14 shows patterns of flows for upward flows; churn, intermittent, annular and bubbly flow. Figure 2.15 shows the downward flow; falling, intermittent, annular and bubbly flows.

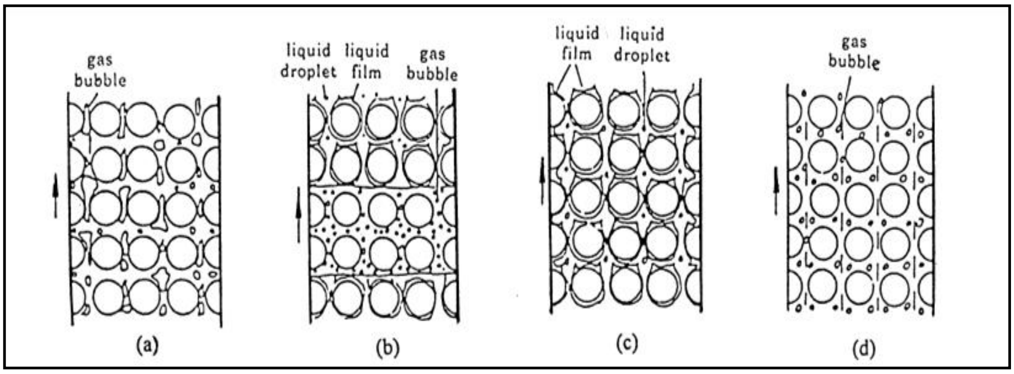

Figure 2.14: Flow pattern in vertical up-flow across horizontal tube bundle (a) churn flow (b) intermittent flow (c) annular flow and (d) bubbly flow [5]

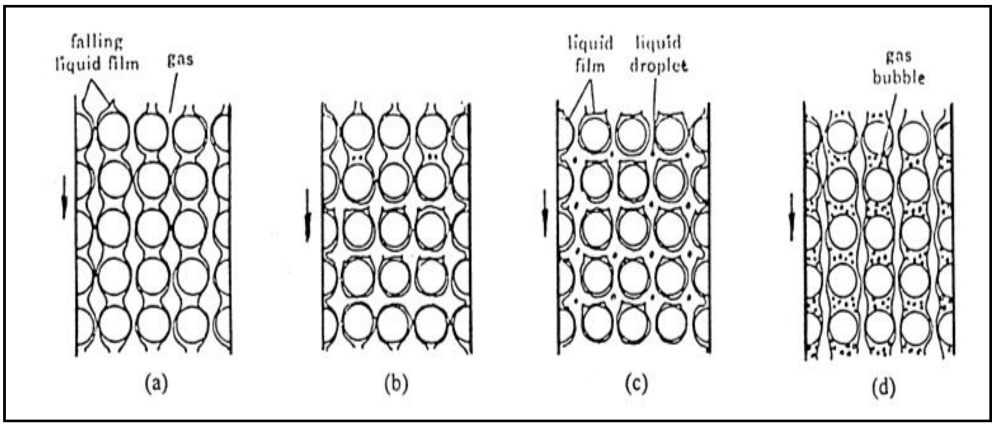

Figure 2.15: Flow pattern in vertical down-flow across horizontal tube bundle (a) falling flow(b) intermittent flow (c) annular flow (c) and (d) bubbly flow [5]

Noghrehkar et al. [47] identified flow regimes similar to those occurring inside circular tubes, including bubbly, intermittent and annular flows, for both in-line and staggered tube configurations consisting of 24 and 26 rows respectively. They reported that visual observations from the outside did not reflect the actual flow pattern that existing inside. They used a resistivity probe to identify two-phase flow regimes using air-water. This void probe was also used to measure the void fraction. The same pitch to diameter ratio was 1.47. Figure 2.16 shows the flow regime map for their bundles.

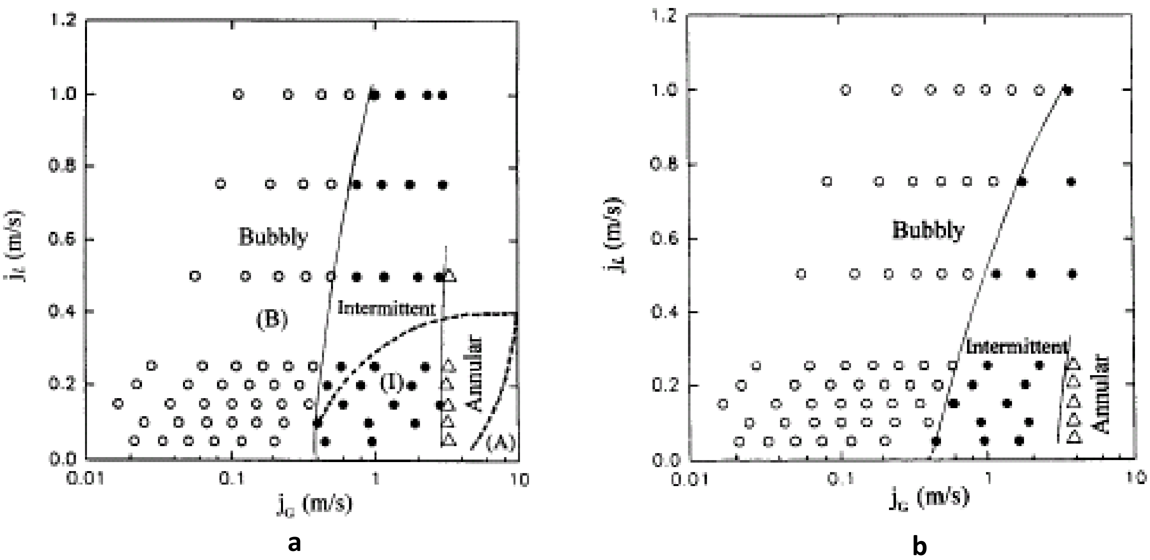

Figure 2.16: (a) Flow regime map for in-line bundle is represented by solid line whereas dotted line show the result of Ulbrich and Mewes [47] (b) Flow regime map for staggered bundle [47]

For the in-line bundle shown in Figure 2.16a, the flow pattern changed depending on the gas velocity. The flow pattern changed from bubbly to intermittent flow at a superficial gas velocity between 0.4 and 1.0 m/s. At superficial air velocity of 3.9 m/s, the flow pattern changed from intermittent to annular flow. For the staggered bundle, Figure 2.16b, the bubbly flow regime occurred below gas superficial velocities between 0.4 and 2.0 m/s while the intermittent regime occurred between 2 and 3.9 m/s. These results suggest that the liquid superficial velocity has little influence on the flow pattern, relative to the vapour velocity.

Ribatski and Thome [48] grouped the flow pattern maps based on above discussion. They found that the transitions between the flow pattern maps based on visual observations, including Grant and Chisholm [45] and Xu et al. [5], were significantly different, as shown in Figure 2.17a, even though the experimental conditions were quite similar. The flow pattern maps based on objective methods, including Ulbrich and Mewes [46] and Noghrehkar et al. [47], were in better agreement as shown in Figure 2.17b .

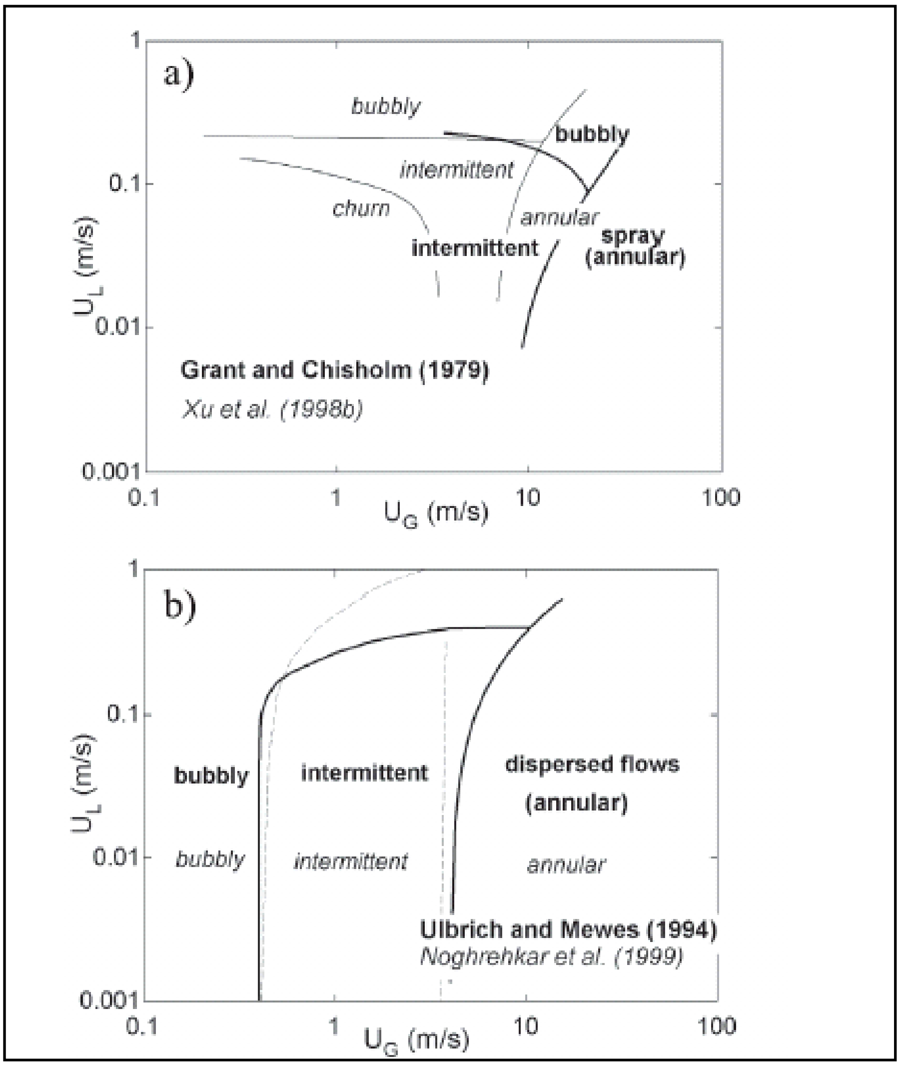

Figure 2.17: Comparison of flow pattern maps based on a) visual observation method b) objective methods

Aprin et al. [49] studied vertical two-phase flow patterns for three hydrocarbons (n-pentane, propane and iso-butane) under saturated conditions. Three flow regimes were identified in the bundle, bubbly, intermittent and annular-dispersed, as shown in Figure 2.18. An optical probe system was used to measure the local void fraction at a central position in the tube bundle and a Probability Density Functions (PDF) was applied to the void probe signal to characterise the flow regimes. The tube bundle consisted of 41 tubes, 19.05 mm in outside diameter arranged in a staggered layout with a pitch-to-diameter ratio of 1.33.

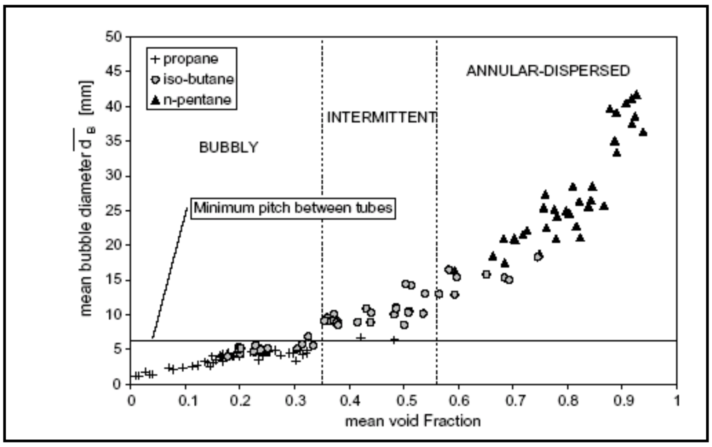

Figure 2.18: Flow pattern based on void fraction [49]

Bubbly flow occurred at void fractions less than 0.35 when the mean bubble diameter was less than the space between the tubes. The intermittent flow regime occurred at a void fraction of between 0.35 and 0.56 when the bubble size was comparable to the minimum space between the tubes. The annular flow regime occurred at void fractions greater than 0.56.

McNeil et al. [50] reports that the pressure drop and void fraction data in in-line heat exchanger are shown to be flow pattern dependent. The flow pattern boundaries are deduced from published flow maps by Noghrehkar et al. [47] and Ulbrich and Mewes [46] as shown in Figure 2.19. The variation of superficial liquid velocity with superficial gas velocity, both based on the minimum gap between the tubes for all of the void fraction and pressure distribution data obtained. The void fraction data sets are shown to span the full range of flow patterns. The pressure distribution data is shown to have one point well within the intermittent flow region of the Noghrehkar et al. [47] flow map with the other three in their annular flow region, while all four points hug the bubbly–intermittent boundary of the Ulbrich and Mewes [46] map. The pressure drop data are analyzed through a one dimensional model that incorporates separation and re-attachment phenomena. The flow is said to be in two regions, the separated flow region and the attached flow region, as shown in Figure 2.20. The separated flow region contains the flow between the separation and re-attachment points. The attached flow region contains the flow between the re-attachment and the separation points. The mechanistic model was deduced for each region. The frictional pressure drop is shown to depend on a liquid layer located on the upper portion of the tubes at low gas velocity and on acceleration effects at high gas velocity.

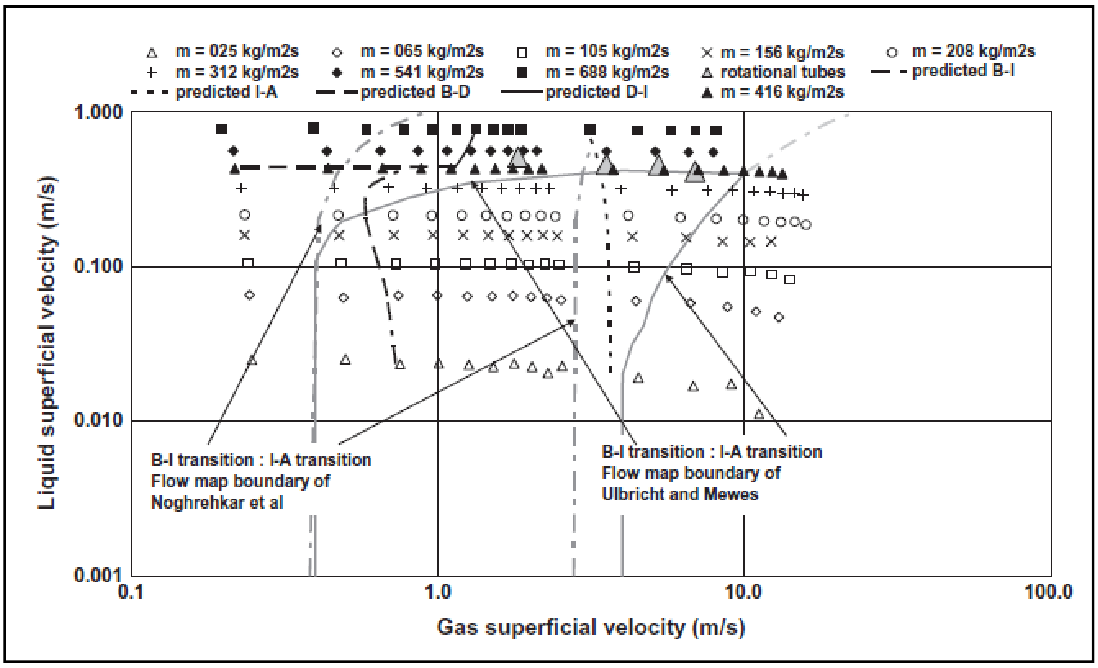

Figure 2.19: Tube bundle flow pattern maps [50]

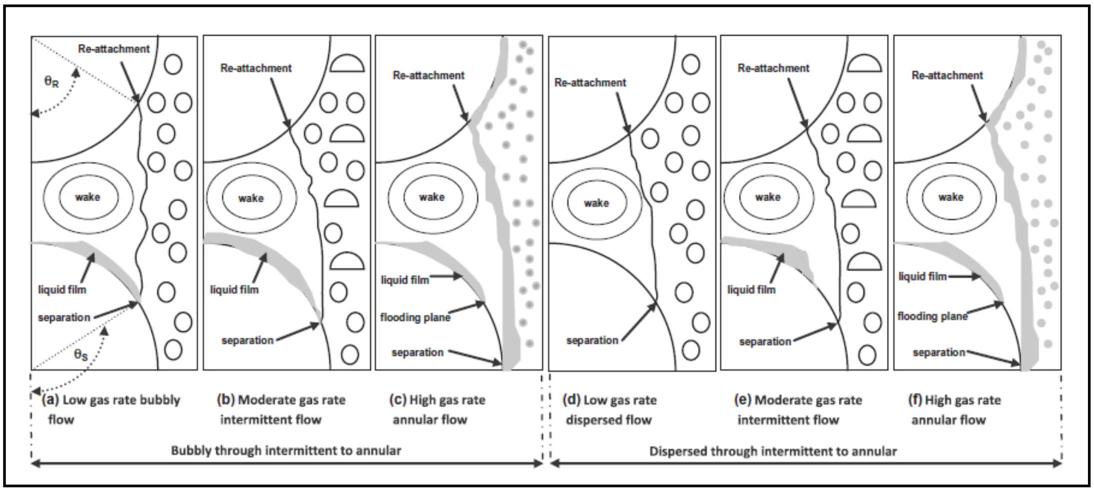

Figure 2.20:Two-phase model flow paths [50]

2.7 Summary of the Literature

Overall, flow regime, pressure drop and void fractions in a kettle reboiler have been widely investigated for the past 50 years. There are a few void fraction correlations, void fraction measurements methods and some results that have been published, thus giving the kettle reboiler design much improvement.

There are many measured pitch void fractions and bundle average void fractions reported in the literatures and that have been used to produce bundle average or pitch average values of frictional pressure drop that were used in the formulation of various correlations. However, none have reported local values in a bundle. Thus, the local values in these gaps will be reported in this research. The correlations were formulated without any reference to the flow phenomena that occurred in the passages between the tubes. Two-phase multiplier correlations are widely used in shell-side tube bundle calculations. Thus, it is implicitly assumed that they act similarly to pipe frictional pressure drops. However, the pressure drop on the shell-side is different. Pipe flow pressure drops are due to wall friction whereas shell-side pressure drops are due to flow separation and reattachment phenomena. Therefore, the void fractions in the maximum gap and the minimum gap between the tubes will be reported because this is where the flow maximum difference is most likely.

Existing void fraction and frictional pressure gradient measurements have only been made for tube diameter less than 20mm. Thus, the measurement of void fraction and frictional pressure drop in larger diameter bundle is warranted, so that existing correlations for void fraction and frictional pressure gradient can be tested for capability on predicting these parameters in larger tube bundles. However, any new correlations can be used for predicting void fraction and pressure drop for tube bundle less than and greater than 20 mm.

Although there has been some interest in pressure drop and void fraction distribution in kettle reboilers, there is a lack of studies on the drag coefficient required for the two-dimensional models. This is a driving force for further study of flow in kettle reboiler and give an insight to more understanding of the flow modelling in a heat exchanger.

CHAPTER 3 - AIR-WATER RIG

This chapter describes the design and instrumentation of 38 mm and 19 mm diameter in-line bundles and a 19 mm diameter staggered bundle used to study the two-phase flow in a tube bundle. The design, fabrication and installation of a gamma-ray densitometer is also discussed here.

Many researchers have used a tube bundle to simulate two-phase flow in a kettle reboiler because it is simple and cheap. However, the difference in density ratio between air-water mixtures and vapour-liquid mixtures typically used in kettle reboilers, causes a difference in gravity and friction pressure drop components when the same operating conditions and the same size of tube bundle is used. Therefore, the bundle size and the operating conditions were modified to produce comparable data. For this, a dimensionless model was developed by Bamardouf [51]. The model was used to identify the required dimensions of the air-water in-bundle rig that gives similar pressure drop components for n-pentane as obtained from the conventional one dimensional (1-D) model that will be described in the following section.

3.1 The one dimensional model description

A conventional 1-D model was used to simulate conditions in a standard kettle reboiler using a n-pentane. The kettle reboiler had 17 rows of tubes in the middle columns with an outside diameter of 19.0 mm and a pitch to diameter ratio of 1.34. The 1-D model assumed that the static pressure head of the liquid at the sides of the bundle, ΔP_l , balances with the two-phase pressure drop due to friction, ΔP_F and gravity , ΔP_G in the bundle so that

$$\Delta P_l = \Delta P_F + \Delta P_G \tag{3.1}$$

The acceleration pressure drop was neglected because it had very low contribution to the overall pressure drop, i.e. < 5% at 50 kW/m². The sum of these two pressure drop components was balanced with the static head by adjusting the mass flux through the bundle. This was calculated based on the horizontal pitch.

The gravitational pressure drop was determined from

$$\Delta P_G = -\rho g P_v \tag{3. 2}$$

where g was the acceleration due to gravity, P_v was the vertical pitch and ρ was the density of the two-phase mixture is given by

$$\rho_{tp} = \alpha\rho_g + (1-\alpha)\rho_l \tag{3. 3}$$

in which ρ_g was the gas density, ρ_l was the liquid density and α was the void fraction obtained from the Schrage et al. [1] correlation, i.e.

$$\alpha = \alpha_h (1 + 0.123 Fr^{-0.191} \ln x) \tag{3. 4}$$

where Fr was the Froude number, obtained from

$$Fr = \frac{G_{\max}}{\rho_l \sqrt{gD}} \tag{3. 5}$$

$G_{\max}$ was mass flux based on the minimum gap between the tubes and D was the tube diameter.

The frictional pressure drop across a cell was calculated from

$$\Delta P_F = \frac{C_L G_{\min}^2 (1-x)^2}{2D\rho_l} \phi_l^2 P \tag{3. 6}$$

where C_L was the single-phase loss coefficient calculated from ESDU [52] and ϕ_l^2 was the two-phase friction multiplier obtained from

$$\phi_l^2 = 1 + \frac{C}{x_{tt}} + \frac{1}{x_{tt}^2} \tag{3. 7}$$

in which C = 8, was recommended by Ishihara et al. [4] and x_{tt} was the Lockhart–Martinelli parameter [29], given by

$$x_{tt}^{\ 2} = \left(\frac{1-x}{x}\right)^{2-m}\left(\frac{\rho_g}{\rho_l}\right)\left(\frac{\mu_l}{\mu_g}\right)^m \tag{3. 8}$$

where μ_l and μ_g were the viscosities of the vapour and liquid phases respectively. The value of m was set equal to 0.2 as suggested by Ishihara et al. [4], Schrage et al. [1] and Dowlati et al. [2].

Bamardouf [51] has shown that the mass flux range of 25 kg/m^{2}s to 688 kg/m^{2}s covers the acceptable normal range of running conditions of a kettle reboiler. Based on this finding, the mass flux range of 25 kg/m^{2}s to 688 kg/m^{2}s was chosen for this study. Moreover, this range covers most of the mass fluxes reported in the literature.

3.2 Rig description

3.2.1 Flow loop

The in-bundle section and the corresponding flow loop used in this study are illustrated in Figure 3.1. Water, driven by a positive displacement pump, entered the test section after passing through one of four differently sized flow nozzles, arranged in parallel, and used to measure the water flow rate. These nozzles had a different throat diameter, allowing a wide range of flows to be measured. The accuracy of water flow measurements was ± 1.0%. A bypass loop allowed the excess flow from the pump to be returned to the supply tanks.

Compressed air flowed from the Ingersoll-rand SSR M110 compressor to one of two magnetically coupled rotameters. A gate valve downstream of each rotameter allowed the air flow rate to be set to the required value. The two parallel flow meters had ranges of 0-

0.0039 and 0-0.034 kg/s. The flow meters were calibrated for the line pressure and were accurate to ±1.6% or reading.

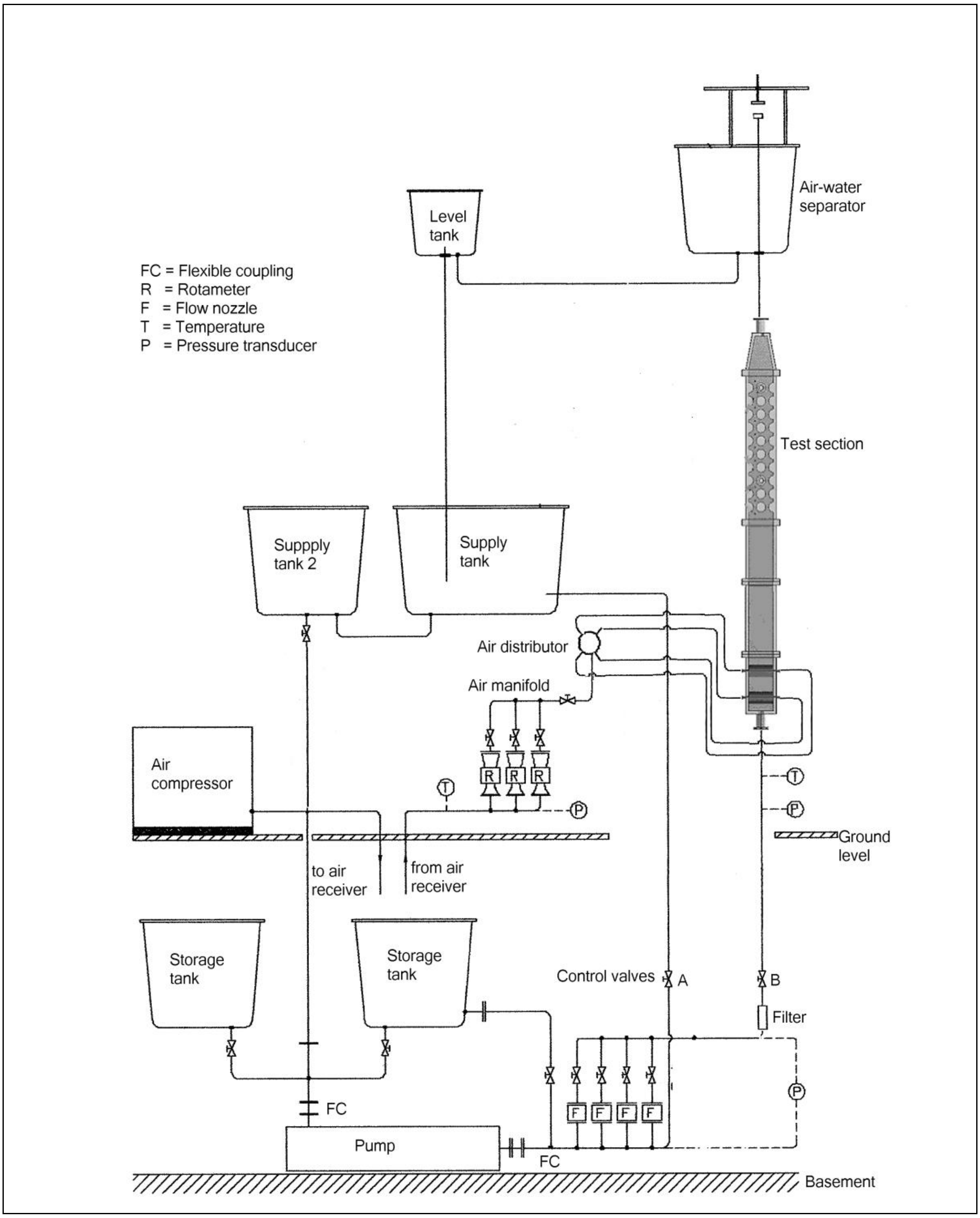

Figure 3.1: Air-water test

The test section consisted of five sections, a bubble generator, a convergent section, a settling length, a tube bundle and a second convergent section, as shown in Figure 3.2. These parts were fabricated from Perspex sheet that was 12 mm thick and Perspex rod that were 38 mm and 19 mm in diameter. Two bundles had an in-line arrangement, one contained tubes 38 mm in diameter and the other tubes 19 mm in diameter. The other bundle had a staggered arrangement and used tubes 19 mm in diameter. The sheets and rods were joins together by bolts and grooves. The clear Perspex provided a transparent view of the flow.

The air and water flows were mixed in the convergent section and settling length before passing through the test section and into the air-water separator.

Compressed air entered the test section through the bubble generator. This produced a reasonably well mixed two-phase flow that passed through the first convergent section and the 244 mm settling length before entering the tube bundle. A further convergent section allowed the test section to be connected to the air-water separator where the air was discharged to the atmosphere and the water was returned to the supply tanks.

The bubble generator, first convergent section, settling length and second convergent section were fixed for all tests. Each tube bundle was used for each tests to measure pressure drop and void fraction. The schematic design of these test sections and bundles are shown in Figure 3.3 – 3.9. The drawing of the test sections were illustrated using SolidWorks Version 2007.

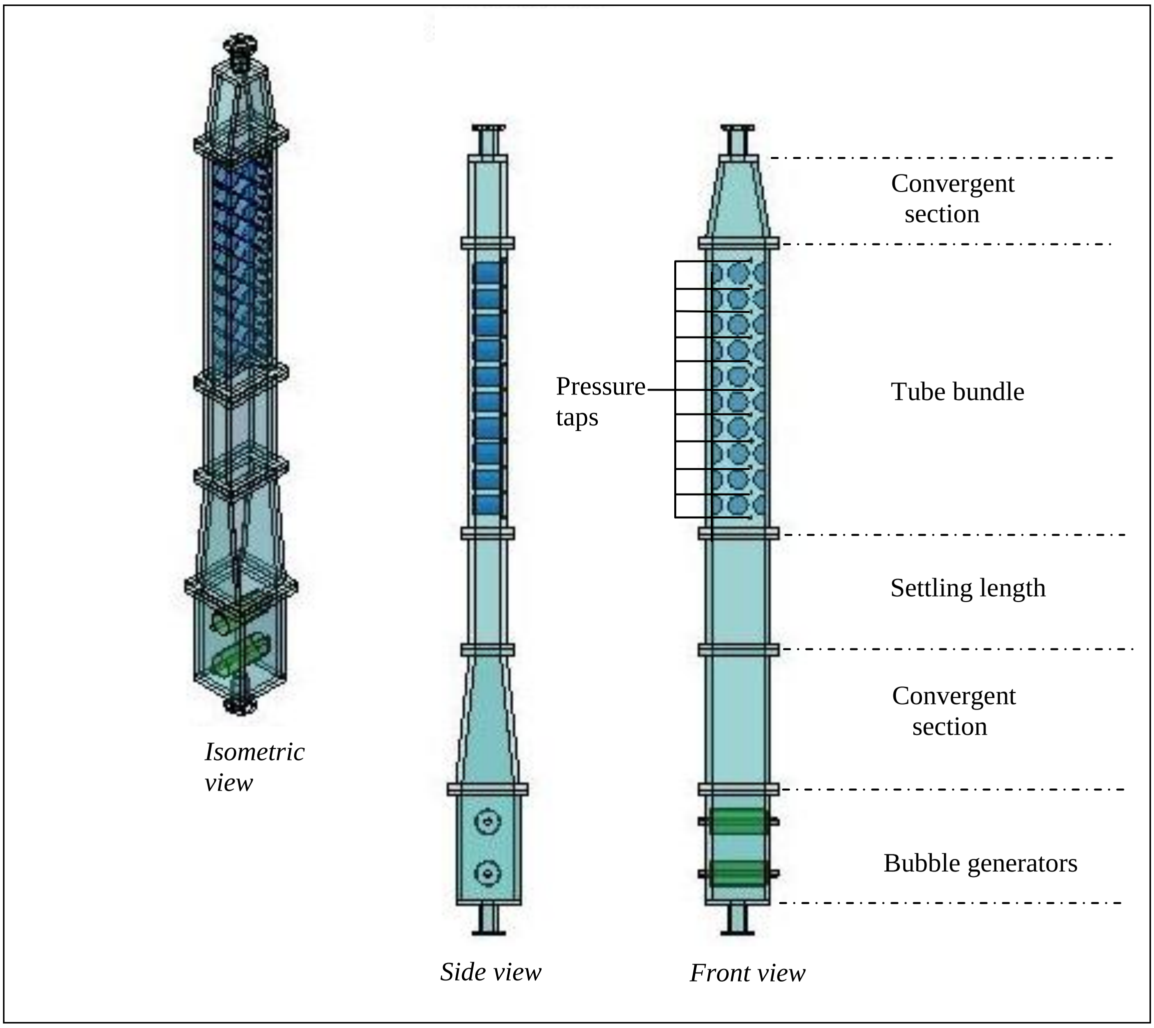

Figure 3.2: Test section of 38 mm in-line tube bundle

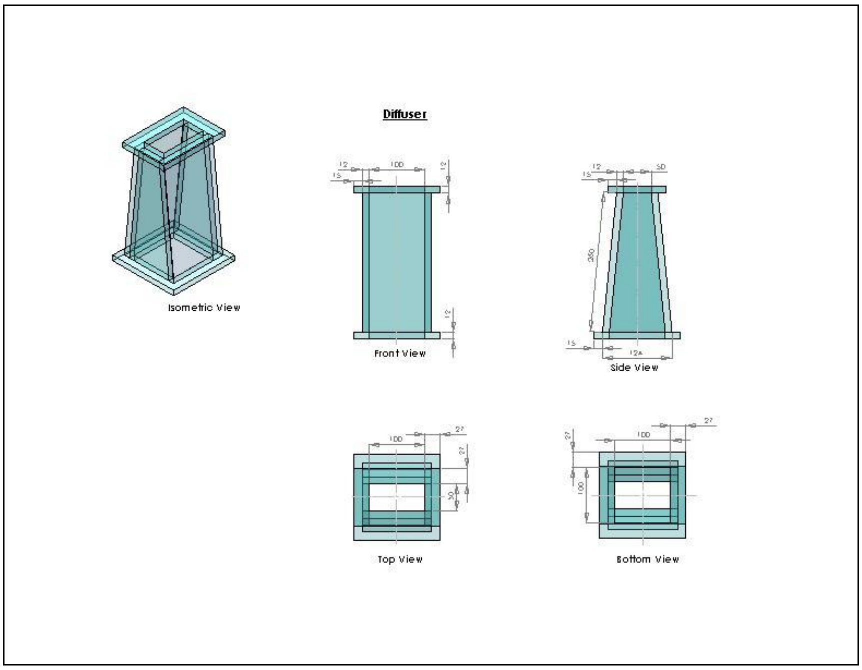

Figure 3.3: Convergent or diffuser section

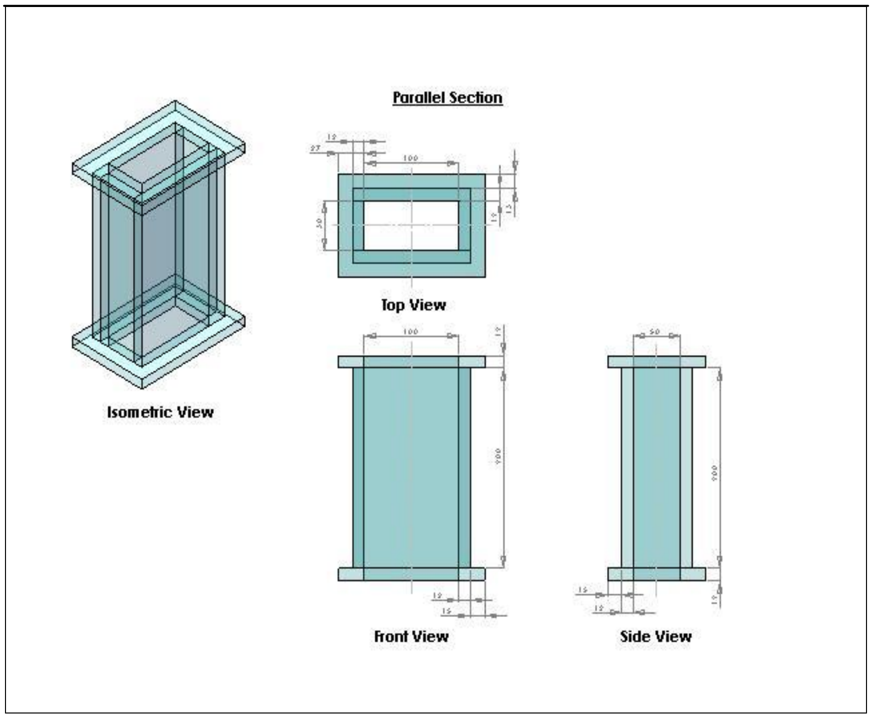

Figure 3.4: Parallel section or settling length

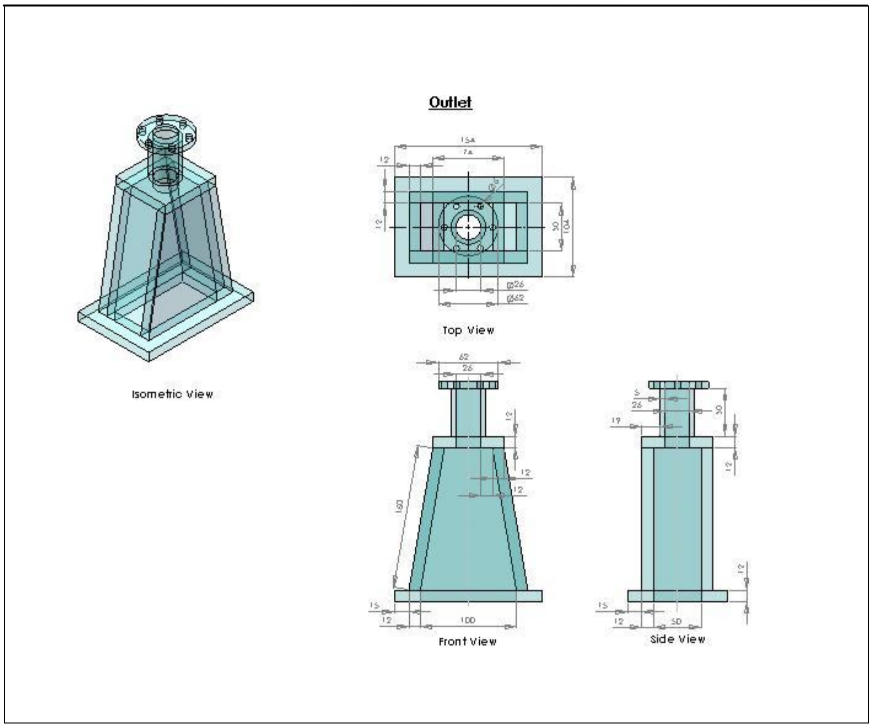

Figure 3.5: Outlet or convergent section

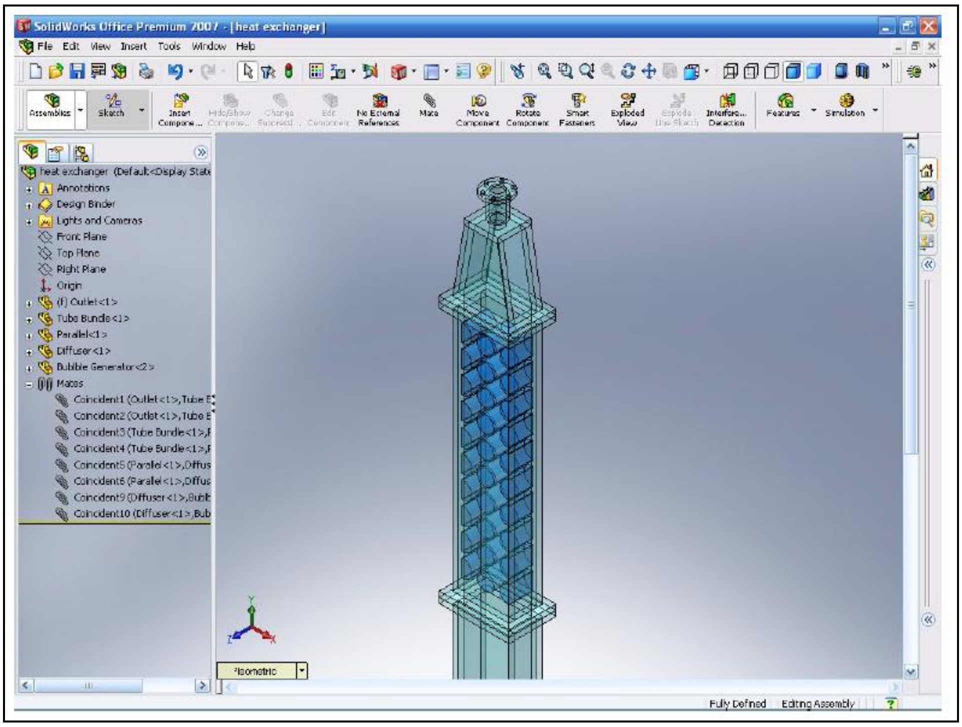

Figure 3.6: Assembly drawing of test section 38 mm in diameter in-line tube bundle, tube bundle and convergent section

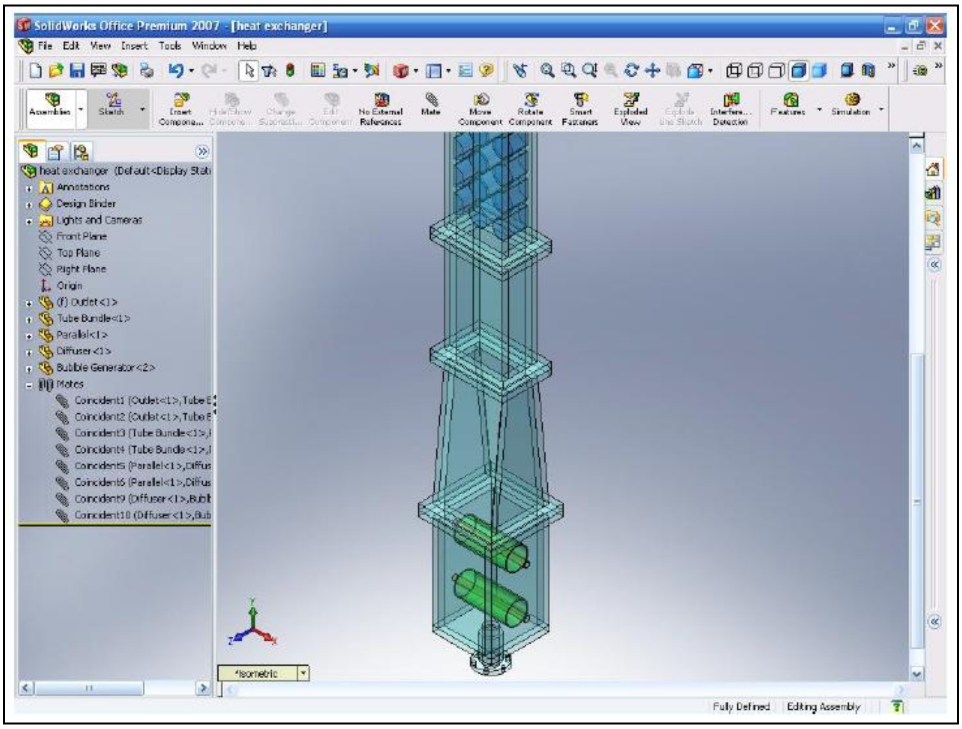

Figure 3.7: Assembly drawing of test section 38 mm in diameter in-line bundle, bubble generator, convergent section and settling length

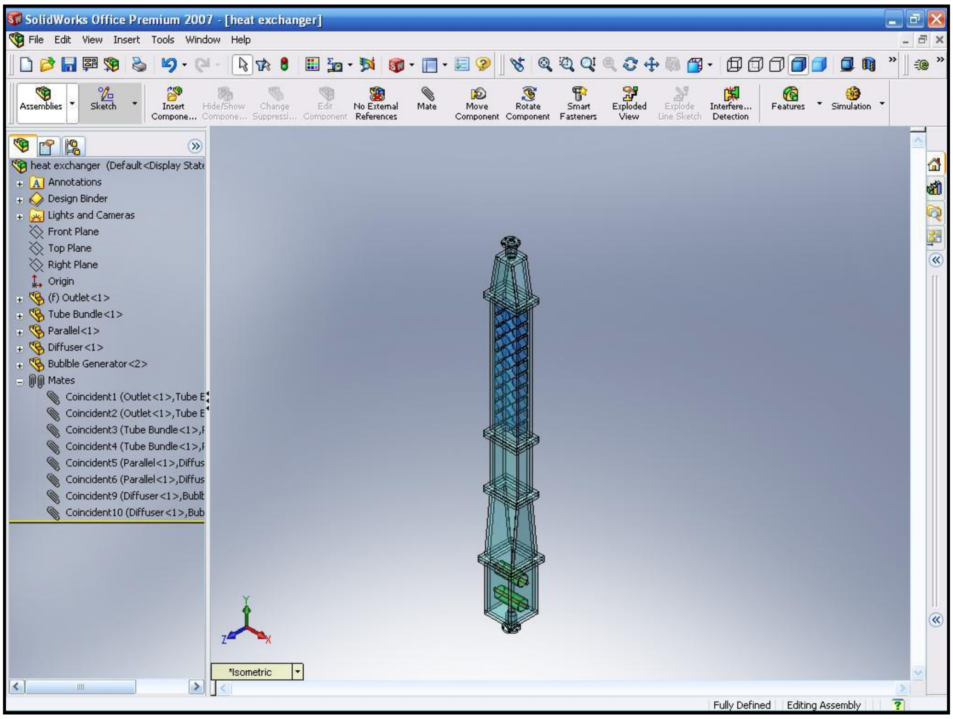

Figure 3.8: Assembly drawing of a full test section

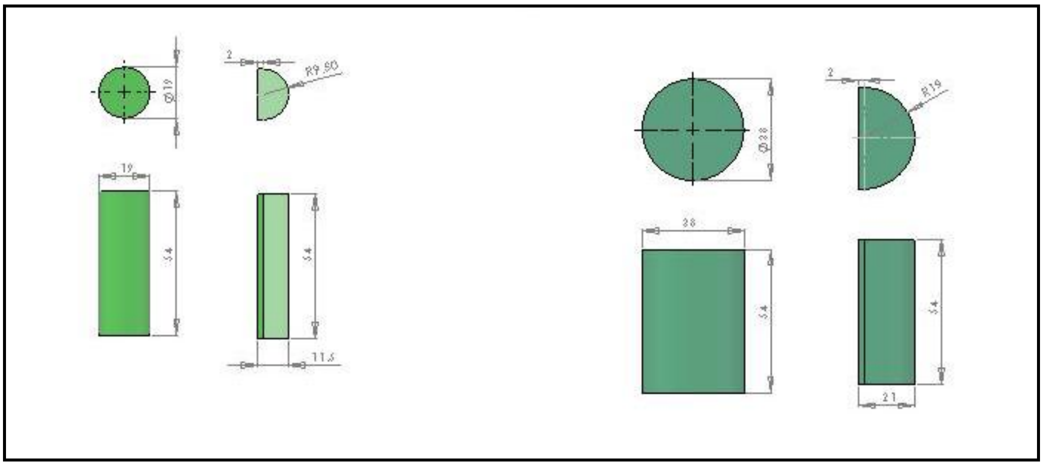

Figure 3.9: Circular and semi-circular tubes for both 38 mm and 19 mm in diameter

3.2.2 Bubble generator

The bubble generator, as with other parts of the test section, was fabricated from Perspex sheets, 12 mm thick and joined together by bolts to provide a transparent view of the flow. Figure 3.10 shows the bubble generator in operation. It consisted of two pieces of porous tube (SIKA-B) manufactured by GKN Sinter Metals. They were 110 mm long and 50.0 mm in outside diameter and they had an effective pore size of 206 microns. They were placed in a rectangular Perspex box 224 mm in height $\times$ 100 mm in depth $\times$100 mm in width as shown in Figure 3.11. The side walls of the bubble generator box contained circular grooves 5.0 mm deep so that each side of the two porous tubes could be located. Rubber seals were placed in the grooves between the wall and the tubes to prevent any leaks that might occur from the tube ends. The pitch between the centers of these tubes was 100 mm.

Figure 3.10: Bubble generator in operation

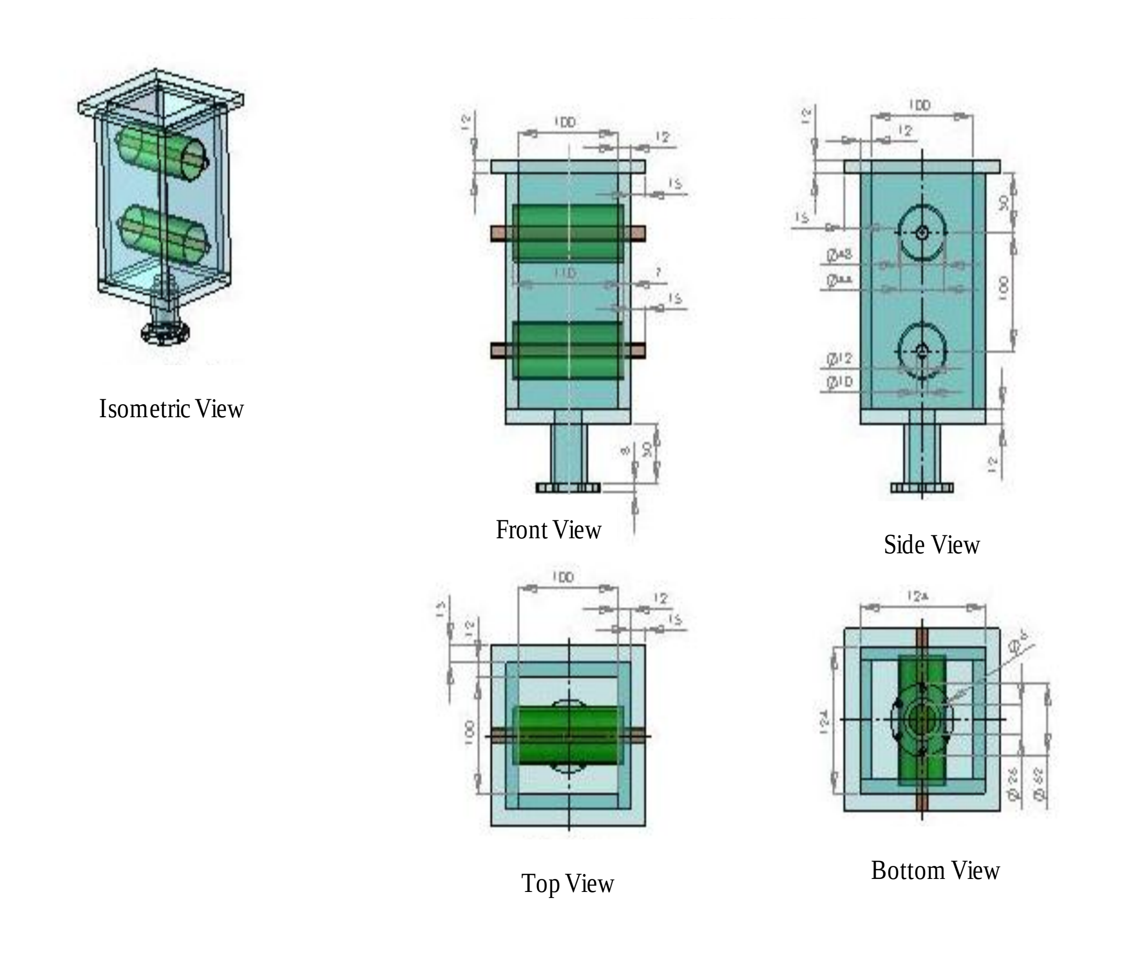

Figure 3.11: Schematic design of bubble generator

To produce a reasonably even two-phase flow, the bubble generator was designed to allow the air to be fed to the porous tubes from both sides. The distributor shown in Figure 3.12 was designed and constructed to improve the distribution of the air evenly to the inlets of the two porous tubes.

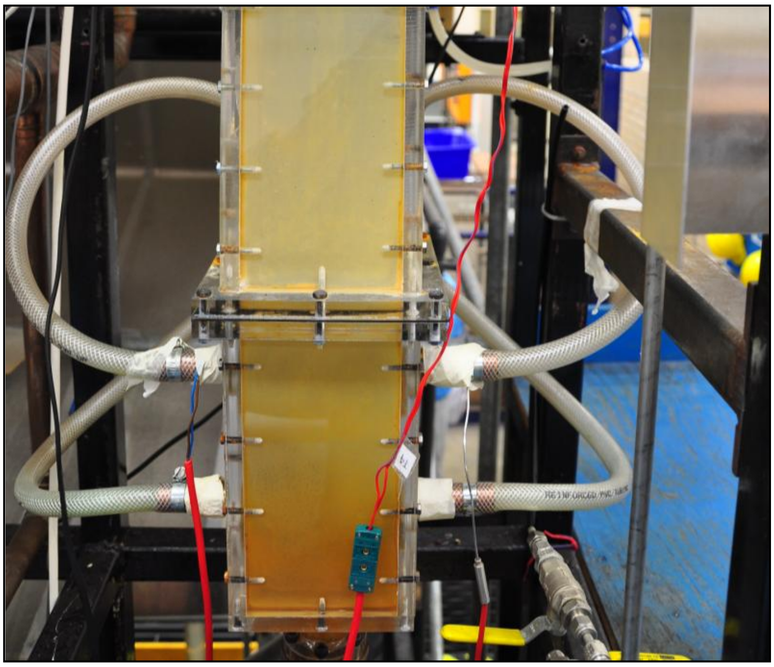

Figure 3.12: Air distributor

3.2.3 Tube bundle

There were three tube bundles used for this research. Tubes 38 mm in diameter in an in-line tube bundle, tubes 19 mm in diameter in an in-line tube bundle and tubes 19 mm in diameter in a staggered tube bundle. The 38 mm tube bundle was constructed by Bamardouf [65]. However, in his work, only pressure drop tests were carried out. Therefore, in this research, void fraction tests were carried out. Pressure drop tests were repeated, but only at the two highest mass fluxes. In this current research, two new bundles were constructed to allow comparison and capability. These were 19 mm in-line bundle and the 19 mm staggered bundle .The drawings of these bundles were made using SolidWork Version 2007. The 38 mm in-line bundle, the bubble generator, both convergent sections and the settling length were redraw using the same software.

3.2.4 38 mm in-line tube bundle

Figure 3.13 shows the tube bundle with tubes 38 mm in diameter. It consisted of ten rows of tubes with an outside diameter of 38.0 mm, with one full central column of tubes and two columns of half tubes placed on the walls to reduce bypass leakage. The tubes were 54.0 mm in length: 50.0 mm of the tube length was exposed to the fluid with the remaining of 4.0 mm inserted into grooves, 2.0 mm in depth, in the front and back walls to locate them. They were arranged in an in-line configuration with a pitch to diameter ratio of 1.32. The tube bundle has eleven pressure taps along a column between each row to allow pressure drops across the tube to be measured. Each pressure taps had push fitting M5x4mm that allowed a soft polyurethane tube to be inserted to the pressure taps holes that connected to the pressure drop purging and measurement system.

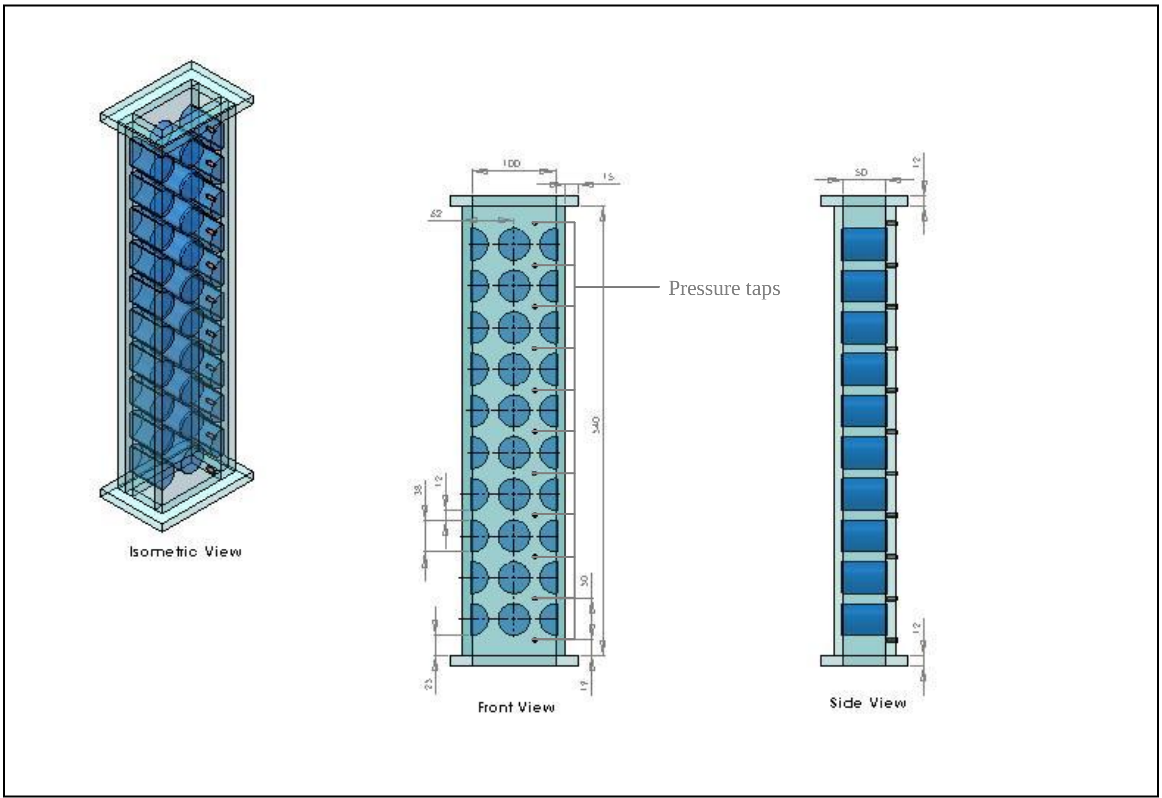

Figure 3.13: The 38 mm in diameter in-line tube bundle

3.2.5 19 mm in-line tube bundle

Figure 3.14 shows the new construction in-line tube bundle. The tube bundle contains 15 rows of tubes with an outside diameter of 19.0 mm. It contained three full columns of tubes and two columns of half tubes placed on the shell walls. There were 45 circular and 30 semi-circular tubes fabricated by a turning process. The tubes were 56.0 mm in length, with 50 mm exposed to the fluid. The remaining 6.0 mm was inserted into 3 mm grooves that were milled using a CNC mill on the front and rear tube sheets. The front and rear sheets were clamped together at the sides with M4 screws and glued with silicon to prevent any leakage. The tubes were arranged on an in-line configuration with a pitch to diameter ratio of 1.32. The material for the sheets and tubes was Perspex. The tube bundle has three pressure taps. The bottom pressure tap was located between rows one and two and between full columns two and three. The middle pressure tap was located between rows nine and ten and between full column one and two. The top pressure tap was located between rows fourteen and fifteen and between full columns two and three. The push fit fittings M5x4mm were inserted to the pressure tap holes so that a connection to the purging and measurement system could be made using a soft polyurethane tube.

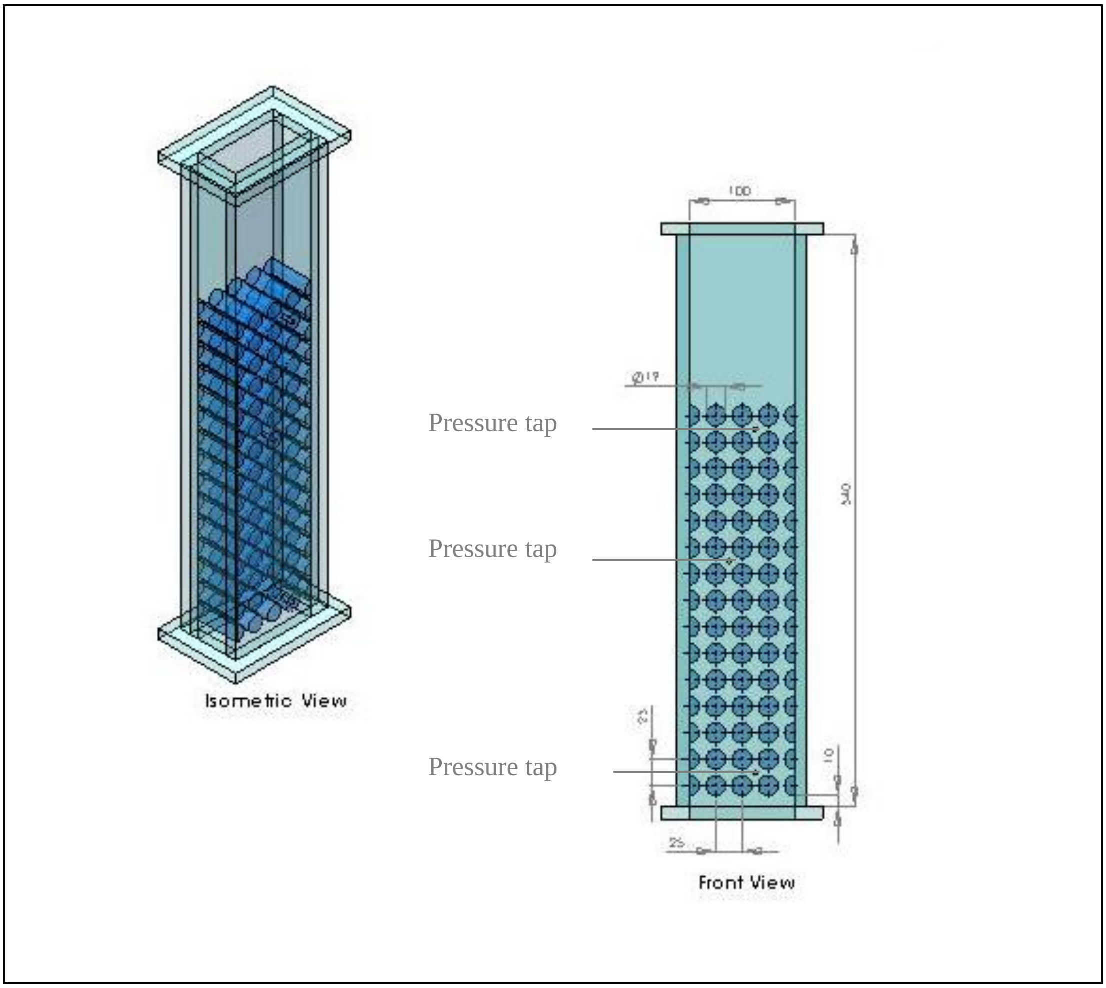

Figure 3.14: The 19 mm in diameter in-line tube bundle

3.2.6 19 mm staggered tube bundle

Figure 3.15 shows the new construction staggered bundle. The tube bundle contains 22 rows of tubes with an outside diameter of 19.0 mm. It contained four full columns of tubes and two columns of half tubes placed on the shell walls. There were 77 circular and

22 semi-circular tubes fabricated by a turning process. The tubes were 56.0 mm in length, with 50 mm exposed to the fluid. The remaining 6.0 mm was inserted into 3 mm grooves that were milled using a CNC mill on the front and rear tube sheets. The front and rear sheets were clamped together at the sides with M4 screws and glued with silicon to prevent any leakage. The tubes were arranged in a staggered triangular configuration with a pitch to diameter ratio of 1.32. The material for the sheets and tubes was Perspex which give a clear view of the flow. The tube bundle had five pressure taps. The two pressure taps at the bottom of the bundle were located between rows one and two. The middle pressure tap was located between rows five and six. The two top pressure taps located between rows fourteen and fifteen and another one at rows fourteen between full column two and three. The push fit fittings M5x4mm were inserted in the pressure taps holes to enable them to be connected to the purging and measurement system using a soft polyurethane tube.

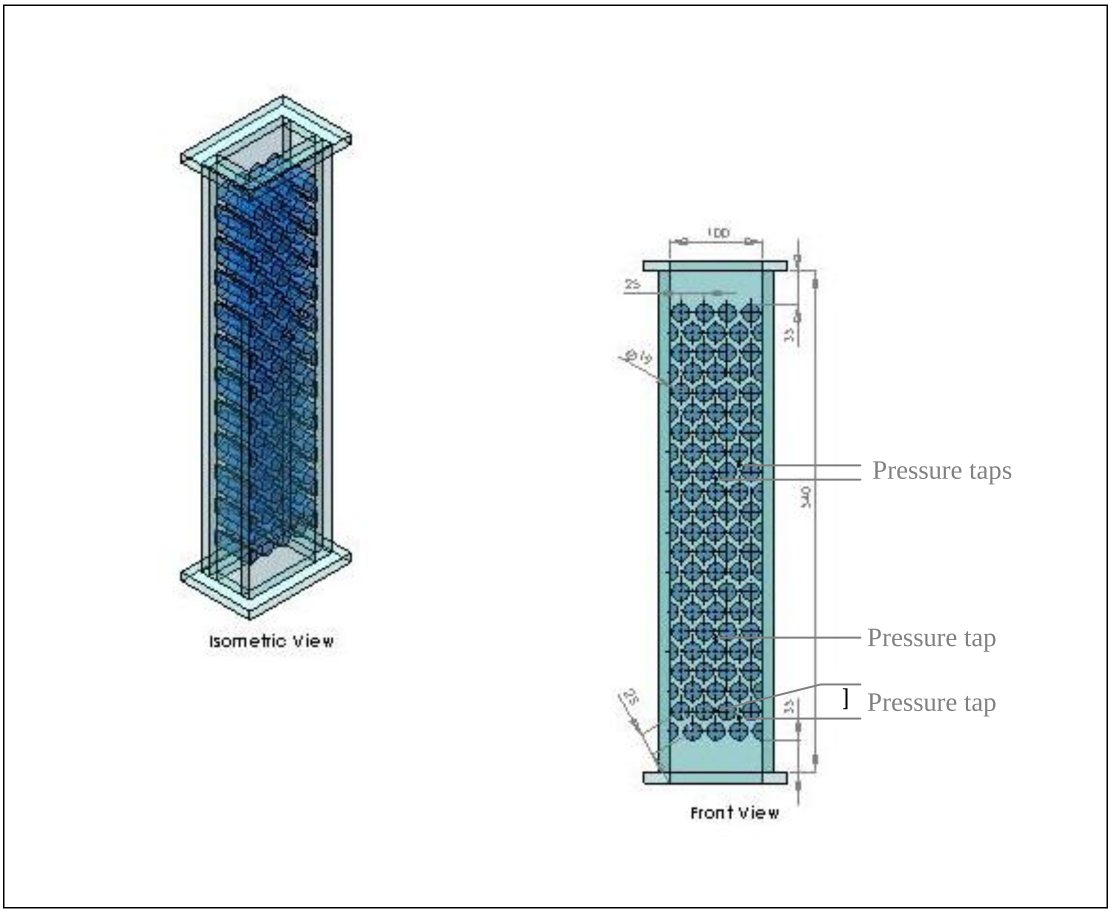

Figure 3.15: The 19 mm in diameter staggered bundle

3.2.7 Filter

A stainless steel filter with a 125 micron mesh was placed before the test section to remove any debris from the water prior to it entering the test section, Figure 3.1. The filter was selected because of its large flow capacity of 120 l/min and its maximum working pressure of 7 bar.

3.2.8 Air –water separator

An air-water separator was placed above the tube bundle to separate the air and the water, Figure 3.1. The separator consisted of number of baffles that provided a large number of direction changes that forced the heavier liquid to separate from the air. A series of holes were placed in the baffle base to drain the water droplets back to the tank. The air left the separator through three 200 mm diameter tubes while the water was returned to the supply tank.

3.3 Instrumentation

3.3.1 Pressure transducer

There were three pressure transducers used in this research. There were the Rosemount SMART transducers capable for measuring pressure drops and pressure. Two SMART Rosemount 3051 pressure drop transducers were used, one for pressure drop and one for water flow rate measurements. A Rosemount 2088 gauge pressure transmitter was used to measure pressure. The current outputs for all of these pressure transducers was 4 mA – 20 mA. This was converted to a 1-5 V signal input to the data acquisition system.

3.3.2 375 Field Communicator

The Rosemount 375 Field Communicator supports HART and FOUNDATION field bus devices, allowing the user to configure or troubleshoot on the bench or in the field. The HART 375 Field Communicator runs on Windows CE, a robust, real-time, operating system. It has a 80 MHz Hitachi® microprocessor SH3and 32 MB of RAM. Figure 3.16 shows the HART 375 Field Communicator.

Figure 3.16: The Rosemount 375 Field Communicator

The HART 375 Field communicator was capable to interrogate and alter the upper and lower pressure and pressure drop limits and to set unit of measurement units. This allowed calibration of a pressure transducer manually to meet each new pressure range the transducer was exposed to for each new experimental condition. This HART 375 Field Communicator was used in this research for calibrating the pressure transducers for pressure drop, pressure and water flow rate.

The HART 375 Field communicator setup will show the range values for URV i.e. Upper Range Value, LRV i.e. Lower Range Value, PV i.e. Primary Variable and AO i.e. Analog Output. These settings need a precision ampere meter or current meter to verify the output during the test, as shown in Figure 3.17. This allows the new pressure range to be calibrated to meet the new experimental condition and set the new range of pressure or pressure drop required. In other words, the HART 375 Field Communicator was used to set the URV and LRV and limits for the test. It had the capability to set a negative LRV, needed for measuring two-phase pressure drop. The ampere meter boxes had three points. One point was connected to the pressure transducer, and another two were connected to Data Acquisition System, described in Section 3.3.5.

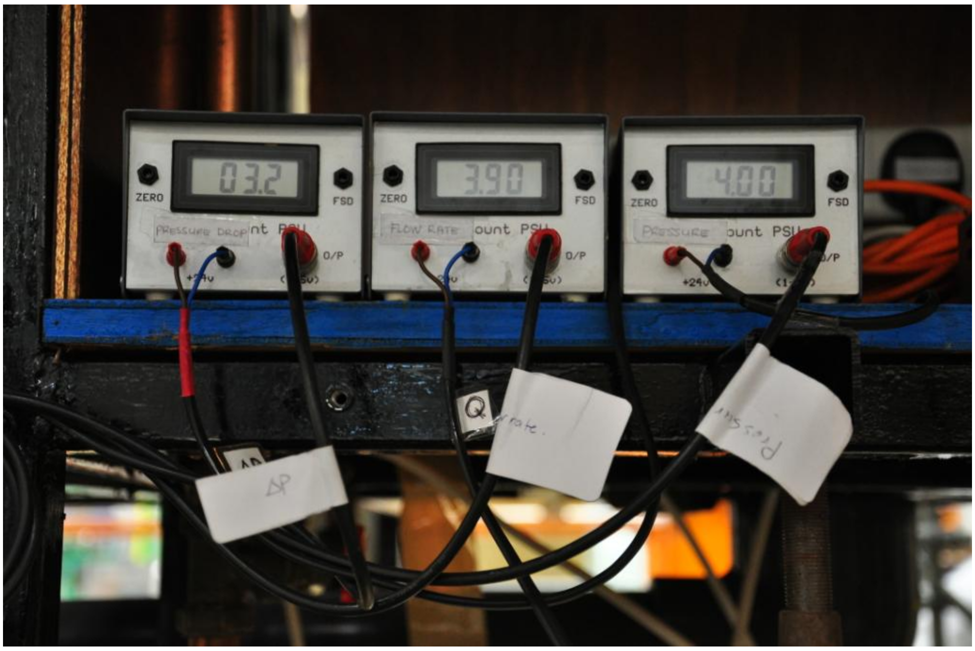

Figure 3.17: The Current meter or Ampere meter showing pressure drop, water flow rate and pressure in milli Ampere

3.3.3 Air flow rate

The air flow was supplied from an Ingersoll-rand SSR M110 compressor, Figure 3.18, to a large receiver that fed the test section through one of two Fisher-Rosemount Brooks air rotameters connected in parallel. The rotameters are shown in Figure 3.19. The mass flow rate range of these rotameters was 0 to 0.0039kg/s, named Rotameter 1, and 0 to 0.034 kg/s, named Rotameter 2. A gate valve was fixed downstream of each magnetically couples rotameter to allow the flow to be set. The accuracy of the flow meters was ±1.6% of full scale and readings were recorded manually.

Figure 3.18: The Ingersoll-rand SSR M110 compressor supply compressed air to test section

Figure 3.19: The Fisher-Rosemount air rotameters

3.3.4 Purging system

A purging system was used to remove air from the pressure drop transducer sampling lines before any pressure drop measurements were taken. The purging system contained solenoid valves controlled from the PC. The selected solenoid valves, Figure 3.20, had a port size of 6.35 mm and a supply voltage of 24 V DC.

Figure 3.20: Solenoid valve

There were thirteen solenoid valves in the purging system. Figure 3.21 shows the solenoid valves connected to the control box. Figure 3.22 shows the solenoid valve arrangement for the 38 mm in-line tube bundle, which had eleven pressure taps. Two solenoids valves, A and B, were fixed at the inlet to the purging system for purging all of the lines. Solenoid valves 1 to 11 were fixed to each pressure tap to allow pressure drop measurement across the tube bundle. These solenoid valves connected the taps to the pressure transducer. The connection of solenoid valves to the high or low end of the pressure transducer depended on the mass flux used. The solenoid valves were connected by a polyurethane tubes with push-in fittings.

These thirteen solenoid valves position were fixed on the rig, independent of the bundle used for the pressure drop tests. For the 38 mm tube diameter in-line bundle, solenoid valves 3 and 10 were used for two-phase pressure drop measurements. The 19 mm diameter tube in-line bundle used solenoid valves 1 and 8 for two-phase pressure drop measurements across the bundle and the 19 mm diameter tube staggered arrangement used solenoid valves 2 and 7.

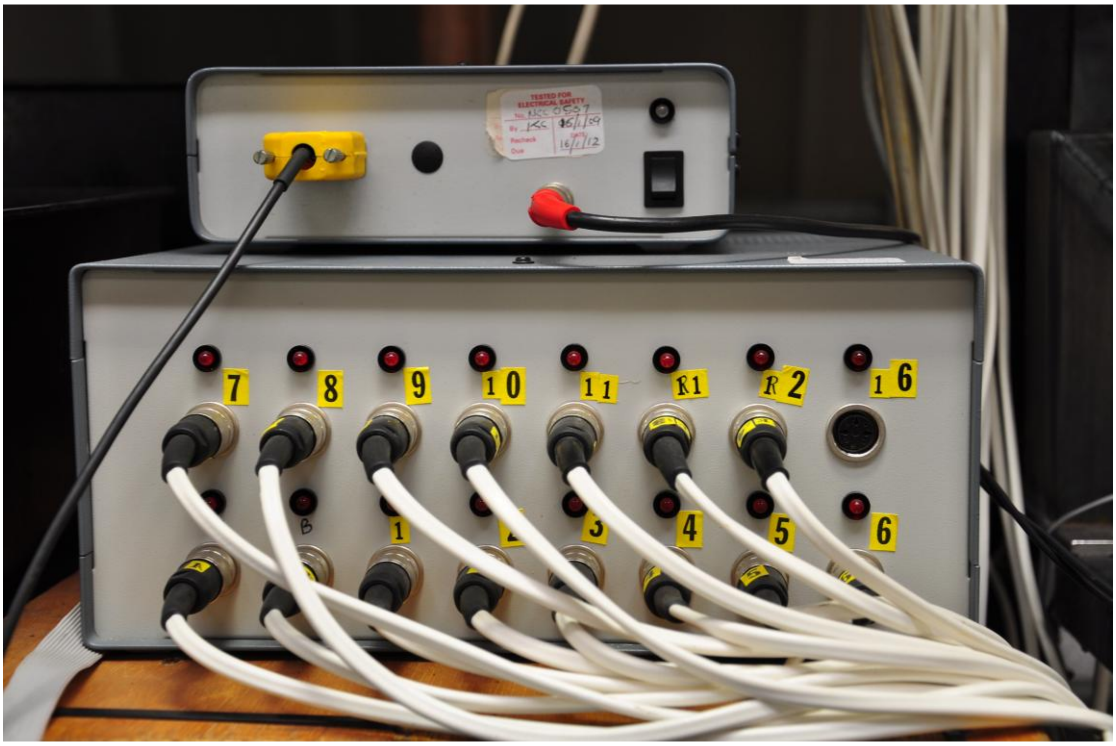

Figure 3.21: Solenoid valves control switch box

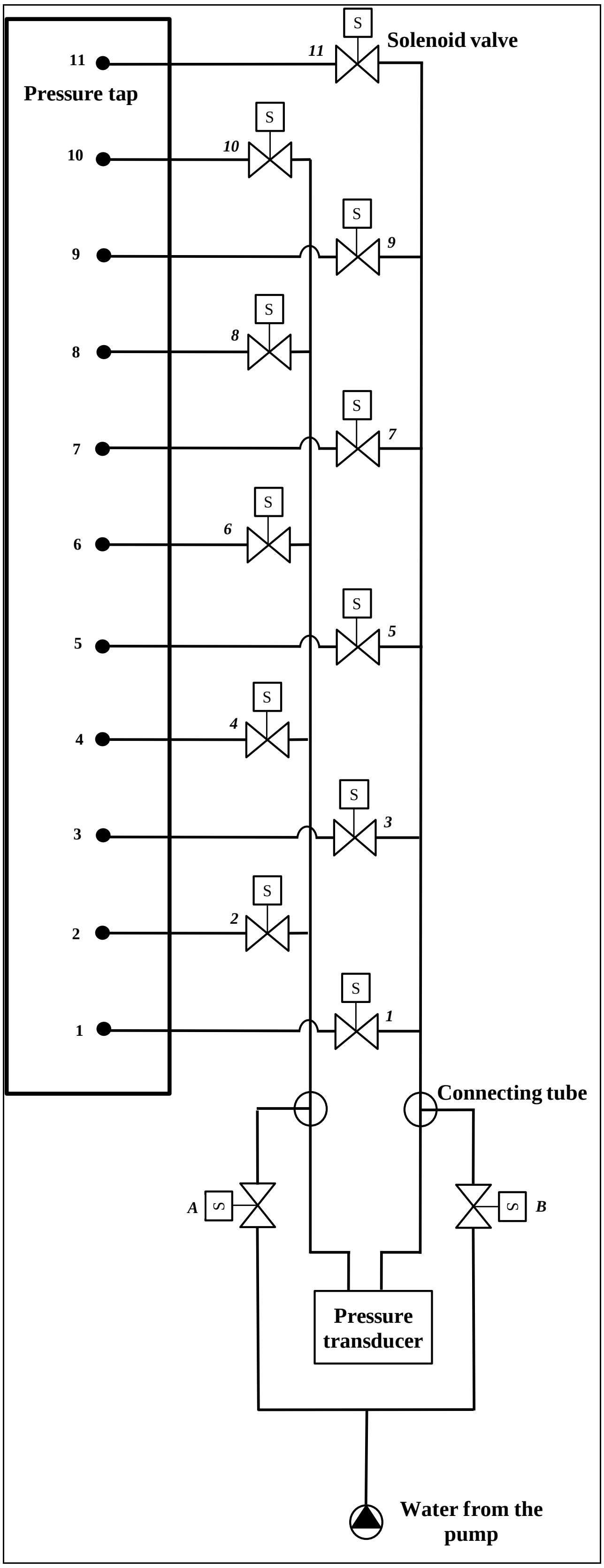

Figure 3.22: Solenoid valves arrangement

3.3.5 Data Acquisition System

A data acquisition system was used to produce repeatable and reliable data from the test facility. Pressure drop, pressure, temperatures, liquid flow rate and void fraction were logged electronically by the data acquisition system. These results were averaged to obtain re-producible results.

The pressure drop, pressure and the water flow rate measurements were recorded as Analog signals ranging from 1-5 V. The signals were sent to the Hewlett Packard (HP) PC through a NI PCI-6514 DAQ board connected to a SCB-68 shielded connector block with 68 screw terminals. These terminals had individual connections to instrument transducers.

The measurements and control of the solenoid valves were automated by an in-house program developed using LabVIEW software. The program will be described in next Section, 3.3.6. The test data from the data acquisition system were stored in a text file format that was accessed from Windows for data analysis.

The temperatures and void fraction measurements were controlled by their own system described later in Section 3.3.9 and Section 3.4 and 3.5.

3.3.6 LabVIEW program

LabView 7.1, is graphical source software which was used to build a program to record and store the experimental data for pressure drop, pressure, temperature, liquid flow rate and void fraction. It was designed to work through two main screens; a block diagram screen and a front panel. The block diagram screen contained the graphical code, including indicators, control objects, control loops, functions and other objects connected together to make the program. The front panel was the user interface, containing control objects connected to the block diagram to simplify changing the settings required to run the program. This included the number of readings to be collected, the frequency to collect them, the time to store the data and the control of the opening and closing of solenoid valves for purging and reading.

Figure 3.23 and 3.24 show the *PURGING* program that allowed the purging of the residual air from the solenoid valve lines before pressure drop readings were taken. There were thirteen solenoid valves. Buttons A and B allowed water to pass through all of the solenoid valves. Button 1 to 11 allowed solenoid valves 1 to 11 to be connected to the pressure transducers.

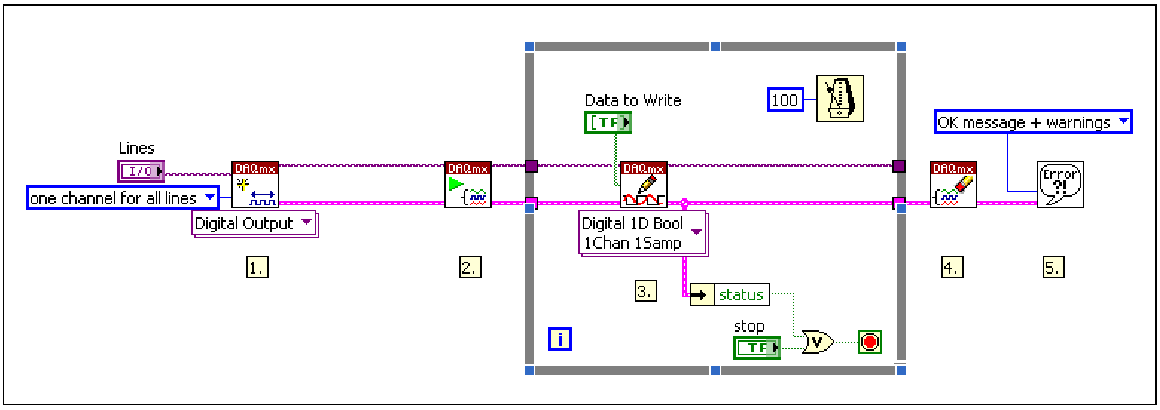

Figure 3.23: Block diagram of *PURGING* program

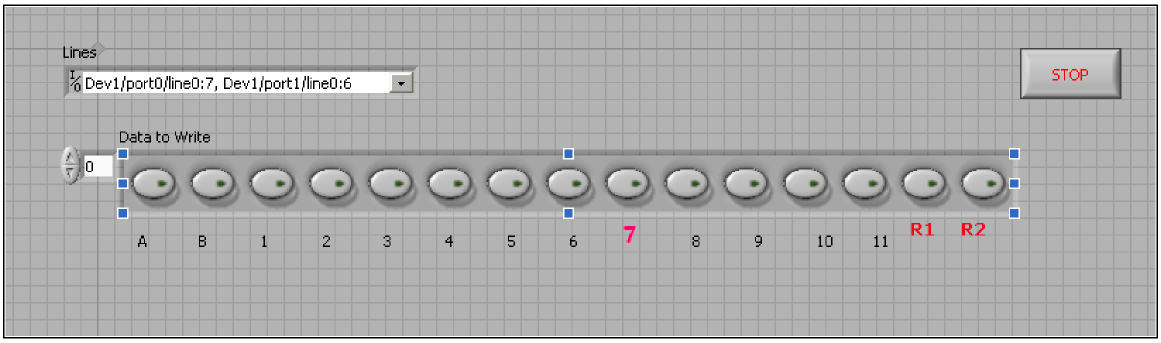

Figure 3.24: Front panel of *PURGING* program

After purging the pressure drop lines, the *TWO-PHASE FLOW* program was run to the pressure drop, pressure, temperatures, liquid flow rate and void fraction data. Figure 3.25 and 3.26 shows the front panel and block diagram respectively. The program has two solenoid valves for reading the pressure drop. The program was divided into two tasks. One task recorded data from the pressure drop tests. Pressure drop, water flow rate, void fraction and pressure data were sent to the data logger. The signal from the pressure drop transducer fluctuated significantly so that 10000 readings were taken at a rate of 1 kHz to ensure representative values were obtained. The other three readings were taken at 1 kHz and 10000 data. The other task recorded the temperatures readings including water, air inlet at right, air inlet at left and two-phase flow at exit bundle. These were recorded at 10 samples at 2 Hz.

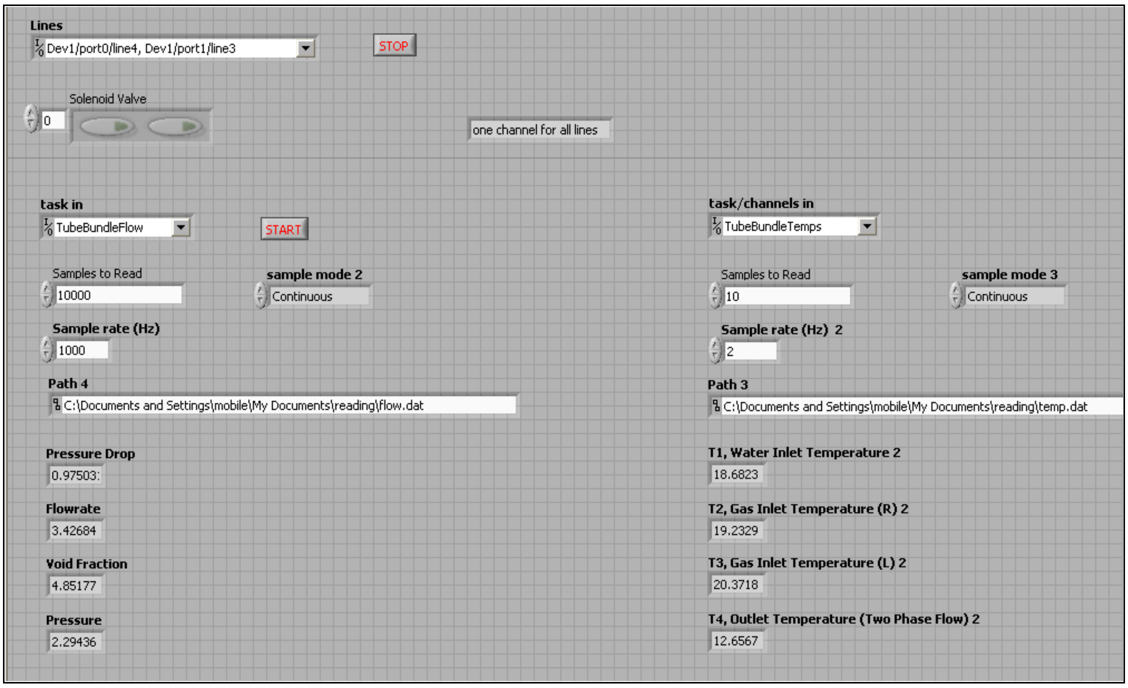

Figure 3.25: Front panel of *TWO-PHASE FLOW* program

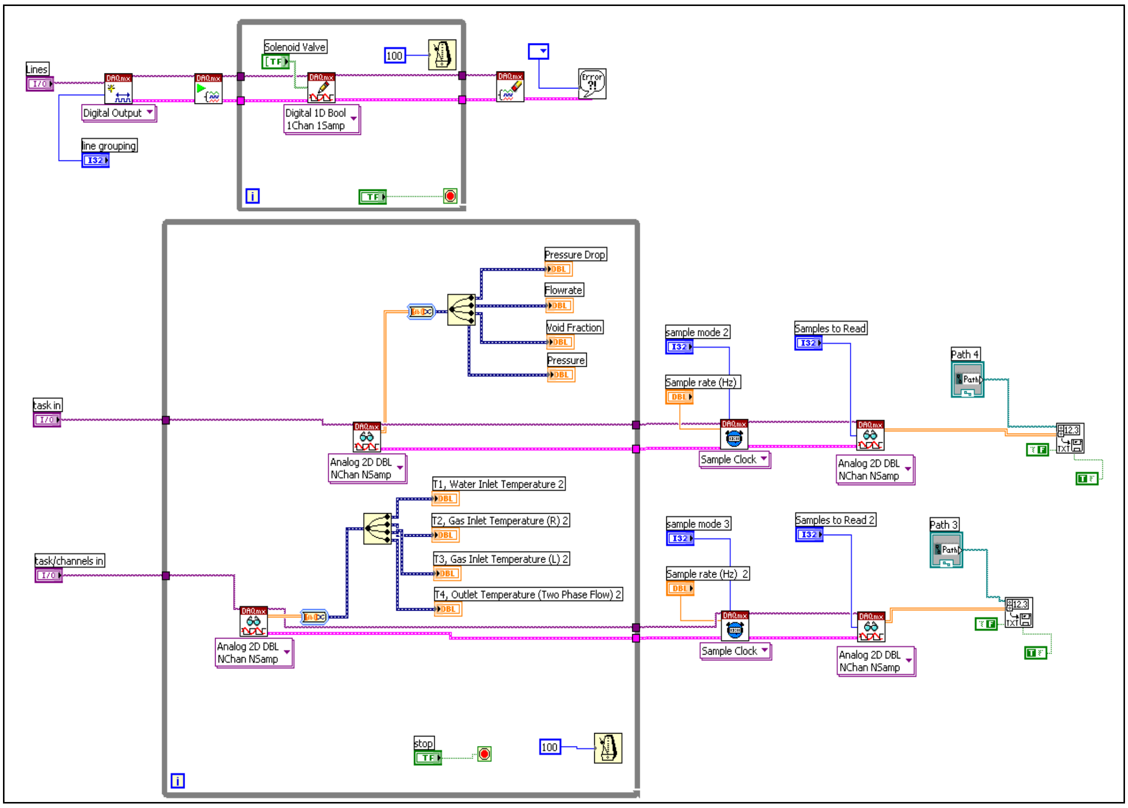

Figure 3.26: Block diagram of *TWO-PHASE FLOW* program

3.3.7 Two-phase flow pressure drop

Only four solenoid valves were used for each pressure drop measurements. The 38 mm in diameter in-line bundle, the 19 mm diameter in-line bundle and the 19 mm in diameter staggered bundle which used solenoid valves A, B and another two; solenoid numbers 3 and 10, 1 and 8, 2 and 7 respectively. The pressure drops were measured by a smart Rosemount pressure transducer, model 3051, able to read positive and negative values. Table 3.1 shows the lines configured for each tube bundles.

Table 3.1: Solenoid valves ports used for pressure drop measurement

Lines	Solenoid valves	38 mm in-line	19 mm in-line	19 mm staggered
Dev1/port0/line0	A	√	√	√
Dev1/port0/line1	B	√	√	√
Dev1/port0/line2	1		√	
Dev1/port0/line3	2			√
Dev1/port0/line4	3	√		
Dev1/port0/line5	4			
Dev1/port0/line6	5			
Dev1/port0/line7	6			
Dev1/port1/line0	7			√
Dev1/port1/line1	8		√	
Dev1/port1/line2	9			
Dev1/port1/line3	10	√		
Dev1/port0/line4	11			

3.3.8 Pressure

The pressure transducer was placed at the bottom of the tube bundle and connected to the pressure tap between rows one and two at all bundles. This pressure transducer enabled the test pressure to be logged by the data acquisition system, described in Section 3.3.5. The pressure transducer generated industry standard process control signals. It was a Rosemount 2088 gauge pressure transmitters, generating 4-20 mA signals that were converted 1-5 V dc signals that were fed to the data acquisition system. The Rosemount pressure transmitters were of a SMART type design. Figure 3.27 shows the pressure transducer connected to the pressure tap on the 38 mm diameter in-line bundle.

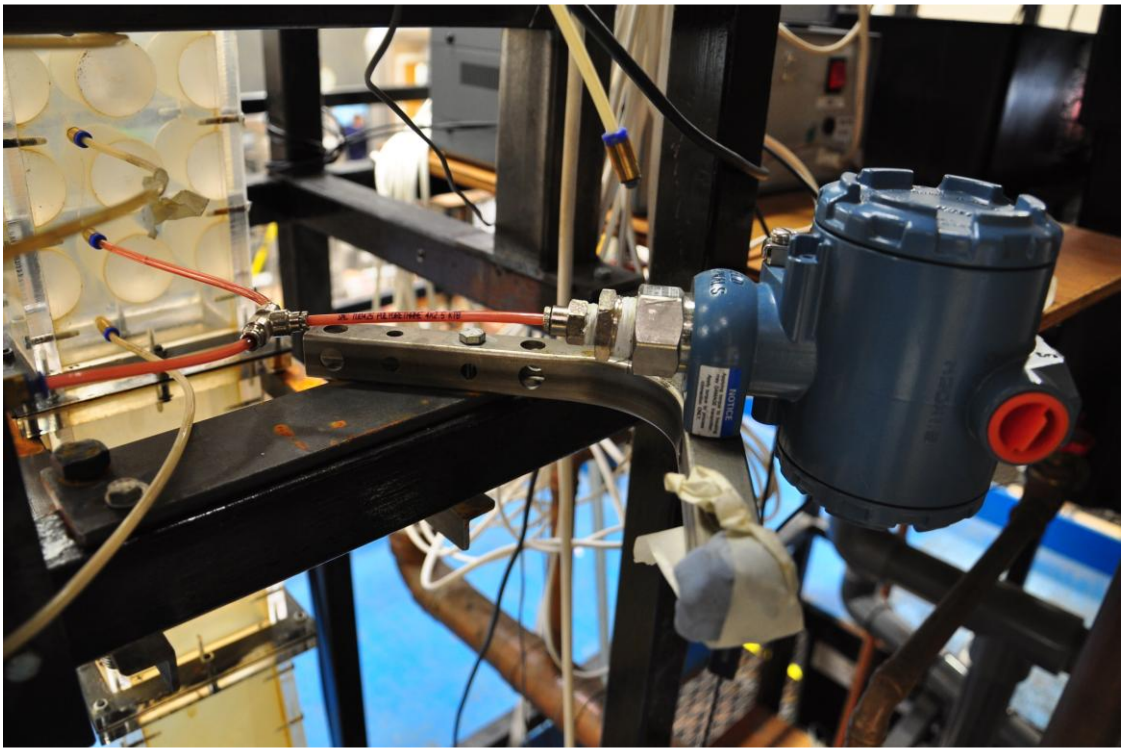

Figure 3.27: Pressure transducer connected to the pressure tap at 38 mm in diameter in-line bundle

3.3.9 Temperature

Four K-type thermocouples were used in the test section as shown in Figure 3.28 - Figure 3.31. One thermocouple was located at the inlet of the test section to measure the water temperature, T_1. Two thermocouples were put at the inlet of the air distributor to measure the inlet air temperature, T_2 and T_3. One thermocouple was located at the outlet of the test section allowing temperature of the two-phase flow to be taken, T_4. These thermocouples were connected to a Thermocouple Input Module NI USB-9211A as shown in Figure 3.31. The thermocouple module had four 24-bit thermocouple input channels, plug-andplay connectivity via USB and 50/60 Hz noise rejection. The signal input ranged ±80 mV, with a maximum sampling rate of 15 S/s and has a sensitivity of that read digitally. These four temperature readings were read and logged into the LabVIEW program as described in Section 3.3.6. These data are needed to obtain the air density entering the test section and the fluid properties.

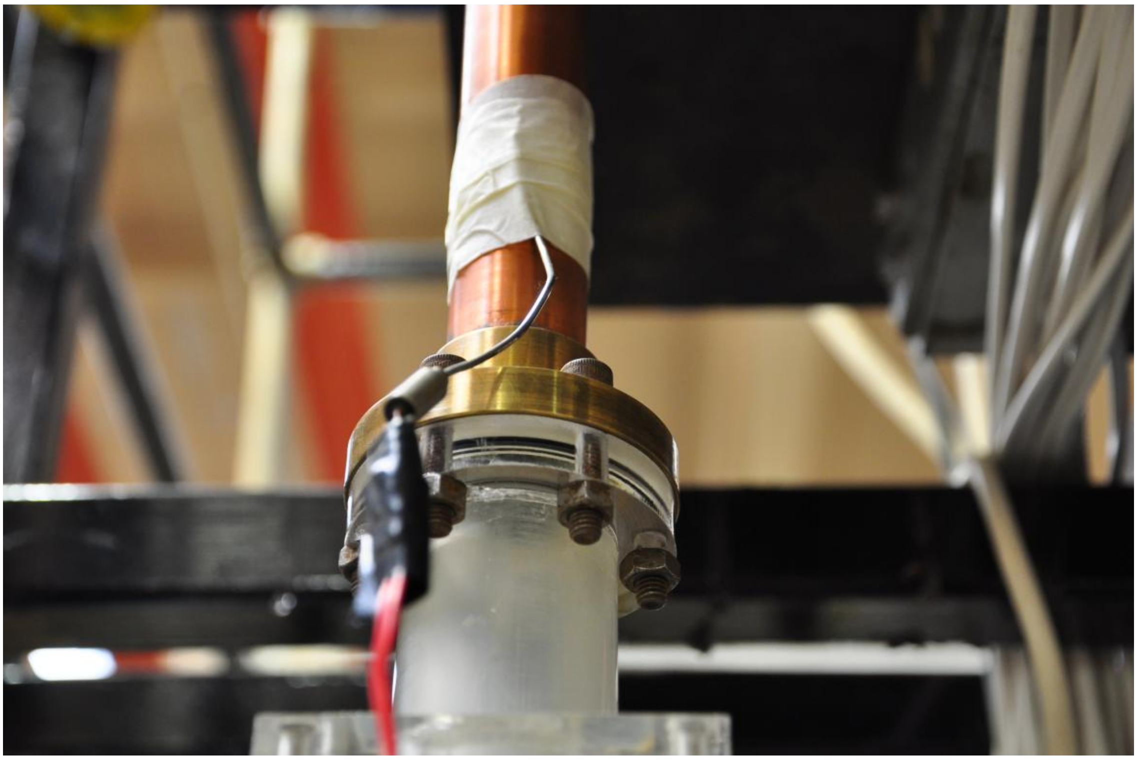

Figure 3.28: Two-phase flow temperature (outlet)

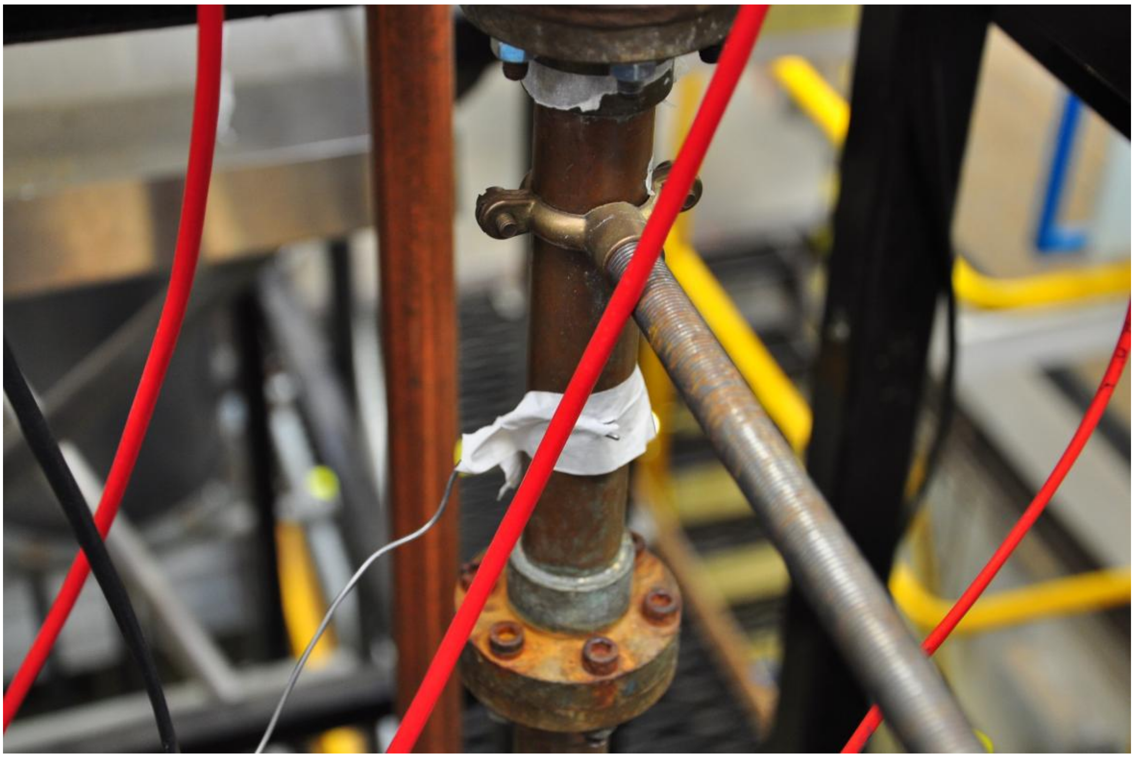

Figure 3.29: Water temperature (inlet)

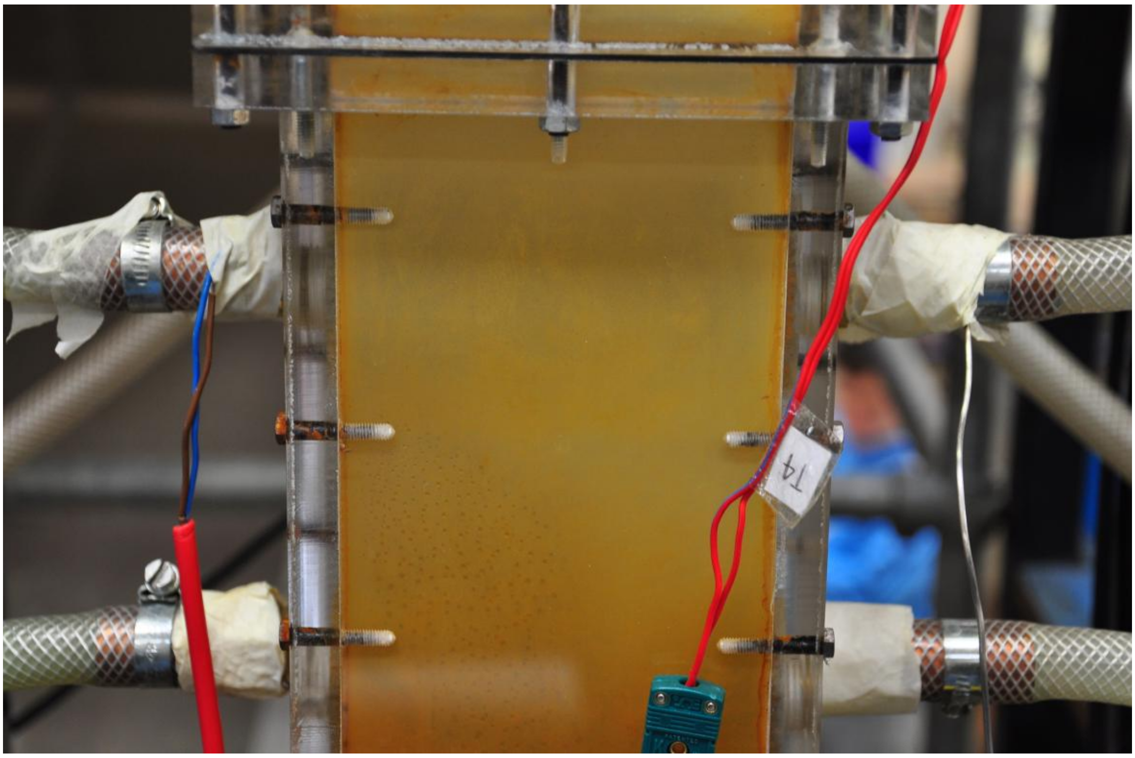

Figure 3.30: Air temperature at two air inlets

Figure 3.31: Thermocouple input Module NI USB-9211A

3.3.10 Water flow rate

The water flow rate was measured by one of four flow nozzles arranged in parallel and placed after the positive displacement pump, as shown in Figure 3.32. The tube diameter, D, the orifice area, A_t, the tube area, A, and the discharged coefficient, C_d, of these nozzles are shown in Table 3.2.

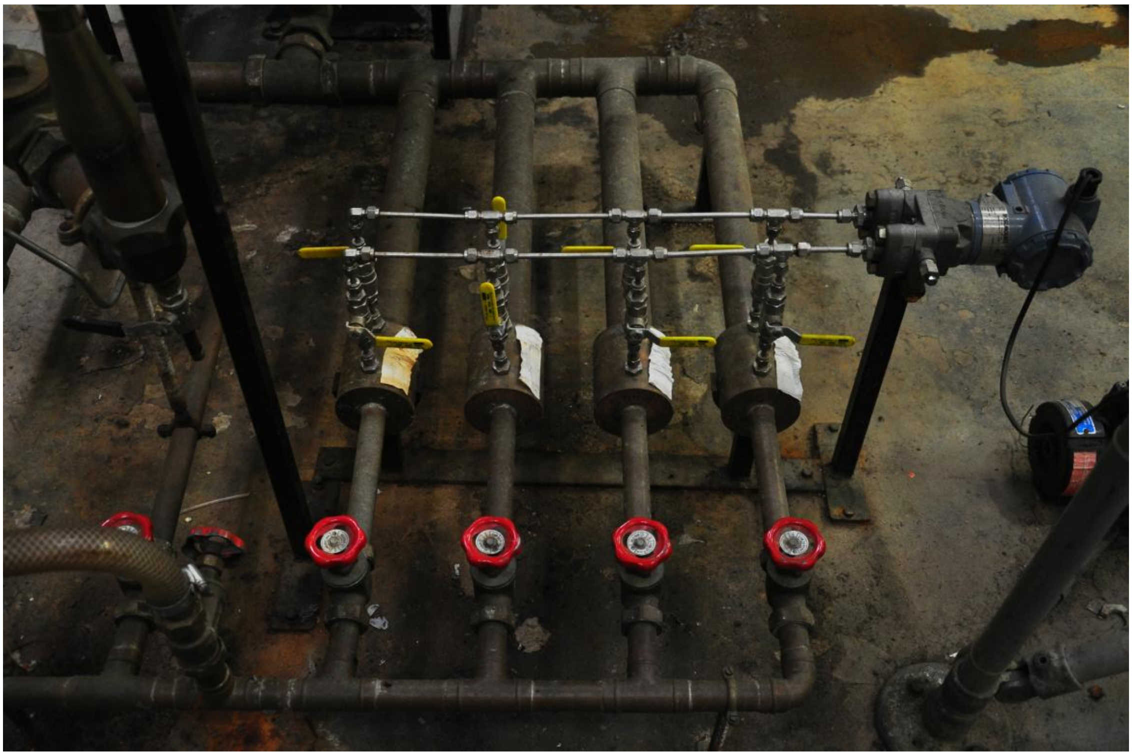

Figure 3.32: Four water nozzles and pressure transducer

Table 3.2: Nozzle geometry

Nozzle No.	D (mm)	C_d	A_t (m^2)	A(m^2)
1	26.02	0.95	5.32E-04	1.96E-03
2	13.60	0.96	1.45E-04	1.96E-03
3	6.44	0.88	3.26E-05	1.96E-03
4	3.50	0.46	7.31E-06	1.96E-03

A Rosemount 3051 differential pressure transducer was used to measure the pressure drop across the nozzles. The HART 375 Field Communicator was used to calibrate 4-20mA output of the flow meter. The voltage setting was set to 0 – 5 Volts.

3.4 Void fraction measurement using gamma-ray densitometer

The void fraction was measured by a gamma-ray densitometer with a 241Am (Americium) isotope as its source because it was readily available to the project. This collimated low-energy source projected a 10 mm diameter beam through the depth of a test section. The attenuation of the gamma-ray beam as it passed through the flow was measured through a photomultiplier tube (PMT) and an electronically controlled pulse counter. An electrical configuration for the coupling of the PMT assembly output to the amplifier discriminator is given in Figure 3.33 [66]. The specification of the system is detailed in Table 3.3.

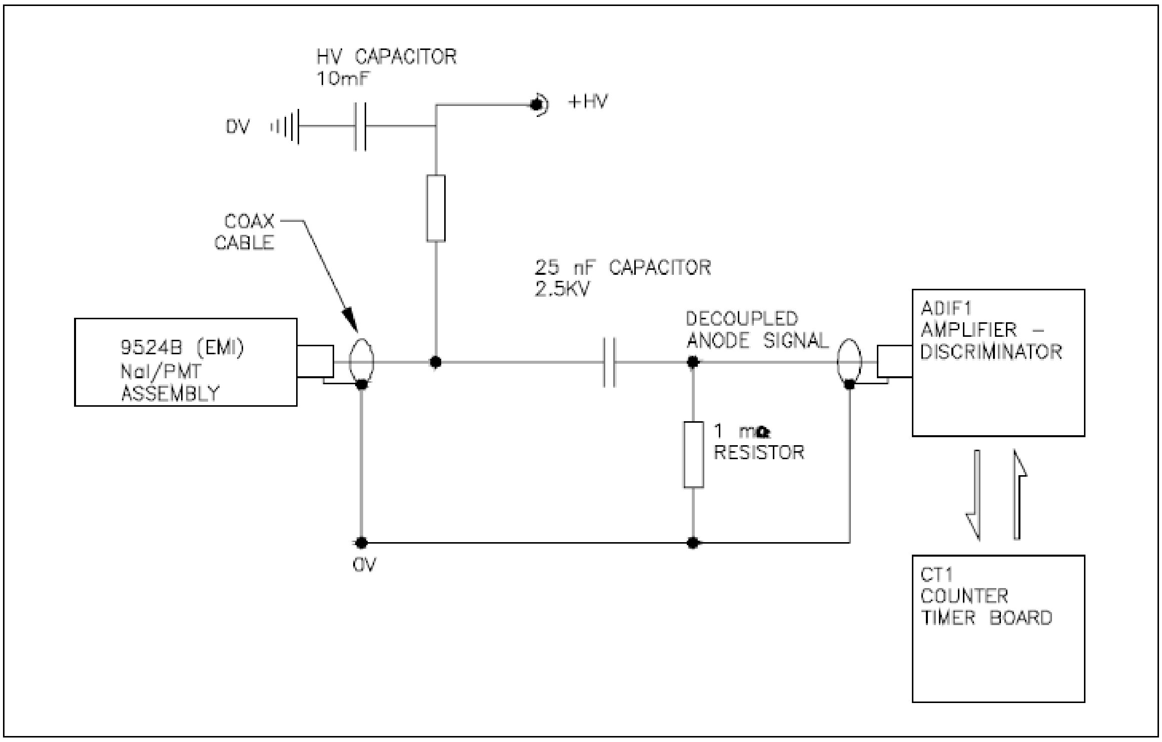

Figure 3.33: Configuration of gamma ray densitometer [53].

Table 3.3: List of component of gamma-ray densitometer [53]

Item	Description	Manufacturer
1	NaI(TL) crystal 1" diameter x 1 mm thick assembly c/w 30 mm 9125 focused photomultiplier. Dark current 0.14 nA	Hilger Crystals Ltd
2	ADIF1 Amplifier-discrimanator & current to frequency module	Electron Tubes Inc
3	CT1 Counter timer board. Counting period accuracy ± 1 μs	Electron Tubes Inc
4	PS2001/12N High voltage modular power, 20 to 2000 V	Electron Tubes Inc

3.4.1 Installation of Gamma Ray Densitometer

The gamma-ray densitometer, relies on the scintillation properties of a Sodium iodide crystal [NaI(Tl)]. When exposed to gamma rays, the crystal emits photons in proportion to the incident rate of the ionising source. By counting the photons emitted by the crystal e.g. detected by the photomultiplier, the attenuation of gamma rays passing through the test section and its contents could be determined.

The 241Am source and the PMT assembly were mounted on a rigid base, at 0.27 cm from the tube bundle base, as shown in Figure 3.34 and Figure 3.35. This collimated low-energy source projected a beam 10 mm in diameter through the flow, parallel to the tubes, onto a photomultiplier tube. The CT1 Counter timer, housed in the Hewlett Packard (HP) PC card based, electronically controlled pulse counter, was used to measure the radiation incident on the photomultiplier. Shims of 50.0 mm, 25.0 mm and 12.5 mm high were fabricated to make it possible for local void fraction measurements to be made in the minimum and maximum gaps between the tubes in the bundles.

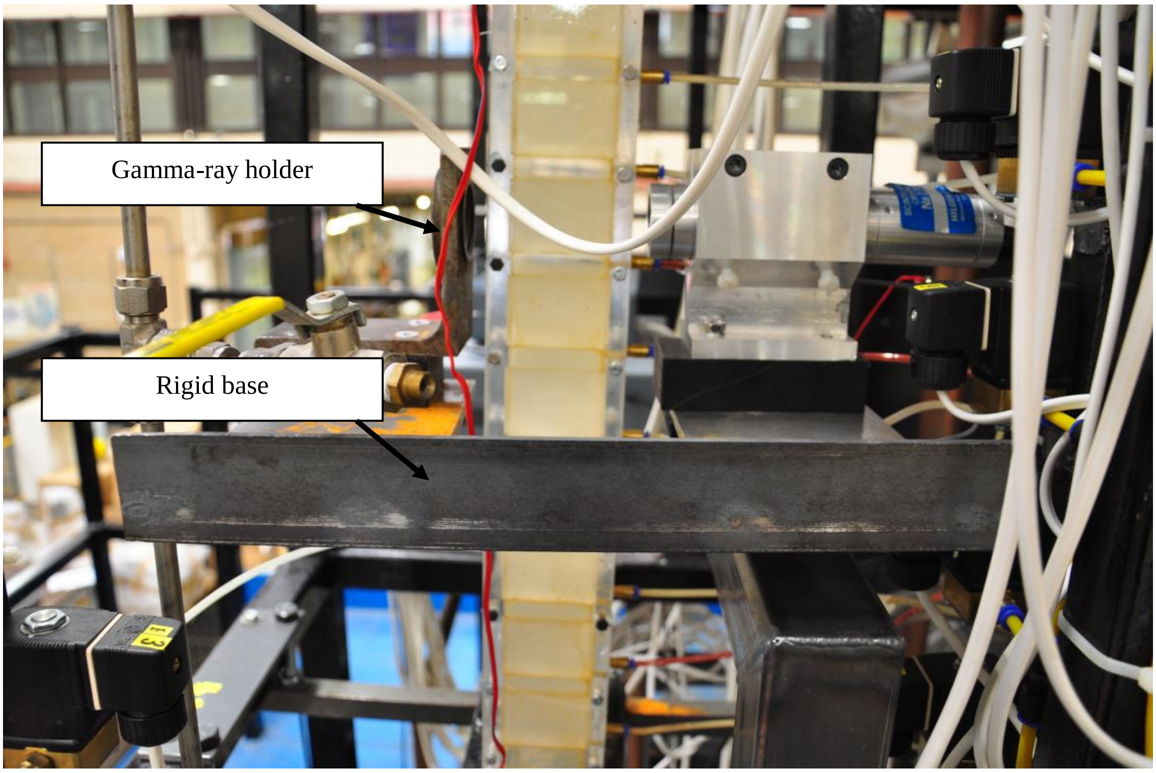

Figure 3.34: Rigid base to mount gamma-ray densitometer

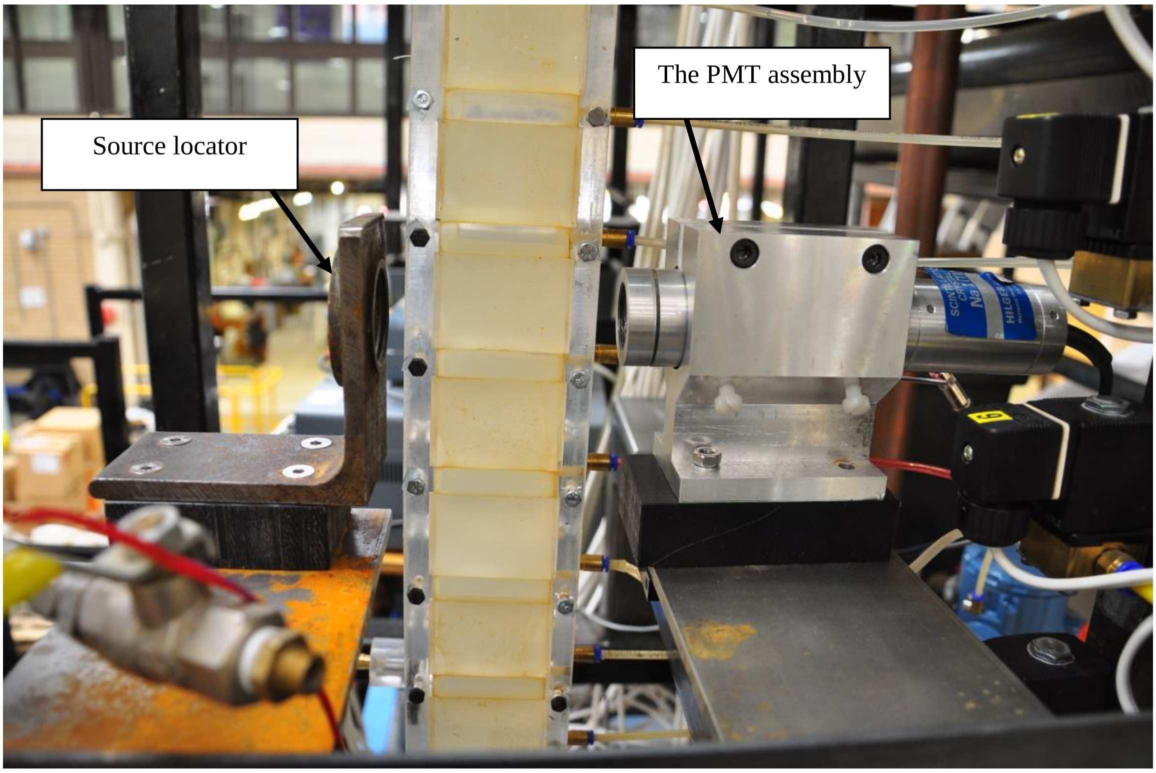

Figure 3.35: The PMT assembly and gamma ray source mounting

The installation of the gamma-ray densitometer was required to adhere several safety procedures. The biggest concern was scatter or the ionising radiation to its immediate surroundings. The 241Am source is shielded in thick metal and kept in a square thick box. Behind the test section, a lead sheet was placed to prevent the radiation dispersing into the surroundings.

CHAPTER 4 - EXPERIMENTAL CONDITIONS, PROCEDURES AND COMISSIONING

The test sections and the instrumentation discussed in Chapter 3, were used to obtain two-phase pressure drop and void fraction data in adiabatic tests. Two test series were conducted for each bundle. The first obtained the pressure drop data and the second obtained the void fraction data. Each data set was obtained at the same nominal conditions. The test conditions, procedures and experimental commissioning are discussed in this chapter.

4.1 Two-phase flow pressure drop

4.1.1 Operation conditions

The two-phase pressure drop measurements in Bamardouf [51] show that the pressure drop across two successive rows are relatively small and the same as each other. Thus, measurements taken across seven rows, between taps 3 and 10, provided approximately seven times the magnitude than the previous set and were therefore more accurate because the uncertainties in the two-phase pressure drop measurements across one row was high because they were small. Therefore, in this study, the pressure drop measurements were taken across the tube bundle to increase their accuracy. In 38 mm in-line tube bundle, the pressure drop across the tube was taken between taps 3 and 10, as shown in the Figure 4.1.

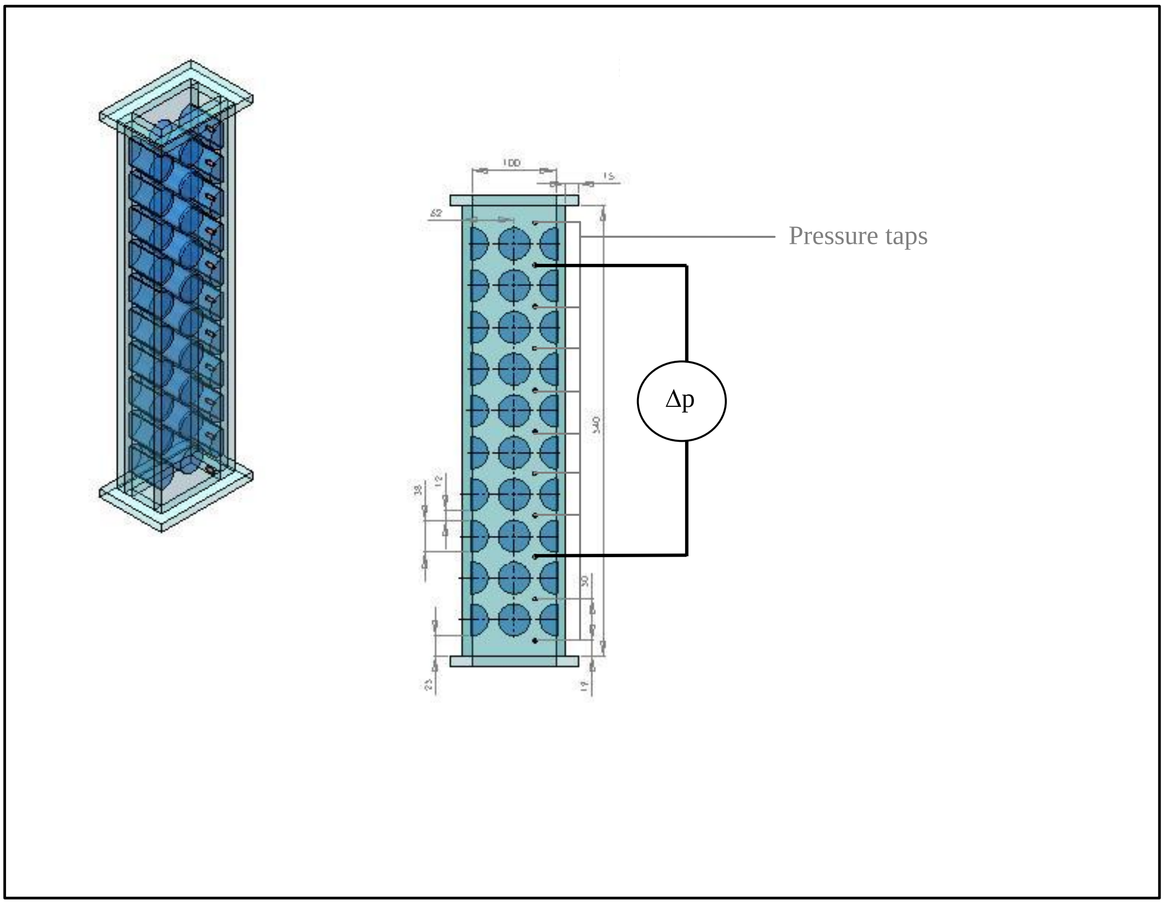

Figure 4.1: Pressure drop measurements in 38 mm in-line tube bundle

In 19 mm in-line tube bundle, the pressure drop across the tube was taken between the bottom and the top pressure taps as shown in Figure 4.2.

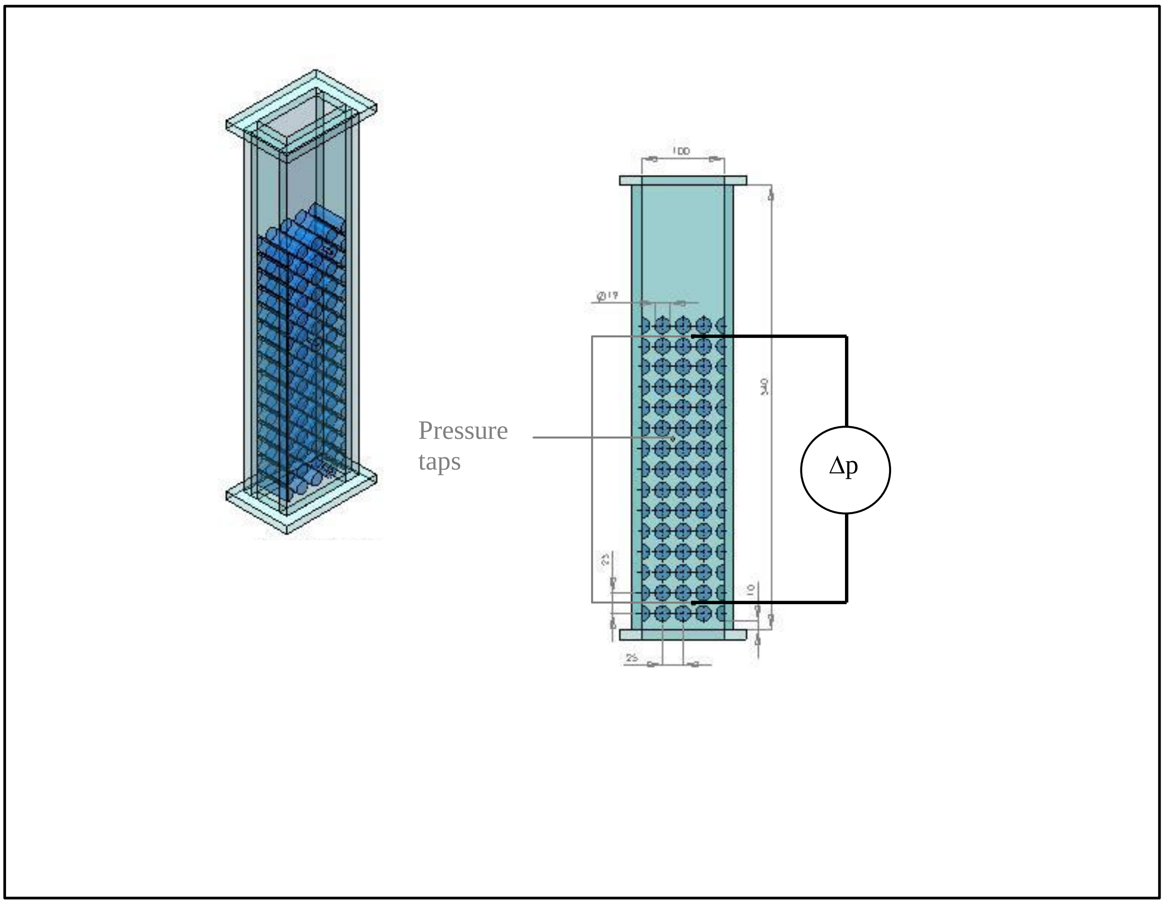

Figure 4.2: Pressure drop measurements in 19 mm in-line tube bundle

In 19 mm staggered tube bundle, the pressure drop across the tube was taken between the bottom and the top pressure taps as shown in Figure 4.3.

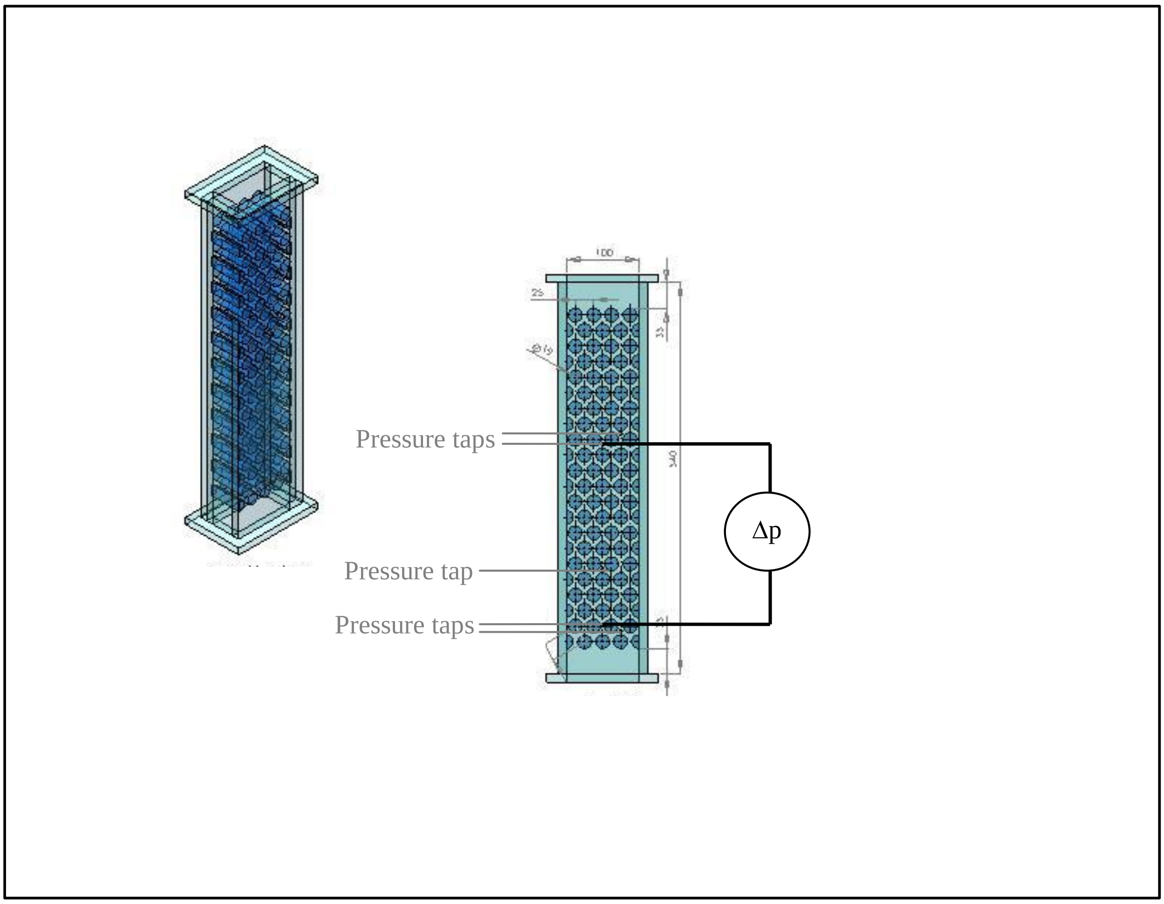

Figure 4.3: Pressure drop measurements in 19 mm staggered tube bundle

The pressure drop and void fraction tests covered a wide range of operating condition. The mass flux range was 25-688 kg/m^{2}s, based on the minimum flow area between the tubes. Nine mass fluxes were used for each data set and the quality for these mass fluxes ranged from 0.00047-0.57. These tests were done at fixed total mass flow rate, thus as the gas mass flow rate increased, the water mass flow rate decreased, similar to what happen in a heat exchanger. At the lower mass flow rate, the gas mass flow rate varied from 0.00039-0.017 kg/s while the water mass flow rate varied from 0.03-0.013 kg/s. At the highest total mass flow rate, the gas mass flow rate varied from 0.00039- 0.0204 kg/s while the water mass flow rate ranged from 0.825-0.805 kg/s. The test conditions are included in Table 4.1 – 4.6.

Table 4.1: Test conditions for 25 kg/m^{2}s and 65 kg/m^{2}s

Mass flux based on min area (kg/m^{2}s)	Total mass flow rate (kg/s)	Air mass flow rate (kg/s)	Water flow rate (Voltage)	Water volume flow rate (m^3/s)	Water mass flow rate (kg/s)	Quality (-)
25.0	0.0302	0.00039	4.58655	0.000030	0.0298	0.01293
25.0	0.0307	0.00078	4.61601	0.000030	0.0299	0.02544
25.0	0.0300	0.00117	4.37445	0.000029	0.0289	0.03895
25.0	0.0302	0.00156	4.31100	0.000029	0.0286	0.05173
25.0	0.0305	0.00195	4.29195	0.000029	0.0285	0.06401
25.0	0.0300	0.00234	4.08904	0.000028	0.0276	0.07810
25.0	0.0304	0.00273	4.10920	0.000028	0.0277	0.08968
25.0	0.0304	0.00312	4.00896	0.000027	0.0273	0.10270
25.0	0.0305	0.00351	3.95772	0.000027	0.0270	0.11494
25.0	0.0306	0.00390	3.88071	0.000027	0.0267	0.12756
25.0	0.0304	0.00680	3.25128	0.000024	0.0236	0.22383
25.0	0.0299	0.01020	4.15403	0.000020	0.0197	0.34074
25.0	0.0305	0.01360	3.32309	0.000017	0.0169	0.44536
25.0	0.0304	0.01700	2.46283	0.000013	0.0134	0.57000
65.0	0.0780	0.00039	3.92879	0.000078	0.0776	0.00500
65.0	0.0779	0.00078	3.89327	0.000077	0.0772	0.01001
65.0	0.0782	0.00117	3.88595	0.000077	0.0771	0.01495
65.0	0.0783	0.00156	3.86514	0.000077	0.0768	0.01991
65.0	0.0780	0.00195	3.81011	0.000076	0.0760	0.02500
65.0	0.0782	0.00234	3.79739	0.000076	0.0759	0.02992
65.0	0.0782	0.00273	3.76637	0.000075	0.0755	0.03492
65.0	0.0780	0.00312	3.72756	0.000075	0.0749	0.03998
65.0	0.0783	0.00351	3.71566	0.000075	0.0748	0.04484
65.0	0.0779	0.00390	3.65827	0.000074	0.0740	0.05009
65.0	0.0778	0.00680	3.44922	0.000071	0.0710	0.08741
65.0	0.0781	0.01020	3.23891	0.000068	0.0679	0.13063
65.0	0.0788	0.01360	3.06777	0.000065	0.0652	0.17251
65.0	0.0780	0.01700	2.80817	0.000061	0.0610	0.21794
65.0	0.0782	0.02040	2.62185	0.000058	0.0578	0.26095
65.0	0.0784	0.02380	2.44838	0.000055	0.0546	0.30358

Table 4.2: Test conditions for 105 kg/m^{2}s and 156 kg/m^{2}s

Mass flux based on min area (kg/m^{2}s)	Total mass flow rate (kg/s)	Air mass flow rate (kg/s)	Water flow rate (Voltage)	Water volume flow rate (m^3/s)	Water mass flow rate (kg/s)	Quality (-)
105.0	0.1257	0.00039	4.17813	0.000125	0.1253	0.00310
105.0	0.1258	0.00078	4.16500	0.000125	0.1250	0.00620
105.0	0.1263	0.00117	4.16794	0.000125	0.1251	0.00927
105.0	0.1261	0.00156	4.14018	0.000125	0.1245	0.01237
105.0	0.1262	0.00195	4.12440	0.000124	0.1242	0.01545
105.0	0.1263	0.00234	4.11091	0.000124	0.1240	0.01853
105.0	0.1261	0.00273	4.08164	0.000123	0.1234	0.02165
105.0	0.1259	0.00312	4.05056	0.000123	0.1228	0.02479
105.0	0.1262	0.00351	4.04591	0.000123	0.1227	0.02782
105.0	0.1262	0.00390	4.02845	0.000122	0.1223	0.03090
105.0	0.1260	0.00680	3.87536	0.000119	0.1192	0.05398
105.0	0.1268	0.01020	3.75067	0.000117	0.1166	0.08047
105.0	0.1250	0.01360	3.51187	0.000111	0.1114	0.10881
105.0	0.1254	0.01700	3.37827	0.000108	0.1084	0.13558
105.0	0.1268	0.02040	3.29160	0.000106	0.1064	0.16089
105.0	0.1273	0.02380	3.17028	0.000104	0.1035	0.18691
156.0	0.1872	0.00039	4.58080	0.000187	0.1868	0.00208
156.0	0.1872	0.00078	4.56927	0.000186	0.1865	0.00417
156.0	0.1867	0.00117	4.53228	0.000185	0.1855	0.00627
156.0	0.1880	0.00156	4.56674	0.000186	0.1864	0.00830
156.0	0.1852	0.00195	4.44794	0.000183	0.1833	0.01053
156.0	0.1878	0.00234	4.52915	0.000185	0.1854	0.01246
156.0	0.1863	0.00273	4.45729	0.000184	0.1835	0.01466
156.0	0.1864	0.00312	4.44886	0.000183	0.1833	0.01674
156.0	0.1868	0.00351	4.44712	0.000183	0.1833	0.01879
156.0	0.1879	0.00390	4.47419	0.000184	0.1840	0.02076
156.0	0.1891	0.00680	4.41261	0.000182	0.1823	0.03595
156.0	0.1870	0.01020	4.20981	0.000177	0.1768	0.05454
156.0	0.1873	0.01360	4.09699	0.000174	0.1737	0.07261
156.0	0.1873	0.01700	3.97851	0.000170	0.1703	0.09074
156.0	0.1878	0.02040	3.87579	0.000167	0.1674	0.10864

Table 4.3: Test conditions for 208 kg/m^{2}s

Mass flux based on min area (kg/m^{2}s)	Total mass flow rate (kg/s)	Air mass flow rate (kg/s)	Water flow rate (Voltage)	Water volume flow rate (m^3/s)	Water mass flow rate (kg/s)	Quality (-)
208.0	0.2487	0.00039	4.16529	0.000248	0.2483	0.00157
208.0	0.2490	0.00078	4.16343	0.000248	0.2483	0.00313
208.0	0.2492	0.00117	4.15792	0.000248	0.2480	0.00469
208.0	0.2512	0.00156	4.19927	0.000250	0.2497	0.00621
208.0	0.2491	0.00195	4.13403	0.000247	0.2471	0.00783
208.0	0.2498	0.00234	4.14229	0.000247	0.2474	0.00937
208.0	0.2500	0.00273	4.13761	0.000247	0.2472	0.01092
208.0	0.2504	0.00312	4.13727	0.000247	0.2472	0.01246
208.0	0.2491	0.00351	4.09475	0.000246	0.2456	0.01409
208.0	0.2486	0.00390	4.07331	0.000245	0.2447	0.01569
208.0	0.2517	0.00680	4.07888	0.000245	0.2449	0.02701
208.0	0.2520	0.01020	4.00114	0.000242	0.2418	0.04047
208.0	0.2445	0.01360	3.73586	0.000231	0.2309	0.05563
208.0	0.2478	0.01700	3.73467	0.000231	0.2308	0.06860
208.0	0.2491	0.02040	3.68419	0.000229	0.2287	0.08190
208.0	0.2507	0.02380	3.64197	0.000227	0.2269	0.09494
208.0	0.2484	0.02720	3.51241	0.000221	0.2212	0.10948
208.0	0.2496	0.03060	3.46171	0.000219	0.2190	0.12259

Table 4.4: Test conditions for 312 kg/m^{2}s

Mass flux based on min area (kg/m^{2}s)	Total mass flow rate (kg/s)	Air mass flow rate (kg/s)	Water flow rate (Voltage)	Water volume flow rate (m^3/s)	Water mass flow rate (kg/s)	Quality (-)
312.0	0.3728	0.00039	4.55901	0.000372	0.3724	0.00105
312.0	0.3748	0.00078	4.59041	0.000374	0.3740	0.00208
312.0	0.3741	0.00117	4.56926	0.000373	0.3729	0.00313
312.0	0.3754	0.00156	4.58639	0.000374	0.3738	0.00416
312.0	0.3741	0.00195	4.55359	0.000372	0.3721	0.00521
312.0	0.3747	0.00234	4.55836	0.000372	0.3724	0.00624
312.0	0.3760	0.00273	4.57625	0.000373	0.3733	0.00726
312.0	0.3755	0.00312	4.55935	0.000372	0.3724	0.00831
312.0	0.3753	0.00351	4.54707	0.000372	0.3718	0.00935
312.0	0.3739	0.00390	4.51286	0.000370	0.3700	0.01043
312.0	0.3764	0.00680	4.50545	0.000370	0.3696	0.01807
312.0	0.3725	0.01020	4.36895	0.000362	0.3623	0.02738
312.0	0.3726	0.01360	4.30725	0.000359	0.3590	0.03650
312.0	0.3737	0.01700	4.26607	0.000357	0.3567	0.04549
312.0	0.3766	0.02040	4.25616	0.000356	0.3562	0.05417
312.0	0.3740	0.02380	4.14727	0.000350	0.3502	0.06364
312.0	0.3737	0.02720	4.08097	0.000346	0.3465	0.07279
312.0	0.3749	0.03060	4.04248	0.000344	0.3443	0.08162
312.0	0.3687	0.03400	3.87506	0.000335	0.3347	0.09221

Table 4.5: Test conditions for 416 kg/m^2s and 541 kg/m^2s

Mass flux based on min area (kg/m^2s)	Total mass flow rate (kg/s)	Air mass flow rate (kg/s)	Water flow rate (Voltage)	Water volume flow rate (m^3/s)	Water mass flow rate (kg/s)	Quality (-)
416.0	0.4952	0.00039	4.59059	0.000495	0.4948	0.00079
416.0	0.5001	0.00078	4.65617	0.000499	0.4993	0.00156
416.0	0.4981	0.00117	4.62181	0.000497	0.4970	0.00235
416.0	0.4984	0.00156	4.61996	0.000497	0.4968	0.00313
416.0	0.4987	0.00195	4.61908	0.000497	0.4968	0.00391
416.0	0.4998	0.00234	4.62838	0.000497	0.4974	0.00468
416.0	0.4988	0.00273	4.60851	0.000496	0.4961	0.00547
416.0	0.4988	0.00312	4.60292	0.000496	0.4957	0.00626
416.0	0.4994	0.00351	4.60563	0.000496	0.4959	0.00703
416.0	0.4997	0.00390	4.60487	0.000496	0.4958	0.00780
416.0	0.5006	0.00680	4.57548	0.000494	0.4938	0.01358
416.0	0.5024	0.01020	4.55218	0.000492	0.4922	0.02030
416.0	0.4994	0.01360	4.46103	0.000486	0.4858	0.02723
416.0	0.4984	0.01700	4.39851	0.000481	0.4814	0.03411
416.0	0.4972	0.02040	4.33323	0.000477	0.4768	0.04103
416.0	0.4989	0.02380	4.30954	0.000475	0.4751	0.04771
416.0	0.4982	0.02720	4.25332	0.000471	0.4710	0.05460
416.0	0.4980	0.03060	4.20350	0.000467	0.4674	0.06145
541.0	0.6472	0.00039	4.57901	0.000647	0.6468	0.00060
541.0	0.6456	0.00078	4.55629	0.000645	0.6448	0.00121
541.0	0.6500	0.00117	4.60109	0.000649	0.6488	0.00180
541.0	0.6500	0.00156	4.59736	0.000648	0.6485	0.00240
541.0	0.6482	0.00195	4.57312	0.000646	0.6463	0.00301
541.0	0.6484	0.00234	4.57006	0.000646	0.6460	0.00361
541.0	0.6481	0.00273	4.56283	0.000645	0.6454	0.00421
541.0	0.6488	0.00312	4.56631	0.000646	0.6457	0.00481
541.0	0.6474	0.00351	4.54627	0.000644	0.6439	0.00542
541.0	0.6479	0.00390	4.54801	0.000644	0.6440	0.00602
541.0	0.6483	0.00680	4.52071	0.000642	0.6415	0.01049
541.0	0.6440	0.01020	4.43661	0.000634	0.6338	0.01584
541.0	0.6499	0.01360	4.46307	0.000636	0.6363	0.02093
541.0	0.6464	0.01700	4.38899	0.000629	0.6294	0.02630

Table 4.6: Test conditions for 688 kg/m^2s

Mass flux based on min area (kg/m^2s)	Total mass flow rate (kg/s)	Air mass flow rate (kg/s)	Water flow rate (Voltage)	Water volume flow rate (m^3/s)	Water mass flow rate (kg/s)	Quality (-)
688.0	0.83204	0.00039	4.34437	0.000832	0.83204	0.00047
688.0	0.82567	0.00078	4.29019	0.000825	0.82567	0.00094
688.0	0.82912	0.00117	4.31464	0.000828	0.82912	0.00141
688.0	0.82848	0.00156	4.30644	0.000827	0.82848	0.00188
688.0	0.83171	0.00195	4.32919	0.000830	0.83171	0.00234
688.0	0.82785	0.00234	4.29519	0.000826	0.82785	0.00283
688.0	0.82764	0.00273	4.29034	0.000825	0.82764	0.0033
688.0	0.8266	0.00312	4.27894	0.000823	0.8266	0.00377
688.0	0.82719	0.00351	4.28057	0.000824	0.82719	0.00424
688.0	0.82499	0.0039	4.25999	0.000821	0.82499	0.00473
688.0	0.82685	0.0068	4.25171	0.000820	0.82685	0.00822
688.0	0.82984	0.0102	4.24851	0.000820	0.82984	0.01229
688.0	0.82427	0.0136	4.17772	0.000811	0.82427	0.0165
688.0	0.82257	0.017	4.13793	0.000806	0.82257	0.02067
688.0	0.82492	0.0204	4.12971	0.000805	0.82492	0.02473

The two-phase pressure drop tests used the purging system to remove any residual air before the pressure drop across the bundle was measured. The purging system consisted of solenoid valves and a purging line of water to remove any residual air in the polyurethane tubes that connects the pressure taps of the bundle through the solenoid valves to the pressure transducer. The LabVIEW program, *PURGING*, described in Section 3.3.6, was used for this purpose. The water flow rate was adjusted using the recirculation valve *A* in Figure 3.1. The flow from the positive displacement pump was reasonable constant. By closing this valve, more flow passed through valve *B*, the flow nozzle and into the test section. The water pressure, had to be made high enough to remove the air in the sampling lines. If the pressure in the purging system was low, valve *B* was closed slightly so that the pressure increased. The pressure gauge in the purging line was maintained between 1.0 bar and 4.0 bar to ensure the purging pressure was sufficient to purge the air throughout the experiment.

The sampling rate and the time for closing and opening the solenoid valves of the purging system were based on trials. It was found that ten seconds was sufficient to purge purging valves, *A* and *B*, two solenoid valves and the lines completely. Five seconds were required to reach a stable condition before the pressure drop, water flow rate, pressure and temperatures data were taken using the LabVIEW program, *TWO-PHASE FLOW* describe in Section 3.3.6. The number of samples and the rate required for pressure drop measurements was fixed at 10000 and 1000 Hz respectively. The water flow rate reading stabilized within 500 readings. No air was observed to enter the system during data recording.

Tests were conducted by setting the required air flow rate and adjusting the water flow rate to the required condition. The flow resistance in the test facility was dependent on these flow rates so that the exact conditions were achieved by making minor adjustments to each as appropriate. The *TWO-PHASE FLOW* program was used to monitor the desired water flow rate as the front panel displayed the new water flow rate each time valve A was turned. The air flow rate was read manually. When the desired conditions were achieved, the water flow rate, pressure and temperature were collected through a data logger connected to a PC controlled by the *TWO-PHASE FLOW* program. Depending on the data set to be taken, measurements of pressure drop or void fraction were made.

The required water flow rate to the test section was adjusted by observing the electrical current, *I*, that ranged between 4 and 20 mA until the required pressure drop across the flow nozzle was reached. The current passed through a 250Ω resistor to give a voltage between 1 and 5 *V*. That was read by the PC. Thus,

$$I = 20 - 4 \times (5 - V) \tag{4.1}$$

where *V*, was calculated from

$$V = \frac{4 \times \Delta p}{URV} + 1 \tag{4. 2}$$

The URV was the upper range value of the pressure drop, set by the HART communicator, and *Δp* was the required pressure drop calculated from

$$\Delta p = \frac{Q^2 \rho_l [1-(A_t / A)^2]}{2(A_t C_d)^2} \qquad (4.\ 3)$$

in which Q, was the required flow rate, A_t and A were the throat and upstream areas of the nozzle and C_d was the discharge coefficient of the nozzle, determined by Stuart [53].

Rearrange Equation (4.3), the water flow rate, Q was obtained from;

$$Q = \sqrt{\frac{2\Delta p(A_t C_d)^2}{\rho_l [1-(A_t / A)^2]}} \qquad (4.4)$$

For example gives the mass flux of 416 kg/m^{2}s, the required water flow rate was 0.499 kg/s when a 0.0004 kg/s air flow rate was set. Using nozzle 2 with the URV set to 7000 Pa, the water flow was adjusted until the reading for liquid flow showing 4.643 *V* in the *TWO-PHASE FLOW* front panel. The measurement of pressure drop or void fraction was then taken because the desired condition had been reached.

The fluid pressure was measured at the pressure tap located between rows one and two of the test tube bundles; the 38 mm diameter in-line, 19 mm diameter in-line or 19 mm diameter staggered. The 4-20 mA current from the pressure transducer was converted to a voltage in the *TWO-PHASE FLOW* program in the signal conditioning unit. The voltage was converted to absolute pressure using Equation (4.5). The fluid pressure data was used to get the density of the gas, and thus the two-phase density, with void fraction obtained from the γ- ray densitometer.

$$p_{abs} = \frac{URV}{4}(V-1) + 101325 \qquad (4.5)$$

The pressure reading was always maintained between 1.0 to 5.0 Volt to ensure accuracy. This was achieved by setting the LRV and URV using the HART 375 Field Communicator.

The pressure reading was observed in the *TWO-PHASE FLOW* program during the test. If the reading was below 1.0 or greater than 5.0, the URV and the LRV was changed until the voltage was ranged between 1.0 and 5.0 Volt. Further checks were made by analyzing the average voltage in a spreadsheet, ensuring that the voltage was within the range. Three readings were taken for each condition to get better accuracy and ensure repeatability. APPENDIX A shows the LRV and URV used for pressure drop, water flow rate and pressure measurements.

The HART 375 Field Communicator, described in Section 3.3.2, was capable of set two a negative value of pressure LRV. It was not set to 0 Pa as used by Bamardouf [51] for his pressure drop tests. Sub-zero LRV's were necessary for the low gravity and high frictional pressure drops obtained at higher mass fluxes, making the total pressure drop higher than the liquid pressure head. Therefore, in this research, two mass fluxes, 541 kg/m^2s and 688 kg/m^2s, of Bamardouf [51] were repeated using a negative pressure drop LRV to get the correct pressure drop. Zero LRV out of the negative values giving an incorrect reading. Note that in APPENDIX A, the LRVs and URVs were always changing to accommodate the increase in mass flux while maintaining accuracy. The transducer pressure was calculated from

$$P_{transducer} = \frac{URV}{4}(V-1) - \frac{LRV}{4}(V-5) \tag{4.6}$$

The equation used to calculate the pressure drop changed according to the connection of the solenoid valves. If the solenoid valve line was connected to the high end of the pressure transducer, the pressure drop was obtained by

$$\Delta P_{\mathrm{high}} = \rho g h - P_{transducer} \tag{4.7}$$

If the solenoid valve line that connected to the low end of pressure transducer, the pressure drop was calculated from

$$\Delta P_{\mathrm{low}} = \rho g h + P_{transducer} \tag{4.8}$$

For example, in the 19 mm in diameter in-line bundle, the solenoid valves used were numbered 1 and 8. For a mass flux of 25 kg/m^2s, the solenoid valve number 1 was connected to the low end of the transducer and the solenoid valve number 8 was connected to the high end. The pressure drop for the bundle was obtained from Equation (4.7). For a mass flux of 541 kg/m^{2}s, the pressure transducer ends were switched. The pressure drop was therefore calculated from Equation (4.8). The connections to the pressure transducer were changing depending on the mass flux used. Those used are included in APPENDIX A.

4.1.2 Pressure drop transducer calibration checks

The pressure drop transducer was checked by setting a known pressure head in the bundle, the pressure drop created when the sampling lines and bundle were filled with water and the pressure drop when the sampling lines were full of water and the bundle was full of air. The HART 375 Field Communicator was used to confirm the tests and the setting of URV and LRV. LabVIEW program, *TWO-PHASE FLOW* was used to record the data. The pressure head in the 38 mm diameter inline bundle was 3433.5 Pa, in the 19 mm diameter in-line bundle it was 3188.25 Pa and in the 19 mm staggered bundle it was 2624.18 Pa. These pressure drops corresponded to the water height across the pressure taps of 0.35 m, 0.325 m and 0.2675 m respectively. The pressure head was calculated from

$$P_{head} = \rho g h \tag{4.9}$$

where ρ is the water density, g is the gravitational acceleration and h is the height of the water. The water filled bundle gave a pressure drop of zero.

The HART 375 Field Communicator was used to calibrate the LRV, URV and the damping time constant. The damping was set to 0.8 ms. Once the static head of water in the bundle was confirmed and both tests were correct, the two-phase pressure drop test was carried out. The calibration of pressure drop check for in-line bundle with 19 mm tubes is given as an example.

The first test was made when only-water was in the bundle. The bundle was filled with water to the height of 0.325 m, just enough to cover the height above the top solenoid valve, number 8, the same height as the pressure tap. The water was static when the reading was taken, using the *TWO-PHASE FLOW* program to record the pressure drop voltage. The transducer pressure drop was zero, which became 3188.25 Pa through Equation (4.7) or (4.8).

The second test was made when air filled the bundle. The transducer pressure drop should show a 3188.25 Pa, which became 0 Pa through Equation (4.7) or (4.8). For each test, the solenoid valves 1 and 8 were purged with water and prior to the pressure drop reading being taken by the *TWO-PHASE FLOW* program.

Table 4.7 shows the result of the pressure head checks. The table show that the pressure head was 3187 Pa for the water test, i.e. a difference of only 1.25 Pa when compared to the set head of 3188.25 Pa, or 0.04%. Meanwhile, the air test gave a pressure drop of 11.13 Pa, a difference is 11.12 Pa when compared to set value of 0 Pa. These checks show that the calibration of the pressure drop transducer in tube bundle had small errors and gave reliable pressure drop reading.

Table 4.7: Result of calibration of pressure head in 19 mm in diameter in-line bundle

	Voltage	URV (pa)	LRV (pa)	$P_{transducer}$ (pa)	P_{head} (pa)	ΔP (pa)
Water-only	1.890	3500	-1000	1.25	3188.25	3187.00
Aor-only	4.713	3500	-1000	3177.13	3188.25	11.12

4.1.3 Calibration check of the local pressure transducer

The local fluid pressure was measured at the pressure tap located between rows two and three of the heat exchanger using the Rosemount 2088 gauge pressure transmitter. This pressure transducer checked against using a Bourdon Gauge. Tests were conducted at a mass flux of 688 kg/m^2s in the 38 mm diameter in-line bundle. The fluid pressures for this bundle are shown in Figure 4.4.

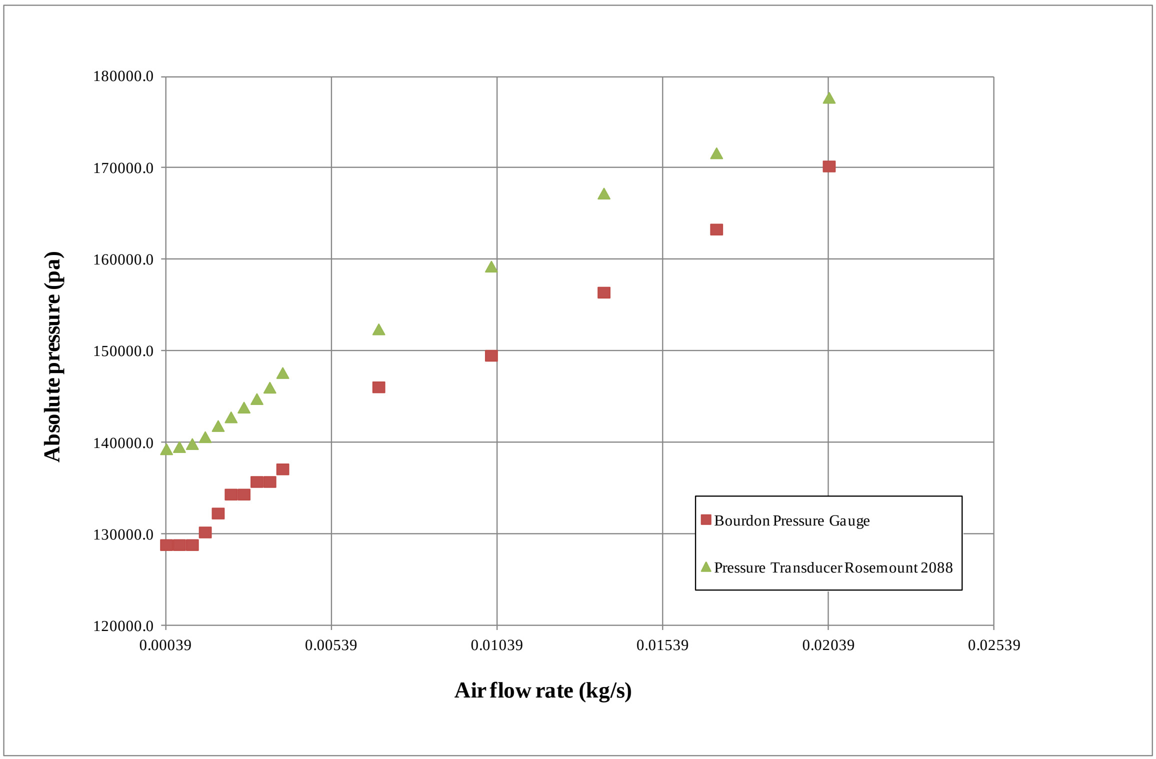

Figure 4.4: Result of measurement of local fluid pressure using Bourdon Pressure Gauge and Rosemount 2088 Gauge Pressure

The absolute pressure measurements made by the Bourdon Gauge and the Rosemount 2088 Gauge Pressure were compared. The RMS error was 6.97% and the mean error was 6.85%. Both pressure gauges showed a good capability of measuring the local fluid pressure. The Rosemount 2088 pressure transducer was used to measure the local fluid pressure in this research as it is more likely that the Bourdon pressure gauge was less accurate.

4.1.4 Pressure drop consistency check

The pressure drop consistency check was done in the 38 mm diameter in-line tube bundle. The tests were repeated twice to ensure repeatability. The mass flux of 105 kg/m^2s was chosen. The results were compared to measured pressure drops of Bamardouf [51]. The test conditions are shown in Table 4.8. Figure 4.5 shows the pressure drop consistency check.

Table 4.8: Test condition of pressure drop commissioning at mass flux of 105 kg/m^{2}s at 38 mm in diameter in-line bundle

Air Rotameter	Air flow rate (%)	Mass flux based on min area (kg/m^{2}s)	Mass flux (kg/m^{2}s)	Total mass flow rate (kg/s)	Air mass flow rate (kg/s)	Water flow rate (Voltage)	Water volume flow rate (m^3/s)	Water mass flow rate (kg/s)	Quality (-)	Pressure drop		Pressure		Water flow rate		Water nozzle
										LRV	URV	LRV	URV	LRV	URV	
Rotameter 1	10	105.0	25.2	0.12639	0.00039	4.178	0.00013	0.126	0.0031	0	3000	0	100000	0	12000	3
	20	105.0	25.2	0.12578	0.00078	4.165	0.00013	0.125	0.0062	0	3000	0	100000	0	12000	3
	30	105.0	25.2	0.12617	0.00117	4.168	0.00013	0.125	0.0093	0	4000	0	100000	0	12000	3
	40	105.0	25.2	0.12656	0.00156	4.140	0.00013	0.125	0.0123	0	4000	0	100000	0	12000	3
	50	105.0	25.2	0.12595	0.00195	4.124	0.00012	0.124	0.0155	0	4000	0	100000	0	12000	3
	60	105.0	25.2	0.12634	0.00234	4.111	0.00012	0.124	0.0185	0	4000	0	100000	0	12000	3
	70	105.0	25.2	0.12673	0.00273	4.082	0.00012	0.124	0.0215	0	4000	0	100000	0	12000	3
	80	105.0	25.2	0.12612	0.00312	4.051	0.00012	0.123	0.0247	0	4000	0	100000	0	12000	3
	90	105.0	25.2	0.12651	0.00351	4.046	0.00012	0.123	0.0277	0	4000	0	100000	0	12000	3
	100	105.0	25.2	0.1259	0.00390	4.028	0.00012	0.122	0.0310	0	4000	0	100000	0	12000	3
Rotameter 2	20	105.0	25.2	0.1258	0.00680	3.875	0.00012	0.119	0.0541	0	3000	0	100000	0	12000	3
	30	105.0	25.2	0.1262	0.01020	3.751	0.00012	0.116	0.0808	0	2800	0	100000	0	12000	3
	40	105.0	25.2	0.1266	0.01360	3.512	0.00011	0.113	0.1074	0	2800	0	100000	0	12000	3
	50	105.0	25.2	0.126	0.01700	3.378	0.00011	0.109	0.1349	0	2800	0	100000	0	12000	3
	60	105.0	25.2	0.1264	0.02040	3.292	0.00011	0.106	0.1614	0	2800	0	100000	0	12000	3
	70	105.0	25.2	0.1258	0.02380	3.170	0.0001	0.102	0.1892	0	2800	0	100000	0	12000	3
	80															
	90															
	100															

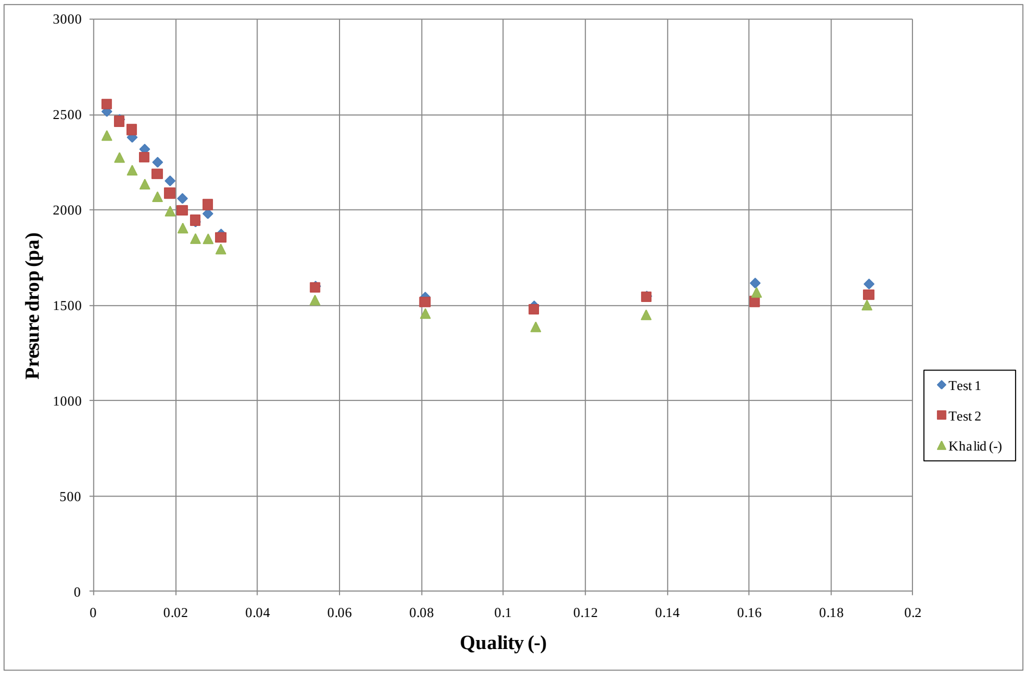

Figure 4.5: Pressure drop measurement in 38 mm in diameter in-line bundle at 105 kg/m^{2}s

Both tests show reasonable agreement. The mean difference is 6.14% and the RMS is 6.69%. This shows that the experiment procedure produces reproducible results that give a small deviation.

4.1.5 Experimental procedures of two-phase pressure drop measurement

The procedure used to obtain the two-phase pressure drop is as below;

1) The LabVIEW programs, the *TWO-PHASE FLOW,* was started to monitor the pressure drop, pressure, water flow rate and temperatures prior to data collection.
2) The LRVs and URVs were set for the pressure drop, pressure and water flow rate transducers. (*Notes: The LRV and URV for the pressure and water flow rate transducers were fixed for each mass flux, 25-688 kg/m^{2}s. The pressure drop transducer, LRV and URV were changing based on the total mass flow rate for each test conditions, see APPENDIX A)*
3) Valve A was opened and valve B closed, Figure 3.1.
4) The water pump was switched on.
5) Valve B was closed to allow water into the test section i.e. the tube bundle.
6) Rosemount 3051 water flow rate differential pressure transducer was purged with water by opening both screws at the sides.
7) The Rosemount 3051 pressure drop differential pressure transducer was purged to remove any air from it.
8) Valve A was adjusted to ensure the pressure at the purging line was between 1.0 and 4.0 bar.
9) The compressor was switched on.
10) The valve downstream of the required air rotameter was adjusted manually to the desired air flow rate.
11) The water flow was adjusted by turning Valve B to set the required water flow. The water flow was checked using the *TWO-PHASE FLOW* program.
12) The Rosemount signal conditioning box displays were monitored to ensure that the pressure drop, pressure and water flow readings were between 4 and 20 mA showing the desired reading.
13) The *PURGING* program was started and all the sampling lines were purged by opening solenoid valves A and B and the two solenoid valves used for the pressure drop measurements. After 10 seconds, the solenoid valves were closed.

14) The *TWO-PHASE FLOW* program was used to open the solenoid valves for pressure drop measurements, wait until the flow stabilized in 5 seconds and take the readings.
15) The pressure drop, pressure, water flow rate and temperatures readings were recorded using the *TWO-PHASE FLOW* program and stored in a Text File.
16) Checks were done after each measurement to ensure the voltage was between 1.0 and 5.0 Volt using a spreadsheet.
17) The purging and measurement were repeated three times to ensure accuracy and repeatability.
18) Step 10 to 17 were repeated for the next test.
19) Valve B was opened to allow water out from the test section i.e. the tube bundle after the tests were completed.
20) The valve downstream of the air rotameter was closed manually to stop the air supply.
21) The compressor and the water pump were shut down.

4.2 Void fraction measurements using the gamma ray densitometer

4.2.1 Operation condition

Void fraction measurements were made using a single beam, gamma-ray densitometer with isotope Americium (Am) 241. This collimated low energy source projected a beam 10 mm in diameter through the flow parallel to the tubes, onto a photomultiplier tube. A PC card-based, electronically controlled pulse counter was used to measure the radiation incident on the photomultiplier. The operating conditions used were nominally the same as the pressure drop tests, i.e. the mass fluxes of $25 \leq G$ based on min area ≤ 688 kg/m^{2}s and qualities of $0.00047 < x < 0.57$, as described in Section 4.1.1.

Prior to testing, the gamma-ray densitometer was set at the desired locations in the tube bundle. In the 38 mm in-line bundle, three locations were used, locations where maximum and minimum gaps occurred. Measurements were made near the tube on row 7 central column. The gap south east of this tube, which was the maximum gap, south of this tube which was the minimum gap; east of this tube which was the minimum gap. Figure 4.6 shows the locations of the void fraction measurements in the bundle. These three tests were carried out separately.

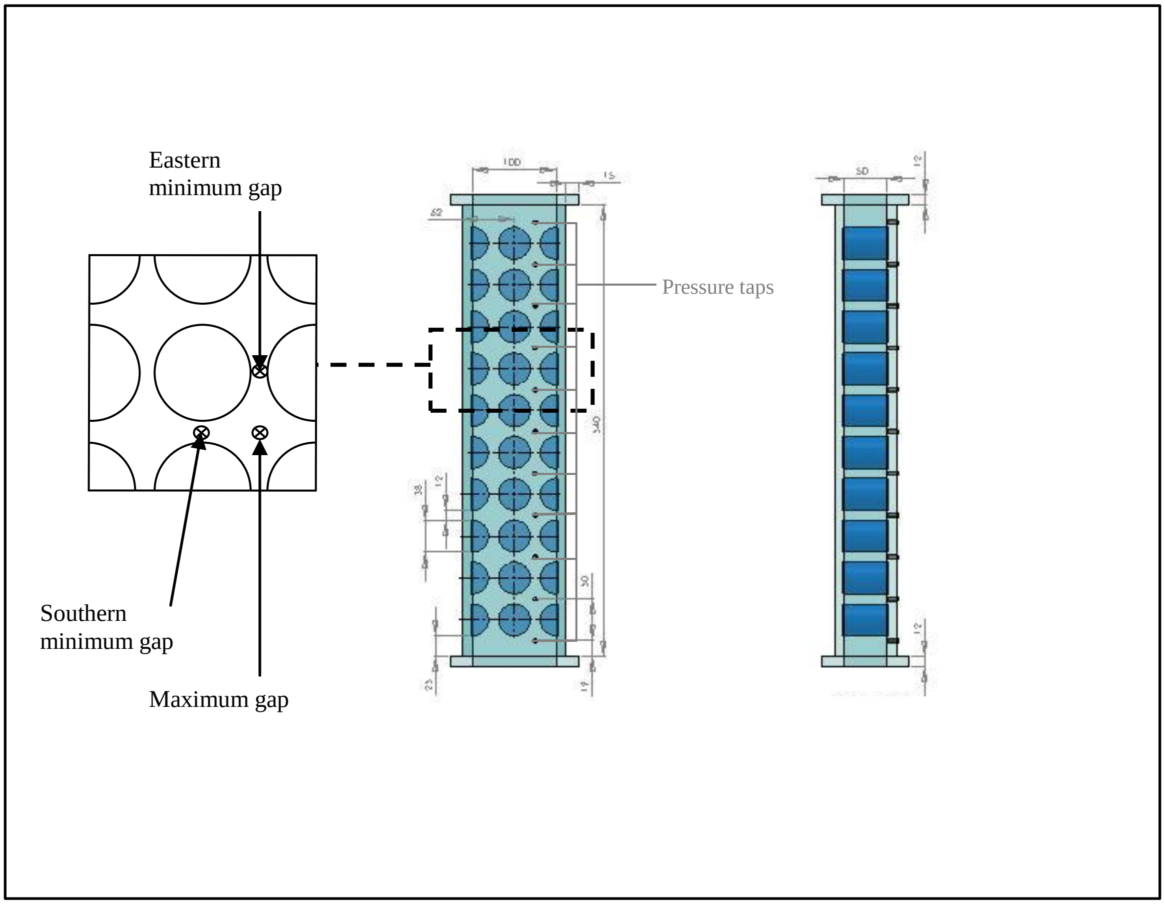

Figure 4.6: Location of void fraction measurements in the 38 mm in-line tube bundle

In the 19 mm diameter in-line bundle, four locations were used for void fraction measurements in maximum and minimum gaps. The central tube in row thirteen was the central location. Void fraction measurements were made north east, which was a maximum gap and at minimum gaps north, east and west of the central tube. These four tests were carried out separately. Figure 4.7 shows the locations of the void fraction measurements in the bundle.

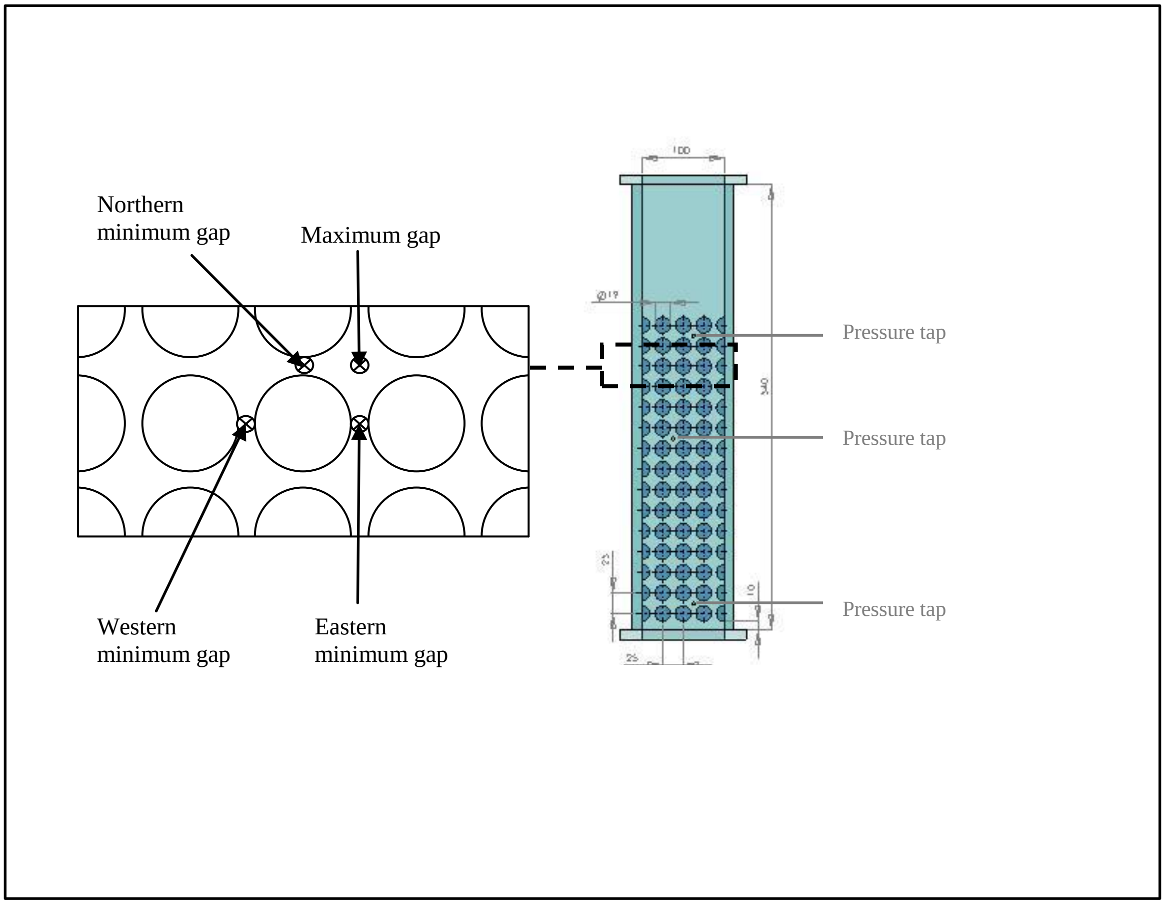

Figure 4.7: Locations of void fraction measurements in 19 mm in-line tube bundle

In the 19 mm diameter staggered bundle, the central tube at row sixteen was the central location. Void fraction measurements were made east and south of the central tube. Both tests were done separately. The locations for the void fraction measurements in this bundle is shown in Figure 4.8.

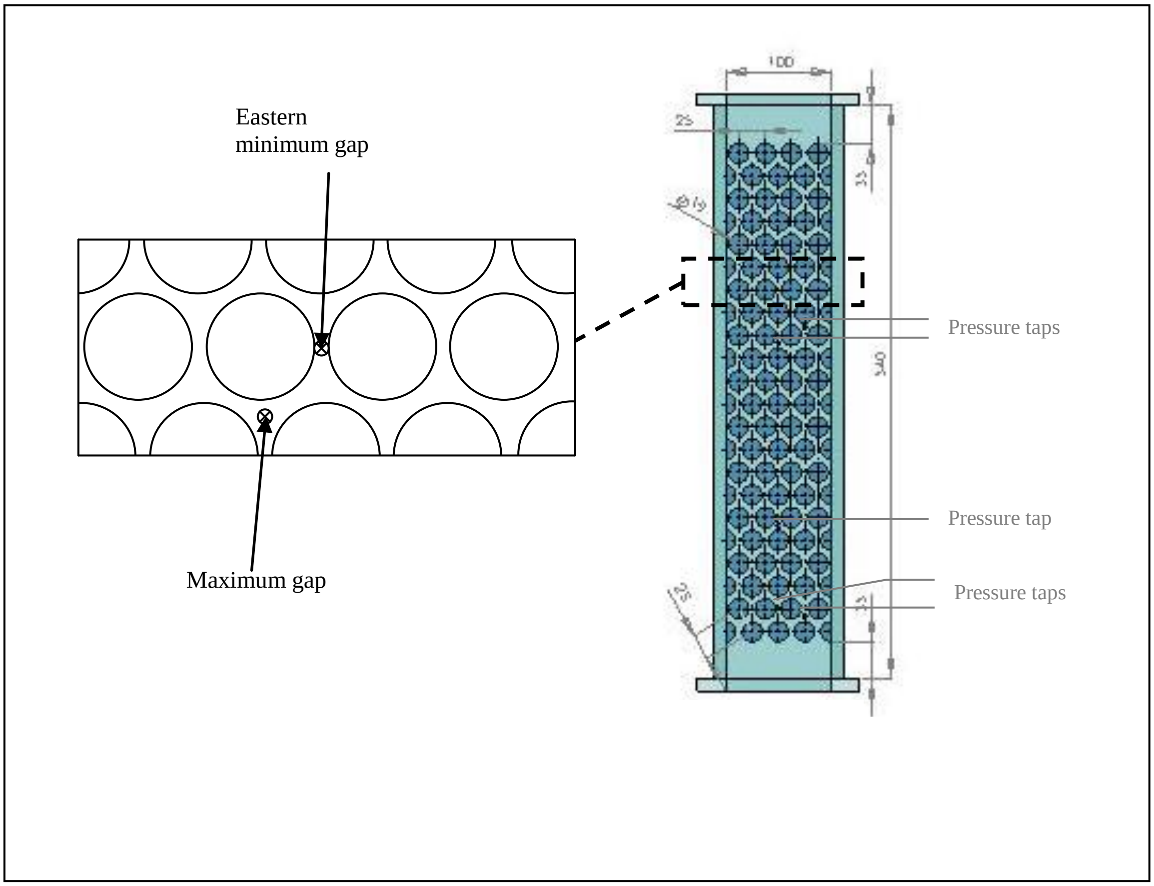

Figure 4.8: Locations of void fraction measurements in 19 mm staggered tube bundle

Background readings, I_B, were taken prior to the Am241 source being installed. After the source was installed, the air-only gamma-ray intensity readings, I_G, were taken. After the water flow in the bundle had been set, the water-only gamma-ray intensity readings, I_L, were taken. The two-phase gamma-ray intensity readings, $I_{2\theta}$, were obtained after the test conditions had been set. All readings were recorded from the electronic counter within the PC via the densitometer's software. One hundred readings were taken over a period of 100 s, allowing a representative average of each data to be achieved. The void fraction, α, is defined as the ratio of the flow area occupied by gas to the total flow area and was found from these measurements through (Patrick and Swanson [54])

$$\alpha = \frac{\ln(I_{2\theta} - I_B) - \ln(I_L - I_B)}{\ln(I_G - I_B) - \ln(I_L - I_B)} \tag{4.10}$$

Safe operation of the gamma-ray densitometer required strict adherence to the University Health and Safety Policy guidelines. These guidelines must be fully understood before handling the gamma-ray source. These were as follows:-

1. The attendance at an officially accredited Radiation Protection Course on the safe handling of the ionising radiation source prior to using the source.
2. A mandatory risk assessment of all working practices and a scheme of work was submitted to the University Radiation Protection Supervisor.
3. The usage of the source was logged in the record book.
4. A designated Controlled Area, encompassing the test facility with warnings against entrance of unauthorised personnel was marked out.
5. The light hazardous warning sign was switched on prior to operating the gamma-ray source being placed in the rig.
6. An appropriate facility for the safe storage of the 241Am source was used when it was not in use.
7. The pre and post-test monitoring of radiation levels within the control area using a Geiger counter.
8. Rig operator wore radiation measuring film badges on the chest and finger when the source was being used. The chest badge was put on the outer clothing while the finger badge was worn at any fingers when handling the gamma-ray source.
9. The 241Am source was lifted up to the test section using a rope and pulley. Carrying the source up a ladder was too dangerous.
10. A ratchet was used to open the lid of the source to make minimum use of unprotected fingers.
11. The source was always pointed out and away from the body when the lid was open.

4.2.2 Void fraction experiment using gamma-ray source experiment commissioning

The capability of the gamma-ray densitometer for measuring void fraction was tested by comparing the results with the correlation of Feenstra et al. [3]. Tests were carried out at a fixed water volume flow rate of 0.000499 m^3/s. The mass flux based on minimum area between the tubes, was varied from 416 – 427 kg/m^2s. The quality range was 0.00078 –

0.002653. The gas mass flow rate was varied from 0.00039-0.0102 kg/s while the water mass flow rate was fixed at 0.4999 kg/s. The commissioning void fraction measurement test using gamma-ray source was repeated three times to confirm accuracy and repeatability. The test condition is shown in Table 4.9.

Figure 4.9 shows the comparison between measured void fraction and the Feenstra et al. correlations [3]. The graph shows that the void fraction measurements using gamma-ray densitometer were repeatable and follow a similar trend to Feenstra et al. [3]. The root mean square (rms) difference is 18.33%, the mean is 17.6% and most predictions lie between upper and lower bounds of ±30%. This is acceptable and show the void fraction measurements using this method are reliable and compatible and that the experiment procedures and methods used are appropriate.

Table 4.9: Test condition for void fraction experiment using gamma-ray source

Air mass flow rate (kg/s)	Test 1 Quality (-)	Test 1 Mass flux min area (kg/m^{2}s)	Test 1 Void fraction measured (-)	Test 1 Void fraction of Feenstra et al [3] (-)	Test 2 Quality (-)	Test 2 Mass flux min area (kg/m^{2}s)	Test 2 Void fraction measured (-)	Test 2 Void fraction of Feenstra et al [3] (-)	Test 3 Quality (-)	Test 3 Mass flux min area (kg/m^{2}s)	Test 3 Void fraction measured (-)
0.00039	**0.00078**	**416**	**0.202**	**0.157**	**0.00078**	**416**	**0.219**	**0.157**	**0.00078**	**416**	**0.199**
0.00078	**0.00156**	**416**	**0.305**	**0.257**	**0.00156**	**416**	**0.309**	**0.257**	**0.00156**	**416**	**0.306**
0.00117	**0.00234**	**417**	**0.383**	**0.329**	**0.00234**	**417**	**0.381**	**0.329**	**0.00234**	**417**	**0.373**
0.00156	**0.00312**	**417**	**0.427**	**0.383**	**0.00312**	**417**	**0.442**	**0.383**	**0.00312**	**417**	**0.437**
0.00195	**0.00389**	**417**	**0.499**	**0.426**	**0.00389**	**417**	**0.489**	**0.426**	**0.00389**	**417**	**0.491**
0.00234	**0.00467**	**418**	**0.538**	**0.462**	**0.00467**	**418**	**0.547**	**0.462**	**0.00467**	**418**	**0.551**
0.00273	**0.00544**	**418**	**0.550**	**0.491**	**0.00544**	**418**	**0.579**	**0.491**	**0.00544**	**418**	**0.558**
0.00312	**0.00621**	**418**	**0.600**	**0.516**	**0.00621**	**418**	**0.610**	**0.516**	**0.00621**	**418**	**0.602**
0.00351	**0.00698**	**419**	**0.619**	**0.538**	**0.00698**	**419**	**0.629**	**0.538**	**0.00698**	**419**	**0.630**
0.0039	**0.01344**	**422**	**0.786**	**0.648**	**0.01344**	**422**	**0.783**	**0.648**	**0.00945**	**420**	**0.717**
0.0068	**0.02003**	**424**	**0.823**	**0.712**	**0.02003**	**424**	**0.830**	**0.712**	**0.01344**	**422**	**0.794**
0.0102	**0.02653**	**427**	**0.841**	**0.749**	**0.02653**	**427**	**0.852**	**0.749**	**0.01609**	**423**	**0.798**

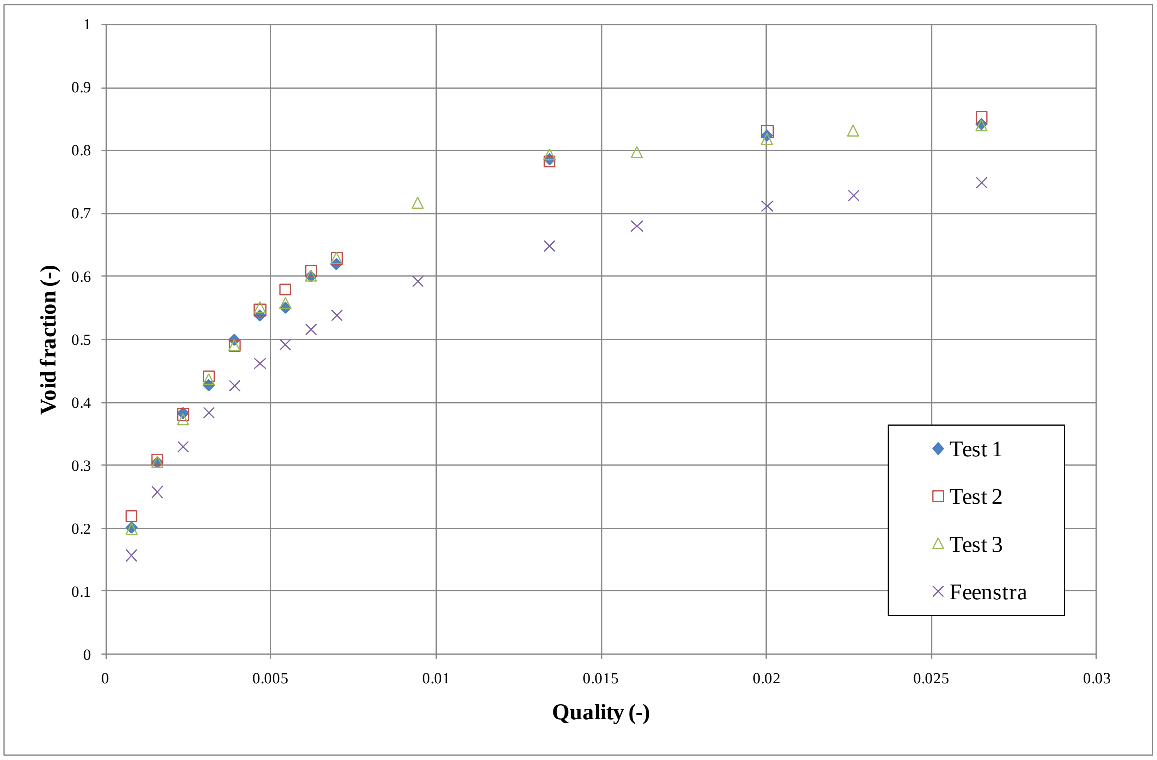

Figure 4.9: Void fractions measurement in 38 mm in diameter bundle and predictions of Feenstra et al. [3]

4.2.3 Experimental procedures for void fraction measurement with the gamma ray densitometer

The procedures for measuring void fraction with the gamma-ray densitometer was as follows;

1) Safe operation procedures for the gamma-ray densitometer was followed at all times.
2) The densitometer's software was started.
3) Readings of background radiation intensity, no source present, I_B, were taken.
4) The Am241 source was carried from safe storage to the rig using the shortest route.
5) The source was mounted and fixed in the rig, Figure 3.35.
6) Readings of intensity of gamma-ray radiation, I_G, were taken.
7) The water pump was switched on, with valves A and B open, Figure 3.1.
8) Valve B was set to fill the test section, i.e. the tube bundle, with water.

9) Readings of intensity of gamma-ray radiation with water-only, I_L were taken.
10) The LabVIEW programs, *TWO-PHASE FLOW*, was started to monitor the pressure, water flow rate and temperatures prior to testing.
11) The LRV and URV were set for pressure and water flow rate. For the *LRV* and *URV* for pressure and water flow rate were fixed for each mass fluxes, 25-688 kg/m^{2}s, refer to APPENDIX A for the test conditions.
12) The current displays on the pressure transducer signal conditioning boxes for pressure and water flow rate, were checked to ensure that the current reading was between 4 and 20 mA.
13) Rosemount 3051 water flow rate differential pressure transducer was purged with water by opening both screws at the sides.
14) The compressor was switched on.
15) The valve downstream of the air rotameter, Figure 3.1, was adjusted to give the desired air flow rate.
16) The water flow was set by adjusting Valve B. The water flow was checked via the *TWO-PHASE FLOW* program.
17) Once the flow stabilized which took about 5 seconds, the *TWO-PHASE FLOW* program took and stored the readings in a Text File. Simultaneously, the gamma-ray densitometer counter was started to obtain the reading of the intensity of the two-phase, *I*.
18) Step15 to 16 were repeated for the next reading.
19) Valve B was opened to allow water out from the test section i.e. the tube bundle after the tests were completed.
20) The valve downstream of the air rotameter was closed manually to stop the air supply.
21) The compressor and the water pump were shut down.

CHAPTER 5 - VOID FRACTION MEASUREMENT USING CONDUCTIVE PROBE

The double-sensor conductivity probe technique is commonly applied to two-phase flow experiments to measure local flow parameters such as void fraction and interfacial area concentration. The double-sensor conductivity probe is used basically a phase identifier in the two-phase mixture. The double sensor probe diagrams are shown in Figures 5.1 – 5.3.

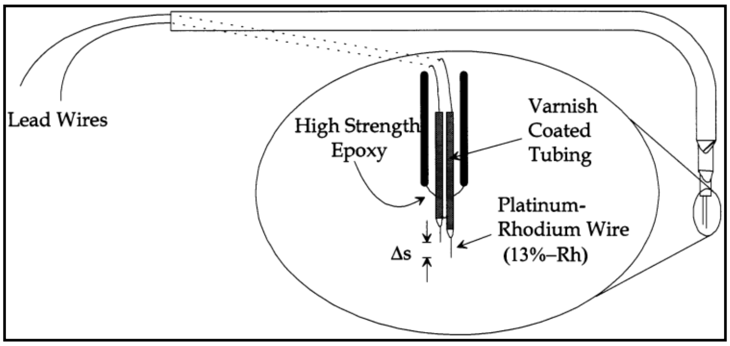

Figure 5.1: Schematic diagram of the double sensor probe [55,56].

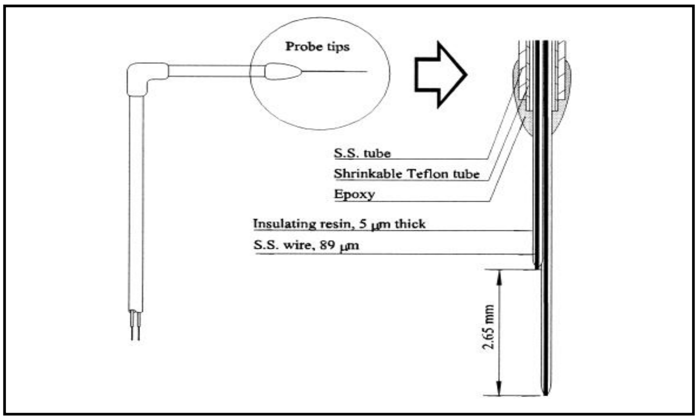

Figure 5.2 Schematic diagram of the double sensor conductivity probe [57]

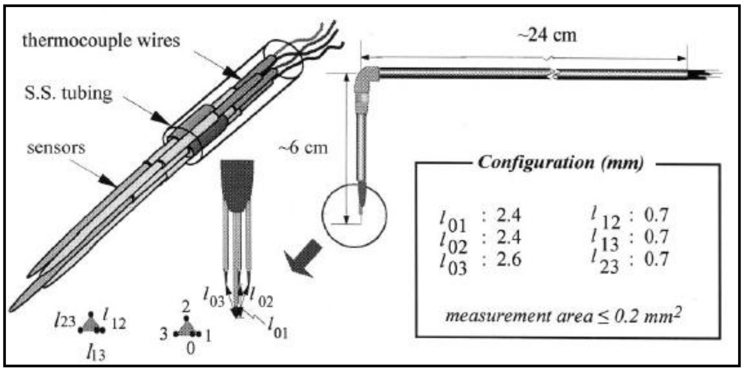

Figure 5.3: Schematic diagram of the four sensor conductivity probes [58]

Basically, the probe is designed with two thin electrodes mostly covered by an insulating resin but exposed at the tips. The probe is submerged in the two phase flow stream with the tips pointing in the direction of the stream; the first electrode found in the direction of motion is denoted as the front tip and the second one as the back tip. The tip of each electrode measures the impedance between the probe tip and the common ground. Due to the large difference in conductivity between the liquid phase and the gas phase, the impedance signal rises sharply when a bubble passes through one of the sensor tips. The double sensor conductivity probe provides two signals, one for each electrode. When a bubble touch the front tip, the impedance signal of this electrode rises sharply, when this same bubble arrives to the second tip then the impedance signal provided by the second electrode also rises sharply.

The information recorded from each signal gives the number of bubbles that hit the sensor, the time that the sensor was exposed to the gas phase, and the relative time between the bubble hitting the upstream and downstream sensors. The time-averaged interfacial velocity, u is calculated by taking into account the distance between the tips of the upstream and downstream sensor and the time difference between the upstream and downstream signal. The void fraction is simply the accumulated time the sensor is exposed to the gas phase divided by the total sampling time of the sensor.

Zhao et al. [59] used the ideal square-wave signal, shown in Figure 5.4, to calculate the number of bubbles that hit the sensor, N_t, which can be measured by counting the number of pulses in the signal.

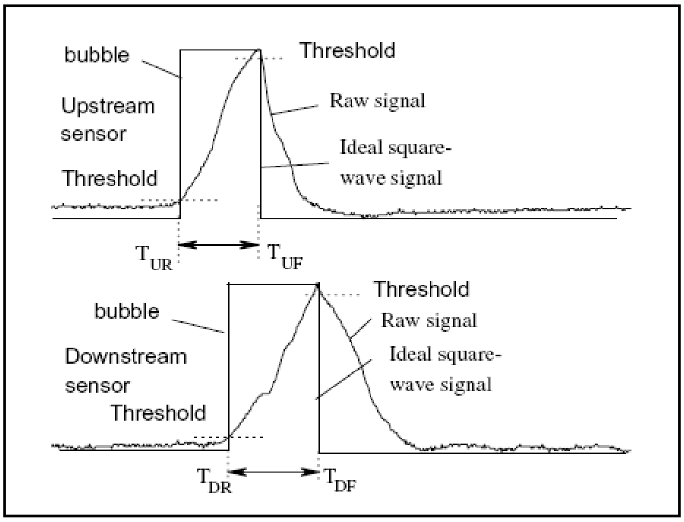

Figure 5.4: Illustration of signals before and after the signal processing [59]

The interfacial velocity in the main flow direction of each interface can be obtained by the distance between the two tips of the double-sensor probe, Δs, and the time delay between the upstream signal, T_{UR} and downstream signal, T_{DR} as below

$$u = \frac{\Delta s}{(T_{DR} - T_{UR})} \tag{5.1}$$

From the local instant formulation of the two-fluid model, the local time-averaged void fraction can be expressed as the ratio between the accumulated pulse widths of the upward or downward sensor and the total sampling time, Δt, during the sampling period.

$$\alpha = \frac{1}{\Delta t} \sum_{j}^{Ns} \left(T_{DR} - T_{UR} \right)_j \tag{5.2}$$

The void fraction can also be calculated by using a simpler equation from Aprin et al. [49]. The void fraction α is defined as the ratio of time, t_G over the total sampling time Δt, where t_G is the total duration of all high level signals when the probe detects vapour.

$$\alpha = \frac{t_G}{\Delta t} \tag{5.3}$$

There are many specifications of the double-sensor developed by many researchers [49, 55-63]. These are shows in Table 5.1. The material for the tips are common thermocouple metals and the distance between the upstream and downstream tips is around 2~4 mm. These distances do not effect the bubble velocity measurement much because it is strongly influenced by both the orientation of bubble velocity and probe spacing relative to the bubble size, according Wu and Ishii [57] and Wu et. al [65]. However, Muñoz-Cobo et al. [66] assumed that the bubble reaches the front tip and may, or may not, reach the back tip depending on the distance between both tips other than the hitting point in the front tip and the velocity direction.

Table 5.1: Conductive probe specifications

Probe specification/ Researcher	Sensor						
	Diameter	Material	Distance between upstream and donstream tip (mm)	Exposed tip length (mm)	Diameter (mm)	Material	Angle elbow bend
Leung et al. [60]	0.120 mm	Platinum-rhodium wire (13% Rh)	2.0 - 4.0	0.24 - 0.36	3.175 OD	stainless steel	90
Hogsett and Ishii [55]	0.127 mm	Platinum-rhodium wire (13% Rh)	3.0	0.4	2.39	stainless steel	90
Hibiki et al. [56]	**0.127 mm**	Platinum-rhodium wire (13% Rh)	**2.0 - 3.0**	**0.15**	**2.39**	stainless steel	90
Wu and Ishii [57]	89.00 μm	**Stainless steel wire**	**2.65**	**N/A**	**N/A**	stainless steel	90
Hibiki and Ishii [61]	0.127 mm	Platinum-rhodium wire (13% Rh)	**2.0 - 3.0**	**0.15**	**2.39**	stainless steel	90
Kim et al. [58]	**0.130 mm**	**Gold acupunture needles**	**2.40**	**N/A**	**3.18**	stainless steel	90
Hibiki et al. [62]	0.127 mm	Platinum-rhodium wire (13% Rh)	**2.0 - 3.0**	**0.15**	**2.39**	stainless steel	90
Hibiki et al. [63]	0.100 OD mm	**Stainless steel acupunture needles**	**1.50**	**0.15**	**2.39**	stainless steel	90
Hibiki et al. [64]	0.130 mm	**Gold acupunture needles**	**2.40**	**N/A**	**N/A**	stainless steel	90
Zhao et al. [59]	0.150 mm	**Stainless steel wire**	**1.84**	**0.2**	**0.9 ID**	stainless steel	90

The measurement system consisted of a double-sensor conductivity probe, a mechanical traverser, a measurement circuit, a digital high-speed acquisition board, and the software used for signal processing. Leung et al. [60], Hogsett and Ishii [55] Hibiki et al. [56,62], Hibiki and Ishii [61] used the A-D converter, MetraByte DAS-20. Hibiki et al. [63] use the A/D converter Keithly-Metrabyte DAS-1801HC. Zhao et al. [59] use a high-speed NI PCI-6110E acquisition board and a personal computer to acquire the voltage signal of the double-sensor probe. A control program developed under NI LabVIEW software environment was used.

Hogsett and Ishii [55] showed the electrical circuit used to measure the potential difference between the exposed tip and the grounded terminal (Figure 5.5). A bias resistor, *R*B, is used to obtain the maximum voltage difference between each phase of the two-phase mixture. The presence of the bias resistor is necessary because of the various levels of cleanliness of water being used. The artificial switch in the circuit represents the state of the surrounding medium. When the switch is open, the tip is exposed to the the gas phase thus the voltage is equivalent to the supplied voltage of 5V. When the switch is closed, the tip is exposed to the liquid phase and the voltage output is lower than the voltage source.

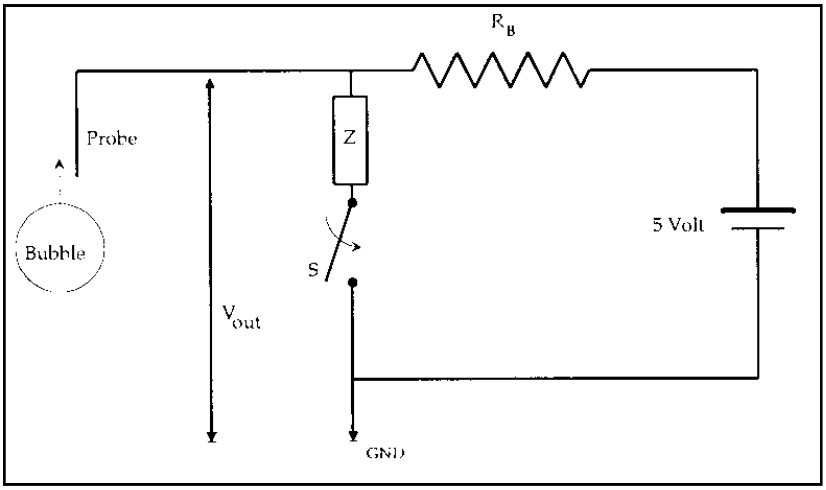

Figure 5.5: Double sensor probe circuit [55]

The difference in impedence between liquid and gas gives the voltage outputs shown in Figure 5.6 in which high and low parts correspond to gas and liquid phase respectively.

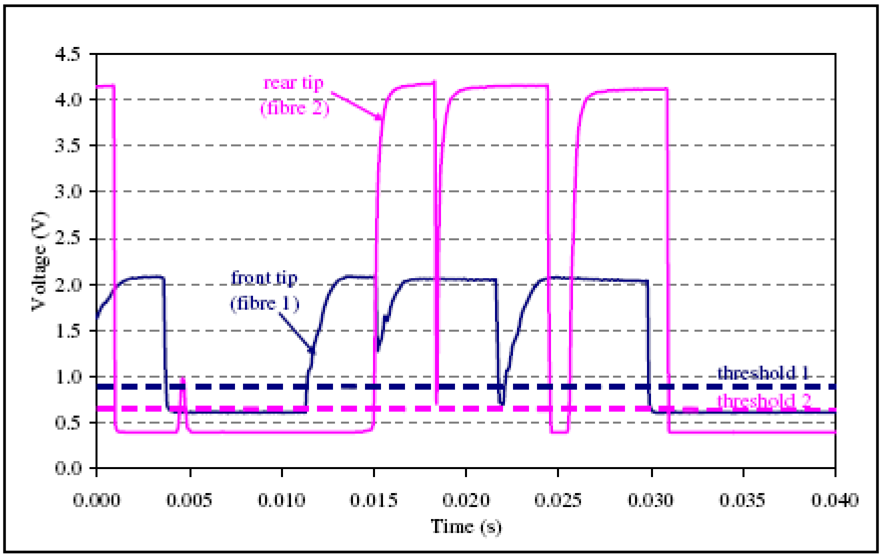

Figure 5.6: Example of raw signals by Chaumat [67]

5.1 Signal processing method

The most commonly used method for processing the signal is to use a threshold technique. This technique is based on the intersection of the raw signal with set level. However, some signal may not be detected if the signal is lower than the set level.

The current research used a model proposed by Van Der Walle [68]. This method was used by Angeli and Hewitt [69]. This technique detects the beginning of the rise or the fall of a signal, and then transforms the raw signal into a rectangular wave, taking as a starting point the change in the signal slope. Therefore, this technique allow every signal to be detected in the change to the rectangular wave signal. The main idea is that each sample of the signal is compared with two self-adjusting trigger levels and its implementation is summarised in Table 5.2.

Table 5.2: Condition method proposed by Van Der Welle [68] for processing the signal data local probe.

Condition	Minimum	Maximum	Output
$\alpha_n > \alpha_{n-1}$	No change	$\alpha_{max} = \alpha_n$	
$\alpha_n = \alpha_{n-1}$	No change	No change	
$\alpha_n < \alpha_{n-1}$	$\alpha_{min} = \alpha_n$	No change	
$\alpha_n > \alpha_{min} + V_{db}$ (Eq. 5.4)			1
$\alpha_n < \alpha_{max} - V_{db}$ (Eq. 5.5)			0
If none of Eq. (5.4) and (5.5) true			No change

This technique also overcomes the delay between the time the probe tip comes in contact with a phase and the time the probe signal takes to register this phase. This delay could be due to the time this phase needs to wet or dewet the whole probe. Other than the tip, the probe is sprayed with lacquer to make it hydrophobic.

The change of the signal slope is the starting point to transform the raw signal to a rectangular wave. The signal amplitude α_n of the n^{th} sample is compared with the amplitude α_{n-1} of the previous sample, with two adjustable parameters, maximum and minimum values, α_{max} and α_{min} respectively. In the beginning two initial values for α_{max} and α_{min} are given. If α_n is greater than α_{n-1} then the maximum α_{max} is changed and is set equal to α_n. If α_n and α_{n-1} are equal then there is no change in the maximum and the minimum values, and if α_n is lower than an α_{n-1} then the minimum changes and is set equal to α_n. The amplitude α_n is then compared with the new maximum and minimum values; in this comparison the margin V_{db} accounts for the signal noise. So if Equation (5.4)

$$\alpha_n > \alpha_{min} + V_{db} \tag{5.4}$$

is true then the output is 1 (which represents the water phase), but if

$$\alpha_n < \alpha_{max} - V_{db} \tag{5.5}$$

is true then the output is 0 (which represents the gas phase). If neither Equation (5.4) nor Equation (5.5) is true then the previous value (1 or 0) is kept. The whole signal is thus converted in a series of 1's and 0's, which represent each one of the two phases. The method assumes that beginning of the change in signal slope represents the interaction of the probe with the liquid-gas interface.

The void fraction, α, can be expressed as the ratio of accumulated signal time in the air phase, t_G to the total sampling time, Δt, i.e., Equation (5.3).

An Excel program was developed to process the void fraction probe signal data using the above method.

5.2 Development of the void fraction probe

A single probe was fabricated to study the capability and the signal from the probe. The probe, shown in Figure 5.7, used a K-type thermocouple wire sealed in a tube by epoxy. The wire tips were exposed as the probe. The exposed wire tube tip length, which is insulated, was 1 cm and the end point is bared to enable a current to flow. The thermocouple was inserted in a stainless steel tube holder with an ID of 2 mm. This void fraction probe was capable of identifying which phase was present in the two-phase flow. Therefore, the probe gave a two level signal, where the lower level represents the liquid phase and the higher the gas phase. When the probe was submerged in the two phase flow stream with the tip pointing in the direction of the stream, the tip of the electrode sensed the impedance between the probe tip and the common ground metal tube. Due to the large difference in conductivity between the liquid phase and the gas phase, the impedance signal rose sharply when a bubble passes the sensor tip. The signal was range between 0 V to 5.5 Volt.

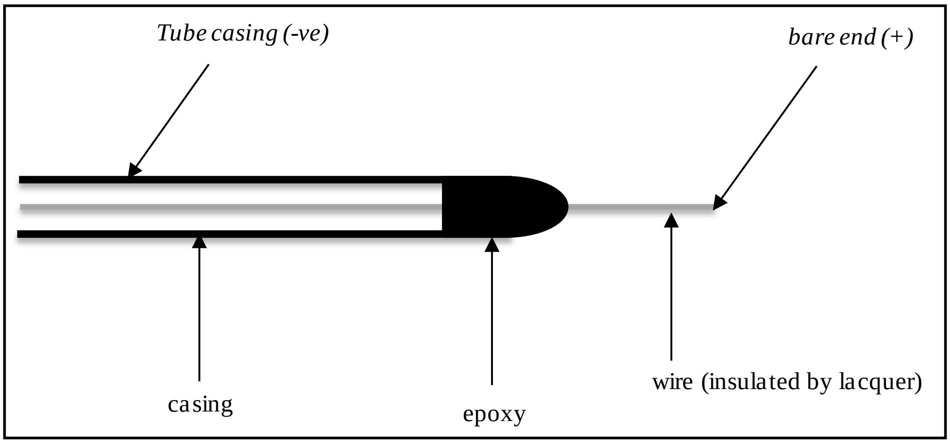

Figure 5.7: The conductive probe

The void fraction signal is based on the circuit shown in Figure 5.5. The void fraction probe was inserted in a tube bundle via a pressure tap as shown in Figure 5.8 to measure the void fraction. It was connected to data logger NI A6220 and read by a computer through a LabVIEW program developed for the purpose. The results had to be post processed to get a void fraction.

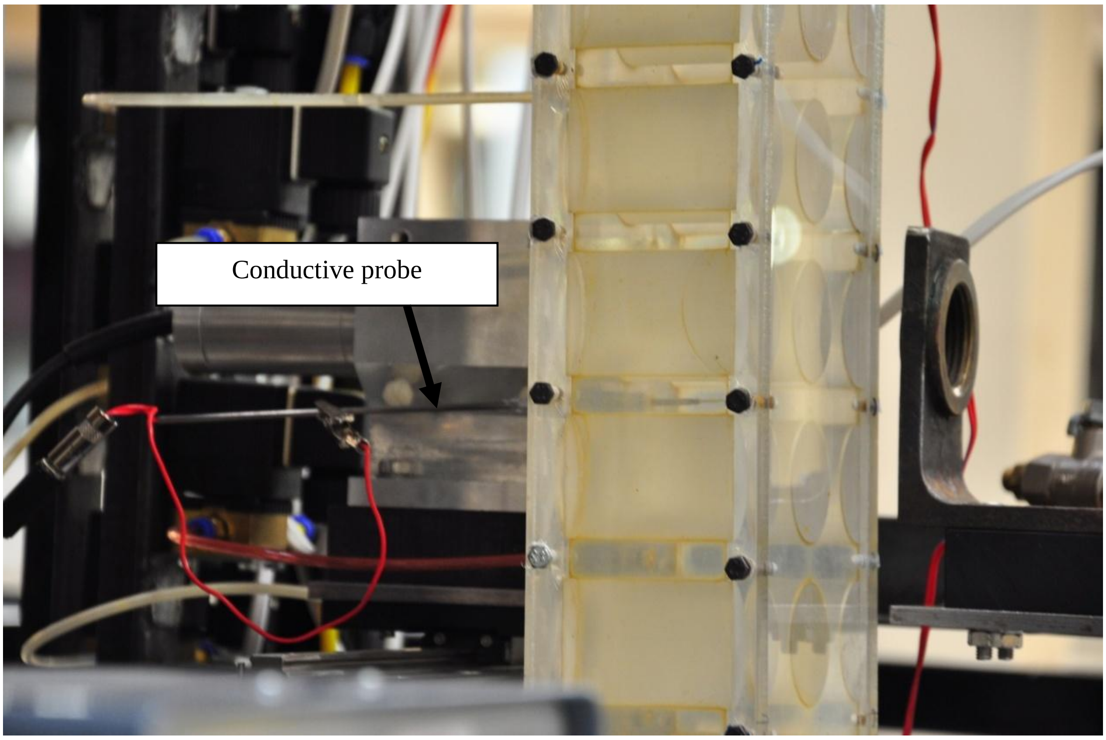

Figure 5.8: Conductive probe at the 38 mm inline bundle

5.3 Void fraction measurement with the conductive probe

5.3.1 Operation condition

The conductive probe, that was built-in in house, was tested to evaluate its capability of producing void fraction measurements. The void fraction test used the same test procedures as the two-phase pressure drop tests, except that the probe was inserted through a pressure tap and solenoid valves and purging of the lines was not necessary involve. The data were measured at the same nominal condition as the pressure drops, as mentioned in Section 4.1.1.

The probe was controlled by a switch box and the signal was send to a LabVIEW program, the *TWO-PHASE FLOW* program, as a voltage. The voltages were converted to void fraction using a spreadsheet based program.

The signal from the probe was analyzes using the method of Angeli and Hewitt [69]. This technique allowed the signal to be detected and changed to a rectangular wave, and reduced the problem caused by the time delay between the probe tip coming into contact with a phase and the signal response. Details of the how the signal was analyzed was discussed in Section 5.1.

5.3.2 Void fraction experiment commissioning

The probe was tested in the 38 mm diameter in-line bundle. Data was collected with a frequency of 10 kHz over a period of 30 s. Some initial experiments, performed over different periods of time, showed that variations in the void fraction were adequately averaged over 30 s. Figure 5.9 shows the range 0 to 0.3 s. This test was carried out at a water flow rate at 0.48 kg/s. The signal was collected using the *TWO PHASE FLOW* program and was processed to get the void fraction signal form shown in Figure 5.10. The void fraction is 0.47. This demonstrates that the probe can detect the air and water phases and is capable of giving a void fraction measurement.

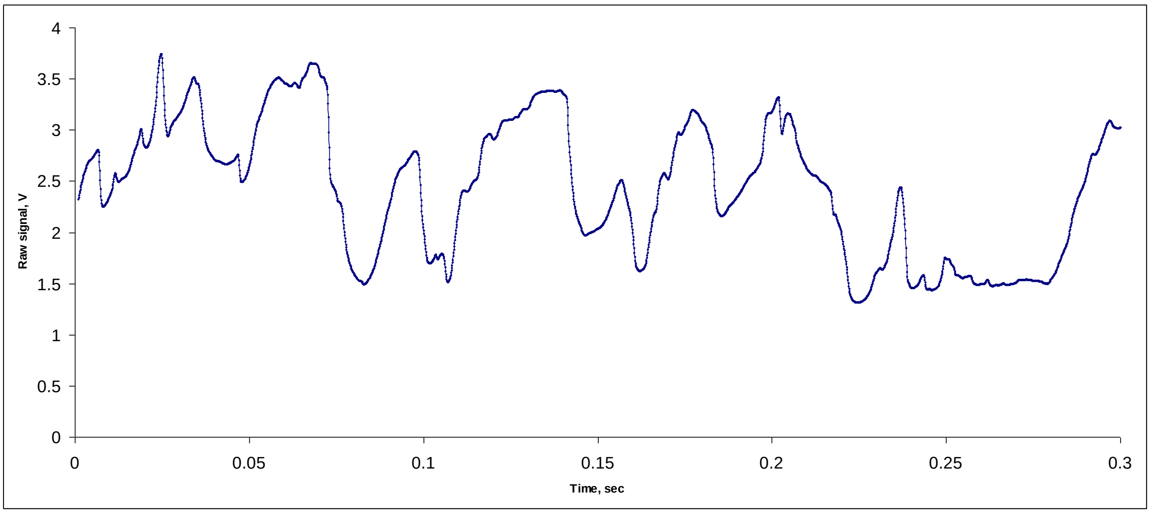

Figure 5.9: Raw signal from the probe

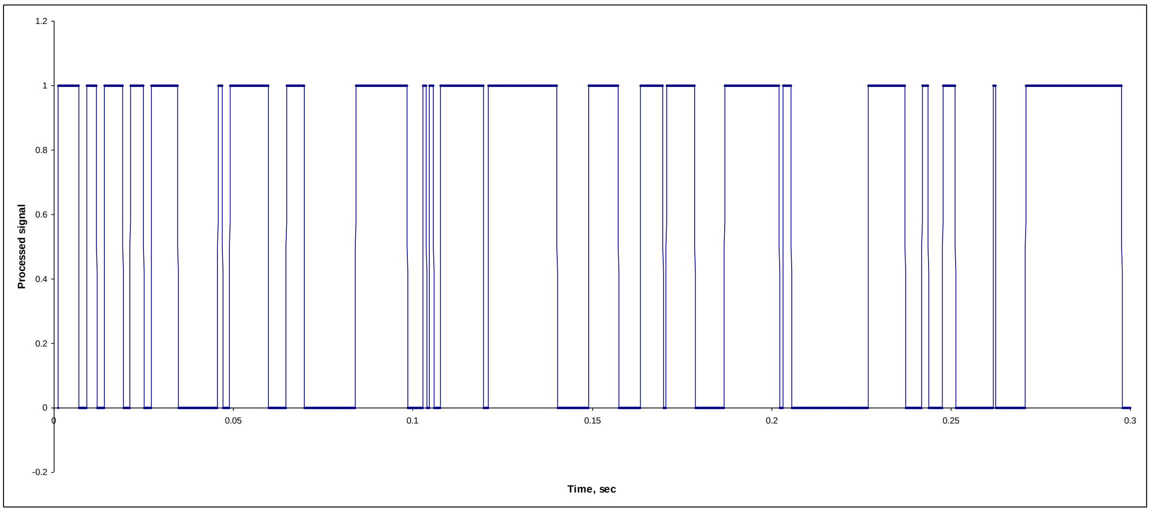

Figure 5.10: Processed signal (in square wave form) after analysing the air and water signal from raw signals

5.3.3 Experimental procedures for void fraction measurement using the conductive probe

Below is the procedure for void fraction measurement using the probe;

1) The LabVIEW program, *TWO-PHASE FLOW* was started to monitor the void fraction, pressure, water flow rate and temperatures prior to testing.
2) The LRV and URV were set for pressure and water flow rate. For the *LRV* and *URV* for pressure and water flow rate were fixed for each mass fluxes, 25-688 kg/m^2s, refer to APPENDIX A for the test conditions.
3) The probe was inserted into the tube bundle through a pressure tap, Figure 5.8.
4) The probe control box was switched on.
5) The water pump was started, with valves A and B open, Figure 3.1.
6) Valve B, Figure 3.1, was adjusted to push water into the test section i.e. the tube bundle.
7) The Rosemount 3051 differential water flow rate pressure transducer was purged with water by opening both screws on its sides.
8) The compressor was started, Figure 3.1.
9) The valve downstream of the air rotameter, Figure 3.1, was adjusted to give desired gas flow rate.
10) The current displays on the signal conditioning boxes for the pressure and water flow rate pressure transducer showed the current readings between 4 to 20 mA.
11) The water flow rate was set by turning valve B, Figure 3.1, until the required current was obtained. The desired water flow was checked using the *TWO-PHASE FLOW* program.
12) Once the flow had stabilized, which took about 5 seconds, the void fraction, pressure, water flow rate and temperatures readings were recorded using the *TWO-PHASE FLOW* program and stored in a Text File.
13) Step 9 to 12 were repeated for the next reading.
14) Valve B was opened to allow water out from the test section i.e. the tube bundle after the tests were completed.
15) The valve downstream of the air rotameter was closed manually to stop the air supply.
16) The compressor and the water pump were shut down.

5.4 Comparison void fraction measurement using conductive probe with void fraction using gamma-ray densitometer

The void fraction data using a single conductive probe was tested on the 38 mm in diameter in-line tube bundle and compared with void fraction measured using gamma-ray densitometer, to see the capability of the probe to measure void fraction. The probe was placed at the pressure tap row 7^{th} of the heat exchanger allowing the void fraction measurement inside the bundle (Figure 5.8). The air mass flow rate varied from 0.00039-0.0306 kg/s while the water mass flow rate varied from 0.2483-0.219 kg/s. The quality range from 0.00157-0.12259 and the mass flux is 208 kg/m^2s.

Void fraction, pressure, water flow rate and temperatures were sent to the data logger. These readings were taken at 1 kHz and 10000 data. The temperatures readings including water, gas inlet at right, gas inlet at left and two-phase flow at exit bundle. These were recorded for 10 samples at 2 Hz. These data were recorded using the *TWO-PHASE FLOW* program and stored in a Text File. Then the post data was done using FORTRAN developed for the purpose, capable of plotting the raw signal captured from the probe, from 0 Volt to 5.5 Volt, Figure 5.11. The program is also capable to processed the signal in a square form after analyzed the air and water signal from raw signal, Fig 5.12. Both figures only showing one second of the data, which is 1000 data per second at 0.00039 kg/s.

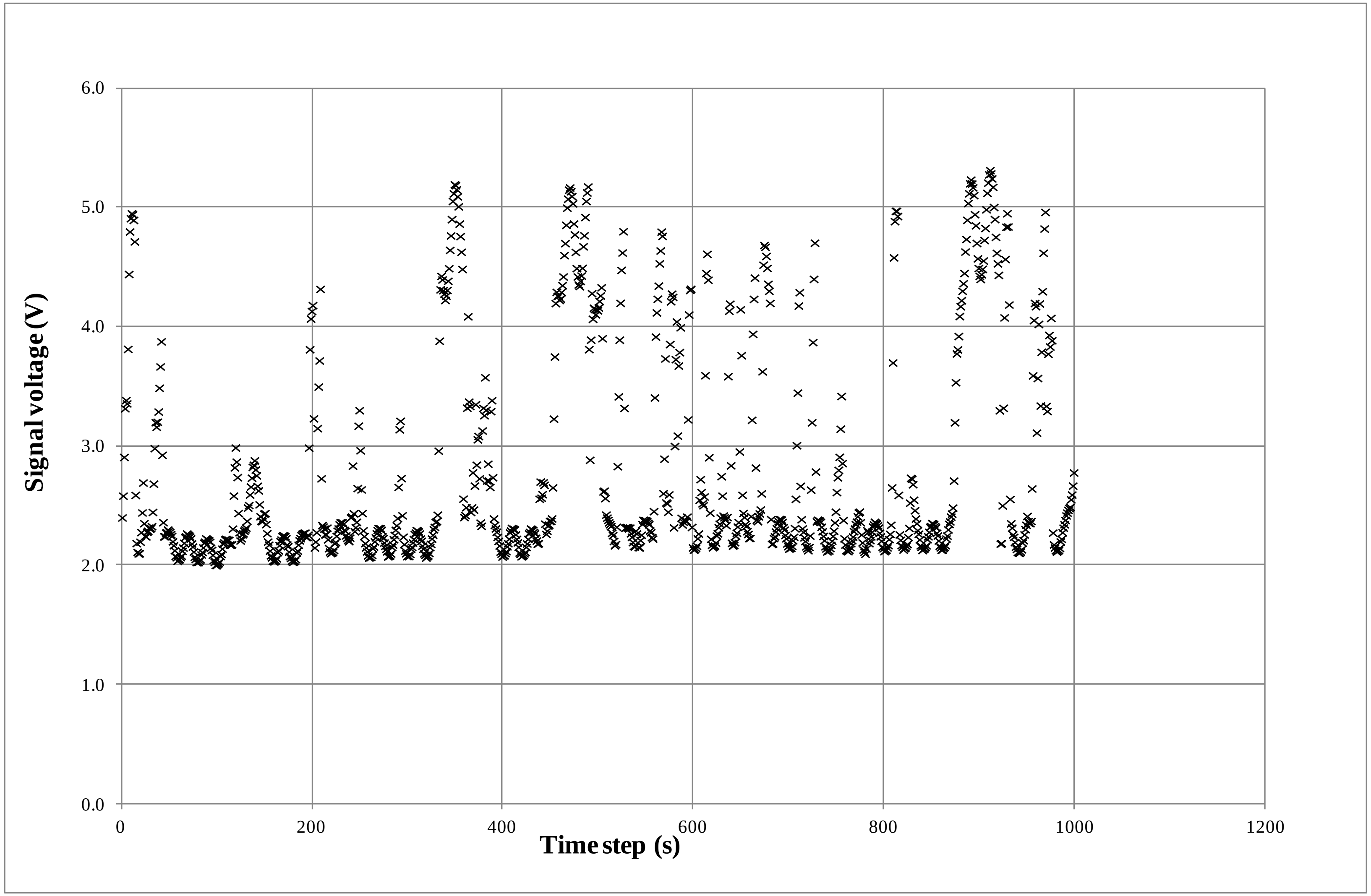

Figure 5.11: Variation of signal voltage against time step

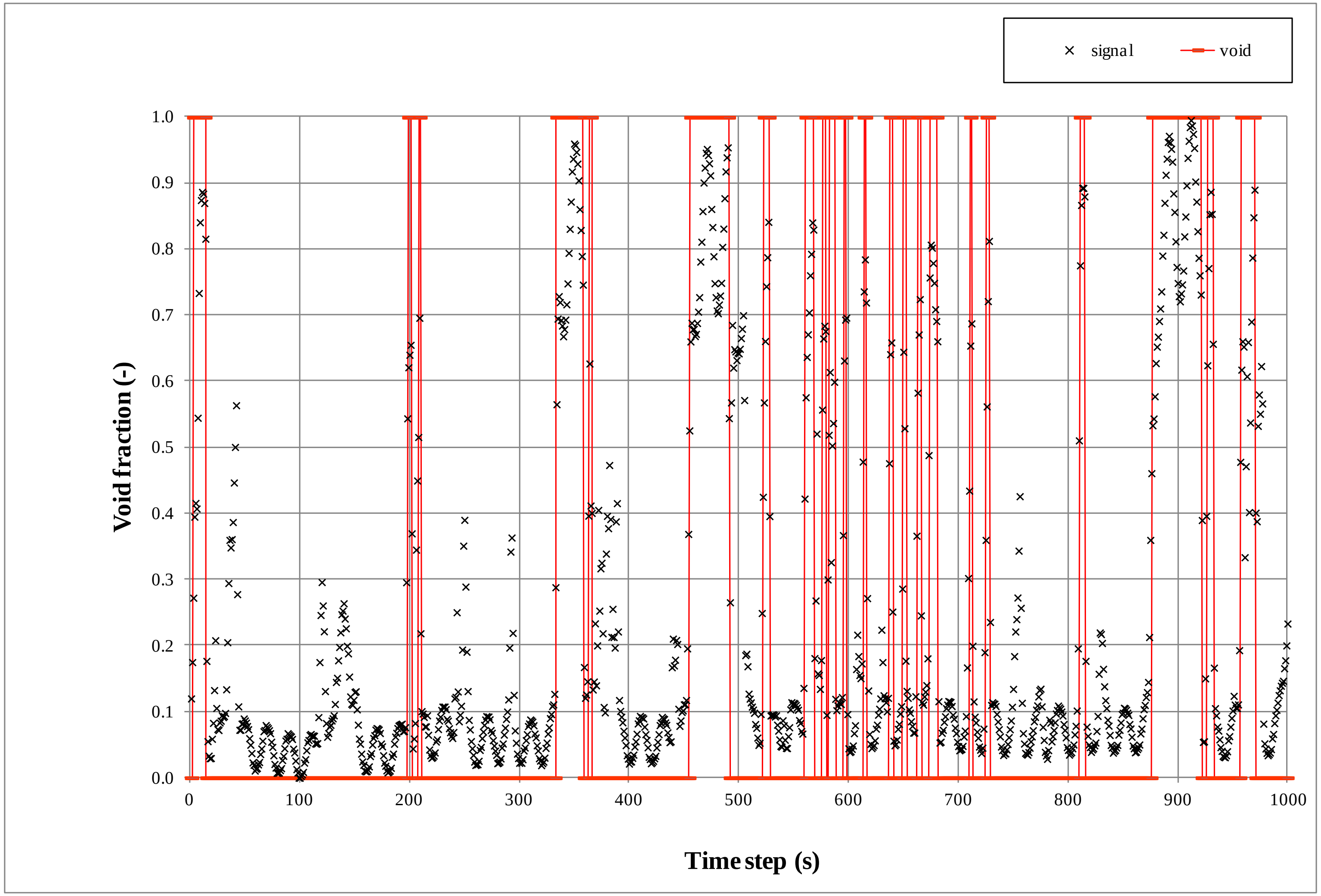

Figure 5.12: Variation of void fraction against time step

The gas mass flow rate was set to various noise levels to get the void fraction using Equation (5.3), (5.4) and (5.5). Then the void fraction is plotted against noise level. Afterwards, the averaged void fraction was obtained from a reasonable portion of the graph, Figure 5.13 for an example. Table 5.3 shows the signal noise and void fraction for each air mass flow rate. The experiment was run at eighteen air mass flow rate, however only eight were shown. It shows that the void fraction is changing when the noise, V_{db} is changed. However, the reasonable portion to get the averaged void fraction obtained from each air mass flow rate is kept changing, that makes the void fraction data from the conductive probe is not reliable. For example, at air flow rate of 0.00039 kg/s, the void fraction is averaged at 16 levels of noise, V_{db} which is from 0.0 until 1.9. On the other hand, at air flow rate of 0.00117 kg/s, the void fraction is averaged at only 5 levels of noise, V_{db} which is 0.4 – 0.8 to get a reasonable void fraction.

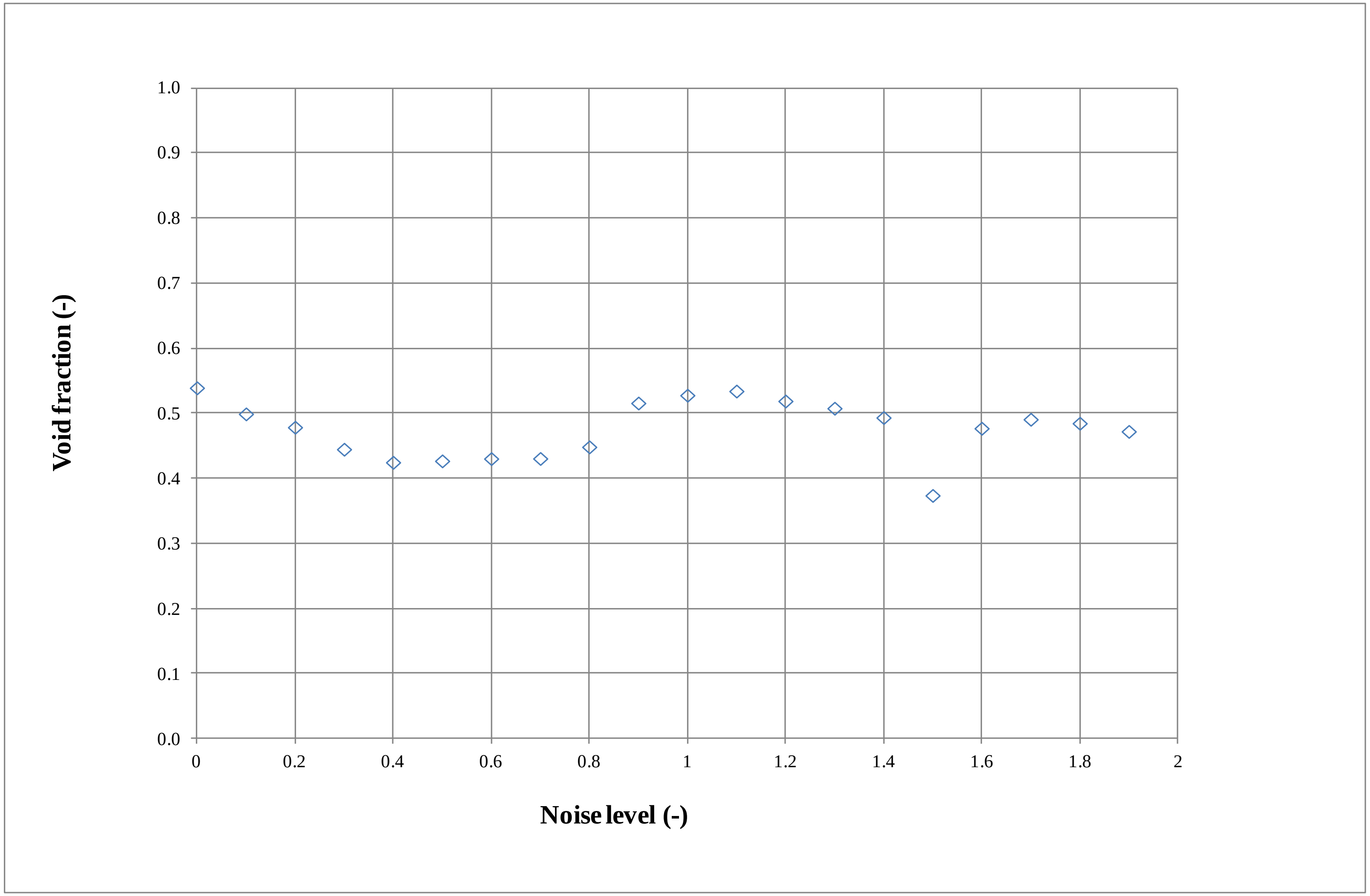

Figure 5.13: Variation of void fraction with noise level for a air mass flow rate of 0.00234 kg/s

Table 5.3: Variation of noise level and void fraction for air mass flow rate from 0.00039 to 0.00312 kg/s

Air mass flowrate (kg/s)															
0.00039		**0.00078**		**0.00117**		**0.00156**		**0.00195**		**0.00234**		**0.00273**		**0.00312**	
Signal noise V	**Void fraction (-)**	**Signal noise V**	**Void fraction (-)**	**Signal noise V**	**Void fraction (-)**	**Signal noise V**	**Void fraction (-)**	**Signal noise V**	**Void fraction (-)**	**Signal noise V**	**Void fraction (-)**	**Signal noise V**	**Void fraction (-)**	**Signal noise V**	**Void fraction (-)**
0.0	0.5343	0.0	0.5354	0.0	0.5416	0.0	0.5391	0.0	0.5436	0.0	0.5400	0.0	0.5351	0.0	0.5428
0.1	0.4703	0.1	0.4769	0.1	0.4935	0.1	0.49	0.1	0.5014	0.1	0.4999	0.1	0.5083	0.1	0.5187
0.2	0.4192	0.2	0.4296	0.2	0.4624	0.2	0.4588	0.2	0.4748	0.2	0.4794	0.2	0.4864	0.2	0.5053
0.3	0.2526	0.3	0.2829	0.3	0.3457	0.3	0.3544	0.3	0.3699	0.3	0.4456	0.3	0.4136	0.3	0.4659
0.4	0.2249	0.4	0.2765	0.4	0.3318	0.4	0.332	0.4	0.3586	0.4	0.4255	0.4	0.4101	0.4	0.4664
0.5	0.2282	0.5	0.2737	0.5	0.3116	0.5	0.3365	0.5	0.3594	0.5	0.4277	0.5	0.3923	0.5	0.4564
0.6	0.2256	0.6	0.2535	0.6	0.3240	0.6	0.3424	0.6	0.3521	0.6	0.4312	0.6	0.3897	0.6	0.4564
0.7	0.2137	0.7	0.2393	0.7	0.312	0.7	0.3309	0.7	0.3541	0.7	0.4314	0.7	0.3963	0.7	0.4781
0.8	0.2348	0.8	0.2433	0.8	0.3129	0.8	0.3251	0.8	0.3590	0.8	0.4492	0.8	0.4196	0.8	0.4833
0.9	0.2446	0.9	0.2567	-	-	0.9	0.3967	0.9	0.3928	0.9	0.5166	0.9	0.5005	0.9	0.5683
1	0.2271	1.0	0.2517	-	-	1.0	0.3833	1.0	0.3948	1.0	0.5286	1.0	0.4848	1	0.5639
1.1	0.2379	-	-	-	-	1.1	0.3722	1.1	0.4011	1.1	0.5350	1.1	0.4880	1.1	0.55
1.2	0.2246	-	-	-	-	1.2	0.3677	1.2	0.4021	1.2	0.5197	1.2	0.4843	1.2	0.5568
1.3	0.2058	-	-	-	-	1.3	0.3862	1.3	0.3996	1.3	0.5086	1.3	0.4684	1.3	0.5453
1.4	0.2181	-	-	-	-	1.4	0.3727	1.4	0.4013	1.4	0.4943	1.4	0.4788	1.4	0.5404
1.5	0.2299	-	-	-	-	1.5	0.3587	1.5	0.3746	1.5	0.3746	1.5	0.4861	1.5	0.5461
1.6	0.2408	-	-	-	-	-	-	1.6	0.3817	1.6	0.4778	1.6	0.4913	1.6	0.5299
1.7	0.2413	-	-	-	-	-	-	1.7	0.4014	1.7	0.4916	1.7	0.4637	1.7	0.52
1.8	0.2449	-	-	-	-	-	-	1.8	0.4147	1.8	0.4855	1.8	0.4327	1.8	0.5108
1.9	0.2307	-	-	-	-	-	-	1.9	0.3871	1.9	0.473	1.9	0.4126	1.9	0.5147
-	-	-	-	-	-	-	-	-	-	-	-	-	-	2	0.5369
AVERAGE VOID FRACTION	**0.2296**		**0.2564**		**0.3185**		**0.3584**		**0.3826**		**0.4914**		**0.4719**		**0.5403**

[Shaded box] The void fraction values chosen to be averaged to get the average void fraction for each air mass flow rate.

Figure 5.14 shows the comparison of void fraction between using a probe and a gamma-ray densitometer and predicted void fraction by Dowlati et al. [2]. Both measured void fraction are increasing with increased of air mass flow rate, same with the predicted values. However, the void fraction measured by the probe shows a bit scatter at a range between 0.00189 – 0.00389 kg/s. The mean average error between the measured void fraction using the conductive probe and predicted by Dowlati et al. [2] is -10% and the RMS error is 16%. On the other hand, the measured void fraction using gamma-ray densitometer shows a better result with a mean average and RMS error are 3.6% and 4% respectively. This shows that the void fraction measurement using the gamma-ray densitometer is in favour.

The conductive probe failed to measure the void fraction correctly because it did not produce a good result when compared with the predicted values by Dowlati et al. [2]. The design of the probe has been improved by using a lacquer to reduce the wetting of the probe tip. So, the respond time of the probe has been increased. However, this improvement did not make the probe capable of measuring the void fraction. The method by Angeli and Hewitt [69] was used to processed the raw signal, between 0 (water phase) and 1 (air phase) is. This has been prove to work to capture the signal and obtained the void fraction. However, the noise level chosen kept changing to give a reasonable averaged void fraction. There is no fix value for each air mass flow rate. This has made the choice and judgement to obtain the void fraction is questionable. Having said all these, the void fraction measurement using gamma-ray densitometer is chosen to be the best method because of the shortcomings of the conductive probe.

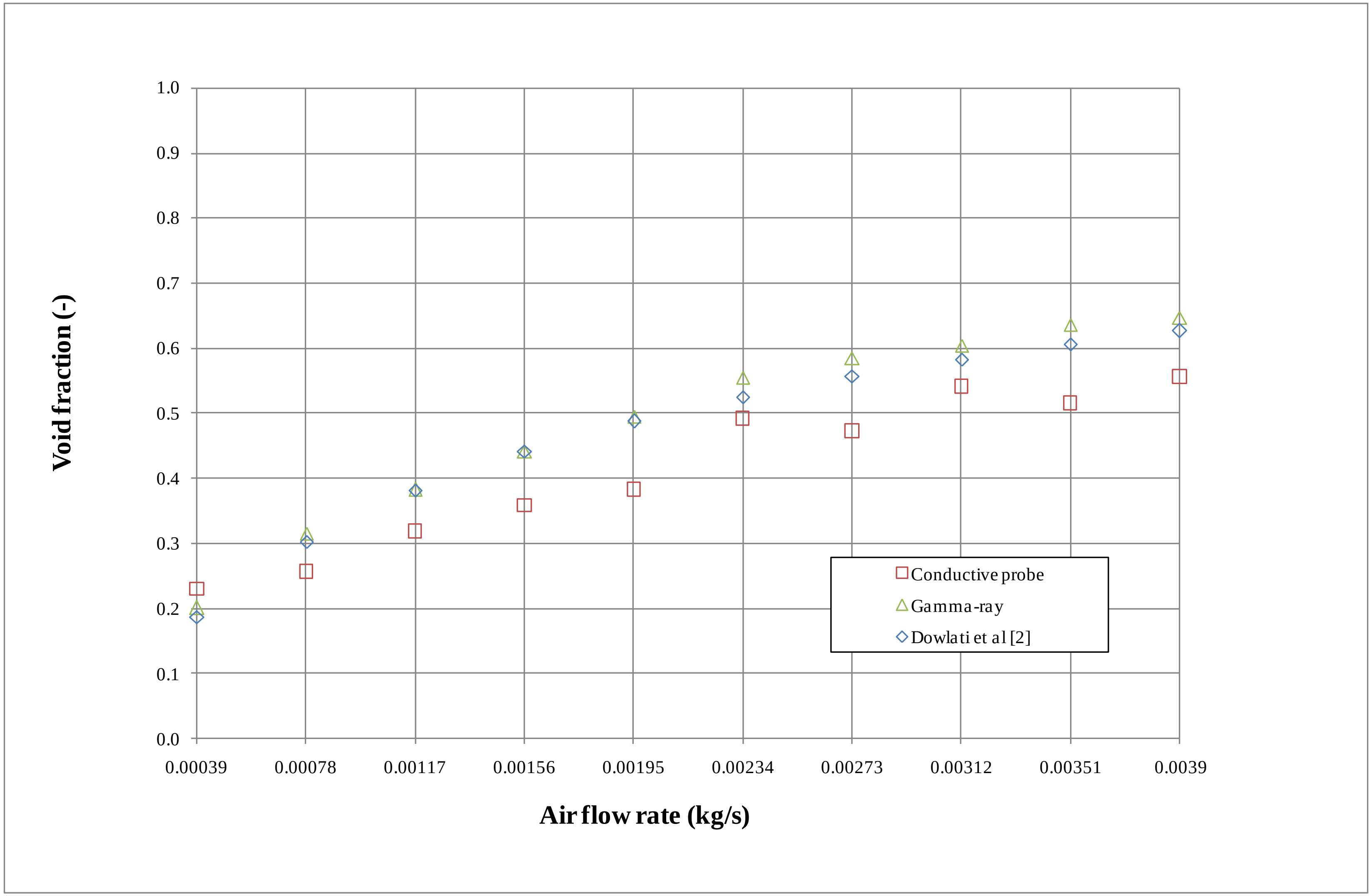

Figure 5.14:Comparison between void fraction using conductive probe, gamma-ray densitometer and predicted void fraction of Dowlati et al. [2]

CHAPTER 6 - VOID FRACTION EXPERIMENTAL RESULTS AND DISCUSSION

The void fractions measurements were taken by traversing the gamma densitometer to a specific position and passing 10 mm in diameter beam through the flow, parallel to the tubes, onto a photomultiplier tube from the Am241 source. There were nine local void fraction measurements taken, three in the 38 mm in diameter square in-line bundle, four in the 19 mm in diameter square in-line bundle and two in the 19 mm in diameter staggered bundle in a 60 degree (equilateral triangle) layout. These three bundles have the same pitch-to-diameter ratio, *P/D* of 1.32. Each location was carefully chosen to give information on local void fraction distribution around the tubes. The void fraction measurements were obtained in the maximum gap and vertical and horizontal minimum gaps between the tubes. The data collected are discussed and analyzed in this chapter. The bundle geometry effect is addressed for each parameter of interest. All tests were done separately. After each experiment, basic statistical analysis was performed for the water flow rate and pressure. This included the averaging of 10000 data points, upper and lower limits, mean average and Root Mean Square (RMS) values. The void fractions and temperature were averages of 100 readings and 10 readings respectively. Data processing was done through an Excel spreadsheet and a series of FORTRAN programs written for specific procedures for void fractions predictions by other researchers [1,2,3,70]. Table 6.1 shows the range of condition for the void fraction experiments.

Table 6.1: Air-water test conditions

Bundle layout	Bundle diameter (mm)	P/D	Minimum gap between tubes (mm)	Mass flux based on min area (kg/m^{2}s)	Flow quality	Air mass flow rate (kg/s)	Water mass flow rate (kg/s)	Pressure (kPa)	Temperature (°C)
In-line	38	1.32	12	25 - 688	0.00047-0.57	0.00039-0.034	0.03-0.82	112 - 121	20 - 23
In-line	19	1.32	6						
Staggered	19	1.32	6						

The void fraction, α is defined as the ratio of the flow area occupied by gas to the total flow area and was found from these measurements through the method of Patrick and Swanson [54], i.e., the measured void fraction, α was obtained from,

$$\alpha = \frac{\ln(I - I_B) - \ln(I_L - I_B)}{\ln(I_G - I_B) - \ln(I_L - I_B)} \tag{6.1}$$

where I is two-phase reading, I_B is the background reading, I_L is the water-only reading and I_G is the air-only readings.

The void fractions for one-dimensional flows has been returned to fall between the maximum slip and homogenous values. Therefore the measured void fractions were compared with these models. The homogeneous and maximum slip models were determined (see e.g. Chisholm [70]),

$$\alpha = \frac{xv_g}{\left(xv_g + k(1-x)v_l\right)} \tag{6.2}$$

in which x is the quality and v_g and v_l are the specific volumes of the gas and liquid phases respectively. The slip ratio, k depends on the model. The homogenous model assumes that the gas and liquid phases travel at the same velocity, giving the slip ratio as unity. The maximum slip model assumes equal momentum flux in the gas and liquid streams of the separated flow model, and is found from

$$k = \sqrt{\frac{v_g}{v_l}} \tag{6.3}$$

Schrage et al. [1] reported that the void fraction could be found from

$$\alpha = \alpha_H R \tag{6.4}$$

where

$$R = \max\left(1 + 0.123\, Fr^{-0.191} \ln x, 0.1\right) \tag{6.5}$$

α_H is the homogenous void fraction, found from Equation (6.2) with a slip ratio of unity, and Fr is the Froude number, defined through

$$Fr = \frac{G_{max}}{\rho_l \sqrt{gD}} \tag{6.6}$$

in which D is the tube diameter.

Feenstra et al. [3] proposed a correlation for the slip ratio, allowing the void fraction to be determined from Equation (6.2). The slip ratio was found from

$$k = 1 + 25.7 \frac{D}{P} \sqrt{Ri\, Ca} \tag{6.7}$$

where P is the tube pitch, Ca is the capillary number and Ri is the Richardson number. The Capillary number is defined as

$$Ca = \frac{\mu_l u_g}{\sigma} \tag{6.8}$$

where μ_l is the dynamic viscosity of the liquid, σ is the surface tension and u_g is the gas velocity in the minimum gap between the tubes calculated from;

$$u_g = \frac{x G_{max}}{\alpha \rho_g} \tag{6.9}$$

where G_{max} is the mass flux based on minimum flow area. The Richardson number is defined through

$$Ri = \frac{(\rho_l - \rho_g)^2 ga}{G_{max}^{\ 2}} \tag{6.10}$$

where a, the gap between the tubes as the basic length scale given by

$$a = P - D \tag{6.11}$$

Dowlati et al. [2] published the void fraction correlations

$$\alpha = 1 - \frac{1}{(1 + C_1 j_g^* + C_2 j_g^{*2})^{1/2}} \tag{6.12}$$

where j_g^* is the Wallis parameter, defined through

$$j_g^* = \frac{\sqrt{\rho_g}\, j_g}{\sqrt{gD(\rho_l - \rho_g)}} \tag{6.13}$$

and C_1 and C_2 are constants that depend on the fluid and the geometry of the tube bundle. For these present data, the values for C_1 was 35 and C_2 was 50 Dowlati et al. [39]. The superficial gas velocity, j_g, is evaluated in the minimum gap between the tubes i.e.

$$j_g = x G_{\max} v_g \tag{6.14}$$

The correlations of Schrage et al. [1], Feenstra et al. [3] and Dowlati et al. [9,2] were based on tube diameter less than 20 mm. Schrage et al. [1] was derived from air-water data obtained from in-line tube bundle containing tubes 7.94 mm in diameter and ratio *P/D* of 1.3 using a quick closing plate valves at near atmospheric conditions. The correlations of Feenstra et al. [3] was obtained from R11 data obtained just upstream of staggered tube bundles containing tubes 6.35 mm and 6.1 mm in diameter on a pitch-to-diameter ratios, *P/D*, of 1.44 and 1.48 respectively. It was also tested against air-water and R113 data sets [2,39,71]. Dowlati et al. [2] void fraction correlation was derived from air-water data obtained from in-line tube bundles containing tubes 12.7 mm and 19.05 mm in diameter on pitch-to-diameter ratios, *P/D*, of 1.75 and 1.3 respectively. More data were collected in staggered bundles under same condition Dowlati et al. [39] that show that tube bundle layout has an insignificant effect. Further work continued on R113 data sets Dowlati et al. [71]. All of these data were based on gamma ray densitometer measurements. The void fraction profiles with regards to row number were relatively uniform, Dowlati et al. [2], for test bundle tube-to-diameter ratio, *P/D* of 1.3 and 1.75. Therefore the void fraction profiles could be readily averaged over the entire bundle to obtain reliable bundle-average void fraction data [2,39]. The measured void fraction of Dowlati et al. [2,39] was a row average void fraction because the gamma-ray beam was spread across a tube pitch. The summary of experimental conditions and tube arrays by these researchers and the present study bundles are tabulated in Table 6.2.

The void fraction correlations [1,2,3] were derived from a database containing several fluids and tube bundles, all of which contained tubes with diameter less than 20 mm. Therefore, these correlations were tested on tube diameter larger than 20 mm to evaluate the capability to predict the void fraction in tube bundles containing larger diameter tubes in adiabatic air-water experiments.

Table 6.2: Summary of experimental conditions and tube array data

Name	Array type[a]	P/D	Tube diameter (mm)	Array size	Fluid temperature[b]	Two-phase flow pressure (kPa)[c]	Two-phase flow temperature[d]	Gas phase density, ρ_g (kg/m^3)	Liquid phase density, ρ_l (kg/m^3)
Present study	NS	1.32	38.0	1 x 10	Air-Water, 20°C	120.7	20°C	1.43[e]	1000
Present study	NS	1.32	19.0	3 x 15	Air-Water, 20°C	119.1	20°C	1.41[e]	1000
Present study	NT	1.32	19.0	4 x 22	Air-Water, 20°C	111.8	23°C	1.41[e]	1000
Feenstra et al [3]	PT	1.44	6.35	4 x 7	R-11, 40°C	-	-	9.65	1440
Dowlati et al [2,9]	NS,NT	1.3	19.05	5 x 20	Air-Water, 25°C	-	-	1.4	997
Dowlati et al [2,9]	NS,NT	1.75	12.7	5 x 20	Air-Water, 25°C	-	-	1.4	997
Noghrehkar [16]	NS,NT	1.47	12.7	5 x 24	Air-Water, 22°C	-	-	1.5	997
Schrage et al [1]	NS	1.3	7.94	4 x 27	Air-Water, 10°C	-	-	2.2	1000
Dowlati et al [71]	NS	1.3	12.7	5 x 20	R-113, 55°C	-	-	9.36	1489
Axisa et al [15]	PT	1.44	19.0	11 x 11	Steam-Water, 260°C	-	-	23.7	784

[a] PT = Parallel triangular, NS = Normal square (in-line), NT = Normal triangular
[b] Fluid temperature are estimated for the air-water studies, all of which were performed near atmospheric conditions.
[c] Two-phase flow pressure was the average pressure measured at the time of experiment for the mass fluxes of 25-688 kg/m^2s.
38 mm in-line bundle – The minimum pressure = 103.7 kPa, maximum pressure = 166.8 kPa
19 mm in-line bundle – The minimum pressure = 105.0 kPa, the maximum pressure = 173.8 kPa
19 mm staggered bundle – The minimum pressure = 105.6 kPa, the maximum pressure = 179.0 kPa
[d] Two-phase flow temperature was the average temperature measured at the time of experiment for the mass fluxes of 25-688 kg/m^2s.
38 mm in-line bundle – The minimum temperature = 15°C, maximum temperature = 22°C
19 mm in-line bundle – The minimum temperature = 16°C, maximum temperature = 23°C
19 mm staggered bundle – The minimum temperature = 16°C, maximum temperature = 26°C
[e] gas phase density is obtained from average two-phase flow pressure and average two-phase flow temperature.

6.1 Void fraction measurement in 38 mm in diameter in-line tube bundle

6.1.1 Local void fraction measurements

The central tube on row 7 of the heat exchanger was the focal tube, see Figure 4.6. The void fractions were measured at three locations around this tube by aligning the single-beam gamma-ray densitometer in the gap to the south east, which was the maximum gap; in the gap to the south, which was the vertical minimum gap, and in the gap to east, which was the horizontal minimum gap. There were 435 data points of the measured void fraction. Both the minimum gaps were 12 mm. The test conditions and procedures are described in Chapter 4. The data are presented in Figures 6.1 to 6.3. The homogenous model and maximum slip model are included in these figures to show a comparison between the measured void fractions and the predictions from these models. The data sets for the three local void fractions measurements, the pitch average and predictions are tabulated in APPENDIX B.

6.1.2 Local void fractions at the maximum and minimum gaps

Figure 6.1 and 6.2 show the variation in measured void fraction with quality for a range of mass fluxes in the southern minimum gap and eastern minimum gap. The variation in measured void fractions in the maximum gap with quality for a range of mass fluxes is shown in Figure 6.3. As seen in Figures 6.1-6.3, the void fraction is shown to increase with increasing quality. It is also shown to increase with increasing mass flux, consistent with other findings [1,2,3]. Included in Figures 6.1-6.3 are the void fraction predictions from the homogeneous and maximum slip models. Void fraction data for one-dimensional flows are said to fall between the maximum slip and the homogeneous values. The current data are shown to be reasonably consistent with this view except at the lowest mass flux.

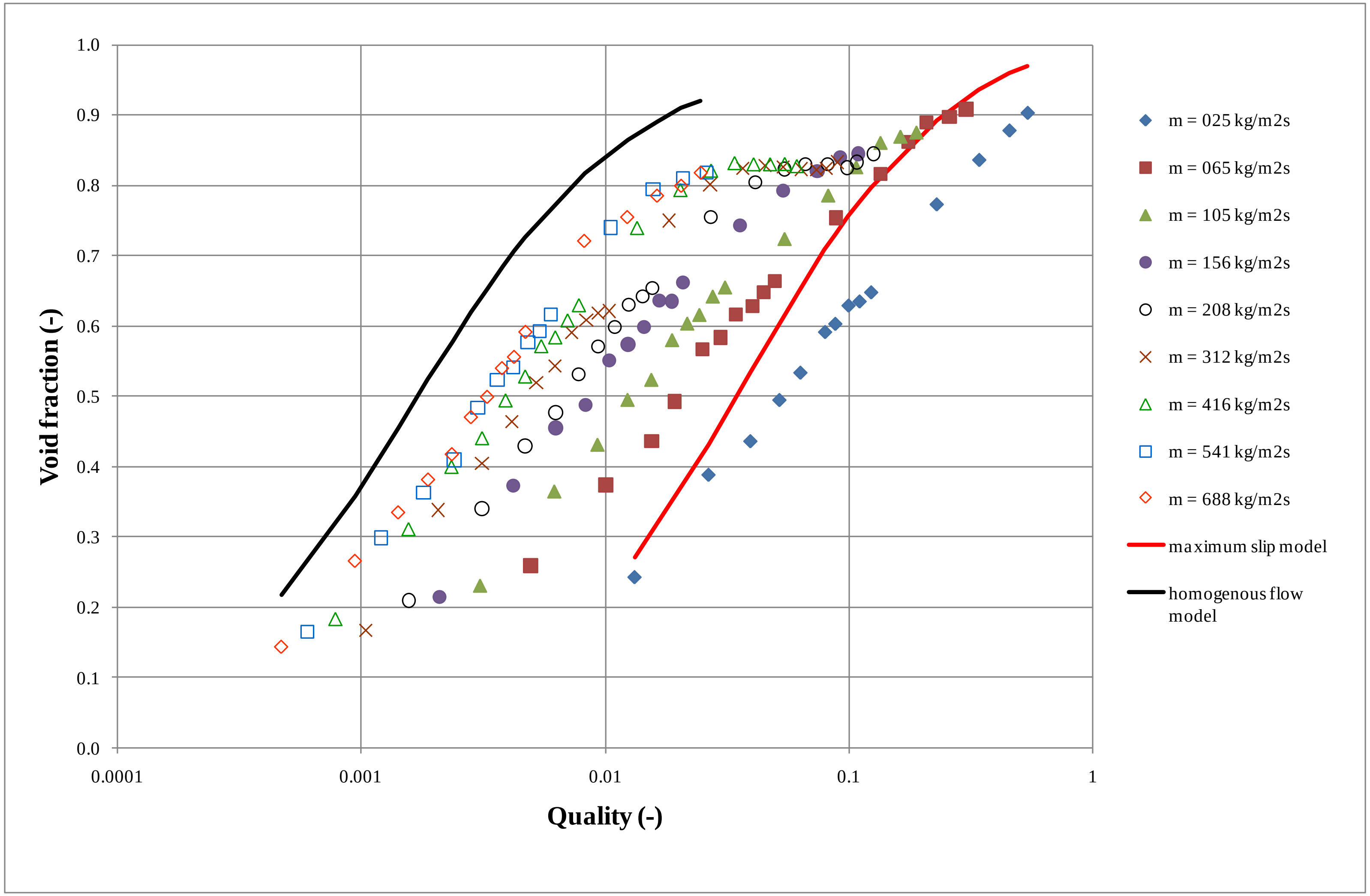

Figure 6.1: Variation of measured void fraction with quality at southern minimum vertical gap (38 mm in-line bundle)

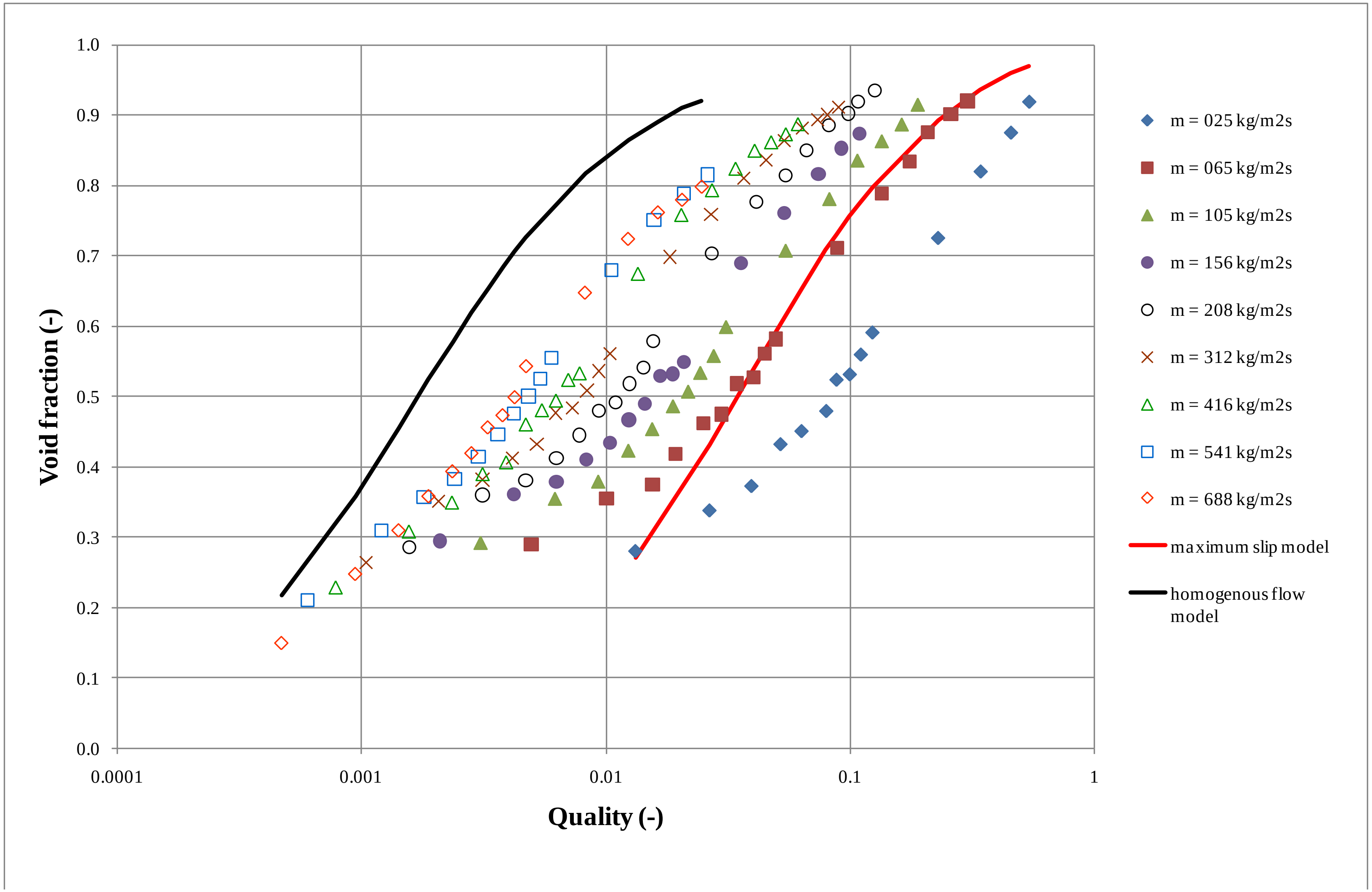

Figure 6.2: Variation of measured void fraction with quality at eastern horizontal minimum gap (38 mm in-line bundle)

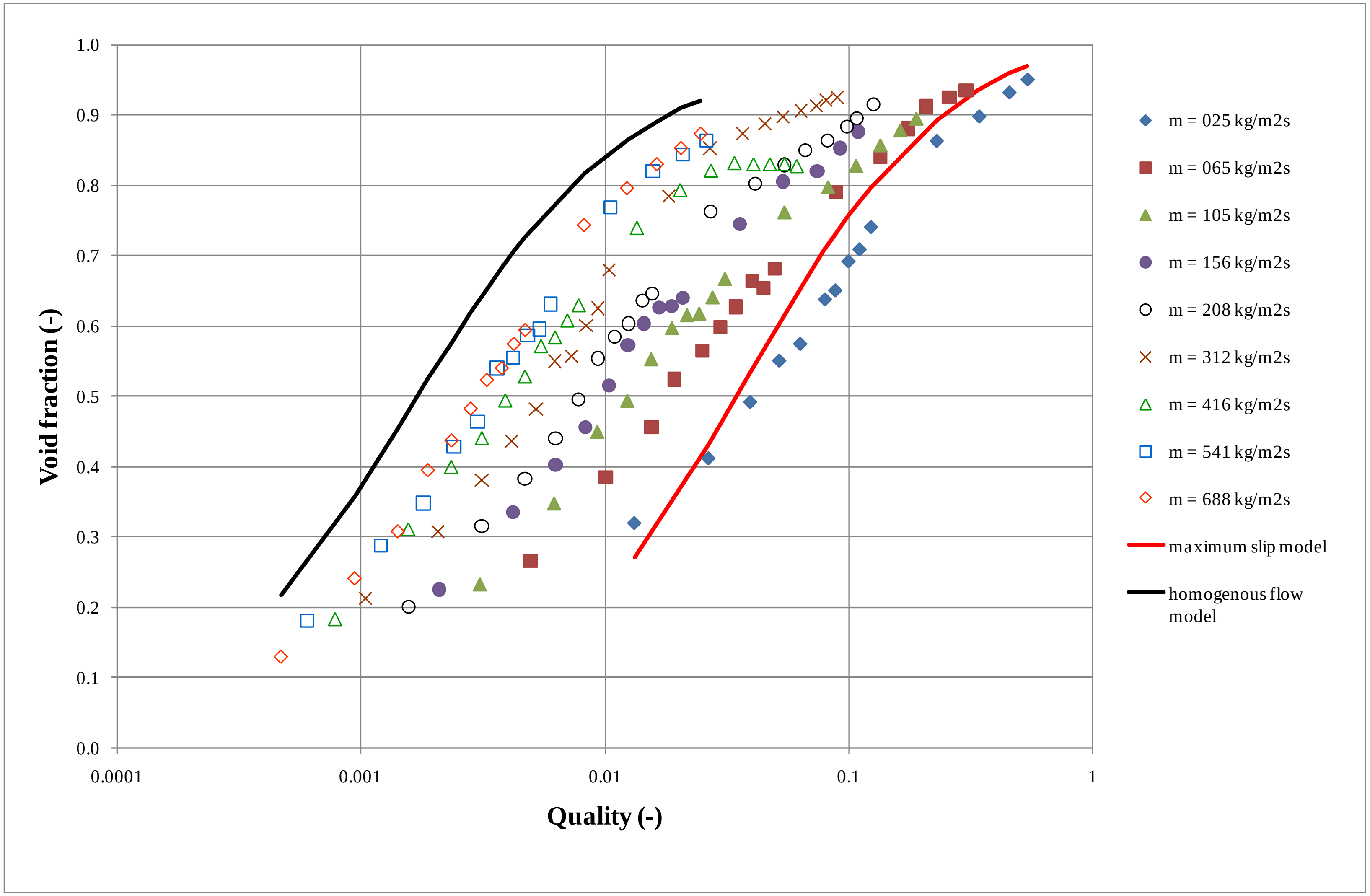

Figure 6.3: Variation of measured void fraction with quality at maximum gap (38 mm in-line bundle)

6.1.3 Comparison of local void fraction measurements

The measured void fractions in the southern vertical minimum gap and eastern horizontal minimum gap are compared to the values in the maximum gap. The comparison of the southern minimum gap and maximum gap is shown in Figure 6.4. For most of the range of void fractions, the maximum and minimum gaps are similar. However, the minimum vertical gap void fractions values tend to a constant at larger values at larger of void fraction, typically at 0.85 but dependent on mass flux.

The measured void fractions east of the central tube behave differently to the maximum gap values as shown in Figure 6.5. These measured local void fractions were in the same flow path but the area of flow was different; 12 mm in minimum gap and up to 50 mm in the maximum gap, assuming the two-phase flow was flowing upward. The void fractions are similar at values less than 0.3, but the minimum gap values are shown to be significantly less than those in the maximum gap, by more than 10%, between 0.4 and 0.75. Above this they are about the same. These data, Figure 6.2 and 6.5, suggest a relatively one-dimensional variation in void fraction. Therefore, the pitch void fractions were taken as the average between the eastern minimum and the maximum gap values. Moreover, these pitch void fractions were used for comparison with the void fraction predictions of Schrage et al. [1], and Feenstra et al. [3] and Dowlati et al. [2] and for other analysis involving two-phase multiplier and drag force [4,5,6,7] later in Chapter 7 and 8. The pitch void fraction variation with quality is shown for a range of mass fluxes in Figure 6.6.

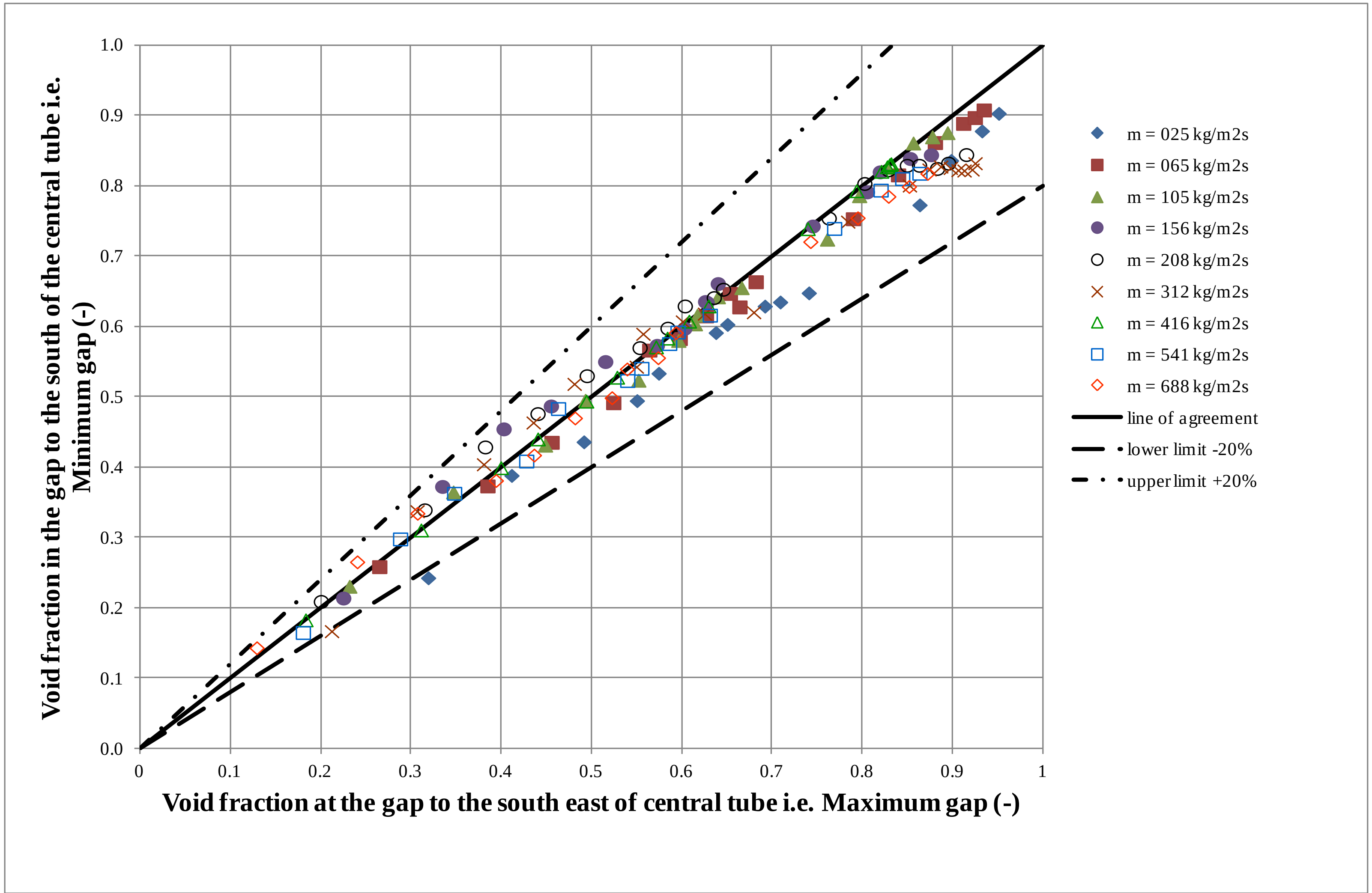

Figure 6.4: Comparison of maximum and vertical minimum gap void fraction (38 mm in-line bundle)

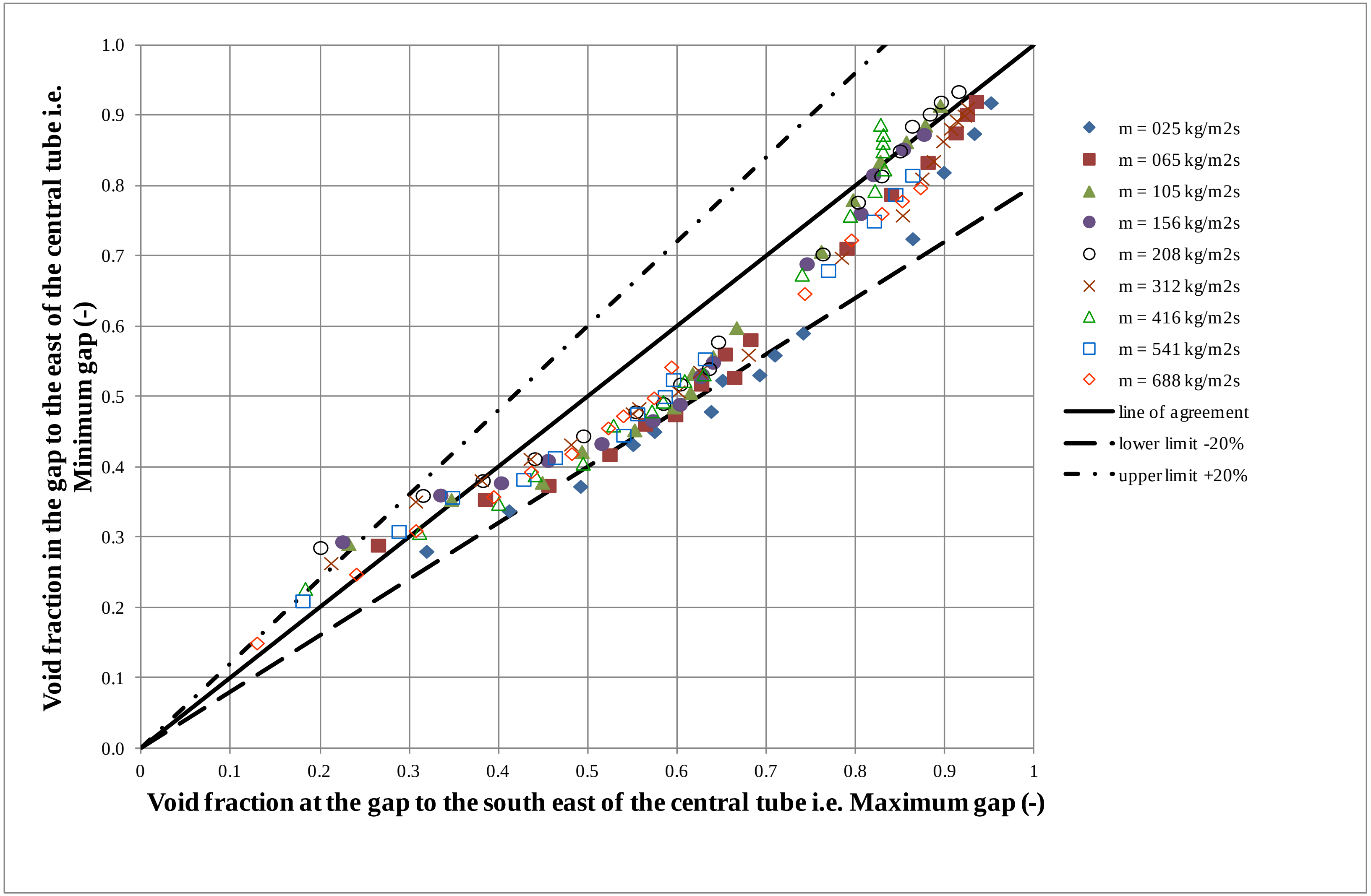

Figure 6.5: Comparison of maximum and horizontal minimum gap void fraction (38 mm in-line bundle)

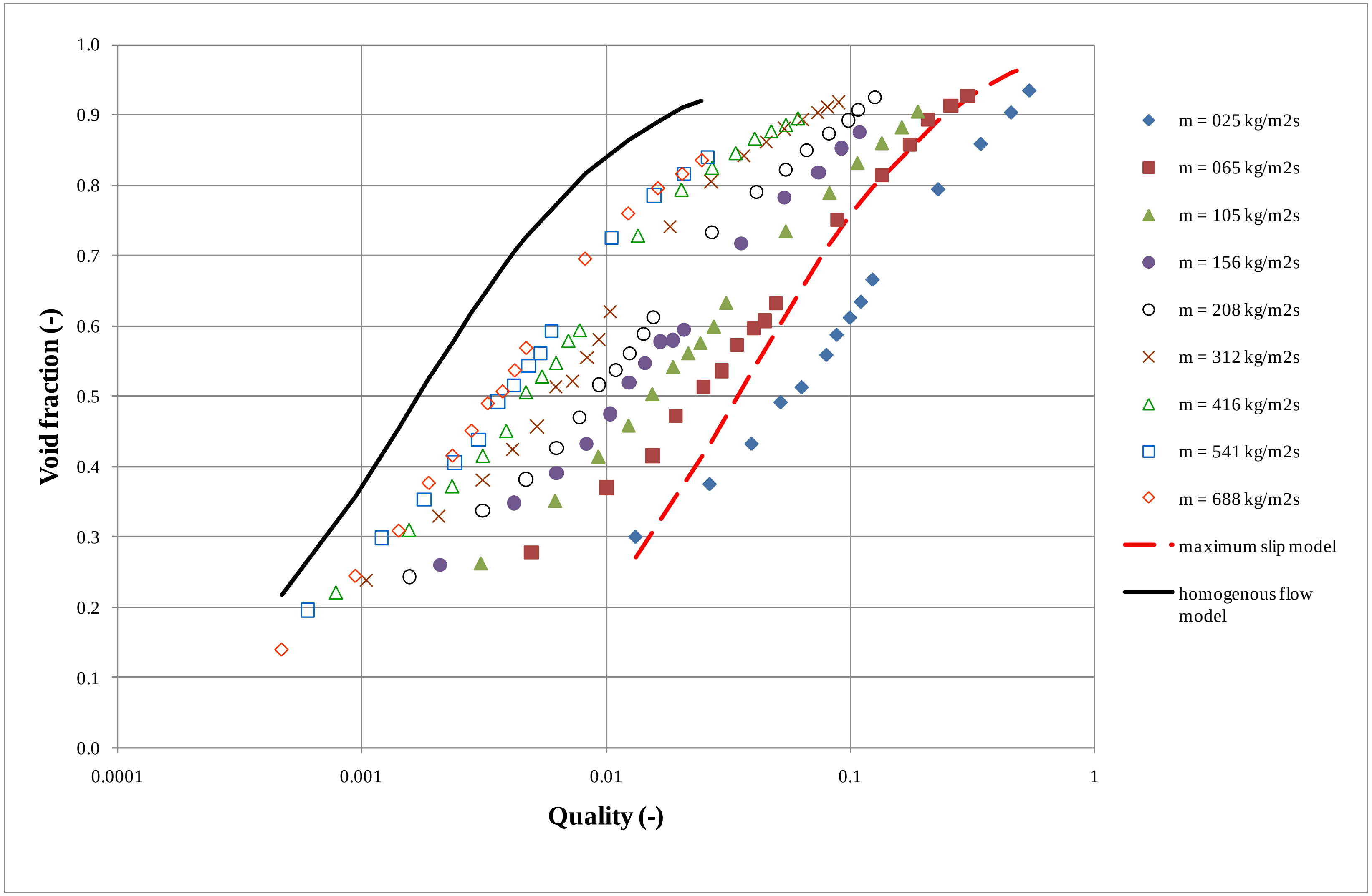

Figure 6.6: Variation of void fraction with quality in the 38 mm in-line bundle

6.1.4 Void fraction comparisons with other models

The measured pitch void fractions are compared with predictions from Schrage et al. [1], Feenstra et al. [3] and Dowlati et al. [2].

The measured and predicted values by Schrage et al. [1] are compared in Figure 6.7. The comparison is poor with most predictions outside the upper and lower limits set at ±30%. This is consistent with other findings [2,3] although at lower mass fluxes of 25 kg/m^{2}s and 65 kg/m^{2}s, some of the void fractions are within the limit sets of ±30%. The RMS error is 152% and the average error is 112%.

The comparison between the measured values and the Feenstra et al. [3] predictions are shown in Figure 6.8. The comparison shows that Feenstra et al. [3] always underpredict the void fraction with most data within ±30%. The RMS error is 19.5% and the average error is 14.7%. This method's predictions are better at the lower mass fluxes than the higher mass fluxes.

The comparison between the measured values and the Dowlati et al. [2] predictions are shown in Figure 6.9. The comparison is reasonably good, with virtually all of the predictions is near with line of agreement and within the upper and lower limits of ±30%. The RMS error is 10.3% and the average error is 2.48%. However, this correlation is poorer at lower mass fluxes than at larger ones.

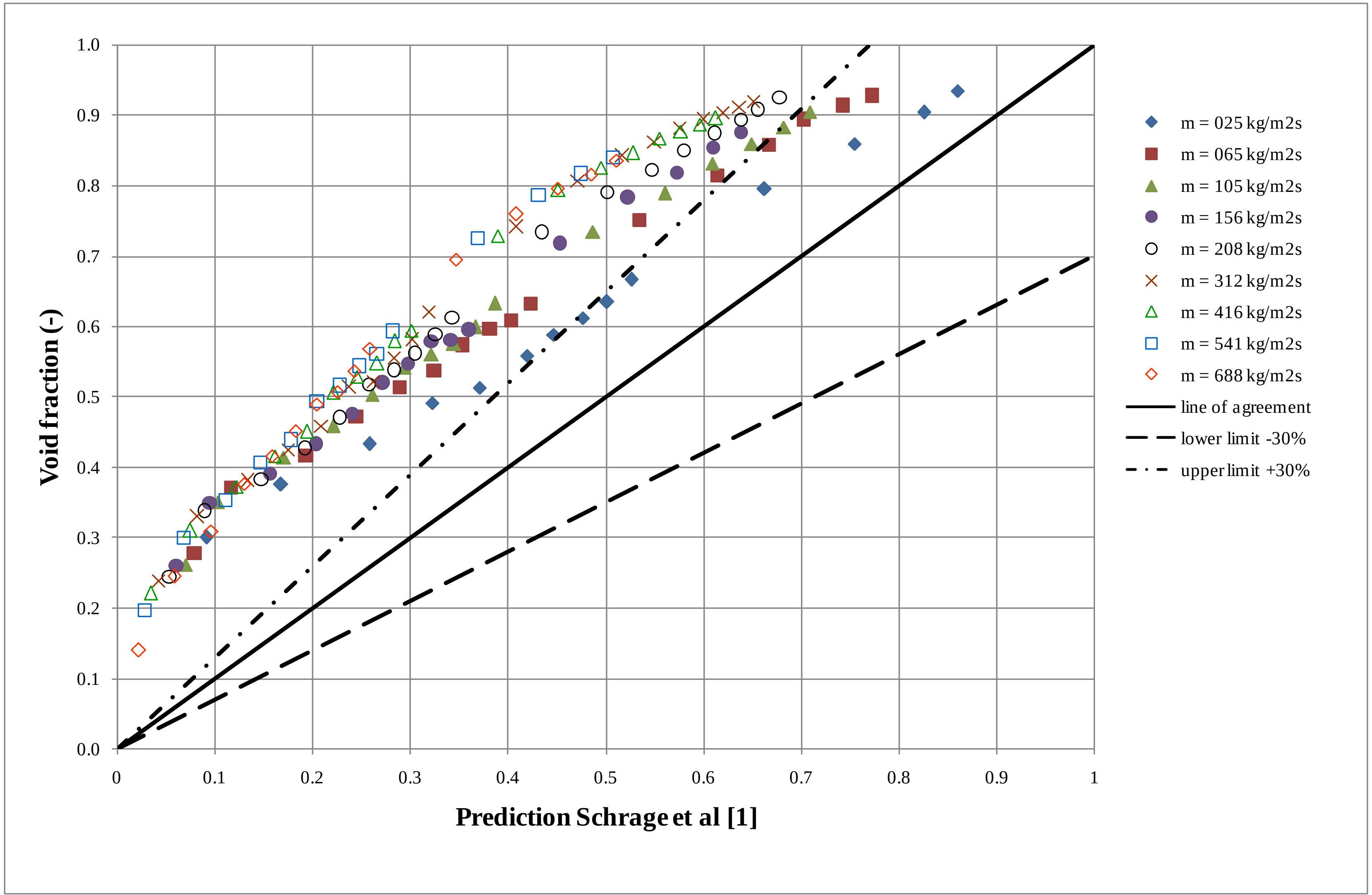

Figure 6.7: Variation of measured and Schrage et al. [1] void fraction for 38 mm in-line bundle

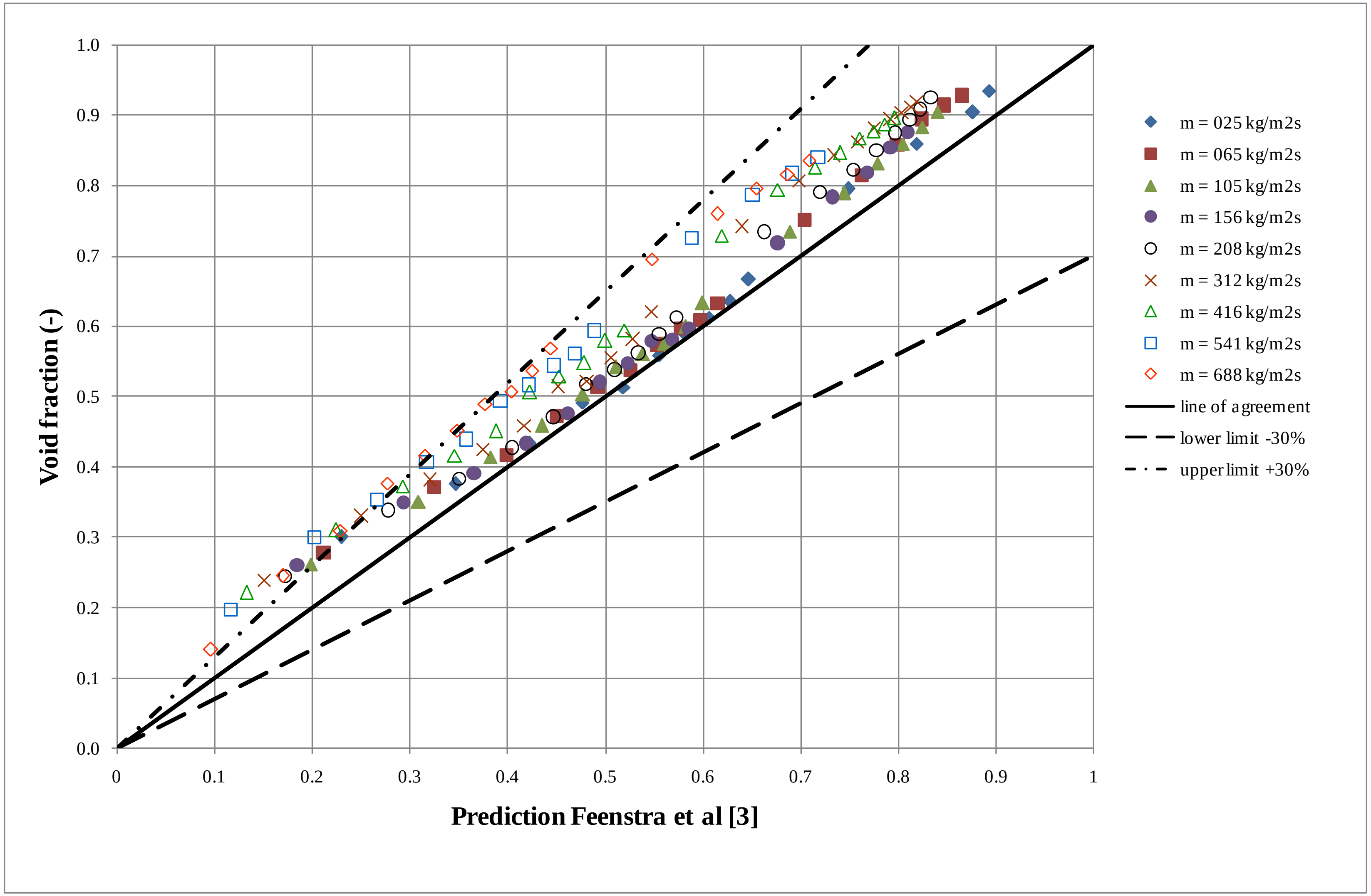

Figure 6.8: Variation of measured and Feenstra et al. [3] void fraction for 38 mm in-line bundle

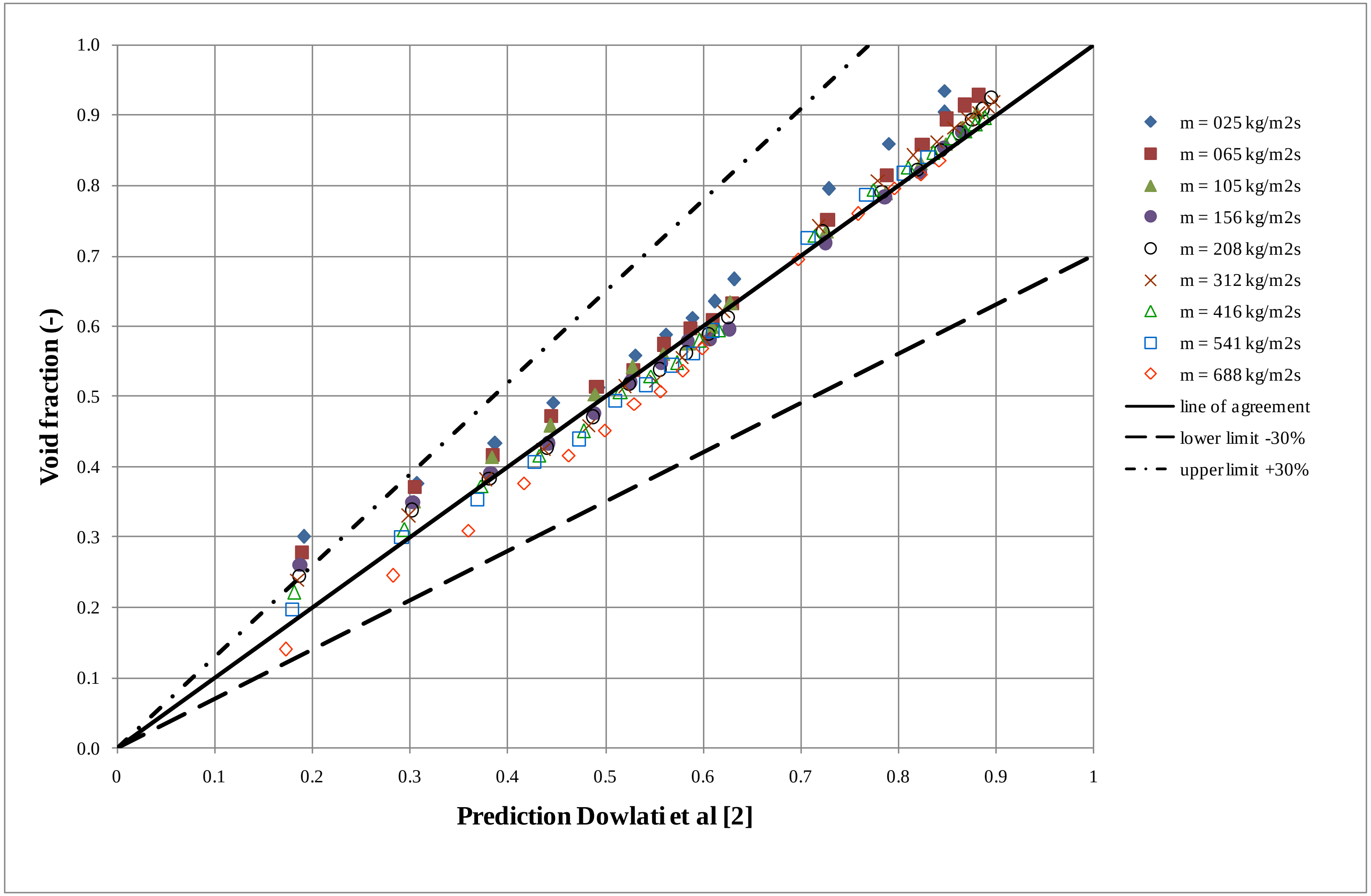

Figure 6.9: Variation of measured and Dowlati et al. [2] void fraction for 38 mm in-line bundle

6.2 Void fraction measurement in the 19 mm in diameter in-line tube bundle

6.2.1 Local void fraction measurements

Void fraction pitch measurements were made at four locations by aligning the single-beam, gamma ray densitometer in the maximum and minimum gaps chosen. The focal tube was the tube in the middle of the row thirteen, see Figure 4.7. The maximum gap used was north east of the central tube. The minimum gaps used were north, east and west of the central tube. The minimum gap between the tubes was 6 mm. The measurements were done separately and there were 580 data points all together. The tests were carried out at the nominal condition described in Chapter 4. The results for the four local void fractions measurements are tabulated in APPENDIX B.

6.2.2 Local Void fraction at the minimum and maximum gap

The measured void fraction variation with quality are shown in Figures 6.10-6.13 for each of the four locations at various of mass fluxes. The first three figures are for the minimum gap between the tubes and the fourth is for the maximum gap between the tubes. The graphs also include the predictions from the homogeneous and maximum slip models**.** The void fraction is shown to increase with increasing quality. Each figure shows void fraction increasing with increasing mass flux, again consistent with other findings [1,2,3]. The measured void fractions also agree well with other findings since the void fraction data for one-dimensional flows are said to fall between the maximum slip and the homogeneous values. The current data are shown to be reasonably consistent with this view, except at the lower mass fluxes.

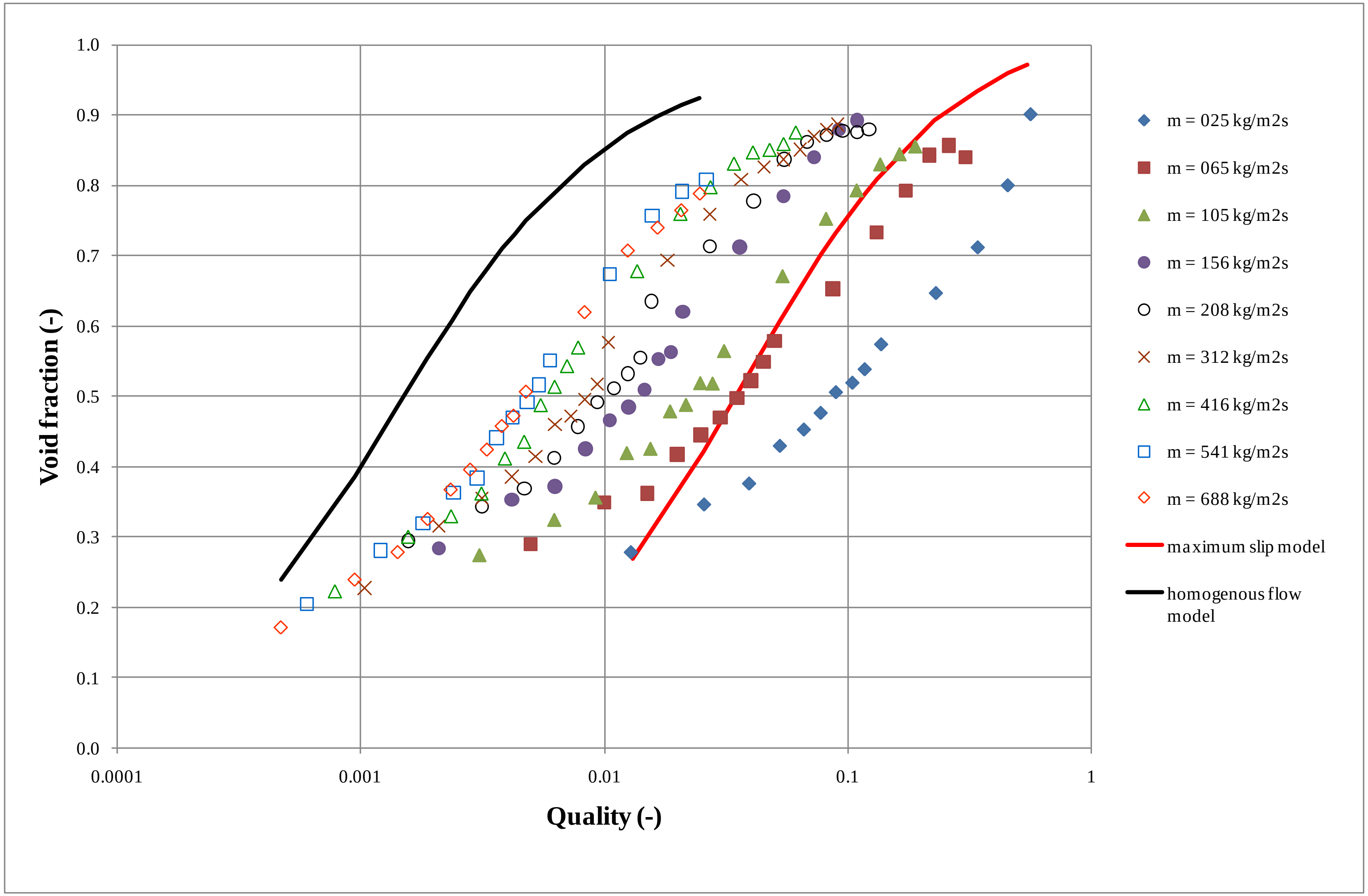

Figure 6.10: Variation of measured void fraction with quality at the gap to the west of central tube i.e. minimum gap (19 mm in-line bundle)

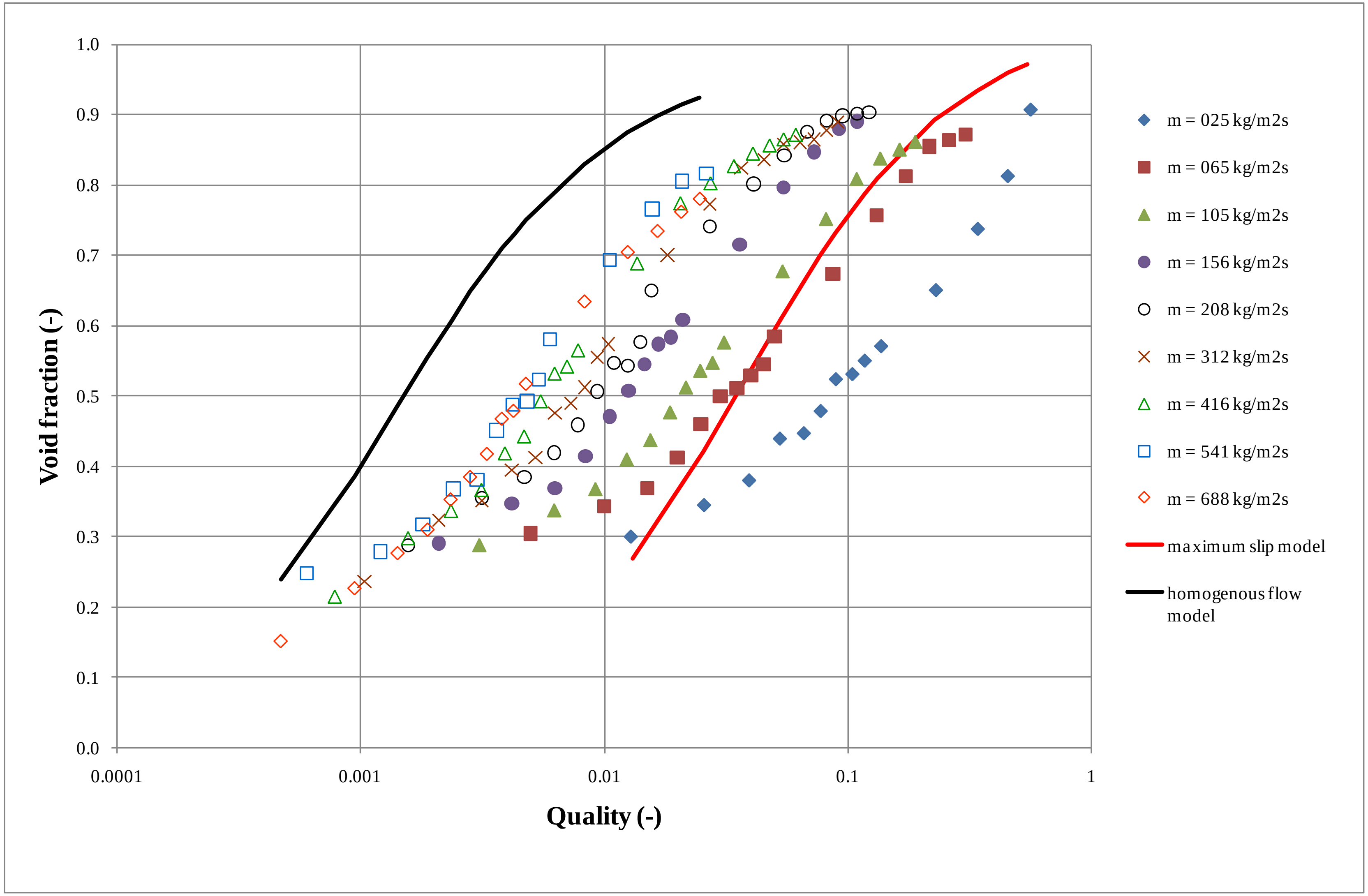

Figure 6.11: Variation of measured void fraction with quality at the gap to the east of central tube i.e. minimum gap (19 mm in-line bundle)

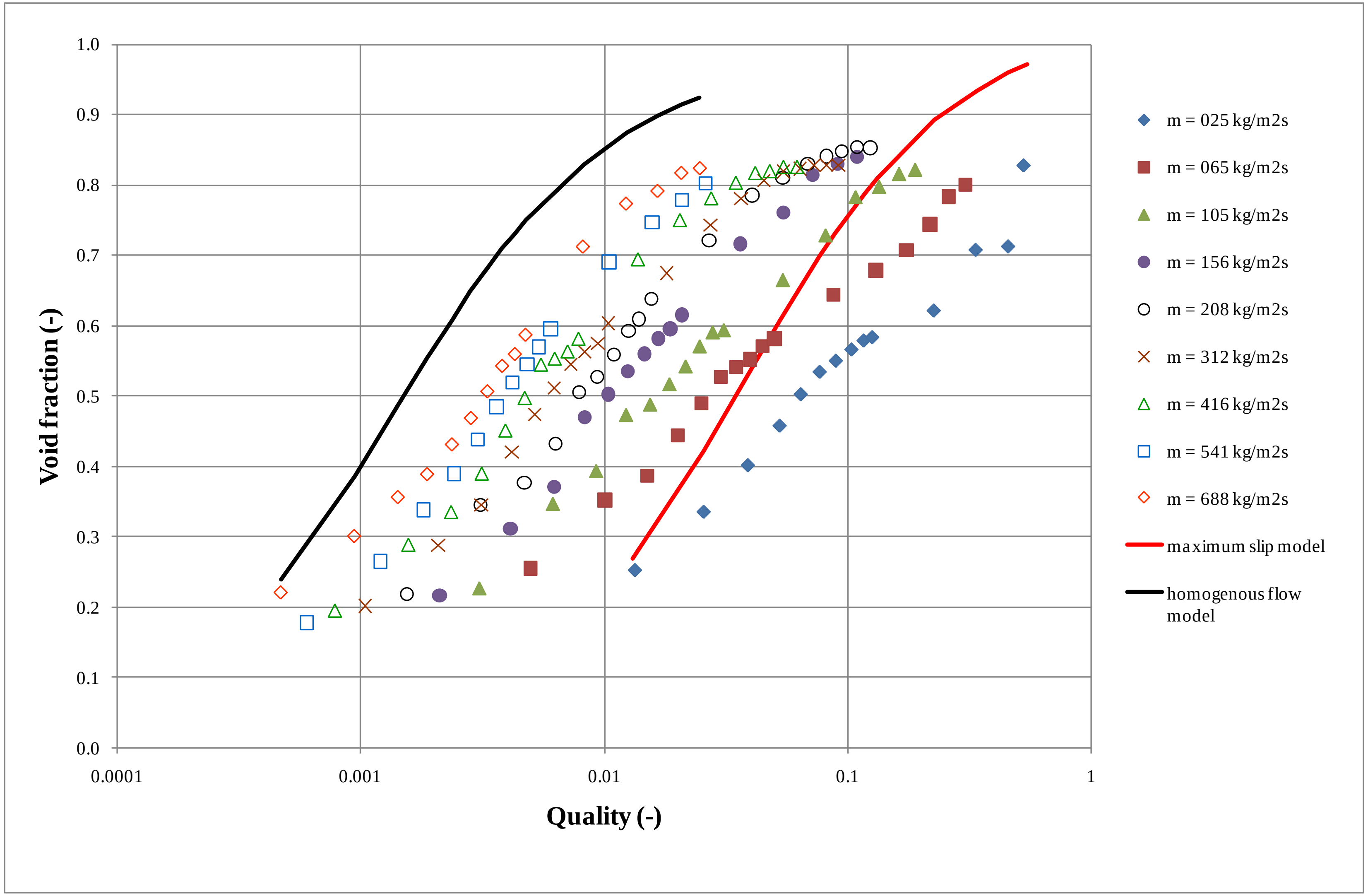

Figure 6.12: Variation of measured void fraction with quality at the gap to the north of central tube i.e. minimum gap (19 mm in-line bundle)

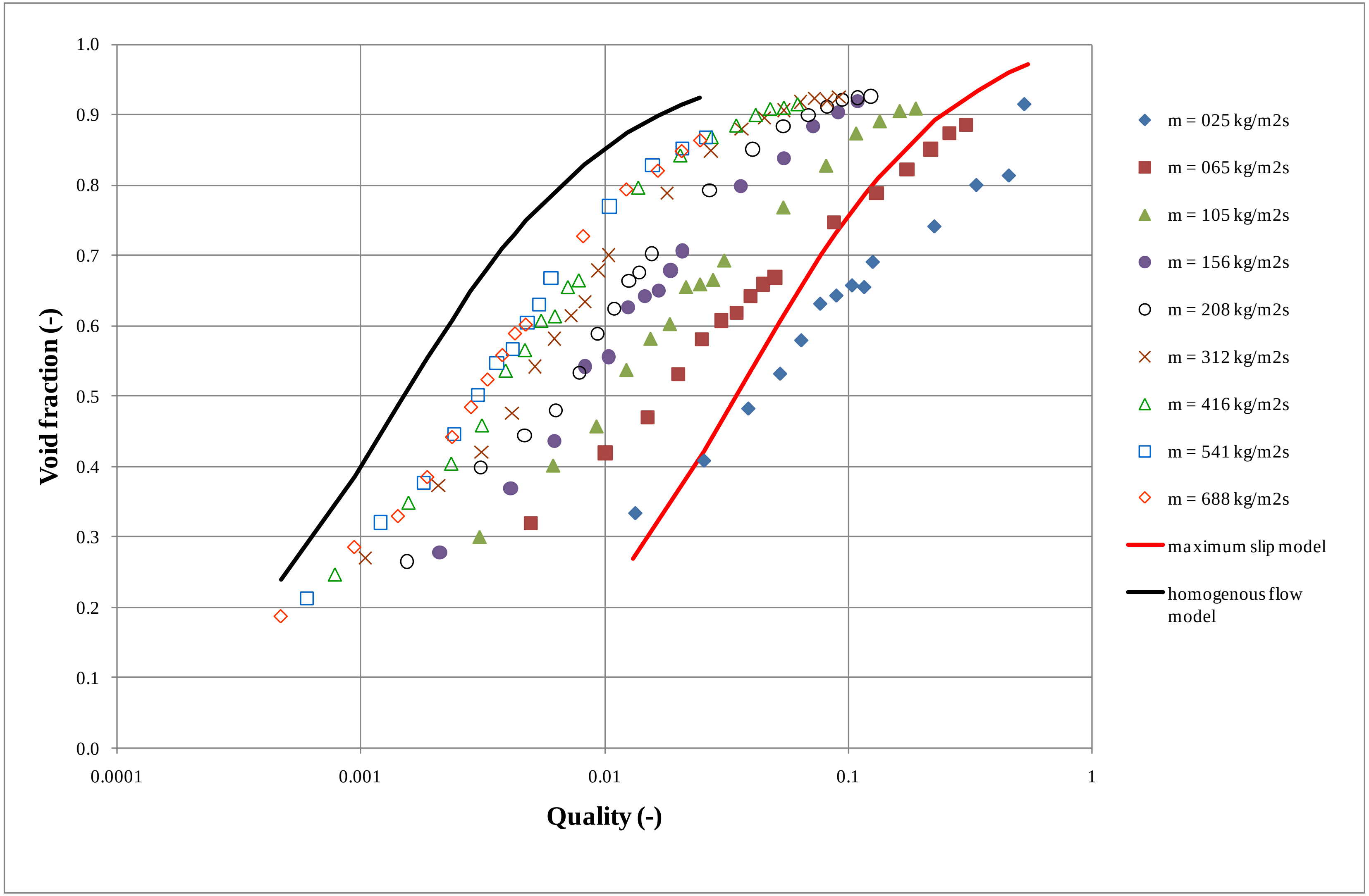

Figure 6.13: Variation of measured void fraction with quality at the gap to the north east of central tube i.e. maximum gap (19 mm in-line bundle)

6.2.3 Comparison of local void fraction measurements

The measured void fractions at the gap to the west and the gap to the east of central tube are compared. These locations were chosen because there are parallel to each other or they were 'mirror images' if the central tube becomes an origin plane. Both locations are in the horizontal minimum gap, which has a 6 mm gap between the tubes. Both locations are also in the line of upward two-phase flow. A comparison of the void fractions data at these locations is shown in Figure 6.14. Most of the measured void fractions at both locations are about the same magnitude and within the line of agreement, set to ±10%. The average difference is 1.5% and RMS difference is 3.1%. Therefore, it can be concluded that the void fractions at these two locations are the same; the flow pattern is also the same. The measured void factions can be treated as symmetrical.

The measured local void fractions in the gaps to the north and east of the central tube (minimum gaps) are compared to the values at the gap to the north east of the central tube (maximum gap).

Figure 6.15 shows the comparison between the void factions measured at the eastern horizontal minimum gap and the maximum gap. Both gaps are in the same vertical flow path of the two-phase flow of air and water except the area of the flow was different. The gap between the tubes for the minimum gap was 6 mm whilst the maximum gap is the maximum area between the tubes at the centre of the flow path and could be 25 mm. Most of the measured void fractions in the minimum gap are significantly lower than the maximum gap values for all mass fluxes, especially between void fractions of 0.4 to 0.8, otherwise the void fractions at both locations move to the agreement line. This is similar to the 38 mm case, Figure 6.5.

Figure 6.16 shows the comparison between measured void fraction in the northern minimum vertical gap and maximum gap between the tubes. This void fraction behaves differently to the measured void faction in the maximum gap. This minimum gap is in the vertical pitch of 25 mm and is 6 mm high and is not in the same vertical flow path. The void fractions measured in the minimum gap were lower than the maximum gap between the tubes for all but the highest mass flux. This is because of the high velocities of the air flow that drag the water up to the top of the bundle that makes barely has any flow in this minimum gap.

The vertical flow direction void fraction measurements, in the eastern horizontal minimum gap and the maximum gap show a big difference. Therefore, the pitch void fractions were taken as the average between these two locations because the flow is treated as one-dimensional. These pitch void fractions were used for comparison to void fractions predictions by Schrage et al. [1], Feenstra et al. [3] and Dowlati et al. [2], and in deducing the two-phase multiplier and drag forces. The two-phase multiplier and drag force will be discussed in Chapter 7 and Chapter 8 respectively. The pitch void fraction measurement variation with quality is shown for a range of mass fluxes in Figure 6.17.

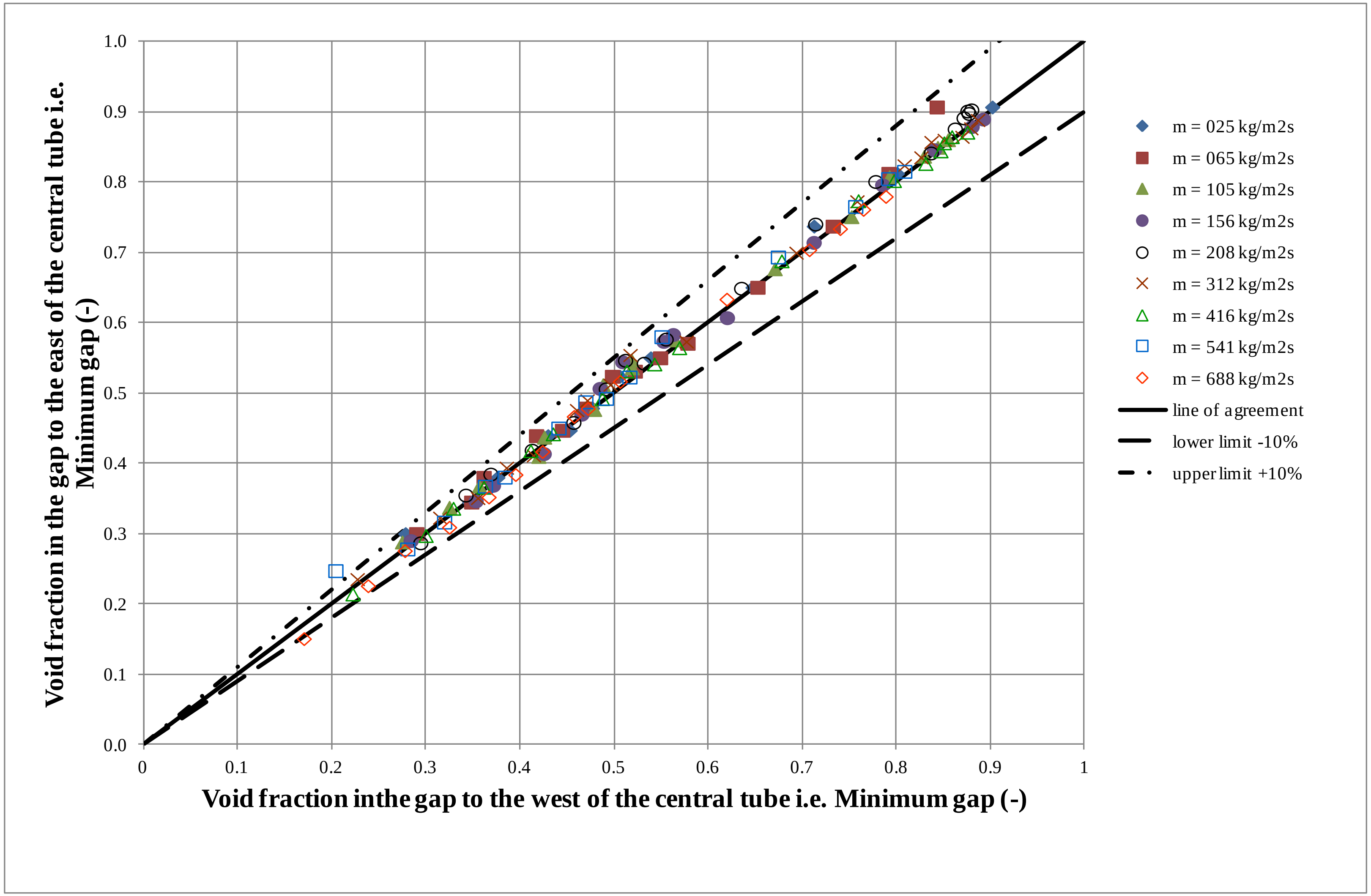

Figure 6.14: Comparison of western and eastern void fraction for 19 mm in-line bundle

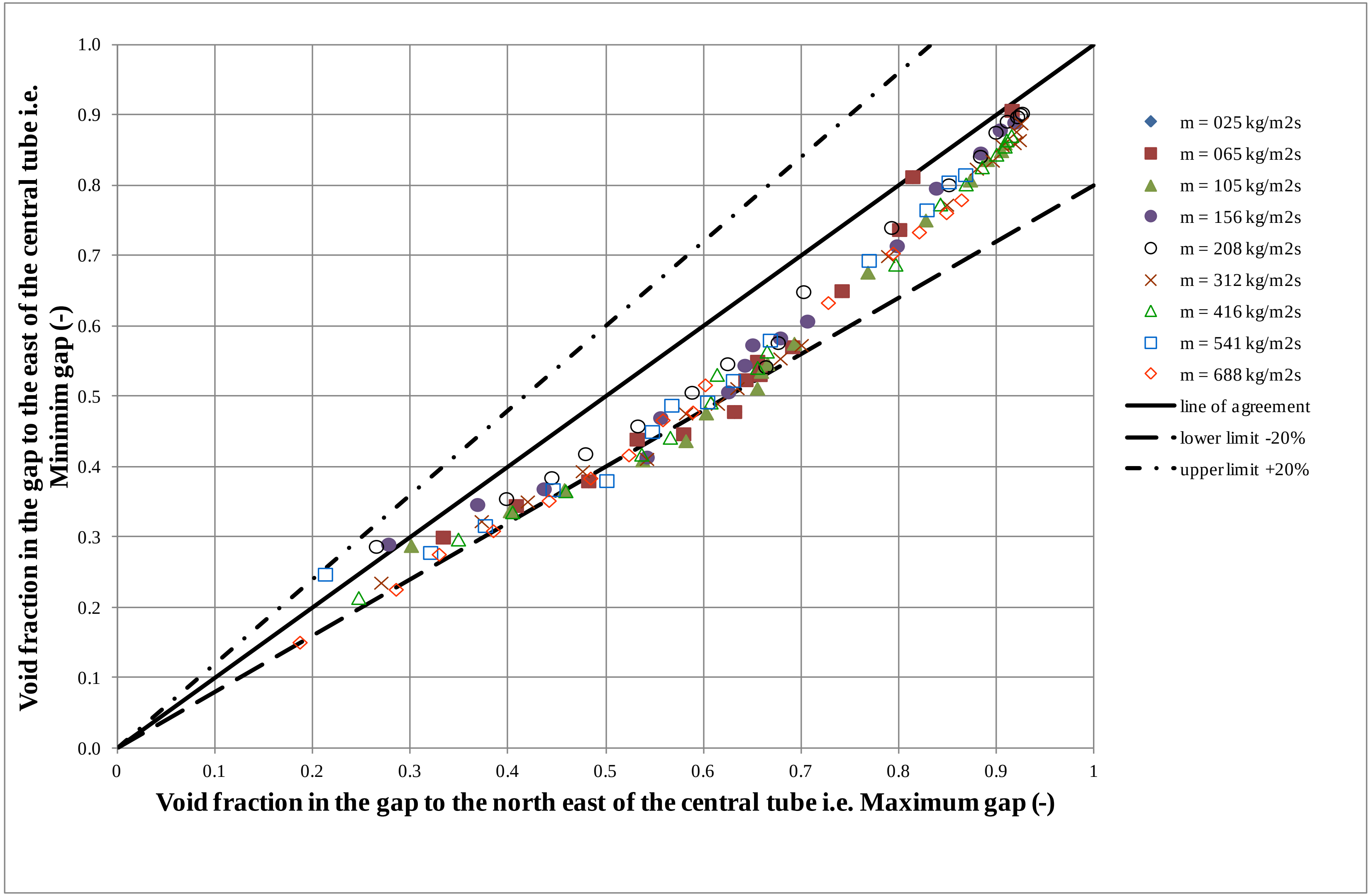

Figure 6.15: Comparison of maximum gap and eastern horizontal minimum gap void fraction for 19 mm in-line bundle

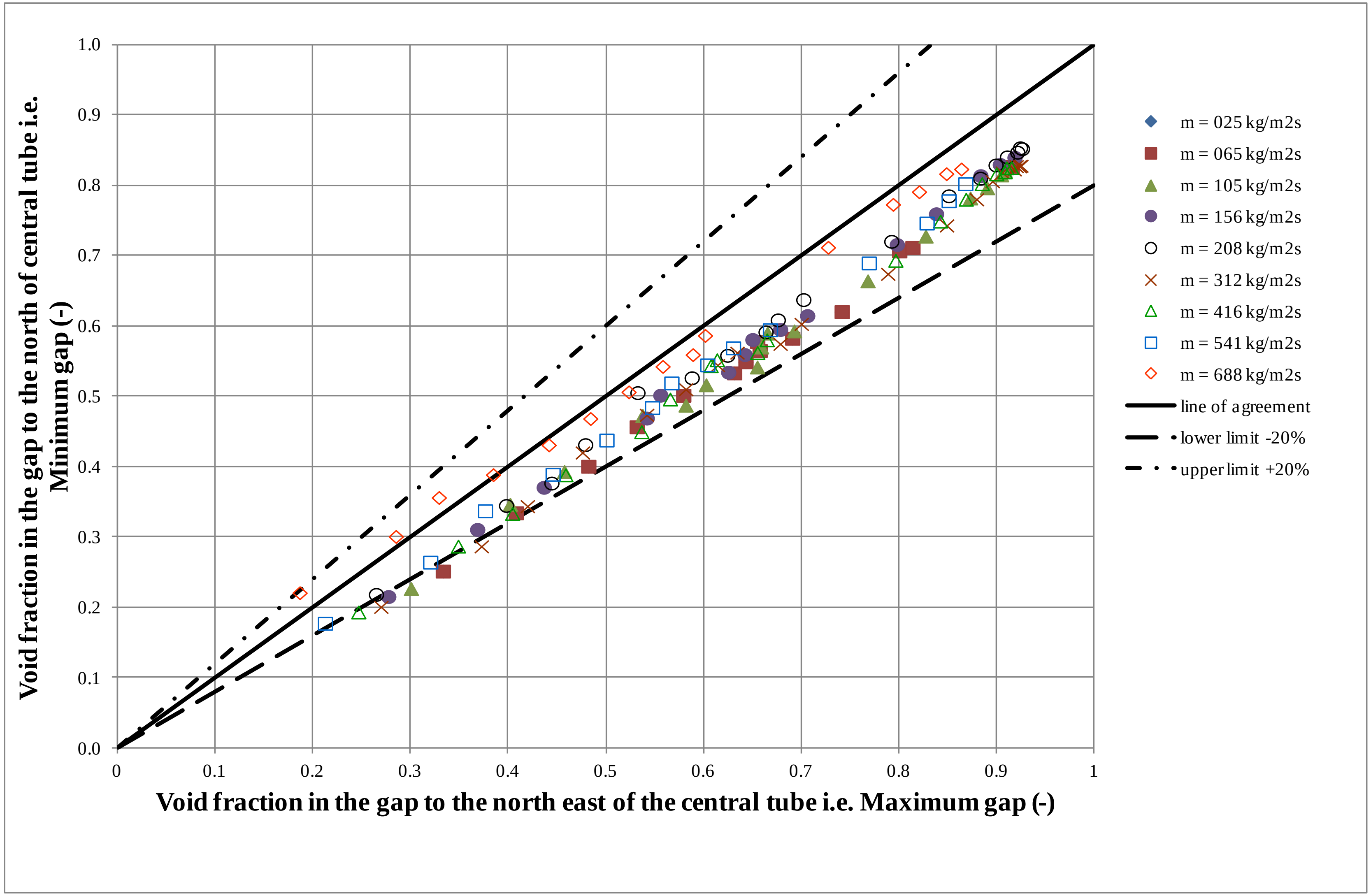

Figure 6.16: Comparison of maximum gap and northern vertical minimum gap void fraction for 19 mm in-line bundle

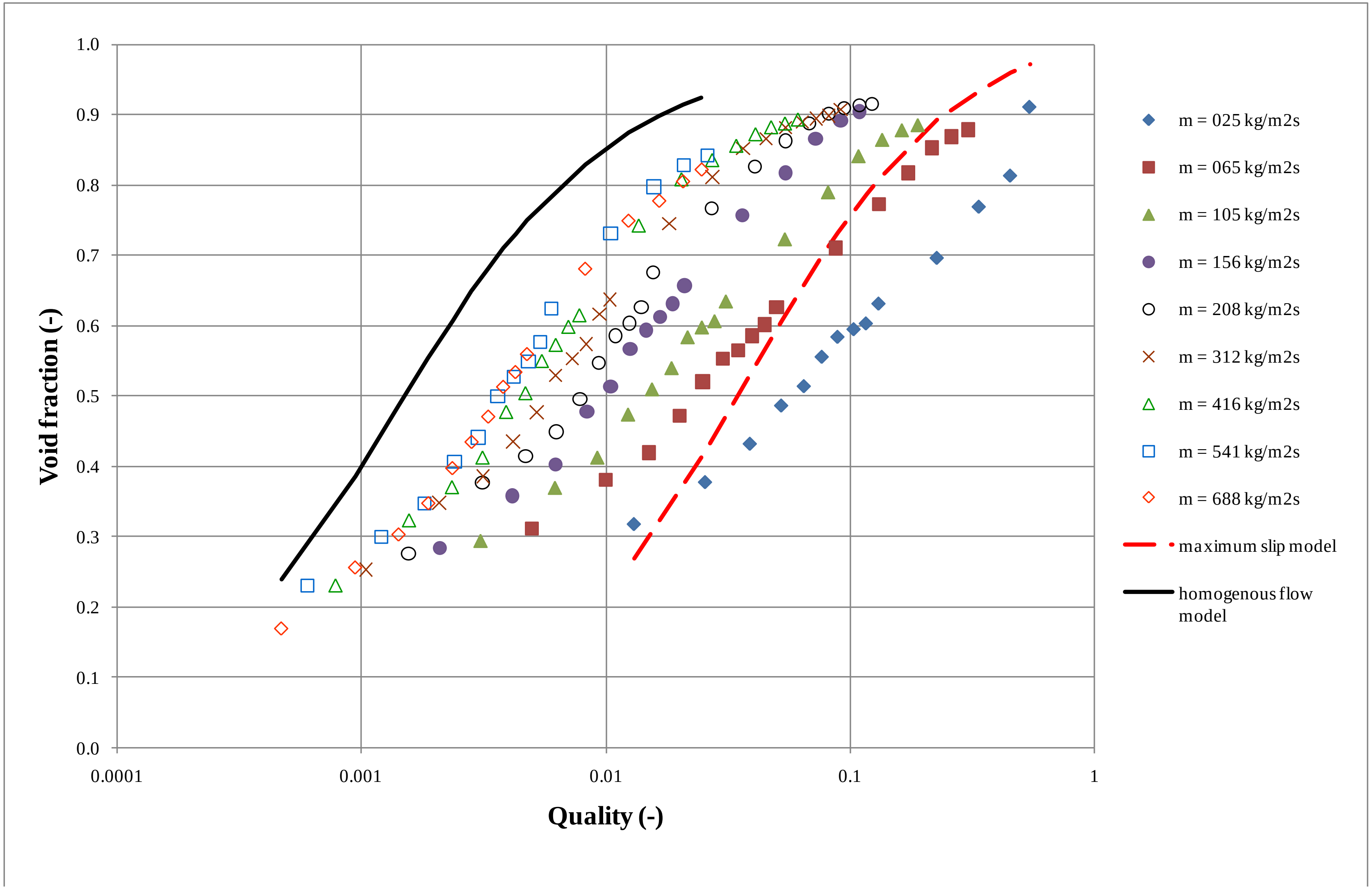

Figure 6.17: Variation of measured void fraction with quality in the 19 mm in-line bundle

6.2.4 Void fraction comparisons with correlations

The pitch void fractions are compared with the correlations of Schrage et al. [1], Feenstra et al. [3] and Dowlati et al. [2].

Schrage et al. [1] used Equation (6.4-6.6) to predict the void fraction. The measured and predicted values are compared in Figure 6.18. The comparison is poor with most predictions outside the upper and lower limits set at ±30%. This is consistent with other findings [2,3]. The RMS error is 127.9% and the average error is 90.13%. However, at the lowest mass flux of 25 kg/m^2s, Schrage et al. [1] predict most of the void fractions reasonably well. Some of the void fractions at 65 kg/m^2s and 105 kg/m^2s are also within the limits of ±30%.

Feenstra et al. [3] used Equation (6.7-6.11) to predict the void fraction. The comparison between the measured values and the predictions by Feenstra et al. [3] correlations are shown in Figure 6.19. The comparison is reasonably good, with virtually all of the data within the upper and lower limits of ±30%. The average error is 0.35% and the RMS error is 9.5%. As seen in Figure 6.19, the predictions by Feenstra et al. [3] is better at larger mass fluxes than it is at lower values.

Figure 6.20 shows the comparison between the measured void fractions and predictions by Dowlati et al. [2]. Dowlati et al. [2] used Equation (6.12-6.14) to model void fraction and the predictions are within the ±30%, with the RMS error of 11.19% and the average of 6.72%. The values for C_1 was 35 and C_2 was 50. At higher void fraction above 0.85, the measured and the predicted values are about the same. Figure 6.20 also shows that the predictions of Dowlati et al. [2] at the lower mass fluxes are better than those at higher mass fluxes, unlike Feenstra et al. [3].

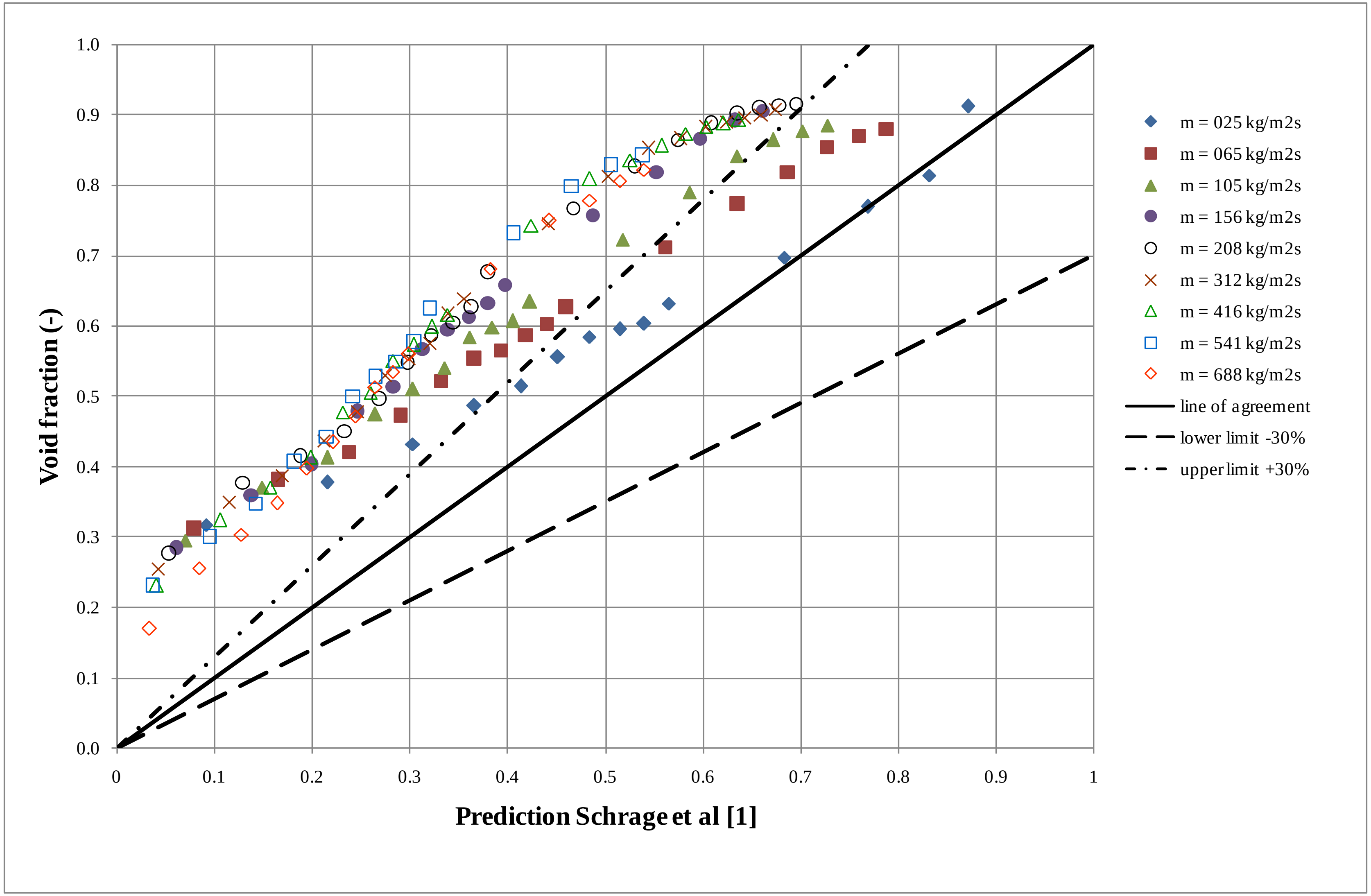

Figure 6.18: Variation of measured and Schrage et al. [1] void fraction for 19 mm in-line bundle

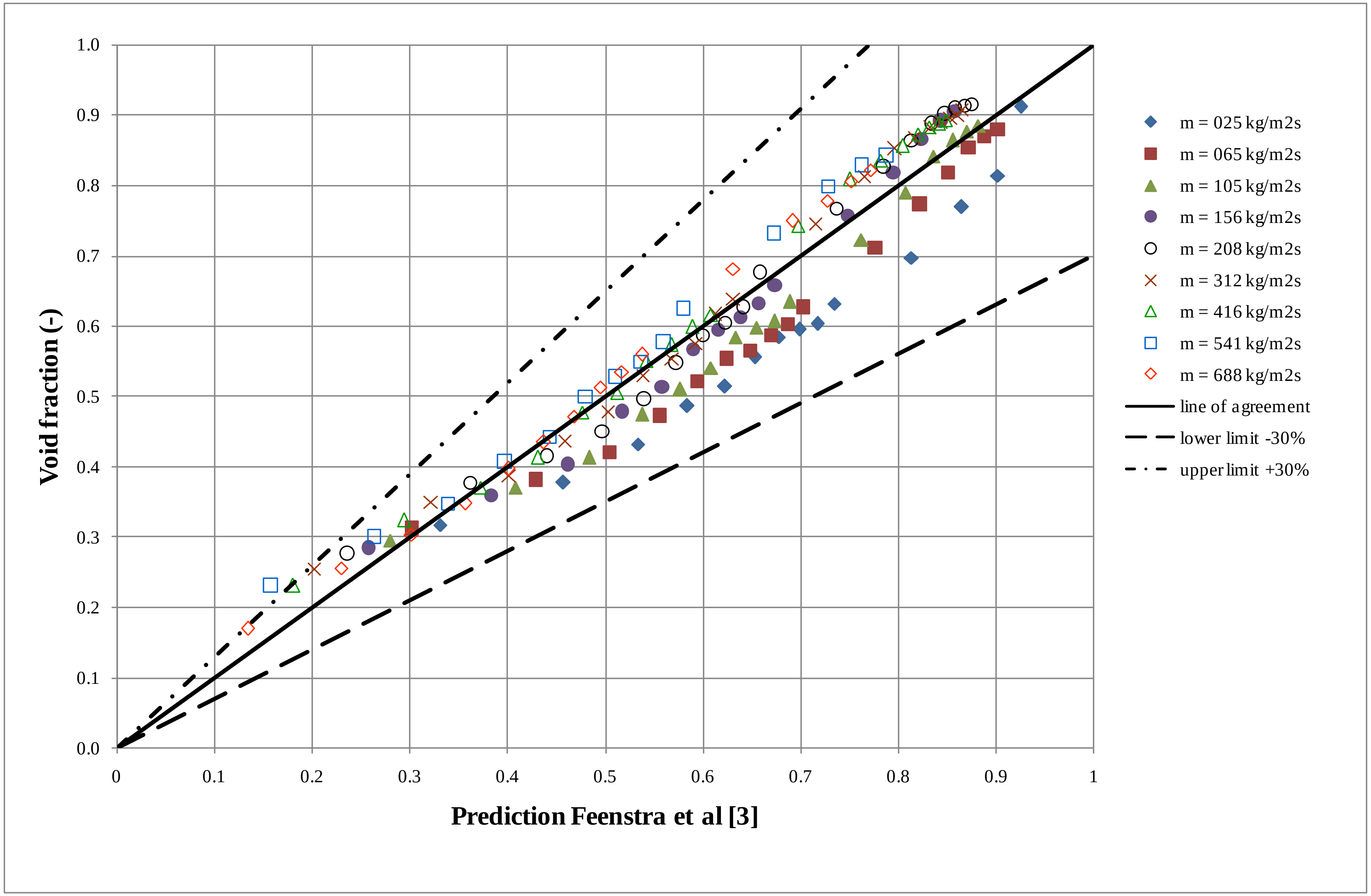

Figure 6.19: Variation of measured and Feenstra et al [3] void fraction for 19 mm in-line bundle

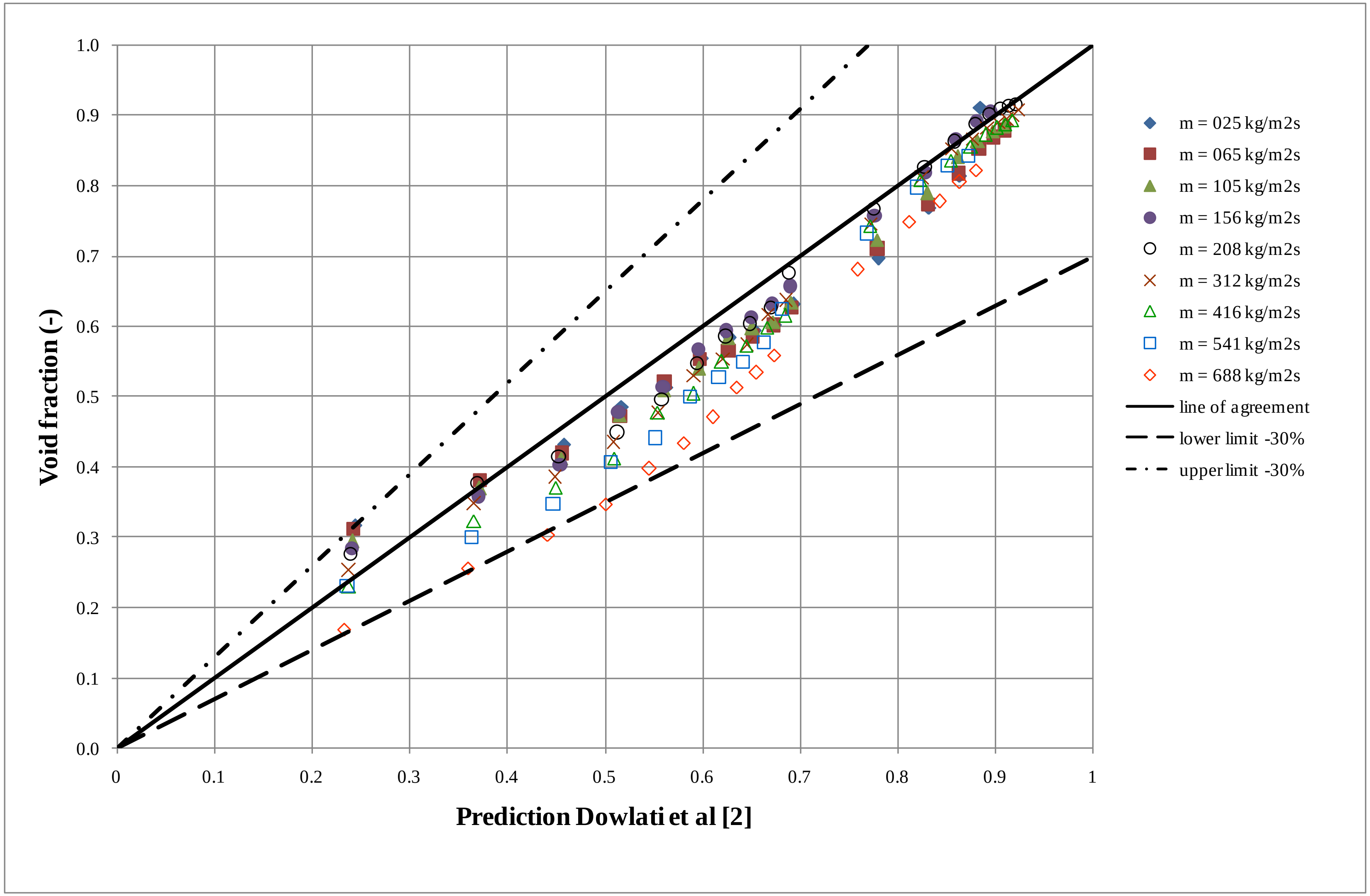

Figure 6.20: Variation of measured and Dowlati et al. [2] void fraction for 19 mm in-line bundle

6.3 Staggered tube bundle with tubes 19 mm in diameter

6.3.1 *Local void fractions measurements*

Void fractions measurements were taken in the staggered tube bundle, which contained 22 rows and 4 full columns of tubes, and half tubes placed on the wall. The outside diameter of the tubes was 19 mm and a pitch to diameter ratio 1.32. The focal tube was in row sixteen, two from left, Figure 4.8. Void fractions measurements were taken at two locations by aligning the single-beam, gamma ray densitometer in the gap to the south of the central tube and at the gap to the east of the central tube. The tests were carried out at the nominal condition described in Chapter 4 and there were 290 data points of void fractions measurement. The two sets of data are included in the APPENDIX B for all mass fluxes. The tests were done separately.

6.3.2 *Local void fractions at the minimum and maximum gaps.*

Figure 6.21 and Figure 6.22 show the local void fraction measurements variation with quality at several mass fluxes in the maximum gap and in the minimum gap between the tubes respectively. The graphs also include the homogenous flow model and maximum slip model**.** The void fraction is shown to increase with increasing quality. It is also shown to increase with increasing mass flux, again consistent with other findings [1,2,3]. The measured void fractions are also consistent with other studies where the void fraction data for one-dimensional flows are said to fall between the maximum slip and the homogenous flow model.

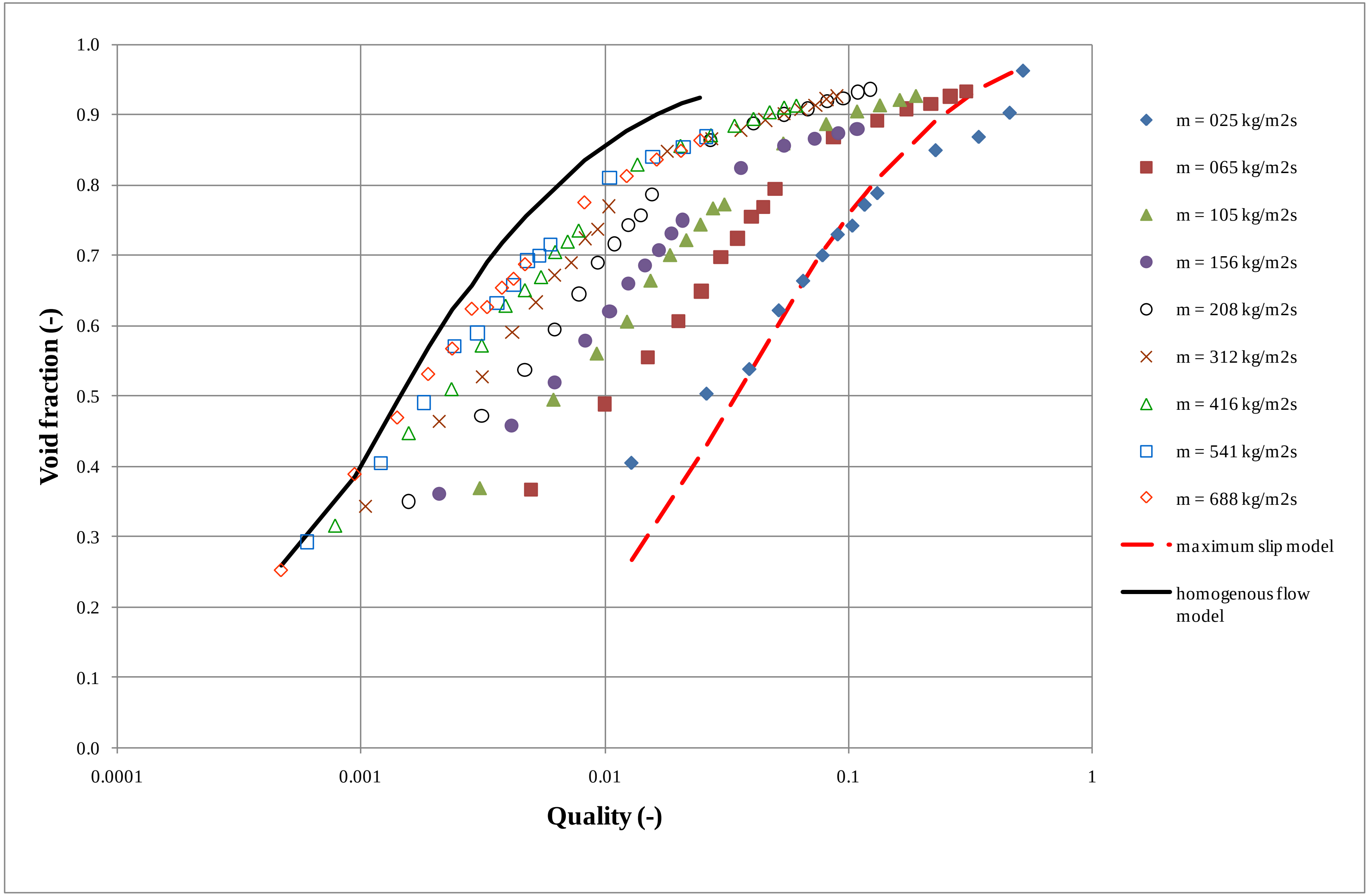

Figure 6.21: Variation of measured void fraction with quality at the gap to the south of central tube i.e. maximum gap (19 mm staggered bundle)

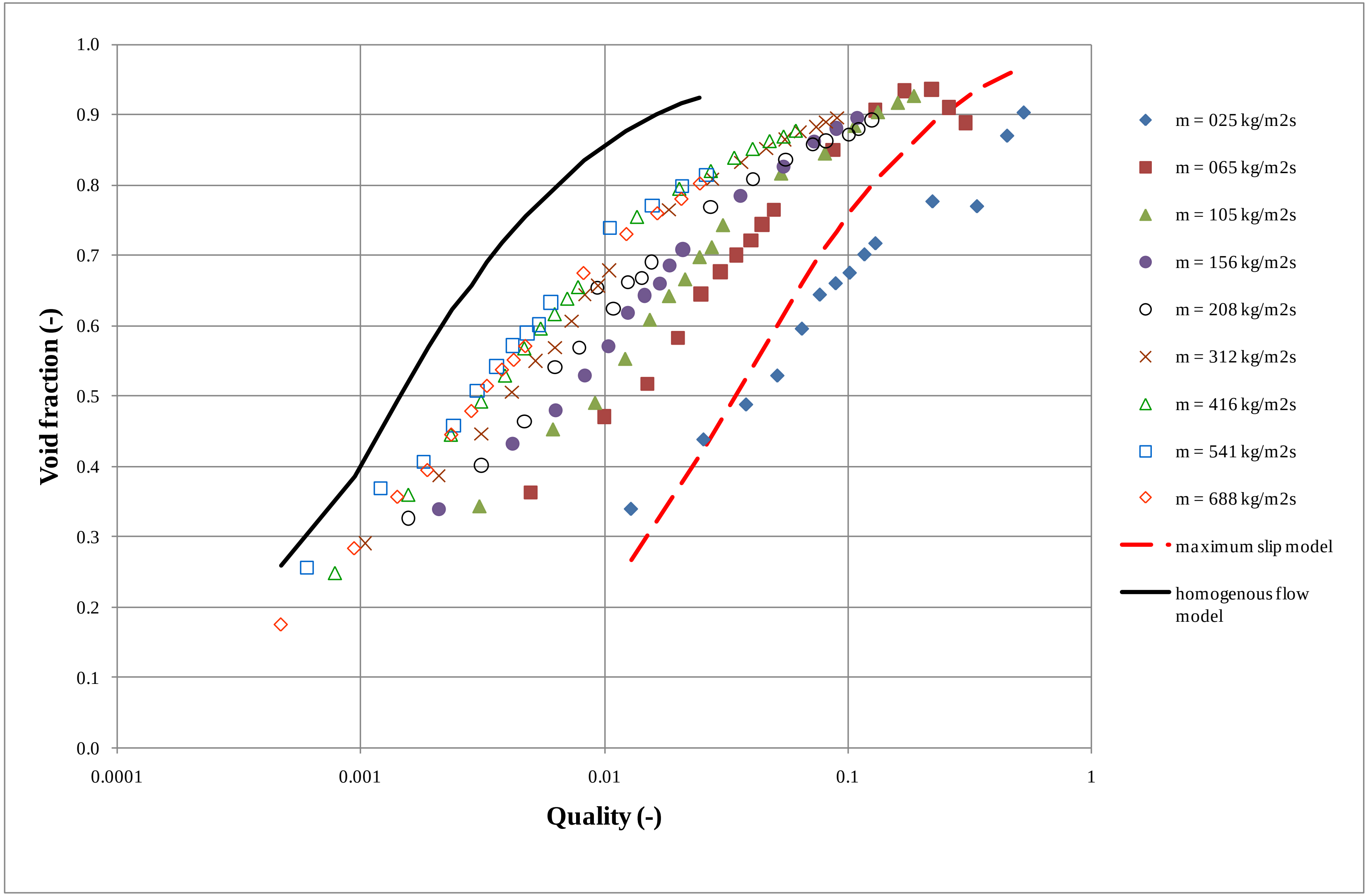

Figure 6.22: Variation of void fraction with quality at the gap to the east of central tube i.e minimum gap (19 mm staggered bundle)

6.3.3 *Comparison of local void fraction measurements*

The measured void fractions in the maximum gap are compared to the values in the minimum gap. The minimum gap between the tubes was 6 mm. The comparison between these two locations is shown in Figure 6.23. The void fractions in the minimum gap are always lower than void fractions in the maximum gap. The differences increase with mass flux. This is because the minimum gap between the tubes was small and the staggered arrangement makes more flow interference. The flow path between these points is complex because of the staggered alignment. At row thirteen, a one-dimensional two-phase flow will passed the tubes and meet in the maximum gap between rows fourteen and fifteen before separated again at row fifteen. Thus, more fluid passes this point and, given that the flow area is bigger than 6 mm, contributes higher void fractions. As for minimum gap between the tubes, the two-phase flow behaves the same way except the flow area is now 6 mm. Therefore the flow area and path affects to the void fraction values.

The pitch void fractions were taken as the average between the maximum and minimum gap values because the flow was treated as one-dimensional. These pitch void fractions were used for comparison with void fractions predictions by [1,2,3]. The two-phase multiplier and drag force analysis, discussed later in Chapter 7 and Chapter 8 respectively, also used the pitch values. The pitch void fraction variation with quality is shown for a range of mass fluxes in Figure 6.24.

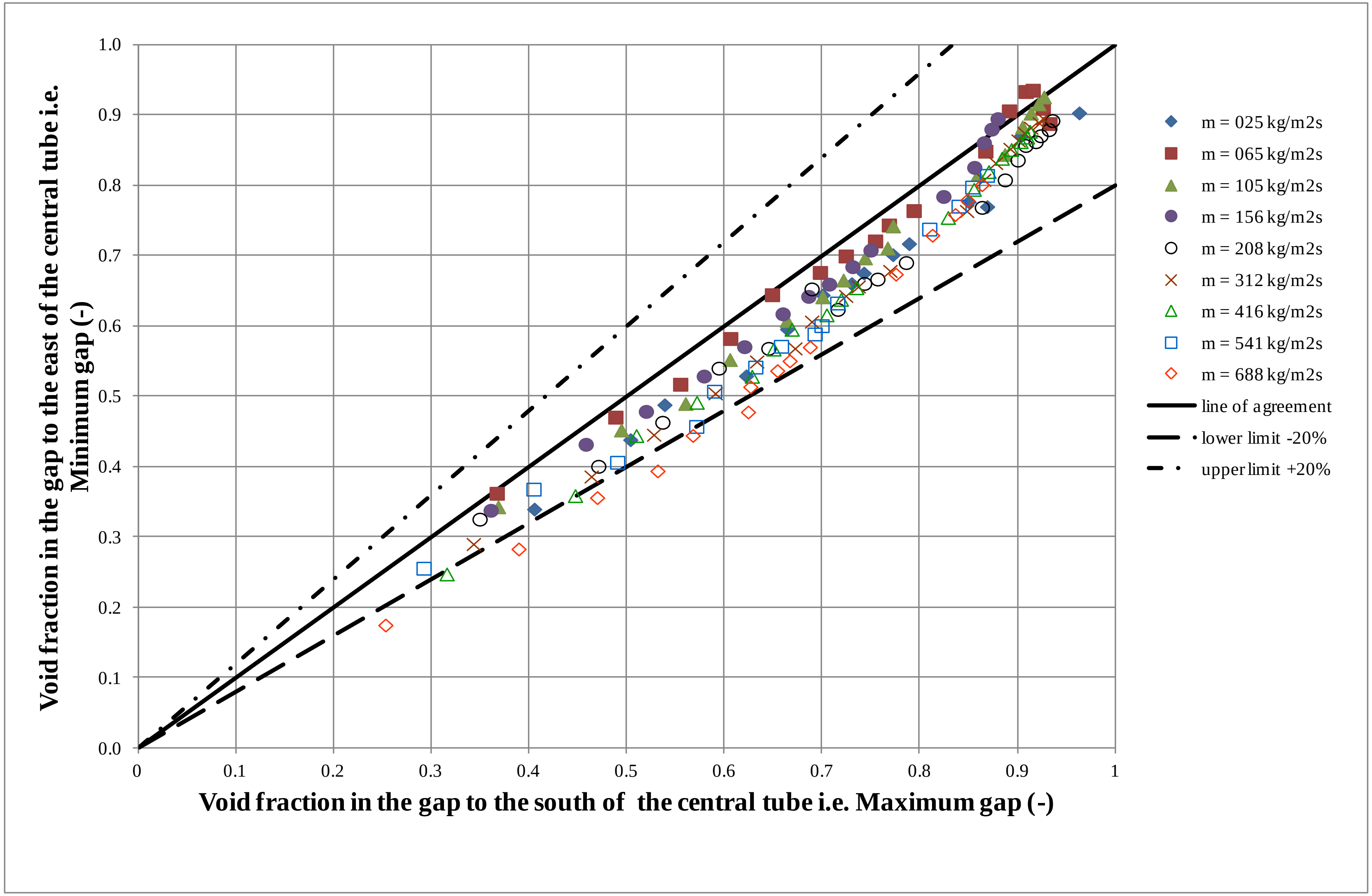

Figure 6.23: Comparison of void fraction at the gap to the south and east of central tube

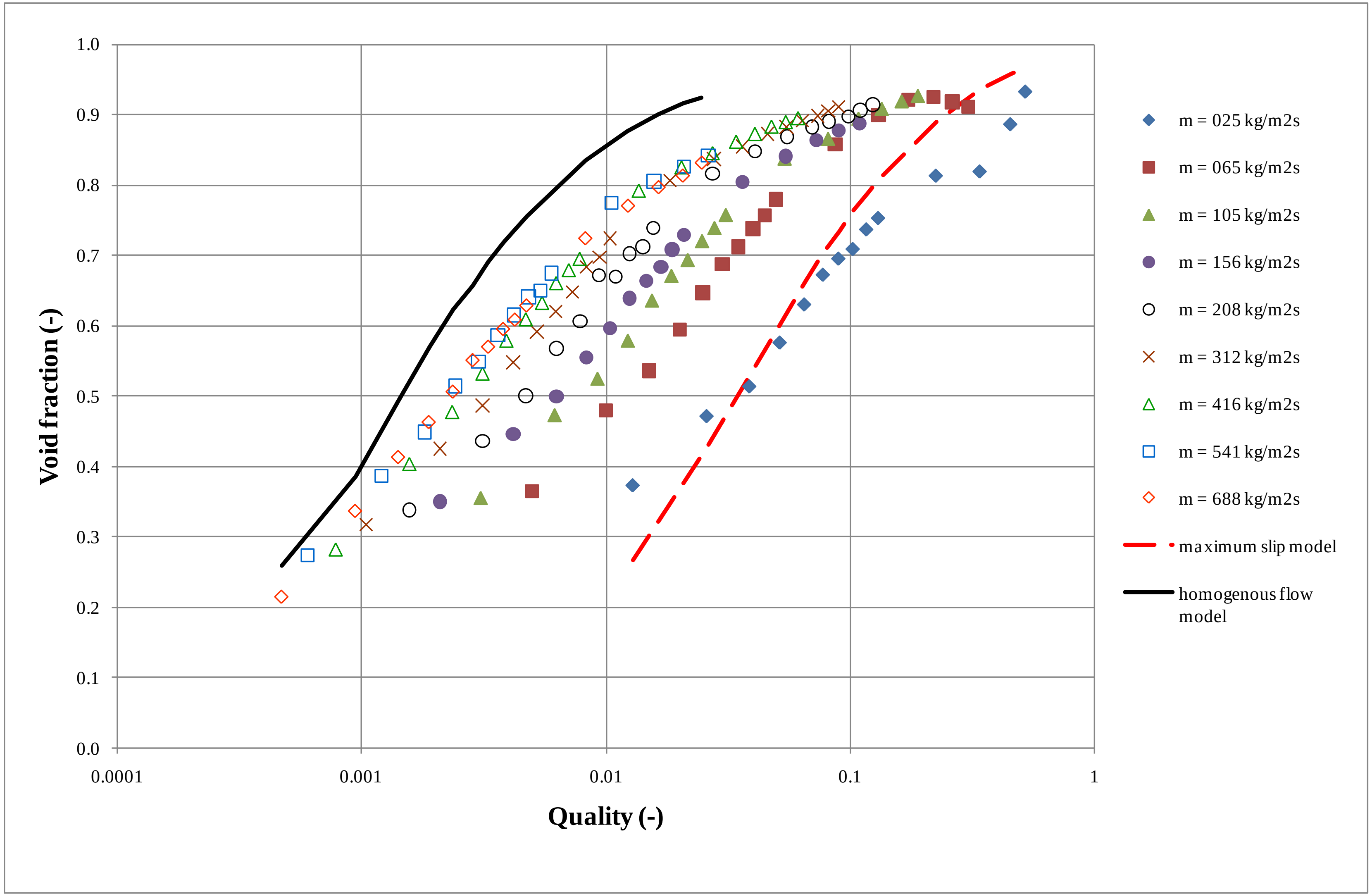

Figure 6.24: Variation of measured void fraction with quality in the 19 mm staggered bundle

6.3.4 *Void fraction comparison with other models*

Figures 6.25-6.27 show the comparison between the measured void fractions and predictions by Schrage et al. [1], Feenstra et al. [3] and Dowlati et al. [2] respectively.

The Schrage et al. [3] predictions and the measured void fractions comparison are shown in Figure 6.25. The figure reveals that the predictions by Schrage et al. [3] is very poor. They were outside of the upper and lower limit, set at ±30%, for all the mass fluxes. However, at the lower mass flux of 25-105 kg/m^{2}s, at void fractions above 0.7, the void fractions are well predicted to within the limits of ±30%. The RMS error is 166% and the mean is 120%.

The measured and predicted values by Feenstra et al. [3] are compared in Figure 6.26. The comparison is reasonable, with most of the predictions within the upper and lower limits of ±30%. The RMS error is 18%, the mean average error is 13%. Figure 6.26 shows that this method's predictions are better at the lower mass fluxes than they are at the larger ones.

Figure 6.27 shows a comparison of the measured void fractions and the predictions of Dowlati et al. [2]. Most of the predictions are within the limits of ±30%. The correlation by Dowlati et al. [2] predicts the void fraction very well at void fractions above 0.3, using C_1 = 35 and C_2 = 50 The RMS error is 12% and the mean average error is 6 %. The Dowlati et al. [2] is good at higher mass fluxes between 312 kg/m^{2}s to 541 kg/m^{2}s but poor at lower mass fluxes at 25 kg/m^{2}s to 105 kg/m^{2}s.

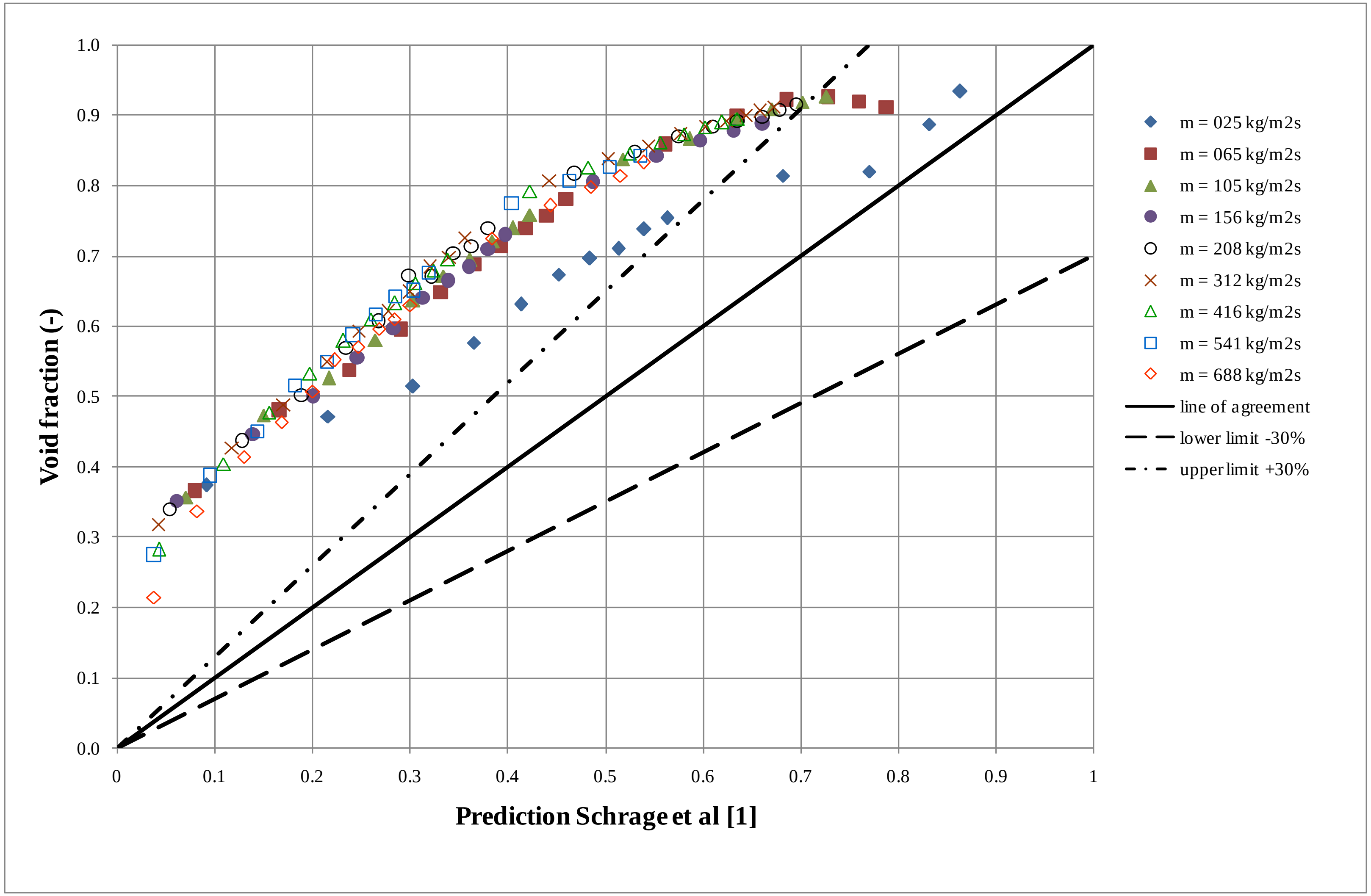

Figure 6.25: Variation of measured and Schrage et al. [1] void fraction for 19 mm staggered bundle

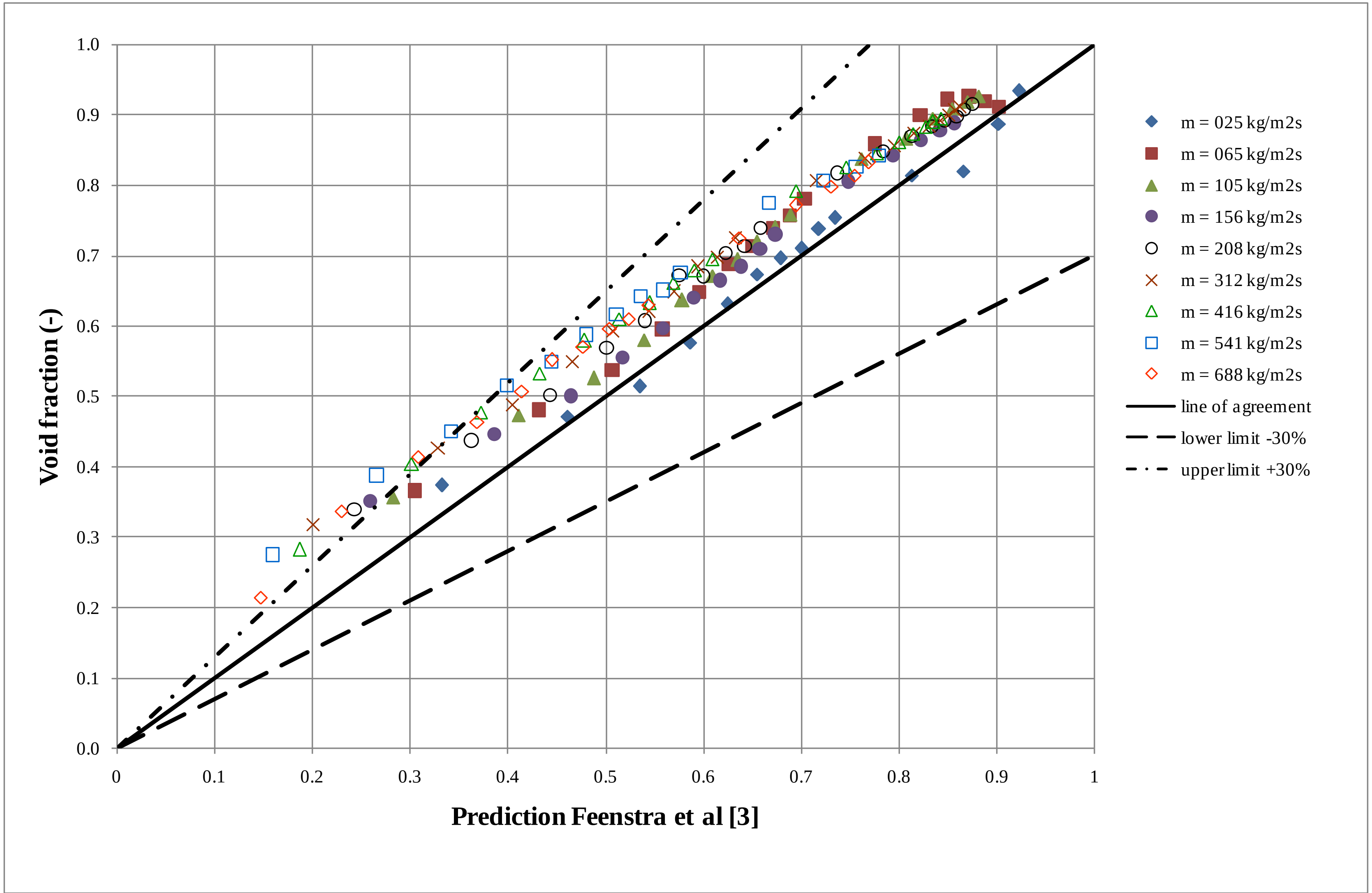

Figure 6.26: Variation of measured and Feenstra et al. [3] void fraction for 19 mm staggered bundle

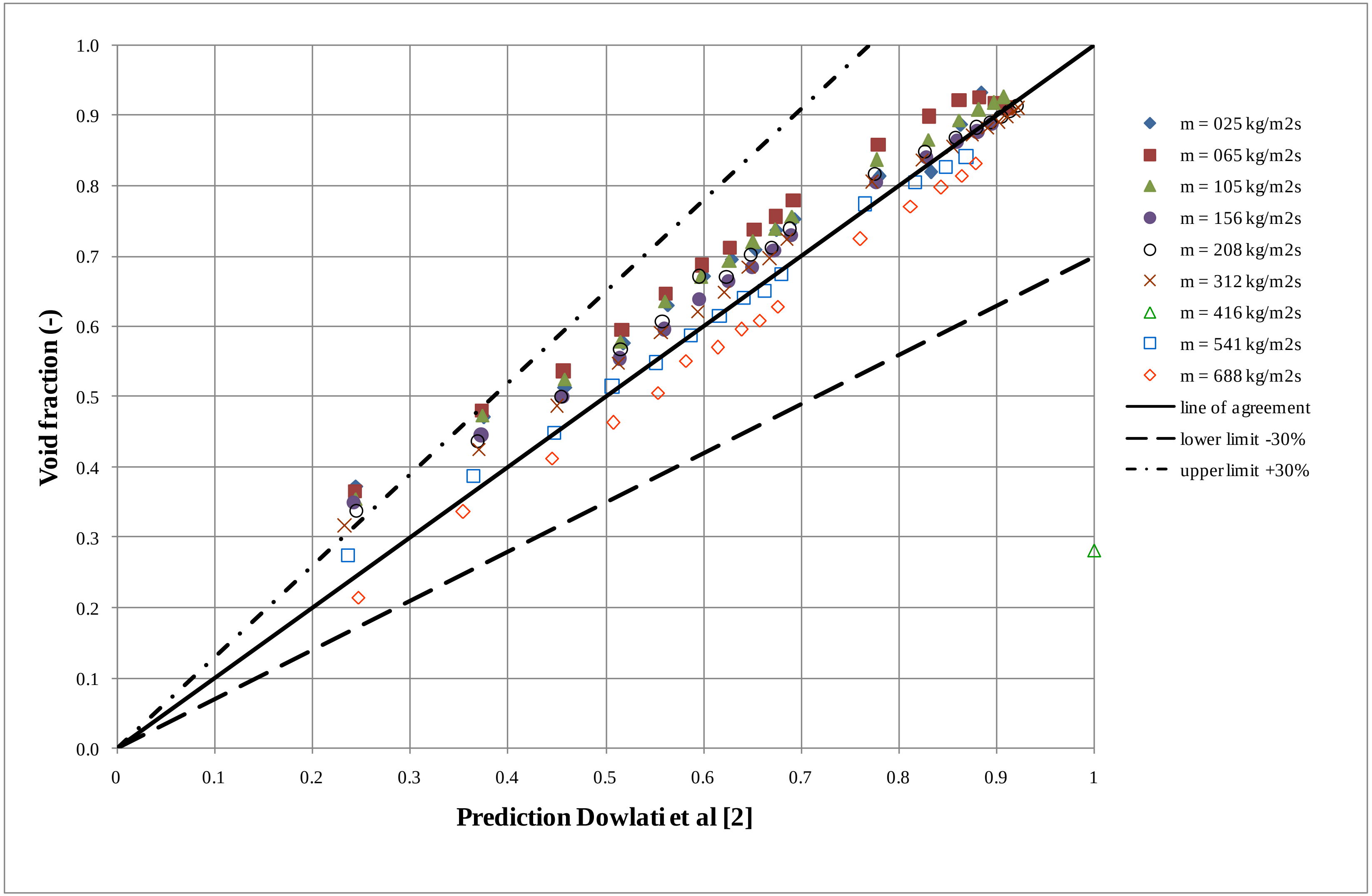

Figure 6.27: Variation of measured and Dowlati et al. [2] void fraction for 19 mm staggered bundle

6.4 Comparison of void fraction measurements from the 38 mm in diameter and 19 mm in diameter in-line tube bundles

The pitch void fractions measurements from the 38 mm in-diameter in-line tube bundle and the 19 mm in-diameter in-line tube bundle are compared in Figure 6.28. Both bundles have the same pitch-to-diameter ratio, *P/D* of 1.32 and the same bundle array geometry, which is a normal square array. The differences between these two bundles are the tube diameter and the pitch. The gaps between the tubes are also different, the 38 mm diameter tube bundle has a 12 mm gap and the 19 mm diameter tube bundle has a 6 mm gap. Finally, the 38 mm bundle has two vertical flow passages whereas the 19 mm bundle has four.

The discussion in sections 6.1 and 6.2 on gaps between the tubes, maximum or minimum of any bundle had given the insight that the between the tubes does not have much effect on the void fraction, Figures 6.1-6.3 and Figures 6.10-6.13. However, the Feenstra et al. [3] correlation used the gap between the tubes in their correlation to predict void fraction, as shown in Equation (6.11). They reported that the gap between the tubes, *a*, was chosen as the characteristic dimension since this is the space through which the flow must pass. This is contrary to some other models which use tube diameter as the characteristic length dimension, e.g. Dowlati et al. [2]. In this research, it is clearly seen that the gap between the tubes do not affect the pitch void fraction, as shown in Figure 6.28. The graph clearly show that the void fraction measurements on both bundles are about the same for all mass fluxes except for minor variations at low mass fluxes of 25 kg/m^{2}s and 65 kg/m^{2}s where the void fraction in the larger diameter bundle were higher than the smaller diameter bundle at larger void fractions. This is strong evidence that gap between the tubes, maximum or minimum, does not affect the void fraction.

The graph in Figure 6.28 also gives strong evidence that larger diameter bundle void fractions are similar to smaller diameter bundle values, i.e., the void fractions are about the same regardless of the sizes of the tube diameter in a same square in-line arrangement. The pitch-to-diameter ratio, *P/D* was the same at 1.32, however the pitch for the bundles were different, 50 mm for 38 mm diameter and 25 mm for 19 mm diameter. An increase in void faction due to an increase in pitch was not observed for the in-line bundle case. This is in agreement with Dowlati et al. [2]. As they reported no apparent pitch-to diameter ratio, *P/D*, affect on void fraction for their test bundles with *P/D* 1.3 and 1.75

and with tube diameters of 12.7 mm and 19.05 mm respectively. So, the measured void fractions in both bundles agree well with the findings by Dowlati et al. [2]. Overall, increasing tube diameter and changing or maintaining the pitch-to-diameter ratio, *P/D* and increasing the pitch does not affect the void fraction in a normal square array bundle arrangement.

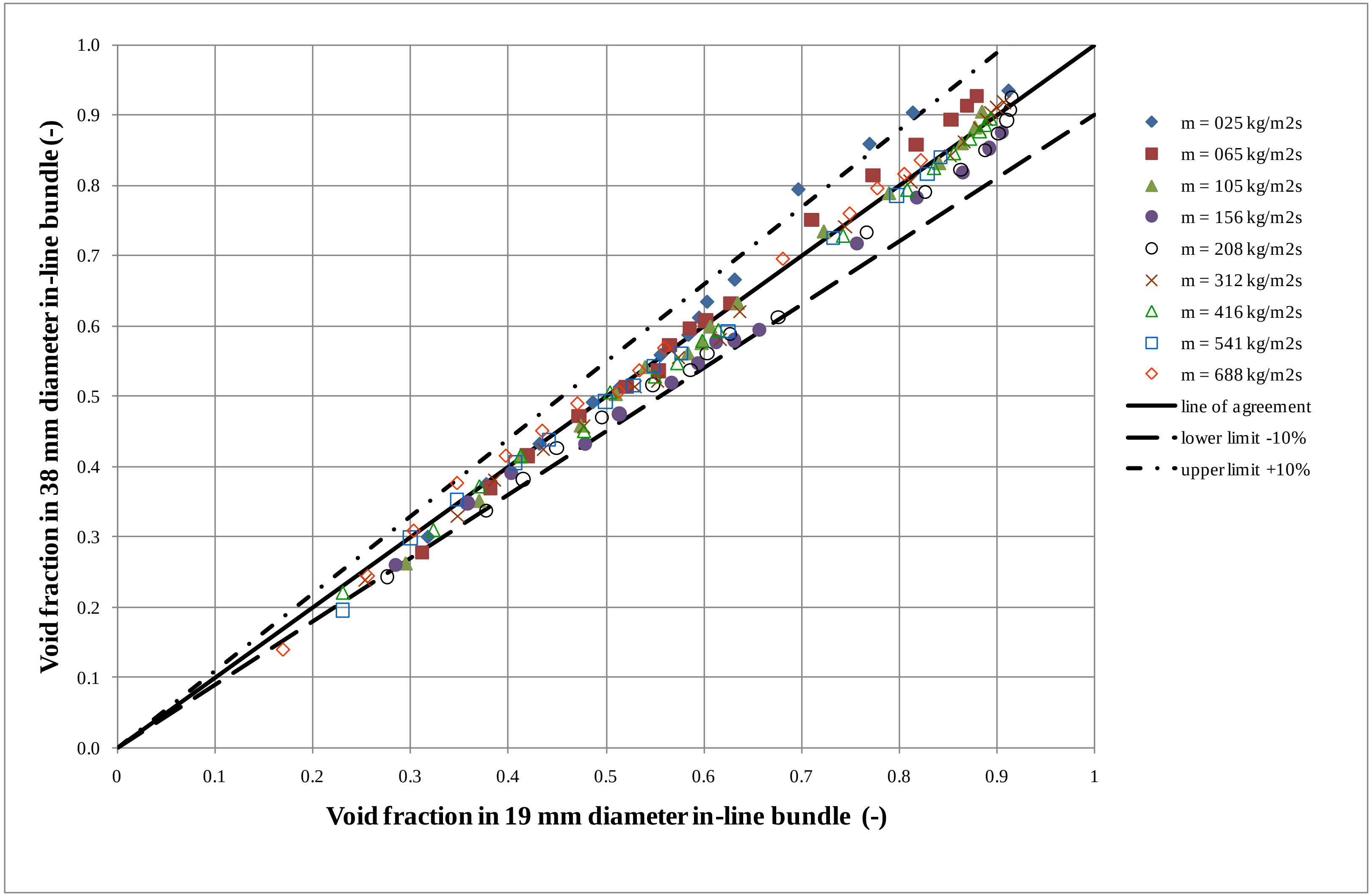

Figure 6.28: Comparison of 19 mm in-line bundle and 38 mm in-line bundle

6.5 Comparison of void fraction measurements from the 19 mm in diameter in-line and staggered bundles

Figure 6.29 shows the comparison between the pitch void fraction measured in the 19 mm diameter in-line bundle and the 19 mm diameter staggered bundle. The data from to the staggered array show a higher void fraction than those from the square in-line array. This may be a result of the flow following a more passages in the staggered array. It should be noted that Dowlati et al. [39] reported, for a given quality, void fraction about 10-15% higher were obtained for staggered rod bundles in comparison with those from in-line rod bundles for the same *P/D* ratio. The measured void fraction in the staggered bundle agree well with the finding by Dowlati et al. [39], as the present data, for a given quality, are observed to be about 14% greater when compared to the in-line bundle for the same pitch-to-diameter ratio, *P/D* of 1.32. This may be a result of higher turbulence in a staggered tube bundle giving higher void fraction because the two phases are mixing better leading to a more homogenous two-phase mixture.

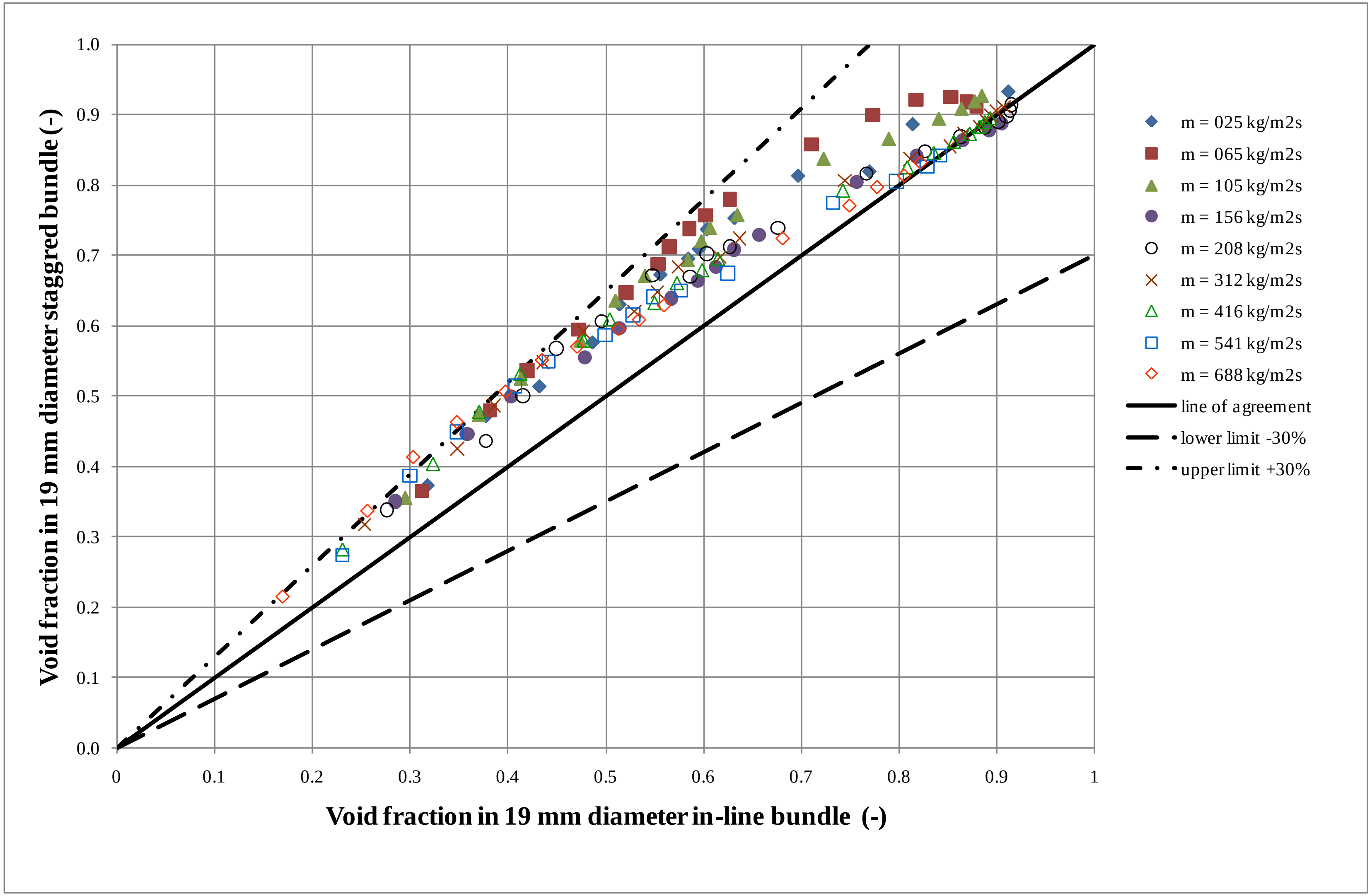

Figure 6.29: Comparison of 19 mm in-line bundle and 19 mm staggered bundle

6.6 Summary of void fraction measurements at three tube bundles

The measured void fraction in the three bundles shows a strong dependency on mass flux and a flow quality as we can be see from Figures 6.1-6.3, 6.6, 6.10-6.13, 6.17, 6.21, 6.22 and 6.24. The measured void fractions increase with increasing mass flux, which agrees with other findings [1,2,3]. The void fraction also increases with increases in quality. The measured void fractions also significantly lower than homogenous flow model values. The difference between the homogenous flow model and the current data is seen to increase with decreasing mass flux and quality. This is because the homogenous flow model assumes no slip between the phases, and the validity of this depends on the degree of mixing achieved by the two phases. At high mass flux, say 688 kg/m^2s, and at low values of quality the void fractions in all bundles tend to approach the values predicted by the homogenous flow model. This is because the turbulence in the liquid phase helps mix the two-phases, allowing the gas and liquid phases to travel at the same velocity, so a more homogenous mixture is obtained, especially in the staggered bundle as shown in Figure 6.24. At low mass fluxes, as seen at 25 kg/m^2s, the effect of buoyancy is significant, especially at low qualities where there is a considerable difference in phase velocities. Therefore, the void fractions measured at low mass flux is far from values predicted by the homogenous flow model. Thus, the separated flow model, maximum slip, was included to compare with the measured void fractions, especially at low mass fluxes. Almost all the measured void fractions fall between the maximum slip and the homogeneous values which is consistent with findings from one-dimensional flows.

Based on the three correlations for void fractions, that were compared to the measured data from the three tube bundles, the correlations of Feenstra et al. [3] and Dowlati et al. [2] are revealed to represent the data best for adiabatic air-water tests as shown in Figures 6.8-6.9, 6.19-6.20 and 6.26-6.27. This is no surprise as the Dowlati et al. [2,39] method was deduced from data sets obtained from tube bundles containing tubes with diameters less than 20 mm. They had test their bundles in air-water rig containing 19.05 mm in diameter tubes with pitch-to-diameter ratio, *P/D* of 1.3 on both in-line and staggered geometry. The present data, also have 19 mm in diameter tube bundles, in-line and staggered, with a 1.32 pitch-to-diameter ratio, in air-water flows. It is therefore expected that Dowlati’s model should fit the data well since the test conditions are the same, although it is shown to be less effective at larger mass fluxes. This is because the method neglected the acceleration affects, which are important at larger mass fluxes. However, the Dowlati et al. [2] method is not general, requiring different coefficients to be set to different fluids. Currently, they are only available for air-water and R113. As for the Feenstra et al. [3] correlations, it was based on Dowlati's data, therefore this model was expected to fit the new data reasonably well. However, this correlation is poorer at lower mass fluxes than the larger ones. The Schrage et al. [1] correlation for void fraction was based on data that used quick-closing technique at atmospheric conditions. This is clearly poor to fit to the data although the model was developed under conditions very similar to Dowlati's data. This is similar with other findings [2,3,39] and is demonstrated in Figures 6.7, 6.18 and 6.25.

Figure 6.28 clearly demonstrated that the measured void fraction in bigger diameter, 38 mm tubes, shows the same void fraction to those in smaller, 19 mm diameter tubes. The effect of tube diameter and void fraction clearly appears to be negligible for a given mass flux. This finding support the view that there is no significant change of void fraction when increasing the pitch for given mass flux as reported by Dowlati et al. [2]. As a result, the Dowlati et al. [2] and Feenstra et al. [3] correlations deduced from data sets with tubes less than 20 mm are capable of predicting void fraction in air-water tube bundles containing tubes larger than 20 mm. Although Feenstra et al. [3] used the gap between the tubes, a, as the characteristic dimension since this is the space through which the flow must pass, Figure 6.28 reveals that the gap between the tubes has no effect on void fraction when increasing or decreasing the gap between the tubes for these two square in-line bundles, 38 mm and 19 mm in diameter. Again, the Schrage et al. [1] correlations fails to predict the void fraction in larger diameter tubes, 38 mm.

Overall, the size of tube diameter and pitch have no clear effect on void fraction. However, the difference in bundle arrangement does effect on void fraction, as seen in Figure 6.29. The mass flux and quality also give strong influence to the void fraction values as demonstrated in Figures 6.1-6.3, 6.6, 6.10-6.13, 6.17, 6.21, 6.22 and 6.24. The best void fraction correlations to predict void fraction are Feenstra et al. [3] and Dowlati et al. [2] as shown in Figures 6.8-6.9, 6.19-6.20 and 6.26-6.27. However, Dowlati et al. [2] correlation is not universal as C_1 and C_2 are only known for air-water and R113 and the Feenstra et al. [3] correlation can be used with any fluid but is based on the wrong length scale.

CHAPTER 7 - PRESSURE DROP EXPERIMENTAL RESULTS AND DISCUSSION

The pressure drop data collected from the adiabatic air-water experiments are discussed and analysed in this chapter. The test conditions and procedures followed the nominal condition described in Chapter 4. The measured pressure drop data are presented in APPENDIX C. Data processing was done through an Excel spreadsheet and a series of FORTRAN programs written for specific procedures for pressure drop and two-phase multipliers predictions using methods by other researchers [4,5].

7.1 Two-phase pressure drop

Two-phase pressure gradients, *dp/dz*, contain three components, the acceleration component, $(dp/dz)_A$, the gravitational component, $(dp/dz)_G$, and the frictional component, $(dp/dz)_F$, thus

$$\frac{dp}{dz} = \left(\frac{dp}{dz}\right)_A + \left(\frac{dp}{dz}\right)_G + \left(\frac{dp}{dz}\right)_F \qquad (7.1)$$

In tube bundles only the latter two are important. The gravitational pressure gradient is given by

$$\left(\frac{dp}{dz}\right)_G = -\rho_{tp}\, g \qquad (7.2)$$

where g is the acceleration due to gravity and ρ_{tp} is the two-phase density, which can be determined from

$$\rho_{tp} = \alpha\, \rho_g + (1-\alpha)\, \rho_l \qquad (7.3)$$

in which ρ_g and ρ_l are the densities of the gas and liquid phases respectively.

7.1.1 Two-phase pressure drop measurements in 38 mm diameter in-line bundle

Pressure drop measurements are shown in Figure 7.1 and Figure 7.2 below as a function of quality for a mass flux range of 25 kg/m^{2}s to 688 kg/m^{2}s. Three data sets were obtained, however, only the average is shown. Table 7.1 shows the example of the three readings to demonstrate repeatability. The pressure drops measurement from 25 kg/m^{2}s to 416 kg/m^{2}s were taken previous by Bamardouf [51] and the later two, mass fluxes of 514 kg/m^{2}s and 688 kg/m^{2}s, were done in this research. As the quality increases, the gravity pressure drop decreases and the friction pressure drop increases. As seen from the Figure 7.1, at the lowest mass flux of 25 kg/m^{2}s, the pressure drop continues to decline as the quality increases because the gravitational pressure drop is more dominant than the frictional pressure drop. This is in contrast to the higher mass flux of 688 kg/m^{2}s where at first the pressure drop decreases as the quality increases until, at a quality of 0.0024, when it starts to increase, and rises above the static liquid pressure head at 3500 Pa, as the frictional pressure drop rise is substantially larger than the gravitational pressure drop decrease.

The predicted pressure drop using the Dowlati et al. [2] void fraction to obtain the gravitational pressure gradient; and the Ishihara et al. [4] correlation and Xu et al. [5] to obtain the frictional pressure gradient. The prediction pressure drop using Dowlati et al. [2] and Ishihara et al. [4] is compared with the measured data in Figure 7.1. The predictions do pick up the trends in the data at a mass flux of 25 kg/m^{2}s, where the pressure drop is continually falling, in line with the measured data. At the larger mass fluxes, the turning characteristic is reproduced. The predicted pressure drop using Xu et al. [5] for frictional pressure drop and Dowlati et al. [2] void fraction to obtain the gravitational pressure drop, is shown Figure 7.2. The predictions show a same characteristic in the data at a mass flux of 25 kg/m^{2}s, where the pressure drop is continually decreasing, same with the measured data. At the larger mass fluxes, the turning point is reproduced.

Both Ishihara et al. [4] and Xu et al. [5] methods are shown to predict most of the pressure drop data to within ±20% if the mass flux lies between 208 and 688 kg/m^{2}s, as shown in Figure 7.3 and Figure 7.4 respectively. Both figures show the predictions pressure drop divided by the measured values varying with quality. However, for mass fluxes out with this range, the predictions are poor, especially for qualities above 0.01

using Ishihara et al. [4], meanwhile predicted pressure drop using Xu et al. [5] are at qualities above 0.02. When comparing both correlations, the predictions by Xu et al. [5] shows better agreement with the measured data with mean error is at -5% and RMS is at 13% while predictions by Ishihara is settled at 14% mean error and 21% RMS.

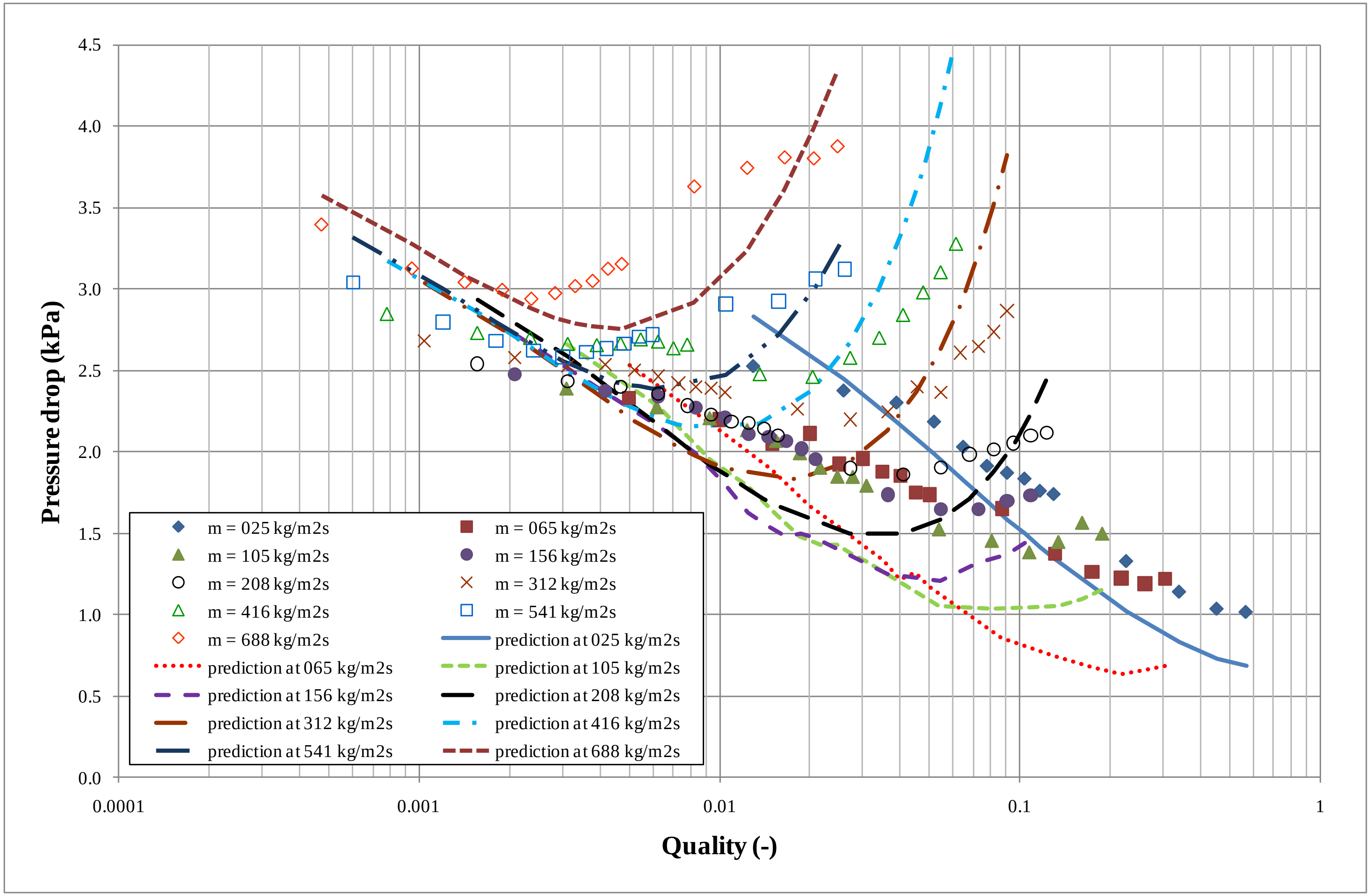

Figure 7.1: Variation of measured pressure drop with quality in 38 mm in diameter in-line bundle and predicted pressure drop using Dowlati et al. [2] void fraction for gravitational pressure drop and Ishihara et al. [4] frictional pressure drop

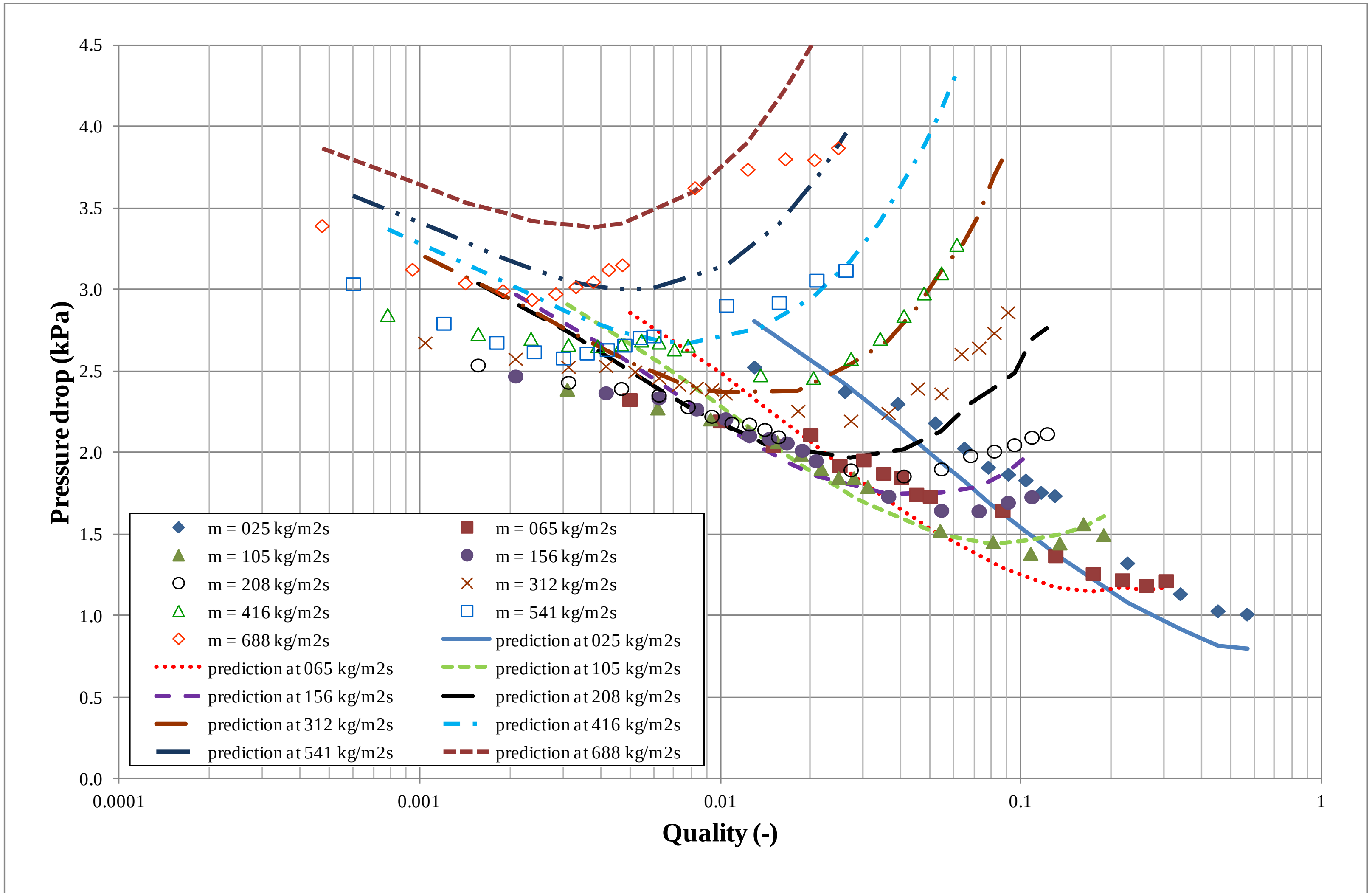

Figure 7.2: Variation of measured pressure drop with quality in 38 mm in diameter in-line bundle and predicted pressure drop using Dowlati et al. [2] void fraction for gravitational pressure drop and Xu et al. [5] frictional pressure drop

Table 7.1: The inlet pressure, two-phase flow temperature, water mass flow rate and pressure drop readings at 541 kg/m^{2}s in 38 mm in diameter in-line tube bundle

Mass flux min are kg/m^{2}s	Air mass flow rate kg/s	Inlet pressure kPa				Two-phase flow temperature °C				Water mass flow rate kg/s				Pressure drop kPa			
		Reading 1	Reading 2	Reading 3	Average	Reading 1	Reading 2	Reading 3	Average	Reading 1	Reading 2	Reading 3	Average	Reading 1	Reading 2	Reading 3	Average
541	0.00039	119.585	119.581	119.596	119.587	24.4	24.4	24.4	24.4	0.64902	0.64875	0.64847	0.64875	3.040	3.053	3.028	3.040
541	0.00078	118.451	118.529	118.427	118.469	24.4	24.5	24.5	24.5	0.64881	0.64896	0.64929	0.64902	2.791	2.794	2.810	2.798
541	0.00117	118.156	118.198	118.169	118.174	24.5	24.6	24.6	24.6	0.64766	0.64731	0.64807	0.64768	2.681	2.683	2.679	2.681
541	0.00156	118.218	118.213	118.226	118.219	24.9	24.9	24.9	24.9	0.64783	0.64751	0.64744	0.64760	2.611	2.622	2.635	2.623
541	0.00195	118.446	118.418	118.526	118.463	24.9	24.9	24.9	24.9	0.64792	0.64703	0.64631	0.64709	2.575	2.569	2.611	2.585
541	0.00234	118.881	118.964	118.894	118.913	25.0	25.0	25.0	25.0	0.64719	0.64655	0.64605	0.64659	2.607	2.601	2.638	2.615
541	0.00273	119.087	119.250	119.184	119.174	25.0	25.1	25.1	25.0	0.64644	0.64727	0.64742	0.64704	2.619	2.631	2.658	2.636
541	0.00312	119.349	119.314	119.571	119.411	25.1	25.2	25.2	25.2	0.64393	0.64390	0.64157	0.64313	2.600	2.696	2.694	2.663
541	0.00351	119.945	119.935	119.848	119.909	25.3	25.3	25.3	25.3	0.64689	0.64685	0.64741	0.64705	2.711	2.717	2.702	2.710
541	0.00390	120.594	120.505	120.384	120.494	25.4	25.4	25.4	25.4	0.64546	0.64481	0.64589	0.64539	2.761	2.684	2.717	2.721
541	0.00680	123.562	124.303	123.732	123.866	25.4	25.4	25.4	25.4	0.64131	0.63989	0.64080	0.64066	2.929	2.949	2.845	2.908
541	0.01020	128.849	128.446	127.989	128.428	25.3	25.4	25.4	25.3	0.63714	0.63781	0.63877	0.63791	2.889	2.918	2.968	2.925
541	0.01360	132.715	134.257	133.587	133.520	25.3	25.3	25.3	25.3	0.63500	0.63453	0.63453	0.63469	3.071	2.998	3.117	3.062
541	0.01700	138.919	139.727	138.813	139.153	25.3	25.4	25.4	25.4	0.63298	0.63114	0.63331	0.63248	3.030	3.121	3.215	3.122

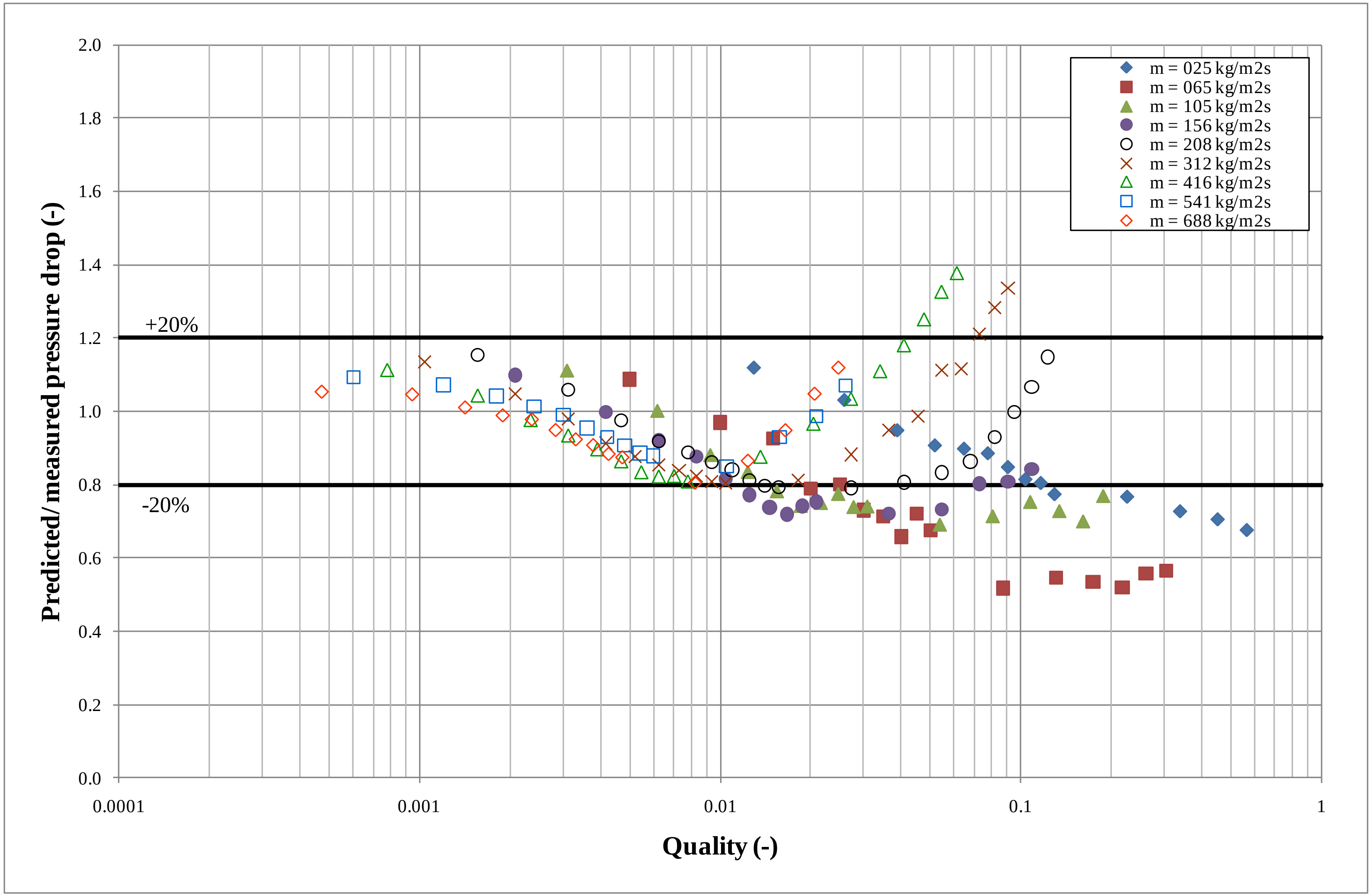

Figure 7.3: Comparison of predicted Ishihara et al. [4] to measured data in 38 mm in diameter in-line bundle

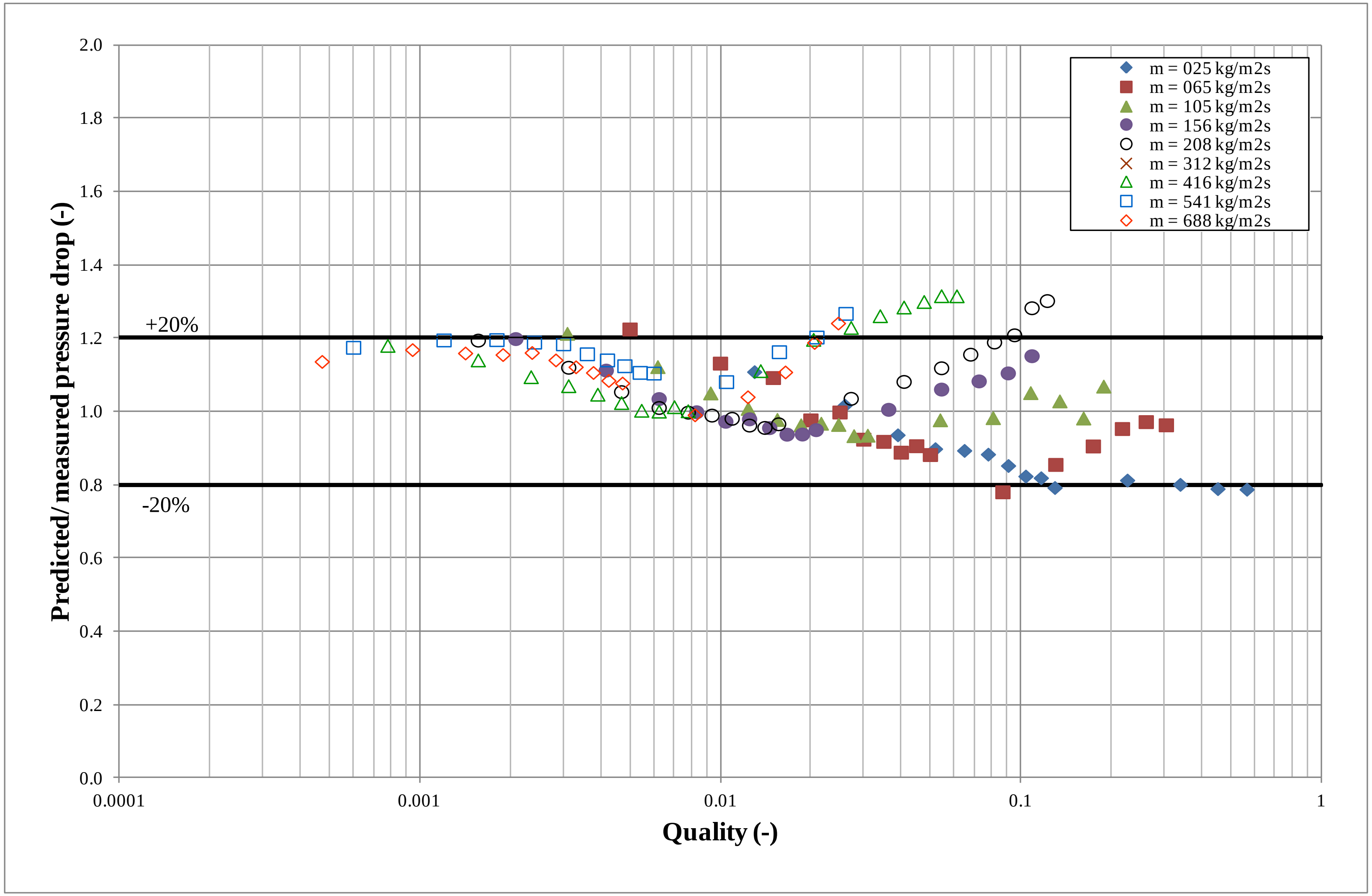

Figure 7.4: Comparison of predicted Xu et al. [5] to measured data in 38 mm in diameter in-line bundle

7.1.2 Two-phase pressure drop measurements in the 19 mm diameter in-line bundle

The pressure drop measurements were made for the 19 mm diameter inline tube bundle. The tests were carried out at the nominal condition described in Chapter 4. Three data sets were obtained, however, only the average is show in Figure 7.5 and Figure 7.6. Table 7.2 shows the example of the three readings to demonstrate repeatability. The lower mass fluxes of 25 kg/m^{2}s and 65 kg/m^{2}s both show a similar pattern to the 38 mm in line bundle. The gravitational pressure drop is dominating as the quality increases, so the pressure drop is gradually decreasing. However, at mass fluxes of 105 kg/m^{2}s and 156 kg/m^{2}s, the pressure drop decreases as the quality increases up to a quality of 0.07. Subsequently the frictional pressure drop starts to dominate, causing the pressure drop to increase. At the higher mass fluxes of 312kg/m^{2}s until 688 kg/m^{2}s, the later trend is repeated but the turning point occurs at lower qualities because, at higher mass flux, the increase in frictional pressure drop is significantly higher than the decrease in gravitational pressure drop. This phenomenon can be seen at 416 kg/m^{2}s where the pressure drop decreases for increasing quality until a quality of 0.004 and increases to 6896 Pa. Thereafter, at the highest two, 541 kg/m^{2}s and 688 kg/m^{2}s, the total pressure drop is always higher than the static liquid pressure head of 3120 Pa but they follow the same pattern as the other mass fluxes.

Figure 7.5 also shows the predicted pressure drop using the Dowlati et al. [2] and the Ishihara et al. [4] correlations for void fraction and two-phase friction multiplier respectively. The predictions do pick up the trends. At the lowest mass flux, 25 kg/m^{2}s, the pressure drop is falling, same as the measured data. At mass flux bigger than 208 kg/m^{2}s, the turning characteristic is reproduced. The measured data is also compared with predictions by Xu et al. [5] for the frictional pressure drop, Figure 7.6. This method is also capable to predict the pressure drop in the tube bundle. At the lowest mass flux, 25 kg/m^{2}s, as the quality increases, the pressure is continually declining. This is same with the measured data. Then, at larger mass flux than 208 kg/m^{2}s, the turning characteristic is reproduced. However, the magnitudes are not accurately reproduced, as is typical of two-phase pressure drop predictions for both.

Figure 7.7 shows the predicted pressure drop by Ishihara et al. [4] divided by the measured pressure drop varying with quality. The predictions show agreement with the data to within ±20% at mass flux between 416 and 688 kg/m^{2}s. However, at lower mass fluxes, the predictions are less reliable, particularly at qualities above 0.005. Xu et al. [5] pressure drop predictions shows better agreement where most of the data is within ±20%, except at lower mass fluxes, at a quality above 0.1, as shown in Figure 7.8. Furthermore, the mean error is 19% and RMS is 33% when using Xu et al. [5] method, meanwhile the mean error is doubled when using Ishihara et al. [4] method, which is 43% and the RMS is 59%.

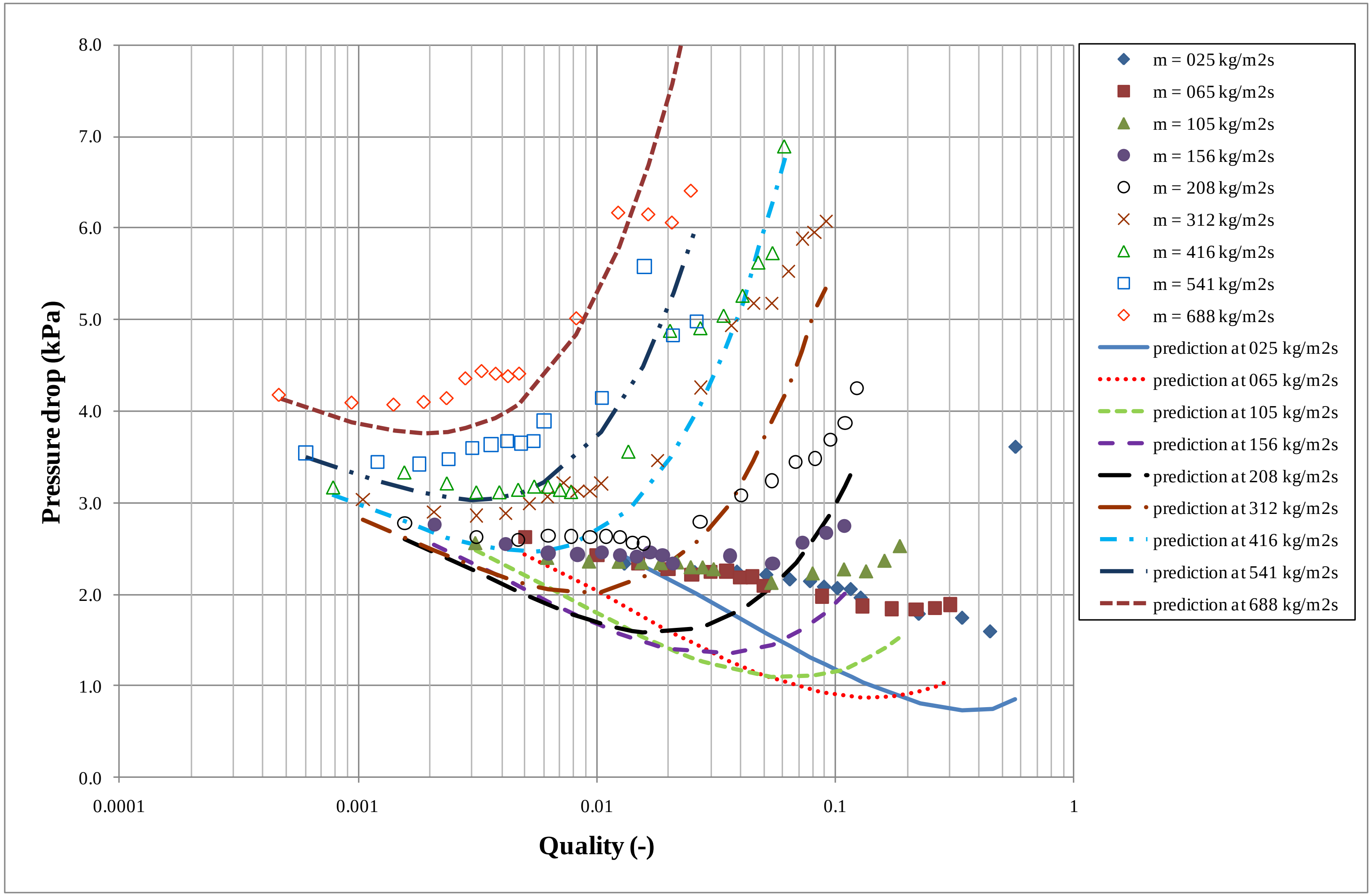

Figure 7.5: Variation of measured pressure drop with quality in 19 mm in diameter in-line bundle and predicted pressure drop using Dowlati et al. [2] void fraction for gravitational pressure drop and Ishihara et al. [4] frictional pressure drop

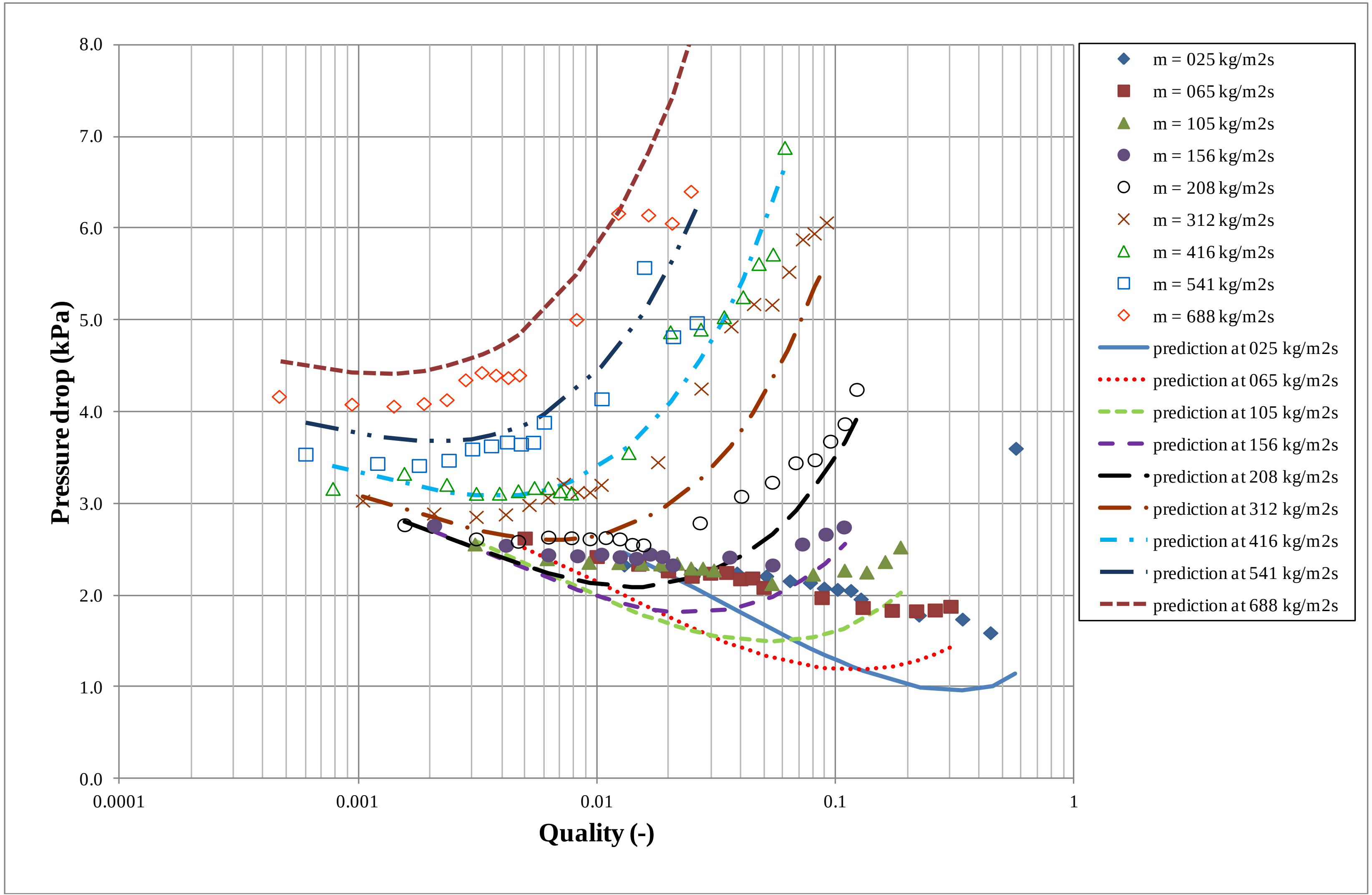

Figure 7.6: Variation of measured pressure drop with quality in 19 mm in diameter in-line bundle and predicted pressure drop using Dowlati et al. [2] void fraction for gravitational pressure drop and Xu et al. [5] frictional pressure drop

Table 7.2: The inlet pressure, two-phase flow temperature, water mass flow rate and pressure drop readings at 65 kg/m^{2}s in 19 mm in diameter in-line tube bundle

Mass flux min are kg/m^{2}s	Air mass flow rate kg/s	Inlet pressure kPa				Two-phase flow temperature °C				Water mass flow rate kg/s				Pressure drop kPa			
		Reading 1	Reading 2	Reading 3	Average	Reading 1	Reading 2	Reading 3	Average	Reading 1	Reading 2	Reading 3	Average	Reading 1	Reading 2	Reading 3	Average
65	0.00039	112.039	112.086	111.960	112.028	22.8	22.9	23.0	22.9	0.07764	0.07766	0.07765	0.07765	2.586	2.602	2.700	2.629
65	0.00078	110.244	110.112	110.239	110.198	22.9	22.9	23.0	22.9	0.07717	0.07714	0.07709	0.07713	2.532	2.383	2.368	2.428
65	0.00117	109.553	109.831	109.952	109.779	23.1	23.1	23.1	23.1	0.07707	0.07682	0.07721	0.07703	2.305	2.431	2.294	2.344
65	0.00156	109.979	109.571	109.455	109.668	23.1	23.2	23.2	23.2	0.07679	0.07666	0.07683	0.07676	2.281	2.298	2.235	2.271
65	0.00195	108.999	108.930	109.082	109.004	23.3	23.4	23.4	23.4	0.07605	0.07605	0.07597	0.07602	2.192	2.223	2.221	2.212
65	0.00234	109.008	108.876	108.832	108.905	23.4	23.4	23.4	23.4	0.07588	0.07590	0.07589	0.07589	2.219	2.168	2.351	2.246
65	0.00273	108.554	108.743	108.726	108.674	23.5	23.5	23.5	23.5	0.07545	0.07549	0.07525	0.07540	2.280	2.222	2.259	2.254
65	0.00312	108.513	108.535	108.525	108.524	23.4	23.5	23.5	23.5	0.07492	0.07482	0.07485	0.07486	2.158	2.180	2.214	2.184
65	0.00351	108.395	108.249	108.384	108.343	23.5	23.5	23.5	23.5	0.07476	0.07474	0.07472	0.07474	2.194	2.194	2.193	2.194
65	0.00390	107.860	108.029	108.053	107.981	23.5	23.5	23.6	23.5	0.07397	0.07389	0.07397	0.07394	2.091	2.089	2.095	2.092
65	0.00680	107.391	107.789	107.142	107.441	23.3	23.3	23.3	23.3	0.07100	0.07055	0.07070	0.07075	1.939	2.029	1.971	1.979
65	0.01020	107.806	107.306	107.536	107.549	22.8	22.8	22.9	22.9	0.06788	0.06785	0.06853	0.06809	1.869	1.869	1.878	1.872
65	0.01360	107.795	108.378	108.300	108.158	22.4	22.4	22.5	22.4	0.06524	0.06510	0.06535	0.06523	1.843	1.838	1.843	1.841
65	0.01700	109.102	109.691	109.691	109.494	22.0	21.9	22.0	22.0	0.06100	0.06085	0.06085	0.06090	1.834	1.836	1.836	1.836

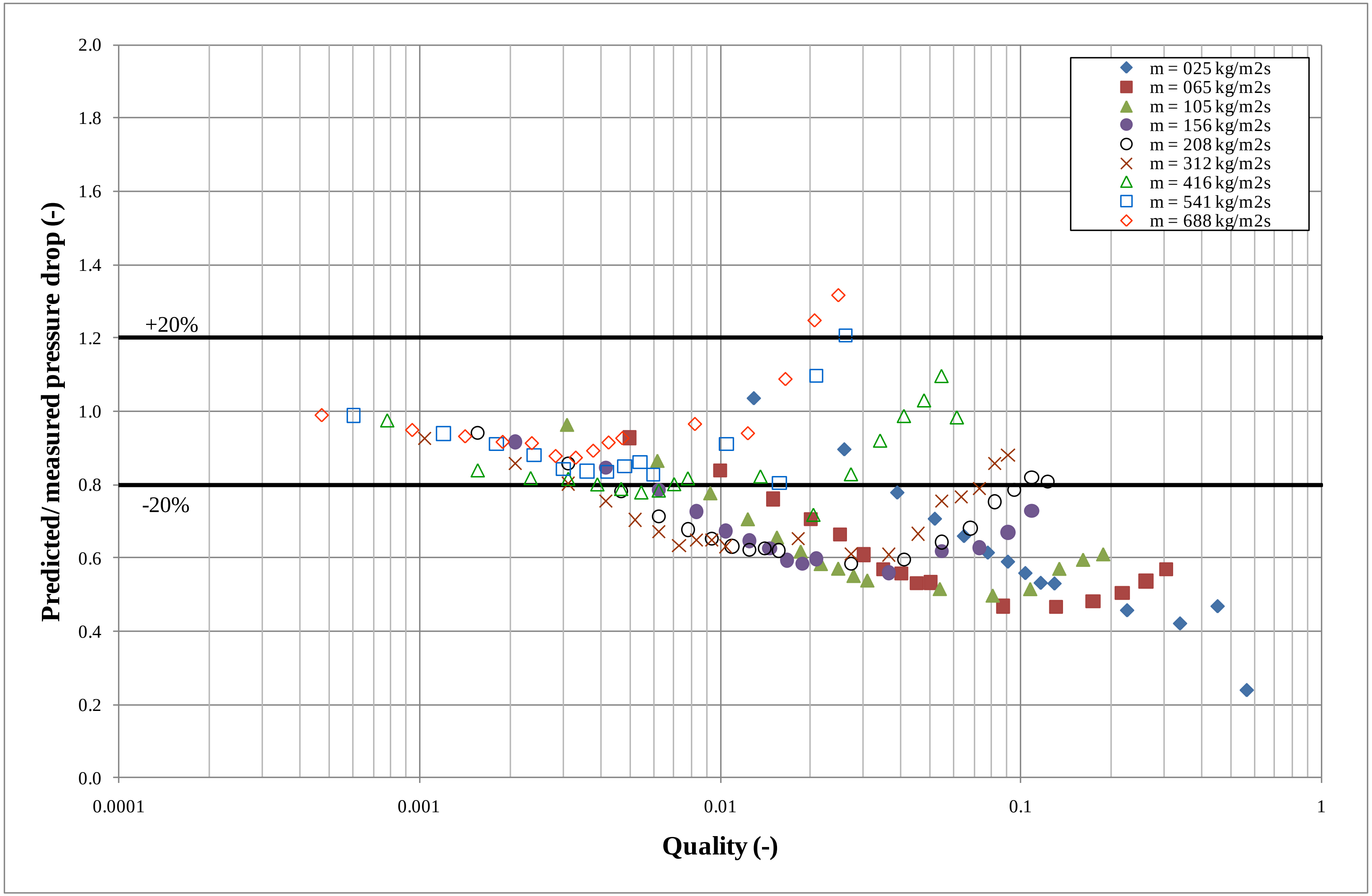

Figure 7.7: Comparison of predicted Ishihara et al. [4] to measured data in 19 mm in diameter in-line bundle

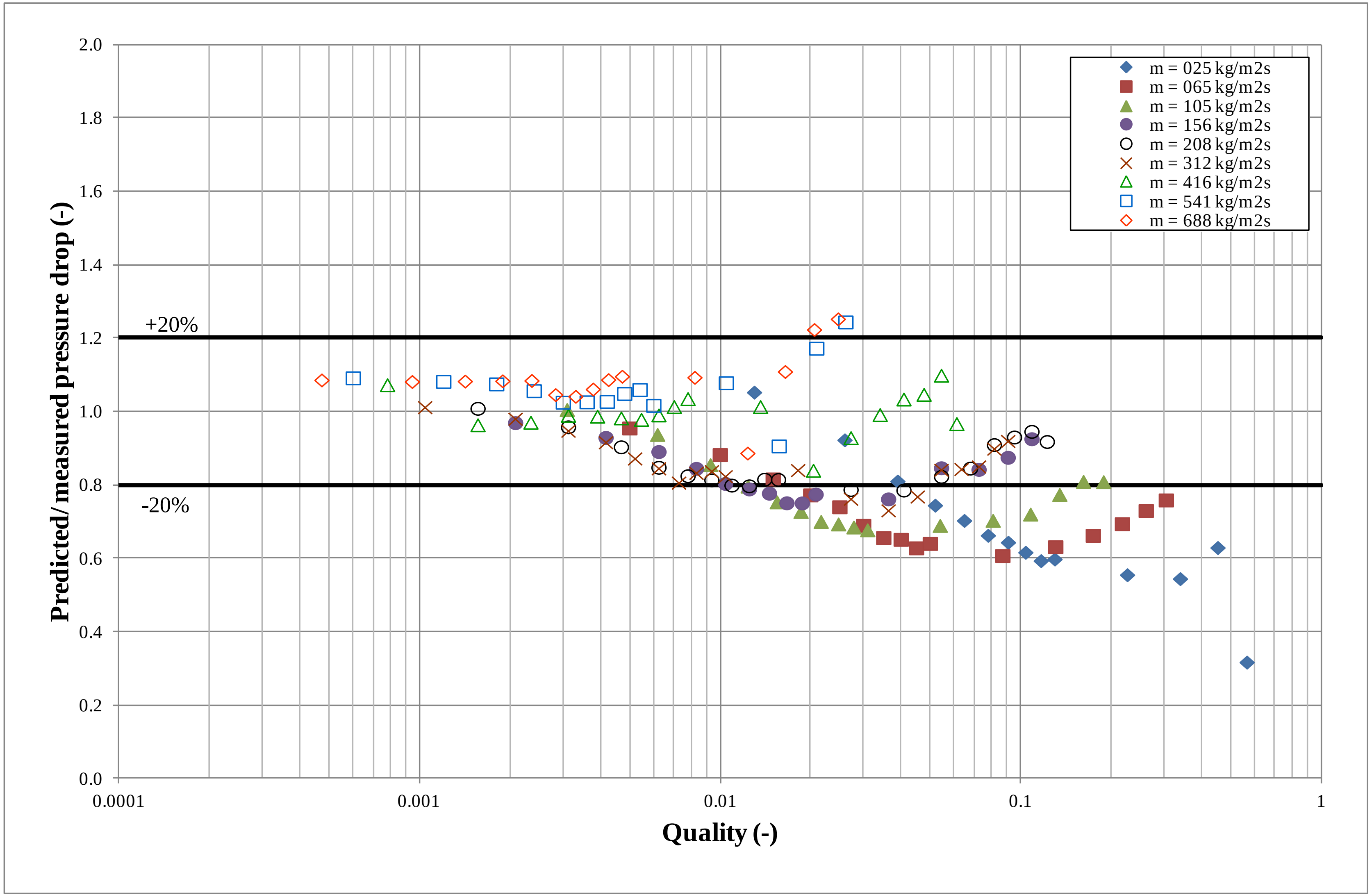

Figure 7.8: Comparison of predicted Xu et al. [5] to measured data in 19 mm in diameter in-line bundle

7.1.3 Two-phase pressure drop measurement in the 19 mm in diameter staggered bundle

Pressure drop measurements for the staggered bundle were made at the same nominal condition described in Chapter 4. Three data sets were obtained, however, only the average is shown in Figure 7.9 and Figure 7.10. Table 7.3 shows the example of the three readings to demonstrate repeatability. It is clearly seen that, overall, the data follow the same trends as the in-line bundle with the same tube diameter. Increasing the quality, causes the gravity pressure drop to decrease and the friction pressure drop to increase. At the lowest mass flux of 25 kg/m^{2}s, the pressure drop continues to decrease as the gas mass fraction increases because the gravitational pressure drop is more significant than the frictional pressure drop. At 65 kg/m^{2}s, the pressure drop continue to decline as the quality increases until 0.05 before increasing to 2660 Pa, just above static liquid pressure head of 2620 Pa which it reaches a quality of 0.30. The pressure drop more than doubles at 156 kg/m^{2}s compared to 105 kg/m^{2}s, from 3440 Pa to 6040 Pa. The total pressure drop trend is different at the higher mass fluxes of 416 kg/m^{2}s, 541 kg/m^{2}s and 688 kg/m^{2}s, where the total pressure drop increases with increasing quality for all quality because the frictional pressure drop is increase always higher than gravitational pressure drop decrease. At the highest mass flux 688 kg/m^{2}s, the pressure drop rises dramatically to 22660 Pa from 4580 Pa, which is twice as much as 12600 Pa achieved at 416 kg/m^{2}s.

The predicted pressure drop is also showed in Figure 7.9 and Figure 7.10. The void fraction used for the prediction of the gravity pressure drop was the correlation of Dowlati et al. [2]. The correlation by Ishihara et al. [4] and Xu et al. [5] were used for the frictional pressure gradient. The measured data agree well with the both predictions for most of the mass fluxes and pick up the trends. The predictions at low mass flux continually fall, while at mass fluxes larger than 208 kg/m^{2}s, the turning trend is reproduced. However, the measured data at the highest mass flux of 688 kg/m^{2}s is far above the prediction.

Figure 7.11 and Figure 7.12 shows both predicted pressure drops divided by the measured values varying with quality, Ishihara et a [4] and Xu et al. [5] respectively. The Ishihara et al. [4] correlations are shown to predict the data well, to within ±20%, if the mass flux lies between 208 kg/m^{2}s and 416 kg/m^{2}s for a range of quality between 0.002 and 0.1. However, other mass fluxes show a poorer prediction. The Xu et al. [5] correlations is also provide better agreement, within ±30%. However, when comparing with the measured data, both methods have a same RMS error at 35%, but the mean errors were different. The mean error for the Xu et al. [5] correlation is -17% while the Ishihara et al. [4]correlation is 11%.

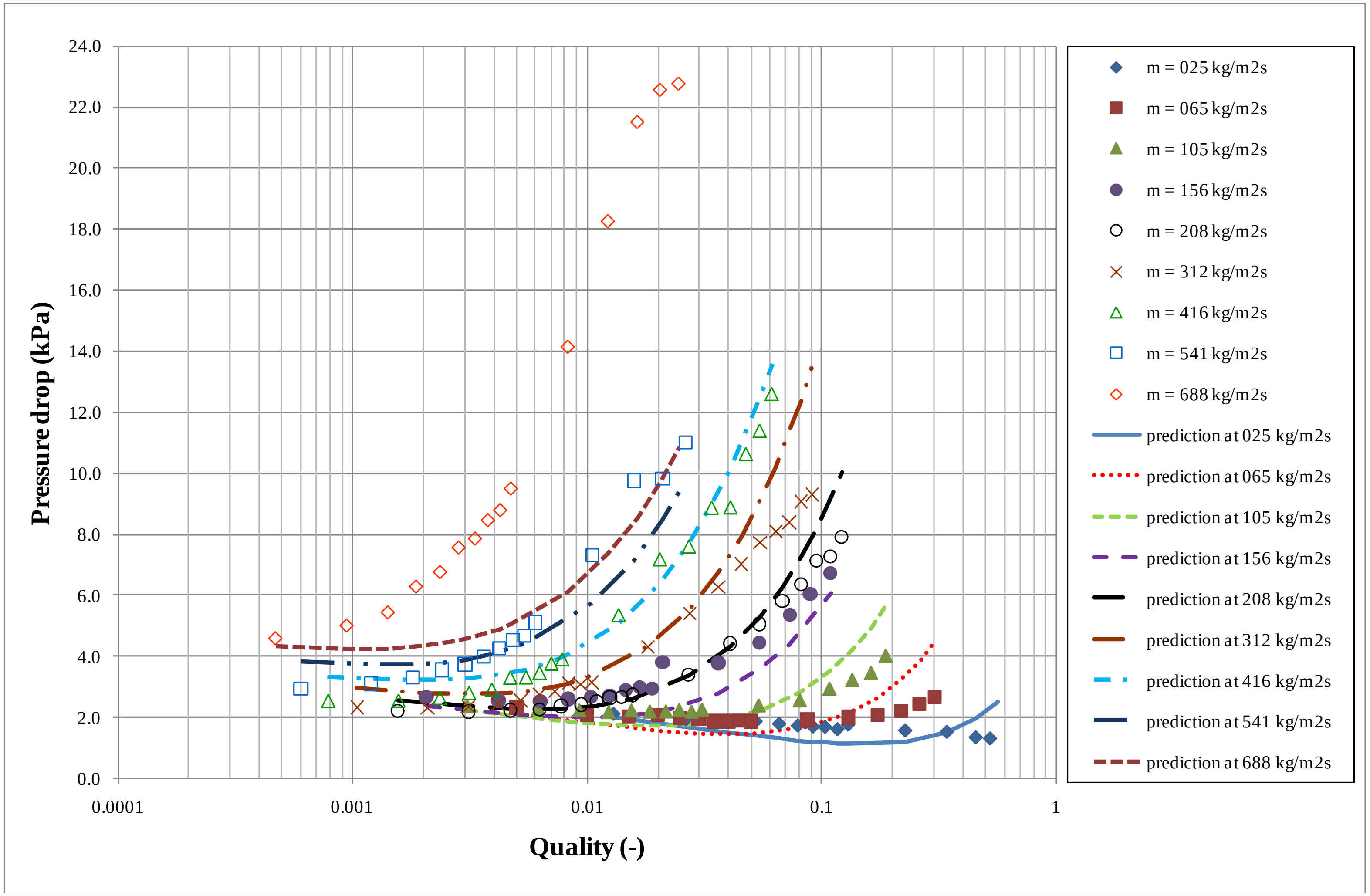

Figure 7.9: Variation of measured pressure drop with quality in 19 mm staggered bundle and predicted pressure drop using Dowlati et al. [2] void fraction for gravitational pressure drop and Ishihara et al. [4] frictional pressure drop

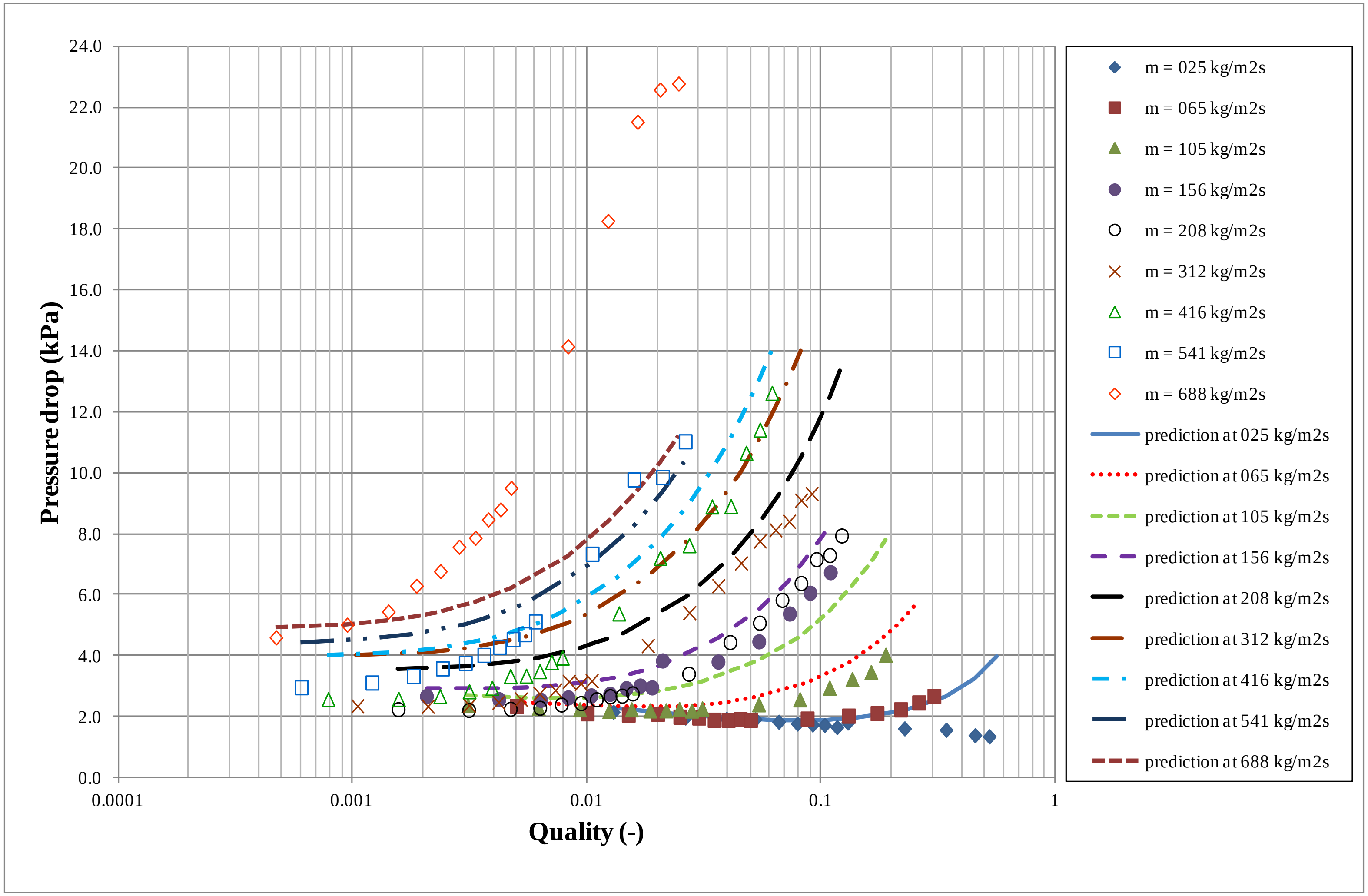

Figure 7.10: Variation of measured pressure drop with quality in 19 mm staggered bundle and predicted pressure drop using Dowlati et al. [2] void fraction for gravitational pressure drop and Xu et al. [5] frictional pressure drop

Table 7.3: The inlet pressure, two-phase flow temperature, water mass flow rate and pressure drop readings at 65 kg/m^{2}s in 19 mm in diameter staggered tube bundle

Mass flux min are kg/m^{2}s	Air mass flow rate kg/s	Inlet pressure kPa				Two-phase flow temperature °C				Water mass flow rate kg/s				Pressure drop kPa			
		Reading 1	Reading 2	Reading 3	Average	Reading 1	Reading 2	Reading 3	Average	Reading 1	Reading 2	Reading 3	Average	Reading 1	Reading 2	Reading 3	Average
208	0.00039	115.737	115.639	115.602	115.659	20.4	20.4	20.5	20.4	0.24943	0.25237	0.24813	0.24997	2.179	2.244	2.243	2.222
208	0.00078	114.390	114.431	114.298	114.373	20.6	20.7	20.7	20.6	0.25144	0.24843	0.24887	0.24958	2.192	2.209	2.193	2.198
208	0.00117	113.827	113.933	113.959	113.907	20.9	21.0	21.0	21.0	0.24638	0.24811	0.24967	0.24805	2.217	2.267	2.221	2.235
208	0.00156	113.453	113.630	113.764	113.616	21.2	21.2	21.2	21.2	0.24663	0.24839	0.24682	0.24728	2.250	2.298	2.258	2.269
208	0.00195	113.582	113.503	113.363	113.482	21.5	21.5	21.5	21.5	0.24952	0.24933	0.25115	0.25000	2.391	2.361	2.376	2.376
208	0.00234	113.689	113.026	113.459	113.391	21.5	21.6	21.6	21.6	0.24580	0.24716	0.24766	0.24688	2.463	2.381	2.424	2.423
208	0.00273	113.365	113.322	113.562	113.416	22.0	22.1	22.1	22.1	0.24719	0.24710	0.24643	0.24691	2.558	2.504	2.580	2.547
208	0.00312	113.136	113.664	113.651	113.484	22.2	22.2	22.2	22.2	0.24531	0.24776	0.24632	0.24646	2.511	2.691	2.742	2.648
208	0.00351	113.469	113.338	113.709	113.506	22.3	22.4	22.4	22.4	0.24675	0.24644	0.24507	0.24608	2.633	2.647	2.717	2.665
208	0.00390	113.376	113.502	114.015	113.631	22.5	22.5	22.5	22.5	0.24757	0.24467	0.24670	0.24632	2.692	2.646	2.884	2.741
208	0.00680	114.523	114.738	115.019	114.760	22.5	22.5	22.6	22.6	0.24478	0.24401	0.24443	0.24441	3.284	3.470	3.403	3.386
208	0.01020	117.562	118.208	117.651	117.807	22.7	22.7	22.6	22.7	0.24060	0.24170	0.23985	0.24071	4.323	4.585	4.369	4.426
208	0.01360	120.326	121.017	121.061	120.801	22.7	22.7	22.7	22.7	0.23695	0.23385	0.23959	0.23679	4.779	5.131	5.272	5.061
208	0.01700	125.871	125.435	125.386	125.564	22.5	22.6	22.5	22.5	0.23180	0.23377	0.23527	0.23362	5.862	5.800	5.773	5.811

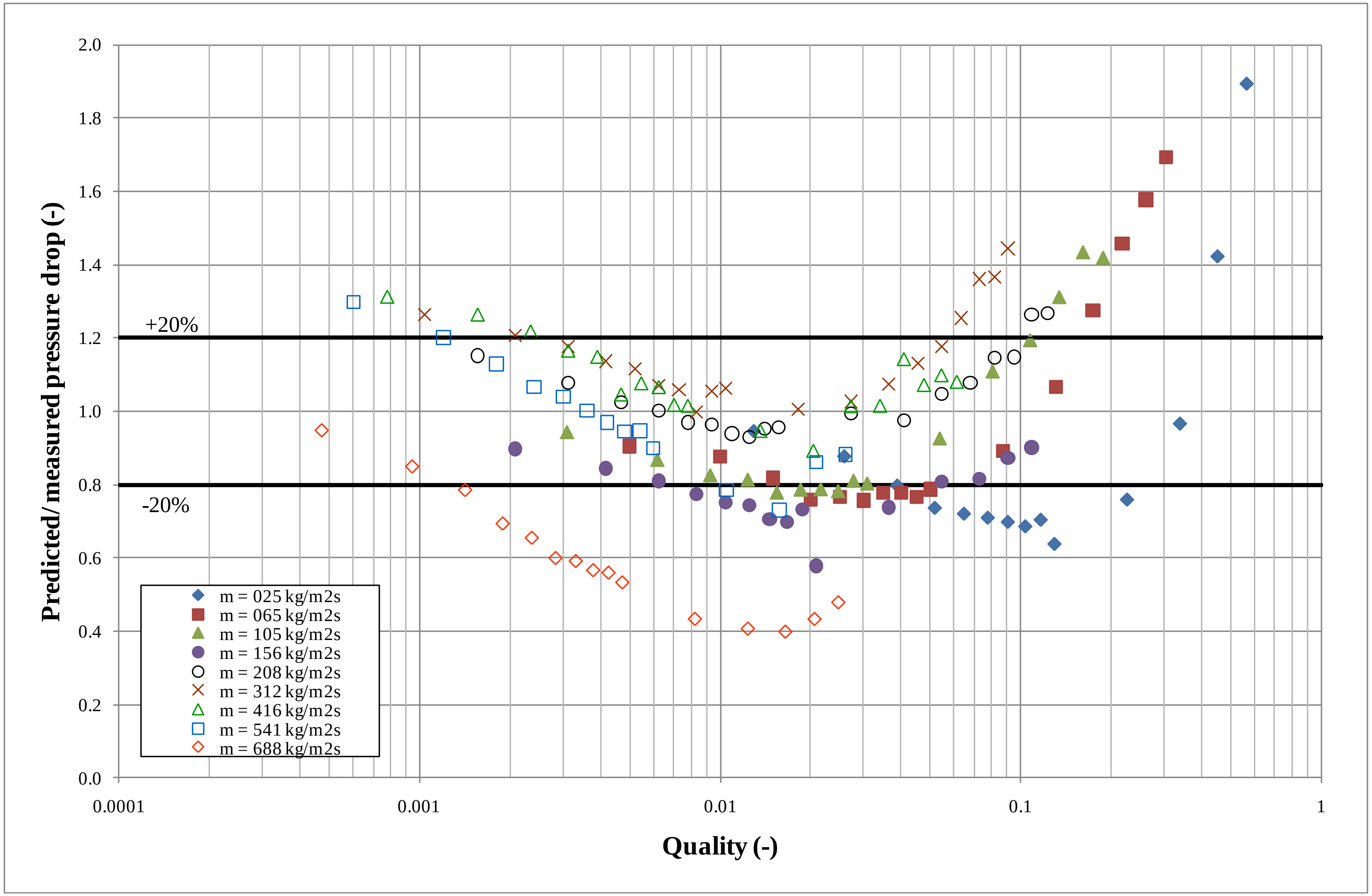

Figure 7.11: Comparison of predicted Ishihara et al. [4] to measured data in 19 mm staggered bundle

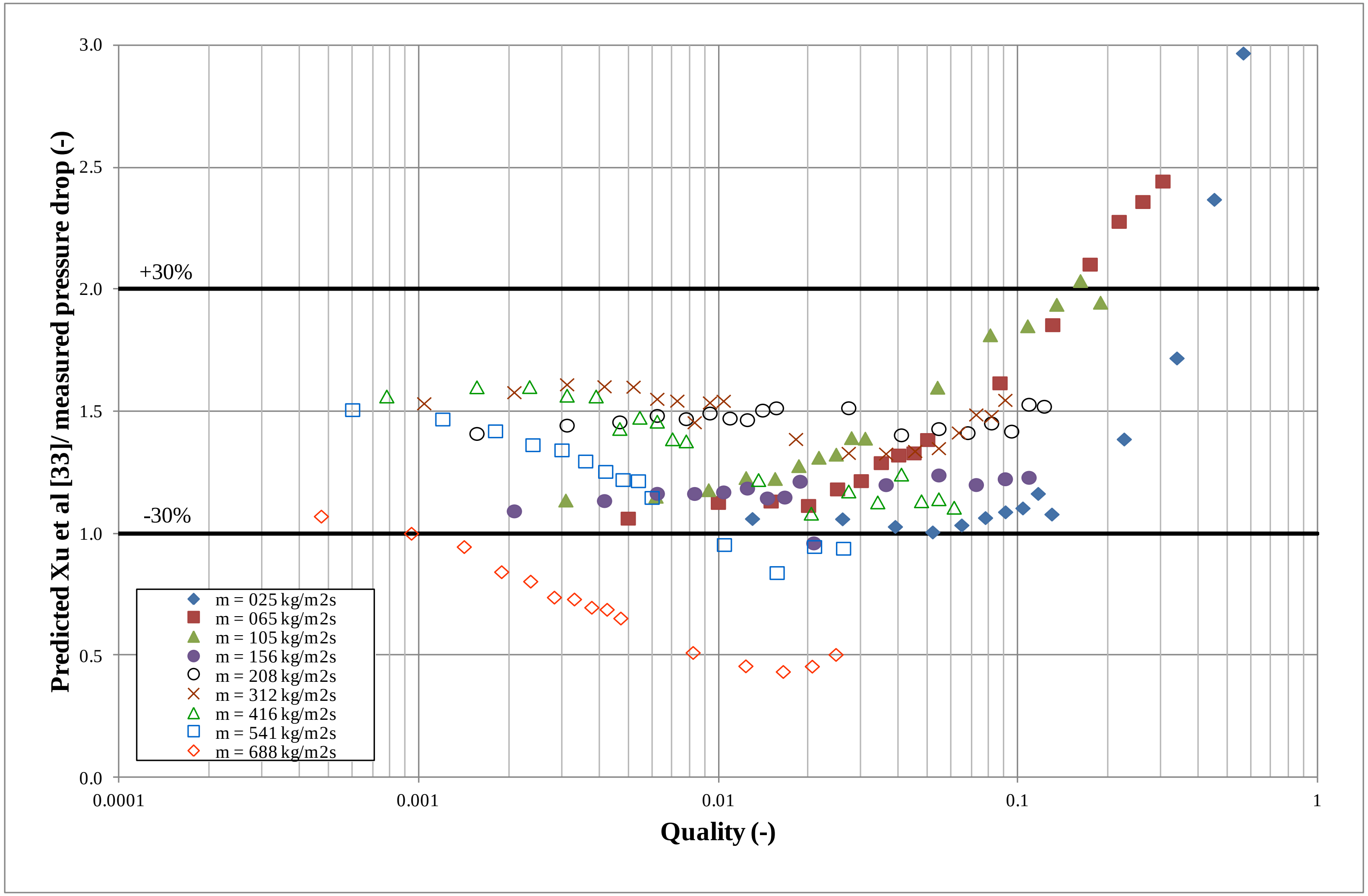

Figure 7.12: Comparison of predicted Xu et al. [5] to measured data in 19 mm staggered bundle

7.1.4 Comparison of two phase pressure drop measurements in three tube bundles

The measured pressure drop in 3 different bundles, 38 mm inline tube bundle, 19 mm inline bundle and 19 mm staggered bundle showed similar trends at most of the mass fluxes tested, as shown in Figures 7.1, 7.2, 7.5, 7.6, 7.9 and 7.10. At low mass fluxes, the pressure drop continues to fall as the quality increases. This is due to decreasing gravitational pressure drop, resulting from increasing void fraction, being more significant than the increase in frictional pressure drop. At larger mass fluxes, the pressure drop show a turning point where the total pressure drop begins to fall with increasing quality at a low quality before increasing with increasing quality. This is due to gravitational pressure drop decreasing at low quality more quickly than the increase in frictional pressure drop. However, frictional pressure drop rises significantly more than the gravitational pressure drop fall at larger qualities, giving an increase in total pressure drop. At higher mass fluxes in the staggered bundle, as shown in Figure 7.9 and 7.10, the frictional pressure drop rise is always higher than gravitational pressure drop fall and hence the total pressure drop always rises.

The effect of tube diameter on pressure drop is shown in Figure 7.13. The limits are set to ±50%. Almost all the measured pressure drops in the larger tube bundle are about 10% - 40% less than those for the smaller diameter tube, especially at the larger mass fluxes. This is due to more complex flow in the smaller tube bundle.

The effect of tube layout on pressure drop is shown in Figure 7.14. The total pressure drop in the staggered 19 mm bundle showed the same pattern as the inline bundle despite the change in configuration, and it agrees well with the correlations, Figures 7.5, 7.6, 7.9 and 7.10. A low mass fluxes, the gravitational pressure drop is dominating and at higher mass fluxes, the frictional pressure dominates; hence causing the total pressure drop to increase with increasing quality. However, the magnitude of the total pressure drop is quite large at larger mass fluxes. The pressure drop in the staggered bundle increases significantly more than for the in-line for mass fluxes in the range 416 – 688 kg/m^{2}s. At 416 kg/m^{2}s, the pressure drop rises by almost 50% at a quality 0.0547 in the staggered bundle. At 541 kg/m^{2}s, the pressure drop increased by up to 55% at a quality of 0.0263. The pressure drop rises dramatically to 22.76 kPa in the staggered bundle compared to 6.41 kPa in the in-line bundle at a quality of 0.0248 and at the mass flux of 688 kg/m^{2}s, a 72% increase. This is due in part to higher void fraction values in the staggered bundle compared to the in-line bundle because the mixing of the two-phases leads to a more homogenous void fraction. A higher void fraction will decrease the gravitational pressure drop. The turbulence in the flow, caused by the change in tube arrangement, creates large frictional pressure drops. The total pressure drop therefore increases.

The predictions of pressure drop using the Dowlati et al. [2] correlation for void fraction; and the Ishihara et al. [4] correlation and the Xu et al. [5] correlation for frictional pressure gradient can be used to predict the two-phase pressure drop. These correlations were deduced from data sets obtained from tube bundles that contained tubes with diameters less than 20 mm. The results presented in Figures 7.1 and 7.2 clearly show that these methods can also be used with tube bundles that contain tubes up to 38 mm in diameter. As seen in Figures 7.1, 7.2, 7.5, 7.6, 7.9 and 7.10, the predictions do pick up the trends, where at low mass flux, the predicted pressure drop continues falling while at larger mass flux, the turning characteristic is reproduced. However, in Figures 7.1 7.2, 7.5 and 7.6 for in-line bundles, the actual magnitudes are not well reproduced, as is typical of two-phase pressure drop. The predicted pressure drop in the staggered bundle, Figures 7.9 an 7.10, shows that the measured data agreed well with the predictions except at the largest mass flux of 688 kg/m^{2}s. However, the prediction frictional pressure drop using Xu et al. [5] for all bundles are shown to predict the best frictional pressure drop compared to Ishihara et al. [4] because it gives better mean average and RMS error for the present data than Ishihara et al. [4].

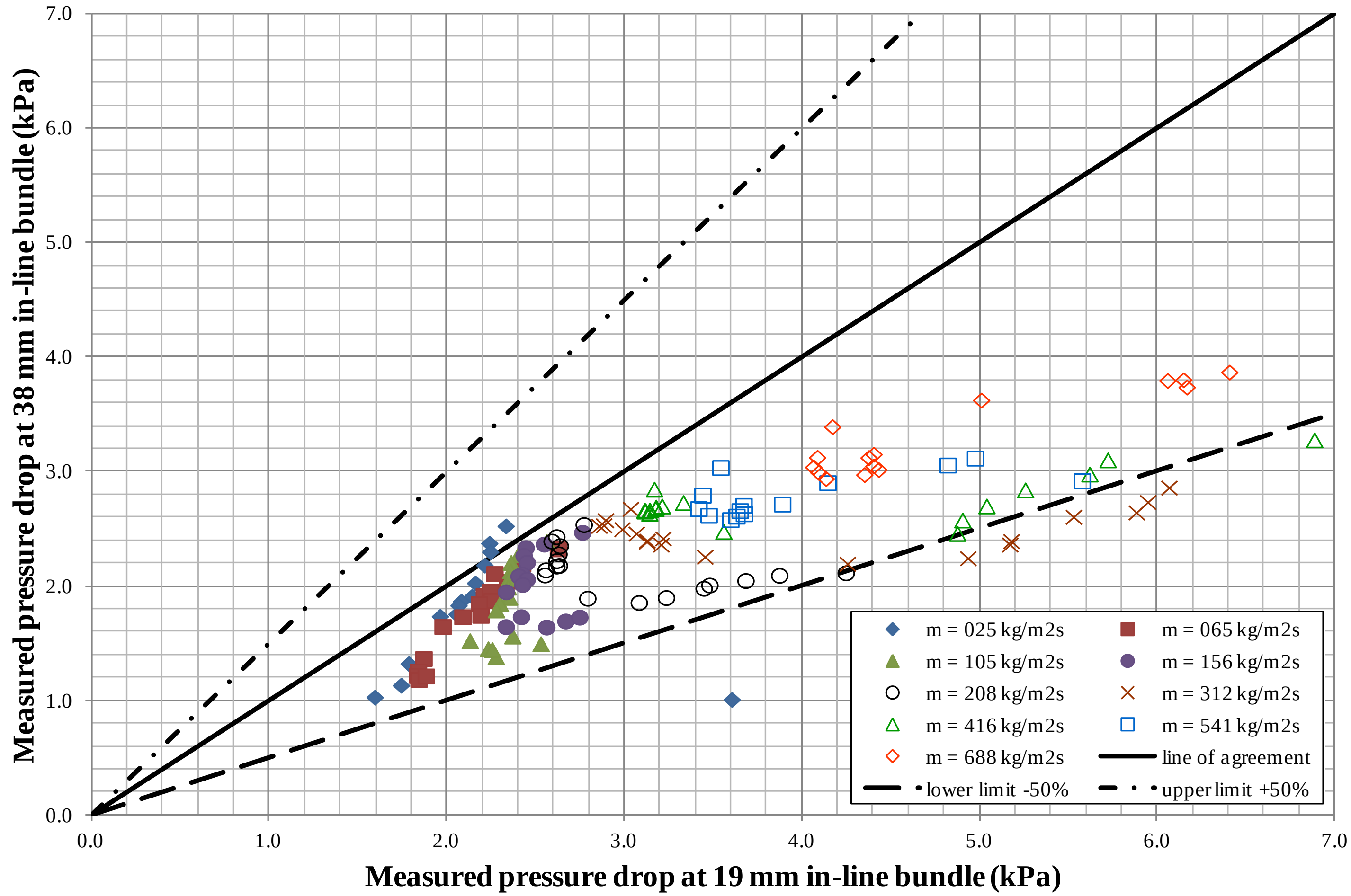

Figure 7.13: Comparison of measured pressure drop in in-line bundles (19 mm and 38 mm in diameter)

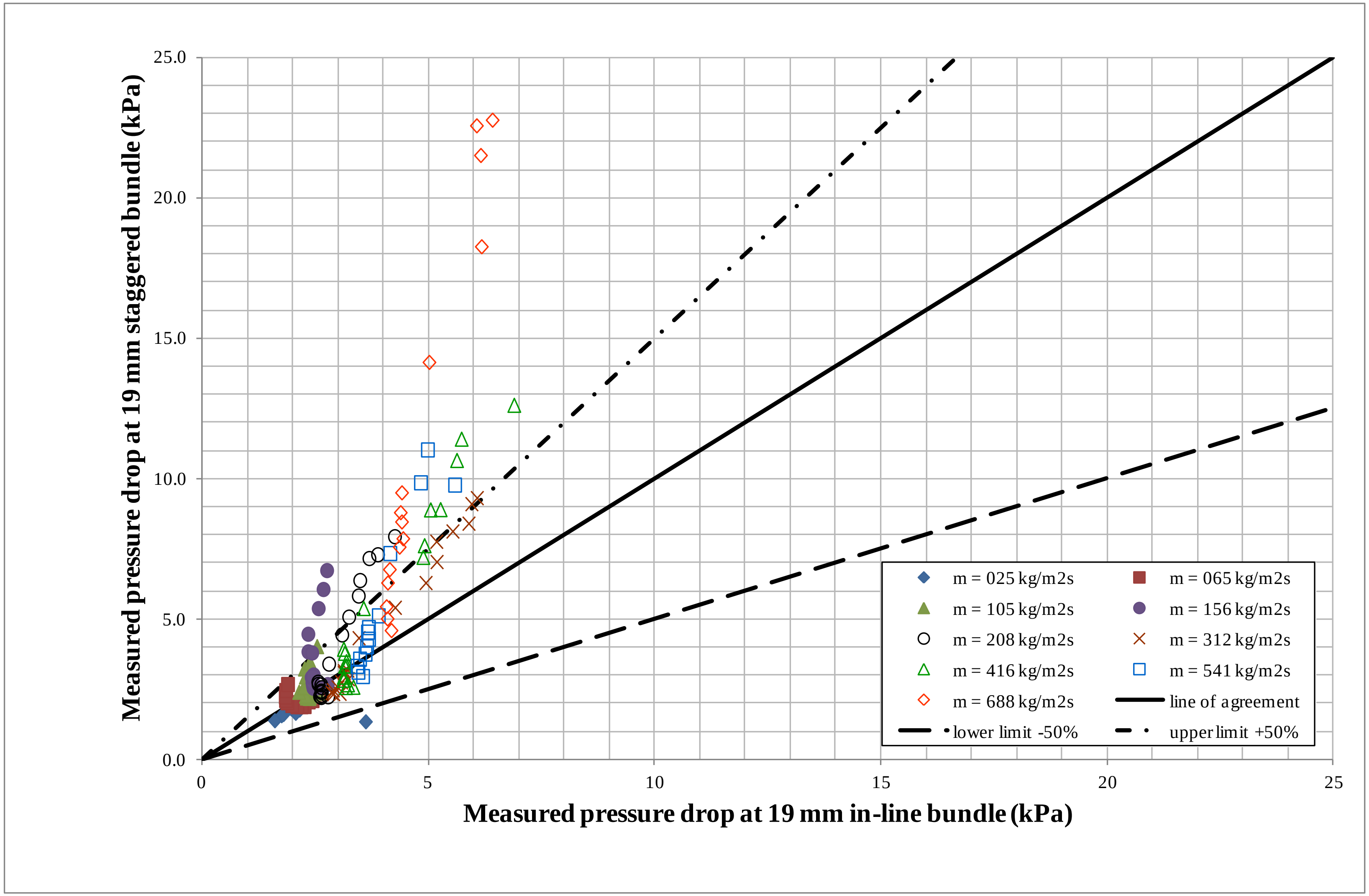

Figure7. 14: Comparison of measured pressure drop in 19 mm in-line bundle and 19 mm staggered bundle

7.2 Two-phase friction multiplier

The measured two-phase multiplier, ϕ_{LE}^2, is related to the frictional pressure gradient through

$$\left(\frac{dp}{dz}\right)_F = \left(\frac{dp}{dz}\right)_l \phi_{LE}^2 \tag{7.4}$$

where $(dp/dz)_l$ is the single-phase frictional pressure gradient that would occur if the liquid portion of the flow passed through the heat exchanger. This was evaluated from ESDU [52] where the pressure loss data are presented in terms of a pressure loss coefficient, C_L, and a single-phase frictional pressure drop related through

$$\left(\frac{dp}{dz}\right)_F = -C_L\left(\frac{\frac{1}{2}\rho_l u^2}{D}\right) \tag{7.5}$$

where u is the stream velocity based on flow area calculated ignoring the area occupied by the tubes. Rearrange Equation (7.5), the single-phase frictional pressure gradient is calculated by

$$\left(\frac{dp}{dz}\right)_F = \frac{-C_L}{2D}\left(\frac{G^2(1-x)^2}{\rho_l}\right) \tag{7.6}$$

The loss coefficient, C_L, or the single-phase friction factor is calculated for in-line arrays from

$$C_L = YF\left(\frac{D_V}{D}\right)\frac{1}{(X-1)^3} \tag{7.7}$$

where the ratio $\left(\frac{D_v}{D}\right)$ is given by

$$\left(\frac{D_V}{D}\right) = \frac{4X^2}{\pi} - \left(\frac{\text{Re}}{\text{Re}+1000}\right) \tag{7.8}$$

and Y is given by

$$Y = \left[\left\{\frac{0.1\text{Re}}{\text{Re}+100}\right\}^2 \Big/ \left\{\frac{a^2}{[0.5(1+0.6\text{a})]^2} + \frac{1}{(1+3a)^2}\right\} + \frac{49}{\text{Re}^{1.95}}\right]^{1/2} \tag{7.9}$$

and a is calculated from

$$a = \frac{\text{Re}}{\text{Re}+10^4} \tag{7.10}$$

For in-line square arrays, F should be taken as unity, i.e. F =1, Equation (7.7).

The loss coefficient, C_L for equilateral triangular arrays is expressed as

$$C_L = Y\left(\frac{D_V}{D}\right)\frac{1}{(X-1)^3} \tag{7.11}$$

where the ratio is $\left(\frac{D_v}{D}\right)$ given by

$$\left(\frac{D_V}{D}\right) = \frac{2\sqrt{3}\,X^2}{\pi} - \left(\frac{\text{Re}}{\text{Re}+10}\right) \tag{7.12}$$

and Y is given by

$$Y = \left[\frac{3.61}{\text{Re}^{0.7}}\left(1+\frac{5}{\text{Re}^{0.8}}\right)^2 + 0.0625(1-\text{a})^2 + 0.01\right]^{1/2} \tag{7.13}$$

where a is given by Equation (7.10).

The experimental gravitational pressure gradient was obtained from the measured pitch void fraction, Equations (7.2). The experimental frictional pressure gradient was calculated by subtracting the measured gravitational pressure gradient from the total measured pressure drop, Equation (7.1). The acceleration pressure gradient was neglected because it had a small value.

Lockhart and Martinelli [29] proposed a model to calculate the two-phase friction multiplier in horizontal tube flow as

$$\phi_l^2 = 1 + \frac{C}{x_{tt}} + \frac{1}{x_{tt}^2} \tag{7.14}$$

where C is a constant, produced from the Chisholm C type, Chisholm [70]. x_{tt} is the Martinelli parameter, determined from

$$x_{tt} = \left(\frac{1-x}{x}\right)^{0.9} \sqrt{\frac{\rho_g}{\rho_l}} \left(\frac{\mu_l}{\mu_g}\right)^{0.1} \tag{7.15}$$

This correlation has been used for shell-side two-phase flow by Ishihara et al. [4] and Schrage et al. [1]. Ishihara et al. [4] found that a constant C of 8 fitted their data best although large scatter was seen for $x_{tt} > 0.2$ and suggested that flow regimes must be identified. The void fraction correlation that was used to compute their friction multiplier values was not specified. Schrage et al. [1] found that the C factor of 8 overpredict their data by 17% and suggested that the C value was dependent on flow pattern. Xu et al. [5] suggested that the constant C deduced on the dimensionless gas velocity, u_g, the Martineli parameter, x_{tt} and the quality ratio, $x / (1 - x)$. The new correlations for the constant C for up-flow in in-line bundles was given as

$$C = 24.45 u_g^{-0.654} \left(\frac{x}{1-x}\right)^{0.336} \tag{7.16}$$

where the dimensionless gas velocity, u_g is expressed as

$$u_g = \frac{G_{\max} x}{\sqrt{\rho_g g D(\rho_l - \rho_g)}} \tag{7.17}$$

The measured frictional pressure drop was compared with two correlations, Ishihara et al. [4] and Xu et al. [5], using the two-phase multiplier deduced from them, see Equation (7.4).

7.2.1 Two-phase multiplier in the 38 mm diameter in-line bundle

A comparison between the measured two-phase multipliers and correlation of Ishihara et al. [4] with Martinelli parameter is shown in Figure 7.15. At small gas quality, the Martinelli parameter is large and the gravitational pressure gradient is high in comparison to the total pressure drop, so that significant errors in the two-phase multipliers would be expected. However, at large quality, the Martinelli parameter is small and the gravitational pressure drop is small in comparison to the total, giving a much smaller error in the measured two-phase multiplier. For example, when the mass flux was 25 kg/m^{2}s, a quality of 0.013 gave a Martinelli parameter of 2.62 and a gravitational pressure drop that was 92% of the total, while a quality of 0.57 gave a Martinelli parameter of 0.048 and a gravitational pressure drop that was 14% of the total. Similarly, when the mass flux was 688 kg/m^{2}s, a quality of 0.00047 gave a Martinelli parameter of 56.96 and a gravitational pressure drop that was 82% of the total, while a quality of 0.025 gave a Martinelli parameter of 1.80 and a gravitational pressure drop that was 13% of the total. Nonetheless, the trends shown for any given mass flux contain little scatter. However, a few data points, in each mass flux run always at the lowest gas mass flow rate, had a gravitational pressure drop that was larger than the total. These have been omitted. The measured two-phase multipliers clearly show a mass flux dependency. At low mass flux, the measured two-phase multiplier is significantly above the predicted value. As the mass flux increases, the data move towards the predicted values, with reasonable agreement occurring for mass fluxes at about 208 kg/m^{2}s. This is consistent with Dowlati et al. [2], where the correlation was said to be valid for mass fluxes greater than 260 kg/m^{2}s.

A comparison between the measured two-phase multipliers and correlation of Ishihara et al. [4] is shown in Figure 7.16. At the lowest mass flux of 25 kg/m^{2}s, the measured two-phase multiplier was considerably above the predicted value with an average difference of 2300% and a RMS difference of 2600%. As the mass flux increases, the data move towards the predicted values, with reasonable agreement occurring for mass fluxes greater than about 208 kg/m^{2}s. At the highest mass flux, 688 kg/m^{2}s, the average and RMS differences were -0.64% and 23% respectively. This is consistent with previous studies, Dowlati et al. [2] where the correlation was said to be valid for mass fluxes greater than 260 kg/m^{2}s.

A comparison between the measured and predicted two-phase multipliers of Xu et al. [5] is shown in Figure 7.17. The average and RMS differences that respectively fell from 370% to 390% at the lowest mass flux to -30% and 34% at the highest mass flux. A reasonable RMS difference of less than 40% is achieved for mass fluxes of 156 kg/m^{2}s and above, although some of the data are less than the predicted values, especially at the small quality in the mass fluxes range from 416 to 688 kg/m^{2}s. At 688 kg/m^{2}s, at the smallest quality, x = 0.00047, the measured data is 0.651, and the predicted values is 1.53. The best agreement with the measured two-phase multipliers was obtained with the Xu et al. [5] correlation. The method fails to capture all of the mass flux dependency, but it does better than the Ishihara et al. [4] method.

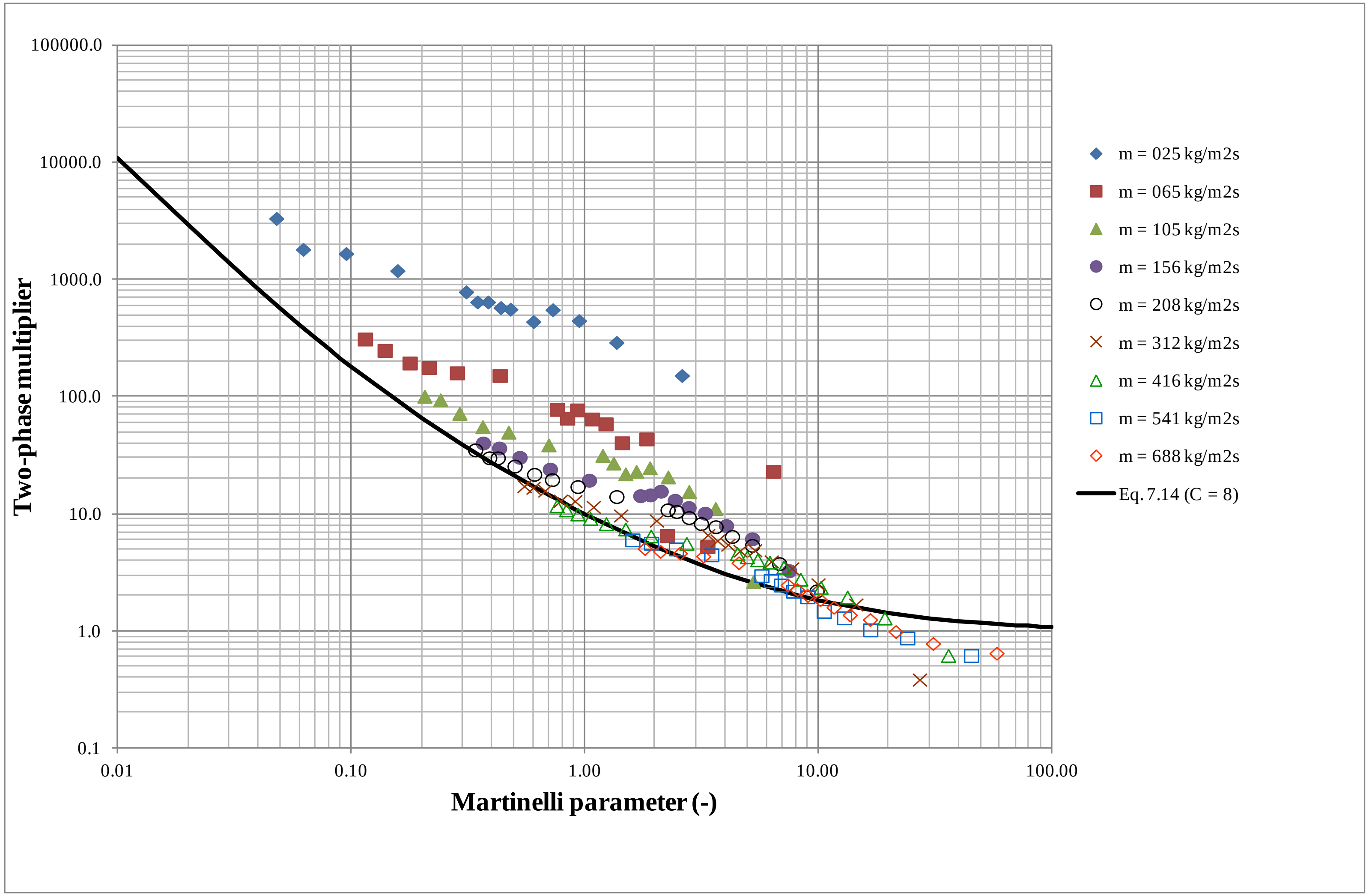

Figure 7.15: Two-phase friction multiplier data with Martinelli paramater in 38 mm in diameter in-line rod bundle

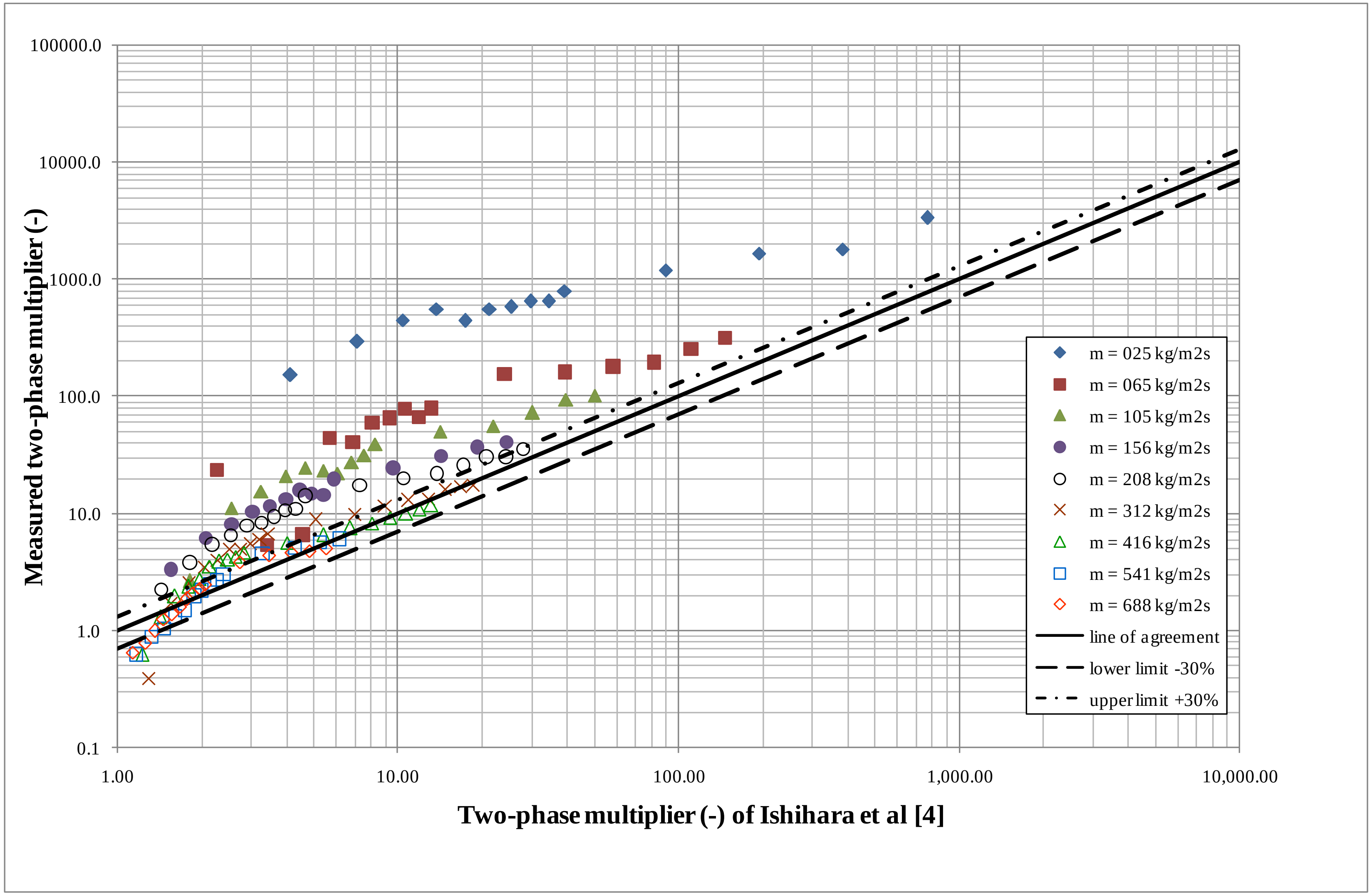

Figure 7.16: Variation of measured with predicted two-phase multipliers of Ishihara et al. [4] in 38 mm in diameter in-line rod bundle

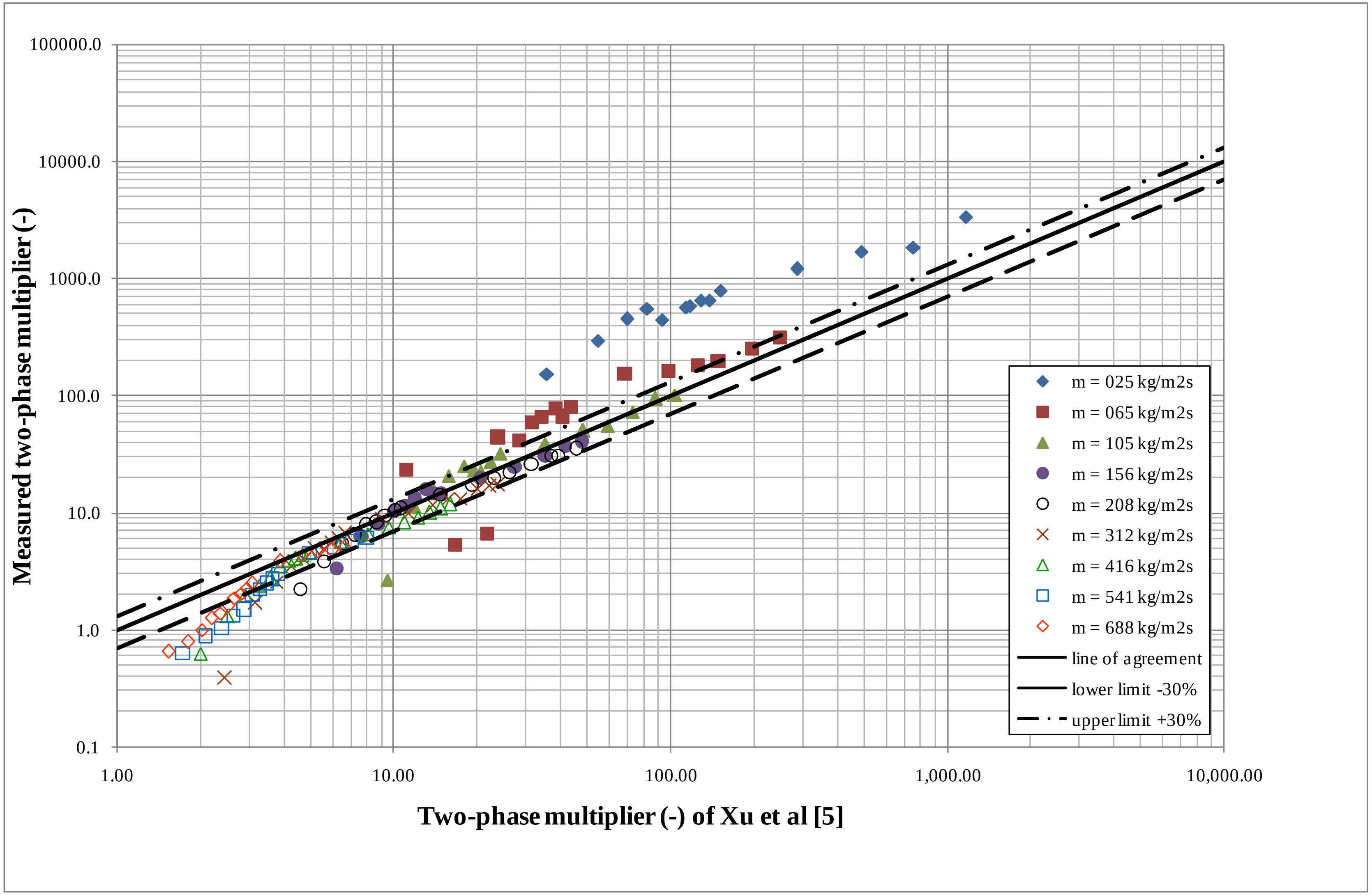

Figure 7.17: Variation of measured with predicted two-phase multipliers of Xu et al. [5] in 38 mm in diameter in-line rod bundle

7.2.2 Two-phase multiplier in the 19 mm diameter in-line bundle

A comparison between the measured and predicted two-phase multipliers by Ishihara et al. [4], varying with Martinelli parameter, is shown in Figure 7.18. The measured two-phase multipliers are almost all above the predicted values except at higher mass flux, 416-688 kg/m^{2}s, where the measured values agree well with the predicted two-phase multipliers. The measured two-phase multipliers also show a clear mass flux dependency. At low mass flux, the measured two-phase multiplier is considerably larger than the predicted value by Ishihara et al. [4]. As the mass flux increases, the data move near the predicted values with reasonable agreement for mass fluxes larger than 208 kg/m^{2}s. This agrees with the study by Dowlati et al. [2], where the correlation was valid for mass fluxes greater than 260 kg/m^{2}s. For this bundle, when the mass flux was 25 kg/m^{2}s, a quality of 0.013 gave a Martinelli parameter of 2.67, while a quality of 0.57 gave a Martinelli parameter of 0.041 and a gravitational pressure drop that was 10% of the total. Similarly, when the mass flux was 688 kg/m^{2}s, a quality of 0.00047 gave a Martinelli parameter of 57.0 and a gravitational pressure drop that was 59% of the total, while a quality of 0.025 gave a Martinelli parameter of 1.752 and a gravitational pressure drop that was 6% of the total.

A comparison between the measured two-phase multipliers and correlation of Ishihara et al. [4] is shown in Figure 7.19. At the lowest mass flux of 25 kg/m^{2}s, the measured two-phase multiplier was considerably above the predicted value with an average difference of 1470% and a RMS difference of 1630%. As the mass flux increases, the data move towards the predicted values, with reasonable agreement occurring for mass fluxes greater than about 208 kg/m^{2}s. At the highest mass flux, 688 kg/m^{2}s, the average and RMS differences were -5.3% and 12% respectively. This is consistent with previous studies, Dowlati et al. [2] where the correlation was said to be valid for mass fluxes greater than 260 kg/m^{2}s.

A comparison between the measured and predicted two-phase multipliers of Xu et al. [5] is shown in Figure 7.20. This gave better average and RMS differences than Ishihara et al. [4]. They fell from 293% to 310% at the lowest mass flux to -21% and 23% at the highest mass flux respectively. A reasonable RMS difference of less than 30% is achieved for mass fluxes of 208 kg/m^{2}s and above. The best agreement with the measured two-phase multipliers was obtained with the Xu et al. [5] correlation. The method fails to capture all of the mass flux dependency, but it does better than the Ishihara et al. [4] method.

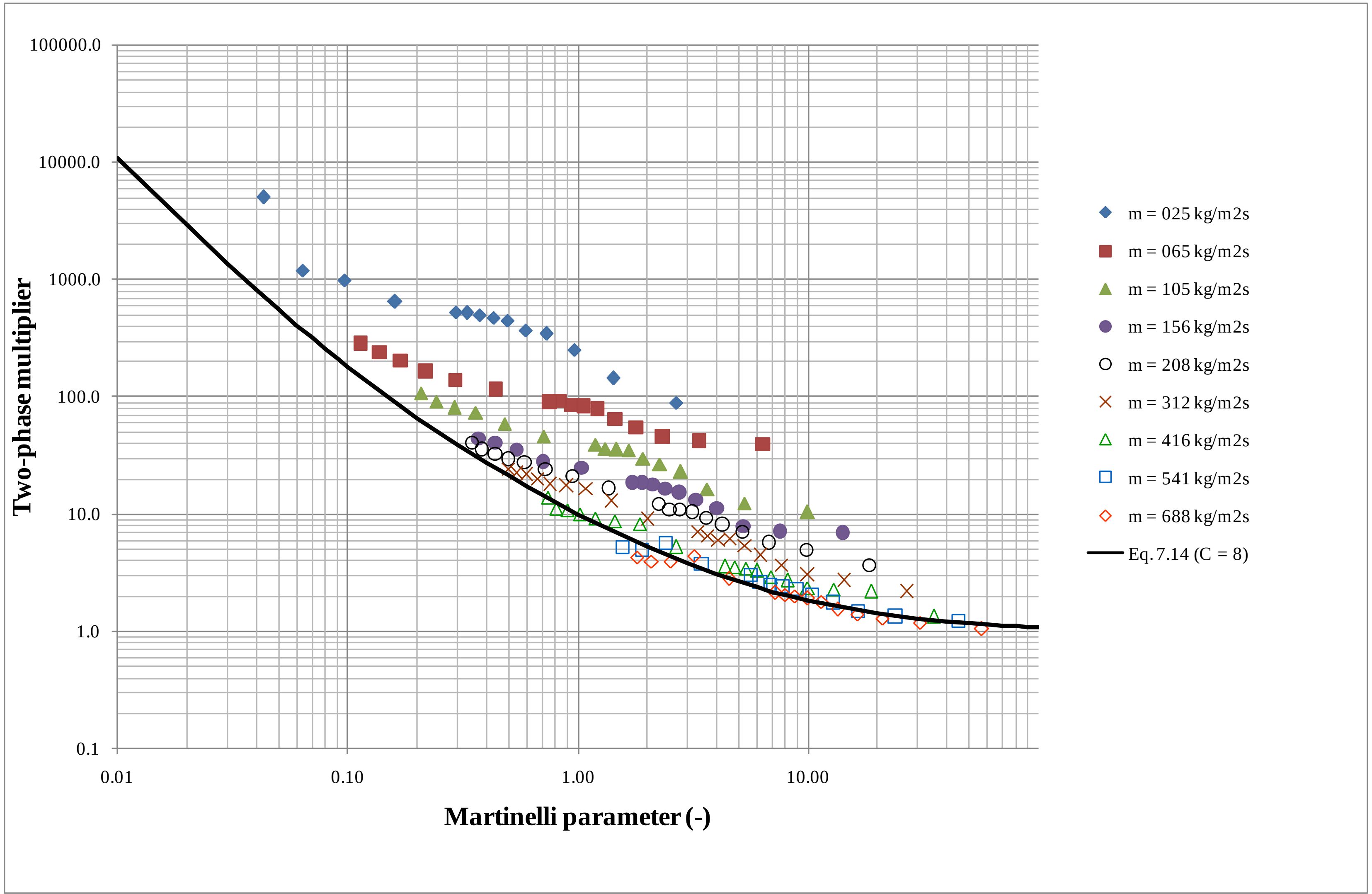

Figure 7.18: Two-phase friction multiplier data with Martinelli paramater in 19 mm in diameter in-line rod bundle

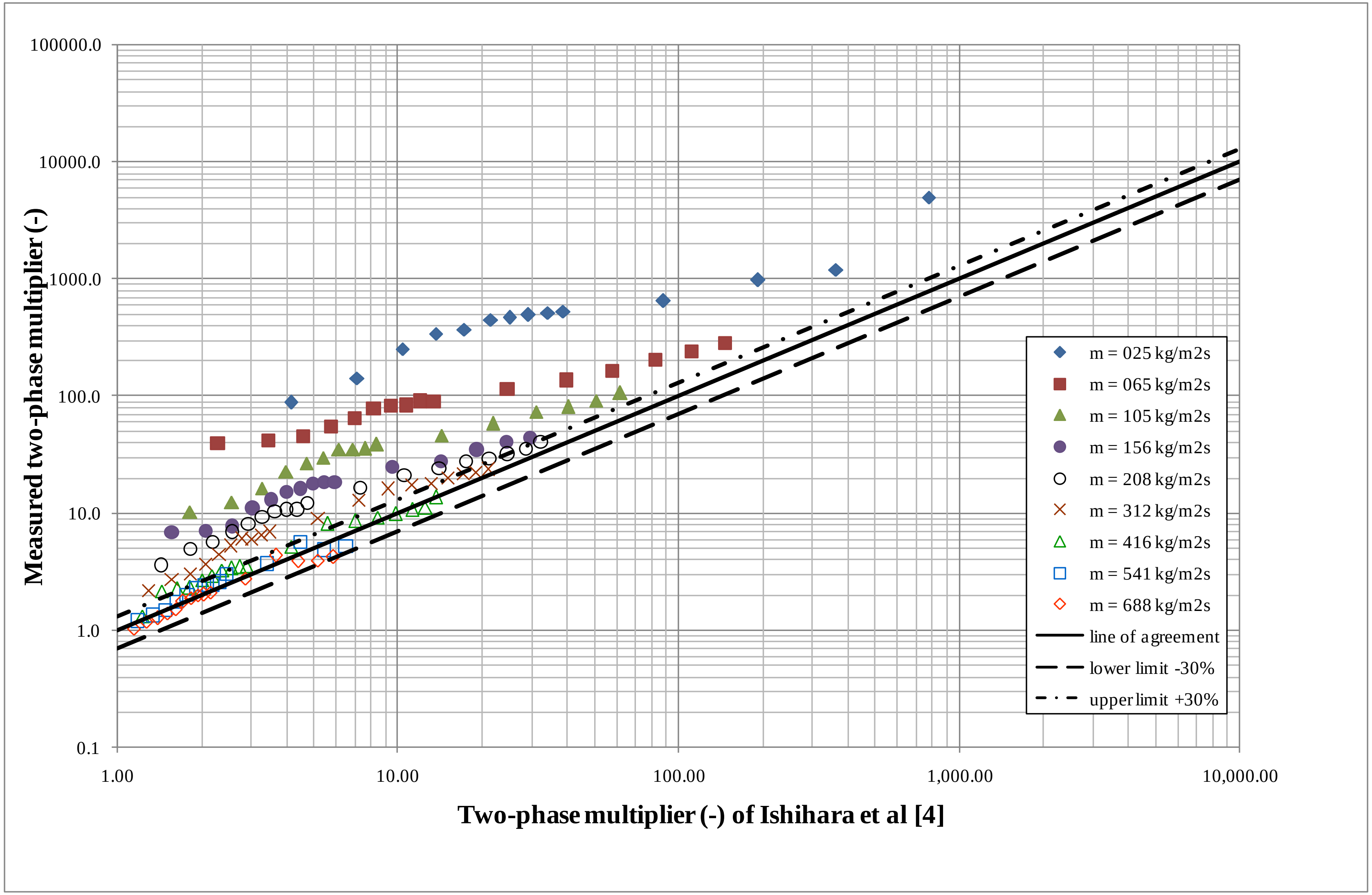

Figure 7.19: Variation of measured with predicted two-phase multipliers of Ishihara et al. [4] in 19 mm in diameter in-line rod bundle

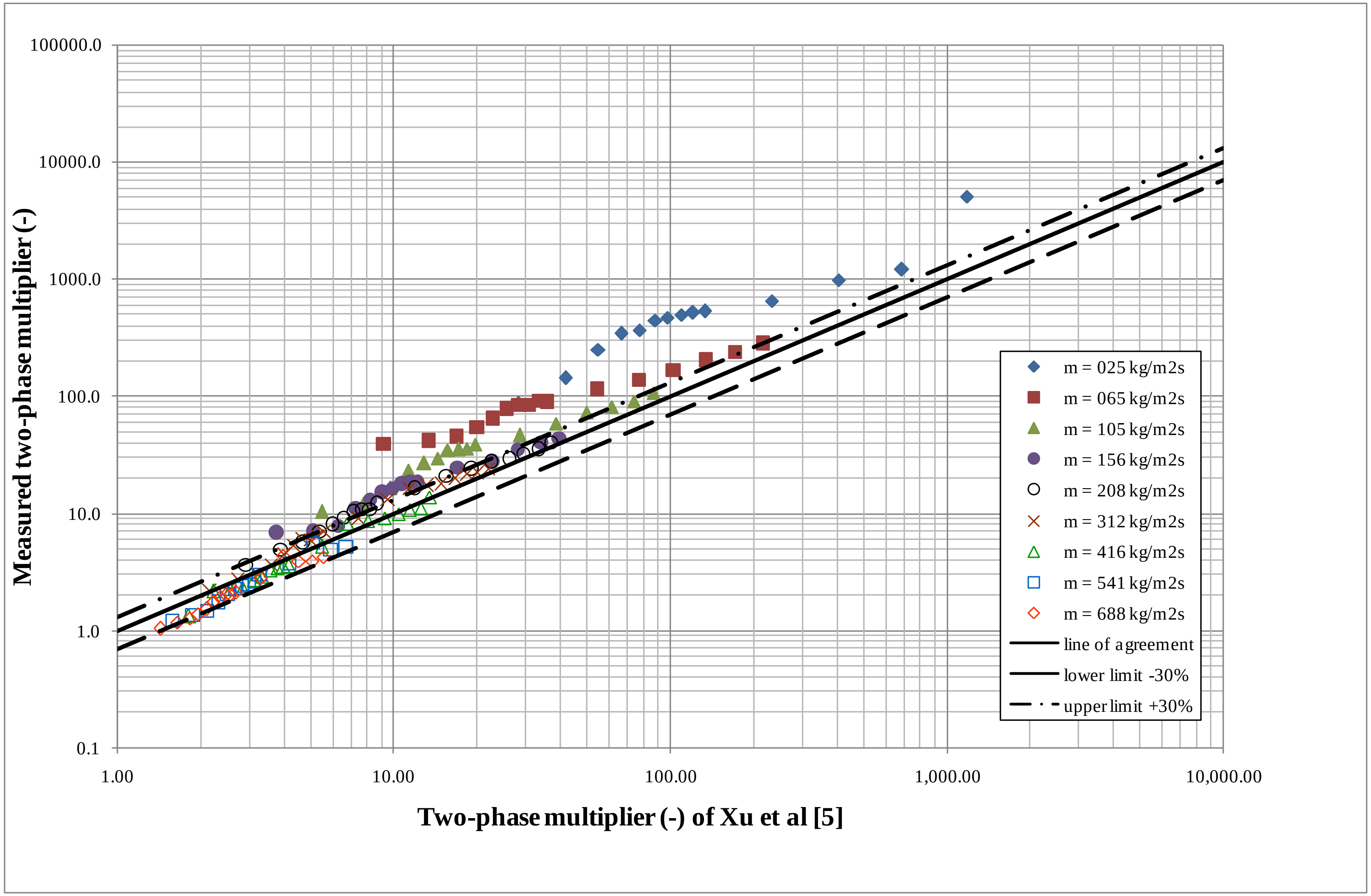

Figure 7.20: Variation of measured with predicted two-phase multipliers of Xu et al. [5] in 19 mm in diameter in-line rod bundle

7.2.3 Two-phase multiplier in the 19 mm diameter staggered bundle

Figure 7.21 shows a comparison between the measured and predicted two-phase multiplier of Ishihara et al. [4] correlation for the 19 mm diameter staggered bundle, varying with Martinelli parameter. The measured two-phase multiplier clearly shows a mass flux dependency, however, the trends shown in the staggered bundle for any given mass flux contains less scatter than the in-line arrays. At small quality, where the Martinelli parameter is large, the gravitational pressure drop is large in comparison to the frictional pressure drop and therefore similar in magnitude to the total pressure drop, potentially giving a significant error in the two-phase multiplier. At large quality, where the Martinelli parameter is small, the frictional pressure drop is more significant than the gravitational pressure drop, giving a small error. As the mass flux increases, the data moves towards the predicted values, with reasonable agreement for mass fluxes above 208 kg/m^{2}s. This is said to be consistent with Dowlati et al. [2], where the correlation works well for mass flux greater than 260 kg/m^{2}s. As seen from the graph, when the mass flux was 25 kg/m^{2}s, a quality of 0.013 gave a Martinelli parameter of 2.66 and a gravitational pressure drop that was 93% of the total, while a quality of 0.52 gave a Martinelli parameter of 0.049 and a gravitational pressure drop that was 23% of the total. Similarly, when the mass flux was 688 kg/m^{2}s, a quality of 0.00047 gave a Martinelli parameter of 57.8 and a gravitational pressure drop that was 44% of the total, while a quality of 0.025 gave a Martinelli parameter of 1.98 and a gravitational pressure drop that was 1.5% of the total.

A comparison between the measured two-phase multipliers and correlation of Ishihara et al. [4] is shown in Figure 7.22. At the lowest mass flux of 25 kg/m^{2}s, the measured two-phase multiplier was considerably above the predicted value with an average difference of 317% and a RMS difference of 430%. As the mass flux increases, the data move towards the predicted values, with reasonable agreement occurring for mass fluxes at 208 kg/m^{2}s to 541 kg/m^{2}s. At 541 kg/m^{2}s, the mean error is -21% and RMS is 31%. This is consistent with previous studies, Dowlati et al. [2] where the correlation was said to be valid for mass fluxes greater than 260 kg/m^{2}s. However, at the highest mass flux, 688 kg/m^{2}s, the average and RMS differences were 85% and 94% respectively. The measured two-phase multipliers are greater than the predicted values and move upward from the agreement line.

Figure 7.23 shows a comparison between the measured and predicted two-phase multipliers of Xu et al. [5]. The comparison gave better average and RMS differences than Ishihara et al. [4]. They fell from -5% to 37% at the lowest mass flux of 25 kg/m^{2}s. At 541 kg/m^{2}s, the mean average is 0.12% and the RMS error is 20%. A reasonable RMS difference of less than 40% is achieved for mass fluxes of 208 kg/m^{2}s to 541 kg/m^{2}s. The best agreement with the measured two-phase multipliers was obtained with the Xu et al. [5] correlation. However, the comparison shows high mean average and RMS error at the highest mass flux, at 688 kg/m^{2}s where the comparison gave 57% and 73% respectively. The mass flux dependency, for the staggered bundle is captured better than for the in-line bundles by this method.

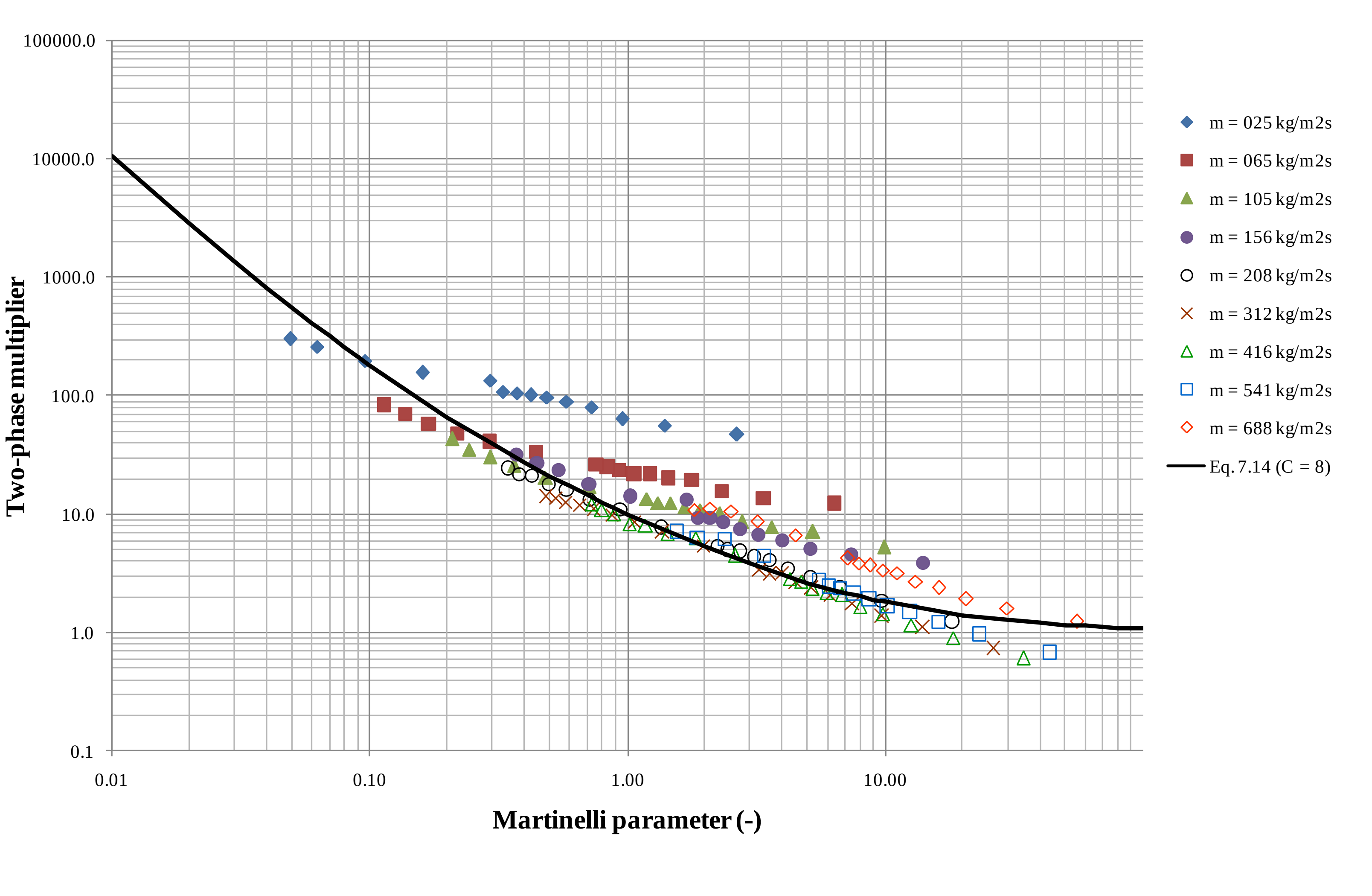

Figure 7.21: Two-phase friction multiplier data with Martinelli paramater 19 mm in diameter in staggered rod bundle

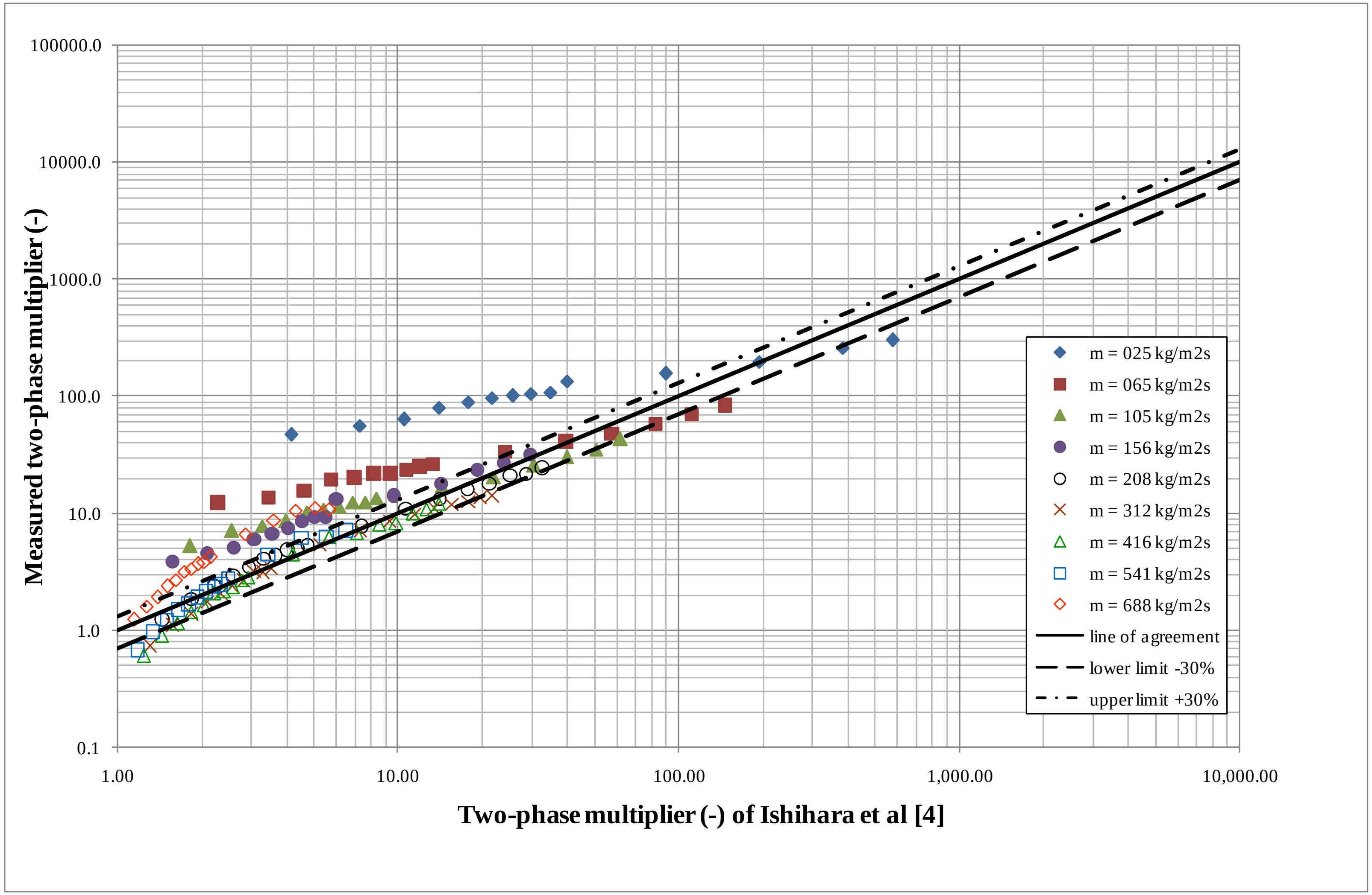

Figure 7.22: Variation of measured with predicted two-phase multipliers of Ishihara et al. [4] in 19 mm in diameter staggered rod bundle

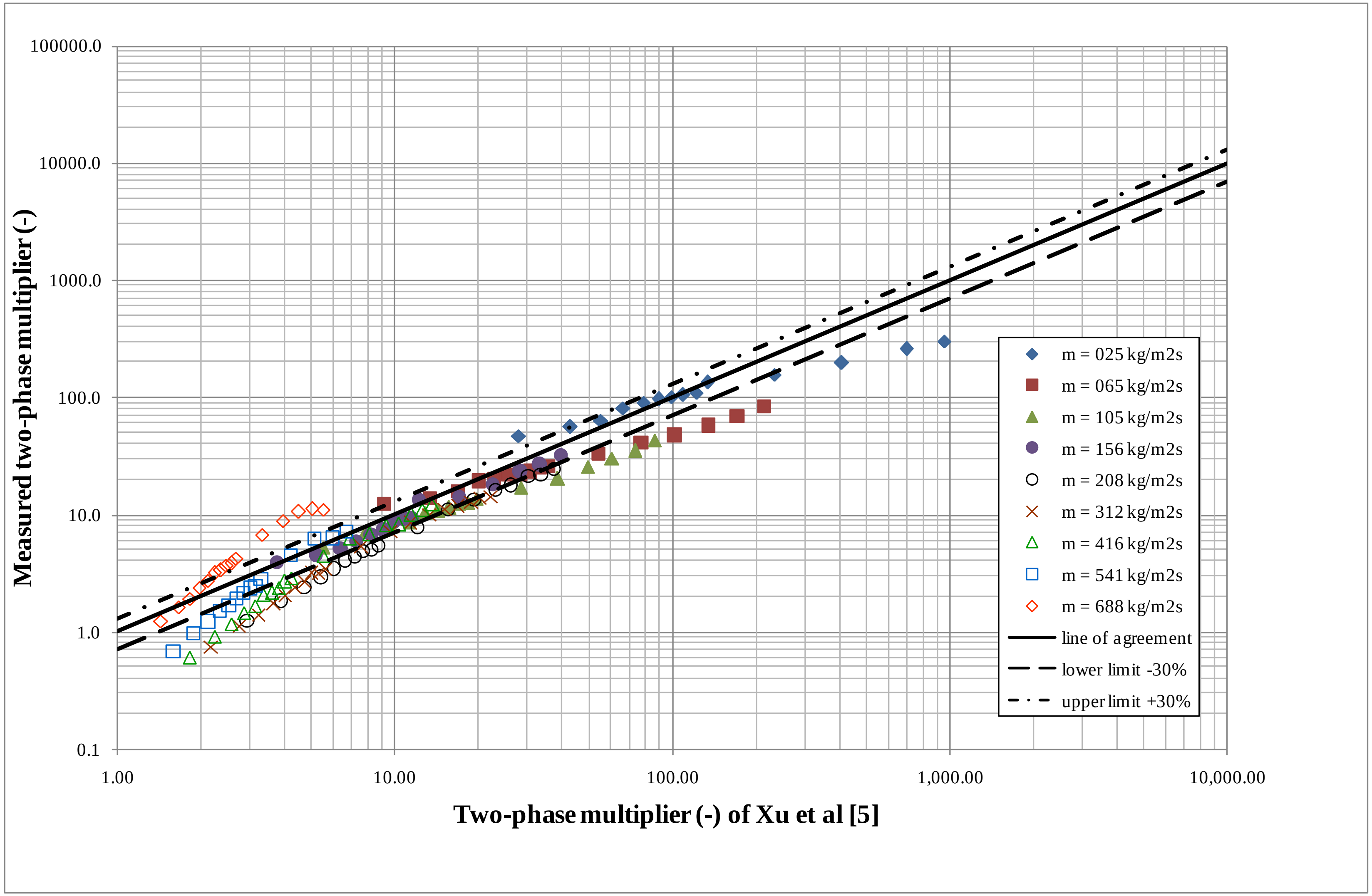

Figure 7.23: Variation of measured with predicted two-phase multipliers of Xu et al. [5] in 19 mm in diameter staggered rod bundle

7.2.4 Comparison of measured two-phase multiplier between the two inline bundles

The comparison between the measured two-phase multipliers for the in-line bundles with different tube diameters is shown in Figure 7.24. At the lower mass fluxes, 25 kg/m^{2}s and 65 kg/m^{2}s, the measured two-phase multiplier agree less well, with many of the two-phase multiplier measured in the 38 mm in-line bundle higher than those in the 19 mm in-line bundle. The measured two-phase multipliers in the larger bundle are slightly lower than the smaller diameter bundle values at the higher mass fluxes of 416 – 688 kg/m^{2}s. Overall, the vast majority of the measured two-phase multipliers in both bundles are shown to be the same for most the data range, regardless of the tube diameter. Recalling that the measured void fraction data in these bundles was also the same, as discussed in Chapter 6. Since the two-phase multiplier is the same, the single-phase friction factor, C_L must account for the different pressure gradient. This is proven by comparing different values of C_L for both bundles at all mass fluxes in Table 7.4.

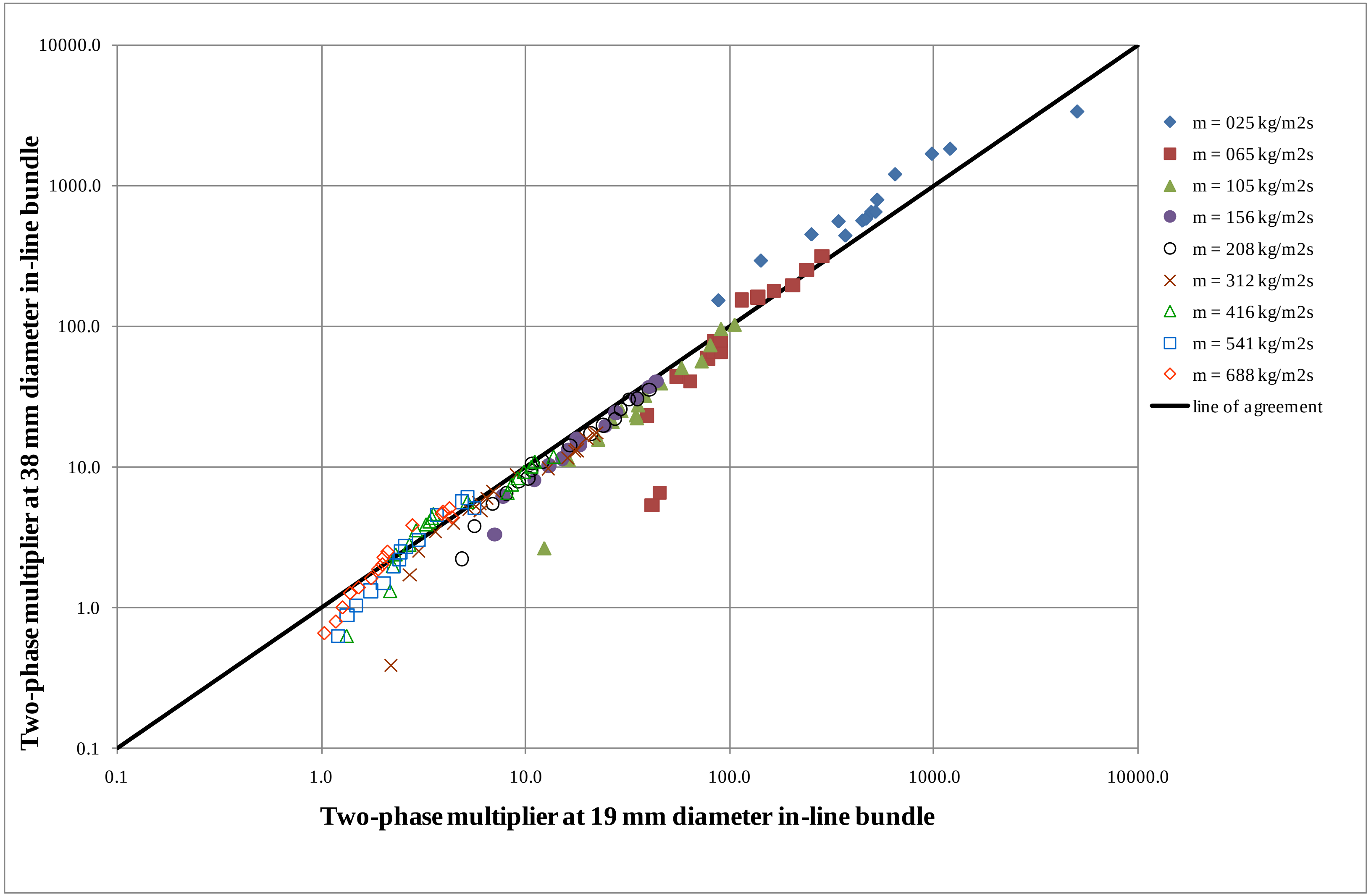

Figure 7.24: Comparison of measured two-phase multiplier in in-line bundles (19 mm and 38 mm diameter)

Table 7.4: Loss coefficient or single-phase friction factor, *C* in in-line tube bundles

Air mass flow rate kg/s	Mass flux minimum flow area (kg/m^2s)																	
	25		65		105		156		208		312		416		541		688	
	Tube 38 mm in-line	Tube 19 mm in-line	Tube 38 mm in-line	Tube 19 mm in-line	Tube 38 mm in-line	Tube 19 mm in-line	Tube 38 mm in-line	Tube 19 mm in-line	Tube 38 mm in-line	Tube 19 mm in-line	Tube 38 mm in-line	Tube 19 mm in-line	Tube 38 mm in-line	Tube 19 mm in-line	Tube 38 mm in-line	Tube 19 mm in-line	Tube 38 mm in-line	Tube 19 mm in-line
	Loss coefficient, C, ESDU [52]	Loss coefficient, C, ESDU [52]	Loss coefficient, C, ESDU [52]	Loss coefficient, C, ESDU [52]	Loss coefficient, C, ESDU [52]	Loss coefficient, C, ESDU [52]	Loss coefficient, C, ESDU [52]	Loss coefficient, C, ESDU [52]	Loss coefficient, C, ESDU [52]	Loss coefficient, C, ESDU [52]	Loss coefficient, C, ESDU [52]	Loss coefficient, C, ESDU [52]	Loss coefficient, C, ESDU [52]	Loss coefficient, C, ESDU [52]	Loss coefficient, C, ESDU [52]	Loss coefficient, C, ESDU [52]	Loss coefficient, C, ESDU [52]	Loss coefficient, C, ESDU [52]
0.000390	5.25	5.95	5.82	5.36	6.11	5.68	6.28	5.93	6.35	6.10	6.27	6.29	6.05	6.35	5.73	6.33	5.38	6.21
0.000780	5.25	5.94	5.81	5.36	6.11	5.67	6.28	5.94	6.35	6.10	6.27	6.29	6.05	6.35	5.74	6.33	5.39	6.21
0.001170	5.25	6.01	5.79	5.36	6.10	5.67	6.28	5.93	6.35	6.10	6.27	6.28	6.05	6.35	5.74	6.33	5.39	6.21
0.001560	5.25	6.05	5.83	5.35	6.10	5.67	6.29	5.93	6.35	6.10	6.27	6.29	6.05	6.35	5.73	6.33	5.38	6.21
0.001950	5.25	6.09	5.80	5.35	6.10	5.67	6.28	5.93	6.35	6.10	6.27	6.28	6.05	6.35	5.74	6.33	5.39	6.21
0.002340	5.24	6.13	5.81	5.35	6.09	5.67	6.28	5.93	6.35	6.10	6.27	6.28	6.05	6.35	5.74	6.33	5.38	6.21
0.002730	5.25	6.13	5.81	5.35	6.10	5.66	6.29	5.93	6.35	6.10	6.28	6.28	6.05	6.35	5.74	6.33	5.38	6.21
0.003120	5.25	6.20	5.79	5.34	6.11	5.66	6.28	5.93	6.35	6.10	6.28	6.28	6.05	6.35	5.74	6.33	5.39	6.22
0.003510	5.25	6.27	5.80	5.34	6.10	5.66	6.28	5.92	6.35	6.10	6.27	6.28	6.05	6.35	5.74	6.33	5.39	6.22
0.003900	5.25	6.33	5.80	5.34	6.09	5.66	6.28	5.92	6.35	6.09	6.27	6.28	6.05	6.35	5.74	6.33	5.39	6.22
0.006800	5.28	6.80	5.75	5.32	6.07	5.64	6.28	5.92	6.35	6.09	6.28	6.28	6.05	6.35	5.75	6.33	5.40	6.22
0.010200	5.40	7.63	5.71	5.30	6.05	5.62	6.27	5.90	6.35	6.09	6.28	6.28	6.07	6.35	5.76	6.33	5.40	6.22
0.013600	5.41	8.83	5.69	5.28	6.05	5.60	6.25	5.89	6.34	6.07	6.29	6.27	6.07	6.35	5.76	6.33	5.40	6.22
0.017000	5.98	10.60	5.70	5.26	6.03	5.58	6.25	5.88	6.35	6.06	6.29	6.27	6.08	6.35	5.77	6.33	5.41	6.23
0.020400			5.63	5.25	6.01	5.56	6.24	5.87	6.34	6.06	6.29	6.27	6.09	6.35			5.42	6.23
0.023800			5.58	5.24	5.99	5.54			6.33	6.05	6.30	6.26	6.09	6.35				
0.027200									6.34	6.04	6.31	6.26	6.11	6.34				
0.030600									6.32	6.03	6.30	6.26	6.11	6.34				
0.034000											6.31	6.25						
0.027200																		
0.030600																		
0.034000																		
AVERAGE	**5.32**	**6.78**	**5.76**	**5.32**	**6.08**	**5.64**	**6.27**	**5.92**	**6.35**	**6.08**	**6.28**	**6.28**	**6.07**	**6.35**	**5.74**	**6.33**	**5.39**	**6.22**
MEAN AVERAGE %	**-20.0**		**8.2**		**7.8**		**6.0**		**4.3**		**0.1**		**-4.5**		**-9.3**		**-13.2**	
RMS %	**22.0**		**8.2**		**7.8**		**6.0**		**4.3**		**0.4**		**4.5**		**9.3**		**13.2**	

7.2.5 Comparison of measured two-phase multiplier in the 19 mm diameter square and staggered bundles

The comparison between the measured two-phase multipliers for the bundles is shown in Figure 7.25. Almost all of the for measured two-phase multipliers for the staggered bundle are smaller than those for the in-line bundle except at high mass flux, 541 kg/m^{2}s and 688 kg/m^{2}s. As we can see from Figures 7.15 and 7.18, at low mass flux, the measured two-phase multipliers for the in-line bundles are above the predicted values. In contrast, the measured two-phase multiplier in the staggered bundle lies near the predicted values, Figure 7.21. A strong mass flux effect was observed at mass fluxes less than 200 kg/m^{2}s in both bundles. Reinke and Jensen [72] investigated and compared the two-phase total pressure drop between an in-line and staggered tube bundle, having the same P/D ratio of 1.3. Based on the comparison of the total pressure drop data obtained in the two bundles, they speculated that at mass fluxes larger than 300 kg/m^{2}s, the two-phase friction multiplier would be greater for the staggered tube bundle than for in-line tube bundle, due to increased turbulence, which resulted from a more homogenous two-phase mixture flow. Dowlati et al. [39] reported that their two-phase friction multiplier, for a given x_{tt}, was found to be greater for the staggered rod bundle than the in-line rod bundle for P/D 1.3. However, they used different C value in Equation (7.14) for both bundles, C = 8 for the in-line bundle and C = 20 for the staggered bundle. So, their judgement and comparison is questionable. The present data used C = 8 for both bundles, which demonstrates the applicability of using C = 8 for any bundle arrangement. Xu et al. [5] is shown to be the best predictor for the two-phase friction multiplier as seen in Figure 7.20 and 7.23. Xu et al. [5] proposed the constant C as a function of mass flux, but this method does not capture the mass flux dependency effectively. It is interesting to note that the C of Xu et al. [5] is correlated based with their data from in-line bundle with tubes 9.79 mm in diameter on a pitch to diameter ratio of 1.28. However, this correlation works well in the staggered bundle, as seen in Figure 7.23. It is better than Ishihara correlation [4], Figure 7.22.

Dowlati et al. [39] found that C = 20 was the best fit to their data for their staggered rod bundles for P/D 1.32 and 1.72. They found a strong mass velocity effect when the Martinelli parameter, x_{tt} < 10, and mass fluxes were less than 200 kg/m^{2}s. However, when x_{tt} > 10, the dependency diminished. The reason of this behaviour is not clear. This behaviour was also seen in their in-line bundle for both P/D 1.32 and 1.75 and with C = 8.

However, the present data, using $C = 8$ do not show the same trend for data with a mass flux less than 200 kg/m^2s, it is not moving towards the Ishihara correlations with increasing Martinelli parameter, x_{tt}.

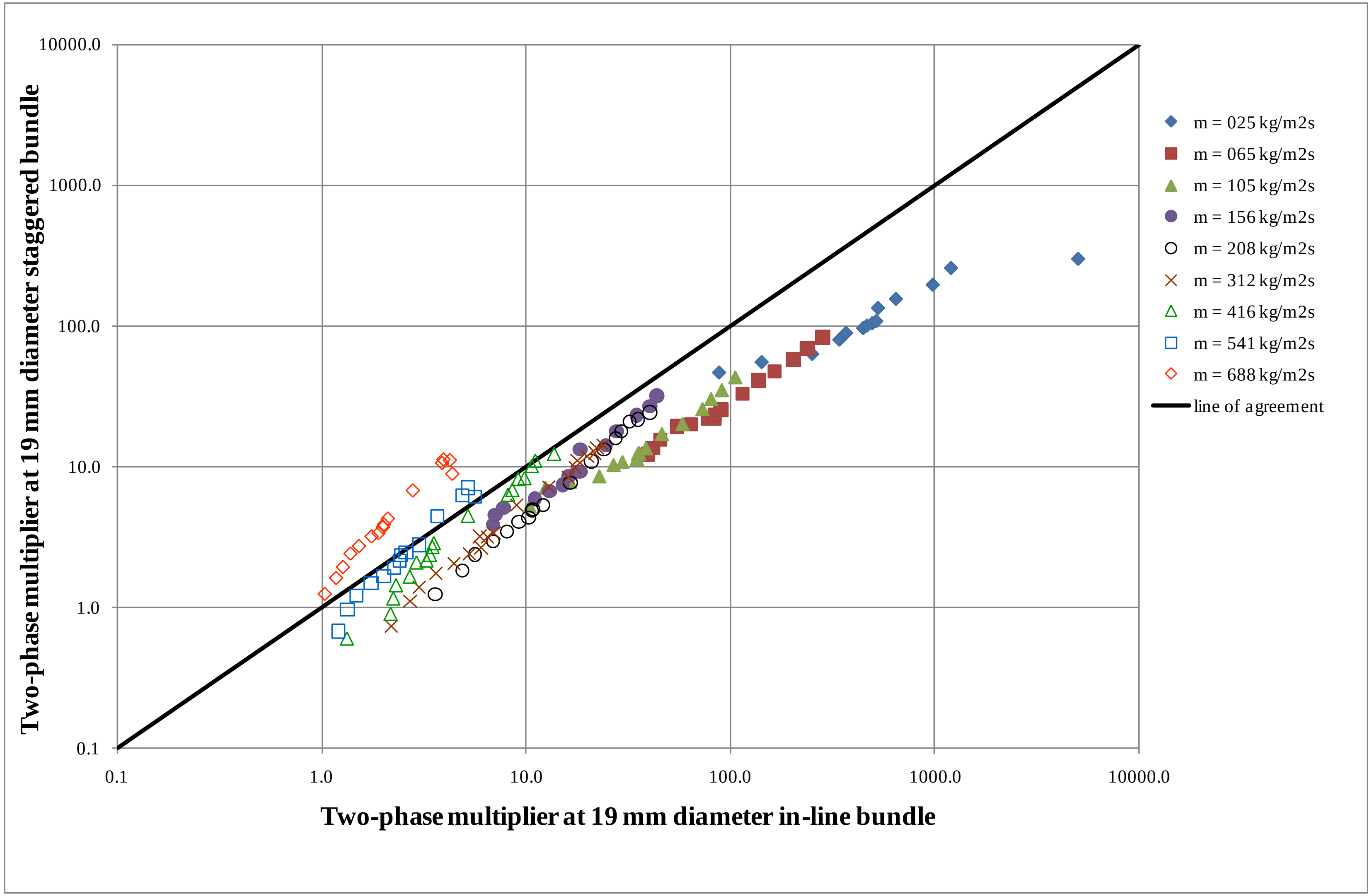

Figure 7.25: Comparison of measured two-phase multipliers in different tube array 19 mm diameter bundle (in-line and staggered bundle)

7.2.6 Summary of measured two-phase multipliers comparisons

The measured frictional pressure drop was obtained by subtracting the gravitational pressure drop, based on the measured void fraction, from the measured total pressure drop. The measured frictional pressure drop was divided by the liquid only pressure loss from ESDU [52] to obtain the two-phase multiplier. These values were compared to the Xu et al. [5] and Ishihara et al. [4] method, which is the most widely quoted correlation for frictional pressure drop for two-phase flow over tube bundles. The Ishihara et al. [4] correlation only dependents on the Martinelli parameter, x_{tt}, that is based on quality and fluid properties as expressed in Equation (7.15). The results have shown that the measured two-phase friction multiplier in Figures 7.15, 7.18 and 7.21 has a large scatter above the correlation of Ishihara, Equation (7.14), especially for in-line bundles, because of its dependence on mass flux. This correlation works well for mass fluxes higher than 200 kg/m^{2}s, which agrees well with other researcher. However, Xu et al. [5] correlation works the best for all tube bundles, as seen in Figure 7.17, 7.20 and 7.23. The correlation of Xu et al. [5] also give better agreement for mass fluxes higher than 200 kg/m^{2}s.

The C value used in the Equation (7.14) is not general for all tube bundle geometries and working fluids. Ishihara et al. [4] suggested that C = 8 is the best fit to their data but Dowlati et al. [2,12,39] tried many values for C = 8, 20, 30, 50 in trying to fit their data to give best prediction of frictional pressured drop for their in-line and staggered bundles with P/D 1.3 and 1.75. Schrage et al. [1] found that a C = 8 over predicted their friction pressure drop data by an average of 17% and suggest that C values dependent on flow pattern. Xu et al. [5] did not get a good representation of their data when using C = 8 as suggested by Ishihara et al. [4]. Dowlati et al. [8] used C = 20, which gave a fairly good correlation both their staggered bundles with P/D 1.3 and 1.75. Although the Ishihara correlation is widely used for the prediction of two-phase multiplier, and the data agree reasonably well with the predicted value at mass flux above 200 kg/m^{2}s, it does not give good predictions of data at lower mass fluxes, as shown by the value lying above the C = 8 curve in Figures 7.9, 7.12 and 7.15. On the other hand, the Xu et al. [5] correlation gave the best agreement with the measured two-phase multipliers. Most of data moves toward the prediction when the C factor in Equation (7.16) is used. It gives better mean average and RMS error for the present data than C = 8 in Equation (7.14) proposed by Ishihara et al. [4].

There is no effect of tube diameter, for the in-line bundles as shown in Figure 7.24, where the measured two-phase friction multiplier for both bundles show good agreement. Therefore the Xu et al. [4] correlation can be used for bundles with tubes up to 38 mm in diameter. The tube layout effect is shown in Figure 7.25. The staggered bundle generated the largest turbulence and has the lower two-phase multiplier. Dowlati et al. [12] speculated that the mass flux effect observed in their data for mass fluxes less than 200 kg/m^2s may occur in two-phase flow conditions where the point of flow separation from the tube moves as the mass flux and void fraction are changed, affecting the drag force and two-phase frictional pressure drop. The variation of separation would also lead to different static forces in the region behind the tube. After separation reached a certain level, at a mass flux around 200 kg/m^2s, the point of separation no longer changes with further increases in mass flux. This variation in two-phase multiplier is also observed in the present data as shown in Figures 7.15, 7.18 and 7.21. This is not surprising as the void fraction is also dependent on mass flux and the flow quality is expected to influence the two-phase friction multiplier pressure drop, as it is used for the Martinelli parameter, x_{tt} in Equation (7.16). The void fraction is increasing with increasing quality, which creates more turbulence and increases the mixing of the phases, making them more homogenous as the mass flux increases. As a result, the frictional pressure drop is increases significantly and the data move toward the prediction of the two-phase multiplier. However, the link to flow separation is not proven. Dowlati et al. [12] also agreed that flow quality should influence the two-phase friction pressure drop over the range of mass fluxes. Based on their data, the mass flux effect occurred a range of Martinelli parameter, X_{tt}, after which the low mass flux data appear to join the remainder of the data. However, the measured data in Figures 7.15, 7.18 and 7.21 behave differently where the data showed a strong mass flux dependency at mass flux less than 200 kg/m^2s but do not show any effect on any range of Martinelli parameter, x_{tt}, and the data at low mass flux do not join the remainder of the data. Furthermore, the dependency of two-phase multiplier on only the Martinelli parameter is questionable, as Ishihara et al. [4] reported for $x_{tt} > 0.2$.

Overall, the measured frictional pressure drop was compared with two correlations, Ishihara et al. [4] and Xu et al. [5], using the two-phase multiplier deduced from them. The use of $C = 8$ and C factor in Equation (7.16) do give a reasonable representation of the data. However, it is shown that the Xu et al. [5] correlation works the best in adiabatic air-water experiment at mass fluxes above 200 kg/m^2s, and gives small mean error and RMS error for all mass flux compared to Ishihara et al. [4]. The Xu et al. [5] correlation does not capture the mass flux dependency completely, although the *C* factor is a function of gas and liquid flow rates. The Xu et al. [5] correlation also works reasonably well in the staggered bundle, despite the correlation being deduced from in-line tube bundle data only.

CHAPTER 8 - PARAMETERS FOR THE TWO-FLUID MODEL

Two-fluid model in a porous domain requires the drag force between the phases and the force on the fluids by the tubes to be specified. The volume of the domain contain of a solid fraction, ε_s, a liquid fraction, ε_l , and a gas fraction, ε_g , so that the total volume fraction is

$$\varepsilon_s + \varepsilon_l + \varepsilon_g = 1 \tag{8.1}$$

The volume fraction available for flow, i.e. the porosity, φ, is

$$\varphi = \varepsilon_g + \varepsilon_l = 1 - \varepsilon_s \tag{8.2}$$

For the square in-line tube bundles, the porosity can be obtained from

$$\varphi = 1 - \frac{\pi}{4}\left(\frac{D}{P}\right)^2 \tag{8.3}$$

For the staggered tube bundle, the porosity can be obtained from

$$\varphi = 1 - \frac{\pi}{2\sqrt{3}}\left(\frac{D}{P}\right)^2 \tag{8.4}$$

The volume fraction of the gas and liquid phases are given by

$$\alpha = \frac{\varepsilon_l}{\varphi} \quad \text{and} \quad 1 - \alpha = \frac{\varepsilon_l}{\varphi} \tag{8.5}$$

For a fully developed flow, the one-dimensional momentum equation for the liquid phase can be written as

$$\varepsilon_l \frac{dp}{dz} = -\varepsilon_l \rho_l g + F_{gl} + F_{sl} \tag{8.6}$$

where F_{gl} is the force on the liquid by the gas per unit volume of domain and F_{sl} is the force on the liquid by the solid per unit volume of domain. The corresponding momentum equation for the gas phase is given by

$$\varepsilon_g \frac{dp}{dz} = -\varepsilon_g \rho_g g + F_{\mathrm{lg}} + F_{sg} \tag{8.7}$$

where F_{lg} is the force on gas by the liquid per unit volume of domain and F_{sg} is the force on the gas by the solid per unit volume of domain.

Combining Equations (8.6) and (8.7), recalling that $F_{lg} = -F_{gl}$, and using Equations (7.3) and (8.5) gives

$$\frac{dp}{dz} = -\rho_{tp} g + \varphi\left(F_{sl} + F_{sg}\right) \tag{8.8}$$

Comparing Equations (7.1) and (8.8) reveals that the force on the fluid by the tubes, F_{sf}, can be found from

$$F_{sf} = F_{sl} + F_{sg} = \varphi\left(\frac{dp}{dz}\right)_F \tag{8.9}$$

An assumption has to be made to split this force into its components applicable to each phase. The assumption made is the same as that made by Rahman et al. [6], i.e. in a boiling flow the gas phase is not in contact with the tubes. Therefore, the force on the gas by the tubes is zero, leaving the force on the liquid by the tubes to be found from Equation (8.9).

Using the same assumption with Equation (8.7), and making use of Equations (8.5), allows the measured pressure drop and void fraction to be used to find the drag force. The drag force is related to the drag coefficient, C_D, through, see, e.g. Simovic et al. [7],

$$F_{gl} = \frac{3}{4}\varphi\alpha\frac{C_D}{D_B}\rho_l(u_g - u_l)\left|u_g - u_l\right| \tag{8.10}$$

where D_B is the bubble diameter and u_g and u_l are the gas and liquid velocities respectively, which can be found from

$$u_g = \frac{M_g}{\varphi \alpha \rho_g A_{he}} \quad \text{and} \quad u_l = \frac{M_l}{\varphi (1-\alpha) \rho_l A_{he}} \tag{8.11}$$

in which A is the unrestricted cross-sectional area of the heat exchanger. Thus, with F_{gl} already determined, and with the measured mass flow rates and void fraction allowing the velocities to be determined, the ratio of the drag coefficient to the bubble diameter can be found from Equation (8.9). This quantity is non-dimensionalised by the Laplace length to give the drag group, D_G, thus

$$D_G = \frac{c_D}{D_B} \sqrt{\frac{\sigma}{g(\rho_l - \rho_h)}} \tag{8.12}$$

Rahman et al. [6] and Simovic et al. [7] have presented drag coefficients from measurements made in one-dimensional air-water flows. Rahman et al. [6] used a different definition from that used here. Their drag coefficient is converted to the current definition through

$$c_D = \frac{2}{3} \frac{\rho_{tp} D_B}{\rho_L \varphi P} c_D^R \tag{8.13}$$

and c_D^R is the Rahman et al. [6] value, given by

$$c_D^R = \frac{c_{D\,bubbly} c_{D\,intermittent}}{\sqrt[4]{c_{D\,bubbly}^4 + c_{D\,intermittent}^4}} \tag{8.14}$$

in which

$$c_{D\,bubbly} = \frac{e^{33.49} \varphi^{3.49}}{\mathrm{Re}_R^{3.68}} \tag{8.15}$$

$$c_{D\,intermittent} = \frac{e^{19.91}\varphi^{1.63}}{\mathrm{Re}_R^{2.10}} \tag{8.16}$$

and

$$\mathrm{Re}_R = \frac{\rho_{tp}\varphi P\left|u_g - u_l\right|}{\mu_l} \tag{8.17}$$

The drag coefficient presented by Simovic et al. [7] also had a two flow pattern approach. The distorted bubble regime value was given by

$$D_{G\,intermittent} = 0.267\left(\frac{1+17.67(1-\alpha)^{9/7}}{18.67(1-\alpha)^{3/2}}\right)^2 \tag{8.18}$$

and the churn flow regime value by

$$D_{G\,churn} = 1.487(1-\alpha)^3(1-0.75\alpha)^2 \tag{8.19}$$

with the actual value determined from

$$D_G = \min(D_{G\,intermittent}, D_{G\,churn}) \tag{8.20}$$

8.1 Two-Fluid Model Comparison in 38 mm in diameter in-line tube bundle

The measured drag group in the 38 mm in diameter in-line bundle and the correlation by Simovic et al. [7] is shown as a function of void fraction in Figure 8.1. The data are shown to trend reasonably well with the predictions, because the void fraction predictions are not overly sensitive to drag coefficient, according to Rahman et al. [6]. It should be noted that all the volume forces and the phase velocities used in the Simovic et al. correlations et al. [7] are functions of void fraction. Simovic et al. [7] had observed two patterns of two-phase flow across the tube bundle, bubby flow for void fractions lower than 0.3, and churn turbulent flow for void fraction higher than 0.3. For bubbly flow, the modified form of the Ishii and Zuber correlation [38] developed for two-phase pipe flow was modified. For churn-turbulent flow, a new correlation was developed with functional dependence on the void fraction. As observed from Figure 8.1, a few data points fall in the bubbly flow regime and most of the data are in churn turbulent or annual flow.

The predictions from the correlation of Simovic et al. [7] are included in Figure 8.2. A significant amount of data is out with the limits set at ±50%. The agreement is reasonable at the lower mass fluxes but deteriorate as the mass flux increases. This method was deduced from air-water data taken in tube bundles with tubes 19 mm in diameter. It extrapolates reasonably well to the tube bundles containing larger diameter tubes. The mean average difference is 82% and the RMS difference is 280%.

When compared to the present data, the predictions of the Rahman et al. correlation [6] were out by a factor of about 12, as shown in Figure 8.3. The gradient of the line of agreement is set to 12. The mass flux dependency is shown to be captured in form but not in magnitude. These drag coefficient predictions from the Rahman et al. [6] compare poorly. They were deduced from the same data sets as Simovic et al. [7] which is from Dowlati et al. [2,39] but they do not extrapolate to tube bundles containing tubes with larger diameters, although the form of the correlation does capture the mass flux dependency. The average difference is 1414% and RMS difference is 1630 %.

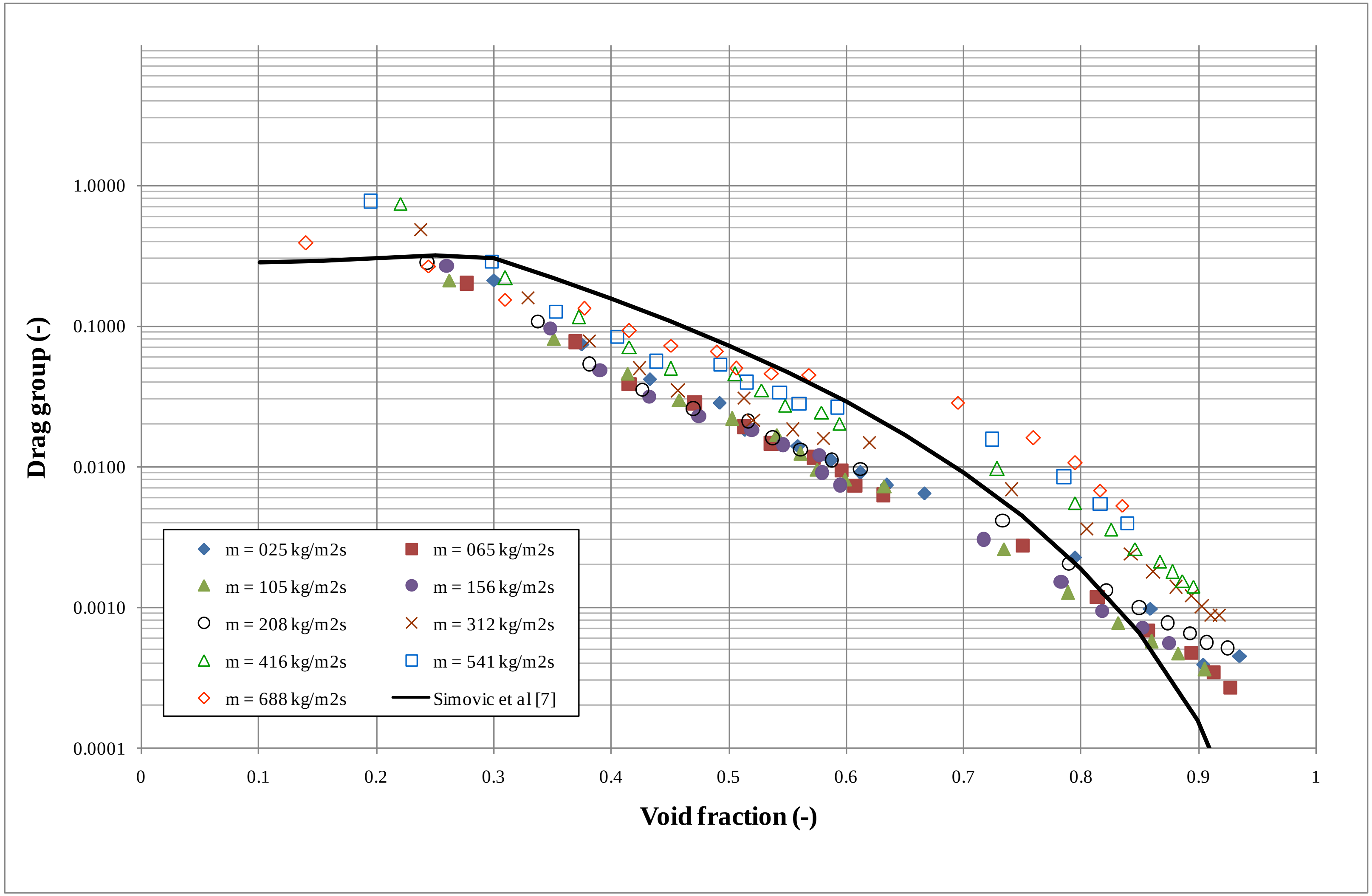

Figure 8.1: Variation of drag group with void fraction at 38 mm in-line bundle

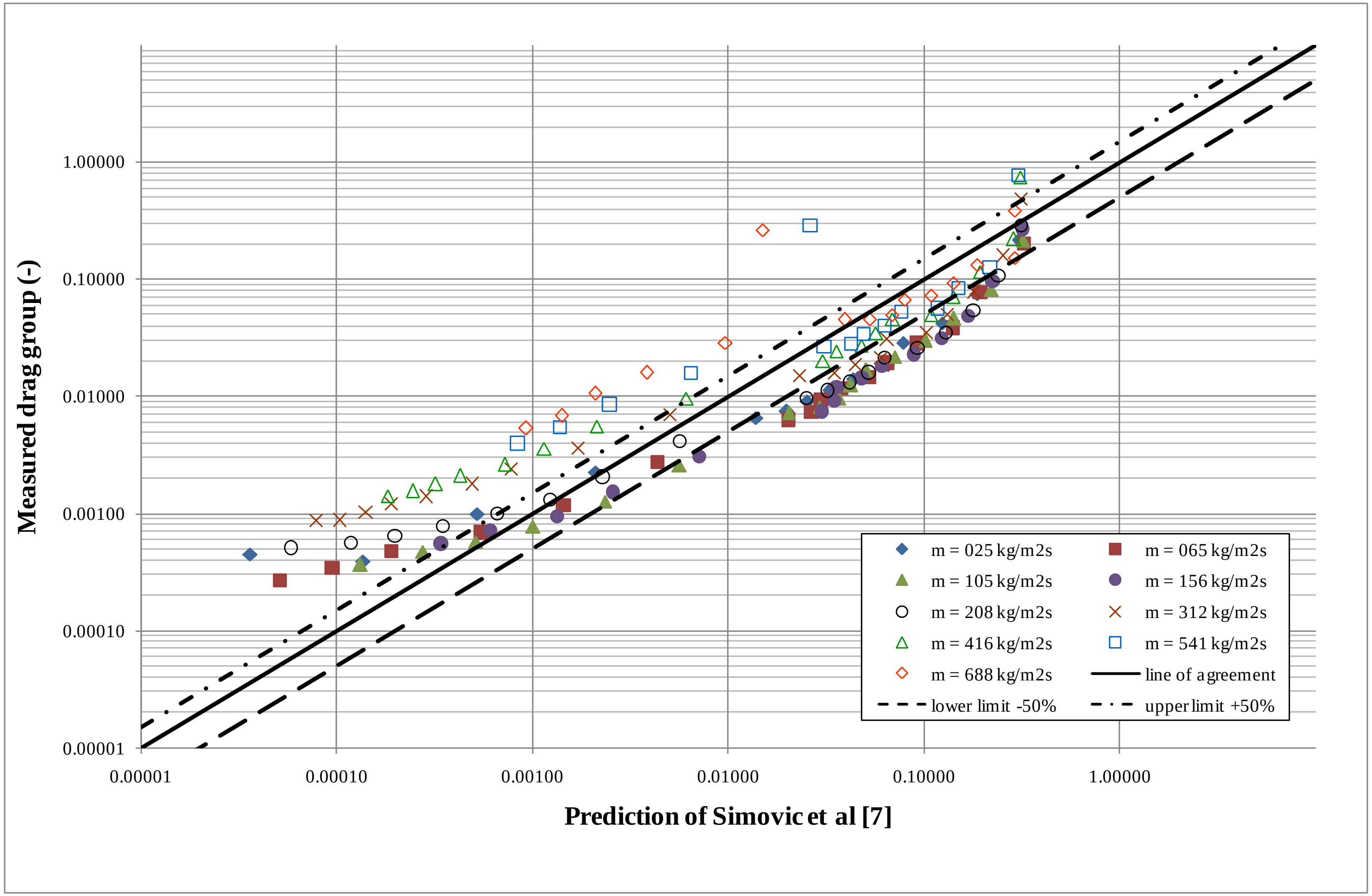

Figure 8.2: Comparison of measured drag group with predictions of Simovic et al. [7] at 38 mm in-line bundle

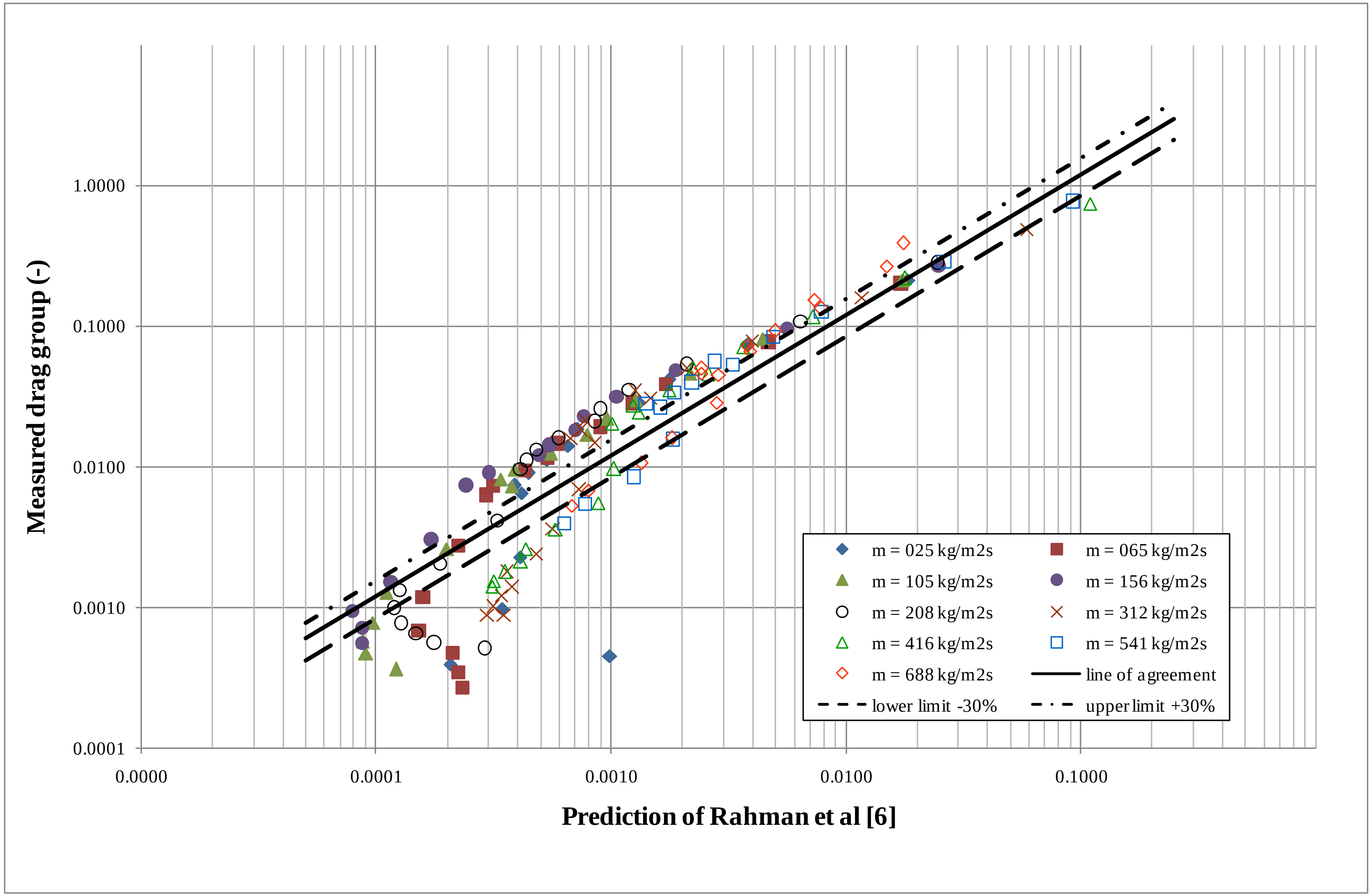

Figure 8.3: Comparison of measured drag group with predictions of Rahman et al. [6] at 38 mm in-line bundle

8.2 Two-Fluid Model Comparison in the 19mm in diameter in-line tube bundle

The measured drag group for the 19 mm in diameter in-line bundle and the predictions from the correlation of Simovic et al. [7] are shown as a function of void fraction in Figure 8.4. The data are shown to trend reasonably well with void fraction. For void fractions values lower than 0.3, which correspond to bubbly flow, the measured drag group shows much higher values than the predictions. For void fraction values higher than 0.3, which correspond to churn or annular flow patterns, both measured and predictions show a sharp decrease in C_d/D_B with increasing void fraction. The data however, show a mass flux dependency and it is evident at the larger void fractions.

The comparison between the measured and predicted values from the Simovic et al. [7] correlation are shown in Figure 8.5. The measured drag group is higher than the predictions at lower drag group in the mass flux range of 156-688 kg/m^{2}s but agreement is obtained at drag groups greater than 0.01. The average difference is 213% and the RMS difference is 445%. Many of the predictions lie outside the upper and lower bounds which are set at ±50%.

The measured drag group and the predictions from the Rahman et al. [6] correlations for the 19 mm in-line bundle is shown in Figure 8.6. The agreement is reasonable, with most predictions inside the upper and lower limits of ±50%. The average difference is -4.1% and the RMS difference is 44%.

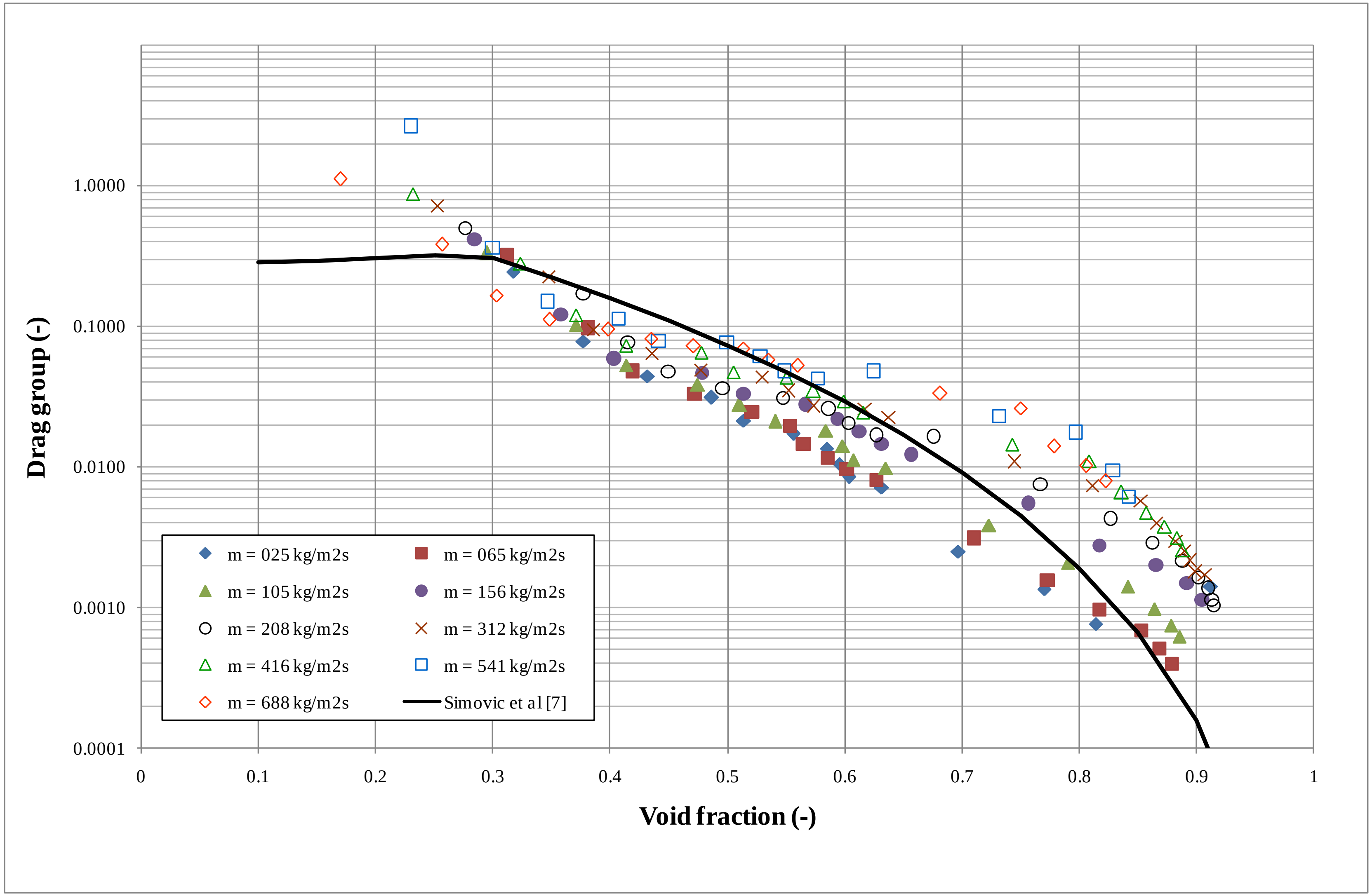

Figure 8.4: Variation of drag group with void fraction in 19 mm in-line bundle

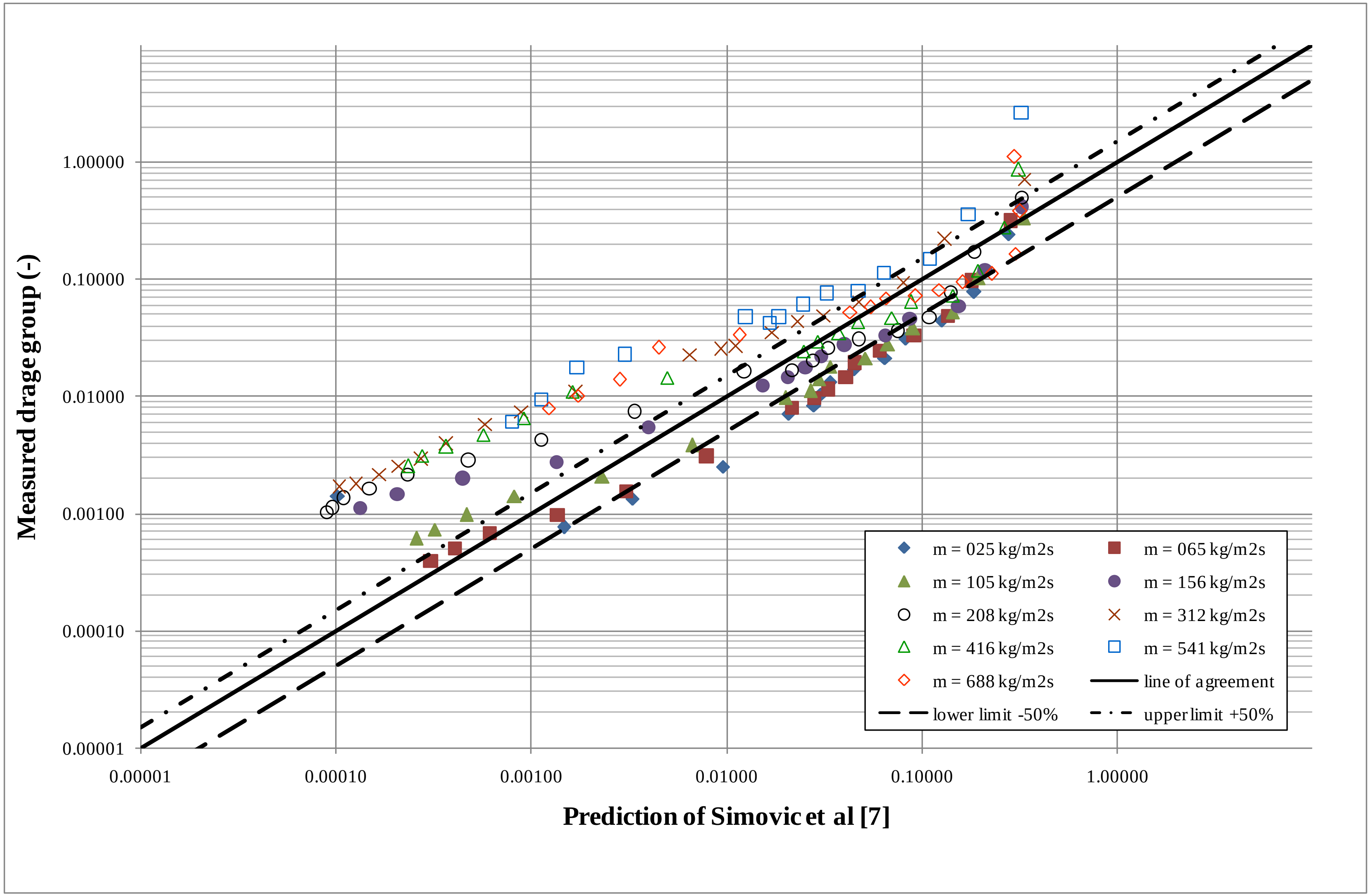

Figure 8.5: Comparison of measured drag group with predictions of Simovic et al. [7] at 19 mm in-line bundle

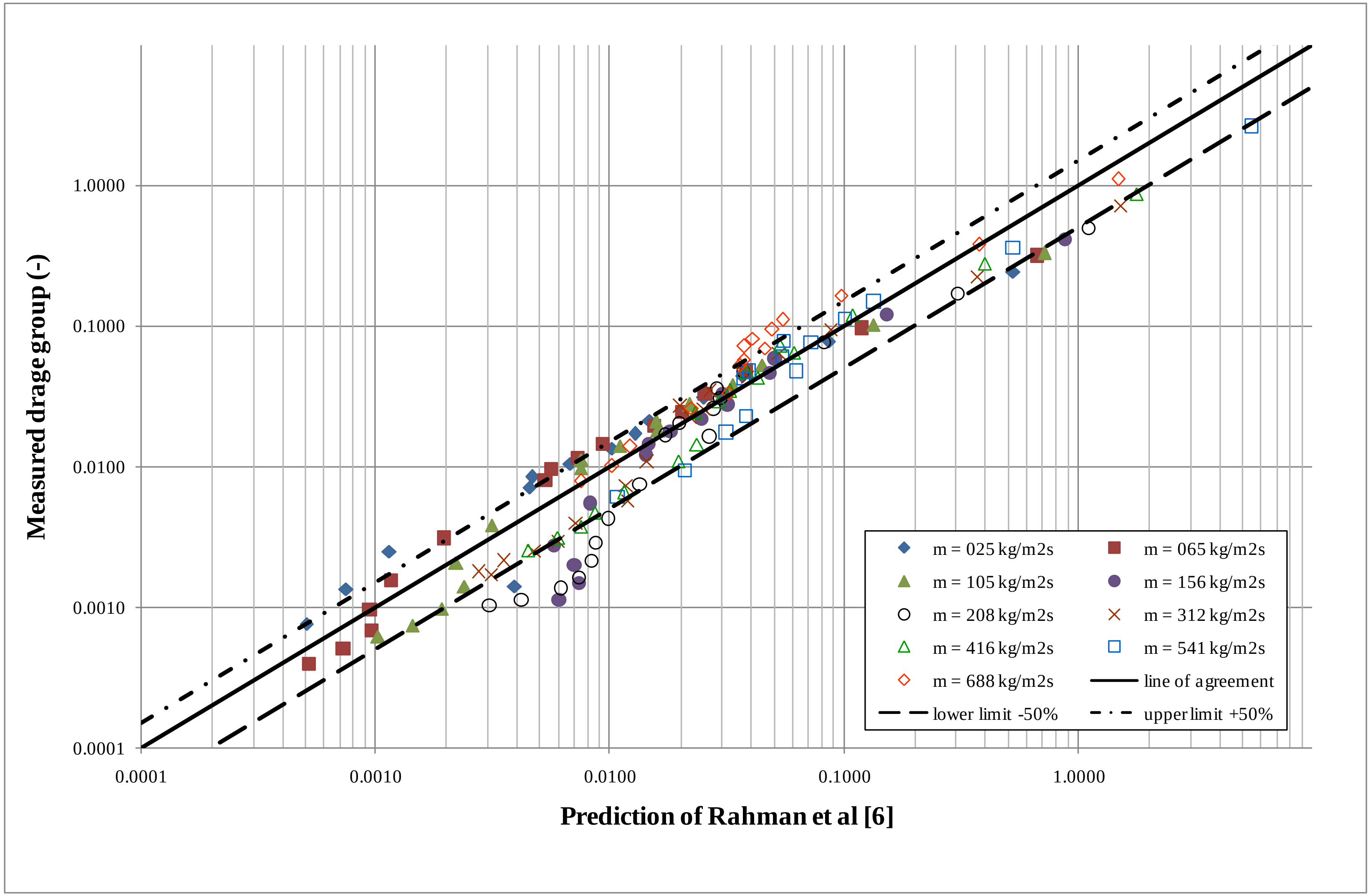

Figure 8.6:Comparison of measured drag group with predictions of Rahman et al. [6] at 19 mm in-line bundle

8.3 Two-Fluid Model Comparison in 19 mm in diameter staggered tube bundle

Figure 8.7 shows the measured drag group and the predictions of Simovic et al. [6] as a function of void fraction. The data trend compare poorly with void fraction. Most of the measured drag group data are above the predictions line, particularly at high mass fluxes. A mass flux dependency is evident. Almost all data can be said to be in annular and churn turbulent flow, since the void fraction is above 0.3. The two-phase flow in staggered bundle is said to be like a homogenous two-phase mixture because of the mixing of phases.

The comparison between the measured and predictions drag group in the staggered bundle is shown in Figure 8.8. The results shown that the measured drag group fall consistently above the ±50% set limit. The average difference is 660% and the RMS difference is 940%, which is shows a poor comparison.

Figure 8.9 compares the measured drag group with the drag group predictions made with the Rahman et al. [6] correlation. The measured drag group is shown to be out with the ±50% of the upper and lower limit, except at low drag groups. The average difference is -40% and the RMS difference is 68%.

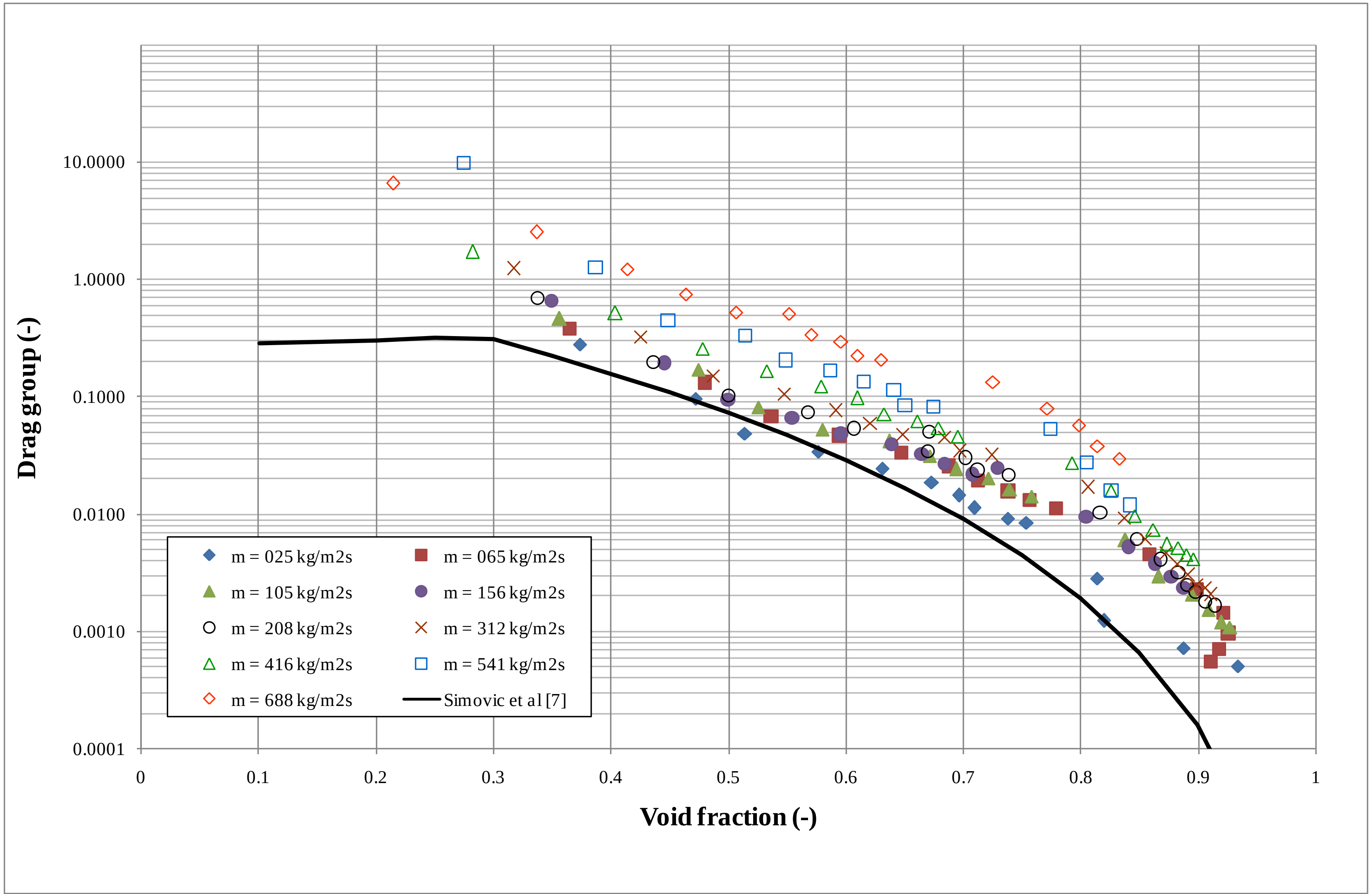

Figure 8.7: Variation of drag group with void fraction in 19 mm staggered bundle

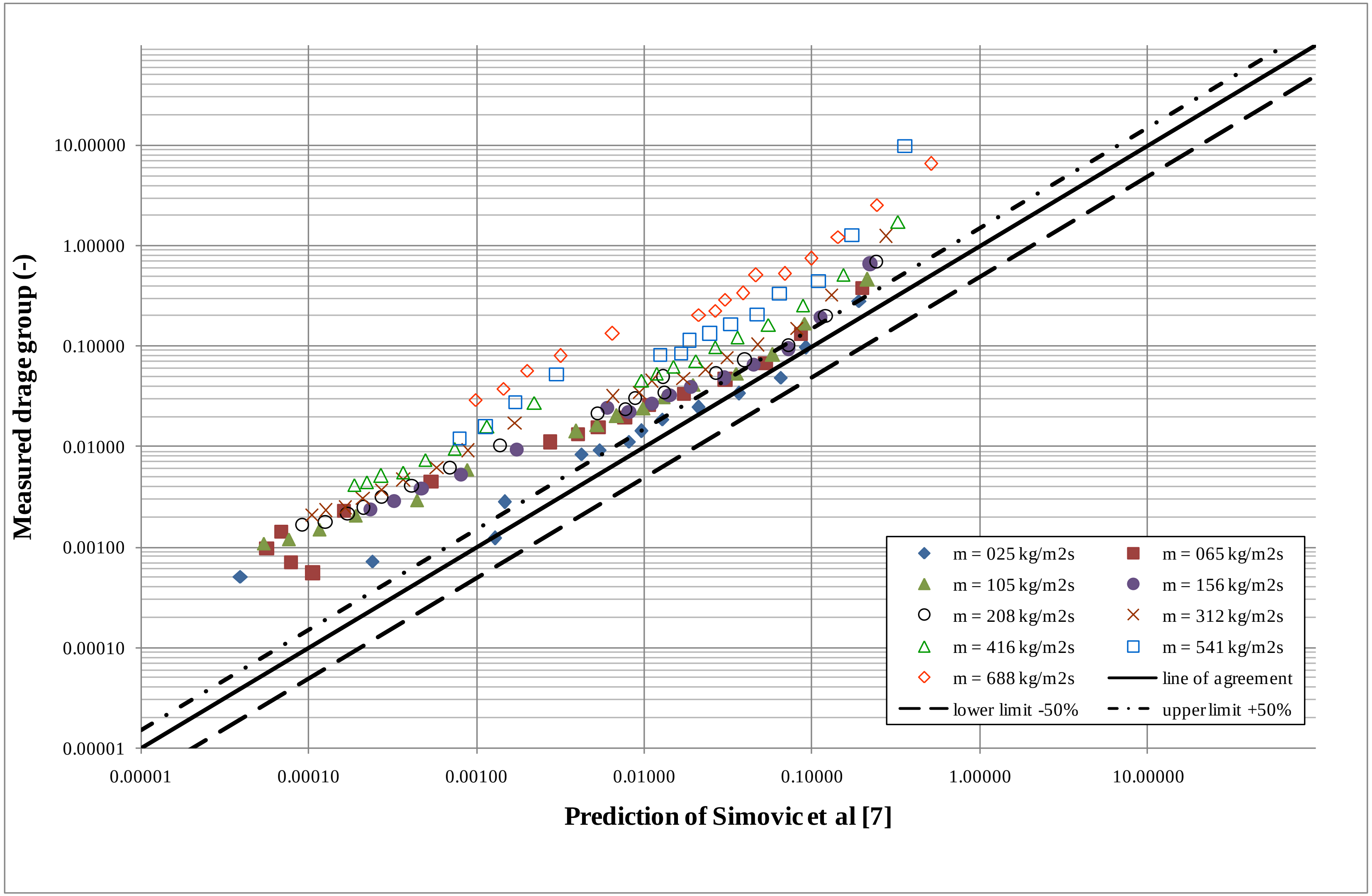

Figure 8.8: Comparison of measured drag group with predictions of Simovic et al. [7] at 19 mm staggered bundle

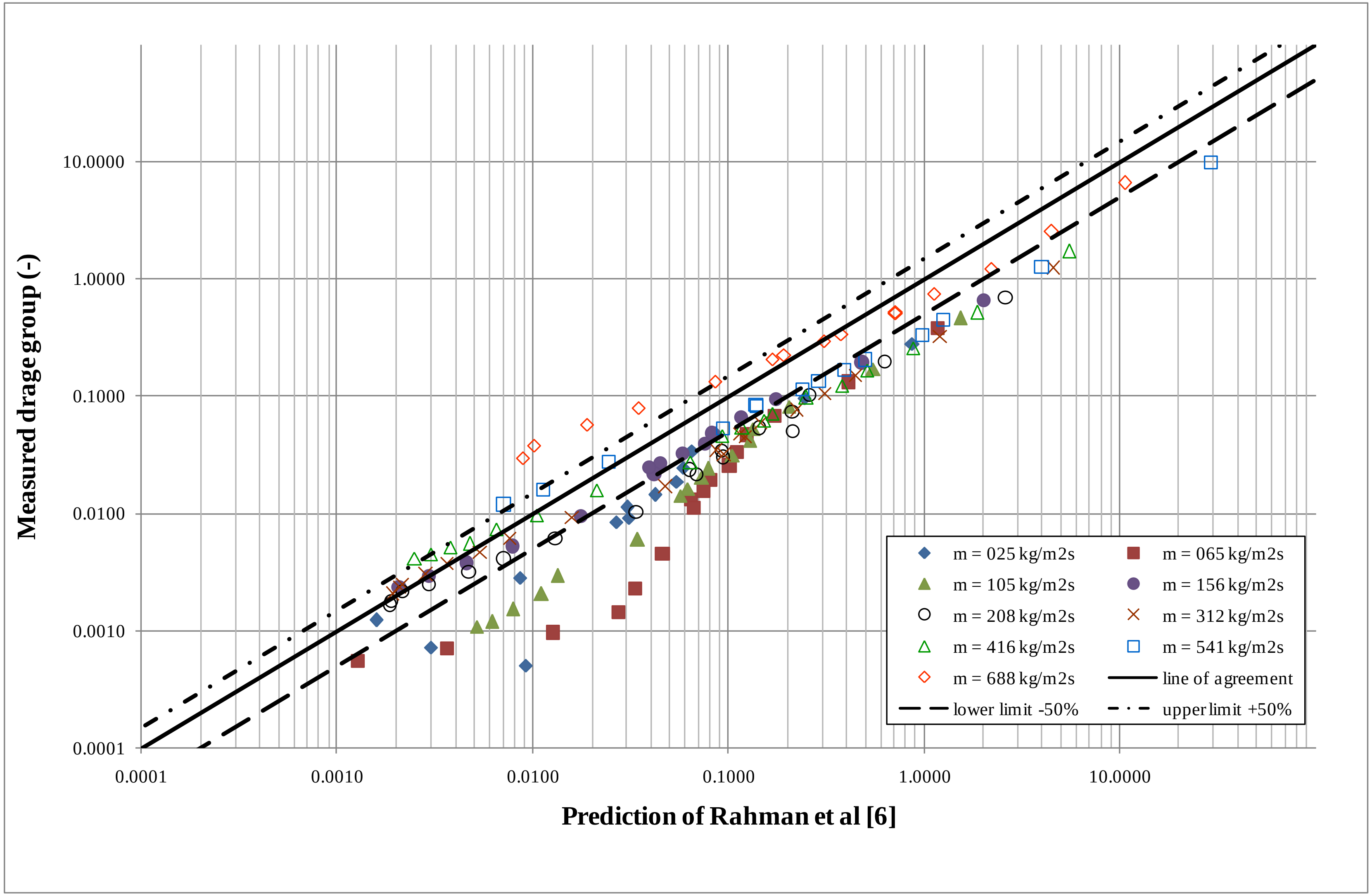

Figure 8.9: Comparison of measured drag group with predictions of Rahman et al. [6] at 19 mm staggered bundle

8.4 Comparison of measured and predicted drag group in three bundles and summary of the Two-Fluid Model.

The measured drag group correlation presented in this research is deduced from the measured void fraction and the measured pressure drop. The measured drag group for in-line bundles with tube diameters of 19 mm and 38 mm in diameter are compared in Figure 8.10. The measured drag group in both in-line bundles are shown to agree well. This is the due to the fact that the drag group is a function of void fraction. The measured void fractions for both bundles are shown to be the same as discussed in Chapter 6. Therefore, the measured drag group for the same arrangement will be the same as have frictional effects, as discussed in Chapter 7.

The Simovic et al. [7] correlation is far better than the Rahman correlation et al. [6]. The drag group prediction from Rahman et al. [6] is not capable of predicting the drag group for larger bundles because it compares poorly with the measured data as shown in Figure 8.3. They used the same data as Simovic et al. [7] but their method does not extrapolate to large diameter bundles, although the correlation does capture the mass flux dependency.

The comparison of measured drag group in difference tube arrangements is shown in Figure 8.11. The measured drag group values for the staggered bundle are higher than those from the in in-line bundles and within of upper limits of ±50%, particularly lower mass flux, where they are strongly correlated. Again, the measured void fractions are different for these bundles, where the measured void fraction in staggered bundle is higher than in-line bundles, as presented in Chapter 6, hence giving a higher drag group due to high friction and turbulence flow with increasing mass flux.

Overall, the porous media approach is an essential tool for the multi-dimensional analysis of flow on the shell-side of a shell and tube heat exchanger. This approach uses a two-fluid model that requires the drag coefficient and the wall forces to be supplied. Simovic et al. [7] used volume fraction weighted, single-phase wall forces. Their approach contains a reasonable method for the drag coefficient, Figure 8.1 and 8.4. Rahman et al. [6] argued that the force on the gas by the tubes was negligible. This allowed two-phase techniques to be directly used for the wall forces but their drag coefficient is not universal, Figure 8.3. Although the Rahman et al. [6] correlations does not extrapolate to larger tube bundles, the comparison between the measured and predicted values for the 19 mm in-line and staggered bundles shows that the Rahman et al. [6] correlation predict the data best, Figures 8.6 and 8.9, with a better average and RMS difference than Simovic et al. [7]. This may be due to the correlation by Simovic et al. [7] being based on a modified pipe flow correlation. The measured drag group that used the measured pressure drop and void fraction from the present study does give a universal variation, but it is independent of tube diameter but not arrangement for adiabatic air-water flows, Figures 8.10 and 8.11. The drag group presented in this research is modelled best by the two-fluid model on the shell side of a heat exchanger using the Simovic et al. [7] correlation.

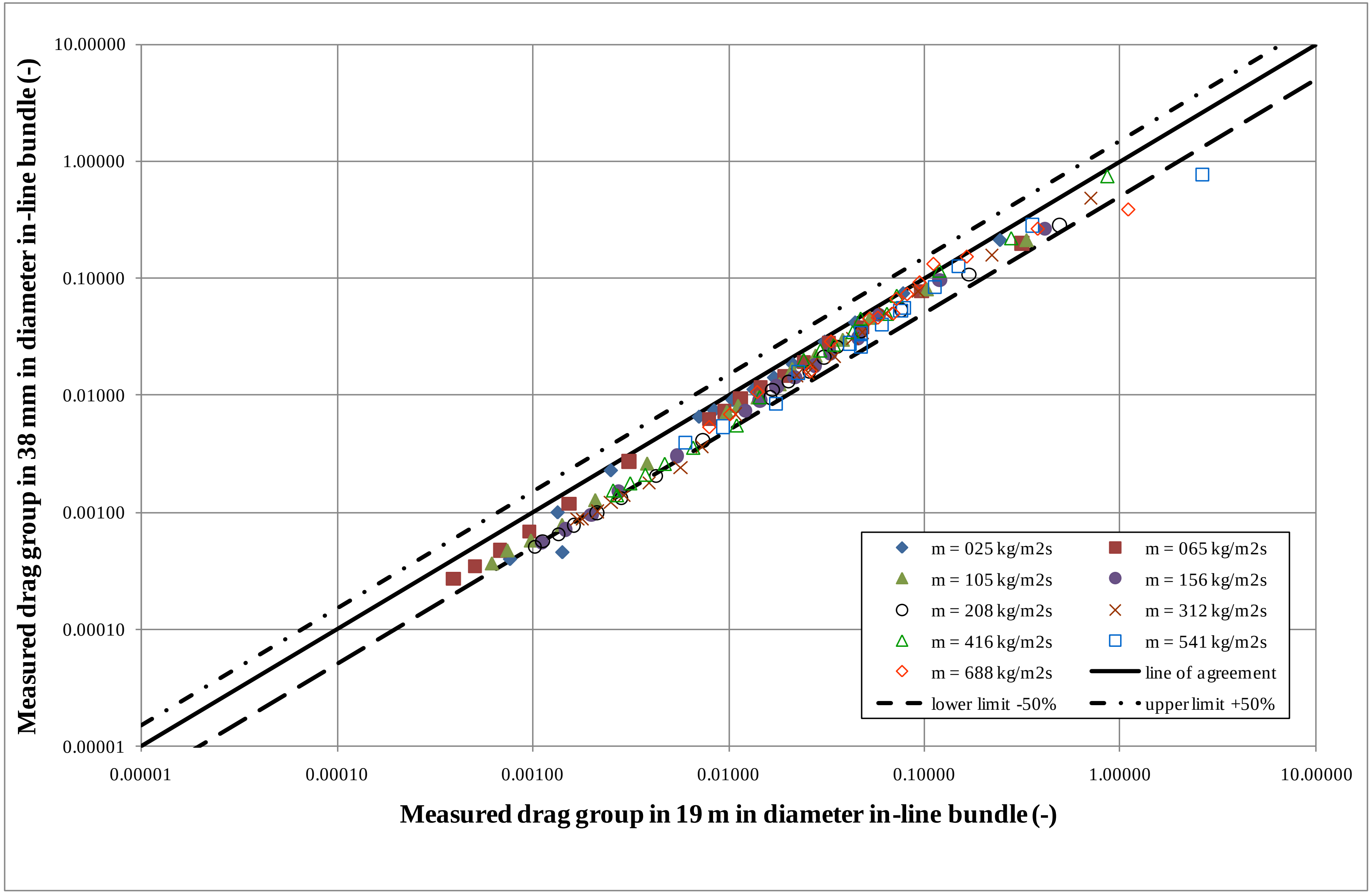

Figure 8.10: Comparison of measured drag group in in-line bundles (19 mm 38 mm in diameter)

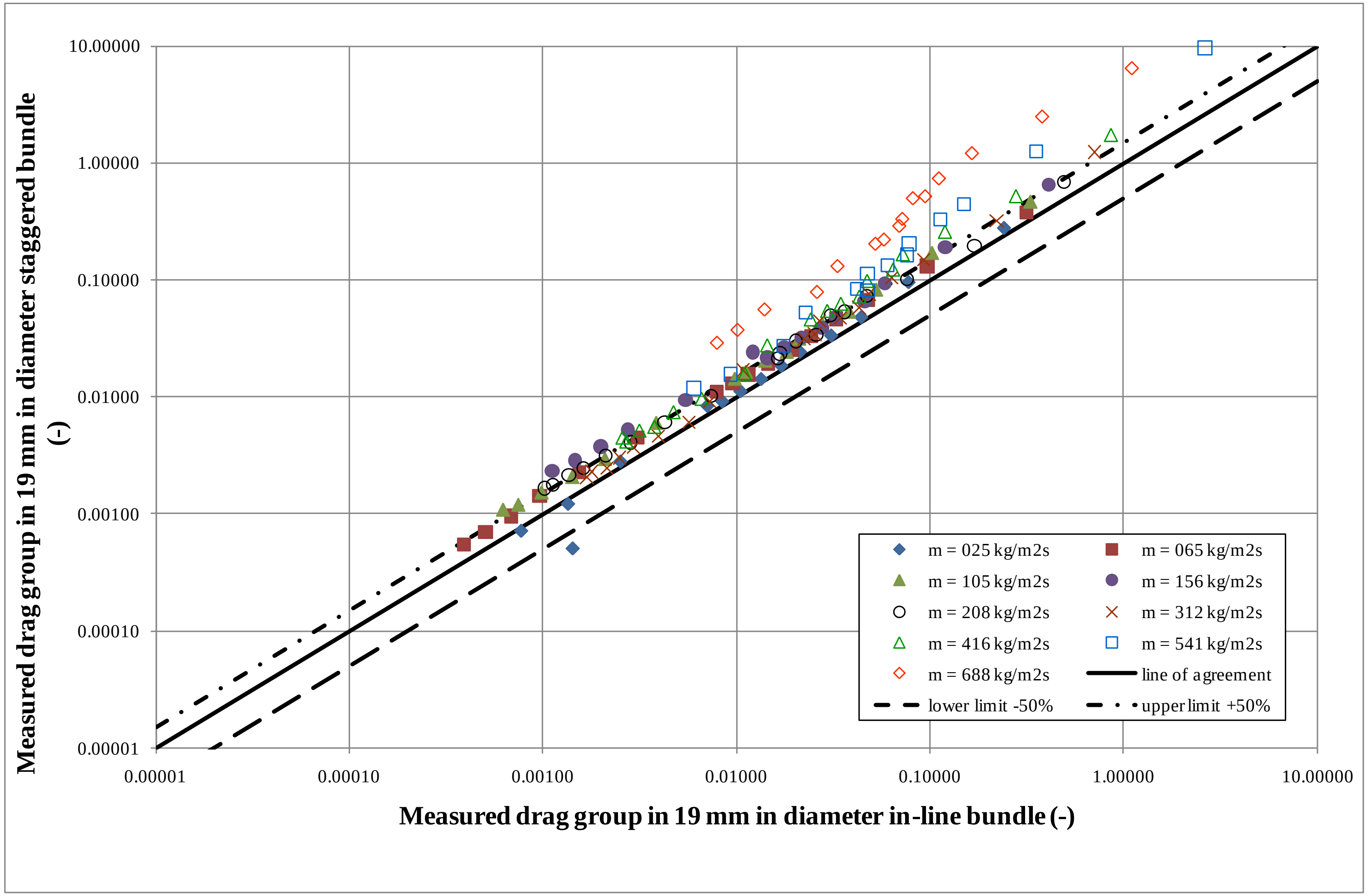

Figure 8.11: Comparison of measured drag group at 19 mm in diameter (in-line and staggered bundles)

CHAPTER 9 - AIR-WATER IN-LINE TUBE BUNDLE SIMULATION

Computational Fluid Dynamics (CFD) is widely used to investigate single-phase fluid flow fields. In the present study, CFX version 14.0 from ANSYS was used to simulate the single-phase flow in the three tube bundles; i.e. the 19 mm and 38 mm diameter in-line bundles and the 19 mm staggered bundle. The simulations were undertaken to inform on how the fluid flowed within the tube passages.

9.1 The models

The flow in a tube passage is assumed to be symmetrical because the geometry and physical conditions causing it are symmetrical and because the flow in any passage between the tubes is likely to be the same as that in any other. So, in the simulations, only a symmetrical half of a flow passage between the tubes is used. The flow is simulated over ten tubes in the flow direction to ensure fully developed flow is achieved. The tube bundles were created in DesignModeler and are shown in Figures 9.1, 9.2 and 9.3.

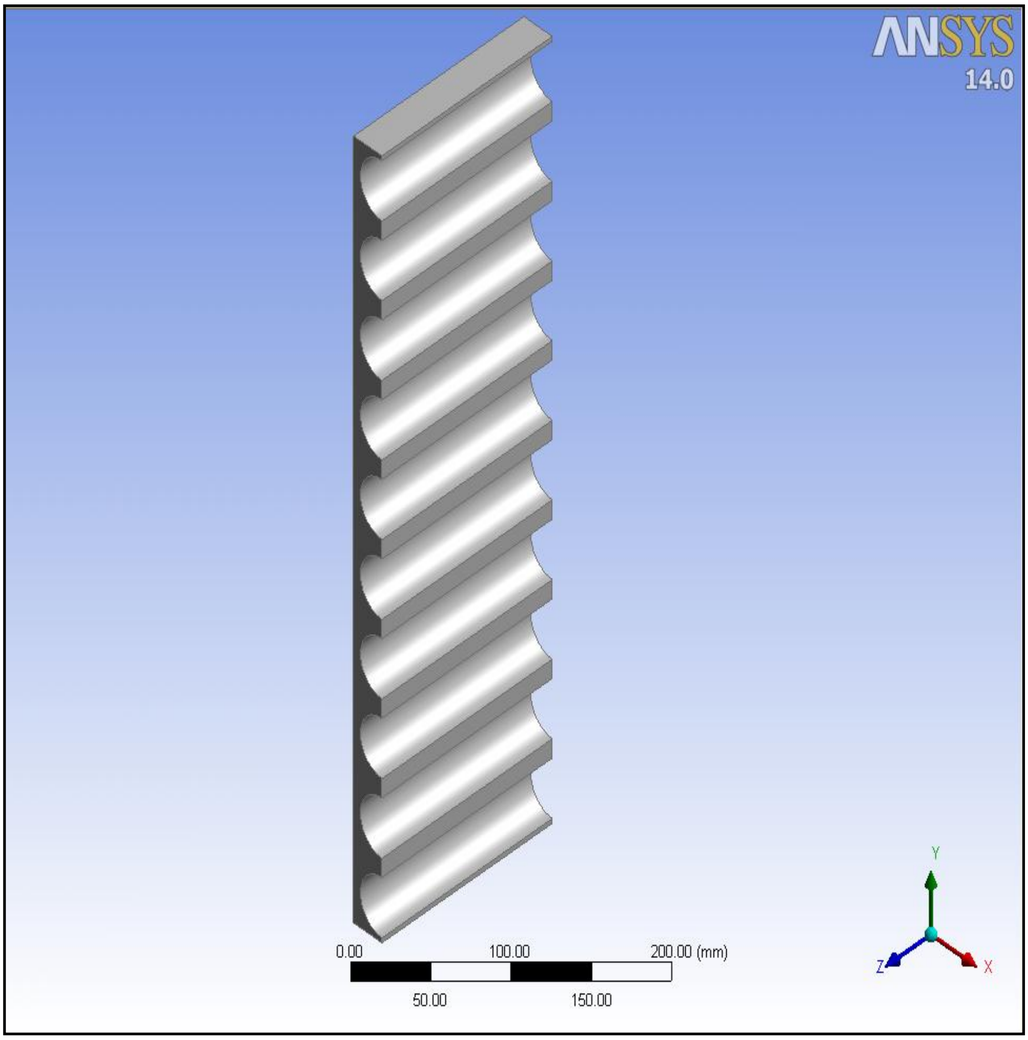

Figure 9.1: The 38 mm in diameter in-line bundle

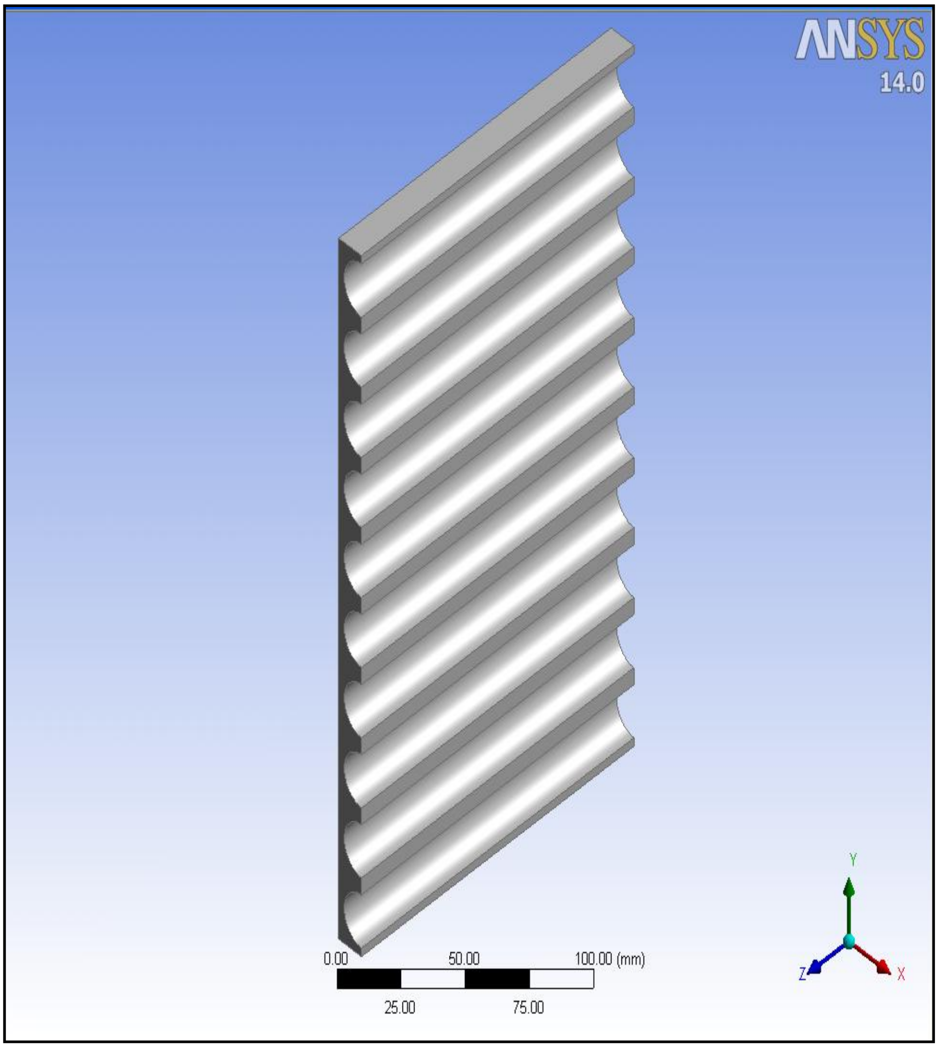

Figure 9.2: The 19 mm in diameter in-line bundle

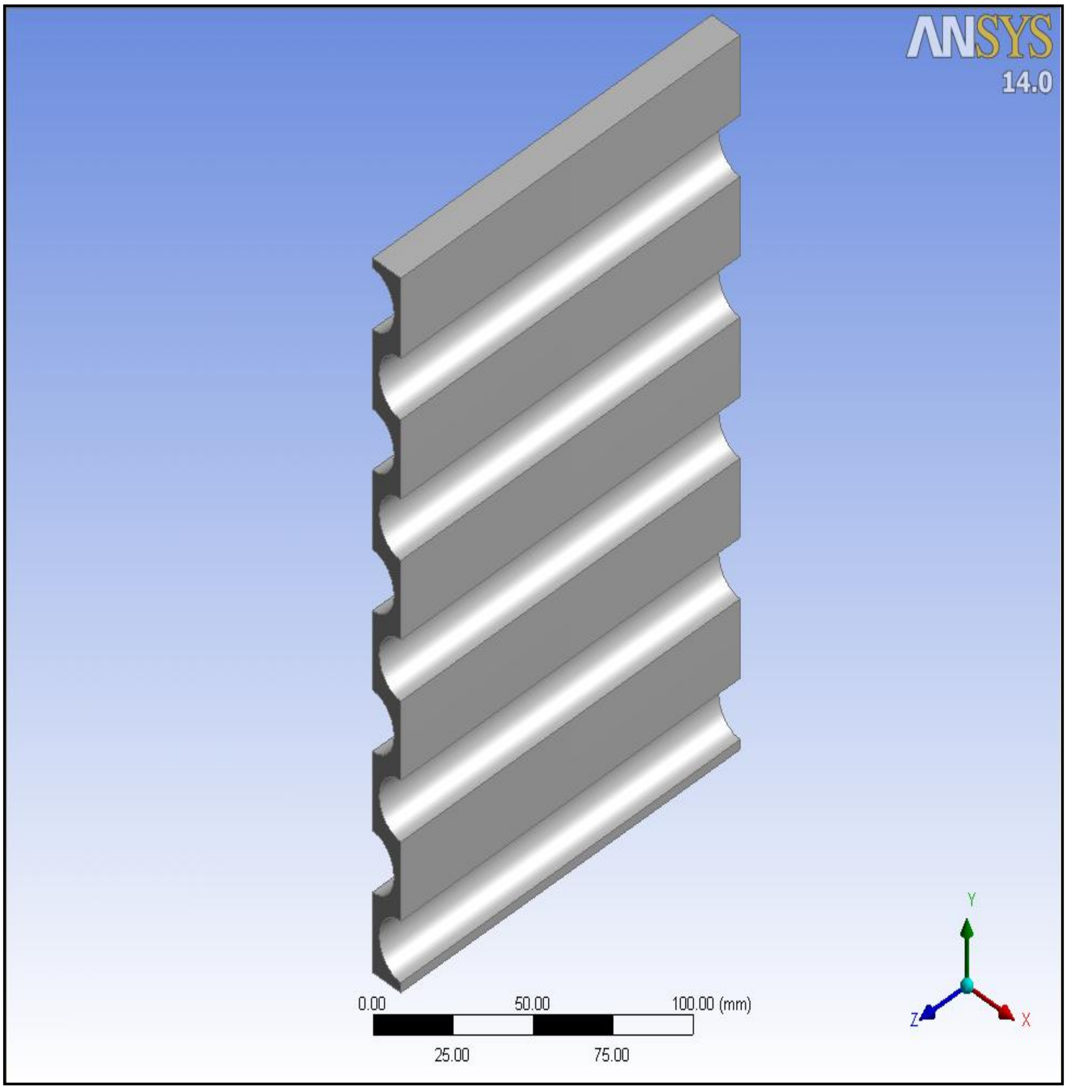

Figure 9.3: The 19 mm in diameter staggered bundle

9.2 The boundary conditions

Two dimensional models for the three bundles were produced in CFX-PRE for the symmetrical half of the water-only bundles. The boundary conditions for the three tube bundles are shown in Figures 9.4, 9.5 and 9.6. The tubes were set to solid surfaces with no slip and the east, west, front and back surfaces set to the symmetrical boundary condition. The opening boundary condition at the top of the bundle was set to atmospheric pressure and the inlet boundary was set to a normal velocity of 6 m/s.

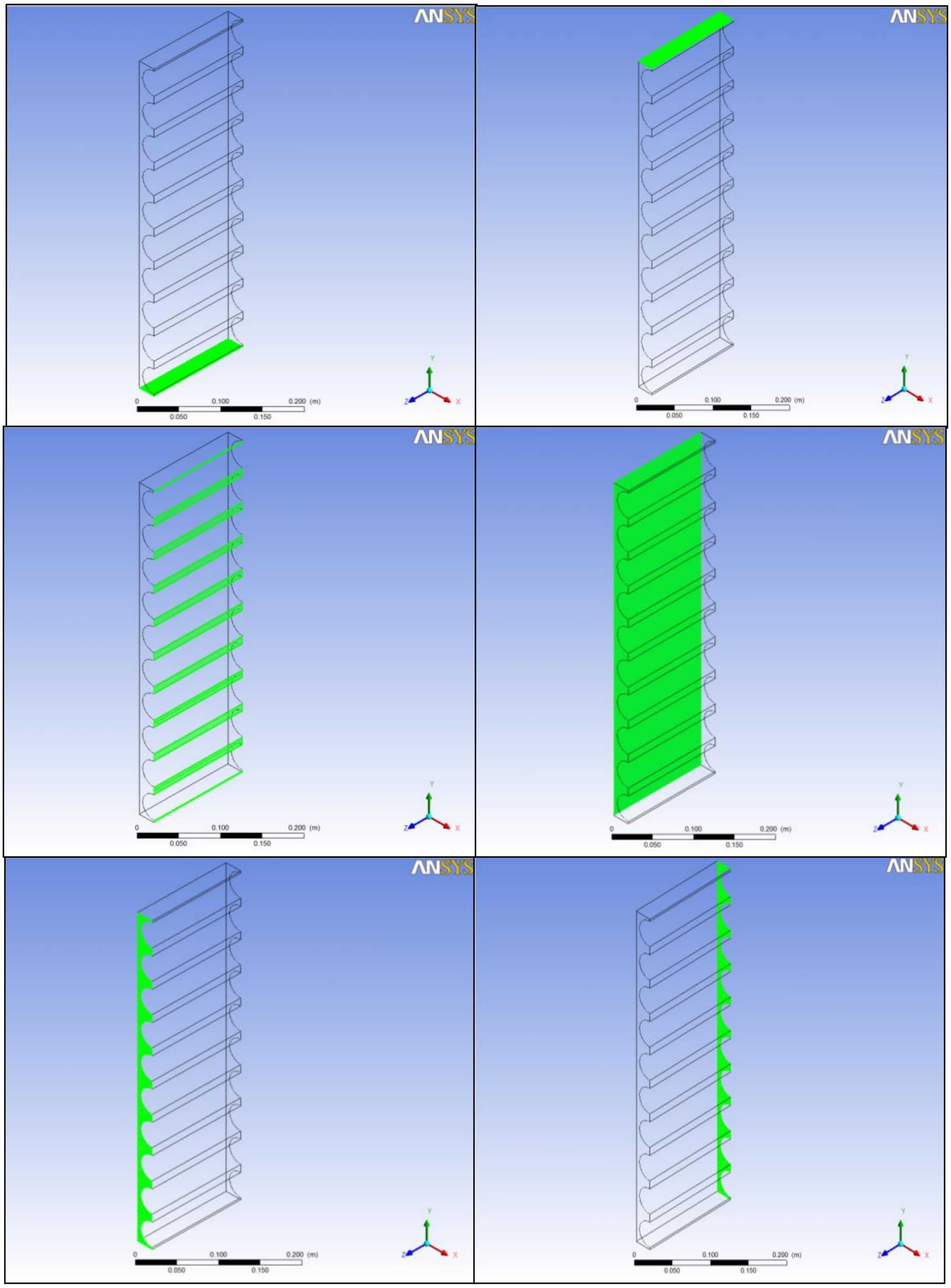

Figure 9.4: Boundary conditions at Tube 1: 38 mm in-line tube bundle. From clockwise; Inlet, Outlet, SymWest, SymBack, SymFront, SymEast. Symmetric is SymWest, SymBack, SymFront and SymEast. No slip condition at the tube surface, u and v = 0

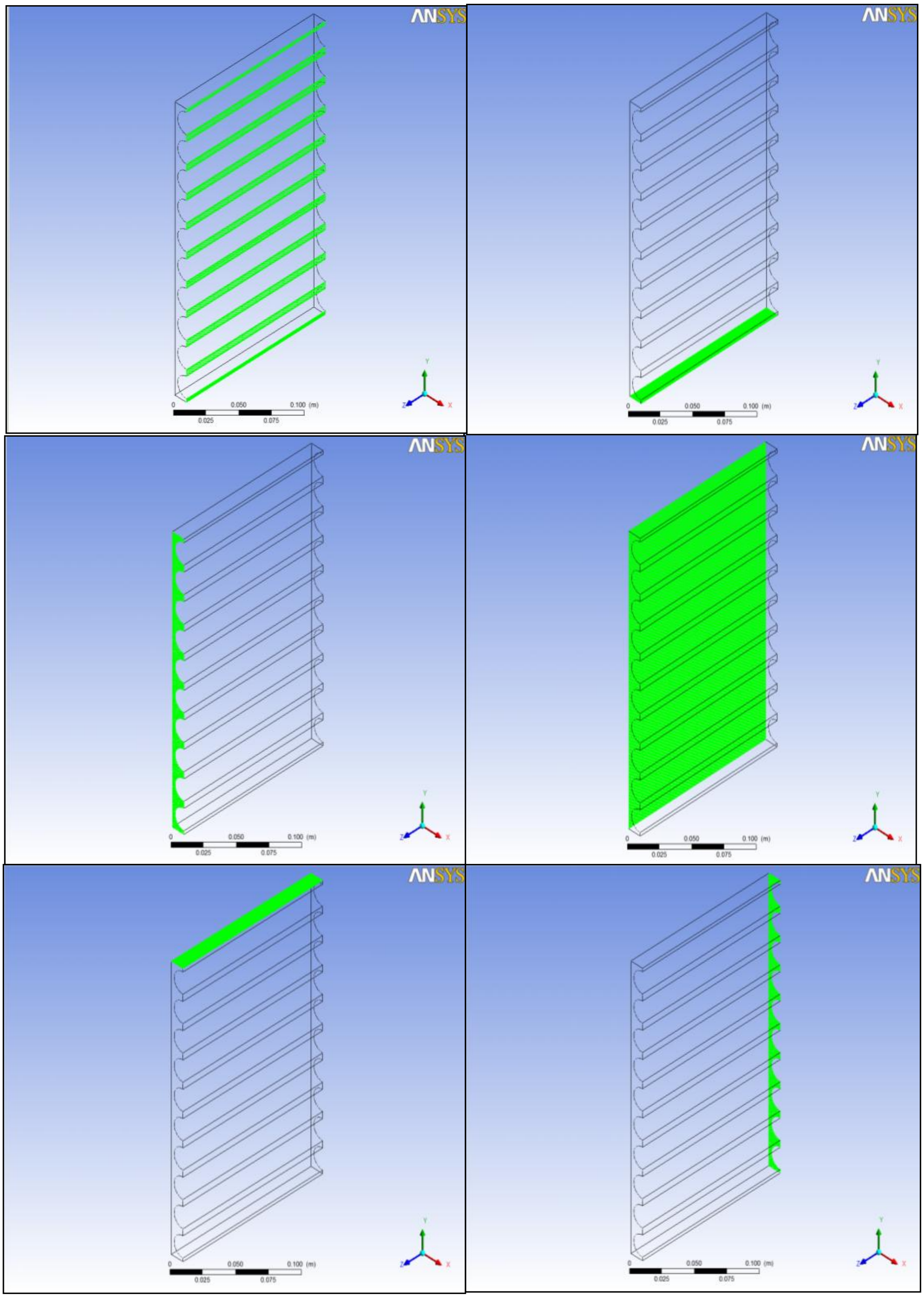

Figure 9.5: Boundary conditions at Tube 2: 19 mm in-line tube bundle. From clockwise; Inlet, Outlet, SymWest, SymBack, SymFront, SymEast. Symmetric is SymWest, SymBack, SymFront and SymEast. No slip condition at the tube surface, *u* and *v* = 0

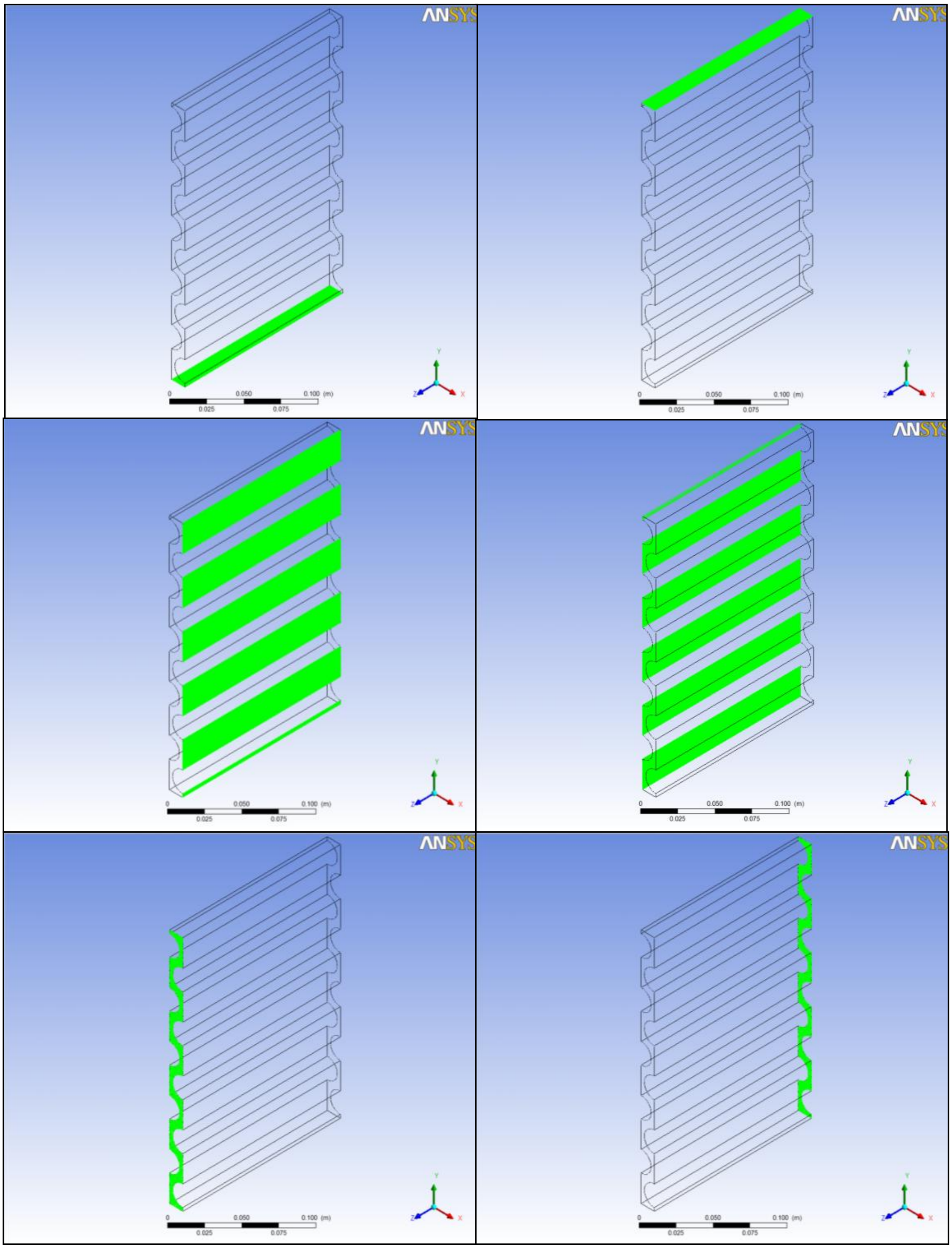

Figure 9.6: Boundary conditions at Tube 3: 19 mm staggered tube bundle. From clockwise; Inlet, Outlet, SymWest, SymBack, SymFront, SymEast. Symmetric is SymWest, SymBack, SymFront and SymEast. No slip condition at the tube surface, *u* and *v* = 0

An inflation layer of 1.0 mm thickness and containing 16 layers with an expansion factor of 1.3 was inserted between the tube walls and the bulk fluid to capture the effects near the wall. The simulation was run until the residual of the pressure and velocities was less than 0.00001. The parameters for the models are shown in Table 9.1.

Table 9.1: Geometric details and boundary conditions of simulated tube bundles

		Tube bundle 1	Tube bundle 2	Tube bundle 3
Geometry	Tube diameter	38 mm	19 mm	19 mm
	Pitch	50 mm square pitch array	25 mm square pitch array	25 mm equilateral triangle
	Pitch to diameter ratio, P/D	1.32	1.32	1.32
	Number of tubes	10	10	5
	Tube length	150 mm		
	Tubes arrangment	In-line square	In-line square	Equilateral staggered
	Working fluid	Water		
Domain	Domain type	Fluid domain		
	Water temperature	25°C		
	Turbulence model	Shear Stress Transport (SST)		
	Wall function	Automatic		
	Reference pressure	1 atm		
	Buoyancy option	Non-Buoyant		
	Domain motion	Stationary		
	Heat transfer model	None		
	Turbulence wall functions	Automatic		
	Reaction or combustion model	None		
	Thermal radiation model option	None		
Boundary condition				
Inlet	Flow regime option	Subsonic		
	Mass and momentum option	Normal speed		
	Normal speed	6 m/s		
Outlet	Flow regime option	Subsonic		
	Mass and momentum option	Static pressure		
	Relative pressure	0 Pa		
	Flow direction	Normal to boundary condition		
	Turbulence option	High intensity		
Symmetry	Boundary type	Symmetry		
Wall	Solid wall	No slip is applied between the fluid and solid		
Solver	2-Dimensional, steady state, axisymmetric			
	Advection Scheme Option	High resolution		
	Timescale control	Auto timescale		
	maximum number of iterations	100		
	Residual type	RMS		
	Residual target	0.00001		

9.3 Grid independency study

In computational fluid dynamics analysis, accuracy of the results is controlled by the selection of the mesh density as finer mesh produces more accurate results but requires more computer time for solving the problem. To this point, simple investigation has been conducted to determine the acceptable mesh division without compromising accuracy of the results. Therefore, a grid independence study was carried out for two meshes for each tube bundles.

In 38 mm inline tube bundle, two mesh configurations of 1,100,000 and 3,200,000 cells were conducted. In 19 mm inline tube bundle, two mesh configurations of 1,300,000 and 3,500,000 cells were made. In 19 mm staggered tube bundle, two mesh configurations 1,000,000 and 2,800,000 cells were investigated. Figures 9.7-9.9 show the results from the tube bundles grid independence study. The tube pitch pressure of each bundle for each mesh configurations were analysed.

The results show there is no significant difference between the two mesh configurations as all lines of both configurations are almost overlapped. These indicate, using finer mesh does not improve the model prediction. Thus, meshing with lower number of mesh cells does not sacrifices the solution accuracy. Since the Central Processing Unit (CPU) time increases exponentially with the number of grids, the lower mesh cells, 1,100,000, 1,300,000 and 1,000,000 were chosen for 38 mm in-line tube bundle,19 mm in-line tube bundle and 19 mm staggered tube bundle respectively. Less mesh cells reduce CPU time during CFD simulation which permits a significant number of cases to be run.

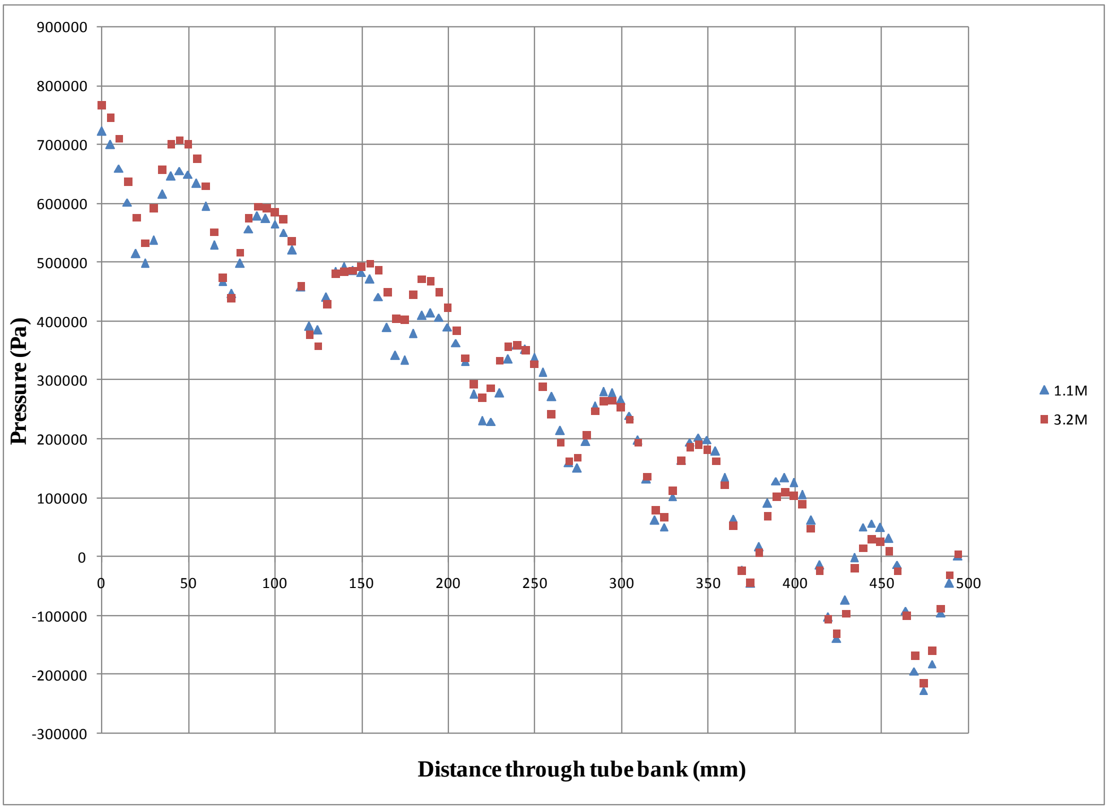

Figure 9.7: Pressure profile comparison between 1.1 million and 3.2 million mesh sizes in 38 mm in-line tube bundle

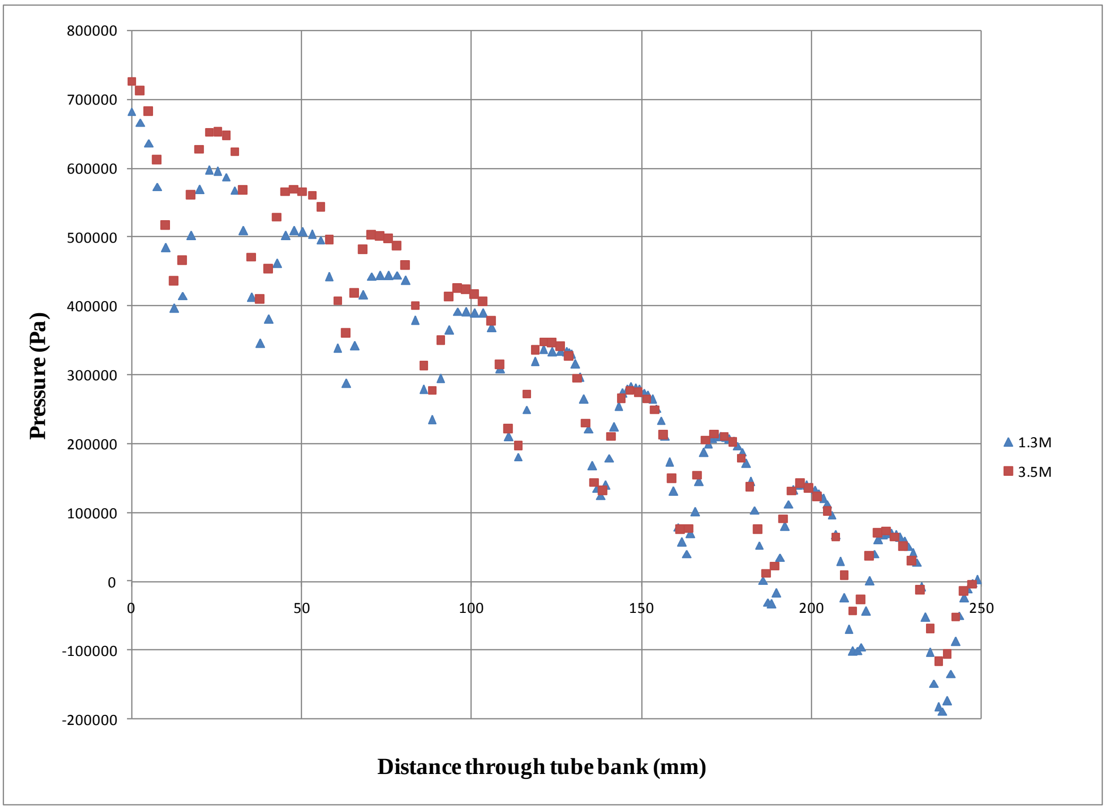

Figure 9.8: Pressure profile comparison between 1.3 million and 3.5 million mesh sizes in 19 mm in-line tube bundle

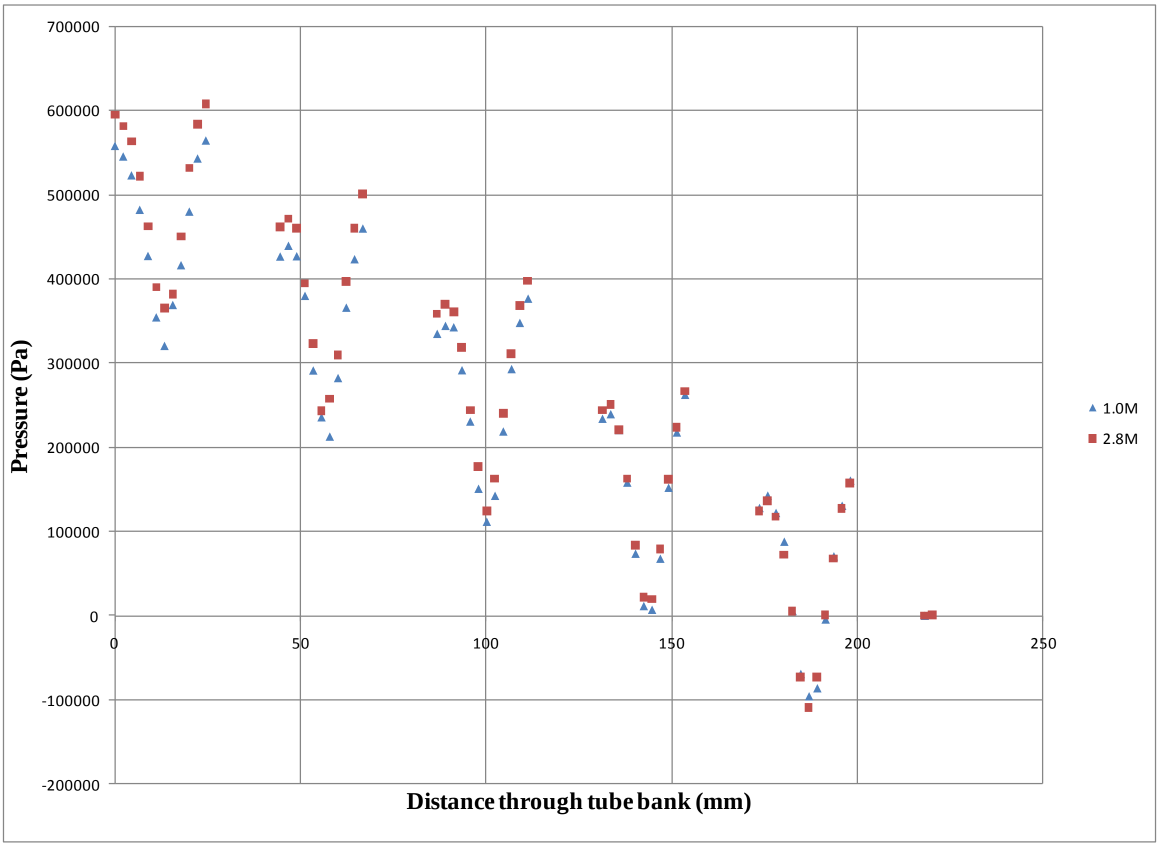

Figure 9.9: Pressure profile comparison between 1.0 million and 2.8 million mesh sizes in 19 mm staggered tube bundle

9.4 Tube bundle 1: 38 mm in diameter in-line tube bundle

The model was constructed with a grid 0.5 mm in length. This gave 1,100,000 elements that consists of prisms as shown in Figure 9.10. The insert picture shows the tube surface inflation was set to rectangular nodes. The meshing gave the total number of nodes as 354,000.

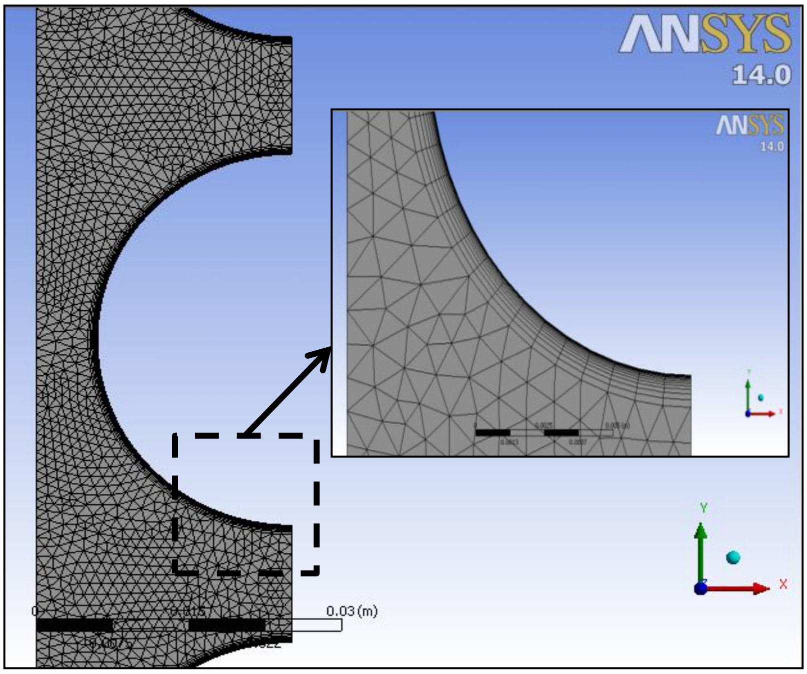

Figure 9.10: The prisms and rectangular grids of model Tube 1: 38 mm in-line bundle

As the fluid flowed past a tube, a thin boundary layer near the surface was expected to develop due to viscous effects. The flow past a series of tubes would create a pressure distribution along the curve surfaces of the tubes for an inviscid flow, the pressure distribution around a tube is such that the stationary fluid at $\theta = 0°$ is accelerated to its maximum velocity at $\theta = 90°$ (minimum gap) and then is decelerated back to zero velocity (stagnation point) at the rear of the tube $\theta = 180°$. This is accomplished by a balance between pressure and inertia effects. Figure 9.11 shows the predicted pressure distributions around the 10 tubes in the bundle.

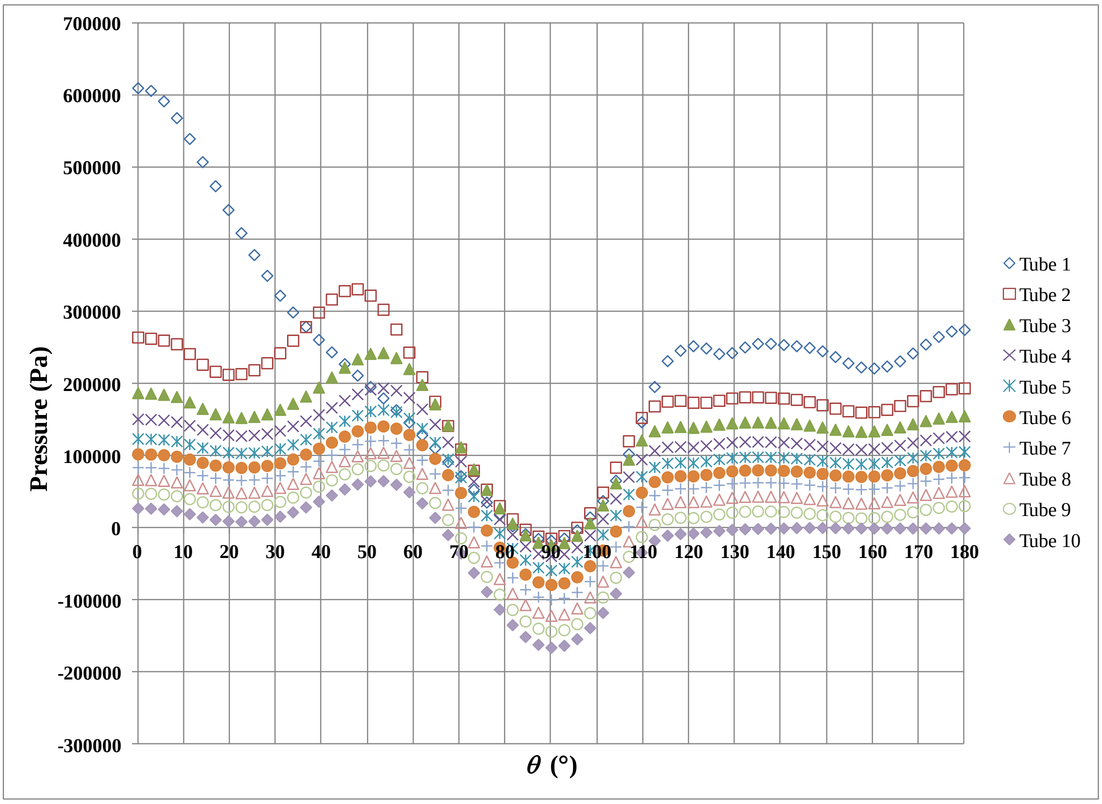

Figure 9.11: Pressure distribution around the tubes surface versus theta at 38 mm in-line bundle

As the fluid flowed through the tube bundle, the fluid losses energy when travelling from tube 1 to tube 10. In its attempt to flow from $\theta = 0°$ to $\theta = 180°$ on tube 1, it experiences the same pressure distribution in the upstream flow as the inviscid flow. However, because of the viscous effects induced by the no slip condition at the tube wall, the fluid particle in the boundary layer experiences a loss of energy as it flows along. This loss means that the particle does not have enough energy to remain attached as the pressure increases ($\theta = 90°$ to $\theta = 180°$) and separates near $\theta = 120°$. The pressure recovers a little after separation for tubes 2-10 flow re-attachment occurs near $\theta = 50°$ and separation near $\theta = 120°$. The pressure drop decreases as the tube number increases as shown in the Figure 9.11. Also shown in Figure 9.11, because of boundary layer separation, the pressure on the rear half of each tube is considerably less than that on the front half. Thus, a drag force is formed on the tubes.

Figure 9.12 shows the velocity vector in the bundle. There are two regions of flow that are clearly shown, the main flow and circulation zones. As the fluid flows past the tubes, separation occurs when the wall shear stress is zero. This results in separation bubbles behind the tubes in which some of the fluid is actually flowing upstream, against the direction of the main flow. The flow forms a circulation between the tubes due to low pressures in the separated wake regions, as shown in Figure 9.13. The separation points occur when the wall shear stress is zero, as indicated in Figure 9.14 where separation occurs at θ_S = 110° and re-attachment at θ_R = 51°.

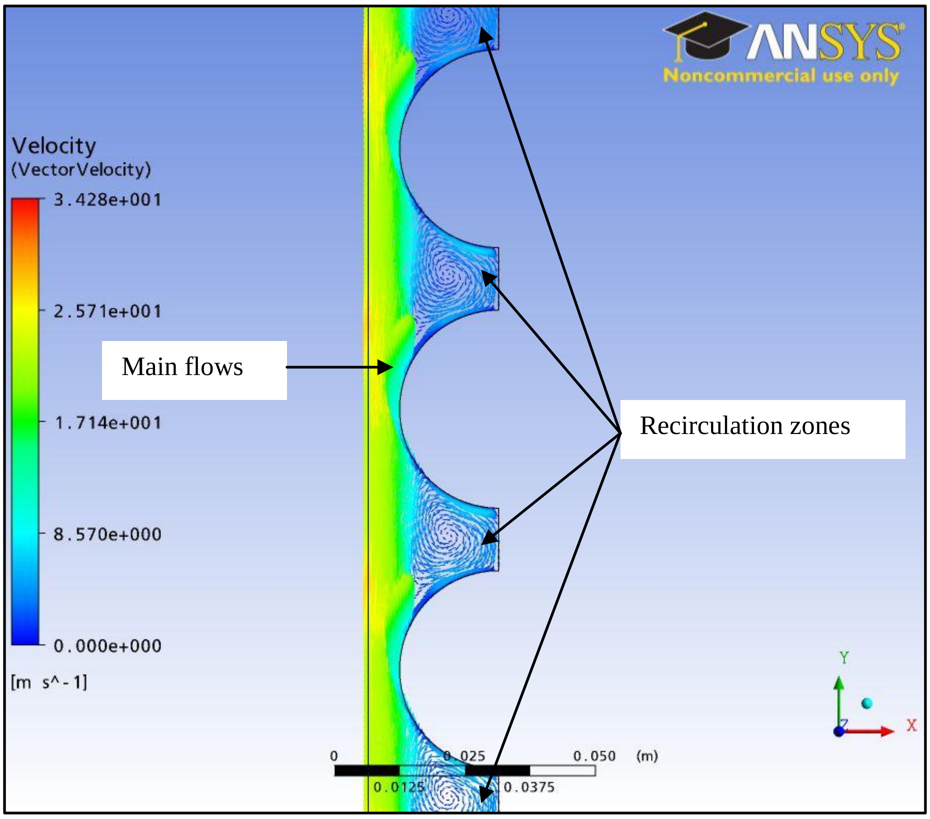

Figure 9.12: Velocity profile at 38 mm in diameter in-line bundle

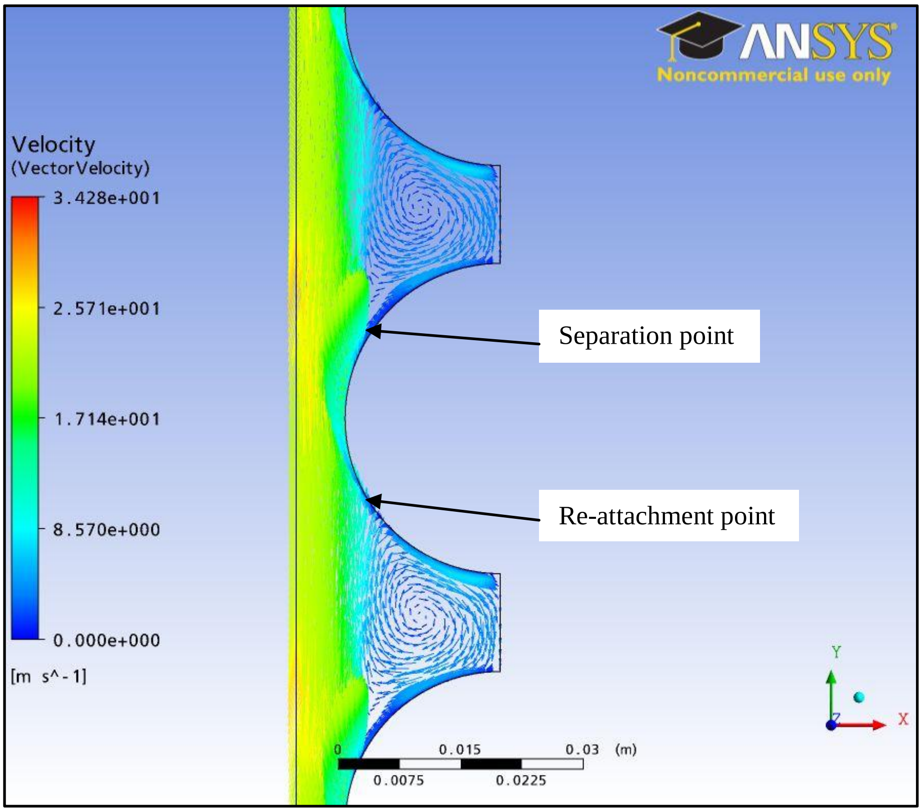

Figure 9.13: Main stream flow and re-circulation zone between the tubes in 38 mm in diameter in-line bundle

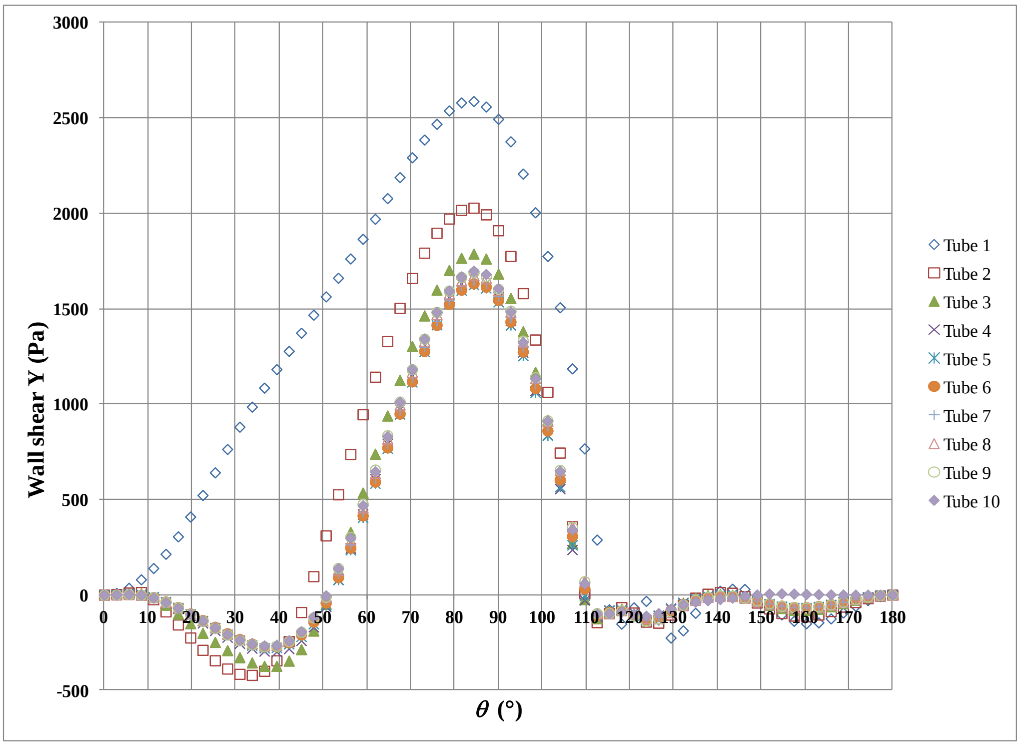

Figure 9.14: Wall shear Y distribution around the tube surface versus theta in 38 mm in-line bundle. The separation point is at θ_S = 110° and re-attachment point is at θ_R = 51°

The pressure is shown to drop significantly as the flow enters the first row of tubes as shown in Figure 9.15. This is caused by the fluid acceleration caused by the reduction in flow area as shown in Figure 9.12. The pressure is shown to subsequently decrease and increase as the flow moves between tubes. The pressure reduction in these tubes is again induced by the reduction in flow area as the flow moves towards the minimum gap as shown in Figure 9.13. The pressure recovery occurs as the flow separates from the tube just after the minimum gap and expands to re-attach to the next tube. There is a net pressure drop across each tube due to friction.

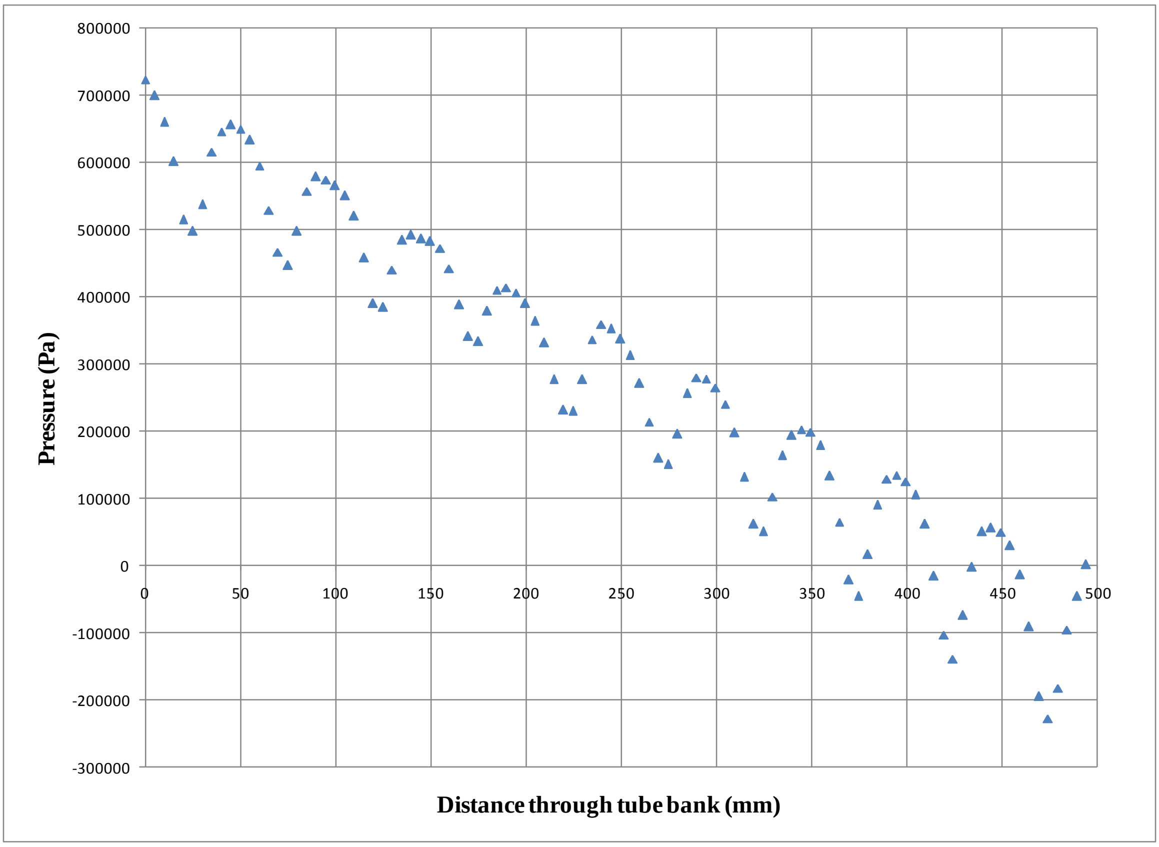

Figure 9.15: Variation of pressure with distance through the tube bank in 38 mm in diameter in-line tube bundle

9.5 Tube bundle 2: 19 mm in diameter in-line tube bundle

The model was constructed with a grid 0.25 mm in length. This gave 1,300,000 elements that consists of prisms. The insert picture in Figure 9.16 shows the tube surface inflation was set to rectangular nodes. The meshing gave a total number of nodes of 421,000.

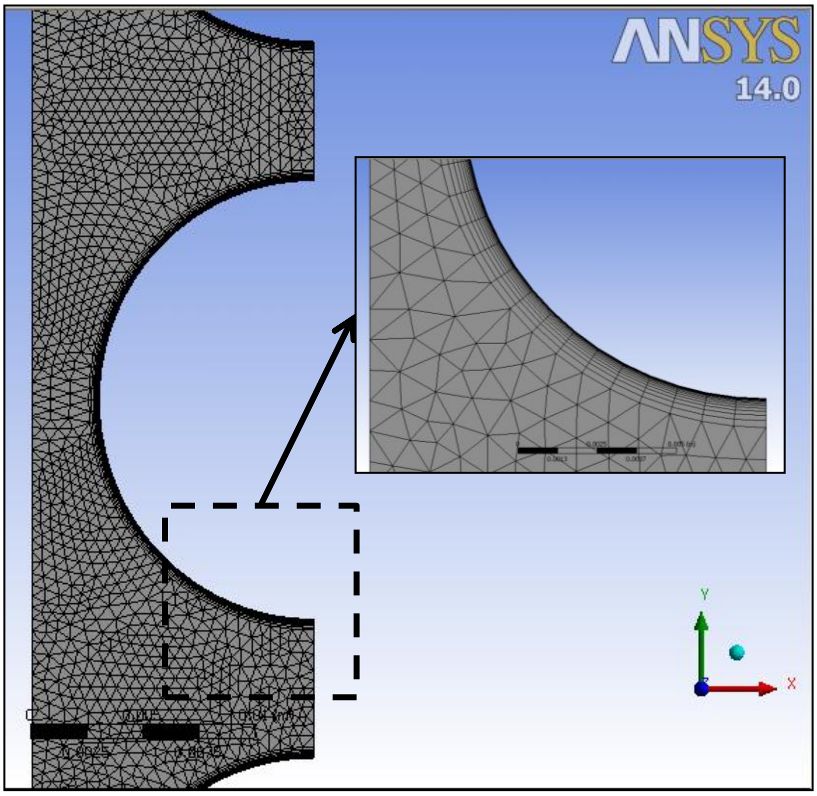

Figure 9.16: The prisms and rectangular grids of model Tube 2: 19 mm in-line bundle

The vector velocity in the tube bundle is shown in Figure 9.17. After the first few tubes, the flow path is fully developed, so that what occurs in one tube pitch is repeated in the others. The main stream has a high velocity due to the area reduction and friction causes re-circulation to occur in the gaps between the tubes due to low pressure in the separated wake regions. This results in a separation bubble behind the tubes in which some of the fluid is actually flowing upstream, against the direction of the main flow. There is a clear similarity between the 38 and 19 mm in-line flow fields, as seen in Figure 9.12. The flow begins at the minimum gap between the tubes and decelerates as a potential flow until it separates at θ_S, where and a wake is formed to the rear of the tubes. The flow is re-attached at θ_R as seen in Figure 9.18.

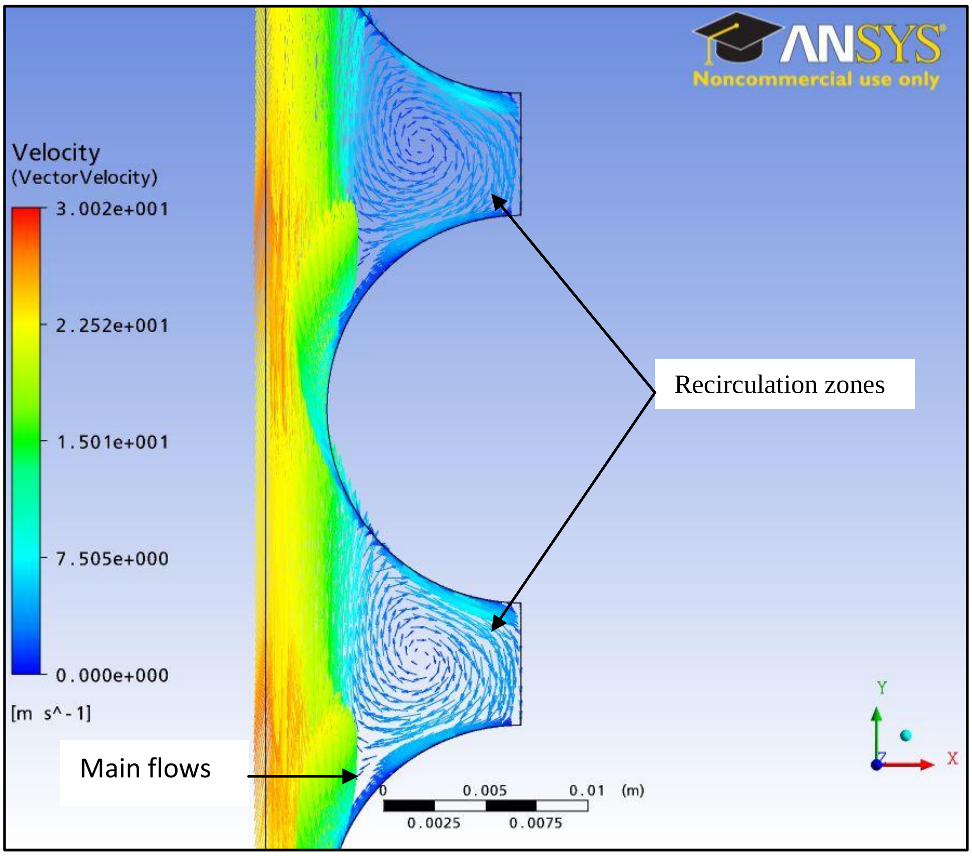

Figure 9.17: Main stream flow and re-circulation zone between the tubes in 19 mm in diameter in-line tube bundle

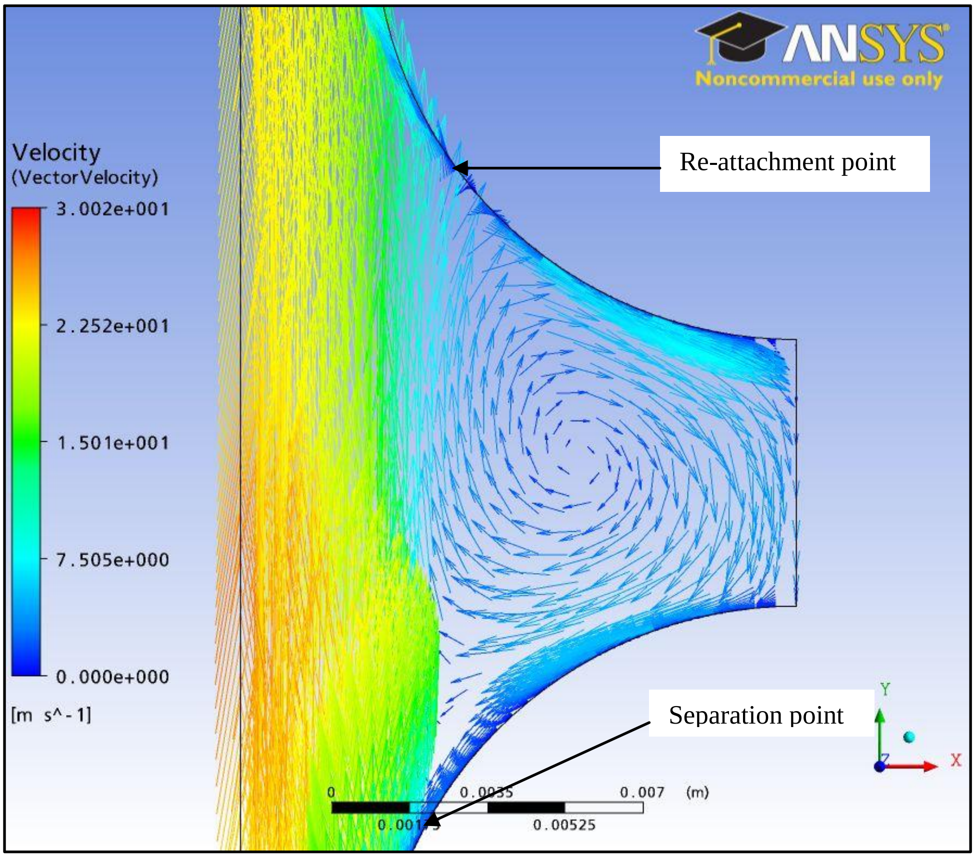

Figure 9.18: Separation and re-attachment points in 19 mm in-diameter in-line bundle

The separation points occur when the wall shear stress is zero, where the water is detached from the tube surface as indicated in the Figure 9.19. The separation point occur at θ_S = 107°. The flow is re-attach at the maximum main flow area at θ_R = 52°. This happens at all tube in fully developed flow. These points are essential values as it helps to analyze a drag force that formed at the rear of the tube banks.

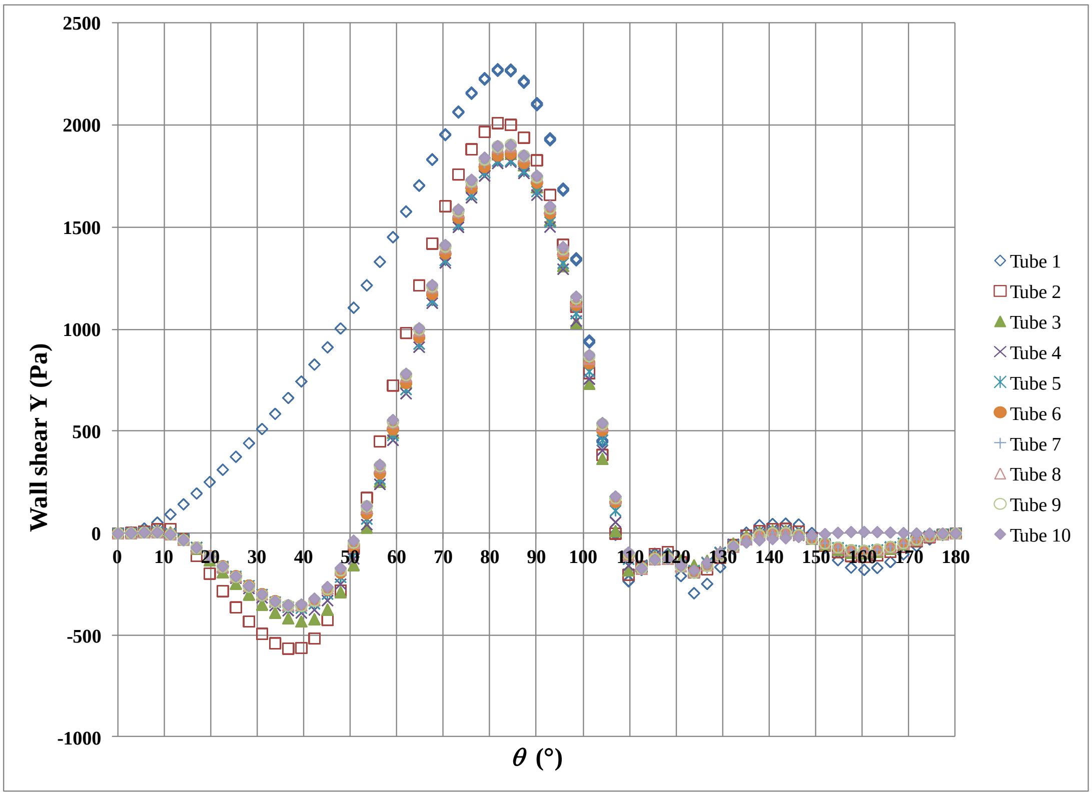

Figure 9.19: Wall shear Y distribution around the tube surface versus theta in 19 mm in-line bundle. Separation flow at θ_S = 107° and re-attachment flow is at θ_R = 52°

Figure 9.20 shows the pressure variation with distance through the tube bundle. The pressure drops considerably as the flow enters the first row of tubes due to fluid acceleration caused by the reduction in the flow area. The pressure is shown to continually rise and fall as the flow moves across the following tubes. The pressure reduction in these tubes is again caused by the reduction in flow area as the flow moves towards the minimum gap. The pressure recovery occurs as the flow separates from the tube just after the minimum gap and expands to re-attach to the next tube. There is a net pressure drop across each tube due to friction.

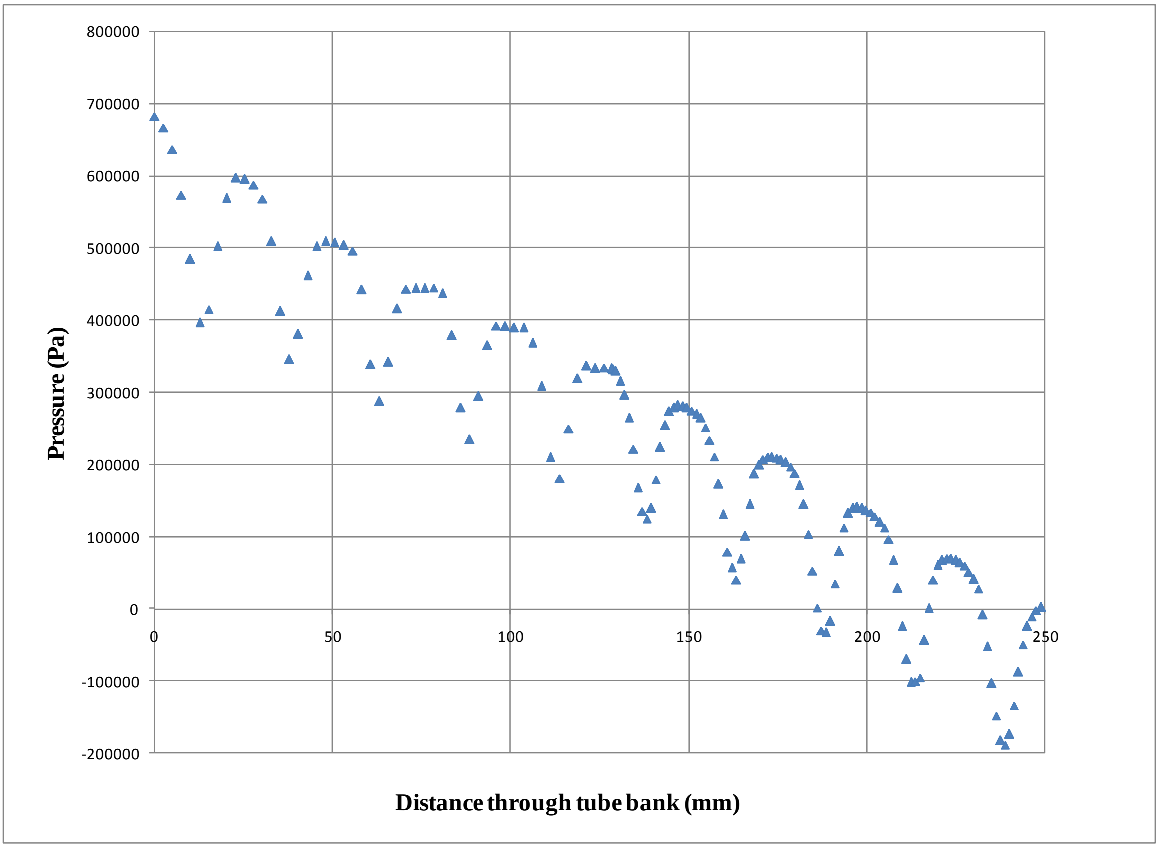

Figure 9.20: Variation of pressure with distance through the tube bank in 19 mm in diameter in-line tube bundle

The pressure distribution around the tubes are shown in Figure 9.21. As the fluid flows past the first tube, there is a considerably drop of pressure because of it is in the entrance region before fully developed flow is reached. The fluid losses energy when travelling from tube 1 to tube 10. Note that the pressure at $\theta = 0°$ is a maximum before the pressure is decreasing at $\theta = 90°$ where it is a minimum. The pressure recovers a little after ($\theta = 90°$) up to separation point which is at $\theta_S = 107°$ where the boundary layer separates from the tube. Due to the boundary layer separation, the pressure on the rear half of each tube is considerably less than that on the front half ($\theta = 90°$ to $\theta = 180°$) giving a significant form loss. The wake region at the rear of the tube will produce a drag force.

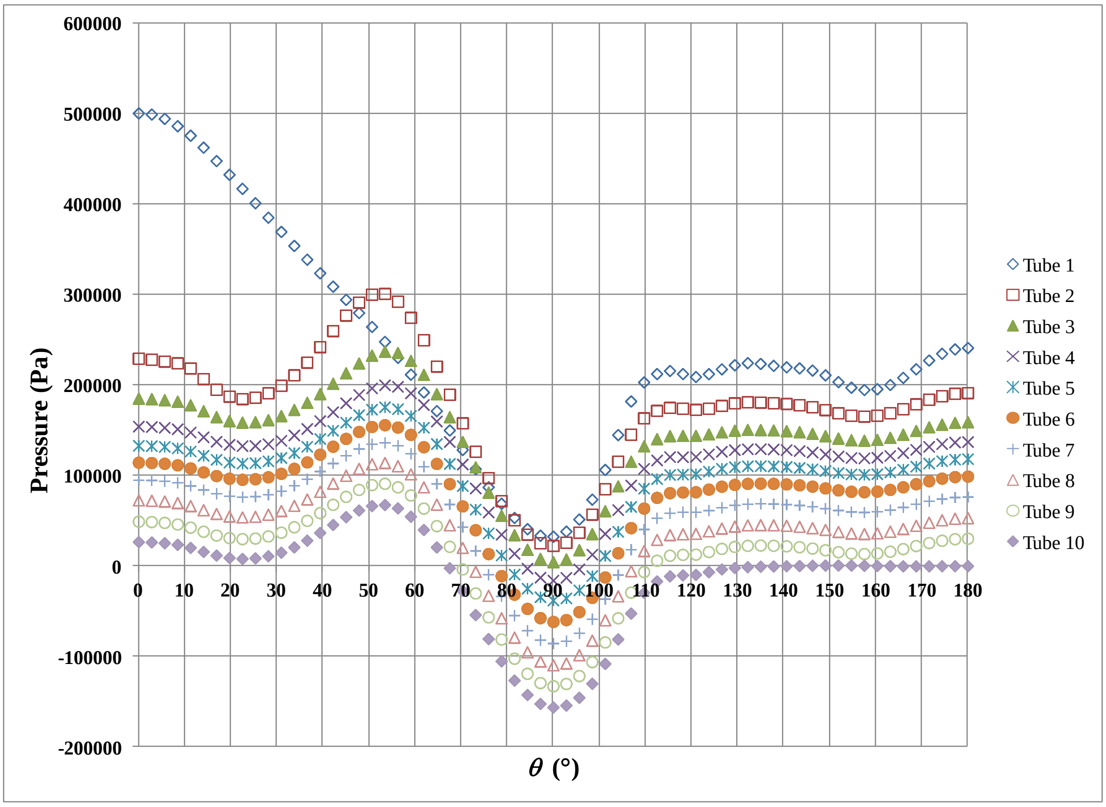

Figure 9.21: Pressure distribution around the tubes surface versus theta at 19 mm in-line bundle

9.6 Tube bundle 3: 19 mm in diameter staggered tube bundle

The model was constructed with a grid 0.25 mm in length. The meshing gave a total of 366,000 nodes and had 1,000,000 elements that consisted of prisms, as shown in Figure 9.22. The inserted picture shows the tube surface inflation was set to rectangular nodes.

.

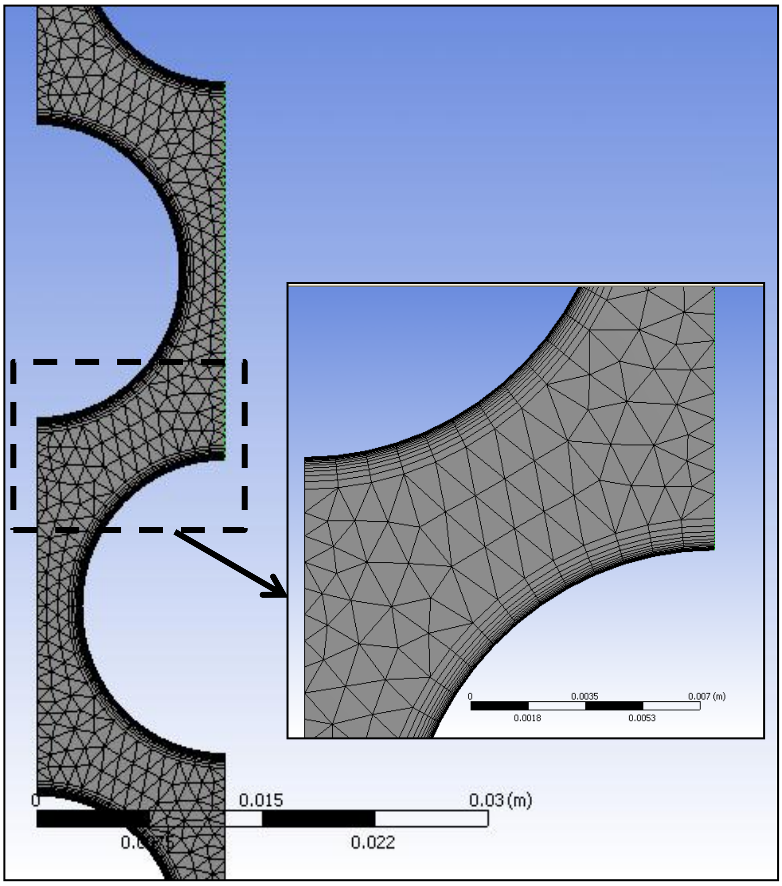

Figure 9.22: The prisms and rectangular grids of model Tube 3: 19 mm staggered bundle

Figure 9.23 shows the velocity vectors for the bundle. The fluid flow is high in the main stream and follow a more torturous path. As the fluid flows past the tubes, which was set to no slip at the wall, the fluid decelerates near the tube surface and creates a thin layer, called the boundary layer, due to viscous effects. The flow is attached to the tube surface until the formation of a wake, evident to the rear of the tube, where some of the fluid is flowing backward against the main flow. The maximum velocity occurs at $\theta = 90°$. Near $\theta = 180°$, the velocity is at a minimum or zero. This is where the circulation happens, see Figure 9.24. The flow re-attaches at the front of the tube.

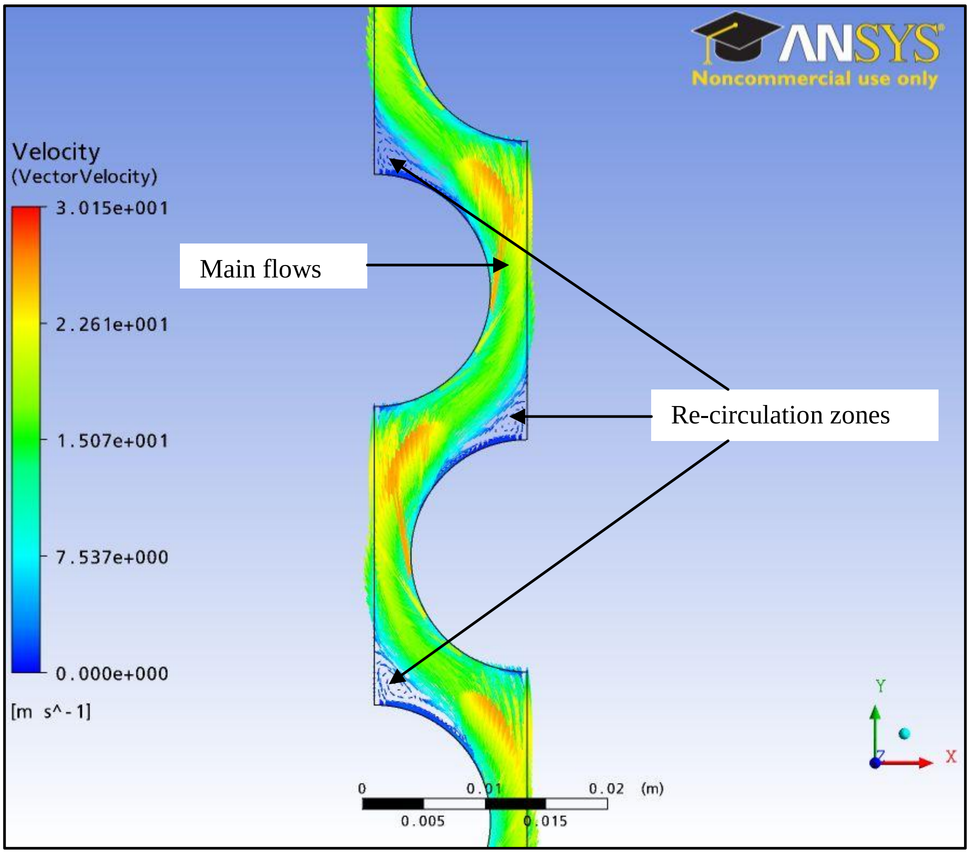

Figure 9.23: Main stream flow and re-circulation zone between the tubes in 19 mm in diameter staggered tube bundle

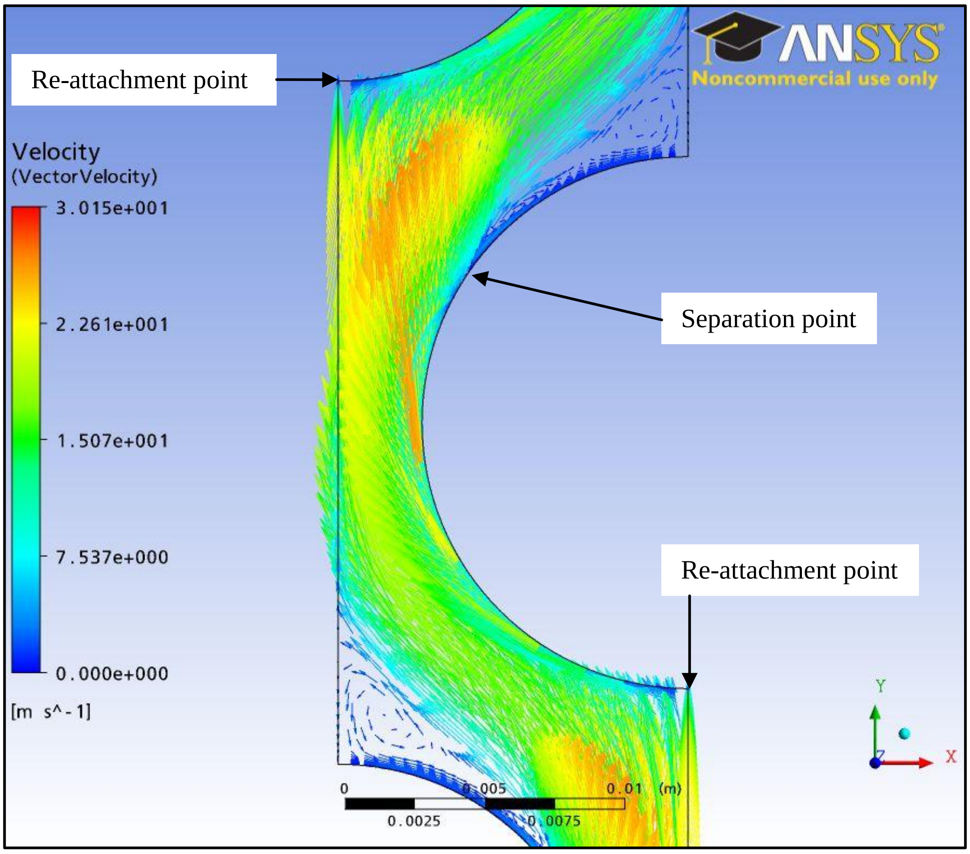

Figure 9.24: Separation point and re-attachment point in 19 mm in-diameter staggered bundle

Flow separation occurs when the shear stress is zero as shown in Figure 9.25. The flow separates at θ_S = 116°. The flow re-attaches at the tube front, as seen in the Figure 9.23 and Figure 9.24, i.e. θ_R = 0°.

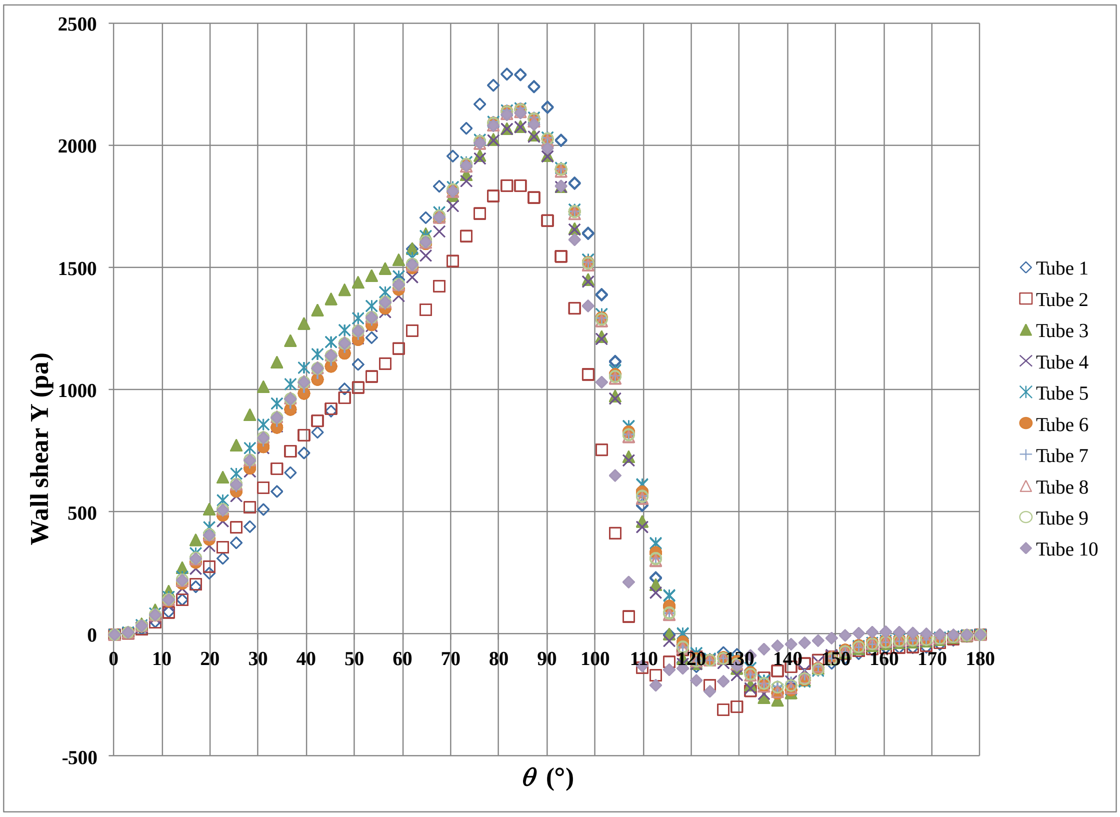

Figure 9.25: Wall shear Y distribution around the tube surface versus theta in 19 mm staggered bundle. Separation flow at θ_S = 116° and re-attachment flow is at θ_R = 0°

The pressure drop is largest on the first row of tubes, as seen in Figure 9.26. This is caused by fluid acceleration due to the reduction in flow area. The staggered alignment gives further reductions in pressure due acceleration and separation from the tube walls. As a result, the friction pressure loss is higher in the staggered bundle. As expected, the pressure is shown to gradually decrease and increase as the flow moves around the tubes. The pressure drop in these tubes is caused by the reduction in flow area as the flow moves towards the minimum gap. Pressure recovery occurs as the flow separates from the tube just after the minimum gap and expands to re-attach to the next tube. There is a net pressure drop across each tube due to friction.

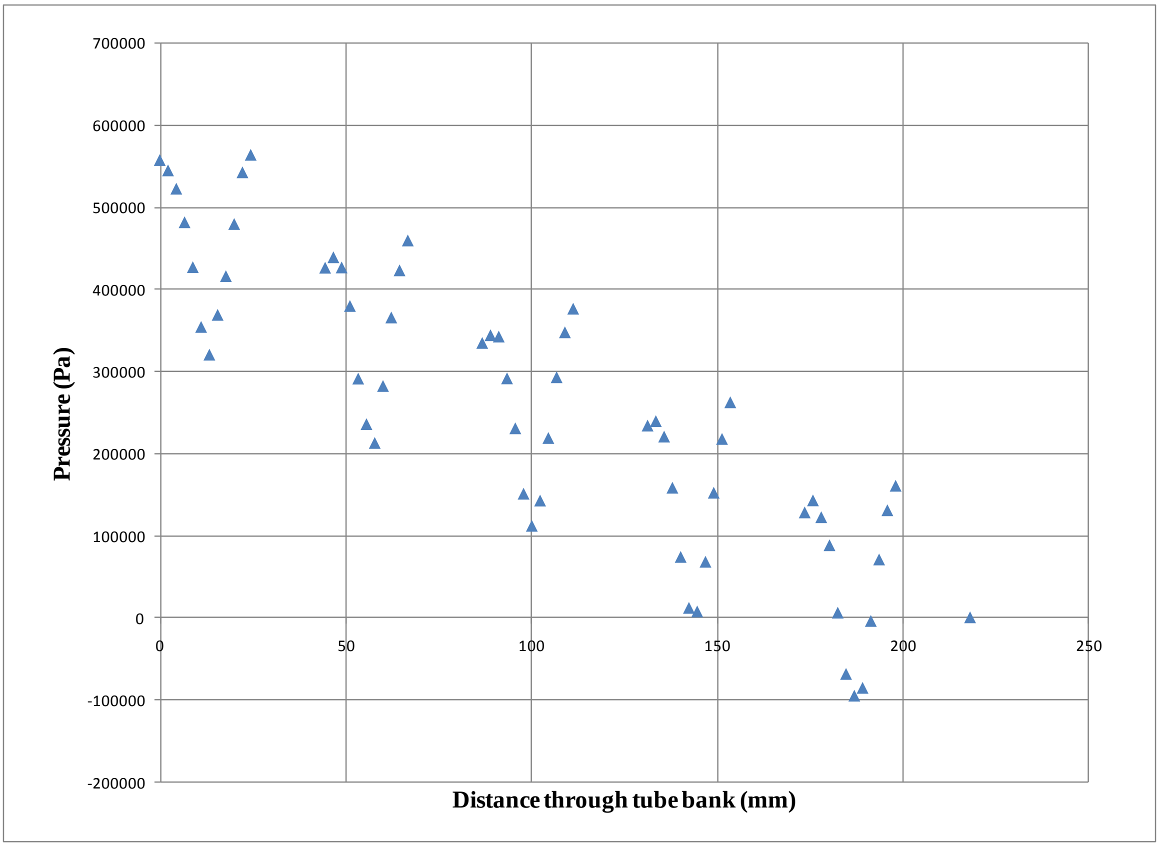

Figure 9.26: Variation of pressure with distance through the tube bank in 19 mm in diameter staggered tube bundle

The pressure distribution around the tubes for the staggered bundle is shown in Figure 9.27. The pressure is highest at θ = 0° and decreases as the flow travels from θ = 0° to θ = 90°, where the pressure reaches a minimum as the maximum velocity occurs at θ = 90°, see Figure 9.24 and Figure 9.25. The pressure recovers a little up to the separation point at θ_S = 115° where the flow separates from the tube surface. The wake region at the rear of the tube will cause a low pressure region due to turbulent dissipation. The drag force results from boundary layer separation, the pressure on the rear half of each tube being considerably less than that on the front half (θ = 90° to θ = 180°). Overall, the loss of energy in the direction of flow is shown. As the fluid flows from θ = 0° to θ = 90°, the pressure falls. The increase in pressure in the direction of flow along the rear half of the tube from θ = 90° to θ = 180° is seen in the figure for all tubes.

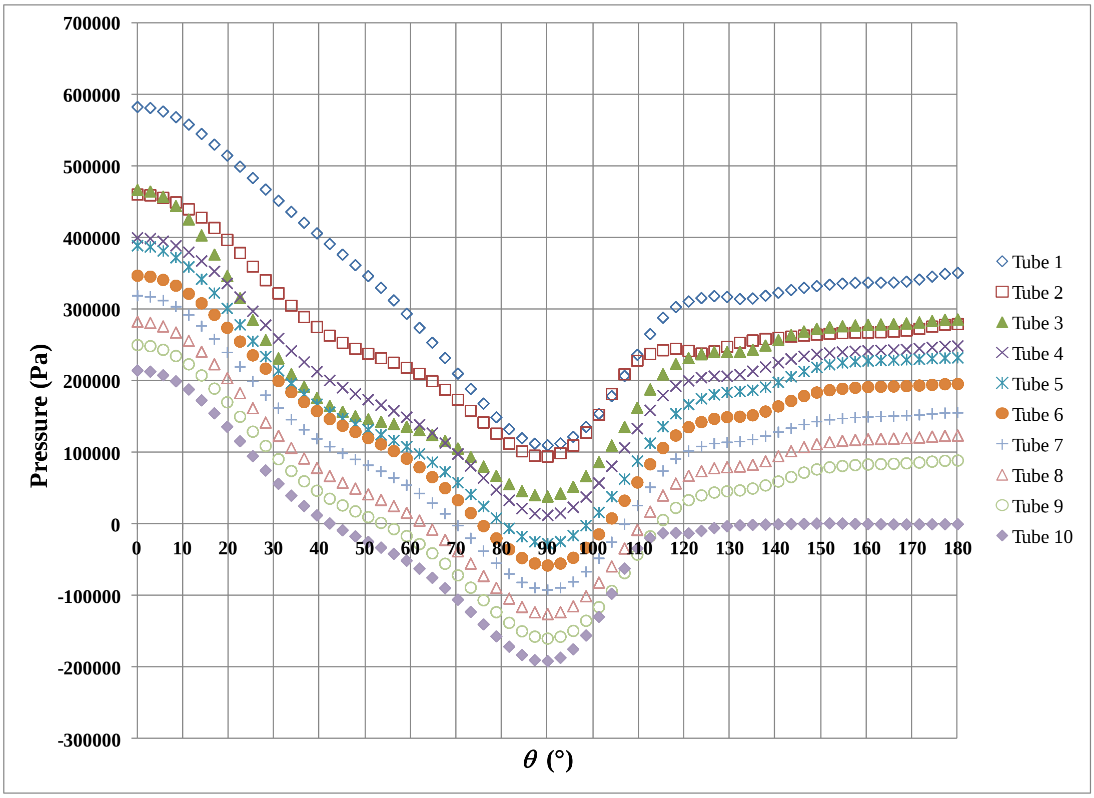

Figure 9.27: Pressure distribution around the tubes surface versus theta at 19 mm staggered bundle

9.7 Summary of velocity and pressure in the tube bundles

The flow passage in the in-line bundles is similar for both tube diameters. High velocity regions occur in the horizontal gaps with the low velocity regions in the vertical gaps. Re-circulation flow is formed in the vertical gaps between the tubes. The flow regimes and the average velocity is the same.

The velocity vectors for the in-line and staggered arrangement are different, as shown in Figure 9.12 and Figure 9.23. The separation and reattachment flows are different. Re-circulation flow is formed in every vertical minimum gap between the tubes, as shown in Figure 9.13 and 9.17, for the 38 mm in-line and 19 mm in-line bundles. For the staggered bundle, the re-circulation flow is formed at the top of the tubes, as shown in Figure 9.24. The water creates a significantly bigger re-circulation zone for both in-line bundles, in comparison to the staggered bundle, where the fluid only creates a small re-circulation zone. However, the in-line and staggered arrangements both have a high velocity in the minimum gaps where the water flow is not separated from the walls.

The separation point in the 38 mm in-line bundle is shown to be at θ_S = 110° and the re-attachment point is at θ_R = 51° in Figure 9.14. The separation point in the 19 mm in-line bundle occurs earlier, where the separation angle is θ_S = 107° and the re-attachment point is at θ_R = 52° as depicted in Figure 9.19. Flow separation is delayed in the staggered arrangement, the separation point is at θ_S = 116° and the re-attachment point occurs at θ_R = 0° as shown in Figure 9.25.

Pressure distributions around the tube surfaces are shown in Figure 9.11, 9.21 and 9.27 for the 38 mm in-line, 19 mm in-line and 19 mm staggered bundles respectively. The trends are the same for all bundles. As the flow is travels from θ = 0° to θ = 180°, the pressure is maximum at the nose of the tube surface, which is at θ = 0°, and decreasing to a minimum as it reached θ = 90°. Due to viscous effects, the fluid can not travel from the front of the tube to the rear of the tube (θ = 0° to θ = 180°). The flow separates from the tube surface and creates drag force in the wake region at the rear of the tubes. Although the pressure recovers a little after θ = 90°, the boundary layer separation makes the pressure on the rear half of each tube is considerably less than that on the front half (θ = 90° to θ = 180°).

The pressure reduces considerably as the flow enters the first row of tubes for both in-line bundles, but not the staggered one, as seen in Figures 9.15, 9.20 and 9.26 respectively. This is caused by fluid acceleration due to the reduction in flow area. The flow area change between these tube bundles contributes to the different pressure drops in staggered and in-line arrangements. As a result, the staggered arrangement has a higher pressure drop, than the in-line arrangement. The larger diameter in-line bundle shows the lowest pressure drop along the tube bundle. The tube diameter also affects the pressure drop in the bundle.

Overall, the purpose of the single-phase CFD simulations was to help gain an understanding of how the flow passes through the heat exchanger. The results from the in-line bundles are similar. The results for staggered bundle are quite different. The re-attachment and separation angles are important because they control the size of the form loss and drag force created by the wakes at the rear of the tubes. The re-attachment angle in single-phase flow suggests it is smaller than two-phase flow, whereas the separation angle in single-phase flow suggests that it is larger than two-phase flow. Therefore, for in-line bundles, the re-attachment point is at θ_R = 55° and separation point is at θ_S = 90° for in-line bundle, deduced from Bamardouf [65]. The re-attachment point is at θ_R = 0° and separation point is at θ_S = 90° for staggered bundle. These values are chosen to best fit to the data, supported by the single-phase CFD simulations presented in this chapter.

CHAPTER 10 - AIR-WATER MODEL DEVELOPMENT

A model for the air-water tests was developed by assuming that the flow was one-dimensional. This is consistent with the void fraction experiments described in Chapter 6. The local flow around tubes in a bundle is two-dimensional, but the dominant flow direction within the whole volume of the bundle is upward. Therefore, a one dimensional flow is presently assumed to model the two-phase flow parameters. The flow is fully developed so that what occurs in one tube pitch is repeated in all others.

The single-phase flow paths in the bundles are discussed in Chapter 9. The flow begins in the minimum gap between the tubes. It decelerates as an ideal flow to the separation point, θ_S where a free expansion takes place to the reattachment point, θ_R with an ideal contraction occurring from there to the next minimum gap. In this chapter, the separation, θ_S, and re-attachment, θ_R, angles will be used to model the air-water test the in in-line and staggered bundles. The re-attachment point is at θ_R = 55° and the separation point is at θ_S = 90° for in-line bundle, deduced from Bamardouf [51] pressure distribution tests, tests that measured the pressure distribution around a tube. The modelling of flow using CFD in Chapter 9 has given an insight into separation and re-attachment angles for staggered bundle. The re-attachment point is at θ_R = 0° and separation point is at θ_S = 90° for the staggered bundle. The local void fraction measurements in the maximum and minimum gaps for all three bundles, presented in Chapter 6, is also used to develop the air-water flow model to predict the void fraction.

10.1 Void fraction model

New void fraction correlations are proposed by analysing the measured local values of void fraction in the maximum and minimum gaps between the tubes.

10.1.1 Prediction of void fraction in in-line bundles

The void fraction measured in the in-line bundles, containing tubes 38 mm in diameter on a 50 mm pitch and tubes 19 mm in diameter on a 25 mm pitch clearly demonstrated that size the of tube diameter and pitch have no significant effect on void fraction, as discussed in Chapter 6. Feenstra et al. [3] proposed the gap between the tubes, *a*, as a characteristic length since this is the space through which the flow must pass. However, the experimental data reveal that the gap between the tubes shows no effect on void fraction. Therefore, a new correlation for the prediction of void fraction is obtained by modifying the correlation by Feenstra et al. [3] for the slip ratio, *k*.

Rearranging Equations (6.7) gives

$$(k-1)\frac{P}{D} = 25.7\left(RiCa\right)^{0.5} \tag{10.1}$$

where the Richardson number is defined through Equation (6.10). The length scale, *a*, in Equation (6.10) is calculated from Equation (6.11). The experimental data show that this length scale, *a*, cannot be the correct length scale. The capillary length is therefore used, i.e.

$$a = \sqrt{\frac{\sigma}{g(\rho_l - \rho_g)}} \tag{10.2}$$

as this is a relevant physical parameter that is not dependent on physical size. The slip ratio, *k*, in Equation (10.1) is obtained from Equation (6.2), which can be re-arranged to give

$$k = \frac{x(1-\alpha)v_g}{\alpha(1-x)v_l} \tag{10.3}$$

Equation (10.1), from Freenstra et al. [3], can be expressed as power law fit i.e.

$$y = bx^n \tag{10.4}$$

where the *y* axis is given by

$$y = (k-1)(P/D) \tag{10.5}$$

and the *x* by

$$x = RiCa \tag{10.6}$$

The measured void fraction in the maximum and minimum gaps for both bundles were combined and the values of constant, *b* and exponent, *n* sought. Figure 10.1 shows the data for both gaps. The maximum gap slip ratio is correlated by

$$k = 1 + 38.3\frac{D}{P}(RiCa)^{0.6} \tag{10.7}$$

and the minimum gap value by

$$k = 1 + 52.3\frac{D}{P}(RiCa)^{0.6} \tag{10.8}$$

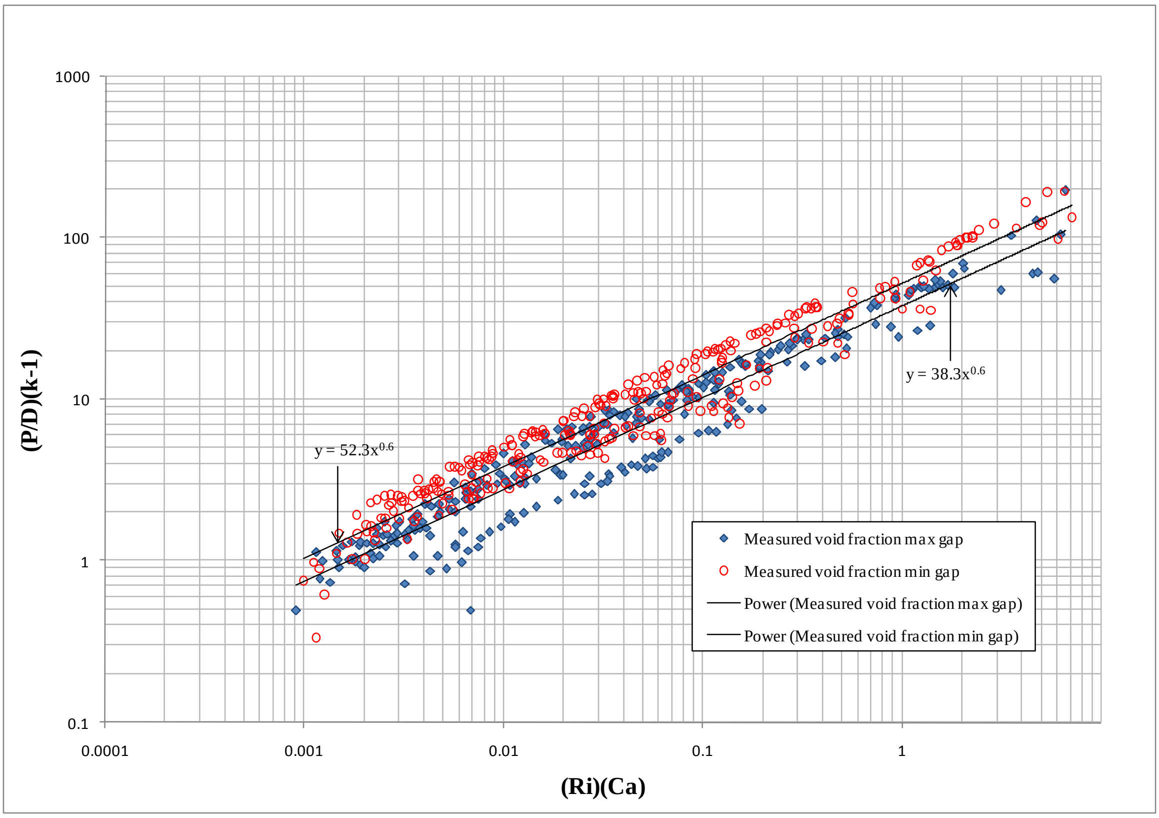

Figure 10.1: Slip model for minimum and maximum gap in inline bundles

The predicted void fraction is then calculated using Equation (6.8-6.10), (10.2), (10.3), (10.7) and (10.8). The predicted and measured void fractions for each bundles maximum and minimum gaps are then compared and shown in Figures 10.2-10.5. The comparison of the 38 mm and 19 mm diameter bundle data from the maximum gap with the predictions are shown in Figures 10.2 and 10.3. The predicted void fraction for the small tube bundle is closer to the measured values than the bigger tube bundle. The mean difference for the 38 mm bundle is -5.25% and the RMS difference is 10.56% while for the 19 mm in-line bundle, the mean difference is 1.95% and RMS difference is 6.67%. The predicted void fraction in the minimum gap of both bundles shows the same trend when compared to measured void fractions in Figure 10.4 and 10.5. The mean difference is -2.06% and the RMS difference is 10.37% for the 38 mm bundle while they are 3.72% and 10.95% respectively for the 19 mm bundle. As discussed in Chapter 6, the measured void fraction for both bundles show almost the same values. Therefore, the predicted void fraction for both bundles in the maximum and minimum gap show only a small difference when comparing against each other. The predicted void fraction values for these gaps will be used in the prediction of the pressure drop in each tube bundle.

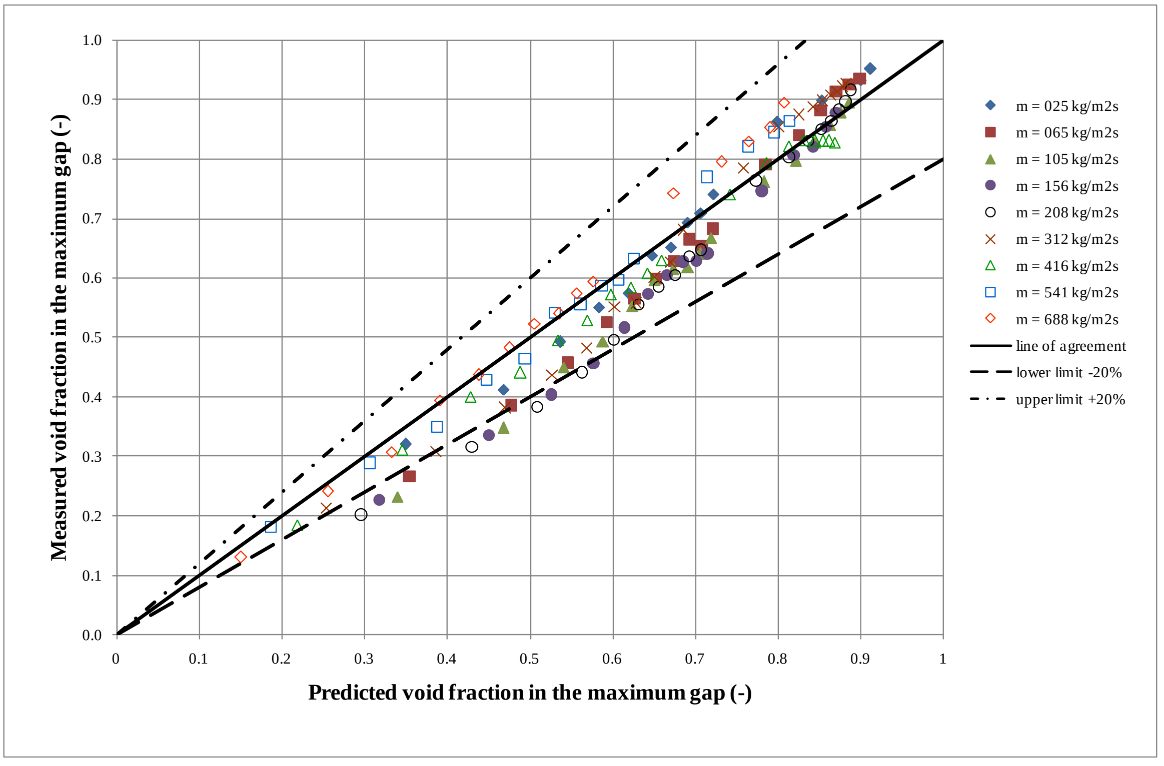

Figure 10.2: Measured void fraction comparison with model prediction in the maximum gap in 38 mm in-line bundle

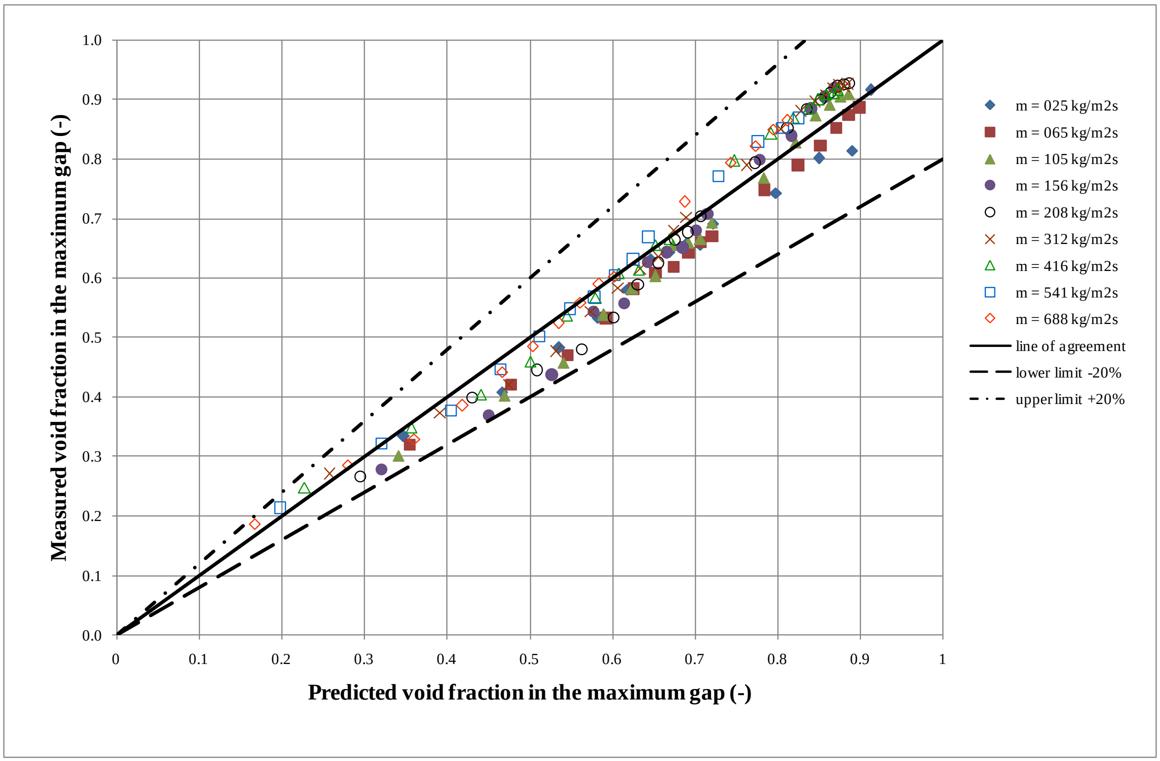

Figure 10.3: Measured void fraction comparison with model prediction in the maximum gap in 19 mm in-line bundle

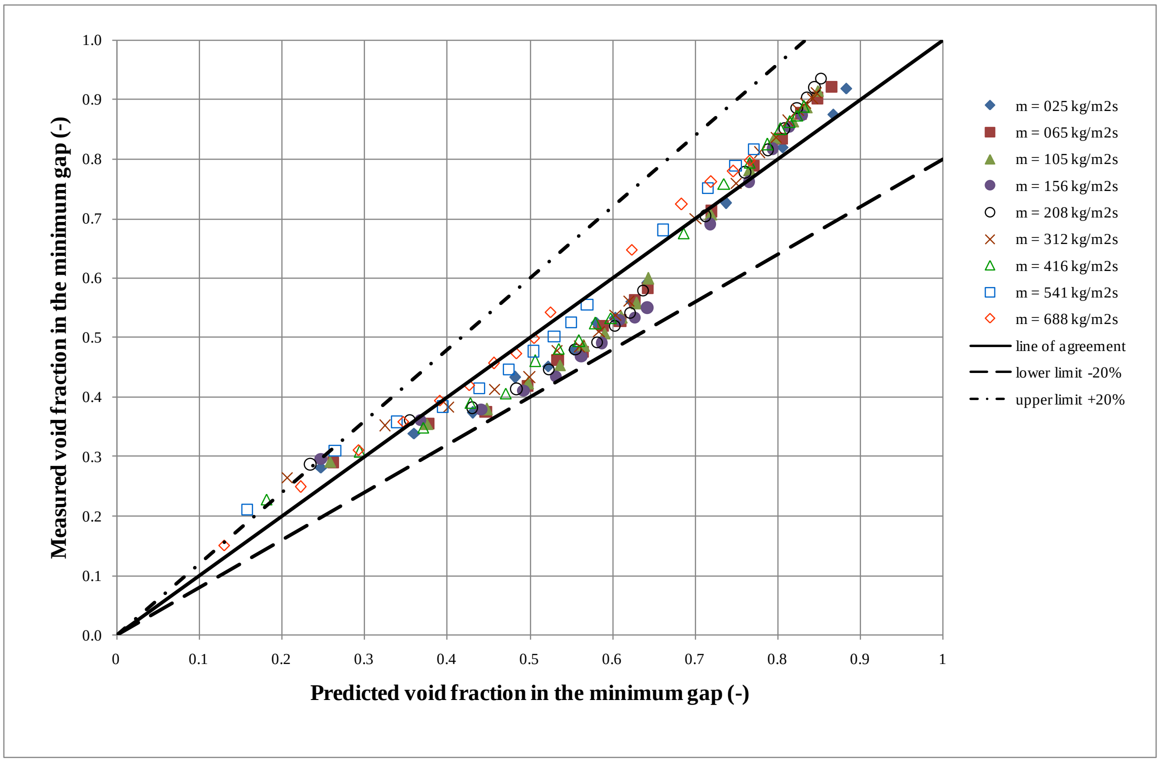

Figure 10.4: Measured void fraction comparison with model prediction in the minimum gap in 38 mm in-line bundle

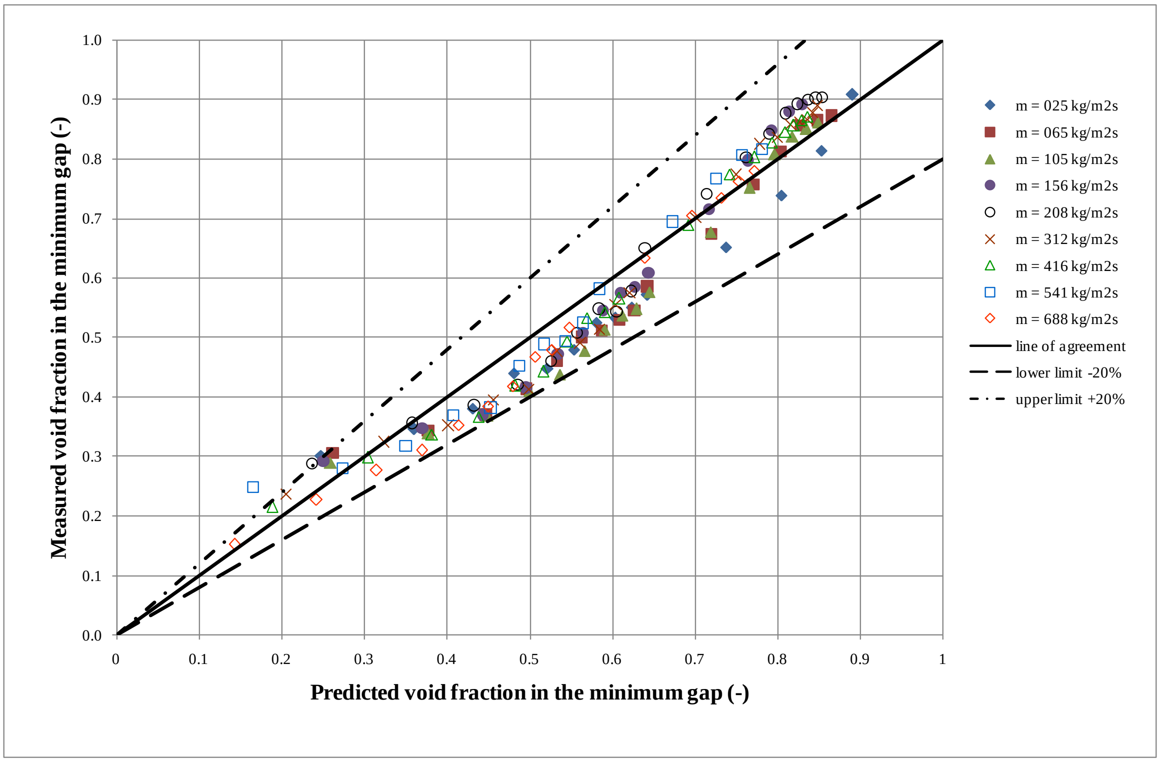

Figure 10.5: Measured void fraction comparison with model prediction in the minimum gap in 19 mm in-line bundle

10.1.2 Prediction of void fraction in staggered bundles

The void fraction correlation is again deduced from the measured local values of void fractions in the maximum and minimum gaps between the tubes. The equations used are the same as those in the in-line bundle, i.e. Equation (10.1) to Equation (10.6), but the slip ratio, *k* is different for both locations. In the maximum gap between the tubes, the slip ratio, *k* is obtained from

$$k = 1 + 29.6\frac{D}{P}(RiCa)^{0.6} \tag{10.9}$$

and the minimum gap value by

$$k = 1 + 34.9\frac{D}{P}(RiCa)^{0.5} \tag{10.10}$$

The values of constant, *b* and exponent, *n* sought from Figure 10.6 that shows the data for both gaps.

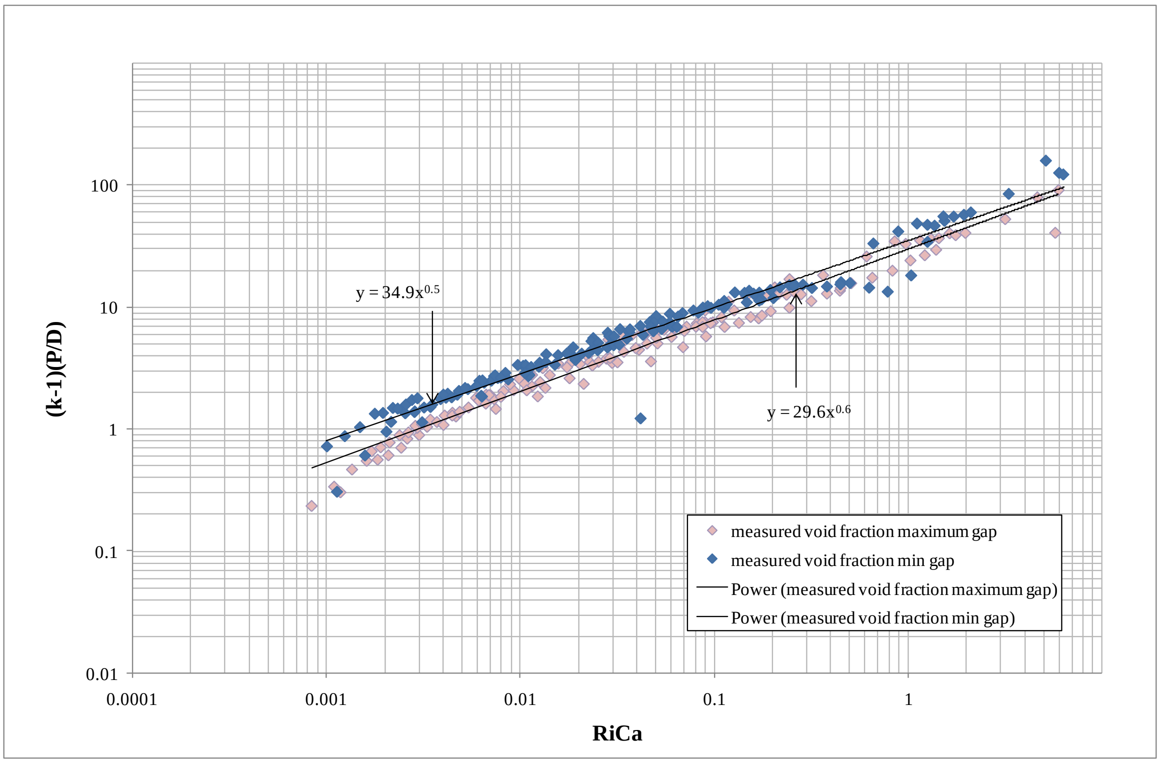

Figure 10.6: Slip model for minimum and maximum gap in the staggered bundle

The predicted void fraction in the staggered bundle is then calculated using Equation (6.8-6.10), and Equation (10.2) and Equation (10.3). Again, instead of using *a*, the characteristic length, which is in Feenstra et al. correlations [3], the proposed new correlation used the characteristic length, *a*, defined in Equation (10.2). The predicted and measured void fraction in the maximum gap between the tubes is shown in Figures 10.7. The predicted void fractions agree well with the measured data within the bounded limit of ± 20%. The average difference is -1.27% and the RMS 5.17%. The predicted void fractions in the minimum gap between the tubes also show a good result where the average difference is -1.18% and the RMS 5.41%.

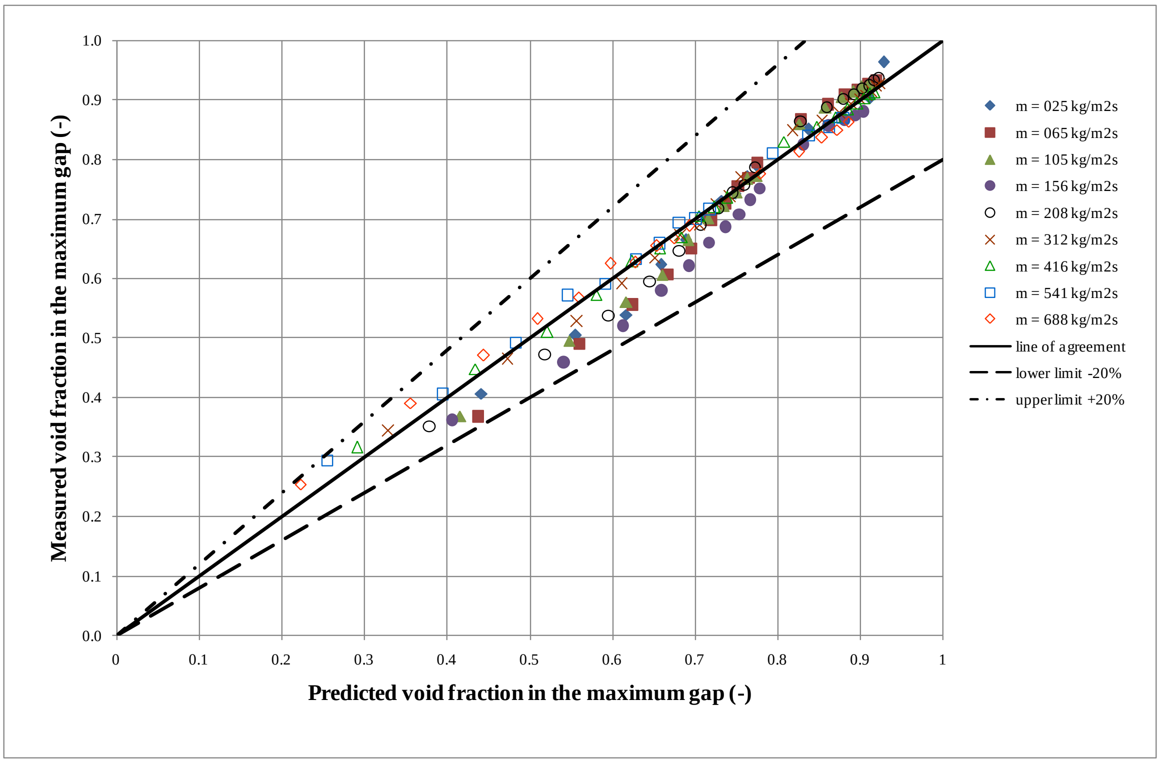

Figure 10.7: Measured void fraction comparison with model prediction in the maximum gap in 19 mm staggered bundle

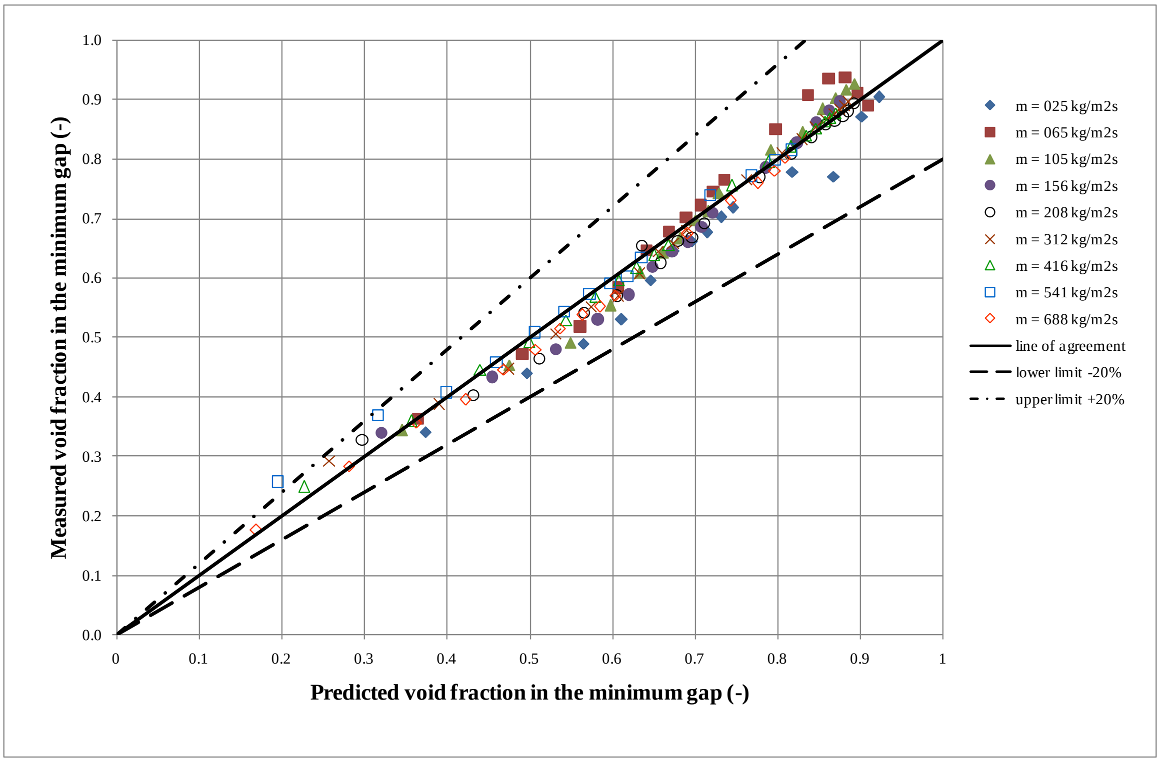

Figure 10.8: Measured void fraction comparison with model prediction in the minimum gap in staggered bundle

10.2 Pressure drop model

The proposed pressure drop model includes a liquid film, an acceleration and a gravitational pressure drop, as shown in Figure 10.9. In the region between re-attachment and separation, acceleration dominates. In the region between separation and re-attachment, the pressure change due is dominated by friction. The flow in the region between the separation point and the top of the tube has a total pressure gradient equivalent to the static liquid value. Thus, a liquid film is assumed to exist on part of the upper half of the tubes. The model uses the void fraction correlations discussed in Section 10.1. The predictions are based on the average of the void fraction measurements in the minimum and the maximum gaps between the tubes. This is applied to in-line and staggered bundles. The flow around the tube and the separated flow that occur behind the tube, affect significantly the mass, momentum and energy transfer. The wake behind the tubes results in shedding of vortices where the large kinetic energy produced by acceleration of the fluid is dissipated in the eddies, i.e. pressure loss, and thus affects the pressure drop in the heat exchanger. The proposed analysis for predicting pressure drop is introduced in the hope of developing a more physical prediction of two-phase flow in heat exchangers.

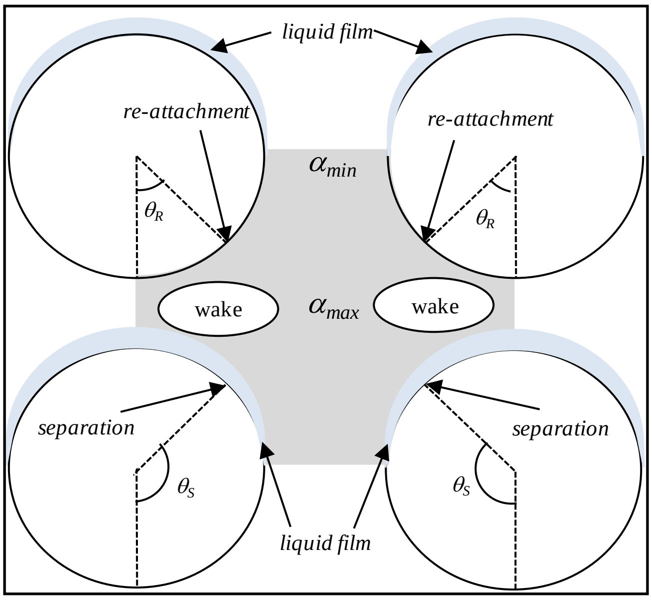

Figure 10.9: The pitch pressure drop model includes a liquid film, an acceleration and a gravitational pressure drop, in the gray shaded area

The most commonly used model for predicting two-phase flow is the homogenous flow model, which assumes that the two phases are well mixed and travelling at the same velocity. However, this model tends to overpredict the momentum fluxes in pipe lengths and the pressure drops in nozzles. Thus, the separated flow model is proposed. The momentum correction factor, c_m, is given by

$$c_m = (x + k(1-x))\left[x + \frac{(1-x)}{k^2} \right] \tag{10.11}$$

The slip ratio is found from the average void fraction in the gap. Equation (10.3) gives

$$k = \frac{x v_g (1-\alpha_{avg})}{\alpha_{avg}(1-x) v_f} \tag{10.12}$$

where the average void fraction, α_{avg}, is calculated using the minimum and maximum void fraction predictions from the correlation proposed in Section 10.1 as

$$\alpha_{avg} = \frac{\alpha_{\max} + \alpha_{\min}}{2} \tag{10.13}$$

The acceleration pressure gradient associated with this model is

$$\left(\frac{dp}{dy}\right)_A = -m \frac{d(c_m v m)}{dy} \tag{10.14}$$

where the mixture specific volume, v is determined from the separated flow model equations, as

$$v = \frac{x v_g + k(1-x) v_l}{x + k(1-x)} \tag{10.15}$$

The product of the correction factor and specific volume, $c_m v$ is assumed constant, i.e.

$$c_m v = \overline{c_m v} = \text{constant} \tag{10.16}$$

Equation (10.15) becomes

$$\left(\frac{dp}{dy}\right)_A = -\overline{c_m v}\frac{d}{dy}\left[\frac{m^2}{2}\right] \tag{10.17}$$

For flow between the re-attachment and separation points, this gives

$$\Delta P_A = \frac{\overline{c_m v}}{2}\left(m_S^2 - m_R^2\right) \tag{10.18}$$

A mass balance between the flow in the passage at θ and the minimum gap gives

$$m(P - D\sin\theta) = m_{\max}(P - D) \tag{10.19}$$

where θ is the angle from the leading point on the cylinder to the vertical position y, as shown in Figure 10.10.

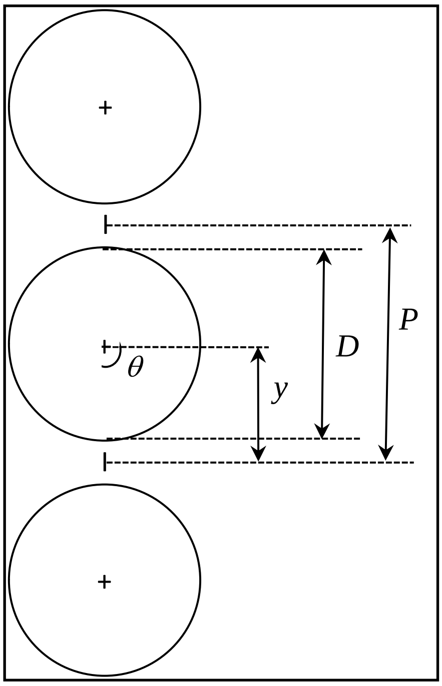

Figure 10.10: The *y* and *θ* in the bundle

The pressure drop due to acceleration is therefore obtained from

$$\Delta p_A = m^2 (P-D)^2 \left[\frac{1}{\left(P - D\sin\theta_s\right)^2} - \frac{1}{\left(P - D\sin\theta_R\right)^2} \right] \frac{\overline{c_m v}}{2} \tag{10.20}$$

It is assumed that the separation angle varies with quality. The separation angle, θ_S is obtained from the angle correlated from the data and gives

$$\theta_S = \max(bx + c, 90) \tag{10.21}$$

where x is a quality. When the quality is equal to zero, the separation angle is the single-phase value of 120°. As quality increases, the separation angle decreases until 90°. The angle is calibrated by decreasing the separation angle from 120° until the model predicts the pressure drop at the largest quality for that mass flux, then the separation angle for the largest quality for that mass flux has been found. This was repeated for all mass fluxes. This produced a straight line i.e. the equation for the separation angle for the model is

$$\theta_S = bx + c \tag{10.22}$$

where b = - 222.44 and c = 109.43 for the 38 mm in-line tube bundle whereas for the 19 mm in-line tube bundle, b = - 488.76 and c = 119.96. Figure 10.11 and 10.12 show the separation angle equations used for both in-line bundles. The separation angle can not go below 90°, so the minimum separation angle is 90°. For the staggered bundle, the separation angle is 90°, obtained from the single-phase simulation in Chapter 9. The re-attachment angle, θ_R = 55° for in-line bundles, and θ_R = 0° for the staggered bundle.

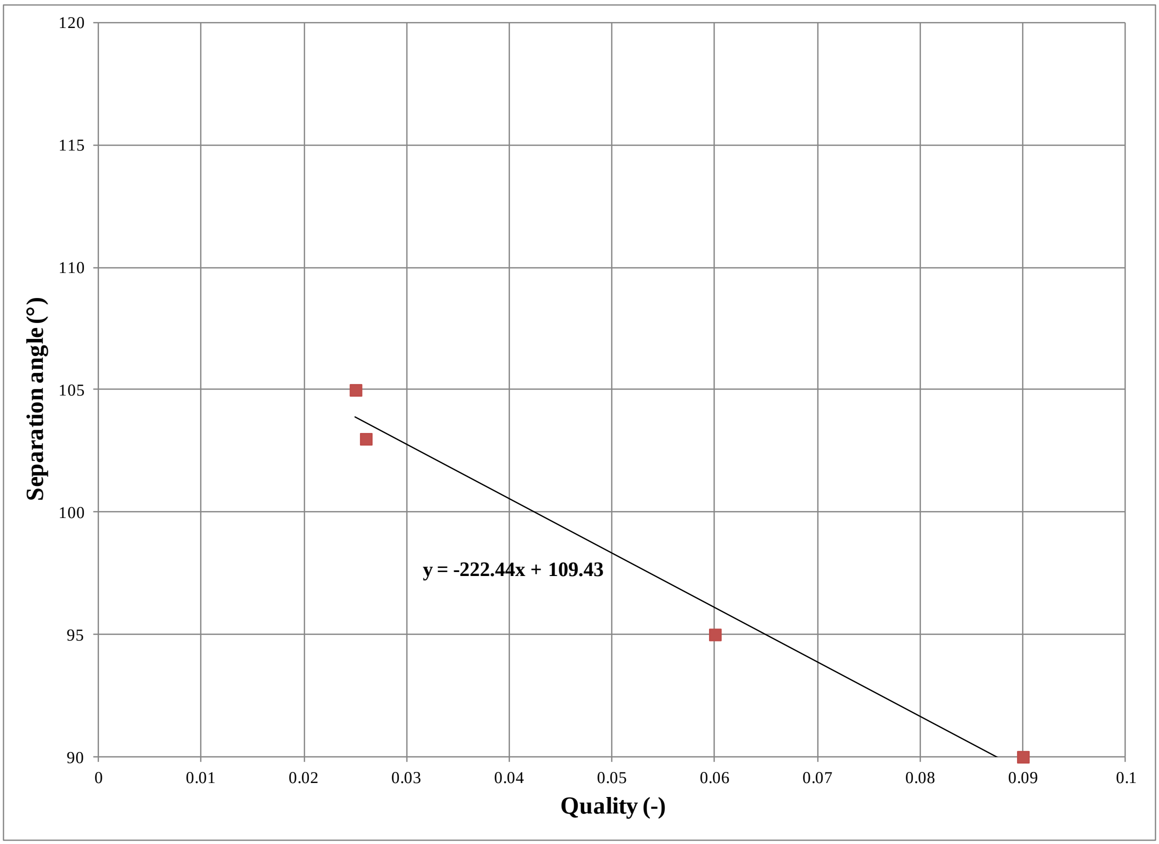

Figure 10.11: The separation angle for 38 mm in-line bundle is θ_s = - 222.44x+ 109.43

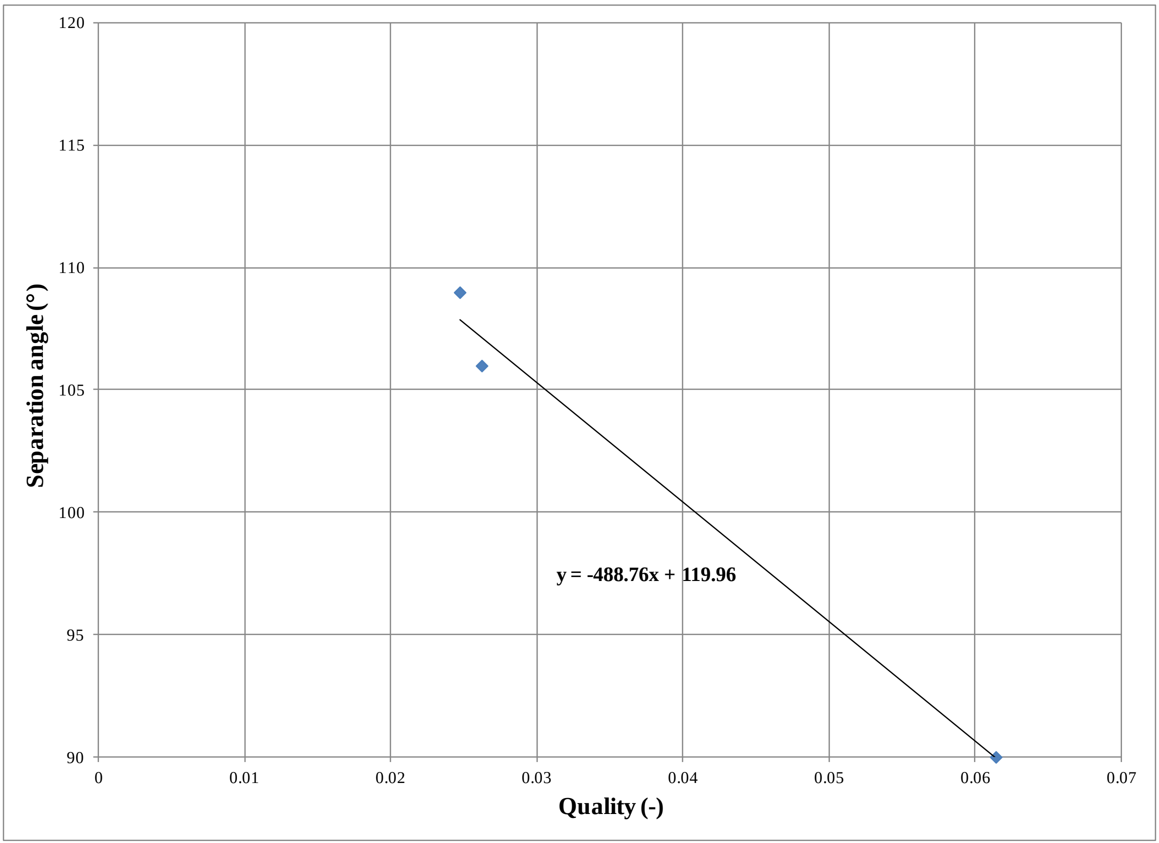

Figure 10.12: The separation angle for 19 mm in-line bundle is θ_s = - 488.76x + 119.96

The total pressure drop is obtained from

$$\frac{dp}{dz} = \left(\frac{dp}{dz}\right)_A + \left(\frac{dp}{dz}\right)_G + \left(\frac{dp}{dz}\right)_{LF} \tag{10.23}$$

where the gravitational pressure drop is calculated using Equation (2.16). The two-phase density is obtained from

$$\rho_{tp} = \alpha_{avg}\rho_g + (1-\alpha_{avg})\rho_l \tag{10.24}$$

where α_{avg} is the average between the maximum and minimum predicted void fractions.

The friction liquid film is a pressure drop due to liquid film trapped above the tubes, and it is obtained from

$$\left(\frac{dp}{dz}\right)_{LF} = \rho_l g \frac{D}{2} C \tag{10.25}$$

where C is a constant for the liquid film that gives the minimum RMS difference between the model predictions and the data. The constant for 38 mm tube in-line, 19 mm tube in-line and 19 mm tube staggered are C_1 = 0.24, C_2 = 0.49 and C_3 = 0.08 respectively. The constant for in-line bundles has doubled when increasing the tube diameter, so Equation (10.25) can be written as

$$\left(\frac{dp}{dz}\right)_{LF} = \rho_l g \frac{C}{2}\frac{D}{P} \tag{10.26}$$

10.2.1 Prediction of pressure drop in in-lines bundles

Figure 10.13 shows the comparison between predicted and measured pressure drops in the 38 mm in-line bundle. The average error is 8% and the RMS error is 15%. The predicted pressure drop compares well at all mass fluxes where most of the data points are within the bounds of ±30%.

A comparison between the predicted and measured pressure drops for the 19 mm in-line bundle is shown in Figure 10.14. The agreement is shown to be reasonable at smaller mass fluxes. The average error is 28% and the RMS error is 35% for the 145 data points.

The predicted pressure drop is a total of pressure drop due to acceleration, gravitational and liquid friction due to the liquid film trapped above the separation point, Equation (10.23). The flow around the tube and the wake at the rear of tube causes the frictional pressure drop. The kinetic energy from the acceleration of the fluid is dissipated in the eddies. The model predictions are compared with the measured data for the lowest, mid and highest mass flux in Figures 10.15, 10.17 and 10.19 respectively for the 38 mm in-line bundle. Also included in the figures is the predicted friction pressure drop from Xu et al. [5], with the predicted void fraction used for the gravity components. These figures compare the new model with the Xu et al. [5] model and the data. These mass fluxes are examples of gravity-dominated and inertia-dominated flow regimes. Shown in Figures 10.16, 10.18 and 10.20 are the corresponding pressure drop components.

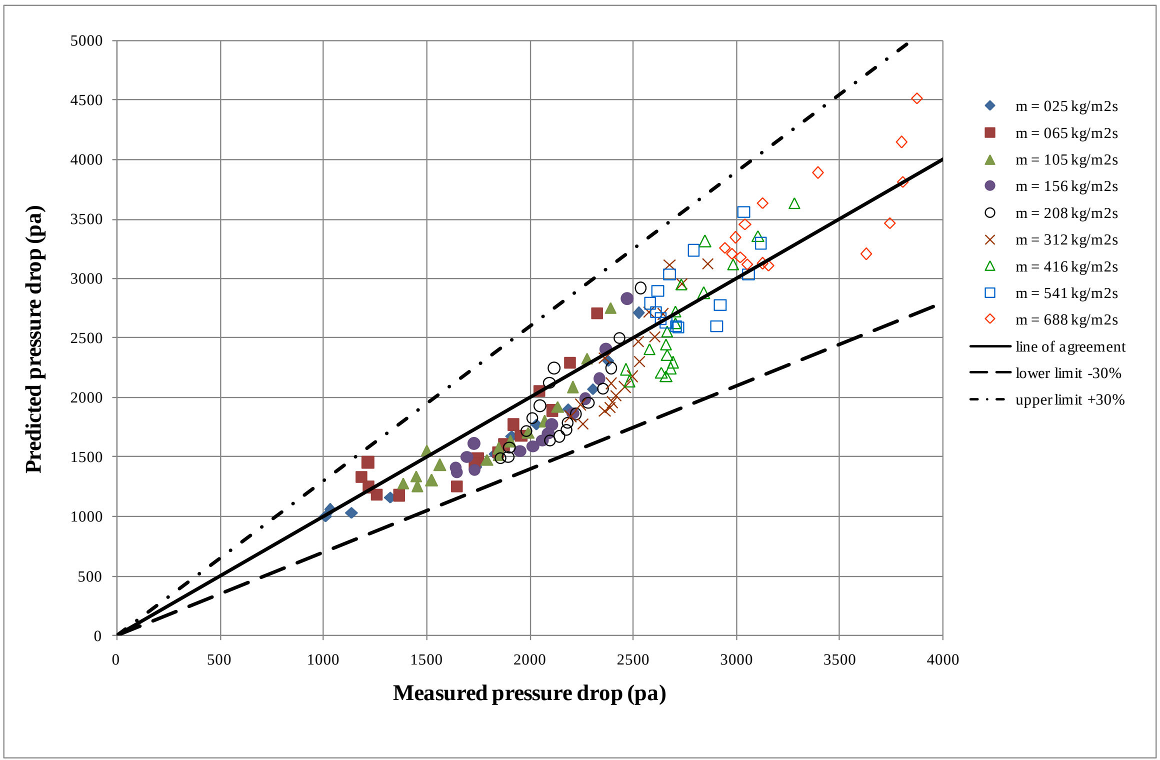

Figure 10.13: Prediction pressure drop against measured pressure drop in 38 mm in-line bundle

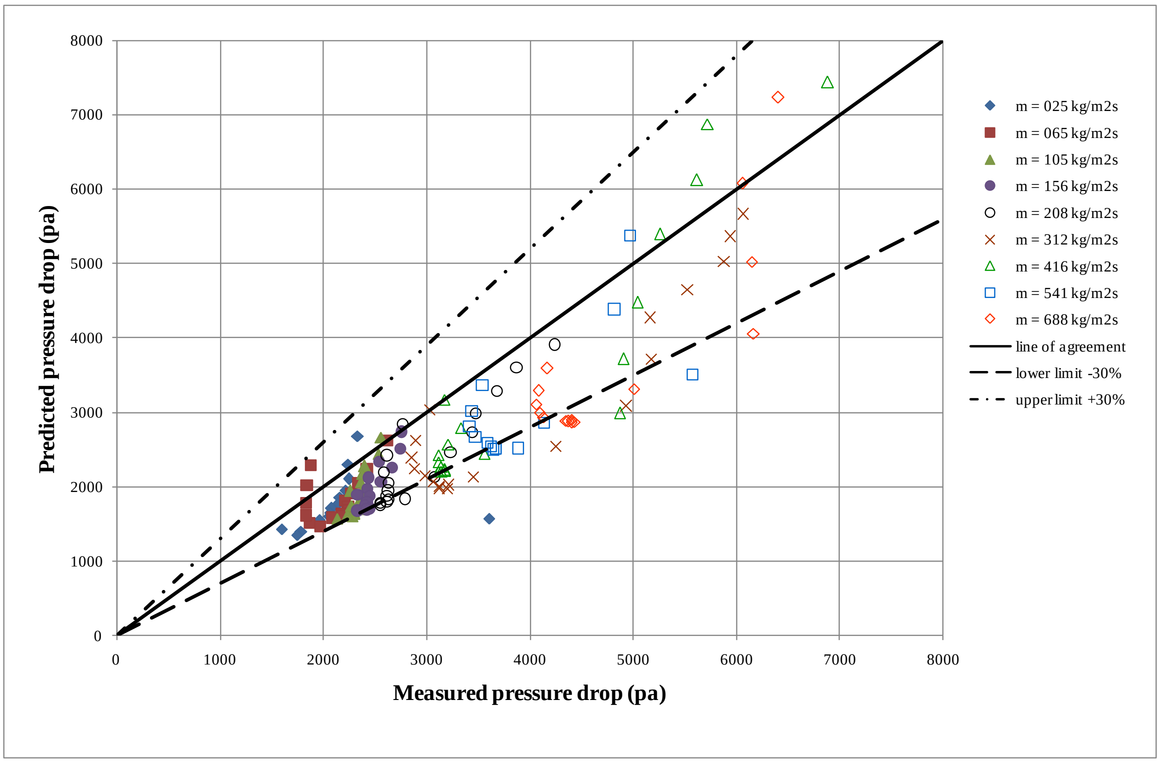

Figure 10.14: Prediction pressure drop against measured pressure drop in 19 mm in-line bundle

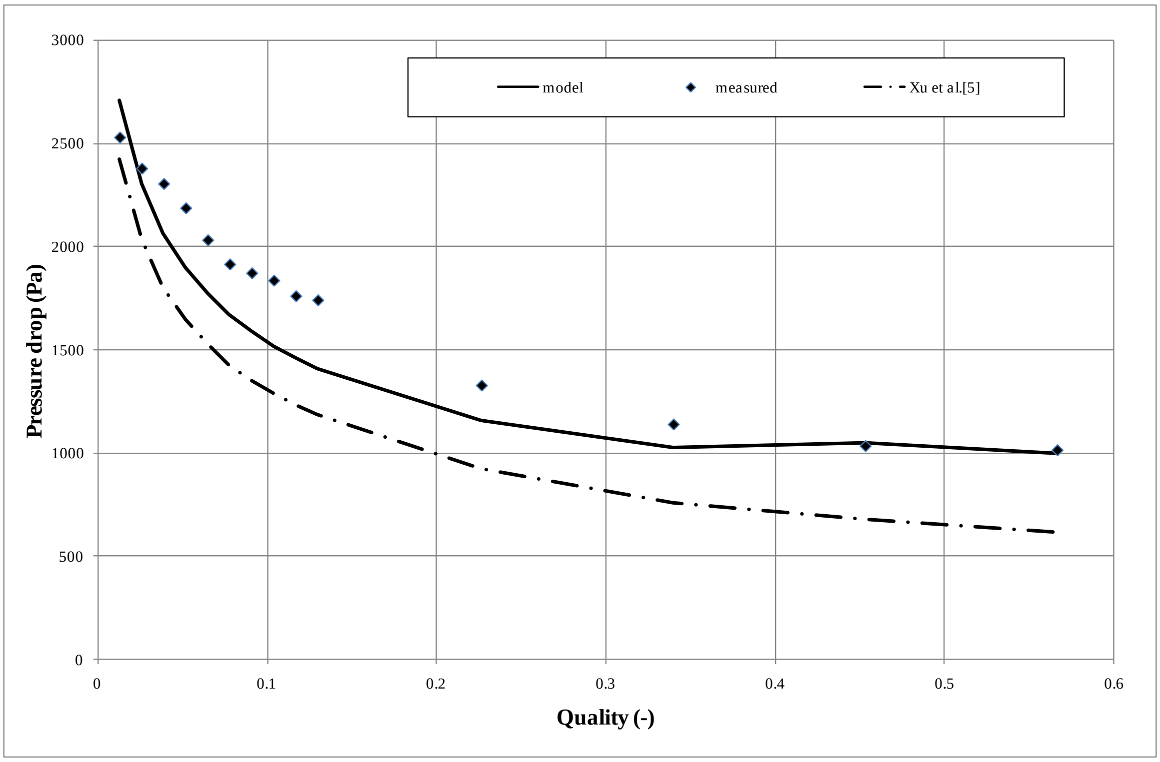

Figure 10.15: Variation of pressure drop with quality at 25 kg/m^{2}s for 38 mm in-line bundle

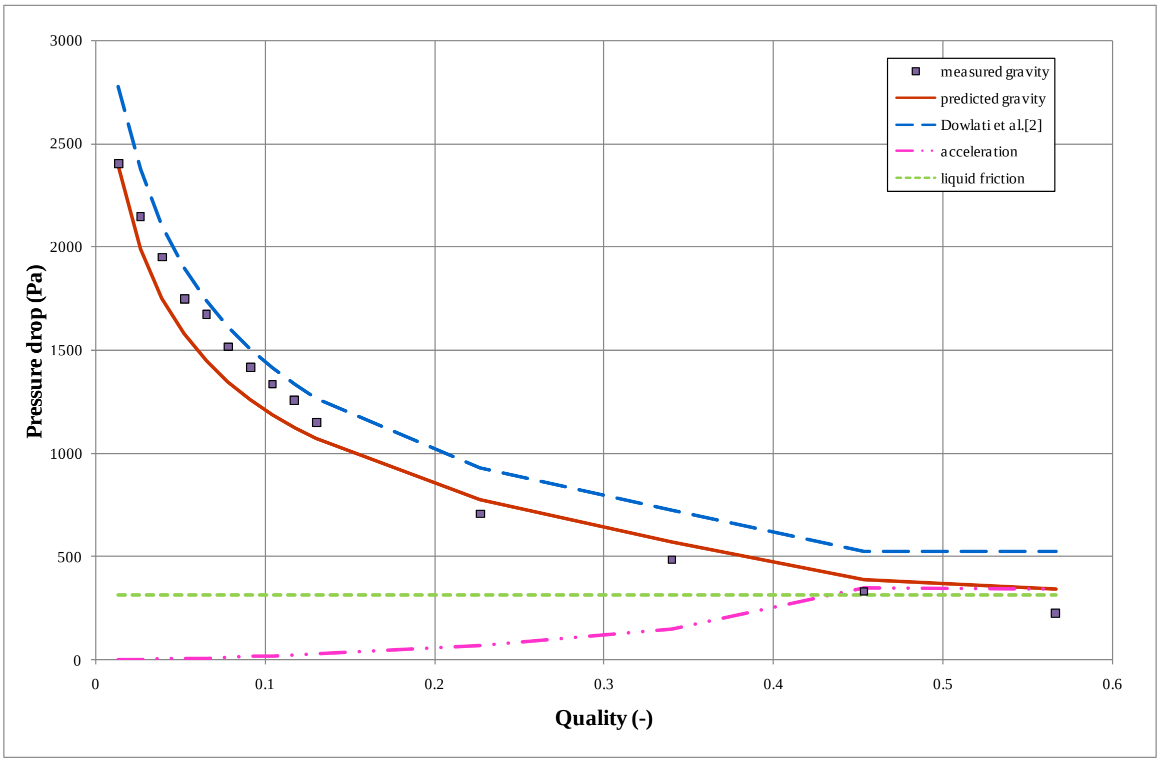

Figure 10.16: Variation of measured gravity and predictions with quality at 25 kg/m^{2}s for 38 mm in-line bundle

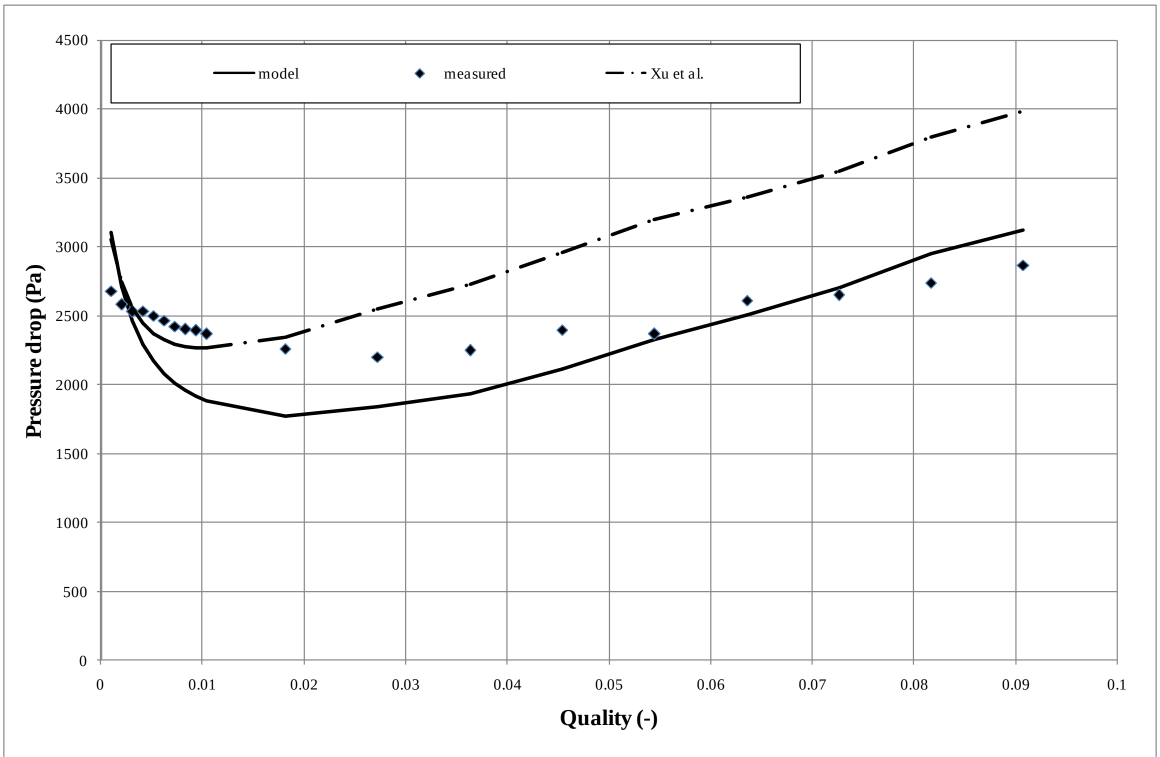

Figure 10.17: Variation of pressure drop with quality at 312 kg/m^{2}s for 38 mm in-line bundle

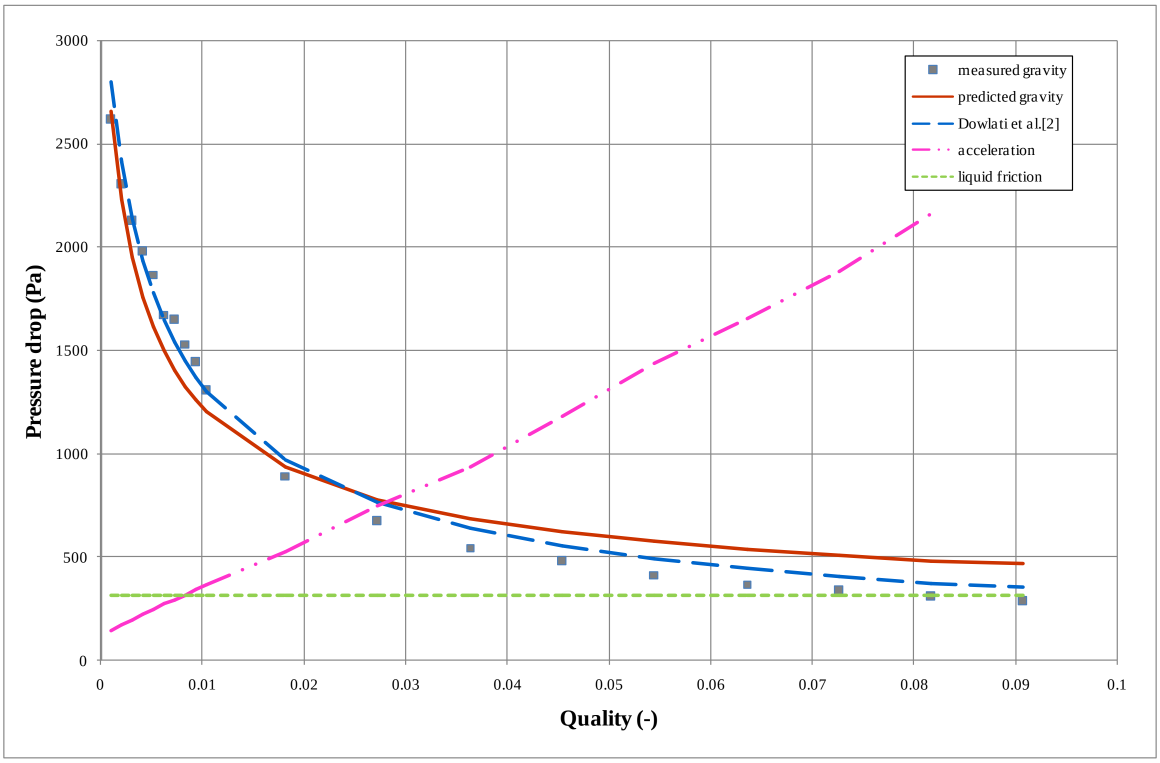

Figure 10.18: Variation of measured gravity and predictions with quality at 312 kg/m^{2}s for 38 mm in-line bundle

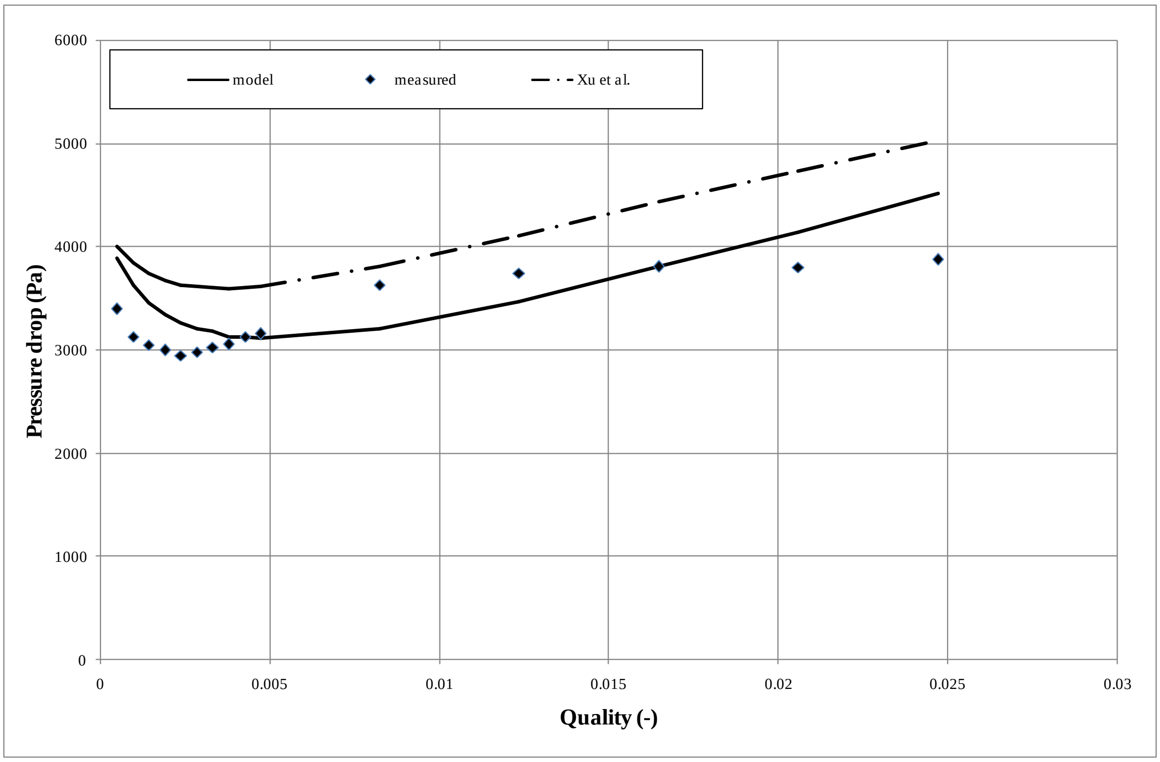

Figure 10.19: Variation of pressure drop with quality at 688 kg/m^{2}s for 38 mm in-line bundle

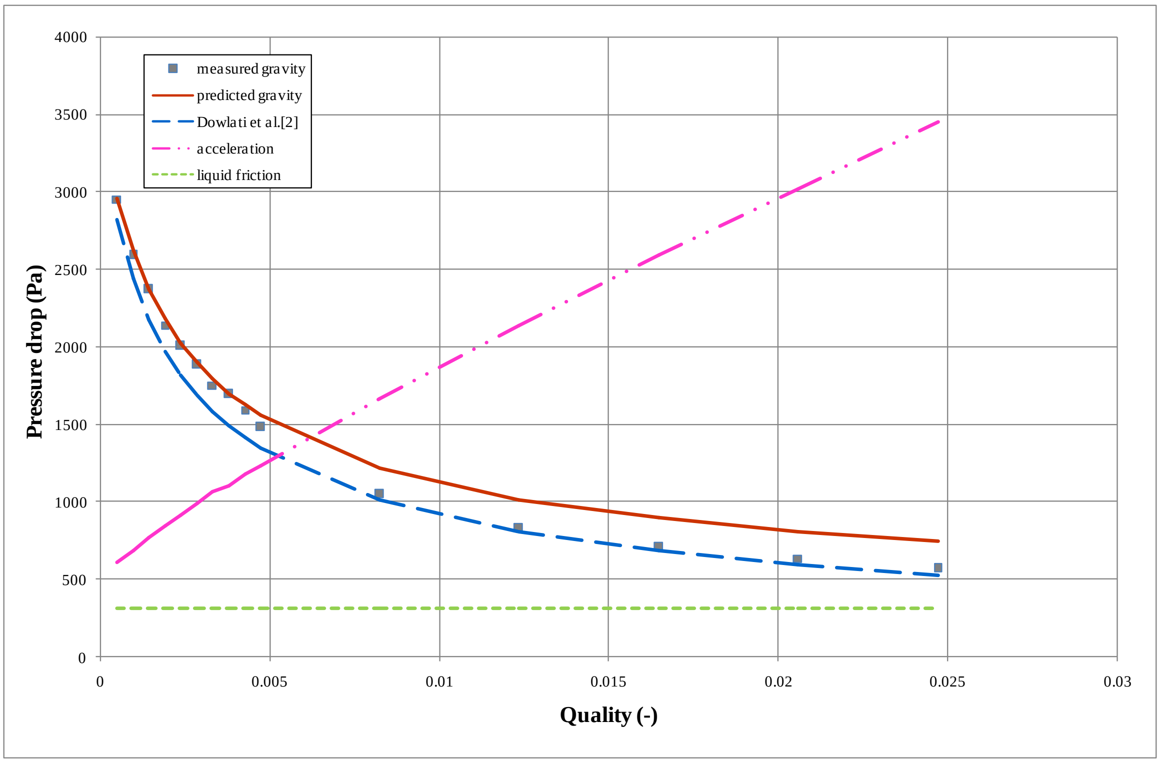

Figure 10.20: Variation of measured gravity and predictions with quality at 688 kg/m^{2}s for 38 mm in-line bundle

The model agrees well with the measured data at the lowest mass flux of 25 kg/m^{2}s, Figure 10.15 and it is better than the prediction of Xu et al. [5]. Figure 10.16 shows the pressure drop components at a mass flux of 25 kg/m^{2}s. At this low mass flux, the gravity pressure drop continues to fall as the quality increases. The gravity pressure drop is decreasing, resulting from the increase of void fraction as the quality increases, faster than the acceleration pressure drop increases. The gravity pressure drop prediction, Figure 10.16 uses the predicted void fraction, and agrees well with the data. The prediction is an improvement on Dowlati et al. [7]. This demonstrates that the model is capable to predict the gravity pressure drop and that low mass flux flows are dominated by gravity.

The comparison between the data and the model and Xu et al. [5] at a mass flux of 312 kg/m^{2}s is shown in Figure 10.17. The model predicts the pressure drop at the mid-range and is an improvement over Xu et al. [5]. The turning point in the pressure drop is produced at lower qualities because the increase in acceleration pressure drop is higher than the decrease in gravitational pressure drop, shown in Figure 10.18.

The model follows the data well at the high mass flux of 688 kg/m^2s, and the turning point is also showed, Figure 10.19. The model again predicts the data better than Xu et al [5]. At low quality, the gravitational component is falling faster than the increase in the acceleration component, Figure 10.20. However, as the quality increases, the acceleration pressure drop continually increases, and dominates at higher qualities. These figures, i.e. Figures 10.16, 10.18 and 10.20 demonstrate that the gravity is dominant at the lower mass fluxes and acceleration is dominant at higher mass fluxes.

The comparison between the measured and total pressure drop model, which contains the acceleration component, gravitational component and liquid film on the top of the tubes for the 19 mm in-line tube bundle is shown in Figures 10.21, 10.23 and 10.25. Also included in the graphs are the Xu et al. [5] prediction. The model is better at the lowest mass flux of 25 kg/m^2s, but poorer at the mid-range and highest mass flux, compared to Xu et al. [5].

Figures 10.22, 10.24 and 10.26 show the model pressure drop components and the gravity predictions and measured data for the lowest, mid and highest mass fluxes respectively for the 19 mm in-line bundle. The trend is similar to the 38 mm tube bundle. These figures also show the gravity dominance at the lower mass fluxes, and acceleration dominance at the higher mass fluxes. However, the model acceleration pressure drop is shown to be low, possibly because of column flow interactions.

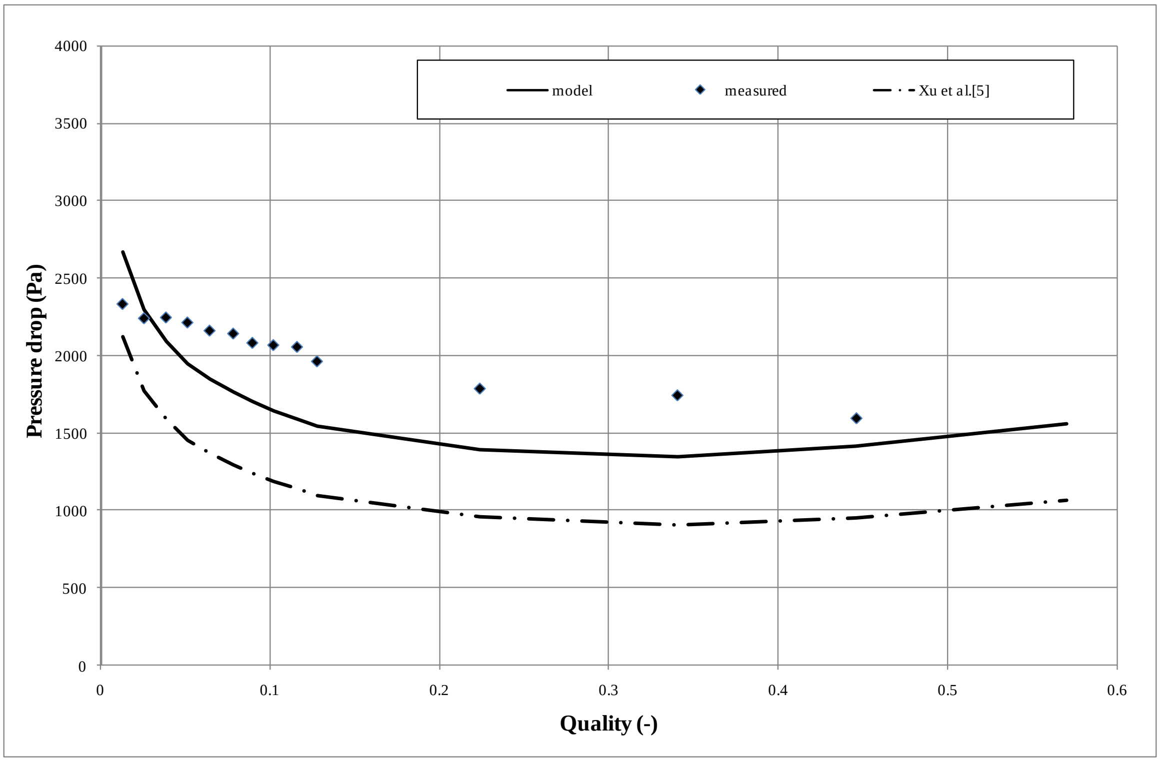

Figure 10.21: Variation of pressure drop with quality at 25 kg/m^{2}s for 19 mm in-line bundle

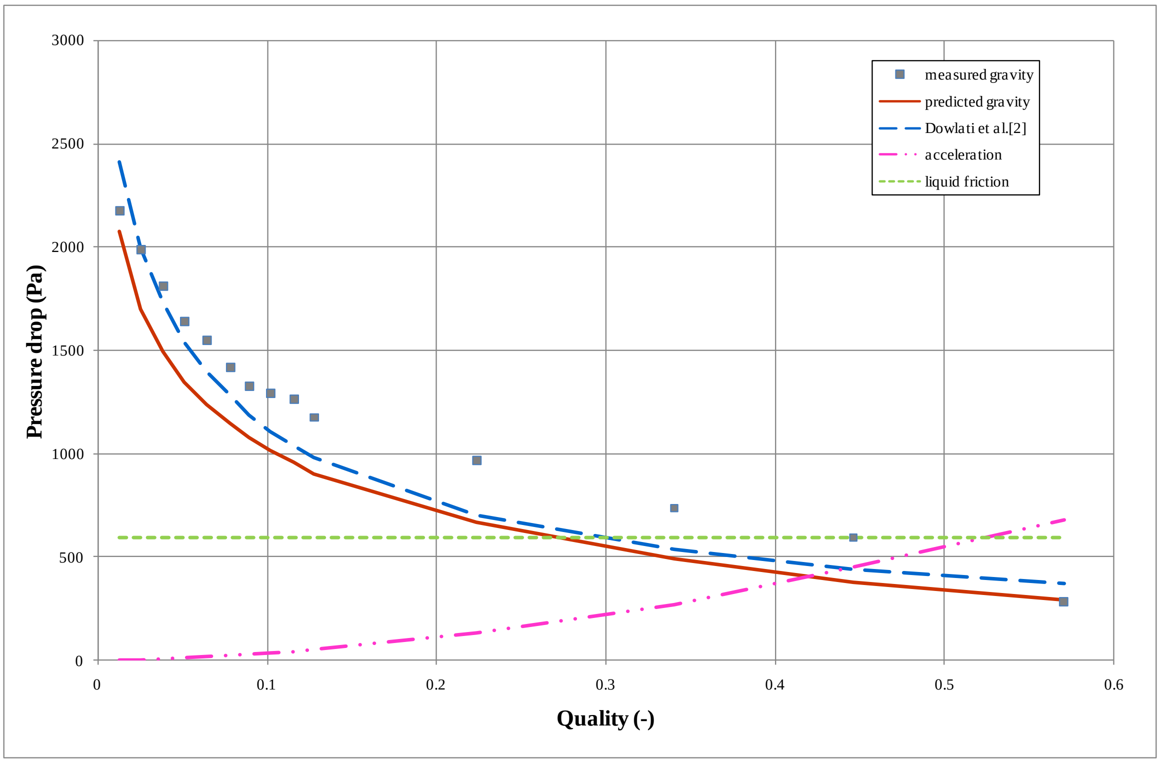

Figure 10.22: Variation of measured gravity and predictions with quality at 25 kg/m^{2}s for 19 mm in-line bundle

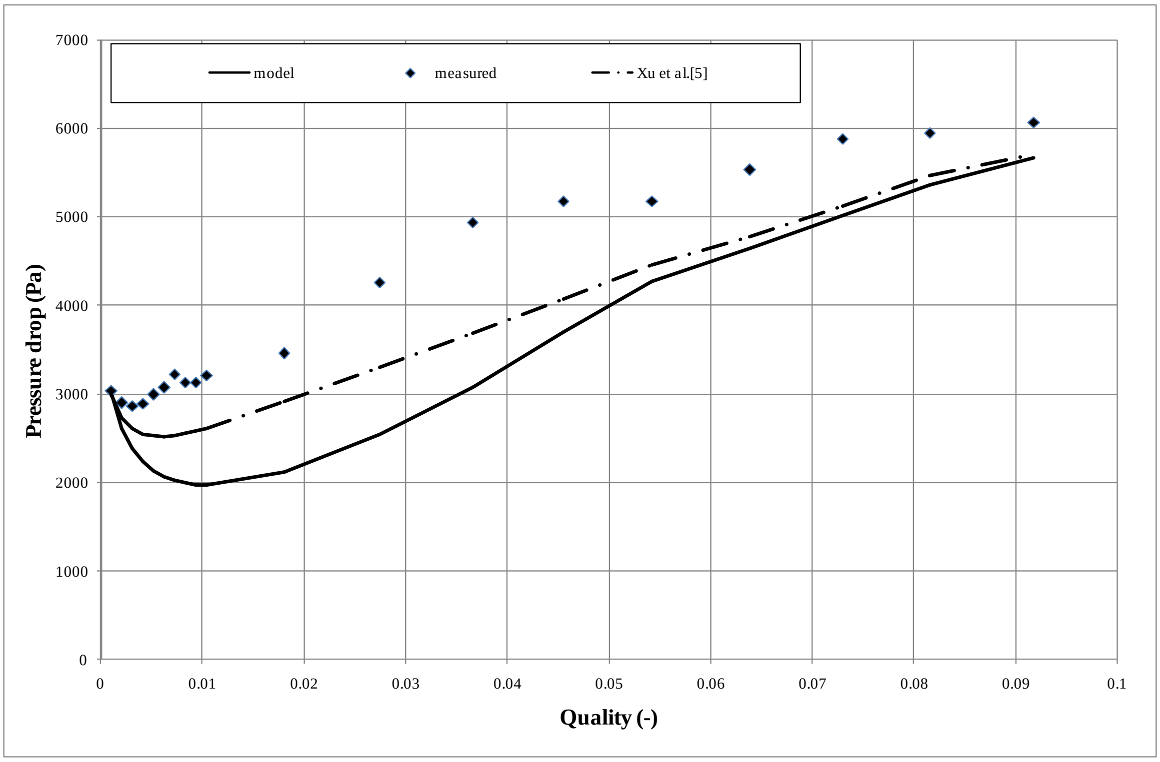

Figure 10.23: Variation of pressure drop with quality at 312 kg/m^{2}s for 19 mm in-line bundle

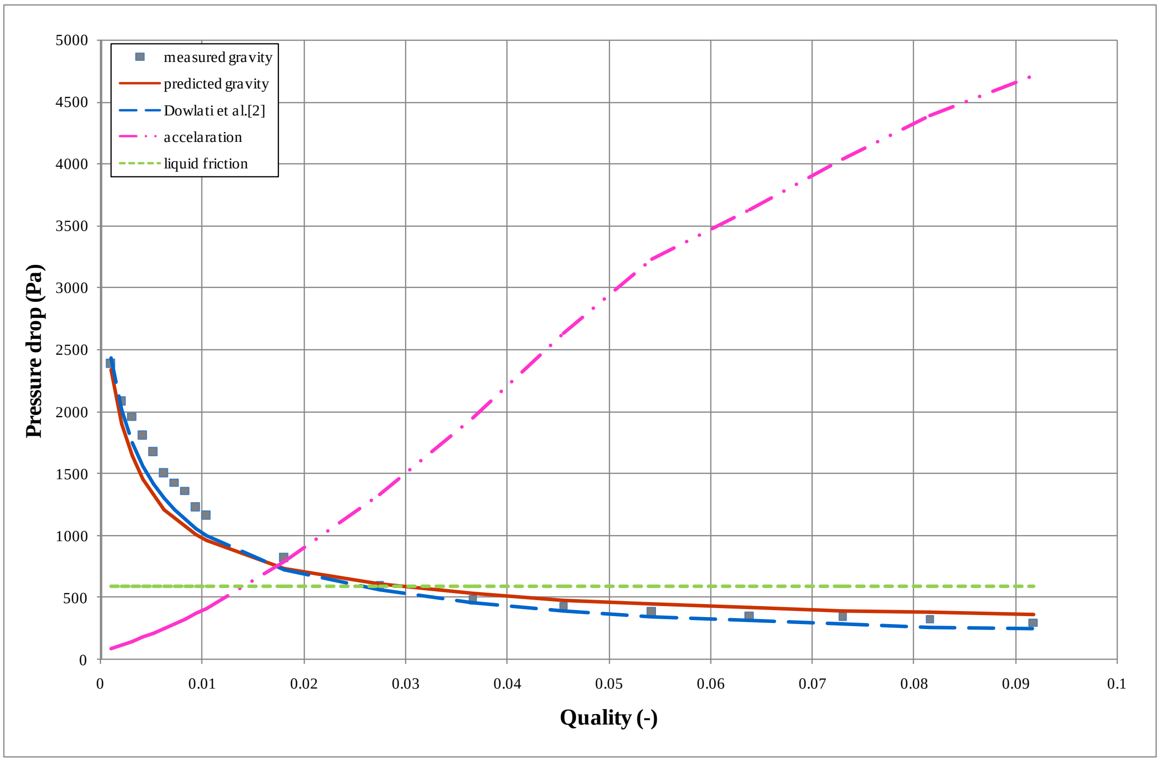

Figure 10.24: Variation of measured gravity and predictions with quality at 312 kg/m^{2}s for 19 mm in-line bundle

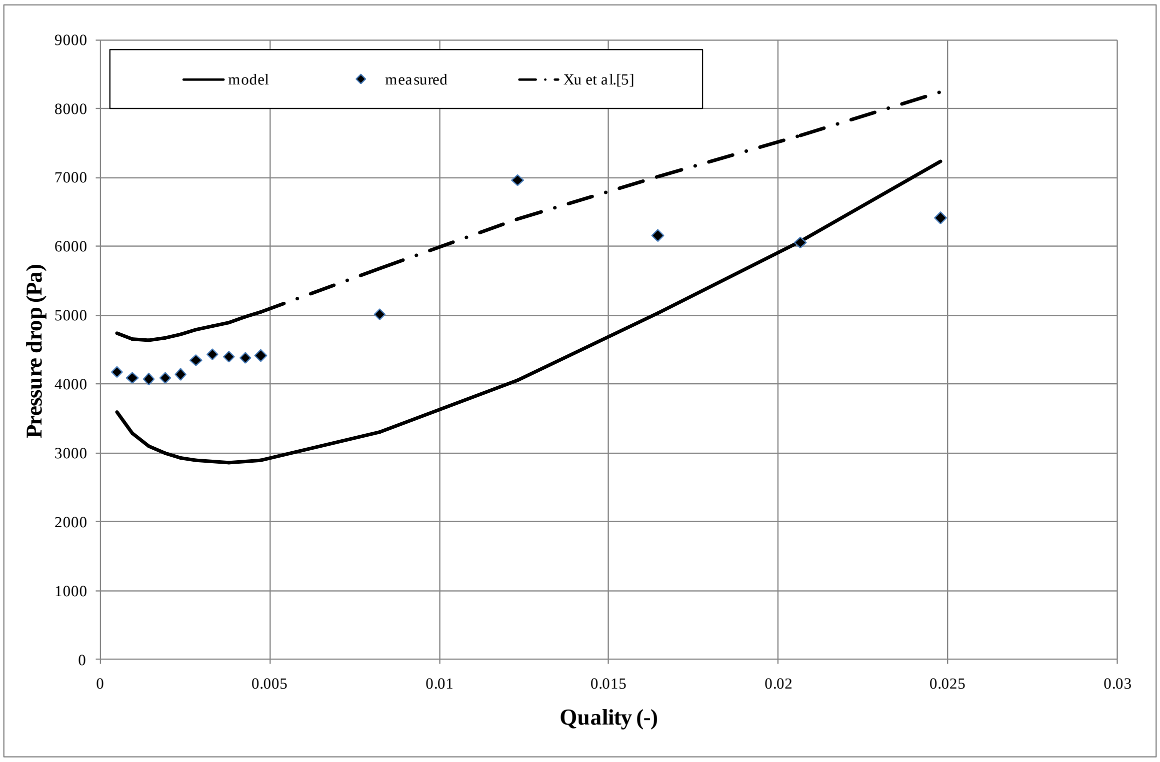

Figure 10.25: Variation of pressure drop with quality at 688 kg/m^{2}s for 19 mm in-line bundle

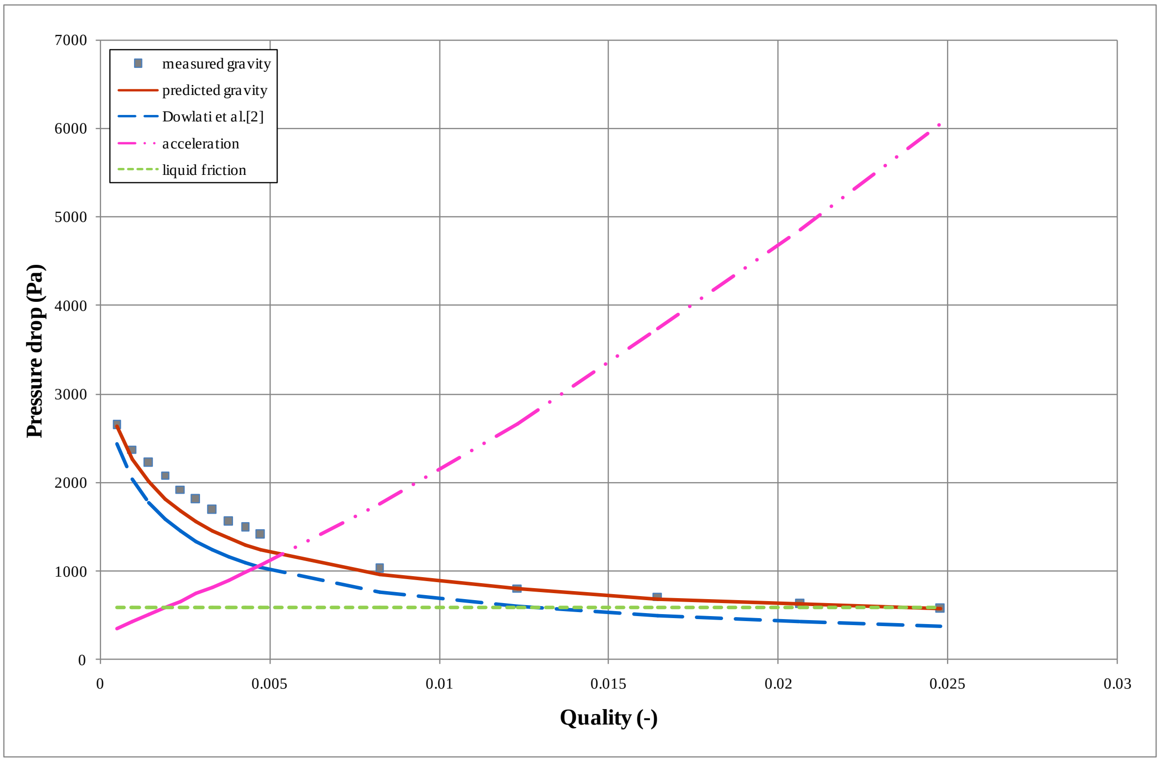

Figure 10.26: Variation of measured gravity and predictions with quality at 688 kg/m^{2}s for 19 mm in-line bundle

10.2.2 Prediction of pressure drop in staggered bundle

Figure 10.27 shows a comparison between the predicted and measured pressure drops for the staggered bundle. Most of the data are within the bounds of ±30%. The mean error is 49% and the RMS error is 72%.

The model predictions are compared with the measured data for the lowest, mid and highest mass fluxes in Figures 10.28, 10.30 and 10.32 respectively. The model predicts poorly at the lowest mass flux but does well at the mid-range and highest mass fluxes.

Figures 10.29, 10.31 and 10.33 show the pressure drop components and a comparison between the measured and gravitational pressure drop. The same trend obtained with the in-line bundle is shown where as the mass fluxes increases again with increasing quality, the gravitational pressure drop continually falls as the void fraction increases, whereas the acceleration and friction pressure drop are increased. These figures show the gravity dominance at the lower mass fluxes and the acceleration dominance at the higher mass fluxes. The relatively poor performance of the model is probably caused by the more complex path followed by the flow.

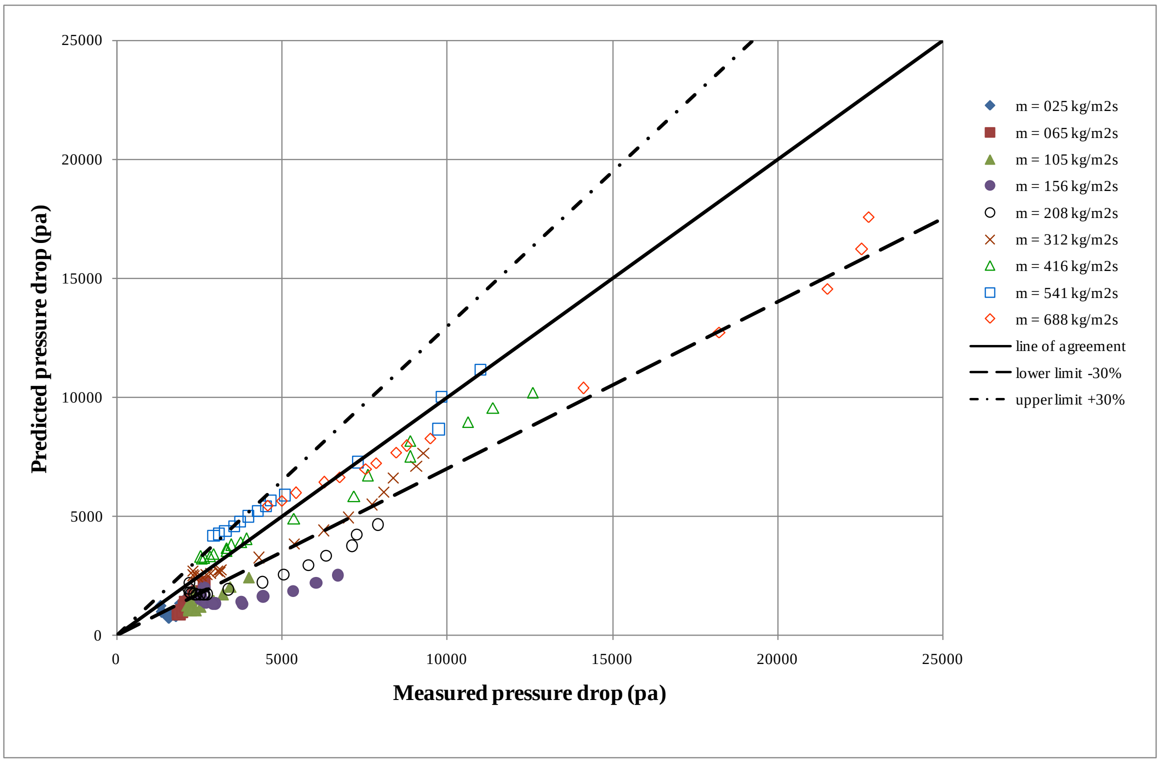

Figure 10.27: Prediction pressure drop against measured pressure drop in 19 mm staggered bundle

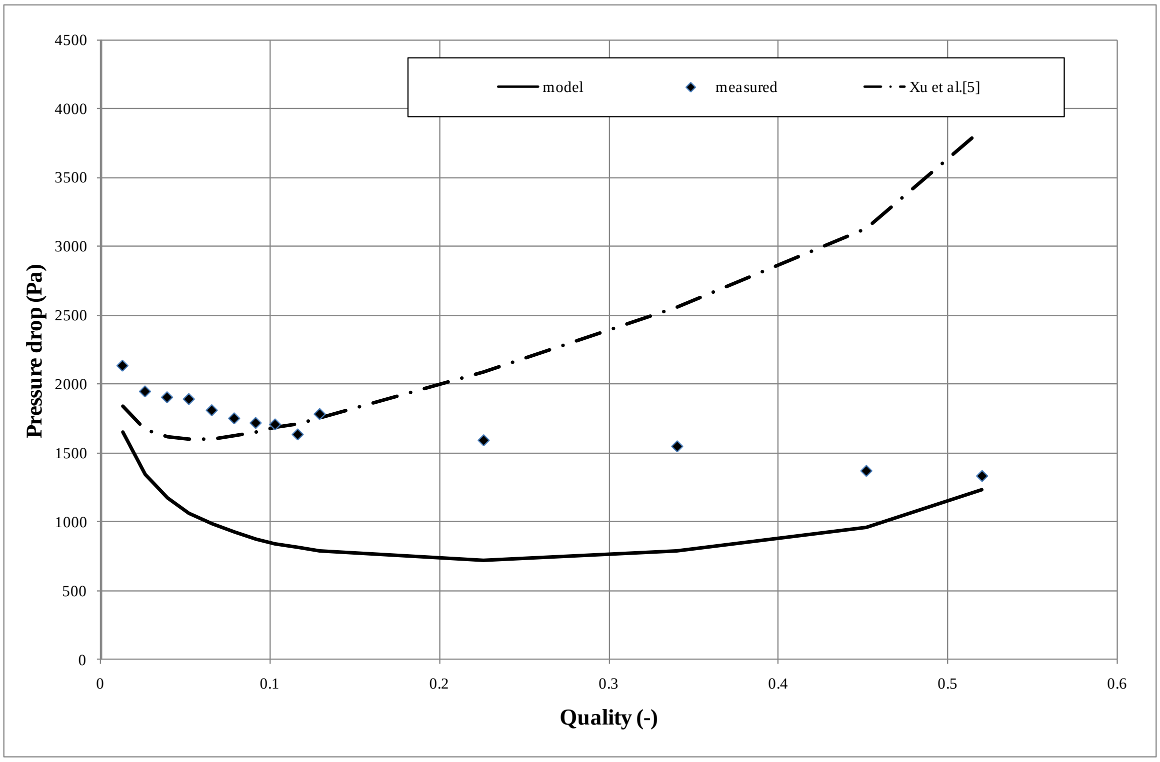

Figure 10.28: Variation of pressure drop with quality at 25 kg/m^{2}s for 19 mm staggered bundle

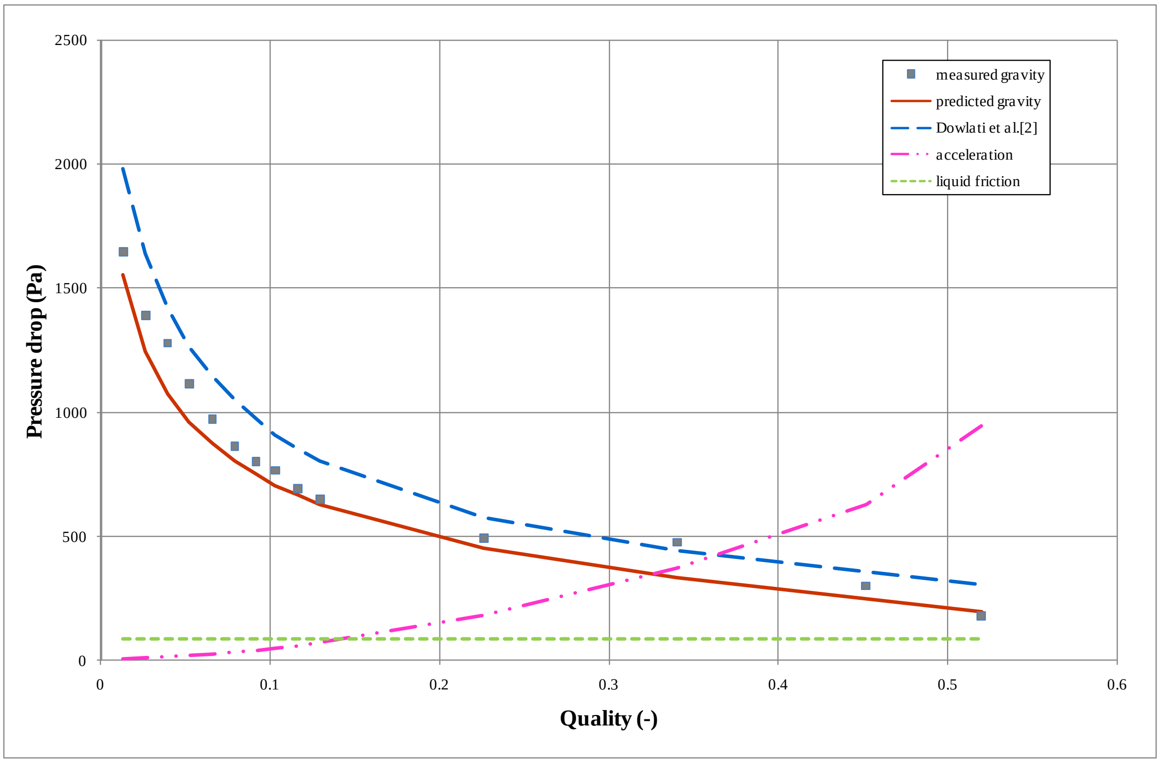

Figure 10.29:Variation of measured gravity and predictions with quality at 25 kg/m^{2}s for 19 mm staggered bundle

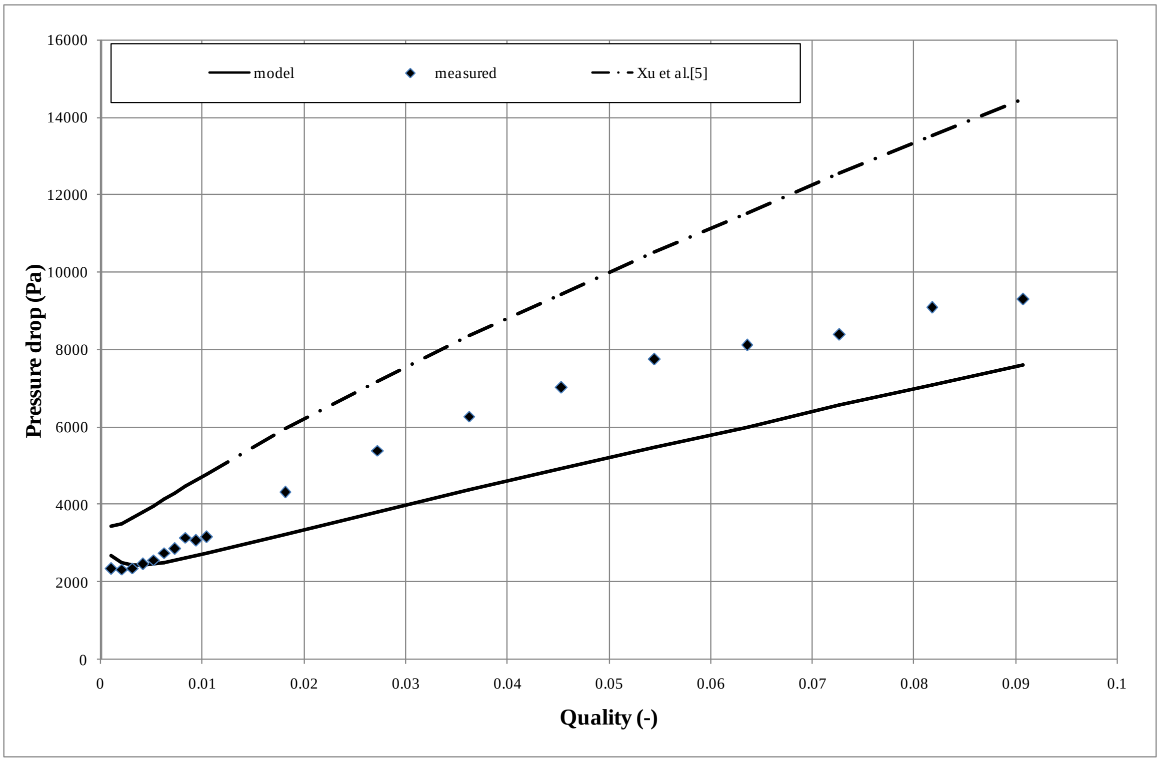

Figure 10.30: Variation of pressure drop with quality at 312 kg/m^{2}s for 19 mm staggered bundle

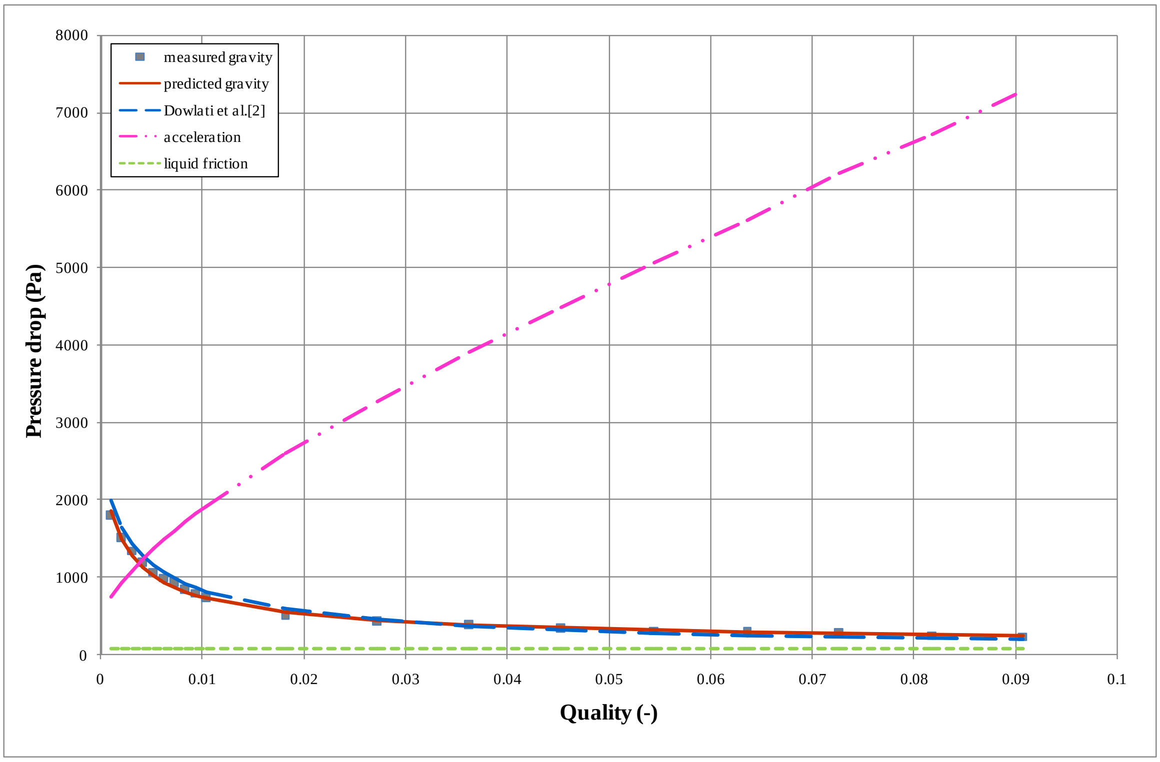

Figure 10.31: Variation of measured gravity and predictions with quality at 312 kg/m^{2}s for 19 mm staggered bundle

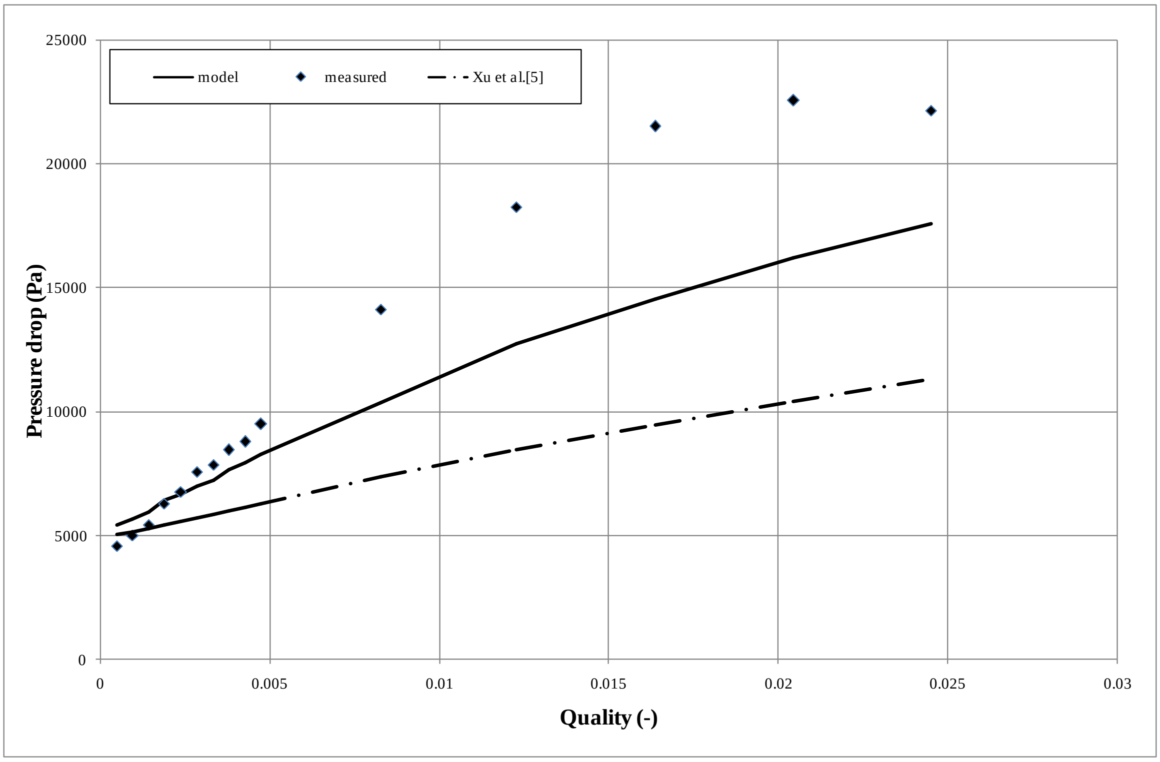

Figure 10.32: Variation of pressure drop with quality at 688 kg/m^{2}s for 19 mm staggered bundle

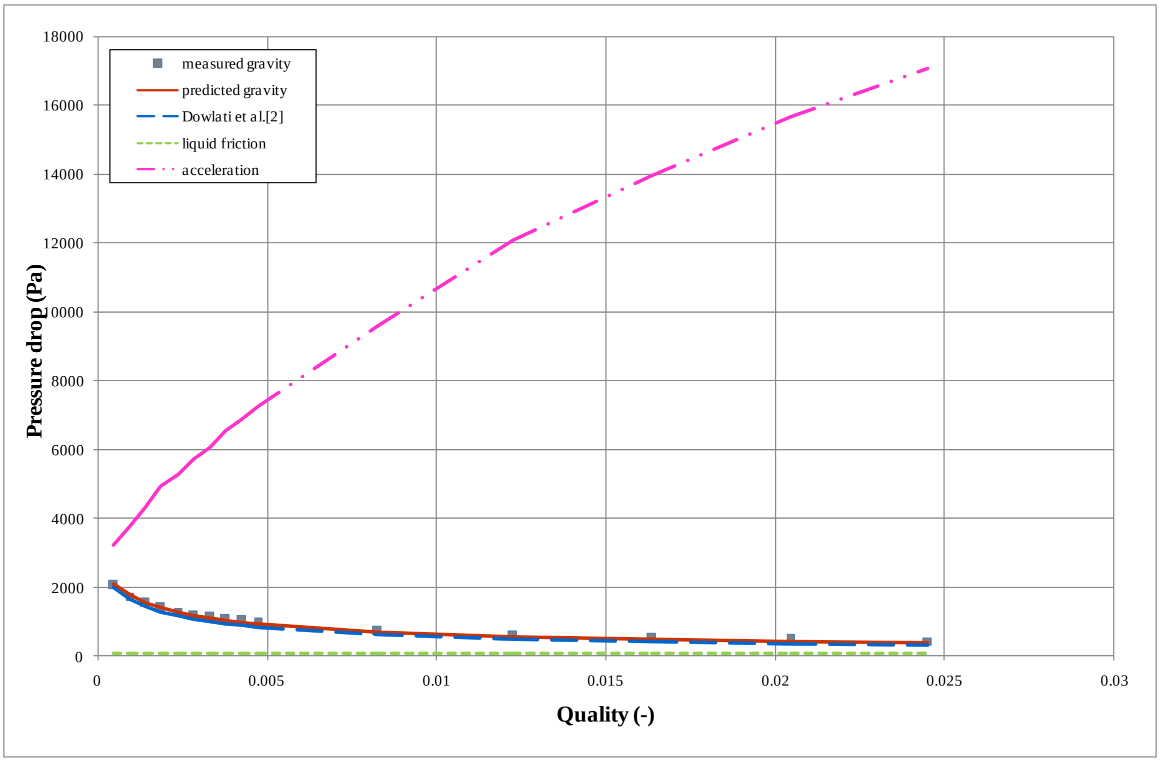

Figure 10.33: Variation of measured gravity and predictions with quality at 688 kg/m^{2}s for 19 mm staggered bundle

10.3 Summary of the proposed model development

The void fraction model proposed gives good predictions for all three bundles, especially the staggered bundle. The model predicts the local void fraction in the minimum and maximum gaps of each tube bundle. The predicted void fraction has captured the data trends reasonably well. The predicted void fractions should be less than those predicted from the homogenous flow model and larger than those predicted by the separated flow model.

The model captures the data trend well for the 38 mm in-line tube bundle, and it is better than the Xu et al. [5] predictions. It works less well for the 19 mm in-line tube bundle, probably because of more interaction between the columns. The model also works less well for the 19 mm staggered bundle, because the model, with its simplistic approach, is not capturing the complexity of the flow path.

The predicted gravitational pressure drop comes from the predicted void fraction. Figures 10.16, 10.18, 10.20, 10.22, 10.24, 10.26, 10.29, 10.31 and 10.33 shows that the predicted gravity pressure drop agree well with the data. These figures also demonstrate the low, mid-range and high mass flux effect to the flow regimes, gravity-dominated and inertia-dominated. These figures also illustrate the significance of the upper tube liquid film at low mass fluxes and the dominance of the acceleration mechanism at high mass fluxes.

The combined predictions of acceleration and liquid film pressure drop; and the predicted friction pressure drop from the correlation of Xu et al. [5] for the in-line bundle show the same trend. At the lower mass flux, both predictions are less than the gravitational pressure drop. As the quality increase, the void fraction increases, resulting in increases in the acceleration and frictional pressure drops, and a decrease in the gravitational pressure drops. The frictional pressure drop results from flow separation and re-attachment that produces wakes, at the rear of the tubes, causes friction between the tubes and the fluid and thus losing the energy as the fluid passes between the tubes. However, at the high mass flux of 688 kg/m^2s, the acceleration effect is dominant, and thus giving higher total predicted pressure drops. Overall, the pressure drop model proposed predicts the pressure drop better for in-line bundles than for the staggered bundle.

CHAPTER 11 – CONCLUSION

The void fraction measurements were compared with correlations of Schrage et al. [1], Feenstra et al. [3] and Dowlati et al. [2]. These methods were deduced from data sets obtained from tube bundles containing tubes with diameters less than 20 mm. The results indicate that the methods of Feenstra et al. [3] and Dowlati et al. [2] can be used with tube bundles that contain tubes up to 38 mm in diameter. The measured void fraction in the 19 mm and 38 mm are shown to be about the same. However, the Schrage et al. [1] correlation shows poor agreement with the data. These studies [1], [3], and [2] reported the measured pitch void fraction or the void fraction bundle average, and none has reported local values before. The data obtained in this study provides local values in the minimum gaps and in the maximum gaps. These local values provide a better understanding of the separation and re-attachment flow phenomenon in the heat exchanger. The data also conform to the view that void fractions should be less than those predicted from homogeneous flow theory and more than those predicted from the maximum slip condition. The correlation of Dowlati et al. [2] is shown to be the best correlations when compared to the measured data. However, the Dowlati et al. [2] method is not universal, requiring different coefficients to be set for different fluids. Currently they are only available for air–water mixtures and R113.

The measured pressure drops for the three bundles were presented. The measured friction pressure drop and measured two-phase multiplier are also reported. The measured frictional pressure drop was deduced by subtracting the gravitational pressure drop, based on the measured void fraction, from the measured total pressure drop. The measured frictional pressure drop was divided by the liquid only pressure loss from ESDU [52] to obtain the two-phase multiplier. The measured data were compared with Ishihara et al. [4] and Xu et al. [5]. The data agree reasonably well with the methods. The frictional pressure drop correlations presented by Ishihara et al. [4] and Xu et al. [5] were deduced from data taken from diameter tube bundles containing tubes with less than 20 mm. These methods were shown to predict the larger 38 mm tube bundle data to similar accuracy. However these correlations are clearly not general and accuracy decreases as mass flux decreases. Shell-side flows are likely to have fairly large mass fluxes, where these correlations are shown to be reasonably accurate. The Xu et al. [5] correlation is the best prediction method for pressure drop and two-phase multiplier, although this correlation does not capture the mass flux dependency completely, even with the *C* factor as a function of gas and liquid flow rates. The Xu et al. [5] correlation also works reasonably well for the staggered bundle, despite the correlation being deduced from in in-line tube bundle data only.

The measured drag groups were presented in this research. The drag force is deduced from the measured void fraction and the measured pressure drop. The Simovic et al. [7] correlation is better than the Rahman correlation et al. [6] in representing the data. The drag group prediction from Rahman et al. [6] does not predict the drag group for the larger bundle, although the correlation does capture the mass flux dependency, and does better than the Simovic et al. correlation [7] for the 19 mm diameter inline and staggered bundles. The measured drag group is independent of tube diameter but not tube bundle arrangement for adiabatic air-water flows, although there are strongly correlated at the lower mass fluxes. The measured drag group was modelled best by the two-fluid model on the shell side of a heat exchanger by the Simovic et al. [7] correlation.

A new model for void fraction is proposed for both bundle arrangements. The model modified the Feenstra et al. [3] correlation by using a different length scale, *a*. This is because the measured void fractions in both in-line bundles demonstrated that the gap size had no significant effect. The predicted void fractions were found to agree well with the measured data.

A new pressure drop model is proposed in this research, which is the total pressure drop from the gravitational and frictional pressure drops. The frictional pressure drop has two components, acceleration and liquid film. The acceleration pressure drop was derived from momentum flux changes from separation to re-attachment points in tube columns. The liquid film is trapped on the top half of the tube. These new models have been deduced from three tube bundles using air-water flows at near atmospheric conditions. The predicted void fractions in the maximum and minimum gaps and some separation angles were the empirical inputs to the model. Other separation and re-attachment angles were suggested from CFD simulations or the previous work of Bamardouf [51]. The predicted acceleration pressure drop was developed using these angles, in conjunction with the predicted void fractions. The predicted total pressure drop, were compared with the measured pressure drop and agree well with the measured data.

Two-phase flow on the shell side of a shell and tube heat exchanger is a complex flow. This study provides further understanding of the pressure drop phenomena that can occur. Further study involving other tube bundle arrangements and other fluids is therefore warranted.

APPENDIX A

A.1 Test conditions for pressure drop and void fraction experiments; the LRV and URV setting for pressure transducers for 19 mm in diameter in-line tube bundle.

Table A.1:Test conditions for G = 25 - 688 kg/m^{2}s for 19 mm diameter in-line tube bundle

Air mass flow rate (kg/s)	Mass flux based on min area (kg/m^{2}s)	PRESSURE DROP		PRESSURE		WATER FLOW RATE		WATER NOZZLE
		LRV	URV	LRV	URV	LRV	URV	
0.00039	25	-1000	1500	0	100000	0	600	3
0.00078	25	-1000	1500	0	100000	0	600	3
0.00117	25	-1000	1500	0	100000	0	600	3
0.00156	25	-1000	1500	0	100000	0	600	3
0.00195	25	-1000	2500	0	100000	0	600	3
0.00234	25	-1000	2500	0	100000	0	600	3
0.00273	25	-1000	2500	0	100000	0	600	3
0.00312	25	-1000	2500	0	100000	0	600	3
0.00351	25	-1000	2500	0	100000	0	600	3
0.00390	25	-1000	2500	0	100000	0	600	3
0.00680	25	-1000	2500	0	100000	0	600	3
0.01020	25	-1000	2500	0	100000	0	300	3
0.01360	25	-1000	2500	0	100000	0	300	3
0.01700	25	-2000	2500	0	100000	0	300	3
0.00039	65	-2000	1500	0	100000	0	5000	3
0.00078	65	-2000	1500	0	100000	0	5000	3
0.00117	65	-2000	1500	0	100000	0	5000	3
0.00156	65	-2000	1500	0	100000	0	5000	3
0.00195	65	-2000	2500	0	100000	0	5000	3
0.00234	65	-2000	2500	0	100000	0	5000	3
0.00273	65	-2000	2500	0	100000	0	5000	3
0.00312	65	-2000	2500	0	100000	0	5000	3
0.00351	65	-2000	2500	0	100000	0	5000	3
0.00390	65	-2000	2500	0	100000	0	5000	3
0.00680	65	-2000	2500	0	100000	0	5000	3
0.01020	65	-2000	2500	0	100000	0	5000	3
0.01360	65	-2000	2500	0	100000	0	5000	3
0.01700	65	-2000	2500	0	100000	0	5000	3
0.02040	65	-2000	2500	0	100000	0	5000	3
0.02380	65	-2000	2500	0	100000	0	5000	3

-continued-

0.00039	105	-2000	2500	0	100000	0	12000	3
0.00078	105	-2000	2500	0	100000	0	12000	3
0.00117	105	-2000	2500	0	100000	0	12000	3
0.00156	105	-2000	2500	0	100000	0	12000	3
0.00195	105	-2000	2500	0	100000	0	12000	3
0.00234	105	-2000	2500	0	100000	0	12000	3
0.00273	105	-2000	2500	0	100000	0	12000	3
0.00312	105	-2000	2500	0	100000	0	12000	3
0.00351	105	-2000	2500	0	100000	0	12000	3
0.00390	105	-2000	2500	0	100000	0	12000	3
0.00680	105	-2000	2500	0	100000	0	12000	3
0.01020	105	-2000	2500	0	100000	0	12000	3
0.01360	105	-2000	2500	0	100000	0	12000	3
0.01700	105	-2000	2500	0	100000	0	12000	3
0.02040	105	-2000	2500	0	100000	0	12000	3
0.02380	105	-2000	2500	0	100000	0	12000	3
0.00039	156	-1000	3500	0	100000	0	1000	2
0.00078	156	-1000	3500	0	100000	0	1000	2
0.00117	156	-1000	3500	0	100000	0	1000	2
0.00156	156	-1000	3500	0	100000	0	1000	2
0.00195	156	-2000	3800	0	100000	0	1000	2
0.00234	156	-2000	3800	0	100000	0	1000	2
0.00273	156	-3000	3900	0	100000	0	1000	2
0.00312	156	-3500	3900	0	100000	0	1000	2
0.00351	156	-4000	4000	0	100000	0	1000	2
0.00390	156	-4000	4000	0	100000	0	1000	2
0.00680	156	-4000	4000	0	100000	0	1000	2
0.01020	156	-4000	4000	0	100000	0	1000	2
0.01360	156	-4000	4000	0	100000	0	1000	2
0.01700	156	-4000	4000	0	100000	0	1000	2
0.02040	156	-4000	4000	0	100000	0	1000	2
0.00039	208	-1000	2000	0	100000	0	2000	2
0.00078	208	-1000	2000	0	100000	0	2000	2
0.00117	208	-2000	3000	0	100000	0	2000	2
0.00156	208	-2000	3000	0	100000	0	2000	2
0.00195	208	-2500	3500	0	100000	0	2000	2
0.00234	208	-2500	3500	0	100000	0	2000	2
0.00273	208	-3000	4000	0	100000	0	2000	2
0.00312	208	-3000	4000	0	100000	0	2000	2
0.00351	208	-3000	2000	0	100000	0	2000	2
0.00390	208	-3000	2000	0	100000	0	2000	2
0.00680	208	-3000	2000	0	100000	0	2000	2
0.01020	208	-3000	2000	0	100000	0	2000	2
0.01360	208	-5000	2500	0	100000	0	2000	2
0.01700	208	-6000	2500	0	100000	0	2000	2
0.02040	208	-6000	2500	0	100000	0	2000	2
0.02380	208	-6000	2500	0	100000	0	2000	2
0.02720	208	-6000	2500	0	100000	0	2000	2
0.03060	208	-6000	2500	0	100000	0	2000	2

-continued-

0.00039	312	-1000	1500	0	100000	0	4000	2
0.00078	312	-1000	1500	0	100000	0	4000	2
0.00117	312	-1000	1500	0	100000	0	4000	2
0.00156	312	-1500	1000	0	100000	0	4000	2
0.00195	312	-1500	1000	0	100000	0	4000	2
0.00234	312	-2500	1000	0	100000	0	4000	2
0.00273	312	-2500	1000	0	100000	0	4000	2
0.00312	312	-2500	2000	0	100000	0	4000	2
0.00351	312	-3000	2000	0	100000	0	4000	2
0.00390	312	-3000	2000	0	100000	0	4000	2
0.00680	312	-7000	1500	0	100000	0	4000	2
0.01020	312	-7000	1500	0	100000	0	4000	2
0.01360	312	-7000	1500	0	100000	0	4000	2
0.01700	312	-7000	1500	0	100000	0	4000	2
0.02040	312	-7000	1500	0	100000	0	4000	2
0.02380	312	-7000	1500	0	100000	0	4000	2
0.02720	312	-7000	1500	0	100000	0	4000	2
0.03060	312	-7000	1500	0	100000	0	4000	2
0.03400	312	-7000	1500	0	100000	0	4000	2
0.00039	416	-1000	1500	0	100000	0	7000	2
0.00078	416	-2000	500	0	100000	0	7000	2
0.00117	416	-2000	500	0	100000	0	7000	2
0.00156	416	-2000	500	0	100000	0	7000	2
0.00195	416	-2000	1500	0	100000	0	7000	2
0.00234	416	-2000	1500	0	100000	0	7000	2
0.00273	416	-2000	1500	0	100000	0	7000	2
0.00312	416	-2500	1500	0	100000	0	7000	2
0.00351	416	-2500	1500	0	100000	0	7000	2
0.00390	416	-2500	1500	0	100000	0	7000	2
0.00680	416	-2500	2500	0	100000	0	7000	2
0.01020	416	-3500	5000	0	100000	0	7000	2
0.01360	416	-3500	5000	0	100000	0	7000	2
0.01700	416	-3500	5000	0	100000	0	7000	2
0.02040	416	-3500	5000	0	100000	0	7000	2
0.02380	416	-3500	5000	0	100000	0	7000	2
0.02720	416	-3500	5000	0	100000	0	7000	2
0.03060	416	-3500	6000	0	100000	0	7000	2
0.00039	541	-1000	1500	0	100000	0	12000	2
0.00078	541	-1000	1500	0	100000	0	12000	2
0.00117	541	-1000	1500	0	100000	0	12000	2
0.00156	541	-1000	1500	0	100000	0	12000	2
0.00195	541	-1000	1500	0	100000	0	12000	2
0.00234	541	-1000	1500	0	100000	0	12000	2
0.00273	541	-1000	1500	0	100000	0	12000	2
0.00312	541	-2000	1500	0	100000	0	12000	2
0.00351	541	-2000	1500	0	100000	0	12000	2
0.00390	541	-2000	2500	0	100000	0	12000	2

-continued-

0.00680	541	-2000	2500	0	100000	0	12000	2
0.01020	541	-2000	4500	0	100000	0	12000	2
0.01360	541	-3000	4500	0	100000	0	12000	2
0.01700	541	-3000	4500	0	100000	0	12000	2
0.00039	688	-1000	1500	0	100000	0	1500	1
0.00078	688	-1000	1500	0	100000	0	1500	1
0.00117	688	-1000	1500	0	100000	0	1500	1
0.00156	688	-1000	1500	0	100000	0	1500	1
0.00195	688	-1000	1500	0	100000	0	1500	1
0.00234	688	-1000	2500	0	100000	0	1500	1
0.00273	688	-1000	2500	0	100000	0	1500	1
0.00312	688	-1000	2500	0	100000	0	1500	1
0.00351	688	-1000	2500	0	100000	0	1500	1
0.00390	688	-1000	2500	0	100000	0	1500	1
0.00680	688	-1000	3500	0	100000	0	1500	1
0.01020	688	-1000	6500	0	100000	0	1500	1
0.01360	688	-3000	6500	0	100000	0	1500	1
0.01700	688	-3000	6500	0	100000	0	1500	1
0.02040	688	-3000	6500	0	100000	0	1500	1

Notes :

- Solenoid valves number 1 and 8 were used for pressure drop experiment.
- For mass fluxes from 25 kg/m^2s to 312 kg/m^2s, solenoid 1 was connected to the low pressure end, while solenoid 8 was connected to the high pressure end.
- For mass fluxes from 416 kg/m^2s to 688 kg/m^2s, solenoid 1 was connected to the high pressure end, while solenoid 8 was connected to the low pressure end.

A.2 Test conditions for pressure drop and void fraction experiments; the LRV and URV setting of pressure transducers for 19 mm in diameter staggered tube bundle.

Table A.2:Test conditions for G = 25 – 688 kg/m^{2}s for 19 mm diameter staggered tube bundle

Air mass flow rate (kg/s)	Mass flux based on min area (kg/m^{2}s)	PRESSURE DROP		PRESSURE		WATER FLOW RATE		WATER NOZZLE
		LRV	URV	LRV	URV	LRV	URV	
0.00039	25	-2500	2000	0	100000	0	600	3
0.00078	25	-2500	2000	0	100000	0	600	3
0.00117	25	-2500	2000	0	100000	0	600	3
0.00156	25	-2500	2000	0	100000	0	600	3
0.00195	25	-2500	2000	0	100000	0	600	3
0.00234	25	-2500	2000	0	100000	0	600	3
0.00273	25	-2500	2000	0	100000	0	600	3
0.00312	25	-2500	2000	0	100000	0	600	3
0.00351	25	-2500	2000	0	100000	0	600	3
0.00390	25	-2500	2000	0	100000	0	600	3
0.00680	25	-2500	2000	0	100000	0	600	3
0.01020	25	-2500	2000	0	100000	0	300	3
0.01360	25	-2500	2000	0	100000	0	300	3
0.01700	25	-2500	2000	0	100000	0	300	3
0.00039	65	-1000	3000	0	100000	0	5000	3
0.00078	65	-1000	3000	0	100000	0	5000	3
0.00117	65	-1000	3000	0	100000	0	5000	3
0.00156	65	-1000	3000	0	100000	0	5000	3
0.00195	65	-2500	2000	0	100000	0	5000	3
0.00234	65	-2500	2000	0	100000	0	5000	3
0.00273	65	-2500	2000	0	100000	0	5000	3
0.00312	65	-2500	2000	0	100000	0	5000	3
0.00351	65	-2500	2000	0	100000	0	5000	3
0.00390	65	-2500	2000	0	100000	0	5000	3
0.00680	65	-2500	2000	0	100000	0	5000	3
0.01020	65	-2500	2000	0	100000	0	5000	3
0.01360	65	-2500	2000	0	100000	0	5000	3
0.01700	65	-2500	2000	0	100000	0	5000	3
0.02040	65	-2500	2000	0	100000	0	5000	3
0.02380	65	-2500	2000	0	100000	0	5000	3

-continued-

0.00039	105	-1000	3000	0	100000	0	12000	3
0.00078	105	-2000	3000	0	100000	0	12000	3
0.00117	105	-2000	3000	0	100000	0	12000	3
0.00156	105	-2000	3000	0	100000	0	12000	3
0.00195	105	-2000	3000	0	100000	0	12000	3
0.00234	105	-2000	3000	0	100000	0	12000	3
0.00273	105	-2000	3000	0	100000	0	12000	3
0.00312	105	-2000	3000	0	100000	0	12000	3
0.00351	105	-2000	3000	0	100000	0	12000	3
0.00390	105	-3000	2500	0	100000	0	12000	3
0.00680	105	-3000	2500	0	100000	0	12000	3
0.01020	105	-3000	2500	0	100000	0	12000	3
0.01360	105	-4000	2000	0	100000	0	12000	3
0.01700	105	-6000	1000	0	100000	0	12000	3
0.02040	105	-6000	1000	0	100000	0	12000	3
0.02380	105	-6000	1000	0	100000	0	12000	3
0.00039	156	-2500	2000	0	100000	0	1000	2
0.00078	156	-2500	2000	0	100000	0	1000	2
0.00117	156	-2500	2000	0	100000	0	1000	2
0.00156	156	-2500	2000	0	100000	0	1000	2
0.00195	156	-2500	2000	0	100000	0	1000	2
0.00234	156	-2500	2000	0	100000	0	1000	2
0.00273	156	-3500	1500	0	100000	0	1000	2
0.00312	156	-3500	1500	0	100000	0	1000	2
0.00351	156	-3500	1500	0	100000	0	1000	2
0.00390	156	-4500	900	0	100000	0	1000	2
0.00680	156	-4500	900	0	100000	0	1000	2
0.01020	156	-8000	100	0	100000	0	1000	2
0.01360	156	-8000	100	0	100000	0	1000	2
0.01700	156	-10000	20	0	100000	0	1000	2
0.02040	156	-10000	20	0	100000	0	1000	2
0.00039	208	-2500	1000	0	100000	0	2000	2
0.00078	208	-2500	1000	0	100000	0	2000	2
0.00117	208	-2500	1000	0	100000	0	2000	2
0.00156	208	-2500	1000	0	100000	0	2000	2
0.00195	208	-2500	1000	0	100000	0	2000	2
0.00234	208	-2500	1000	0	100000	0	2000	2
0.00273	208	-2500	2500	0	100000	0	2000	2
0.00312	208	-2500	2500	0	100000	0	2000	2
0.00351	208	-2500	2500	0	100000	0	2000	2
0.00390	208	-2500	2500	0	100000	0	2000	2
0.00680	208	-2500	2500	0	100000	0	2000	2
0.01020	208	-2500	6000	0	100000	0	2000	2
0.01360	208	-2500	6000	0	100000	0	2000	2
0.01700	208	-2500	6000	0	100000	0	2000	2
0.02040	208	-2500	8500	0	100000	0	2000	2
0.02380	208	-2500	8500	0	100000	0	2000	2
0.02720	208	-2500	8500	0	100000	0	2000	2
0.03060	208	-2500	8500	0	100000	0	2000	2

-continued-

0.00039	312	-2500	1000	0	100000	0	4000	2
0.00078	312	-2500	1000	0	100000	0	4000	2
0.00117	312	-2500	1000	0	100000	0	4000	2
0.00156	312	-2500	1000	0	100000	0	4000	2
0.00195	312	-2500	1000	0	100000	0	4000	2
0.00234	312	-2500	2500	0	100000	0	4000	2
0.00273	312	-2500	2500	0	100000	0	4000	2
0.00312	312	-2500	2500	0	100000	0	4000	2
0.00351	312	-2500	2500	0	100000	0	4000	2
0.00390	312	-2500	2500	0	100000	0	4000	2
0.00680	312	-2500	4000	0	100000	0	4000	2
0.01020	312	-2000	8000	0	100000	0	4000	2
0.01360	312	-2000	8000	0	100000	0	4000	2
0.01700	312	-2000	8000	0	100000	0	4000	2
0.02040	312	-2000	8000	0	100000	0	4000	2
0.02380	312	-2000	8000	0	100000	0	4000	2
0.02720	312	-2000	10000	0	100000	0	4000	2
0.03060	312	-2000	10000	0	100000	0	4000	2
0.03400	312	-2000	10000	0	100000	0	4000	2
0.00039	416	-1000	1000	0	100000	0	7000	2
0.00078	416	-1000	1000	0	100000	0	7000	2
0.00117	416	-1000	1000	0	100000	0	7000	2
0.00156	416	-1000	1000	0	100000	0	7000	2
0.00195	416	-1000	1000	0	100000	0	7000	2
0.00234	416	-2000	2500	0	100000	0	7000	2
0.00273	416	-2000	2500	0	100000	0	7000	2
0.00312	416	-2000	2500	0	100000	0	7000	2
0.00351	416	-2000	2500	0	100000	0	7000	2
0.00390	416	-2000	3500	0	100000	0	7000	2
0.00680	416	-1000	5000	0	100000	0	7000	2
0.01020	416	-1000	10000	0	100000	0	7000	2
0.01360	416	-1000	10000	0	100000	0	7000	2
0.01700	416	-1000	10000	0	100000	0	7000	2
0.02040	416	-1000	10000	0	100000	0	7000	2
0.02380	416	-1000	13000	0	100000	0	7000	2
0.02720	416	-1000	13000	0	100000	0	7000	2
0.03060	416	-1000	14000	0	100000	0	7000	2
0.00039	541	-1000	1000	0	100000	0	12000	2
0.00078	541	-1000	1000	0	100000	0	12000	2
0.00117	541	-1000	1000	0	100000	0	12000	2
0.00156	541	-1000	2000	0	100000	0	12000	2
0.00195	541	-1000	2000	0	100000	0	12000	2
0.00234	541	-1000	3500	0	100000	0	12000	2
0.00273	541	-1000	3500	0	100000	0	12000	2
0.00312	541	-1000	3500	0	100000	0	12000	2
0.00351	541	-1000	3500	0	100000	0	12000	2
0.00390	541	-1000	5000	0	100000	0	12000	2

-continued-

0.00680	541	-500	8000	0	100000	0	12000	2
0.01020	541	0	12000	0	100000	0	12000	2
0.01360	541	0	12000	0	100000	0	12000	2
0.01700	541	0	12000	0	100000	0	12000	2
0.00039	688	-1000	3000	0	100000	0	1500	1
0.00078	688	-1000	3000	0	100000	0	1500	1
0.00117	688	-1000	5000	0	100000	0	1500	1
0.00156	688	-1000	5000	0	100000	0	1500	1
0.00195	688	-1000	5000	0	100000	0	1500	1
0.00234	688	-1000	8000	0	100000	0	1500	1
0.00273	688	-1000	8000	0	100000	0	1500	1
0.00312	688	-1000	8000	0	100000	0	1500	1
0.00351	688	-1000	8000	0	100000	0	1500	1
0.00390	688	-1000	12000	0	100000	0	1500	1
0.00680	688	-1000	16000	0	100000	0	1500	1
0.01020	688	-1000	22000	0	100000	0	1500	1
0.01360	688	-1000	28000	0	100000	0	1500	1
0.01700	688	-1000	28000	0	100000	0	1500	1
0.02040	688	-1000	28000	0	100000	0	1500	1

Notes

- Solenoid valves number 2 and 7 were used for pressure drop experiment.
- For mass fluxes from 25 kg/m^{2}s to 156 kg/m^{2}s, solenoid 2 was connected to the low pressure end, while solenoid 7 was connected to the high pressure end.
- For mass fluxes from 208 kg/m^{2}s to 688 kg/m^{2}s, solenoid 2 was connected to the high pressure end, while solenoid 7 was connected to the low pressure end.

A.3 Test conditions for pressure drop and void fraction experiments; the LRV and URV setting of pressure transducers for 38 mm in diameter in-line tube bundle

Table A.3: Test conditions for G = 25 kg/m^{2}s for 38 mm diameter in-line tube bundle

Air mass flow rate (kg/s)	Mass flux based on min area (kg/m^{2}s)	PRESSURE DROP		PRESSURE		WATER FLOW RATE		WATER NOZZLE
		LRV	URV	LRV	URV	LRV	URV	
0.00039	25			0	100000	0	600	3
0.00078	25			0	100000	0	600	3
0.00117	25			0	100000	0	600	3
0.00156	25			0	100000	0	600	3
0.00195	25			0	100000	0	600	3
0.00234	25			0	100000	0	600	3
0.00273	25			0	100000	0	600	3
0.00312	25			0	100000	0	600	3
0.00351	25			0	100000	0	600	3
0.00390	25			0	100000	0	600	3
0.00680	25			0	100000	0	600	3
0.01020	25			0	100000	0	300	3
0.01360	25			0	100000	0	300	3
0.01700	25			0	100000	0	300	3
0.00039	65			0	100000	0	5000	3
0.00078	65			0	100000	0	5000	3
0.00117	65			0	100000	0	5000	3
0.00156	65			0	100000	0	5000	3
0.00195	65			0	100000	0	5000	3
0.00234	65			0	100000	0	5000	3
0.00273	65			0	100000	0	5000	3
0.00312	65			0	100000	0	5000	3
0.00351	65			0	100000	0	5000	3
0.00390	65			0	100000	0	5000	3
0.00680	65			0	100000	0	5000	3
0.01020	65			0	100000	0	5000	3
0.01360	65			0	100000	0	5000	3
0.01700	65			0	100000	0	5000	3
0.02040	65			0	100000	0	5000	3
0.02380	65			0	100000	0	5000	3

-continued-

0.00039	105			0	100000	0	12000	3
0.00078	105			0	100000	0	12000	3
0.00117	105			0	100000	0	12000	3
0.00156	105			0	100000	0	12000	3
0.00195	105			0	100000	0	12000	3
0.00234	105			0	100000	0	12000	3
0.00273	105			0	100000	0	12000	3
0.00312	105			0	100000	0	12000	3
0.00351	105			0	100000	0	12000	3
0.00390	105			0	100000	0	12000	3
0.00680	105			0	100000	0	12000	3
0.01020	105			0	100000	0	12000	3
0.01360	105			0	100000	0	12000	3
0.01700	105			0	100000	0	12000	3
0.02040	105			0	100000	0	12000	3
0.02380	105			0	100000	0	12000	3
0.00039	156			0	100000	0	1000	2
0.00078	156			0	100000	0	1000	2
0.00117	156			0	100000	0	1000	2
0.00156	156			0	100000	0	1000	2
0.00195	156			0	100000	0	1000	2
0.00234	156			0	100000	0	1000	2
0.00273	156			0	100000	0	1000	2
0.00312	156			0	100000	0	1000	2
0.00351	156			0	100000	0	1000	2
0.00390	156			0	100000	0	1000	2
0.00680	156			0	100000	0	1000	2
0.01020	156			0	100000	0	1000	2
0.01360	156			0	100000	0	1000	2
0.01700	156			0	100000	0	1000	2
0.02040	156			0	100000	0	1000	2
0.00039	208			0	100000	0	2000	2
0.00078	208			0	100000	0	2000	2
0.00117	208			0	100000	0	2000	2
0.00156	208			0	100000	0	2000	2
0.00195	208			0	100000	0	2000	2
0.00234	208			0	100000	0	2000	2
0.00273	208			0	100000	0	2000	2
0.00312	208			0	100000	0	2000	2
0.00351	208			0	100000	0	2000	2
0.00390	208			0	100000	0	2000	2
0.00680	208			0	100000	0	2000	2
0.01020	208			0	100000	0	2000	2
0.01360	208			0	100000	0	2000	2
0.01700	208			0	100000	0	2000	2
0.02040	208			0	100000	0	2000	2
0.02380	208			0	100000	0	2000	2
0.02720	208			0	100000	0	2000	2
0.03060	208			0	100000	0	2000	2

-continued-

0.00039	312			0	100000	0	4000	2
0.00078	312			0	100000	0	4000	2
0.00117	312			0	100000	0	4000	2
0.00156	312			0	100000	0	4000	2
0.00195	312			0	100000	0	4000	2
0.00234	312			0	100000	0	4000	2
0.00273	312			0	100000	0	4000	2
0.00312	312			0	100000	0	4000	2
0.00351	312			0	100000	0	4000	2
0.00390	312			0	100000	0	4000	2
0.00680	312			0	100000	0	4000	2
0.01020	312			0	100000	0	4000	2
0.01360	312			0	100000	0	4000	2
0.01700	312			0	100000	0	4000	2
0.02040	312			0	100000	0	4000	2
0.02380	312			0	100000	0	4000	2
0.02720	312			0	100000	0	4000	2
0.03060	312			0	100000	0	4000	2
0.03400	312			0	100000	0	4000	2
0.00039	416			0	100000	0	7000	2
0.00078	416			0	100000	0	7000	2
0.00117	416			0	100000	0	7000	2
0.00156	416			0	100000	0	7000	2
0.00195	416			0	100000	0	7000	2
0.00234	416			0	100000	0	7000	2
0.00273	416			0	100000	0	7000	2
0.00312	416			0	100000	0	7000	2
0.00351	416			0	100000	0	7000	2
0.00390	416			0	100000	0	7000	2
0.00680	416			0	100000	0	7000	2
0.01020	416			0	100000	0	7000	2
0.01360	416			0	100000	0	7000	2
0.01700	416			0	100000	0	7000	2
0.02040	416			0	100000	0	7000	2
0.02380	416			0	100000	0	7000	2
0.02720	416			0	100000	0	7000	2
0.03060	416			0	100000	0	7000	2

-continued-

0.00039	541	-3000	3000	0	100000	0	12000	2
0.00078	541	-3000	3000	0	100000	0	12000	2
0.00117	541	-3000	3000	0	100000	0	12000	2
0.00156	541	-3000	3000	0	100000	0	12000	2
0.00195	541	-3000	3000	0	100000	0	12000	2
0.00234	541	-3000	3000	0	100000	0	12000	2
0.00273	541	-4000	2000	0	100000	0	12000	2
0.00312	541	-4000	2000	0	100000	0	12000	2
0.00351	541	-4000	2000	0	100000	0	12000	2
0.00390	541	-4000	2000	0	100000	0	12000	2
0.00680	541	-4000	2000	0	100000	0	12000	2
0.01020	541	-4000	2000	0	100000	0	12000	2
0.01360	541	-4000	2000	0	100000	0	12000	2
0.01700	541	-4000	2000	0	100000	0	12000	2
0.00039	688	-3000	3000	0	100000	0	1500	1
0.00078	688	-3000	3000	0	100000	0	1500	1
0.00117	688	-3000	3000	0	100000	0	1500	1
0.00156	688	-3000	3000	0	100000	0	1500	1
0.00195	688	-3000	3000	0	100000	0	1500	1
0.00234	688	-3000	3000	0	100000	0	1500	1
0.00273	688	-3000	3000	0	100000	0	1500	1
0.00312	688	-3000	3000	0	100000	0	1500	1
0.00351	688	-3000	3000	0	100000	0	1500	1
0.00390	688	-3000	3000	0	100000	0	1500	1
0.00680	688	-3000	3000	0	100000	0	1500	1
0.01020	688	-3000	3000	0	100000	0	1500	1
0.01360	688	-3000	3000	0	100000	0	1500	1
0.01700	688	-3000	3000	0	100000	0	1500	1
0.02040	688	-3000	3000	0	100000	0	1500	1

Notes

- Solenoid valves number 3 and 10 were used for pressure drop experiment.
- Solenoid 3 was connected to the high pressure end, while solenoid 10 was connected to the low pressure end.

APPENDIX B

B.1 Void fraction data sets for the three local void fractions measurements and the pitch average in the 38 mm in-line bundle

Table B.1: Void fraction in the maximum gap between the tubes

Air Rotameter	Air flow rate (%)	Mass flux based on min area (kg/m^2s)	Mass flux (kg/m^2s)	Two-pahse flow pressure (Pa)	Two-phase flow temperature (K)	Total mass flow rate (kg/s)	Quality (-)	Void fraction at the gap to the south east of central tube (max gap)(-)
Rotameter 1	10	25.0	6.1	110187.9	294.39	0.0295	0.0132	0.319
	20	25.0	6.1	108860.9	294.31	0.0294	0.0265	0.412
	30	25.0	6.1	108390.7	294.27	0.0297	0.0394	0.492
	40	25.0	6.1	108088.1	294.20	0.0301	0.0518	0.551
	50	25.0	6.1	107741.1	294.09	0.0309	0.0631	0.575
	60	25.0	6.1	107425.1	294.10	0.0294	0.0797	0.638
	70	25.0	6.1	107224.6	294.05	0.0311	0.0878	0.651
	80	25.0	6.1	106918.6	293.84	0.0314	0.0994	0.693
	90	25.0	6.1	106921.8	293.76	0.0318	0.1103	0.710
	100	25.0	6.1	106822.6	293.71	0.0317	0.1231	0.741
Rotameter 2	20	25.0	6.1	105013.4	292.23	0.0298	0.2282	0.864
	30	25.0	6.1	103919.6	291.72	0.0299	0.3408	0.899
	40	25.0	6.1	103747.3	290.14	0.0359	0.4533	0.933
	50	25.0	6.1	112047.2	287.82	0.0316	0.5383	0.952
	60							
	70							
	80							
	90							
	100							
Rotameter 1	10	65.0	15.6	112357.1	293.95	0.0787	0.0050	0.265
	20	65.0	15.6	110763.0	293.86	0.0775	0.0101	0.385
	30	65.0	15.6	110034.4	293.86	0.0754	0.0155	0.456
	40	65.0	15.6	109471.9	293.86	0.0808	0.0193	0.525
	50	65.0	15.6	109362.5	293.85	0.0777	0.0251	0.565
	60	65.0	15.6	108837.9	293.83	0.0785	0.0298	0.598
	70	65.0	15.6	108512.1	293.82	0.0794	0.0344	0.627
	80	65.0	15.6	108282.9	293.79	0.0778	0.0401	0.664
	90	65.0	15.6	108208.9	293.78	0.0787	0.0446	0.654
	100	65.0	15.6	107954.2	293.75	0.0788	0.0495	0.682
Rotameter 2	20	65.0	15.6	107242.0	293.64	0.0767	0.0886	0.790
	30	65.0	15.6	107099.6	293.15	0.0759	0.1344	0.840
	40	65.0	15.6	107806.5	292.71	0.0776	0.1752	0.881
	50	65.0	15.6	108552.9	292.54	0.0816	0.2083	0.912
	60	65.0	15.6	109974.6	292.14	0.0789	0.2586	0.925
	70	65.0	15.6	110590.0	291.92	0.0786	0.3030	0.935
	80							
	90							
	100							

-continued-

Rotameter 1	10	105.0	25.2	114185.9	294.07	0.1275	0.0031	0.232
	20	105.0	25.2	112744.4	294.18	0.1264	0.0062	0.347
	30	105.0	25.2	111919.0	294.21	0.1261	0.0093	0.449
	40	105.0	25.2	111266.2	293.15	0.1266	0.0123	0.493
	50	105.0	25.2	111091.3	294.26	0.1264	0.0154	0.552
	60	105.0	25.2	110964.6	294.20	0.1246	0.0188	0.597
	70	105.0	25.2	110650.3	294.17	0.1260	0.0217	0.615
	80	105.0	25.2	110434.6	294.24	0.1284	0.0243	0.617
	90	105.0	25.2	110146.3	294.22	0.1273	0.0276	0.641
	100	105.0	25.2	110192.4	293.15	0.1259	0.0310	0.667
Rotameter 2	20	105.0	25.2	109130.3	294.03	0.1251	0.0544	0.762
	30	105.0	25.2	109630.5	293.81	0.1242	0.0821	0.797
	40	105.0	25.2	111229.9	293.62	0.1271	0.1070	0.828
	50	105.0	25.2	112845.2	293.51	0.1263	0.1346	0.857
	60	105.0	25.2	115002.6	293.28	0.1255	0.1625	0.878
	70	105.0	25.2	117164.7	293.14	0.1259	0.1891	0.895
	80							
	90							
	100							
Rotameter 1	10	156.0	37.4	114860.0	292.22	0.1865	0.0021	0.225
	20	156.0	37.4	113074.3	292.24	0.1861	0.0042	0.335
	30	156.0	37.4	112447.2	292.30	0.1870	0.0063	0.403
	40	156.0	37.4	112021.1	292.17	0.1880	0.0083	0.456
	50	156.0	37.4	111396.0	292.24	0.1875	0.0104	0.516
	60	156.0	37.4	111326.7	292.17	0.1884	0.0124	0.573
	70	156.0	37.4	111048.0	292.13	0.1898	0.0144	0.603
	80	156.0	37.4	110853.8	292.17	0.1865	0.0167	0.626
	90	156.0	37.4	110579.7	292.20	0.1877	0.0187	0.628
	100	156.0	37.4	110624.8	292.21	0.1875	0.0208	0.640
Rotameter 2	20	156.0	37.4	108937.7	292.11	0.1907	0.0357	0.745
	30	156.0	37.4	109292.5	292.02	0.1896	0.0538	0.806
	40	156.0	37.4	110956.4	291.75	0.1836	0.0741	0.820
	50	156.0	37.4	113251.6	291.53	0.1848	0.0920	0.853
	60	156.0	37.4	115457.7	291.58	0.1874	0.1089	0.877
	70							
	80							
	90							
	100							
Rotameter 1	10	208.0	49.9	115938.4	292.64	0.2497	0.0016	0.201
	20	208.0	49.9	114324.1	292.61	0.2498	0.0031	0.315
	30	208.0	49.9	113745.6	292.56	0.2496	0.0047	0.383
	40	208.0	49.9	113248.0	292.59	0.2483	0.0063	0.441
	50	208.0	49.9	113168.5	292.55	0.2497	0.0078	0.495
	60	208.0	49.9	112978.2	292.55	0.2508	0.0093	0.554
	70	208.0	49.9	112809.0	292.64	0.2501	0.0109	0.585
	80	208.0	49.9	112809.0	292.72	0.2505	0.0125	0.604
	90	208.0	49.9	112751.1	292.68	0.2468	0.0142	0.636
	100	208.0	49.9	112642.9	292.62	0.2492	0.0157	0.646

-continued-

Rotameter 2	20	208.0	49.9	113210.7	292.54	0.2502	0.0272	0.763
	30	208.0	49.9	113980.2	292.51	0.2478	0.0412	0.803
	40	208.0	49.9	116573.9	292.40	0.2499	0.0544	0.829
	50	208.0	49.9	119773.6	292.37	0.2563	0.0663	0.850
	60	208.0	49.9	122393.8	292.27	0.2493	0.0818	0.863
	70	208.0	49.9	126383.0	292.28	0.2419	0.0984	0.883
	80	208.0	49.9	129469.6	292.21	0.2512	0.1083	0.896
	90	208.0	49.9	133722.6	292.15	0.2427	0.1261	0.916
	100							
Rotameter 1	10	312.0	74.8	120155.4	292.98	0.3747	0.0010	0.212
	20	312.0	74.8	118693.8	292.98	0.3760	0.0021	0.307
	30	312.0	74.8	118126.5	292.99	0.3740	0.0031	0.381
	40	312.0	74.8	117915.8	293.01	0.3749	0.0042	0.436
	50	312.0	74.8	117906.1	292.98	0.3743	0.0052	0.481
	60	312.0	74.8	117908.0	293.02	0.3748	0.0062	0.550
	70	312.0	74.8	118074.6	293.00	0.3730	0.0073	0.558
	80	312.0	74.8	118074.6	292.97	0.3734	0.0084	0.601
	90	312.0	74.8	117840.1	292.99	0.3752	0.0094	0.626
	100	312.0	74.8	118061.8	293.01	0.3750	0.0104	0.680
Rotameter 2	20	312.0	74.8	119655.3	292.98	0.3729	0.0182	0.784
	30	312.0	74.8	121801.8	292.97	0.3782	0.0270	0.853
	40	312.0	74.8	125796.1	292.91	0.3703	0.0367	0.875
	50	312.0	74.8	130020.4	292.89	0.3744	0.0454	0.888
	60	312.0	74.8	134676.7	292.87	0.3798	0.0537	0.898
	70	312.0	74.8	137872.8	292.86	0.3723	0.0639	0.907
	80	312.0	74.8	142566.1	292.91	0.3709	0.0733	0.913
	90	312.0	74.8	145411.2	292.89	0.3775	0.0811	0.922
	100	312.0	74.8	154183.1	292.71	0.3796	0.0896	0.926
Rotameter 1	10	416.0	99.8	125787.4	293.45	0.5003	0.0008	0.184
	20	416.0	99.8	124607.3	293.41	0.5011	0.0016	0.311
	30	416.0	99.8	124251.5	293.41	0.5007	0.0023	0.400
	40	416.0	99.8	123952.9	293.40	0.4998	0.0031	0.441
	50	416.0	99.8	124264.7	293.49	0.5003	0.0039	0.495
	60	416.0	99.8	124454.0	293.53	0.4986	0.0047	0.529
	70	416.0	99.8	124546.4	293.54	0.4998	0.0055	0.572
	80	416.0	99.8	124546.4	293.51	0.5001	0.0062	0.584
	90	416.0	99.8	125217.6	293.51	0.5008	0.0070	0.608
	100	416.0	99.8	125339.8	293.58	0.4999	0.0078	0.630
Rotameter 2	20	416.0	99.8	125339.8	293.54	0.5028	0.0135	0.740
	30	416.0	99.8	131535.3	293.55	0.5006	0.0204	0.794
	40	416.0	99.8	135755.2	293.49	0.4994	0.0272	0.822
	50	416.0	99.8	140090.1	293.45	0.4998	0.0340	0.832
	60	416.0	99.8	143514.0	293.44	0.5010	0.0407	0.831
	70	416.0	99.8	149845.5	293.41	0.5001	0.0476	0.831
	80	416.0	99.8	155871.7	293.40	0.4977	0.0546	0.831
	90	416.0	99.8	160796.9	293.32	0.4994	0.0613	0.828
	100							

-continued-

Rotameter 1	10	541.0	129.6	123439.4	293.00	0.6495	0.0006	0.181
	20	541.0	129.6	122420.6	293.04	0.6483	0.0012	0.288
	30	541.0	129.6	122306.7	293.10	0.6492	0.0018	0.348
	40	541.0	129.6	122559.2	293.36	0.6501	0.0024	0.428
	50	541.0	129.6	123084.3	293.39	0.6493	0.0030	0.464
	60	541.0	129.6	123711.8	293.54	0.6492	0.0036	0.540
	70	541.0	129.6	124065.9	293.55	0.6492	0.0042	0.556
	80	541.0	129.6	124428.8	293.69	0.6482	0.0048	0.587
	90	541.0	129.6	125295.6	293.77	0.6498	0.0054	0.596
	100	541.0	129.6	125749.2	293.81	0.6503	0.0060	0.632
Rotameter 2	20	541.0	129.6	129339.8	293.91	0.6476	0.0105	0.769
	30	541.0	129.6	134523.2	293.86	0.6486	0.0157	0.821
	40	541.0	129.6	139178.9	293.88	0.6498	0.0209	0.845
	50	541.0	129.6	145316.0	293.97	0.6490	0.0262	0.864
	60							
	70							
	80							
	90							
	100							
Rotameter 1	10	688.0	165.5	130871.2	291.85	0.8291	0.0005	0.129
	20	688.0	165.5	130659.1	292.09	0.8271	0.0009	0.241
	30	688.0	165.5	130809.5	292.21	0.8247	0.0014	0.308
	40	688.0	165.5	131374.7	292.38	0.8289	0.0019	0.395
	50	688.0	165.5	132267.4	292.50	0.8276	0.0024	0.437
	60	688.0	165.5	133018.8	292.62	0.8297	0.0028	0.482
	70	688.0	165.5	134165.7	292.66	0.8306	0.0033	0.523
	80	688.0	165.5	134988.0	292.84	0.8250	0.0038	0.540
	90	688.0	165.5	135888.7	294.50	0.8282	0.0042	0.574
	100	688.0	165.5	137134.8	294.51	0.8263	0.0047	0.594
Rotameter 2	20	688.0	165.5	142241.9	294.48	0.8275	0.0082	0.743
	30	688.0	165.5	148365.1	294.52	0.8270	0.0123	0.795
	40	688.0	165.5	156109.4	294.55	0.8322	0.0163	0.829
	50	688.0	165.5	160994.1	294.60	0.8283	0.0205	0.852
	60	688.0	165.5	166792.9	294.65	0.8256	0.0247	0.873
	70							
	80							
	90							
	100							

Table B.2: Void fraction in the minimum gap between the tubes (to the south of central tube)

Air Rotameter	Air flow rate (%)	Mass flux based on min area (kg/m^2s)	Mass flux (kg/m^2s)	Two-pahse flow pressure (Pa)	Two-phase flow temperature (K)	Total mass flow rate (kg/s)	Quality (-)	Void fraction at the gap to the south of central tube (min gap) (-)
Rotameter 1	10	25.0	6.1	110187.9	294.39	0.0295	0.0132	0.243
	20	25.0	6.1	108860.9	294.31	0.0294	0.0265	0.389
	30	25.0	6.1	108390.7	294.27	0.0297	0.0394	0.437
	40	25.0	6.1	108088.1	294.20	0.0301	0.0518	0.495
	50	25.0	6.1	107741.1	294.09	0.0309	0.0631	0.534
	60	25.0	6.1	107425.1	294.10	0.0294	0.0797	0.592
	70	25.0	6.1	107224.6	294.05	0.0311	0.0878	0.604
	80	25.0	6.1	106918.6	293.84	0.0314	0.0994	0.630
	90	25.0	6.1	106921.8	293.76	0.0318	0.1103	0.636
	100	25.0	6.1	106822.6	293.71	0.0317	0.1231	0.649
Rotameter 2	20	25.0	6.1	105013.4	292.23	0.0298	0.2282	0.774
	30	25.0	6.1	103919.6	291.72	0.0299	0.3408	0.837
	40	25.0	6.1	103747.3	290.14	0.0359	0.4533	0.879
	50	25.0	6.1	112047.2	287.82	0.0316	0.5383	0.904
	60							
	70							
	80							
	90							
	100							
Rotameter 1	10	65.0	15.6	112357.1	293.95	0.0787	0.0050	0.259
	20	65.0	15.6	110763.0	293.86	0.0775	0.0101	0.374
	30	65.0	15.6	110034.4	293.86	0.0754	0.0155	0.436
	40	65.0	15.6	109471.9	293.86	0.0808	0.0193	0.492
	50	65.0	15.6	109362.5	293.85	0.0777	0.0251	0.567
	60	65.0	15.6	108837.9	293.83	0.0785	0.0298	0.584
	70	65.0	15.6	108512.1	293.82	0.0794	0.0344	0.616
	80	65.0	15.6	108282.9	293.79	0.0778	0.0401	0.629
	90	65.0	15.6	108208.9	293.78	0.0787	0.0446	0.648
	100	65.0	15.6	107954.2	293.75	0.0788	0.0495	0.664
Rotameter 2	20	65.0	15.6	107242.0	293.64	0.0767	0.0886	0.754
	30	65.0	15.6	107099.6	293.15	0.0759	0.1344	0.816
	40	65.0	15.6	107806.5	292.71	0.0776	0.1752	0.862
	50	65.0	15.6	108552.9	292.54	0.0816	0.2083	0.890
	60	65.0	15.6	109974.6	292.14	0.0789	0.2586	0.898
	70	65.0	15.6	110590.0	291.92	0.0786	0.3030	0.909
	80							
	90							
	100							

-continued-

Rotameter 1	10	105.0	25.2	114185.9	294.07	0.1275	0.0031	0.231
	20	105.0	25.2	112744.4	294.18	0.1264	0.0062	0.366
	30	105.0	25.2	111919.0	294.21	0.1261	0.0093	0.432
	40	105.0	25.2	111266.2	293.15	0.1266	0.0123	0.496
	50	105.0	25.2	111091.3	294.26	0.1264	0.0154	0.524
	60	105.0	25.2	110964.6	294.20	0.1246	0.0188	0.581
	70	105.0	25.2	110650.3	294.17	0.1260	0.0217	0.605
	80	105.0	25.2	110434.6	294.24	0.1284	0.0243	0.617
	90	105.0	25.2	110146.3	294.22	0.1273	0.0276	0.643
	100	105.0	25.2	110192.4	293.15	0.1259	0.0310	0.656
Rotameter 2	20	105.0	25.2	109130.3	294.03	0.1251	0.0544	0.725
	30	105.0	25.2	109630.5	293.81	0.1242	0.0821	0.787
	40	105.0	25.2	111229.9	293.62	0.1271	0.1070	0.827
	50	105.0	25.2	112845.2	293.51	0.1263	0.1346	0.862
	60	105.0	25.2	115002.6	293.28	0.1255	0.1625	0.871
	70	105.0	25.2	117164.7	293.14	0.1259	0.1891	0.877
	80							
	90							
	100							
Rotameter 1	10	156.0	37.4	114860.0	292.22	0.1865	0.0021	0.215
	20	156.0	37.4	113074.3	292.24	0.1861	0.0042	0.373
	30	156.0	37.4	112447.2	292.30	0.1870	0.0063	0.455
	40	156.0	37.4	112021.1	292.17	0.1880	0.0083	0.488
	50	156.0	37.4	111396.0	292.24	0.1875	0.0104	0.551
	60	156.0	37.4	111326.7	292.17	0.1884	0.0124	0.574
	70	156.0	37.4	111048.0	292.13	0.1898	0.0144	0.598
	80	156.0	37.4	110853.8	292.17	0.1865	0.0167	0.636
	90	156.0	37.4	110579.7	292.20	0.1877	0.0187	0.635
	100	156.0	37.4	110624.8	292.21	0.1875	0.0208	0.662
Rotameter 2	20	156.0	37.4	108937.7	292.11	0.1907	0.0357	0.744
	30	156.0	37.4	109292.5	292.02	0.1896	0.0538	0.792
	40	156.0	37.4	110956.4	291.75	0.1836	0.0741	0.821
	50	156.0	37.4	113251.6	291.53	0.1848	0.0920	0.840
	60	156.0	37.4	115457.7	291.58	0.1874	0.1089	0.845
	70							
	80							
	90							
	100							
Rotameter 1	10	208.0	49.9	115938.4	292.64	0.2497	0.0016	0.210
	20	208.0	49.9	114324.1	292.61	0.2498	0.0031	0.340
	30	208.0	49.9	113745.6	292.56	0.2496	0.0047	0.430
	40	208.0	49.9	113248.0	292.59	0.2483	0.0063	0.477
	50	208.0	49.9	113168.5	292.55	0.2497	0.0078	0.531
	60	208.0	49.9	112978.2	292.55	0.2508	0.0093	0.571
	70	208.0	49.9	112809.0	292.64	0.2501	0.0109	0.598
	80	208.0	49.9	112809.0	292.72	0.2505	0.0125	0.630
	90	208.0	49.9	112751.1	292.68	0.2468	0.0142	0.642
	100	208.0	49.9	112642.9	292.62	0.2492	0.0157	0.654

-continued-

Rotameter 2	20	208.0	49.9	113210.7	292.54	0.2502	0.0272	0.755
	30	208.0	49.9	113980.2	292.51	0.2478	0.0412	0.804
	40	208.0	49.9	116573.9	292.40	0.2499	0.0544	0.824
	50	208.0	49.9	119773.6	292.37	0.2563	0.0663	0.830
	60	208.0	49.9	122393.8	292.27	0.2493	0.0818	0.830
	70	208.0	49.9	126383.0	292.28	0.2419	0.0984	0.826
	80	208.0	49.9	129469.6	292.21	0.2512	0.1083	0.833
	90	208.0	49.9	133722.6	292.15	0.2427	0.1261	0.845
	100							
Rotameter 1	10	312.0	74.8	120155.4	292.98	0.3747	0.0010	0.168
	20	312.0	74.8	118693.8	292.98	0.3760	0.0021	0.338
	30	312.0	74.8	118126.5	292.99	0.3740	0.0031	0.405
	40	312.0	74.8	117915.8	293.01	0.3749	0.0042	0.464
	50	312.0	74.8	117906.1	292.98	0.3743	0.0052	0.519
	60	312.0	74.8	117908.0	293.02	0.3748	0.0062	0.544
	70	312.0	74.8	118074.6	293.00	0.3730	0.0073	0.590
	80	312.0	74.8	118074.6	292.97	0.3734	0.0084	0.608
	90	312.0	74.8	117840.1	292.99	0.3752	0.0094	0.619
	100	312.0	74.8	118061.8	293.01	0.3750	0.0104	0.621
Rotameter 2	20	312.0	74.8	119655.3	292.98	0.3729	0.0182	0.750
	30	312.0	74.8	121801.8	292.97	0.3782	0.0270	0.801
	40	312.0	74.8	125796.1	292.91	0.3703	0.0367	0.824
	50	312.0	74.8	130020.4	292.89	0.3744	0.0454	0.828
	60	312.0	74.8	134676.7	292.87	0.3798	0.0537	0.826
	70	312.0	74.8	137872.8	292.86	0.3723	0.0639	0.823
	80	312.0	74.8	142566.1	292.91	0.3709	0.0733	0.823
	90	312.0	74.8	145411.2	292.89	0.3775	0.0811	0.824
	100	312.0	74.8	154183.1	292.71	0.3796	0.0896	0.833
Rotameter 1	10	416.0	99.8	125787.4	293.45	0.5003	0.0008	0.184
	20	416.0	99.8	124607.3	293.41	0.5011	0.0016	0.311
	30	416.0	99.8	124251.5	293.41	0.5007	0.0023	0.400
	40	416.0	99.8	123952.9	293.40	0.4998	0.0031	0.441
	50	416.0	99.8	124264.7	293.49	0.5003	0.0039	0.495
	60	416.0	99.8	124454.0	293.53	0.4986	0.0047	0.529
	70	416.0	99.8	124546.4	293.54	0.4998	0.0055	0.572
	80	416.0	99.8	124546.4	293.51	0.5001	0.0062	0.584
	90	416.0	99.8	125217.6	293.51	0.5008	0.0070	0.608
	100	416.0	99.8	125339.8	293.58	0.4999	0.0078	0.630
Rotameter 2	20	416.0	99.8	125339.8	293.54	0.5028	0.0135	0.740
	30	416.0	99.8	131535.3	293.55	0.5006	0.0204	0.794
	40	416.0	99.8	135755.2	293.49	0.4994	0.0272	0.822
	50	416.0	99.8	140090.1	293.45	0.4998	0.0340	0.832
	60	416.0	99.8	143514.0	293.44	0.5010	0.0407	0.831
	70	416.0	99.8	149845.5	293.41	0.5001	0.0476	0.831
	80	416.0	99.8	155871.7	293.40	0.4977	0.0546	0.831
	90	416.0	99.8	160796.9	293.32	0.4994	0.0613	0.828
	100							

-continued-

Rotameter 1	10	541.0	129.6	123439.4	293.00	0.6495	0.0006	0.166
	20	541.0	129.6	122420.6	293.04	0.6483	0.0012	0.299
	30	541.0	129.6	122306.7	293.10	0.6492	0.0018	0.364
	40	541.0	129.6	122559.2	293.36	0.6501	0.0024	0.410
	50	541.0	129.6	123084.3	293.39	0.6493	0.0030	0.484
	60	541.0	129.6	123711.8	293.54	0.6492	0.0036	0.524
	70	541.0	129.6	124065.9	293.55	0.6492	0.0042	0.541
	80	541.0	129.6	124428.8	293.69	0.6482	0.0048	0.577
	90	541.0	129.6	125295.6	293.77	0.6498	0.0054	0.593
	100	541.0	129.6	125749.2	293.81	0.6503	0.0060	0.617
Rotameter 2	20	541.0	129.6	129339.8	293.91	0.6476	0.0105	0.740
	30	541.0	129.6	134523.2	293.86	0.6486	0.0157	0.795
	40	541.0	129.6	139178.9	293.88	0.6498	0.0209	0.811
	50	541.0	129.6	145316.0	293.97	0.6490	0.0262	0.819
	60							
	70							
	80							
	90							
	100							
Rotameter 1	10	688.0	165.5	130871.2	291.85	0.8291	0.0005	0.144
	20	688.0	165.5	130659.1	292.09	0.8271	0.0009	0.266
	30	688.0	165.5	130809.5	292.21	0.8247	0.0014	0.335
	40	688.0	165.5	131374.7	292.38	0.8289	0.0019	0.382
	50	688.0	165.5	132267.4	292.50	0.8276	0.0024	0.418
	60	688.0	165.5	133018.8	292.62	0.8297	0.0028	0.471
	70	688.0	165.5	134165.7	292.66	0.8306	0.0033	0.500
	80	688.0	165.5	134988.0	292.84	0.8250	0.0038	0.540
	90	688.0	165.5	135888.7	294.50	0.8282	0.0042	0.556
	100	688.0	165.5	137134.8	294.51	0.8263	0.0047	0.592
Rotameter 2	20	688.0	165.5	142241.9	294.48	0.8275	0.0082	0.722
	30	688.0	165.5	148365.1	294.52	0.8270	0.0123	0.755
	40	688.0	165.5	156109.4	294.55	0.8322	0.0163	0.786
	50	688.0	165.5	160994.1	294.60	0.8283	0.0205	0.800
	60	688.0	165.5	166792.9	294.65	0.8256	0.0247	0.819
	70							
	80							
	90							
	100							

Table B.3: Void fraction in the minimum gap between the tubes (to the east of central tube)

Air Rotameter	Air flow rate (%)	Mass flux based on min area (kg/m^{2}s)	Mass flux (kg/m^{2}s)	Two-pahse flow pressure (Pa)	Two-phase flow temperature (K)	Total mass flow rate (kg/s)	Quality (-)	Void fraction at the gap to the east of central tube (min gap)(-)
Rotameter 1	10	25.0	6.1	110187.9	294.39	0.0295	0.0132	0.281
	20	25.0	6.1	108860.9	294.31	0.0294	0.0265	0.339
	30	25.0	6.1	108390.7	294.27	0.0297	0.0394	0.373
	40	25.0	6.1	108088.1	294.20	0.0301	0.0518	0.433
	50	25.0	6.1	107741.1	294.09	0.0309	0.0631	0.451
	60	25.0	6.1	107425.1	294.10	0.0294	0.0797	0.480
	70	25.0	6.1	107224.6	294.05	0.0311	0.0878	0.524
	80	25.0	6.1	106918.6	293.84	0.0314	0.0994	0.532
	90	25.0	6.1	106921.8	293.76	0.0318	0.1103	0.560
	100	25.0	6.1	106822.6	293.71	0.0317	0.1231	0.591
Rotameter 2	20	25.0	6.1	105013.4	292.23	0.0298	0.2282	0.726
	30	25.0	6.1	103919.6	291.72	0.0299	0.3408	0.820
	40	25.0	6.1	103747.3	290.14	0.0359	0.4533	0.875
	50	25.0	6.1	112047.2	287.82	0.0316	0.5383	0.919
	60							
	70							
	80							
	90							
	100							
Rotameter 1	10	65.0	15.6	112357.1	293.95	0.0787	0.0050	0.290
	20	65.0	15.6	110763.0	293.86	0.0775	0.0101	0.355
	30	65.0	15.6	110034.4	293.86	0.0754	0.0155	0.375
	40	65.0	15.6	109471.9	293.86	0.0808	0.0193	0.418
	50	65.0	15.6	109362.5	293.85	0.0777	0.0251	0.462
	60	65.0	15.6	108837.9	293.83	0.0785	0.0298	0.475
	70	65.0	15.6	108512.1	293.82	0.0794	0.0344	0.519
	80	65.0	15.6	108282.9	293.79	0.0778	0.0401	0.528
	90	65.0	15.6	108208.9	293.78	0.0787	0.0446	0.562
	100	65.0	15.6	107954.2	293.75	0.0788	0.0495	0.582
Rotameter 2	20	65.0	15.6	107242.0	293.64	0.0767	0.0886	0.712
	30	65.0	15.6	107099.6	293.15	0.0759	0.1344	0.789
	40	65.0	15.6	107806.5	292.71	0.0776	0.1752	0.834
	50	65.0	15.6	108552.9	292.54	0.0816	0.2083	0.876
	60	65.0	15.6	109974.6	292.14	0.0789	0.2586	0.902
	70	65.0	15.6	110590.0	291.92	0.0786	0.3030	0.921
	80							
	90							
	100							

-continued-

Rotameter 1	10	105.0	25.2	114185.9	294.07	0.1275	0.0031	0.292
	20	105.0	25.2	112744.4	294.18	0.1264	0.0062	0.354
	30	105.0	25.2	111919.0	294.21	0.1261	0.0093	0.379
	40	105.0	25.2	111266.2	293.15	0.1266	0.0123	0.423
	50	105.0	25.2	111091.3	294.26	0.1264	0.0154	0.454
	60	105.0	25.2	110964.6	294.20	0.1246	0.0188	0.486
	70	105.0	25.2	110650.3	294.17	0.1260	0.0217	0.507
	80	105.0	25.2	110434.6	294.24	0.1284	0.0243	0.534
	90	105.0	25.2	110146.3	294.22	0.1273	0.0276	0.558
	100	105.0	25.2	110192.4	293.15	0.1259	0.0310	0.599
Rotameter 2	20	105.0	25.2	109130.3	294.03	0.1251	0.0544	0.708
	30	105.0	25.2	109630.5	293.81	0.1242	0.0821	0.781
	40	105.0	25.2	111229.9	293.62	0.1271	0.1070	0.836
	50	105.0	25.2	112845.2	293.51	0.1263	0.1346	0.863
	60	105.0	25.2	115002.6	293.28	0.1255	0.1625	0.887
	70	105.0	25.2	117164.7	293.14	0.1259	0.1891	0.915
	80							
	90							
	100							
Rotameter 1	10	156.0	37.4	114860.0	292.22	0.1865	0.0021	0.294
	20	156.0	37.4	113074.3	292.24	0.1861	0.0042	0.361
	30	156.0	37.4	112447.2	292.30	0.1870	0.0063	0.378
	40	156.0	37.4	112021.1	292.17	0.1880	0.0083	0.410
	50	156.0	37.4	111396.0	292.24	0.1875	0.0104	0.434
	60	156.0	37.4	111326.7	292.17	0.1884	0.0124	0.467
	70	156.0	37.4	111048.0	292.13	0.1898	0.0144	0.490
	80	156.0	37.4	110853.8	292.17	0.1865	0.0167	0.529
	90	156.0	37.4	110579.7	292.20	0.1877	0.0187	0.532
	100	156.0	37.4	110624.8	292.21	0.1875	0.0208	0.550
Rotameter 2	20	156.0	37.4	108937.7	292.11	0.1907	0.0357	0.690
	30	156.0	37.4	109292.5	292.02	0.1896	0.0538	0.761
	40	156.0	37.4	110956.4	291.75	0.1836	0.0741	0.817
	50	156.0	37.4	113251.6	291.53	0.1848	0.0920	0.853
	60	156.0	37.4	115457.7	291.58	0.1874	0.1089	0.874
	70							
	80							
	90							
	100							
Rotameter 1	10	208.0	49.9	115938.4	292.64	0.2497	0.0016	0.286
	20	208.0	49.9	114324.1	292.61	0.2498	0.0031	0.360
	30	208.0	49.9	113745.6	292.56	0.2496	0.0047	0.381
	40	208.0	49.9	113248.0	292.59	0.2483	0.0063	0.413
	50	208.0	49.9	113168.5	292.55	0.2497	0.0078	0.445
	60	208.0	49.9	112978.2	292.55	0.2508	0.0093	0.479
	70	208.0	49.9	112809.0	292.64	0.2501	0.0109	0.491
	80	208.0	49.9	112809.0	292.72	0.2505	0.0125	0.519
	90	208.0	49.9	112751.1	292.68	0.2468	0.0142	0.541
	100	208.0	49.9	112642.9	292.62	0.2492	0.0157	0.579

-continued-

Rotameter 2	20	208.0	49.9	113210.7	292.54	0.2502	0.0272	0.704
	30	208.0	49.9	113980.2	292.51	0.2478	0.0412	0.777
	40	208.0	49.9	116573.9	292.40	0.2499	0.0544	0.815
	50	208.0	49.9	119773.6	292.37	0.2563	0.0663	0.850
	60	208.0	49.9	122393.8	292.27	0.2493	0.0818	0.886
	70	208.0	49.9	126383.0	292.28	0.2419	0.0984	0.903
	80	208.0	49.9	129469.6	292.21	0.2512	0.1083	0.920
	90	208.0	49.9	133722.6	292.15	0.2427	0.1261	0.935
	100							
Rotameter 1	10	312.0	74.8	120155.4	292.98	0.3747	0.0010	0.264
	20	312.0	74.8	118693.8	292.98	0.3760	0.0021	0.352
	30	312.0	74.8	118126.5	292.99	0.3740	0.0031	0.382
	40	312.0	74.8	117915.8	293.01	0.3749	0.0042	0.412
	50	312.0	74.8	117906.1	292.98	0.3743	0.0052	0.433
	60	312.0	74.8	117908.0	293.02	0.3748	0.0062	0.477
	70	312.0	74.8	118074.6	293.00	0.3730	0.0073	0.484
	80	312.0	74.8	118074.6	292.97	0.3734	0.0084	0.508
	90	312.0	74.8	117840.1	292.99	0.3752	0.0094	0.536
	100	312.0	74.8	118061.8	293.01	0.3750	0.0104	0.560
Rotameter 2	20	312.0	74.8	119655.3	292.98	0.3729	0.0182	0.698
	30	312.0	74.8	121801.8	292.97	0.3782	0.0270	0.759
	40	312.0	74.8	125796.1	292.91	0.3703	0.0367	0.811
	50	312.0	74.8	130020.4	292.89	0.3744	0.0454	0.836
	60	312.0	74.8	134676.7	292.87	0.3798	0.0537	0.864
	70	312.0	74.8	137872.8	292.86	0.3723	0.0639	0.882
	80	312.0	74.8	142566.1	292.91	0.3709	0.0733	0.893
	90	312.0	74.8	145411.2	292.89	0.3775	0.0811	0.901
	100	312.0	74.8	154183.1	292.71	0.3796	0.0896	0.911
Rotameter 1	10	416.0	99.8	125787.4	293.45	0.5003	0.0008	0.228
	20	416.0	99.8	124607.3	293.41	0.5011	0.0016	0.308
	30	416.0	99.8	124251.5	293.41	0.5007	0.0023	0.349
	40	416.0	99.8	123952.9	293.40	0.4998	0.0031	0.390
	50	416.0	99.8	124264.7	293.49	0.5003	0.0039	0.406
	60	416.0	99.8	124454.0	293.53	0.4986	0.0047	0.460
	70	416.0	99.8	124546.4	293.54	0.4998	0.0055	0.481
	80	416.0	99.8	124546.4	293.51	0.5001	0.0062	0.494
	90	416.0	99.8	125217.6	293.51	0.5008	0.0070	0.524
	100	416.0	99.8	125339.8	293.58	0.4999	0.0078	0.533
Rotameter 2	20	416.0	99.8	125339.8	293.54	0.5028	0.0135	0.675
	30	416.0	99.8	131535.3	293.55	0.5006	0.0204	0.759
	40	416.0	99.8	135755.2	293.49	0.4994	0.0272	0.794
	50	416.0	99.8	140090.1	293.45	0.4998	0.0340	0.825
	60	416.0	99.8	143514.0	293.44	0.5010	0.0407	0.850
	70	416.0	99.8	149845.5	293.41	0.5001	0.0476	0.862
	80	416.0	99.8	155871.7	293.40	0.4977	0.0546	0.874
	90	416.0	99.8	160796.9	293.32	0.4994	0.0613	0.888
	100							

-continued-

Rotameter 1	10	541.0	129.6	123439.4	293.00	0.6495	0.0006	0.210
	20	541.0	129.6	122420.6	293.04	0.6483	0.0012	0.309
	30	541.0	129.6	122306.7	293.10	0.6492	0.0018	0.358
	40	541.0	129.6	122559.2	293.36	0.6501	0.0024	0.383
	50	541.0	129.6	123084.3	293.39	0.6493	0.0030	0.414
	60	541.0	129.6	123711.8	293.54	0.6492	0.0036	0.446
	70	541.0	129.6	124065.9	293.55	0.6492	0.0042	0.476
	80	541.0	129.6	124428.8	293.69	0.6482	0.0048	0.501
	90	541.0	129.6	125295.6	293.77	0.6498	0.0054	0.525
	100	541.0	129.6	125749.2	293.81	0.6503	0.0060	0.555
Rotameter 2	20	541.0	129.6	129339.8	293.91	0.6476	0.0105	0.680
	30	541.0	129.6	134523.2	293.86	0.6486	0.0157	0.751
	40	541.0	129.6	139178.9	293.88	0.6498	0.0209	0.788
	50	541.0	129.6	145316.0	293.97	0.6490	0.0262	0.816
	60							
	70							
	80							
	90							
	100							
Rotameter 1	10	688.0	165.5	130871.2	291.85	0.8291	0.0005	0.150
	20	688.0	165.5	130659.1	292.09	0.8271	0.0009	0.248
	30	688.0	165.5	130809.5	292.21	0.8247	0.0014	0.310
	40	688.0	165.5	131374.7	292.38	0.8289	0.0019	0.359
	50	688.0	165.5	132267.4	292.50	0.8276	0.0024	0.394
	60	688.0	165.5	133018.8	292.62	0.8297	0.0028	0.420
	70	688.0	165.5	134165.7	292.66	0.8306	0.0033	0.456
	80	688.0	165.5	134988.0	292.84	0.8250	0.0038	0.474
	90	688.0	165.5	135888.7	294.50	0.8282	0.0042	0.499
	100	688.0	165.5	137134.8	294.51	0.8263	0.0047	0.543
Rotameter 2	20	688.0	165.5	142241.9	294.48	0.8275	0.0082	0.648
	30	688.0	165.5	148365.1	294.52	0.8270	0.0123	0.724
	40	688.0	165.5	156109.4	294.55	0.8322	0.0163	0.761
	50	688.0	165.5	160994.1	294.60	0.8283	0.0205	0.779
	60	688.0	165.5	166792.9	294.65	0.8256	0.0247	0.798
	70							
	80							
	90							
	100							

Table B.4: Pitch void fraction

Air Rotameter	Air flow rate (%)	Mass flux based on min area (kg/m^{2}s)	Mass flux (kg/m^{2}s)	Two-pahse flow pressure (Pa)	Two-phase flow temperature (K)	Total mass flow rate (kg/s)	Quality (-)	Void fraction pitch (-)
Rotameter 1	10	25.0	6.1	110187.9	294.39	0.0295	0.0132	0.300
	20	25.0	6.1	108860.9	294.31	0.0294	0.0265	0.375
	30	25.0	6.1	108390.7	294.27	0.0297	0.0394	0.433
	40	25.0	6.1	108088.1	294.20	0.0301	0.0518	0.492
	50	25.0	6.1	107741.1	294.09	0.0309	0.0631	0.513
	60	25.0	6.1	107425.1	294.10	0.0294	0.0797	0.559
	70	25.0	6.1	107224.6	294.05	0.0311	0.0878	0.588
	80	25.0	6.1	106918.6	293.84	0.0314	0.0994	0.612
	90	25.0	6.1	106921.8	293.76	0.0318	0.1103	0.635
	100	25.0	6.1	106822.6	293.71	0.0317	0.1231	0.666
Rotameter 2	20	25.0	6.1	105013.4	292.23	0.0298	0.2282	0.795
	30	25.0	6.1	103919.6	291.72	0.0299	0.3408	0.859
	40	25.0	6.1	103747.3	290.14	0.0359	0.4533	0.904
	50	25.0	6.1	112047.2	287.82	0.0316	0.5383	0.935
	60							
	70							
	80							
	90							
	100							
Rotameter 1	10	65.0	15.6	112357.1	293.95	0.0787	0.0050	0.277
	20	65.0	15.6	110763.0	293.86	0.0775	0.0101	0.370
	30	65.0	15.6	110034.4	293.86	0.0754	0.0155	0.415
	40	65.0	15.6	109471.9	293.86	0.0808	0.0193	0.471
	50	65.0	15.6	109362.5	293.85	0.0777	0.0251	0.513
	60	65.0	15.6	108837.9	293.83	0.0785	0.0298	0.537
	70	65.0	15.6	108512.1	293.82	0.0794	0.0344	0.573
	80	65.0	15.6	108282.9	293.79	0.0778	0.0401	0.596
	90	65.0	15.6	108208.9	293.78	0.0787	0.0446	0.608
	100	65.0	15.6	107954.2	293.75	0.0788	0.0495	0.632
Rotameter 2	20	65.0	15.6	107242.0	293.64	0.0767	0.0886	0.751
	30	65.0	15.6	107099.6	293.15	0.0759	0.1344	0.814
	40	65.0	15.6	107806.5	292.71	0.0776	0.1752	0.858
	50	65.0	15.6	108552.9	292.54	0.0816	0.2083	0.894
	60	65.0	15.6	109974.6	292.14	0.0789	0.2586	0.914
	70	65.0	15.6	110590.0	291.92	0.0786	0.3030	0.928
	80							
	90							
	100							

-continued-

Rotameter 1	10	105.0	25.2	114185.9	294.07	0.1275	0.0031	0.262
	20	105.0	25.2	112744.4	294.18	0.1264	0.0062	0.351
	30	105.0	25.2	111919.0	294.21	0.1261	0.0093	0.414
	40	105.0	25.2	111266.2	293.15	0.1266	0.0123	0.458
	50	105.0	25.2	111091.3	294.26	0.1264	0.0154	0.503
	60	105.0	25.2	110964.6	294.20	0.1246	0.0188	0.541
	70	105.0	25.2	110650.3	294.17	0.1260	0.0217	0.561
	80	105.0	25.2	110434.6	294.24	0.1284	0.0243	0.576
	90	105.0	25.2	110146.3	294.22	0.1273	0.0276	0.599
	100	105.0	25.2	110192.4	293.15	0.1259	0.0310	0.633
Rotameter 2	20	105.0	25.2	109130.3	294.03	0.1251	0.0544	0.735
	30	105.0	25.2	109630.5	293.81	0.1242	0.0821	0.789
	40	105.0	25.2	111229.9	293.62	0.1271	0.1070	0.832
	50	105.0	25.2	112845.2	293.51	0.1263	0.1346	0.860
	60	105.0	25.2	115002.6	293.28	0.1255	0.1625	0.883
	70	105.0	25.2	117164.7	293.14	0.1259	0.1891	0.905
	80							
	90							
	100							
Rotameter 1	10	156.0	37.4	114860.0	292.22	0.1865	0.0021	0.260
	20	156.0	37.4	113074.3	292.24	0.1861	0.0042	0.348
	30	156.0	37.4	112447.2	292.30	0.1870	0.0063	0.391
	40	156.0	37.4	112021.1	292.17	0.1880	0.0083	0.433
	50	156.0	37.4	111396.0	292.24	0.1875	0.0104	0.475
	60	156.0	37.4	111326.7	292.17	0.1884	0.0124	0.520
	70	156.0	37.4	111048.0	292.13	0.1898	0.0144	0.547
	80	156.0	37.4	110853.8	292.17	0.1865	0.0167	0.578
	90	156.0	37.4	110579.7	292.20	0.1877	0.0187	0.580
	100	156.0	37.4	110624.8	292.21	0.1875	0.0208	0.595
Rotameter 2	20	156.0	37.4	108937.7	292.11	0.1907	0.0357	0.718
	30	156.0	37.4	109292.5	292.02	0.1896	0.0538	0.784
	40	156.0	37.4	110956.4	291.75	0.1836	0.0741	0.818
	50	156.0	37.4	113251.6	291.53	0.1848	0.0920	0.853
	60	156.0	37.4	115457.7	291.58	0.1874	0.1089	0.875
	70							
	80							
	90							
	100							
Rotameter 1	10	208.0	49.9	115938.4	292.64	0.2497	0.0016	0.243
	20	208.0	49.9	114324.1	292.61	0.2498	0.0031	0.338
	30	208.0	49.9	113745.6	292.56	0.2496	0.0047	0.382
	40	208.0	49.9	113248.0	292.59	0.2483	0.0063	0.427
	50	208.0	49.9	113168.5	292.55	0.2497	0.0078	0.470
	60	208.0	49.9	112978.2	292.55	0.2508	0.0093	0.517
	70	208.0	49.9	112809.0	292.64	0.2501	0.0109	0.538
	80	208.0	49.9	112809.0	292.72	0.2505	0.0125	0.561
	90	208.0	49.9	112751.1	292.68	0.2468	0.0142	0.588
	100	208.0	49.9	112642.9	292.62	0.2492	0.0157	0.612

-continued-

Rotameter 2	20	208.0	49.9	113210.7	292.54	0.2502	0.0272	0.734
	30	208.0	49.9	113980.2	292.51	0.2478	0.0412	0.790
	40	208.0	49.9	116573.9	292.40	0.2499	0.0544	0.822
	50	208.0	49.9	119773.6	292.37	0.2563	0.0663	0.850
	60	208.0	49.9	122393.8	292.27	0.2493	0.0818	0.875
	70	208.0	49.9	126383.0	292.28	0.2419	0.0984	0.893
	80	208.0	49.9	129469.6	292.21	0.2512	0.1083	0.908
	90	208.0	49.9	133722.6	292.15	0.2427	0.1261	0.925
	100							
Rotameter 1	10	312.0	74.8	120155.4	292.98	0.3747	0.0010	0.238
	20	312.0	74.8	118693.8	292.98	0.3760	0.0021	0.329
	30	312.0	74.8	118126.5	292.99	0.3740	0.0031	0.381
	40	312.0	74.8	117915.8	293.01	0.3749	0.0042	0.424
	50	312.0	74.8	117906.1	292.98	0.3743	0.0052	0.457
	60	312.0	74.8	117908.0	293.02	0.3748	0.0062	0.514
	70	312.0	74.8	118074.6	293.00	0.3730	0.0073	0.521
	80	312.0	74.8	118074.6	292.97	0.3734	0.0084	0.555
	90	312.0	74.8	117840.1	292.99	0.3752	0.0094	0.581
	100	312.0	74.8	118061.8	293.01	0.3750	0.0104	0.620
Rotameter 2	20	312.0	74.8	119655.3	292.98	0.3729	0.0182	0.741
	30	312.0	74.8	121801.8	292.97	0.3782	0.0270	0.806
	40	312.0	74.8	125796.1	292.91	0.3703	0.0367	0.843
	50	312.0	74.8	130020.4	292.89	0.3744	0.0454	0.862
	60	312.0	74.8	134676.7	292.87	0.3798	0.0537	0.881
	70	312.0	74.8	137872.8	292.86	0.3723	0.0639	0.894
	80	312.0	74.8	142566.1	292.91	0.3709	0.0733	0.903
	90	312.0	74.8	145411.2	292.89	0.3775	0.0811	0.911
	100	312.0	74.8	154183.1	292.71	0.3796	0.0896	0.918
Rotameter 1	10	416.0	99.8	125787.4	293.45	0.5003	0.0008	0.221
	20	416.0	99.8	124607.3	293.41	0.5011	0.0016	0.310
	30	416.0	99.8	124251.5	293.41	0.5007	0.0023	0.372
	40	416.0	99.8	123952.9	293.40	0.4998	0.0031	0.415
	50	416.0	99.8	124264.7	293.49	0.5003	0.0039	0.451
	60	416.0	99.8	124454.0	293.53	0.4986	0.0047	0.506
	70	416.0	99.8	124546.4	293.54	0.4998	0.0055	0.528
	80	416.0	99.8	124546.4	293.51	0.5001	0.0062	0.548
	90	416.0	99.8	125217.6	293.51	0.5008	0.0070	0.579
	100	416.0	99.8	125339.8	293.58	0.4999	0.0078	0.594
Rotameter 2	20	416.0	99.8	125339.8	293.54	0.5028	0.0135	0.729
	30	416.0	99.8	131535.3	293.55	0.5006	0.0204	0.794
	40	416.0	99.8	135755.2	293.49	0.4994	0.0272	0.825
	50	416.0	99.8	140090.1	293.45	0.4998	0.0340	0.847
	60	416.0	99.8	143514.0	293.44	0.5010	0.0407	0.867
	70	416.0	99.8	149845.5	293.41	0.5001	0.0476	0.878
	80	416.0	99.8	155871.7	293.40	0.4977	0.0546	0.887
	90	416.0	99.8	160796.9	293.32	0.4994	0.0613	0.896
	100							

-continued-

Rotameter 1	10	541.0	129.6	123439.4	293.00	0.6495	0.0006	0.195
	20	541.0	129.6	122420.6	293.04	0.6483	0.0012	0.299
	30	541.0	129.6	122306.7	293.10	0.6492	0.0018	0.353
	40	541.0	129.6	122559.2	293.36	0.6501	0.0024	0.406
	50	541.0	129.6	123084.3	293.39	0.6493	0.0030	0.439
	60	541.0	129.6	123711.8	293.54	0.6492	0.0036	0.493
	70	541.0	129.6	124065.9	293.55	0.6492	0.0042	0.516
	80	541.0	129.6	124428.8	293.69	0.6482	0.0048	0.544
	90	541.0	129.6	125295.6	293.77	0.6498	0.0054	0.560
	100	541.0	129.6	125749.2	293.81	0.6503	0.0060	0.593
Rotameter 2	20	541.0	129.6	129339.8	293.91	0.6476	0.0105	0.725
	30	541.0	129.6	134523.2	293.86	0.6486	0.0157	0.786
	40	541.0	129.6	139178.9	293.88	0.6498	0.0209	0.817
	50	541.0	129.6	145316.0	293.97	0.6490	0.0262	0.840
	60							
	70							
	80							
	90							
	100							
Rotameter 1	10	688.0	165.5	130871.2	291.85	0.8291	0.0005	0.140
	20	688.0	165.5	130659.1	292.09	0.8271	0.0009	0.245
	30	688.0	165.5	130809.5	292.21	0.8247	0.0014	0.309
	40	688.0	165.5	131374.7	292.38	0.8289	0.0019	0.377
	50	688.0	165.5	132267.4	292.50	0.8276	0.0024	0.415
	60	688.0	165.5	133018.8	292.62	0.8297	0.0028	0.451
	70	688.0	165.5	134165.7	292.66	0.8306	0.0033	0.490
	80	688.0	165.5	134988.0	292.84	0.8250	0.0038	0.507
	90	688.0	165.5	135888.7	294.50	0.8282	0.0042	0.537
	100	688.0	165.5	137134.8	294.51	0.8263	0.0047	0.569
Rotameter 2	20	688.0	165.5	142241.9	294.48	0.8275	0.0082	0.695
	30	688.0	165.5	148365.1	294.52	0.8270	0.0123	0.760
	40	688.0	165.5	156109.4	294.55	0.8322	0.0163	0.795
	50	688.0	165.5	160994.1	294.60	0.8283	0.0205	0.816
	60	688.0	165.5	166792.9	294.65	0.8256	0.0247	0.835
	70							
	80							
	90							
	100							

B.1.1 Predicted void fractions [1,2,3,70] for 38 mm in-line tube bundle

Table B.5: Predicted void fractions

Air flow rate (%)	Mass flux based on min area (kg/m^2s)	Mass flux (kg/m^2s)	Void fraction pitch (-) (present study)	Void fraction (-) prediction by Schrage et al [1]	Void fraction (-) prediction by Feenstra et al [3]	Void fraction (-) prediction by Dowlati et al [2]	Maximum slip model by Chisholm [70]	Homogenous model by Chisholm [70]
10	25	6.07	0.300	0.091	0.230	0.191	0.271	0.911
20	25	6.07	0.375	0.167	0.347	0.307	0.432	0.955
30	25	6.07	0.433	0.258	0.422	0.387	0.534	0.970
40	25	6.07	0.492	0.323	0.476	0.446	0.604	0.977
50	25	6.07	0.513	0.371	0.518	0.493	0.654	0.981
60	25	6.07	0.559	0.419	0.555	0.531	0.708	0.986
70	25	6.07	0.588	0.447	0.582	0.562	0.730	0.987
80	25	6.07	0.612	0.476	0.606	0.588	0.756	0.989
90	25	6.07	0.635	0.501	0.627	0.611	0.777	0.990
100	25	6.07	0.666	0.526	0.647	0.631	0.798	0.991
20	25	6.07	0.795	0.662	0.749	0.729	0.893	0.996
30	25	6.07	0.859	0.754	0.818	0.790	0.936	0.998
40	25	6.07	0.904	0.826	0.876	0.847	0.959	0.999
50	25	6.07	0.935	0.860	0.892	0.847	0.969	0.999
10	65	15.63	0.277	0.079	0.212	0.189	0.120	0.789
20	65	15.63	0.370	0.116	0.325	0.305	0.219	0.886
30	65	15.63	0.415	0.193	0.399	0.385	0.304	0.924
40	65	15.63	0.471	0.244	0.451	0.445	0.353	0.938
50	65	15.63	0.513	0.290	0.493	0.491	0.417	0.952
60	65	15.63	0.537	0.324	0.526	0.529	0.461	0.960
70	65	15.63	0.573	0.354	0.553	0.561	0.498	0.965
80	65	15.63	0.596	0.381	0.578	0.587	0.538	0.970
90	65	15.63	0.608	0.403	0.597	0.610	0.566	0.973
100	65	15.63	0.632	0.424	0.615	0.630	0.593	0.976
20	65	15.63	0.751	0.534	0.705	0.728	0.732	0.987
30	65	15.63	0.814	0.614	0.763	0.788	0.813	0.992
40	65	15.63	0.858	0.667	0.799	0.825	0.856	0.994
50	65	15.63	0.894	0.703	0.825	0.850	0.880	0.995
60	65	15.63	0.914	0.743	0.847	0.868	0.906	0.996
70	65	15.63	0.928	0.773	0.865	0.882	0.923	0.997
10	105	25.22	0.262	0.069	0.198	0.188	0.077	0.694
20	105	25.22	0.351	0.103	0.309	0.304	0.145	0.823
30	105	25.22	0.414	0.170	0.382	0.384	0.205	0.876
40	105	25.22	0.458	0.220	0.435	0.443	0.256	0.904
50	105	25.22	0.503	0.260	0.477	0.490	0.302	0.923
60	105	25.22	0.541	0.294	0.511	0.527	0.346	0.936
70	105	25.22	0.561	0.321	0.538	0.559	0.380	0.944
80	105	25.22	0.576	0.344	0.561	0.585	0.408	0.950
90	105	25.22	0.599	0.366	0.582	0.609	0.440	0.956
100	105	25.22	0.633	0.386	0.599	0.628	0.469	0.961
20	105	25.22	0.735	0.487	0.689	0.727	0.615	0.978
30	105	25.22	0.789	0.560	0.745	0.787	0.713	0.986
40	105	25.22	0.832	0.609	0.779	0.823	0.767	0.989
50	105	25.22	0.860	0.649	0.805	0.848	0.810	0.991
60	105	25.22	0.883	0.682	0.824	0.866	0.840	0.993
70	105	25.22	0.905	0.709	0.840	0.880	0.862	0.994
10	156	37.44	0.260	0.060	0.185	0.187	0.054	0.605
20	156	37.44	0.348	0.095	0.293	0.303	0.103	0.757
30	156	37.44	0.391	0.157	0.366	0.383	0.147	0.824
40	156	37.44	0.433	0.203	0.419	0.442	0.186	0.862
50	156	37.44	0.475	0.241	0.462	0.489	0.224	0.888
60	156	37.44	0.520	0.272	0.495	0.526	0.257	0.904
70	156	37.44	0.547	0.298	0.523	0.558	0.286	0.917
80	156	37.44	0.578	0.322	0.548	0.584	0.319	0.928
90	156	37.44	0.580	0.342	0.569	0.608	0.344	0.935
100	156	37.44	0.595	0.360	0.586	0.628	0.369	0.942
20	156	37.44	0.718	0.454	0.676	0.726	0.506	0.966
30	156	37.44	0.784	0.523	0.733	0.787	0.612	0.978
40	156	37.44	0.818	0.574	0.768	0.823	0.687	0.984
50	156	37.44	0.853	0.610	0.792	0.848	0.734	0.987
60	156	37.44	0.875	0.639	0.810	0.866	0.767	0.989
10	208	49.92	0.243	0.053	0.173	0.187	0.040	0.531
20	208	49.92	0.338	0.090	0.278	0.302	0.078	0.697
30	208	49.92	0.382	0.147	0.351	0.381	0.113	0.777
40	208	49.92	0.427	0.192	0.405	0.441	0.147	0.824
50	208	49.92	0.470	0.228	0.447	0.487	0.177	0.854
60	208	49.92	0.517	0.258	0.481	0.525	0.204	0.875
70	208	49.92	0.538	0.283	0.510	0.556	0.231	0.892
80	208	49.92	0.561	0.305	0.534	0.583	0.256	0.904
90	208	49.92	0.588	0.326	0.555	0.606	0.283	0.915

-continued-

100	208	49.92	0.612	0.343	0.574	0.626	0.303	0.922
20	208	49.92	0.734	0.435	0.663	0.723	0.432	0.954
30	208	49.92	0.790	0.501	0.720	0.784	0.538	0.969
40	208	49.92	0.822	0.547	0.755	0.820	0.607	0.976
50	208	49.92	0.850	0.580	0.778	0.845	0.653	0.980
60	208	49.92	0.875	0.612	0.797	0.863	0.700	0.984
70	208	49.92	0.893	0.639	0.812	0.876	0.738	0.986
80	208	49.92	0.908	0.656	0.823	0.887	0.756	0.987
90	208	49.92	0.925	0.678	0.833	0.896	0.783	0.989
10	312	74.8	0.238	0.042	0.151	0.184	0.027	0.422
20	312	74.8	0.329	0.081	0.250	0.299	0.052	0.596
30	312	74.8	0.381	0.134	0.321	0.378	0.077	0.691
40	312	74.8	0.424	0.175	0.375	0.437	0.100	0.749
50	312	74.8	0.457	0.209	0.417	0.483	0.123	0.789
60	312	74.8	0.514	0.237	0.452	0.521	0.144	0.818
70	312	74.8	0.521	0.262	0.481	0.552	0.164	0.840
80	312	74.8	0.555	0.283	0.506	0.578	0.184	0.857
90	312	74.8	0.581	0.302	0.528	0.602	0.201	0.871
100	312	74.8	0.620	0.319	0.547	0.622	0.219	0.882
20	312	74.8	0.741	0.408	0.640	0.719	0.330	0.929
30	312	74.8	0.806	0.471	0.699	0.779	0.421	0.950
40	312	74.8	0.843	0.517	0.734	0.815	0.496	0.962
50	312	74.8	0.862	0.550	0.759	0.840	0.547	0.969
60	312	74.8	0.881	0.576	0.776	0.858	0.586	0.973
70	312	74.8	0.894	0.601	0.792	0.872	0.628	0.977
80	312	74.8	0.903	0.621	0.804	0.883	0.658	0.979
90	312	74.8	0.911	0.637	0.814	0.893	0.680	0.981
100	312	74.8	0.918	0.651	0.819	0.899	0.697	0.982
10	416	99.84	0.221	0.034	0.132	0.181	0.020	0.343
20	416	99.84	0.310	0.074	0.224	0.294	0.039	0.513
30	416	99.84	0.372	0.122	0.292	0.373	0.057	0.614
40	416	99.84	0.415	0.161	0.346	0.432	0.075	0.680
50	416	99.84	0.451	0.193	0.388	0.478	0.092	0.726
60	416	99.84	0.506	0.221	0.423	0.515	0.109	0.761
70	416	99.84	0.528	0.245	0.453	0.547	0.125	0.788
80	416	99.84	0.548	0.266	0.478	0.573	0.140	0.809
90	416	99.84	0.579	0.284	0.500	0.596	0.155	0.826
100	416	99.84	0.594	0.301	0.520	0.616	0.169	0.841
20	416	99.84	0.729	0.389	0.619	0.715	0.262	0.902
30	416	99.84	0.794	0.451	0.677	0.774	0.345	0.930
40	416	99.84	0.825	0.495	0.714	0.811	0.411	0.946
50	416	99.84	0.847	0.528	0.740	0.836	0.463	0.955
60	416	99.84	0.867	0.554	0.761	0.855	0.507	0.961
70	416	99.84	0.878	0.577	0.774	0.868	0.542	0.966
80	416	99.84	0.887	0.596	0.786	0.879	0.573	0.969
90	416	99.84	0.896	0.613	0.796	0.888	0.599	0.972
10	541	129.6	0.195	0.028	0.116	0.179	0.015	0.281
20	541	129.6	0.299	0.068	0.202	0.291	0.030	0.442
30	541	129.6	0.353	0.111	0.266	0.369	0.044	0.542
40	541	129.6	0.406	0.147	0.317	0.428	0.058	0.611
50	541	129.6	0.439	0.178	0.358	0.473	0.071	0.661
60	541	129.6	0.493	0.204	0.393	0.510	0.084	0.700
70	541	129.6	0.516	0.228	0.422	0.541	0.097	0.731
80	541	129.6	0.544	0.248	0.448	0.568	0.109	0.756
90	541	129.6	0.560	0.266	0.469	0.590	0.120	0.775
100	541	129.6	0.593	0.282	0.489	0.610	0.132	0.792
20	541	129.6	0.725	0.370	0.589	0.708	0.208	0.867
30	541	129.6	0.786	0.431	0.651	0.768	0.280	0.904
40	541	129.6	0.817	0.475	0.691	0.806	0.338	0.924
50	541	129.6	0.840	0.507	0.718	0.831	0.387	0.937
10	688	165.5	0.140	0.022	0.096	0.173	0.011	0.217
20	688	165.5	0.245	0.058	0.170	0.282	0.022	0.358
30	688	165.5	0.309	0.096	0.229	0.359	0.033	0.455
40	688	165.5	0.377	0.129	0.276	0.417	0.044	0.525
50	688	165.5	0.415	0.158	0.315	0.462	0.054	0.578
60	688	165.5	0.451	0.183	0.348	0.499	0.063	0.620
70	688	165.5	0.490	0.205	0.377	0.530	0.073	0.653
80	688	165.5	0.507	0.225	0.404	0.556	0.083	0.684
90	688	165.5	0.537	0.243	0.425	0.579	0.092	0.706
100	688	165.5	0.569	0.259	0.444	0.598	0.101	0.726
20	688	165.5	0.695	0.346	0.548	0.697	0.162	0.818
30	688	165.5	0.760	0.408	0.614	0.758	0.221	0.866
40	688	165.5	0.795	0.451	0.655	0.796	0.269	0.891
50	688	165.5	0.816	0.485	0.687	0.823	0.315	0.910
60	688	165.5	0.835	0.511	0.709	0.842	0.352	0.921

B.2 Void fraction data sets for the four local void fractions measurements and the pitch average in the 19 mm in-line bundle

Table B.6: Void fraction in the minimum gap between the tubes (to the east of central tube)

Air Rotameter	Air flow rate (%)	Mass flux based on min area (kg/m^2s)	Mass flux (kg/m^2s)	Two-pahse flow pressure (Pa)	Two-phase flow temperature (K)	Total mass flow rate (kg/s)	Quality (-)	Void fraction at the gap to the east of central tube (min gap)(-)
Rotameter 1	10	25.0	6.1	110576.3	294.24	0.0304	0.0128	0.301
	20	25.0	6.1	109488.8	294.04	0.0304	0.0257	0.346
	30	25.0	6.1	108295.7	293.80	0.0298	0.0393	0.381
	40	25.0	6.1	108614.0	293.88	0.0297	0.0526	0.440
	50	25.0	6.1	107900.4	293.83	0.0296	0.0659	0.448
	60	25.0	6.1	107626.9	293.87	0.0303	0.0773	0.479
	70	25.0	6.1	107768.1	293.81	0.0306	0.0893	0.525
	80	25.0	6.1	107499.4	293.99	0.0299	0.1043	0.532
	90	25.0	6.1	107371.1	293.90	0.0299	0.1172	0.551
	100	25.0	6.1	107096.6	293.85	0.0285	0.1369	0.572
Rotameter 2	20	25.0	6.1	105702.0	293.62	0.0296	0.2298	0.651
	30	25.0	6.1	105592.3	291.98	0.0299	0.3412	0.738
	40	25.0	6.1	105500.7	290.96	0.0300	0.4531	0.813
	50	25.0	6.1	105266.3	287.39	0.0302	0.5623	0.908
	60							
	70							
	80							
	90							
	100							
Rotameter 1	10	65.0	15.6	112059.9	292.59	0.0782	0.0050	0.305
	20	65.0	15.6	110549.9	292.55	0.0781	0.0100	0.343
	30	65.0	15.6	109896.1	292.71	0.0778	0.0150	0.369
	40	65.0	15.6	109948.4	292.87	0.0781	0.0200	0.413
	50	65.0	15.6	109482.2	292.96	0.0783	0.0249	0.460
	60	65.0	15.6	109234.7	293.20	0.0781	0.0300	0.500
	70	65.0	15.6	109150.2	293.48	0.0779	0.0351	0.511
	80	65.0	15.6	109116.4	293.61	0.0782	0.0399	0.529
	90	65.0	15.6	108818.3	293.65	0.0780	0.0450	0.545
	100	65.0	15.6	108652.8	293.74	0.0781	0.0499	0.585
Rotameter 2	20	65.0	15.6	107668.2	293.45	0.0783	0.0869	0.674
	30	65.0	15.6	107746.0	293.19	0.0778	0.1311	0.757
	40	65.0	15.6	109551.0	292.95	0.0785	0.1733	0.812
	50	65.0	15.6	110168.8	292.52	0.0785	0.2166	0.855
	60	65.0	15.6	110823.1	292.25	0.0781	0.2611	0.865
	70	65.0	15.6	111301.0	291.89	0.0782	0.3045	0.872
	80							
	90							
	100							

-continued-

Rotameter 1	10	105.0	25.2	112675.7	291.78	0.1269	0.0031	0.289
	20	105.0	25.2	111214.8	292.22	0.1252	0.0062	0.338
	30	105.0	25.2	110893.0	292.50	0.1273	0.0092	0.368
	40	105.0	25.2	110284.1	292.70	0.1262	0.0124	0.411
	50	105.0	25.2	110216.9	292.87	0.1262	0.0155	0.438
	60	105.0	25.2	110024.4	292.93	0.1257	0.0186	0.477
	70	105.0	25.2	109850.0	293.05	0.1263	0.0216	0.513
	80	105.0	25.2	109595.0	293.43	0.1261	0.0247	0.536
	90	105.0	25.2	109466.6	293.34	0.1263	0.0278	0.548
	100	105.0	25.2	109367.8	293.44	0.1259	0.0310	0.576
Rotameter 2	20	105.0	25.2	109078.8	293.38	0.1264	0.0538	0.677
	30	105.0	25.2	110487.7	293.31	0.1257	0.0811	0.752
	40	105.0	25.2	111362.0	293.14	0.1255	0.1084	0.808
	50	105.0	25.2	113735.0	292.95	0.1256	0.1354	0.838
	60	105.0	25.2	115054.7	292.77	0.1256	0.1625	0.850
	70	105.0	25.2	117950.8	292.59	0.1263	0.1884	0.861
	80							
	90							
	100							
Rotameter 1	10	156.0	37.4	114218.2	295.77	0.1870	0.0021	0.291
	20	156.0	37.4	112755.1	295.58	0.1873	0.0042	0.347
	30	156.0	37.4	112071.4	295.65	0.1868	0.0063	0.370
	40	156.0	37.4	111598.1	295.24	0.1865	0.0084	0.415
	50	156.0	37.4	111472.5	295.36	0.1856	0.0105	0.471
	60	156.0	37.4	111154.7	295.94	0.1861	0.0126	0.507
	70	156.0	37.4	111956.5	296.15	0.1870	0.0146	0.545
	80	156.0	37.4	111094.1	295.61	0.1873	0.0167	0.574
	90	156.0	37.4	111101.8	294.76	0.1861	0.0189	0.584
	100	156.0	37.4	110613.6	294.90	0.1855	0.0210	0.608
Rotameter 2	20	156.0	37.4	111197.3	294.33	0.1886	0.0361	0.715
	30	156.0	37.4	112180.8	294.68	0.1872	0.0545	0.797
	40	156.0	37.4	113762.4	295.02	0.1876	0.0725	0.847
	50	156.0	37.4	114980.3	294.94	0.1850	0.0919	0.880
	60	156.0	37.4	117568.0	295.06	0.1868	0.1092	0.891
	70							
	80							
	90							
	100							
Rotameter 1	10	208.0	49.9	114863.1	293.41	0.2487	0.0016	0.288
	20	208.0	49.9	113352.6	293.58	0.2485	0.0031	0.356
	30	208.0	49.9	112841.7	293.57	0.2493	0.0047	0.385
	40	208.0	49.9	112552.4	293.35	0.2497	0.0062	0.419
	50	208.0	49.9	112206.3	293.86	0.2494	0.0078	0.459
	60	208.0	49.9	111937.4	293.99	0.2500	0.0094	0.507
	70	208.0	49.9	111880.8	294.42	0.2488	0.0110	0.547
	80	208.0	49.9	111958.8	294.55	0.2498	0.0125	0.543
	90	208.0	49.9	112187.7	294.53	0.2498	0.0141	0.577
	100	208.0	49.9	111657.4	294.62	0.2503	0.0156	0.650

-continued-

Rotameter 2	20	208.0	49.9	112791.6	294.82	0.2503	0.0272	0.741
	30	208.0	49.9	113120.9	294.85	0.2488	0.0410	0.802
	40	208.0	49.9	116113.0	294.57	0.2486	0.0547	0.842
	50	208.0	49.9	117900.2	294.71	0.2503	0.0679	0.876
	60	208.0	49.9	122088.2	294.45	0.2493	0.0818	0.892
	70	208.0	49.9	124037.4	294.35	0.2497	0.0953	0.898
	80	208.0	49.9	127375.5	294.17	0.2497	0.1089	0.902
	90	208.0	49.9	131893.5	294.00	0.2503	0.1222	0.904
	100							
Rotameter 1	10	312.0	74.8	117317.5	283.24	0.3758	0.0010	0.236
	20	312.0	74.8	115849.2	283.46	0.3743	0.0021	0.323
	30	312.0	74.8	115198.1	283.99	0.3724	0.0031	0.351
	40	312.0	74.8	115014.7	284.16	0.3741	0.0042	0.395
	50	312.0	74.8	115216.0	284.77	0.3731	0.0052	0.412
	60	312.0	74.8	114890.2	284.91	0.3737	0.0063	0.477
	70	312.0	74.8	114714.0	285.23	0.3732	0.0073	0.490
	80	312.0	74.8	114631.1	285.64	0.3745	0.0083	0.513
	90	312.0	74.8	114956.5	286.08	0.3742	0.0094	0.555
	100	312.0	74.8	114917.1	286.24	0.3746	0.0104	0.574
Rotameter 2	20	312.0	74.8	117243.7	286.50	0.3741	0.0182	0.700
	30	312.0	74.8	119312.6	286.65	0.3744	0.0272	0.774
	40	312.0	74.8	122545.9	286.91	0.3734	0.0364	0.825
	50	312.0	74.8	124902.9	287.11	0.3739	0.0455	0.836
	60	312.0	74.8	127621.9	287.33	0.3740	0.0546	0.858
	70	312.0	74.8	132432.7	287.50	0.3722	0.0640	0.861
	80	312.0	74.8	135834.6	287.77	0.3735	0.0728	0.865
	90	312.0	74.8	142311.9	287.88	0.3754	0.0815	0.877
	100	312.0	74.8	150336.3	288.12	0.3732	0.0911	0.889
Rotameter 1	10	416.0	99.8	118778.5	291.81	0.4989	0.0008	0.215
	20	416.0	99.8	117531.9	291.81	0.4989	0.0016	0.298
	30	416.0	99.8	117134.4	292.02	0.4985	0.0023	0.337
	40	416.0	99.8	117106.5	292.35	0.4984	0.0031	0.367
	50	416.0	99.8	117026.7	292.25	0.4990	0.0039	0.419
	60	416.0	99.8	117180.6	292.37	0.4991	0.0047	0.443
	70	416.0	99.8	117376.3	292.47	0.4980	0.0055	0.493
	80	416.0	99.8	117678.8	292.72	0.4989	0.0063	0.532
	90	416.0	99.8	117727.3	292.82	0.4989	0.0070	0.542
	100	416.0	99.8	117829.0	292.87	0.4992	0.0078	0.565
Rotameter 2	20	416.0	99.8	120667.0	292.91	0.4977	0.0137	0.689
	30	416.0	99.8	124651.2	292.93	0.4959	0.0206	0.774
	40	416.0	99.8	128231.0	292.95	0.4973	0.0273	0.803
	50	416.0	99.8	132571.2	293.00	0.4979	0.0341	0.827
	60	416.0	99.8	134706.5	293.08	0.4993	0.0409	0.845
	70	416.0	99.8	141411.9	292.99	0.4973	0.0479	0.857
	80	416.0	99.8	147410.2	293.00	0.4982	0.0546	0.865
	90	416.0	99.8	152205.6	292.84	0.4994	0.0613	0.872
	100							

-continued-

Rotameter 1	10	541.0	129.6	120784.9	289.03	0.6484	0.0006	0.248
	20	541.0	129.6	119927.7	289.22	0.6468	0.0012	0.279
	30	541.0	129.6	119677.3	289.40	0.6494	0.0018	0.317
	40	541.0	129.6	119803.6	289.77	0.6488	0.0024	0.368
	50	541.0	129.6	119899.5	289.92	0.6482	0.0030	0.381
	60	541.0	129.6	120887.6	290.36	0.6488	0.0036	0.451
	70	541.0	129.6	120984.7	290.40	0.6486	0.0042	0.488
	80	541.0	129.6	121455.5	290.63	0.6485	0.0048	0.493
	90	541.0	129.6	121967.9	291.02	0.6486	0.0054	0.524
	100	541.0	129.6	121632.8	291.10	0.6492	0.0060	0.581
Rotameter 2	20	541.0	129.6	125449.5	291.23	0.6481	0.0105	0.694
	30	541.0	129.6	131177.3	291.37	0.6486	0.0157	0.766
	40	541.0	129.6	137229.7	291.53	0.6498	0.0209	0.806
	50	541.0	129.6	138992.6	291.64	0.6485	0.0262	0.816
	60							
	70							
	80							
	90							
	100							
Rotameter 1	10	688.0	165.5	127322.7	293.72	0.8273	0.0005	0.151
	20	688.0	165.5	127514.2	293.85	0.8244	0.0009	0.227
	30	688.0	165.5	127927.0	293.86	0.8244	0.0014	0.276
	40	688.0	165.5	128522.2	293.96	0.8284	0.0019	0.310
	50	688.0	165.5	129322.2	294.23	0.8333	0.0023	0.353
	60	688.0	165.5	130894.7	294.47	0.8319	0.0028	0.385
	70	688.0	165.5	132158.2	294.58	0.8293	0.0033	0.418
	80	688.0	165.5	133077.7	294.74	0.8234	0.0038	0.467
	90	688.0	165.5	134710.6	294.88	0.8294	0.0042	0.479
	100	688.0	165.5	135340.4	295.03	0.8199	0.0048	0.517
Rotameter 2	20	688.0	165.5	143268.4	295.07	0.8224	0.0083	0.634
	30	688.0	165.5	151092.2	295.14	0.8207	0.0124	0.705
	40	688.0	165.5	157716.5	295.19	0.8262	0.0165	0.735
	50	688.0	165.5	166674.7	295.21	0.8256	0.0206	0.762
	60	688.0	165.5	172563.6	295.23	0.8316	0.0245	0.780
	70							
	80							
	90							
	100							

Table B.7: Void fraction in the minimum gap between the tubes (to the west of central tube)

Air Rotameter	Air flow rate (%)	Mass flux based on min area (kg/m^{2}s)	Mass flux (kg/m^{2}s)	Two-pahse flow pressure (Pa)	Two-phase flow temperature (K)	Total mass flow rate (kg/s)	Quality (-)	Void fraction at the gap to the west of central tube (min gap)(-)
Rotameter 1	10	25.0	6.1	110576.3	294.24	0.0304	0.0128	0.279
	20	25.0	6.1	109488.8	294.04	0.0304	0.0257	0.347
	30	25.0	6.1	108295.7	293.80	0.0298	0.0393	0.376
	40	25.0	6.1	108614.0	293.88	0.0297	0.0526	0.430
	50	25.0	6.1	107900.4	293.83	0.0296	0.0659	0.453
	60	25.0	6.1	107626.9	293.87	0.0303	0.0773	0.477
	70	25.0	6.1	107768.1	293.81	0.0306	0.0893	0.506
	80	25.0	6.1	107499.4	293.99	0.0299	0.1043	0.520
	90	25.0	6.1	107371.1	293.90	0.0299	0.1172	0.539
	100	25.0	6.1	107096.6	293.85	0.0285	0.1369	0.575
Rotameter 2	20	25.0	6.1	105702.0	293.62	0.0296	0.2298	0.648
	30	25.0	6.1	105592.3	291.98	0.0299	0.3412	0.713
	40	25.0	6.1	105500.7	290.96	0.0300	0.4531	0.801
	50	25.0	6.1	105266.3	287.39	0.0302	0.5623	0.902
	60							
	70							
	80							
	90							
	100							
Rotameter 1	10	65.0	15.6	112059.9	292.59	0.0782	0.0050	0.290
	20	65.0	15.6	110549.9	292.55	0.0781	0.0100	0.349
	30	65.0	15.6	109896.1	292.71	0.0778	0.0150	0.362
	40	65.0	15.6	109948.4	292.87	0.0781	0.0200	0.418
	50	65.0	15.6	109482.2	292.96	0.0783	0.0249	0.445
	60	65.0	15.6	109234.7	293.20	0.0781	0.0300	0.470
	70	65.0	15.6	109150.2	293.48	0.0779	0.0351	0.498
	80	65.0	15.6	109116.4	293.61	0.0782	0.0399	0.522
	90	65.0	15.6	108818.3	293.65	0.0780	0.0450	0.549
	100	65.0	15.6	108652.8	293.74	0.0781	0.0499	0.578
Rotameter 2	20	65.0	15.6	107668.2	293.45	0.0783	0.0869	0.653
	30	65.0	15.6	107746.0	293.19	0.0778	0.1311	0.733
	40	65.0	15.6	109551.0	292.95	0.0785	0.1733	0.792
	50	65.0	15.6	110168.8	292.52	0.0785	0.2166	0.843
	60	65.0	15.6	110823.1	292.25	0.0781	0.2611	0.857
	70	65.0	15.6	111301.0	291.89	0.0782	0.3045	0.841
	80							
	90							
	100							

-continued-

Rotameter 1	10	105.0	25.2	112675.7	291.78	0.1269	0.0031	0.275
	20	105.0	25.2	111214.8	292.22	0.1252	0.0062	0.325
	30	105.0	25.2	110893.0	292.50	0.1273	0.0092	0.357
	40	105.0	25.2	110284.1	292.70	0.1262	0.0124	0.420
	50	105.0	25.2	110216.9	292.87	0.1262	0.0155	0.426
	60	105.0	25.2	110024.4	292.93	0.1257	0.0186	0.479
	70	105.0	25.2	109850.0	293.05	0.1263	0.0216	0.488
	80	105.0	25.2	109595.0	293.43	0.1261	0.0247	0.519
	90	105.0	25.2	109466.6	293.34	0.1263	0.0278	0.519
	100	105.0	25.2	109367.8	293.44	0.1259	0.0310	0.565
Rotameter 2	20	105.0	25.2	109078.8	293.38	0.1264	0.0538	0.671
	30	105.0	25.2	110487.7	293.31	0.1257	0.0811	0.753
	40	105.0	25.2	111362.0	293.14	0.1255	0.1084	0.793
	50	105.0	25.2	113735.0	292.95	0.1256	0.1354	0.830
	60	105.0	25.2	115054.7	292.77	0.1256	0.1625	0.844
	70	105.0	25.2	117950.8	292.59	0.1263	0.1884	0.855
	80							
	90							
	100							
Rotameter 1	10	156.0	37.4	114218.2	295.77	0.1870	0.0021	0.284
	20	156.0	37.4	112755.1	295.58	0.1873	0.0042	0.353
	30	156.0	37.4	112071.4	295.65	0.1868	0.0063	0.372
	40	156.0	37.4	111598.1	295.24	0.1865	0.0084	0.426
	50	156.0	37.4	111472.5	295.36	0.1856	0.0105	0.466
	60	156.0	37.4	111154.7	295.94	0.1861	0.0126	0.485
	70	156.0	37.4	111956.5	296.15	0.1870	0.0146	0.509
	80	156.0	37.4	111094.1	295.61	0.1873	0.0167	0.553
	90	156.0	37.4	111101.8	294.76	0.1861	0.0189	0.563
	100	156.0	37.4	110613.6	294.90	0.1855	0.0210	0.620
Rotameter 2	20	156.0	37.4	111197.3	294.33	0.1886	0.0361	0.713
	30	156.0	37.4	112180.8	294.68	0.1872	0.0545	0.785
	40	156.0	37.4	113762.4	295.02	0.1876	0.0725	0.840
	50	156.0	37.4	114980.3	294.94	0.1850	0.0919	0.880
	60	156.0	37.4	117568.0	295.06	0.1868	0.1092	0.893
	70							
	80							
	90							
	100							
Rotameter 1	10	208.0	49.9	114863.1	293.41	0.2487	0.0016	0.294
	20	208.0	49.9	113352.6	293.58	0.2485	0.0031	0.343
	30	208.0	49.9	112841.7	293.57	0.2493	0.0047	0.369
	40	208.0	49.9	112552.4	293.35	0.2497	0.0062	0.413
	50	208.0	49.9	112206.3	293.86	0.2494	0.0078	0.457
	60	208.0	49.9	111937.4	293.99	0.2500	0.0094	0.492
	70	208.0	49.9	111880.8	294.42	0.2488	0.0110	0.512
	80	208.0	49.9	111958.8	294.55	0.2498	0.0125	0.532
	90	208.0	49.9	112187.7	294.53	0.2498	0.0141	0.555
	100	208.0	49.9	111657.4	294.62	0.2503	0.0156	0.636

-continued-

Rotameter 2	20	208.0	49.9	112791.6	294.82	0.2503	0.0272	0.714
	30	208.0	49.9	113120.9	294.85	0.2488	0.0410	0.778
	40	208.0	49.9	116113.0	294.57	0.2486	0.0547	0.837
	50	208.0	49.9	117900.2	294.71	0.2503	0.0679	0.863
	60	208.0	49.9	122088.2	294.45	0.2493	0.0818	0.872
	70	208.0	49.9	124037.4	294.35	0.2497	0.0953	0.877
	80	208.0	49.9	127375.5	294.17	0.2497	0.1089	0.876
	90	208.0	49.9	131893.5	294.00	0.2503	0.1222	0.880
	100							
Rotameter 1	10	312.0	74.8	117317.5	283.24	0.3758	0.0010	0.227
	20	312.0	74.8	115849.2	283.46	0.3743	0.0021	0.315
	30	312.0	74.8	115198.1	283.99	0.3724	0.0031	0.356
	40	312.0	74.8	115014.7	284.16	0.3741	0.0042	0.386
	50	312.0	74.8	115216.0	284.77	0.3731	0.0052	0.415
	60	312.0	74.8	114890.2	284.91	0.3737	0.0063	0.461
	70	312.0	74.8	114714.0	285.23	0.3732	0.0073	0.472
	80	312.0	74.8	114631.1	285.64	0.3745	0.0083	0.496
	90	312.0	74.8	114956.5	286.08	0.3742	0.0094	0.517
	100	312.0	74.8	114917.1	286.24	0.3746	0.0104	0.577
Rotameter 2	20	312.0	74.8	117243.7	286.50	0.3741	0.0182	0.694
	30	312.0	74.8	119312.6	286.65	0.3744	0.0272	0.759
	40	312.0	74.8	122545.9	286.91	0.3734	0.0364	0.809
	50	312.0	74.8	124902.9	287.11	0.3739	0.0455	0.827
	60	312.0	74.8	127621.9	287.33	0.3740	0.0546	0.837
	70	312.0	74.8	132432.7	287.50	0.3722	0.0640	0.851
	80	312.0	74.8	135834.6	287.77	0.3735	0.0728	0.870
	90	312.0	74.8	142311.9	287.88	0.3754	0.0815	0.880
	100	312.0	74.8	150336.3	288.12	0.3732	0.0911	0.887
Rotameter 1	10	416.0	99.8	118778.5	291.81	0.4989	0.0008	0.222
	20	416.0	99.8	117531.9	291.81	0.4989	0.0016	0.300
	30	416.0	99.8	117134.4	292.02	0.4985	0.0023	0.329
	40	416.0	99.8	117106.5	292.35	0.4984	0.0031	0.362
	50	416.0	99.8	117026.7	292.25	0.4990	0.0039	0.412
	60	416.0	99.8	117180.6	292.37	0.4991	0.0047	0.435
	70	416.0	99.8	117376.3	292.47	0.4980	0.0055	0.488
	80	416.0	99.8	117678.8	292.72	0.4989	0.0063	0.514
	90	416.0	99.8	117727.3	292.82	0.4989	0.0070	0.543
	100	416.0	99.8	117829.0	292.87	0.4992	0.0078	0.570
Rotameter 2	20	416.0	99.8	120667.0	292.91	0.4977	0.0137	0.678
	30	416.0	99.8	124651.2	292.93	0.4959	0.0206	0.760
	40	416.0	99.8	128231.0	292.95	0.4973	0.0273	0.798
	50	416.0	99.8	132571.2	293.00	0.4979	0.0341	0.831
	60	416.0	99.8	134706.5	293.08	0.4993	0.0409	0.847
	70	416.0	99.8	141411.9	292.99	0.4973	0.0479	0.851
	80	416.0	99.8	147410.2	293.00	0.4982	0.0546	0.859
	90	416.0	99.8	152205.6	292.84	0.4994	0.0613	0.876
	100							

-continued-

Rotameter 1	10	541.0	129.6	120784.9	289.03	0.6484	0.0006	0.204
	20	541.0	129.6	119927.7	289.22	0.6468	0.0012	0.281
	30	541.0	129.6	119677.3	289.40	0.6494	0.0018	0.320
	40	541.0	129.6	119803.6	289.77	0.6488	0.0024	0.363
	50	541.0	129.6	119899.5	289.92	0.6482	0.0030	0.384
	60	541.0	129.6	120887.6	290.36	0.6488	0.0036	0.441
	70	541.0	129.6	120984.7	290.40	0.6486	0.0042	0.470
	80	541.0	129.6	121455.5	290.63	0.6485	0.0048	0.492
	90	541.0	129.6	121967.9	291.02	0.6486	0.0054	0.517
	100	541.0	129.6	121632.8	291.10	0.6492	0.0060	0.551
Rotameter 2	20	541.0	129.6	125449.5	291.23	0.6481	0.0105	0.675
	30	541.0	129.6	131177.3	291.37	0.6486	0.0157	0.757
	40	541.0	129.6	137229.7	291.53	0.6498	0.0209	0.792
	50	541.0	129.6	138992.6	291.64	0.6485	0.0262	0.809
	60							
	70							
	80							
	90							
	100							
Rotameter 1	10	688.0	165.5	127322.7	293.72	0.8273	0.0005	0.171
	20	688.0	165.5	127514.2	293.85	0.8244	0.0009	0.239
	30	688.0	165.5	127927.0	293.86	0.8244	0.0014	0.278
	40	688.0	165.5	128522.2	293.96	0.8284	0.0019	0.325
	50	688.0	165.5	129322.2	294.23	0.8333	0.0023	0.367
	60	688.0	165.5	130894.7	294.47	0.8319	0.0028	0.396
	70	688.0	165.5	132158.2	294.58	0.8293	0.0033	0.424
	80	688.0	165.5	133077.7	294.74	0.8234	0.0038	0.458
	90	688.0	165.5	134710.6	294.88	0.8294	0.0042	0.472
	100	688.0	165.5	135340.4	295.03	0.8199	0.0048	0.507
Rotameter 2	20	688.0	165.5	143268.4	295.07	0.8224	0.0083	0.620
	30	688.0	165.5	151092.2	295.14	0.8207	0.0124	0.708
	40	688.0	165.5	157716.5	295.19	0.8262	0.0165	0.741
	50	688.0	165.5	166674.7	295.21	0.8256	0.0206	0.765
	60	688.0	165.5	172563.6	295.23	0.8316	0.0245	0.789
	70							
	80							
	90							
	100							

Table B.8: Void fraction in the maximum gap between the tubes

Air Rotameter	Air flow rate (%)	Mass flux based on min area (kg/m^{2}s)	Mass flux (kg/m^{2}s)	Two-pahse flow pressure (Pa)	Two-phase flow temperature (K)	Total mass flow rate (kg/s)	Quality (-)	Void fraction at the gap to the north east of central tube (max gap)(-)
Rotameter 1	10	25.0	6.1	111695.1	294.96	0.0292	0.0133	0.333
	20	25.0	6.1	110853.5	294.94	0.0305	0.0256	0.408
	30	25.0	6.1	109624.0	294.98	0.0301	0.0389	0.482
	40	25.0	6.1	109300.2	294.93	0.0297	0.0525	0.532
	50	25.0	6.1	108944.1	294.96	0.0304	0.0641	0.580
	60	25.0	6.1	108824.7	295.05	0.0305	0.0767	0.632
	70	25.0	6.1	108899.7	294.98	0.0306	0.0893	0.643
	80	25.0	6.1	108416.6	295.06	0.0301	0.1036	0.658
	90	25.0	6.1	108687.5	295.08	0.0302	0.1162	0.655
	100	25.0	6.1	107835.2	295.08	0.0310	0.1260	0.691
Rotameter 2	20	25.0	6.1	106420.8	294.28	0.0301	0.2256	0.742
	30	25.0	6.1	107943.6	294.28	0.0304	0.3354	0.801
	40	25.0	6.1	105539.3	292.07	0.0298	0.4560	0.814
	50	25.0	6.1	104694.3	290.14	0.0322	0.5277	0.916
	60							
	70							
	80							
	90							
	100							
Rotameter 1	10	65.0	15.6	111716.5	292.73	0.0780	0.0050	0.319
	20	65.0	15.6	110457.6	292.59	0.0777	0.0100	0.419
	30	65.0	15.6	109659.6	292.67	0.0782	0.0150	0.470
	40	65.0	15.6	109461.9	292.87	0.0780	0.0200	0.532
	50	65.0	15.6	109216.4	292.95	0.0779	0.0250	0.581
	60	65.0	15.6	109161.8	293.09	0.0778	0.0301	0.608
	70	65.0	15.6	108963.0	293.21	0.0784	0.0348	0.618
	80	65.0	15.6	108451.6	293.38	0.0783	0.0399	0.642
	90	65.0	15.6	108520.9	293.49	0.0784	0.0448	0.659
	100	65.0	15.6	108195.9	293.61	0.0780	0.0500	0.669
Rotameter 2	20	65.0	15.6	107553.4	293.39	0.0779	0.0872	0.748
	30	65.0	15.6	107968.2	293.17	0.0782	0.1305	0.789
	40	65.0	15.6	108033.8	292.98	0.0782	0.1738	0.822
	50	65.0	15.6	108837.9	292.76	0.0782	0.2174	0.851
	60	65.0	15.6	109913.7	292.44	0.0781	0.2611	0.873
	70	65.0	15.6	111754.0	292.08	0.0779	0.3055	0.886
	80							
	90							
	100							

-continued-

Rotameter 1	10	105.0	25.2	113561.5	293.24	0.1264	0.0031	0.301
	20	105.0	25.2	111953.9	293.41	0.1263	0.0062	0.402
	30	105.0	25.2	111424.9	293.48	0.1259	0.0093	0.458
	40	105.0	25.2	110410.4	293.53	0.1266	0.0123	0.538
	50	105.0	25.2	110620.2	293.67	0.1261	0.0155	0.582
	60	105.0	25.2	110310.6	293.78	0.1261	0.0186	0.603
	70	105.0	25.2	110093.4	293.95	0.1263	0.0216	0.655
	80	105.0	25.2	110059.4	294.07	0.1265	0.0247	0.659
	90	105.0	25.2	109907.8	294.29	0.1258	0.0279	0.666
	100	105.0	25.2	109509.2	294.23	0.1259	0.0310	0.693
Rotameter 2	20	105.0	25.2	109600.1	294.10	0.1257	0.0541	0.769
	30	105.0	25.2	109937.4	293.95	0.1260	0.0809	0.828
	40	105.0	25.2	111116.9	293.79	0.1266	0.1074	0.874
	50	105.0	25.2	112129.6	293.65	0.1267	0.1341	0.891
	60	105.0	25.2	114436.6	293.47	0.1260	0.1619	0.905
	70	105.0	25.2	116400.3	293.34	0.1263	0.1884	0.909
	80							
	90							
	100							
Rotameter 1	10	156.0	37.4	115092.6	296.18	0.1851	0.0021	0.278
	20	156.0	37.4	114301.1	295.99	0.1891	0.0041	0.369
	30	156.0	37.4	113409.6	296.05	0.1882	0.0062	0.437
	40	156.0	37.4	113082.4	296.23	0.1868	0.0084	0.542
	50	156.0	37.4	112602.3	296.14	0.1878	0.0104	0.556
	60	156.0	37.4	113066.2	296.18	0.1865	0.0125	0.626
	70	156.0	37.4	112647.2	296.20	0.1861	0.0147	0.643
	80	156.0	37.4	112479.5	296.22	0.1864	0.0167	0.651
	90	156.0	37.4	112135.2	296.25	0.1878	0.0187	0.679
	100	156.0	37.4	112153.0	296.24	0.1862	0.0209	0.707
Rotameter 2	20	156.0	37.4	113210.1	296.10	0.1873	0.0363	0.798
	30	156.0	37.4	114267.9	295.99	0.1876	0.0544	0.839
	40	156.0	37.4	115615.9	295.83	0.1891	0.0719	0.884
	50	156.0	37.4	117603.9	295.64	0.1870	0.0909	0.904
	60	156.0	37.4	120746.8	295.47	0.1866	0.1093	0.919
	70							
	80							
	90							
	100							
Rotameter 1	10	208.0	49.9	116118.1	292.61	0.2521	0.0015	0.265
	20	208.0	49.9	114054.2	292.68	0.2510	0.0031	0.398
	30	208.0	49.9	113725.0	292.77	0.2494	0.0047	0.445
	40	208.0	49.9	113230.0	292.96	0.2482	0.0063	0.479
	50	208.0	49.9	113447.0	293.03	0.2474	0.0079	0.533
	60	208.0	49.9	113580.9	293.25	0.2495	0.0094	0.588
	70	208.0	49.9	113150.9	293.32	0.2501	0.0109	0.625
	80	208.0	49.9	113216.9	293.44	0.2478	0.0126	0.664
	90	208.0	49.9	113454.9	293.78	0.2535	0.0138	0.677
	100	208.0	49.9	113427.1	293.77	0.2491	0.0157	0.703

-continued-

Rotameter 2	20	208.0	49.9	114049.4	293.66	0.2519	0.0270	0.793
	30	208.0	49.9	116400.7	293.70	0.2517	0.0405	0.852
	40	208.0	49.9	118869.5	293.61	0.2518	0.0540	0.884
	50	208.0	49.9	120148.2	293.59	0.2484	0.0684	0.900
	60	208.0	49.9	124816.4	293.50	0.2496	0.0817	0.911
	70	208.0	49.9	129179.5	293.42	0.2519	0.0945	0.922
	80	208.0	49.9	133363.2	293.31	0.2490	0.1092	0.925
	90	208.0	49.9	136876.8	293.22	0.2475	0.1236	0.927
	100							
Rotameter 1	10	312.0	74.8	117453.9	294.17	0.3746	0.0010	0.270
	20	312.0	74.8	116154.8	294.11	0.3756	0.0021	0.373
	30	312.0	74.8	115592.6	294.20	0.3747	0.0031	0.420
	40	312.0	74.8	115390.7	294.51	0.3739	0.0042	0.476
	50	312.0	74.8	115358.3	294.46	0.3758	0.0052	0.542
	60	312.0	74.8	115291.1	294.58	0.3756	0.0062	0.582
	70	312.0	74.8	115106.1	294.68	0.3748	0.0073	0.615
	80	312.0	74.8	115211.2	294.89	0.3752	0.0083	0.635
	90	312.0	74.8	115326.1	294.97	0.3724	0.0094	0.679
	100	312.0	74.8	115780.6	295.05	0.3759	0.0104	0.701
Rotameter 2	20	312.0	74.8	116202.0	295.23	0.3752	0.0181	0.789
	30	312.0	74.8	119387.5	295.36	0.3736	0.0273	0.849
	40	312.0	74.8	122338.6	295.20	0.3734	0.0364	0.880
	50	312.0	74.8	125886.2	295.24	0.3738	0.0455	0.896
	60	312.0	74.8	128592.3	295.11	0.3737	0.0546	0.906
	70	312.0	74.8	132552.4	295.04	0.3744	0.0636	0.919
	80	312.0	74.8	139085.7	294.95	0.3755	0.0724	0.924
	90	312.0	74.8	142237.1	294.84	0.3742	0.0818	0.921
	100	312.0	74.8	149770.7	294.68	0.3714	0.0916	0.926
Rotameter 1	10	416.0	99.8	118672.9	293.23	0.4992	0.0008	0.247
	20	416.0	99.8	117621.2	293.05	0.4984	0.0016	0.349
	30	416.0	99.8	117288.1	293.22	0.4993	0.0023	0.405
	40	416.0	99.8	117215.2	293.51	0.4983	0.0031	0.459
	50	416.0	99.8	117362.6	293.42	0.4979	0.0039	0.537
	60	416.0	99.8	117493.8	293.49	0.4980	0.0047	0.566
	70	416.0	99.8	117954.4	293.57	0.4983	0.0055	0.608
	80	416.0	99.8	117513.6	293.69	0.5003	0.0062	0.614
	90	416.0	99.8	118311.7	293.77	0.4981	0.0070	0.656
	100	416.0	99.8	117983.9	293.83	0.4994	0.0078	0.665
Rotameter 2	20	416.0	99.8	120127.9	293.88	0.4967	0.0137	0.797
	30	416.0	99.8	123953.6	293.92	0.5008	0.0204	0.843
	40	416.0	99.8	126999.2	293.92	0.4969	0.0274	0.869
	50	416.0	99.8	131520.6	293.92	0.4920	0.0345	0.885
	60	416.0	99.8	136977.2	293.88	0.4915	0.0415	0.900
	70	416.0	99.8	141295.9	293.81	0.4999	0.0476	0.909
	80	416.0	99.8	143186.5	293.77	0.5021	0.0542	0.911
	90	416.0	99.8	151408.4	293.70	0.4966	0.0616	0.916
	100							

-continued-

Rotameter 1	10	541.0	129.6	120565.6	294.53	0.6487	0.0006	0.213
	20	541.0	129.6	119906.1	294.49	0.6493	0.0012	0.320
	30	541.0	129.6	119575.7	294.60	0.6472	0.0018	0.377
	40	541.0	129.6	119761.3	294.65	0.6478	0.0024	0.446
	50	541.0	129.6	119770.9	295.12	0.6477	0.0030	0.501
	60	541.0	129.6	120166.4	295.22	0.6488	0.0036	0.548
	70	541.0	129.6	120846.8	295.30	0.6491	0.0042	0.568
	80	541.0	129.6	121366.4	295.39	0.6485	0.0048	0.604
	90	541.0	129.6	121325.0	295.50	0.6489	0.0054	0.631
	100	541.0	129.6	121683.0	295.59	0.6479	0.0060	0.669
Rotameter 2	20	541.0	129.6	124748.1	295.64	0.6504	0.0105	0.770
	30	541.0	129.6	129986.1	295.65	0.6485	0.0157	0.829
	40	541.0	129.6	133405.1	295.62	0.6501	0.0209	0.852
	50	541.0	129.6	137945.8	295.60	0.6495	0.0262	0.869
	60							
	70							
	80							
	90							
	100							
Rotameter 1	10	688.0	165.5	125842.9	294.70	0.8296	0.0005	0.187
	20	688.0	165.5	125852.2	295.01	0.8281	0.0009	0.285
	30	688.0	165.5	126276.8	295.17	0.8223	0.0014	0.329
	40	688.0	165.5	127028.7	295.18	0.8307	0.0019	0.385
	50	688.0	165.5	128094.6	295.20	0.8211	0.0024	0.442
	60	688.0	165.5	129336.2	295.30	0.8238	0.0028	0.485
	70	688.0	165.5	130183.9	295.43	0.8223	0.0033	0.524
	80	688.0	165.5	131366.6	295.56	0.8168	0.0038	0.559
	90	688.0	165.5	132304.1	295.66	0.8156	0.0043	0.589
	100	688.0	165.5	133600.0	295.75	0.8190	0.0048	0.602
Rotameter 2	20	688.0	165.5	144309.2	295.91	0.8296	0.0082	0.728
	30	688.0	165.5	151203.8	295.97	0.8275	0.0123	0.794
	40	688.0	165.5	162031.4	296.10	0.8194	0.0166	0.821
	50	688.0	165.5	170490.7	295.95	0.8172	0.0208	0.849
	60	688.0	165.5	175041.1	295.93	0.8235	0.0248	0.864
	70							
	80							
	90							
	100							

Table B.9: Void fraction in the minimum gap between the tubes (to the north of central tube)

Air Rotameter	Air flow rate (%)	Mass flux based on min area (kg/m^{2}s)	Mass flux (kg/m^{2}s)	Two-pahse flow pressure (Pa)	Two-phase flow temperature (K)	Total mass flow rate (kg/s)	Quality (-)	Void fraction at the gap to the north of central tube (min gap)(-)
Rotameter 1	10	25.0	6.1	111695.1	294.96	0.0292	0.0133	0.252
	20	25.0	6.1	110853.5	294.94	0.0305	0.0256	0.335
	30	25.0	6.1	109624.0	294.98	0.0301	0.0389	0.401
	40	25.0	6.1	109300.2	294.93	0.0297	0.0525	0.458
	50	25.0	6.1	108944.1	294.96	0.0304	0.0641	0.502
	60	25.0	6.1	108824.7	295.05	0.0305	0.0767	0.534
	70	25.0	6.1	108899.7	294.98	0.0306	0.0893	0.550
	80	25.0	6.1	108416.6	295.06	0.0301	0.1036	0.566
	90	25.0	6.1	108687.5	295.08	0.0302	0.1162	0.579
	100	25.0	6.1	107835.2	295.08	0.0310	0.1260	0.583
Rotameter 2	20	25.0	6.1	106420.8	294.28	0.0301	0.2256	0.621
	30	25.0	6.1	107943.6	294.28	0.0304	0.3354	0.708
	40	25.0	6.1	105539.3	292.07	0.0298	0.4560	0.713
	50	25.0	6.1	104694.3	290.14	0.0322	0.5277	0.828
	60							
	70							
	80							
	90							
	100							
Rotameter 1	10	65.0	15.6	111716.5	292.73	0.0780	0.0050	0.255
	20	65.0	15.6	110457.6	292.59	0.0777	0.0100	0.352
	30	65.0	15.6	109659.6	292.67	0.0782	0.0150	0.387
	40	65.0	15.6	109461.9	292.87	0.0780	0.0200	0.444
	50	65.0	15.6	109216.4	292.95	0.0779	0.0250	0.490
	60	65.0	15.6	109161.8	293.09	0.0778	0.0301	0.527
	70	65.0	15.6	108963.0	293.21	0.0784	0.0348	0.542
	80	65.0	15.6	108451.6	293.38	0.0783	0.0399	0.552
	90	65.0	15.6	108520.9	293.49	0.0784	0.0448	0.571
	100	65.0	15.6	108195.9	293.61	0.0780	0.0500	0.582
Rotameter 2	20	65.0	15.6	107553.4	293.39	0.0779	0.0872	0.644
	30	65.0	15.6	107968.2	293.17	0.0782	0.1305	0.679
	40	65.0	15.6	108033.8	292.98	0.0782	0.1738	0.708
	50	65.0	15.6	108837.9	292.76	0.0782	0.2174	0.745
	60	65.0	15.6	109913.7	292.44	0.0781	0.2611	0.784
	70	65.0	15.6	111754.0	292.08	0.0779	0.3055	0.801
	80							
	90							
	100							

-continued-

Rotameter 1	10	105.0	25.2	113561.5	293.24	0.1264	0.0031	0.227
	20	105.0	25.2	111953.9	293.41	0.1263	0.0062	0.347
	30	105.0	25.2	111424.9	293.48	0.1259	0.0093	0.394
	40	105.0	25.2	110410.4	293.53	0.1266	0.0123	0.474
	50	105.0	25.2	110620.2	293.67	0.1261	0.0155	0.488
	60	105.0	25.2	110310.6	293.78	0.1261	0.0186	0.517
	70	105.0	25.2	110093.4	293.95	0.1263	0.0216	0.543
	80	105.0	25.2	110059.4	294.07	0.1265	0.0247	0.571
	90	105.0	25.2	109907.8	294.29	0.1258	0.0279	0.591
	100	105.0	25.2	109509.2	294.23	0.1259	0.0310	0.594
Rotameter 2	20	105.0	25.2	109600.1	294.10	0.1257	0.0541	0.665
	30	105.0	25.2	109937.4	293.95	0.1260	0.0809	0.729
	40	105.0	25.2	111116.9	293.79	0.1266	0.1074	0.783
	50	105.0	25.2	112129.6	293.65	0.1267	0.1341	0.797
	60	105.0	25.2	114436.6	293.47	0.1260	0.1619	0.816
	70	105.0	25.2	116400.3	293.34	0.1263	0.1884	0.822
	80							
	90							
	100							
Rotameter 1	10	156.0	37.4	115092.6	296.18	0.1851	0.0021	0.216
	20	156.0	37.4	114301.1	295.99	0.1891	0.0041	0.312
	30	156.0	37.4	113409.6	296.05	0.1882	0.0062	0.371
	40	156.0	37.4	113082.4	296.23	0.1868	0.0084	0.470
	50	156.0	37.4	112602.3	296.14	0.1878	0.0104	0.502
	60	156.0	37.4	113066.2	296.18	0.1865	0.0125	0.535
	70	156.0	37.4	112647.2	296.20	0.1861	0.0147	0.560
	80	156.0	37.4	112479.5	296.22	0.1864	0.0167	0.582
	90	156.0	37.4	112135.2	296.25	0.1878	0.0187	0.596
	100	156.0	37.4	112153.0	296.24	0.1862	0.0209	0.616
Rotameter 2	20	156.0	37.4	113210.1	296.10	0.1873	0.0363	0.717
	30	156.0	37.4	114267.9	295.99	0.1876	0.0544	0.760
	40	156.0	37.4	115615.9	295.83	0.1891	0.0719	0.815
	50	156.0	37.4	117603.9	295.64	0.1870	0.0909	0.831
	60	156.0	37.4	120746.8	295.47	0.1866	0.1093	0.841
	70							
	80							
	90							
	100							
Rotameter 1	10	208.0	49.9	116118.1	292.61	0.2521	0.0015	0.219
	20	208.0	49.9	114054.2	292.68	0.2510	0.0031	0.346
	30	208.0	49.9	113725.0	292.77	0.2494	0.0047	0.377
	40	208.0	49.9	113230.0	292.96	0.2482	0.0063	0.432
	50	208.0	49.9	113447.0	293.03	0.2474	0.0079	0.506
	60	208.0	49.9	113580.9	293.25	0.2495	0.0094	0.527
	70	208.0	49.9	113150.9	293.32	0.2501	0.0109	0.559
	80	208.0	49.9	113216.9	293.44	0.2478	0.0126	0.592
	90	208.0	49.9	113454.9	293.78	0.2535	0.0138	0.610
	100	208.0	49.9	113427.1	293.77	0.2491	0.0157	0.638

-continued-

Rotameter 2	20	208.0	49.9	114049.4	293.66	0.2519	0.0270	0.721
	30	208.0	49.9	116400.7	293.70	0.2517	0.0405	0.786
	40	208.0	49.9	118869.5	293.61	0.2518	0.0540	0.811
	50	208.0	49.9	120148.2	293.59	0.2484	0.0684	0.830
	60	208.0	49.9	124816.4	293.50	0.2496	0.0817	0.841
	70	208.0	49.9	129179.5	293.42	0.2519	0.0945	0.848
	80	208.0	49.9	133363.2	293.31	0.2490	0.1092	0.854
	90	208.0	49.9	136876.8	293.22	0.2475	0.1236	0.853
	100							
Rotameter 1	10	312.0	74.8	117453.9	294.17	0.3746	0.0010	0.201
	20	312.0	74.8	116154.8	294.11	0.3756	0.0021	0.288
	30	312.0	74.8	115592.6	294.20	0.3747	0.0031	0.345
	40	312.0	74.8	115390.7	294.51	0.3739	0.0042	0.421
	50	312.0	74.8	115358.3	294.46	0.3758	0.0052	0.474
	60	312.0	74.8	115291.1	294.58	0.3756	0.0062	0.511
	70	312.0	74.8	115106.1	294.68	0.3748	0.0073	0.545
	80	312.0	74.8	115211.2	294.89	0.3752	0.0083	0.563
	90	312.0	74.8	115326.1	294.97	0.3724	0.0094	0.575
	100	312.0	74.8	115780.6	295.05	0.3759	0.0104	0.604
Rotameter 2	20	312.0	74.8	116202.0	295.23	0.3752	0.0181	0.675
	30	312.0	74.8	119387.5	295.36	0.3736	0.0273	0.744
	40	312.0	74.8	122338.6	295.20	0.3734	0.0364	0.781
	50	312.0	74.8	125886.2	295.24	0.3738	0.0455	0.807
	60	312.0	74.8	128592.3	295.11	0.3737	0.0546	0.819
	70	312.0	74.8	132552.4	295.04	0.3744	0.0636	0.824
	80	312.0	74.8	139085.7	294.95	0.3755	0.0724	0.828
	90	312.0	74.8	142237.1	294.84	0.3742	0.0818	0.828
	100	312.0	74.8	149770.7	294.68	0.3714	0.0916	0.829
Rotameter 1	10	416.0	99.8	118672.9	293.23	0.4992	0.0008	0.194
	20	416.0	99.8	117621.2	293.05	0.4984	0.0016	0.288
	30	416.0	99.8	117288.1	293.22	0.4993	0.0023	0.334
	40	416.0	99.8	117215.2	293.51	0.4983	0.0031	0.389
	50	416.0	99.8	117362.6	293.42	0.4979	0.0039	0.451
	60	416.0	99.8	117493.8	293.49	0.4980	0.0047	0.497
	70	416.0	99.8	117954.4	293.57	0.4983	0.0055	0.544
	80	416.0	99.8	117513.6	293.69	0.5003	0.0062	0.553
	90	416.0	99.8	118311.7	293.77	0.4981	0.0070	0.563
	100	416.0	99.8	117983.9	293.83	0.4994	0.0078	0.581
Rotameter 2	20	416.0	99.8	120127.9	293.88	0.4967	0.0137	0.694
	30	416.0	99.8	123953.6	293.92	0.5008	0.0204	0.750
	40	416.0	99.8	126999.2	293.92	0.4969	0.0274	0.781
	50	416.0	99.8	131520.6	293.92	0.4920	0.0345	0.803
	60	416.0	99.8	136977.2	293.88	0.4915	0.0415	0.817
	70	416.0	99.8	141295.9	293.81	0.4999	0.0476	0.820
	80	416.0	99.8	143186.5	293.77	0.5021	0.0542	0.826
	90	416.0	99.8	151408.4	293.70	0.4966	0.0616	0.826
	100							

-continued-

Rotameter 1	10	541.0	129.6	120565.6	294.53	0.6487	0.0006	0.178
	20	541.0	129.6	119906.1	294.49	0.6493	0.0012	0.265
	30	541.0	129.6	119575.7	294.60	0.6472	0.0018	0.338
	40	541.0	129.6	119761.3	294.65	0.6478	0.0024	0.390
	50	541.0	129.6	119770.9	295.12	0.6477	0.0030	0.439
	60	541.0	129.6	120166.4	295.22	0.6488	0.0036	0.485
	70	541.0	129.6	120846.8	295.30	0.6491	0.0042	0.520
	80	541.0	129.6	121366.4	295.39	0.6485	0.0048	0.546
	90	541.0	129.6	121325.0	295.50	0.6489	0.0054	0.570
	100	541.0	129.6	121683.0	295.59	0.6479	0.0060	0.596
Rotameter 2	20	541.0	129.6	124748.1	295.64	0.6504	0.0105	0.691
	30	541.0	129.6	129986.1	295.65	0.6485	0.0157	0.747
	40	541.0	129.6	133405.1	295.62	0.6501	0.0209	0.779
	50	541.0	129.6	137945.8	295.60	0.6495	0.0262	0.803
	60							
	70							
	80							
	90							
	100							
Rotameter 1	10	688.0	165.5	125842.9	294.70	0.8296	0.0005	0.222
	20	688.0	165.5	125852.2	295.01	0.8281	0.0009	0.302
	30	688.0	165.5	126276.8	295.17	0.8223	0.0014	0.357
	40	688.0	165.5	127028.7	295.18	0.8307	0.0019	0.389
	50	688.0	165.5	128094.6	295.20	0.8211	0.0024	0.432
	60	688.0	165.5	129336.2	295.30	0.8238	0.0028	0.469
	70	688.0	165.5	130183.9	295.43	0.8223	0.0033	0.507
	80	688.0	165.5	131366.6	295.56	0.8168	0.0038	0.543
	90	688.0	165.5	132304.1	295.66	0.8156	0.0043	0.560
	100	688.0	165.5	133600.0	295.75	0.8190	0.0048	0.587
Rotameter 2	20	688.0	165.5	144309.2	295.91	0.8296	0.0082	0.713
	30	688.0	165.5	151203.8	295.97	0.8275	0.0123	0.774
	40	688.0	165.5	162031.4	296.10	0.8194	0.0166	0.792
	50	688.0	165.5	170490.7	295.95	0.8172	0.0208	0.817
	60	688.0	165.5	175041.1	295.93	0.8235	0.0248	0.824
	70							
	80							
	90							
	100							

Table B.10: Pitch void fraction

Air Rotameter	Air flow rate (%)	Mass flux based on min area (kg/m^2s)	Mass flux (kg/m^2s)	Two-pahse flow pressure (Pa)	Two-phase flow temperature (K)	Total mass flow rate (kg/s)	Quality (-)	Void fraction pitch (-)
Rotameter 1	10	25.0	6.1	111135.7	294.60	0.0298	0.0131	0.317
	20	25.0	6.1	110171.2	294.49	0.0304	0.0256	0.377
	30	25.0	6.1	108959.8	294.39	0.0299	0.0391	0.432
	40	25.0	6.1	108957.1	294.40	0.0297	0.0525	0.486
	50	25.0	6.1	108422.3	294.39	0.0300	0.0650	0.514
	60	25.0	6.1	108225.8	294.46	0.0304	0.0770	0.556
	70	25.0	6.1	108333.9	294.39	0.0306	0.0893	0.584
	80	25.0	6.1	107958.0	294.53	0.0300	0.1040	0.595
	90	25.0	6.1	108029.3	294.49	0.0301	0.1167	0.603
	100	25.0	6.1	107465.9	294.47	0.0297	0.1314	0.631
Rotameter 2	20	25.0	6.1	106061.4	293.95	0.0299	0.2277	0.697
	30	25.0	6.1	106768.0	293.13	0.0302	0.3383	0.770
	40	25.0	6.1	105520.0	291.51	0.0299	0.4545	0.814
	50	25.0	6.1	104980.3	288.76	0.0312	0.5450	0.912
	60							
	70							
	80							
	90							
	100							
Rotameter 1	10	65.0	15.6	111888.2	292.66	0.0781	0.0050	0.312
	20	65.0	15.6	110503.8	292.57	0.0779	0.0100	0.381
	30	65.0	15.6	109777.9	292.69	0.0780	0.0150	0.419
	40	65.0	15.6	109705.2	292.87	0.0781	0.0200	0.472
	50	65.0	15.6	109349.3	292.96	0.0781	0.0250	0.521
	60	65.0	15.6	109198.3	293.14	0.0779	0.0300	0.554
	70	65.0	15.6	109056.6	293.34	0.0781	0.0349	0.565
	80	65.0	15.6	108784.0	293.49	0.0782	0.0399	0.586
	90	65.0	15.6	108669.6	293.57	0.0782	0.0449	0.602
	100	65.0	15.6	108424.3	293.68	0.0781	0.0500	0.627
Rotameter 2	20	65.0	15.6	107610.8	293.42	0.0781	0.0871	0.711
	30	65.0	15.6	107857.1	293.18	0.0780	0.1308	0.773
	40	65.0	15.6	108792.4	292.96	0.0784	0.1736	0.817
	50	65.0	15.6	109503.4	292.64	0.0783	0.2170	0.853
	60	65.0	15.6	110368.4	292.35	0.0781	0.2611	0.869
	70	65.0	15.6	111527.5	291.98	0.0780	0.3050	0.879
	80							
	90							
	100							

-continued-

Rotameter 1	10	105.0	25.2	113118.6	292.51	0.1266	0.0031	0.295
	20	105.0	25.2	111584.4	292.82	0.1258	0.0062	0.370
	30	105.0	25.2	111158.9	292.99	0.1266	0.0092	0.413
	40	105.0	25.2	110347.3	293.11	0.1264	0.0123	0.474
	50	105.0	25.2	110418.6	293.27	0.1262	0.0155	0.510
	60	105.0	25.2	110167.5	293.35	0.1259	0.0186	0.540
	70	105.0	25.2	109971.7	293.50	0.1263	0.0216	0.584
	80	105.0	25.2	109827.2	293.75	0.1263	0.0247	0.598
	90	105.0	25.2	109687.2	293.82	0.1261	0.0278	0.607
	100	105.0	25.2	109438.5	293.84	0.1259	0.0310	0.635
Rotameter 2	20	105.0	25.2	109339.4	293.74	0.1260	0.0540	0.723
	30	105.0	25.2	110212.6	293.63	0.1259	0.0810	0.790
	40	105.0	25.2	111239.4	293.46	0.1261	0.1079	0.841
	50	105.0	25.2	112932.3	293.30	0.1261	0.1348	0.864
	60	105.0	25.2	114745.7	293.12	0.1258	0.1622	0.878
	70	105.0	25.2	117175.6	292.96	0.1263	0.1884	0.885
	80							
	90							
	100							
Rotameter 1	10	156.0	37.4	114655.4	295.97	0.1860	0.0021	0.284
	20	156.0	37.4	113528.1	295.78	0.1882	0.0041	0.358
	30	156.0	37.4	112740.5	295.85	0.1875	0.0062	0.403
	40	156.0	37.4	112340.2	295.73	0.1866	0.0084	0.478
	50	156.0	37.4	112037.4	295.75	0.1867	0.0104	0.513
	60	156.0	37.4	112110.4	296.06	0.1863	0.0126	0.567
	70	156.0	37.4	112301.9	296.17	0.1866	0.0146	0.594
	80	156.0	37.4	111786.8	295.92	0.1868	0.0167	0.612
	90	156.0	37.4	111618.5	295.51	0.1869	0.0188	0.631
	100	156.0	37.4	111383.3	295.57	0.1858	0.0210	0.657
Rotameter 2	20	156.0	37.4	112203.7	295.22	0.1879	0.0362	0.757
	30	156.0	37.4	113224.4	295.33	0.1874	0.0544	0.818
	40	156.0	37.4	114689.1	295.43	0.1883	0.0722	0.866
	50	156.0	37.4	116292.1	295.29	0.1860	0.0914	0.892
	60	156.0	37.4	119157.4	295.26	0.1867	0.1093	0.905
	70							
	80							
	90							
	100							
Rotameter 1	10	208.0	49.9	115490.6	293.01	0.2504	0.0016	0.276
	20	208.0	49.9	113703.4	293.13	0.2498	0.0031	0.377
	30	208.0	49.9	113283.4	293.17	0.2494	0.0047	0.415
	40	208.0	49.9	112891.2	293.15	0.2489	0.0063	0.449
	50	208.0	49.9	112826.6	293.45	0.2484	0.0079	0.496
	60	208.0	49.9	112759.2	293.62	0.2498	0.0094	0.548
	70	208.0	49.9	112515.9	293.87	0.2495	0.0109	0.586
	80	208.0	49.9	112587.9	294.00	0.2488	0.0125	0.604
	90	208.0	49.9	112821.3	294.16	0.2516	0.0140	0.627
	100	208.0	49.9	112542.3	294.20	0.2497	0.0156	0.676

-continued-

Rotameter 2	20	208.0	49.9	113420.5	294.24	0.2511	0.0271	0.767
	30	208.0	49.9	114760.8	294.28	0.2502	0.0408	0.827
	40	208.0	49.9	117491.3	294.09	0.2502	0.0544	0.863
	50	208.0	49.9	119024.2	294.15	0.2494	0.0682	0.888
	60	208.0	49.9	123452.3	293.97	0.2495	0.0818	0.902
	70	208.0	49.9	126608.5	293.89	0.2508	0.0949	0.910
	80	208.0	49.9	130369.3	293.74	0.2494	0.1091	0.913
	90	208.0	49.9	134385.2	293.61	0.2489	0.1229	0.915
	100							
Rotameter 1	10	312.0	74.8	117385.7	288.71	0.3752	0.0010	0.253
	20	312.0	74.8	116002.0	288.78	0.3749	0.0021	0.348
	30	312.0	74.8	115395.4	289.09	0.3736	0.0031	0.386
	40	312.0	74.8	115202.7	289.33	0.3740	0.0042	0.435
	50	312.0	74.8	115287.1	289.62	0.3745	0.0052	0.477
	60	312.0	74.8	115090.7	289.74	0.3746	0.0062	0.529
	70	312.0	74.8	114910.1	289.96	0.3740	0.0073	0.553
	80	312.0	74.8	114921.2	290.26	0.3749	0.0083	0.574
	90	312.0	74.8	115141.3	290.53	0.3733	0.0094	0.617
	100	312.0	74.8	115348.8	290.65	0.3752	0.0104	0.637
Rotameter 2	20	312.0	74.8	116722.9	290.87	0.3746	0.0182	0.745
	30	312.0	74.8	119350.0	291.01	0.3740	0.0273	0.811
	40	312.0	74.8	122442.3	291.06	0.3734	0.0364	0.852
	50	312.0	74.8	125394.5	291.18	0.3739	0.0455	0.866
	60	312.0	74.8	128107.1	291.22	0.3738	0.0546	0.882
	70	312.0	74.8	132492.5	291.27	0.3733	0.0638	0.890
	80	312.0	74.8	137460.1	291.36	0.3745	0.0726	0.895
	90	312.0	74.8	142274.5	291.36	0.3748	0.0816	0.899
	100	312.0	74.8	150053.5	291.40	0.3723	0.0913	0.907
Rotameter 1	10	416.0	99.8	118725.7	292.52	0.4990	0.0008	0.231
	20	416.0	99.8	117576.6	292.43	0.4986	0.0016	0.324
	30	416.0	99.8	117211.3	292.62	0.4989	0.0023	0.371
	40	416.0	99.8	117160.8	292.93	0.4984	0.0031	0.413
	50	416.0	99.8	117194.7	292.83	0.4984	0.0039	0.478
	60	416.0	99.8	117337.2	292.93	0.4985	0.0047	0.504
	70	416.0	99.8	117665.3	293.02	0.4981	0.0055	0.550
	80	416.0	99.8	117596.2	293.20	0.4996	0.0062	0.573
	90	416.0	99.8	118019.5	293.29	0.4985	0.0070	0.599
	100	416.0	99.8	117906.5	293.35	0.4993	0.0078	0.615
Rotameter 2	20	416.0	99.8	120397.5	293.39	0.4972	0.0137	0.743
	30	416.0	99.8	124302.4	293.42	0.4984	0.0205	0.809
	40	416.0	99.8	127615.1	293.43	0.4971	0.0274	0.836
	50	416.0	99.8	132045.9	293.46	0.4950	0.0343	0.856
	60	416.0	99.8	135841.8	293.48	0.4954	0.0412	0.873
	70	416.0	99.8	141353.9	293.40	0.4986	0.0477	0.883
	80	416.0	99.8	145298.4	293.38	0.5001	0.0544	0.888
	90	416.0	99.8	151807.0	293.27	0.4980	0.0614	0.894
	100							

-continued-

Rotameter 1	10	541.0	129.6	120675.2	291.78	0.6486	0.0006	0.230
	20	541.0	129.6	119916.9	291.85	0.6480	0.0012	0.300
	30	541.0	129.6	119626.5	292.00	0.6483	0.0018	0.347
	40	541.0	129.6	119782.4	292.21	0.6483	0.0024	0.407
	50	541.0	129.6	119835.2	292.52	0.6479	0.0030	0.441
	60	541.0	129.6	120527.0	292.79	0.6488	0.0036	0.499
	70	541.0	129.6	120915.8	292.85	0.6488	0.0042	0.528
	80	541.0	129.6	121410.9	293.01	0.6485	0.0048	0.549
	90	541.0	129.6	121646.4	293.26	0.6488	0.0054	0.577
	100	541.0	129.6	121657.9	293.34	0.6485	0.0060	0.625
Rotameter 2	20	541.0	129.6	125098.8	293.43	0.6492	0.0105	0.732
	30	541.0	129.6	130581.7	293.51	0.6486	0.0157	0.798
	40	541.0	129.6	135317.4	293.57	0.6500	0.0209	0.829
	50	541.0	129.6	138469.2	293.62	0.6490	0.0262	0.842
	60							
	70							
	80							
	90							
	100							
Rotameter 1	10	688.0	165.5	126582.8	294.21	0.8285	0.0005	0.169
	20	688.0	165.5	126683.2	294.43	0.8263	0.0009	0.256
	30	688.0	165.5	127101.9	294.51	0.8234	0.0014	0.303
	40	688.0	165.5	127775.5	294.57	0.8295	0.0019	0.347
	50	688.0	165.5	128708.4	294.72	0.8272	0.0024	0.397
	60	688.0	165.5	130115.5	294.88	0.8279	0.0028	0.435
	70	688.0	165.5	131171.0	295.00	0.8258	0.0033	0.471
	80	688.0	165.5	132222.1	295.15	0.8201	0.0038	0.513
	90	688.0	165.5	133507.3	295.27	0.8225	0.0043	0.534
	100	688.0	165.5	134470.2	295.39	0.8195	0.0048	0.560
Rotameter 2	20	688.0	165.5	143788.8	295.49	0.8260	0.0082	0.681
	30	688.0	165.5	151148.0	295.56	0.8241	0.0124	0.750
	40	688.0	165.5	159873.9	295.65	0.8228	0.0165	0.778
	50	688.0	165.5	168582.7	295.58	0.8214	0.0207	0.806
	60	688.0	165.5	173802.4	295.58	0.8275	0.0247	0.822
	70							
	80							
	90							
	100							

B.2.1 Predicted void fractions [1,2,3,70] for 19 mm in-line tube bundle

Table B.11: Predictions of void fraction

Air flow rate (%)	Mass flux based on min area (kg/m^2s)	Mass flux (kg/m^2s)	Void fraction pitch (-) (present study)	Void fraction (-) prediction by Schrage et al [1]	Void fraction (-) prediction by Feenstra et al [3]	Void fraction (-) prediction by Dowlati et al [2]	Maximum slip model by Chisholm [70]	Homogenous model by Chisholm [70]
10	25	6.07	0.317	0.091	0.330	0.244	0.268	0.910
20	25	6.07	0.377	0.215	0.457	0.373	0.421	0.953
30	25	6.07	0.432	0.303	0.533	0.458	0.531	0.969
40	25	6.07	0.486	0.366	0.584	0.517	0.607	0.977
50	25	6.07	0.514	0.413	0.623	0.563	0.660	0.982
60	25	6.07	0.556	0.451	0.653	0.599	0.700	0.985
70	25	6.07	0.584	0.484	0.677	0.628	0.732	0.987
80	25	6.07	0.595	0.515	0.699	0.653	0.765	0.989
90	25	6.07	0.603	0.540	0.717	0.674	0.787	0.990
100	25	6.07	0.631	0.564	0.734	0.694	0.809	0.992
20	25	6.07	0.697	0.683	0.813	0.781	0.893	0.996
30	25	6.07	0.770	0.769	0.865	0.833	0.935	0.998
40	25	6.07	0.814	0.832	0.902	0.864	0.959	0.998
50	25	6.07	0.912	0.871	0.926	0.885	0.971	0.999
10	65	15.63	0.312	0.079	0.302	0.243	0.121	0.790
20	65	15.63	0.381	0.165	0.429	0.373	0.218	0.885
30	65	15.63	0.419	0.238	0.505	0.456	0.296	0.921
40	65	15.63	0.472	0.291	0.556	0.516	0.361	0.940
50	65	15.63	0.521	0.332	0.594	0.562	0.415	0.952
60	65	15.63	0.554	0.366	0.625	0.598	0.462	0.960
70	65	15.63	0.565	0.394	0.649	0.627	0.502	0.965
80	65	15.63	0.586	0.418	0.670	0.652	0.536	0.970
90	65	15.63	0.602	0.440	0.688	0.674	0.567	0.973
100	65	15.63	0.627	0.460	0.703	0.692	0.595	0.976
20	65	15.63	0.711	0.562	0.776	0.780	0.727	0.987
30	65	15.63	0.773	0.635	0.822	0.832	0.808	0.992
40	65	15.63	0.817	0.687	0.851	0.863	0.854	0.994
50	65	15.63	0.853	0.727	0.872	0.884	0.885	0.995
60	65	15.63	0.869	0.760	0.889	0.899	0.907	0.996
70	65	15.63	0.879	0.788	0.902	0.910	0.923	0.997
10	105	25.22	0.295	0.070	0.279	0.242	0.078	0.696
20	105	25.22	0.370	0.149	0.407	0.372	0.146	0.825
30	105	25.22	0.413	0.215	0.484	0.455	0.204	0.876
40	105	25.22	0.474	0.265	0.538	0.515	0.256	0.905
50	105	25.22	0.510	0.303	0.577	0.561	0.302	0.923
60	105	25.22	0.540	0.335	0.608	0.597	0.344	0.935
70	105	25.22	0.584	0.361	0.633	0.627	0.379	0.944
80	105	25.22	0.598	0.384	0.655	0.652	0.412	0.951
90	105	25.22	0.607	0.405	0.673	0.673	0.443	0.957
100	105	25.22	0.635	0.423	0.688	0.691	0.470	0.961
20	105	25.22	0.723	0.518	0.762	0.779	0.613	0.978
30	105	25.22	0.790	0.586	0.807	0.831	0.709	0.985
40	105	25.22	0.841	0.634	0.836	0.862	0.769	0.989
50	105	25.22	0.864	0.671	0.855	0.883	0.810	0.991
60	105	25.22	0.878	0.702	0.870	0.898	0.840	0.993
70	105	25.22	0.885	0.727	0.882	0.909	0.861	0.994
10	156	37.44	0.284	0.061	0.258	0.242	0.054	0.609
20	156	37.44	0.358	0.137	0.383	0.371	0.102	0.757
30	156	37.44	0.403	0.200	0.462	0.455	0.147	0.825
40	156	37.44	0.478	0.246	0.517	0.514	0.188	0.864
50	156	37.44	0.513	0.283	0.558	0.560	0.225	0.889
60	156	37.44	0.567	0.313	0.590	0.596	0.259	0.906
70	156	37.44	0.594	0.338	0.616	0.625	0.290	0.918
80	156	37.44	0.612	0.360	0.638	0.651	0.319	0.928
90	156	37.44	0.631	0.380	0.657	0.672	0.345	0.936
100	156	37.44	0.657	0.398	0.674	0.690	0.372	0.942
20	156	37.44	0.757	0.487	0.749	0.777	0.508	0.966
30	156	37.44	0.818	0.552	0.795	0.829	0.612	0.977
40	156	37.44	0.866	0.597	0.823	0.861	0.679	0.983
50	156	37.44	0.892	0.633	0.844	0.882	0.731	0.987
60	156	37.44	0.905	0.661	0.858	0.896	0.766	0.989
10	208	49.92	0.276	0.053	0.236	0.240	0.040	0.532
20	208	49.92	0.377	0.129	0.362	0.370	0.079	0.699
30	208	49.92	0.415	0.188	0.441	0.453	0.114	0.778
40	208	49.92	0.449	0.233	0.497	0.513	0.147	0.825
50	208	49.92	0.496	0.268	0.539	0.559	0.178	0.855
60	208	49.92	0.548	0.298	0.572	0.595	0.205	0.876
70	208	49.92	0.586	0.323	0.600	0.625	0.233	0.892
80	208	49.92	0.604	0.344	0.623	0.649	0.258	0.905
90	208	49.92	0.627	0.363	0.641	0.671	0.279	0.914
100	208	49.92	0.676	0.380	0.659	0.689	0.303	0.923
20	208	49.92	0.767	0.468	0.737	0.776	0.432	0.954
30	208	49.92	0.827	0.531	0.785	0.828	0.535	0.969
40	208	49.92	0.863	0.574	0.814	0.859	0.606	0.976

-continued-

50	208	49.92	0.888	0.608	0.834	0.880	0.661	0.981
60	208	49.92	0.902	0.635	0.848	0.895	0.700	0.984
70	208	49.92	0.910	0.658	0.859	0.906	0.730	0.986
80	208	49.92	0.913	0.678	0.868	0.915	0.757	0.988
90	208	49.92	0.915	0.696	0.876	0.922	0.778	0.989
10	312	74.8	0.253	0.043	0.202	0.238	0.027	0.423
20	312	74.8	0.348	0.115	0.321	0.366	0.053	0.598
30	312	74.8	0.386	0.170	0.401	0.450	0.078	0.693
40	312	74.8	0.435	0.212	0.459	0.510	0.101	0.751
50	312	74.8	0.477	0.247	0.503	0.555	0.123	0.791
60	312	74.8	0.529	0.275	0.539	0.591	0.145	0.820
70	312	74.8	0.553	0.300	0.568	0.621	0.165	0.842
80	312	74.8	0.574	0.321	0.592	0.646	0.184	0.859
90	312	74.8	0.617	0.340	0.613	0.668	0.203	0.873
100	312	74.8	0.637	0.356	0.631	0.686	0.220	0.884
20	312	74.8	0.745	0.442	0.716	0.773	0.331	0.930
30	312	74.8	0.811	0.503	0.766	0.825	0.426	0.952
40	312	74.8	0.852	0.545	0.797	0.856	0.497	0.963
50	312	74.8	0.866	0.577	0.818	0.877	0.552	0.969
60	312	74.8	0.882	0.603	0.833	0.893	0.596	0.974
70	312	74.8	0.890	0.625	0.845	0.904	0.631	0.977
80	312	74.8	0.895	0.643	0.853	0.912	0.659	0.979
90	312	74.8	0.899	0.660	0.861	0.919	0.683	0.981
100	312	74.8	0.907	0.674	0.866	0.925	0.704	0.982
10	416	99.84	0.231	0.040	0.180	0.238	0.020	0.356
20	416	99.84	0.324	0.105	0.294	0.366	0.040	0.528
30	416	99.84	0.371	0.157	0.372	0.450	0.059	0.627
40	416	99.84	0.413	0.198	0.431	0.509	0.078	0.693
50	416	99.84	0.478	0.231	0.476	0.555	0.095	0.738
60	416	99.84	0.504	0.259	0.512	0.591	0.112	0.772
70	416	99.84	0.550	0.283	0.542	0.620	0.128	0.798
80	416	99.84	0.573	0.304	0.568	0.645	0.144	0.818
90	416	99.84	0.599	0.322	0.589	0.666	0.159	0.835
100	416	99.84	0.615	0.339	0.608	0.685	0.174	0.849
20	416	99.84	0.743	0.424	0.697	0.772	0.268	0.907
30	416	99.84	0.809	0.484	0.750	0.824	0.352	0.934
40	416	99.84	0.836	0.526	0.782	0.855	0.419	0.949
50	416	99.84	0.856	0.557	0.804	0.875	0.473	0.958
60	416	99.84	0.873	0.582	0.820	0.891	0.517	0.964
70	416	99.84	0.883	0.603	0.831	0.902	0.550	0.968
80	416	99.84	0.888	0.621	0.841	0.911	0.581	0.971
90	416	99.84	0.894	0.637	0.848	0.917	0.607	0.973
10	541	129.6	0.230	0.037	0.157	0.236	0.016	0.295
20	541	129.6	0.300	0.095	0.263	0.364	0.031	0.457
30	541	129.6	0.347	0.143	0.339	0.447	0.046	0.559
40	541	129.6	0.407	0.182	0.397	0.507	0.060	0.628
50	541	129.6	0.441	0.214	0.443	0.552	0.074	0.679
60	541	129.6	0.499	0.242	0.480	0.588	0.087	0.716
70	541	129.6	0.528	0.265	0.511	0.617	0.100	0.746
80	541	129.6	0.549	0.286	0.537	0.642	0.113	0.770
90	541	129.6	0.577	0.304	0.560	0.664	0.125	0.790
100	541	129.6	0.625	0.321	0.580	0.682	0.137	0.807
20	541	129.6	0.732	0.406	0.674	0.769	0.215	0.877
30	541	129.6	0.798	0.466	0.729	0.821	0.289	0.912
40	541	129.6	0.829	0.506	0.763	0.852	0.348	0.930
50	541	129.6	0.842	0.538	0.788	0.873	0.399	0.942
10	688	165.5	0.169	0.033	0.134	0.233	0.012	0.239
20	688	165.5	0.256	0.084	0.230	0.360	0.024	0.387
30	688	165.5	0.303	0.127	0.302	0.442	0.035	0.486
40	688	165.5	0.347	0.163	0.356	0.501	0.046	0.555
50	688	165.5	0.397	0.194	0.401	0.546	0.057	0.608
60	688	165.5	0.435	0.220	0.437	0.581	0.067	0.648
70	688	165.5	0.471	0.244	0.468	0.610	0.078	0.682
80	688	165.5	0.513	0.264	0.495	0.635	0.088	0.710
90	688	165.5	0.534	0.282	0.517	0.656	0.097	0.731
100	688	165.5	0.560	0.298	0.537	0.674	0.107	0.751
20	688	165.5	0.681	0.382	0.631	0.759	0.168	0.830
30	688	165.5	0.750	0.443	0.692	0.812	0.229	0.876
40	688	165.5	0.778	0.484	0.728	0.843	0.279	0.899
50	688	165.5	0.806	0.515	0.752	0.864	0.322	0.914
60	688	165.5	0.822	0.540	0.772	0.880	0.358	0.925

B.3 Void fraction data sets for the two local void fractions measurements and the pitch average in the 19 mm staggered bundle

Table B.12: Void fraction in the maximum gap between the tubes

Air Rotameter	Air flow rate (%)	Mass flux based on min area (kg/m^{2}s)	Mass flux (kg/m^{2}s)	Two-phase flow pressure (Pa)	Two-phase flow temperature (K)	Total mass flow rate (kg/s)	Quality (-)	Void fraction at the gap to the south of central tube (max gap)(-)
Rotameter 1	10	25.0	6.1	109836.6	297.93	0.0302	0.0129	0.406
	20	25.0	6.1	108686.6	297.85	0.0298	0.0262	0.504
	30	25.0	6.1	108791.3	297.79	0.0298	0.0392	0.539
	40	25.0	6.1	108032.7	297.69	0.0301	0.0518	0.623
	50	25.0	6.1	107811.0	297.63	0.0299	0.0651	0.665
	60	25.0	6.1	107878.4	297.53	0.0299	0.0782	0.701
	70	25.0	6.1	107626.7	297.46	0.0303	0.0902	0.731
	80	25.0	6.1	107314.4	297.42	0.0301	0.1036	0.743
	90	25.0	6.1	107584.0	297.31	0.0302	0.1163	0.773
	100	25.0	6.1	107371.4	297.31	0.0298	0.1310	0.789
Rotameter 2	20	25.0	6.1	106416.2	296.18	0.0300	0.2269	0.850
	30	25.0	6.1	106452.5	295.06	0.0299	0.3407	0.869
	40	25.0	6.1	105708.6	291.49	0.0298	0.4561	0.904
	50	25.0	6.1	105250.8	289.36	0.0329	0.5172	0.963
	60							
	70							
	80							
	90							
	100							
Rotameter 1	10	65.0	15.6	111852.0	296.11	0.0780	0.0050	0.367
	20	65.0	15.6	110352.5	296.19	0.0780	0.0100	0.489
	30	65.0	15.6	109859.1	296.29	0.0781	0.0150	0.555
	40	65.0	15.6	109112.5	296.37	0.0781	0.0200	0.606
	50	65.0	15.6	109107.2	296.42	0.0782	0.0249	0.649
	60	65.0	15.6	108876.0	296.50	0.0783	0.0299	0.698
	70	65.0	15.6	108978.6	296.54	0.0780	0.0350	0.725
	80	65.0	15.6	108810.3	296.62	0.0780	0.0400	0.755
	90	65.0	15.6	108695.6	296.68	0.0782	0.0449	0.769
	100	65.0	15.6	108831.2	296.71	0.0780	0.0500	0.794
Rotameter 2	20	65.0	15.6	108749.1	296.38	0.0783	0.0869	0.868
	30	65.0	15.6	108778.6	296.05	0.0779	0.1309	0.892
	40	65.0	15.6	110417.5	295.78	0.0785	0.1733	0.909
	50	65.0	15.6	111532.0	295.49	0.0781	0.2176	0.916
	60	65.0	15.6	112254.1	294.90	0.0778	0.2621	0.926
	70	65.0	15.6	112990.7	294.58	0.0780	0.3050	0.933
	80							
	90							
	100							

-continued-

Rotameter 1	10	105.0	25.2	112067.3	294.74	0.1263	0.0031	0.369
	20	105.0	25.2	110261.5	294.91	0.1262	0.0062	0.495
	30	105.0	25.2	109544.2	294.96	0.1258	0.0093	0.560
	40	105.0	25.2	109663.5	295.09	0.1261	0.0124	0.606
	50	105.0	25.2	109773.4	295.18	0.1264	0.0154	0.664
	60	105.0	25.2	109522.6	295.26	0.1262	0.0185	0.701
	70	105.0	25.2	109604.7	295.29	0.1263	0.0216	0.722
	80	105.0	25.2	110255.3	295.37	0.1262	0.0247	0.744
	90	105.0	25.2	109793.0	295.41	0.1262	0.0278	0.767
	100	105.0	25.2	109637.2	295.47	0.1260	0.0310	0.773
Rotameter 2	20	105.0	25.2	110525.4	295.36	0.1261	0.0539	0.860
	30	105.0	25.2	111192.6	295.21	0.1262	0.0808	0.887
	40	105.0	25.2	112730.9	295.02	0.1258	0.1081	0.905
	50	105.0	25.2	114036.4	294.85	0.1268	0.1341	0.914
	60	105.0	25.2	116272.9	294.79	0.1262	0.1616	0.922
	70	105.0	25.2	118603.5	294.68	0.1264	0.1882	0.927
	80							
	90							
	100							
Rotameter 1	10	156.0	37.4	113207.0	293.99	0.1867	0.0021	0.361
	20	156.0	37.4	111993.8	294.10	0.1874	0.0042	0.459
	30	156.0	37.4	111371.7	294.12	0.1871	0.0063	0.520
	40	156.0	37.4	111096.3	294.15	0.1875	0.0083	0.579
	50	156.0	37.4	111040.0	294.25	0.1867	0.0104	0.621
	60	156.0	37.4	111275.5	294.38	0.1872	0.0125	0.660
	70	156.0	37.4	111283.0	294.34	0.1866	0.0146	0.686
	80	156.0	37.4	111385.8	294.37	0.1870	0.0167	0.708
	90	156.0	37.4	110952.3	294.58	0.1874	0.0187	0.732
	100	156.0	37.4	111263.2	294.54	0.1874	0.0208	0.750
Rotameter 2	20	156.0	37.4	112046.1	294.64	0.1878	0.0362	0.825
	30	156.0	37.4	114482.9	294.37	0.1871	0.0545	0.856
	40	156.0	37.4	114874.6	294.31	0.1876	0.0725	0.866
	50	156.0	37.4	117758.5	294.22	0.1878	0.0905	0.874
	60	156.0	37.4	120710.9	294.16	0.1879	0.1086	0.880
	70							
	80							
	90							
	100							
Rotameter 1	10	208.0	49.9	114553.5	295.14	0.2495	0.0016	0.350
	20	208.0	49.9	113283.5	295.23	0.2499	0.0031	0.471
	30	208.0	49.9	112759.2	295.33	0.2496	0.0047	0.537
	40	208.0	49.9	112150.9	295.44	0.2498	0.0062	0.595
	50	208.0	49.9	112316.4	295.54	0.2491	0.0078	0.645
	60	208.0	49.9	112438.7	295.64	0.2498	0.0094	0.690
	70	208.0	49.9	113178.9	295.73	0.2498	0.0109	0.716
	80	208.0	49.9	113050.8	295.78	0.2490	0.0125	0.743
	90	208.0	49.9	113283.0	295.83	0.2497	0.0141	0.757
	100	208.0	49.9	113028.1	296.04	0.2497	0.0156	0.786

-continued-

Rotameter 2	20	208.0	49.9	114350.1	295.88	0.2497	0.0272	0.864
	30	208.0	49.9	116530.7	295.79	0.2495	0.0409	0.888
	40	208.0	49.9	118915.3	295.68	0.2495	0.0545	0.901
	50	208.0	49.9	120960.1	295.71	0.2487	0.0684	0.909
	60	208.0	49.9	125778.3	295.55	0.2488	0.0820	0.919
	70	208.0	49.9	129125.4	295.51	0.2500	0.0952	0.924
	80	208.0	49.9	133869.2	295.38	0.2487	0.1094	0.933
	90	208.0	49.9	135765.5	295.36	0.2500	0.1224	0.936
	100							
Rotameter 1	10	312.0	74.8	116563.7	294.44	0.3744	0.0010	0.343
	20	312.0	74.8	115379.3	294.48	0.3738	0.0021	0.464
	30	312.0	74.8	114917.4	294.50	0.3730	0.0031	0.528
	40	312.0	74.8	114634.7	294.56	0.3741	0.0042	0.591
	50	312.0	74.8	114760.0	294.61	0.3740	0.0052	0.633
	60	312.0	74.8	114976.3	294.69	0.3743	0.0063	0.673
	70	312.0	74.8	115724.9	294.75	0.3743	0.0073	0.690
	80	312.0	74.8	115281.5	294.82	0.3737	0.0083	0.725
	90	312.0	74.8	116294.5	294.86	0.3741	0.0094	0.737
	100	312.0	74.8	115941.4	294.87	0.3743	0.0104	0.770
Rotameter 2	20	312.0	74.8	119554.4	294.90	0.3750	0.0181	0.848
	30	312.0	74.8	122661.4	294.85	0.3721	0.0274	0.866
	40	312.0	74.8	125915.7	294.99	0.3756	0.0362	0.878
	50	312.0	74.8	130969.6	294.82	0.3729	0.0456	0.893
	60	312.0	74.8	134388.0	294.72	0.3740	0.0545	0.901
	70	312.0	74.8	138068.8	294.85	0.3734	0.0637	0.907
	80	312.0	74.8	144348.3	294.65	0.3711	0.0733	0.914
	90	312.0	74.8	150821.0	294.61	0.3765	0.0813	0.923
	100	312.0	74.8	157952.9	294.51	0.3780	0.0900	0.926
Rotameter 1	10	416.0	99.8	118179.1	295.36	0.4999	0.0008	0.316
	20	416.0	99.8	117187.0	295.41	0.4985	0.0016	0.448
	30	416.0	99.8	116915.5	295.34	0.4986	0.0023	0.510
	40	416.0	99.8	117030.9	295.40	0.4995	0.0031	0.572
	50	416.0	99.8	117274.9	295.44	0.4983	0.0039	0.629
	60	416.0	99.8	118053.8	295.54	0.4982	0.0047	0.651
	70	416.0	99.8	118257.5	295.58	0.4988	0.0055	0.669
	80	416.0	99.8	119282.8	295.62	0.4988	0.0063	0.705
	90	416.0	99.8	119496.3	295.67	0.4984	0.0070	0.720
	100	416.0	99.8	119162.5	295.73	0.4991	0.0078	0.735
Rotameter 2	20	416.0	99.8	124150.6	295.75	0.4989	0.0136	0.829
	30	416.0	99.8	129413.5	295.76	0.4981	0.0205	0.856
	40	416.0	99.8	135126.4	295.77	0.4979	0.0273	0.871
	50	416.0	99.8	139165.7	295.75	0.4979	0.0341	0.884
	60	416.0	99.8	145566.2	295.70	0.4993	0.0409	0.894
	70	416.0	99.8	150921.4	295.68	0.5000	0.0476	0.904
	80	416.0	99.8	158623.9	295.70	0.4982	0.0546	0.910
	90	416.0	99.8	164854.5	295.58	0.4993	0.0613	0.913
	100							

-continued-

Rotameter 1	10	541.0	129.6	120132.4	296.10	0.6488	0.0006	0.293
	20	541.0	129.6	119589.7	296.33	0.6486	0.0012	0.405
	30	541.0	129.6	119563.8	296.46	0.6486	0.0018	0.491
	40	541.0	129.6	119852.3	296.61	0.6479	0.0024	0.572
	50	541.0	129.6	120303.1	296.57	0.6487	0.0030	0.590
	60	541.0	129.6	121206.8	296.65	0.6472	0.0036	0.632
	70	541.0	129.6	121762.5	296.84	0.6466	0.0042	0.658
	80	541.0	129.6	122621.5	296.92	0.6481	0.0048	0.693
	90	541.0	129.6	123278.3	297.09	0.6494	0.0054	0.700
	100	541.0	129.6	124978.2	297.17	0.6492	0.0060	0.716
Rotameter 2	20	541.0	129.6	131727.6	297.29	0.6489	0.0105	0.810
	30	541.0	129.6	137455.0	297.14	0.6496	0.0157	0.840
	40	541.0	129.6	143930.0	297.24	0.6490	0.0210	0.854
	50	541.0	129.6	150187.5	297.18	0.6495	0.0262	0.869
	60							
	70							
	80							
	90							
	100							
Rotameter 1	10	688.0	165.5	122836.6	297.71	0.8295	0.0005	0.253
	20	688.0	165.5	122836.6	297.65	0.8276	0.0009	0.390
	30	688.0	165.5	122900.0	297.70	0.8299	0.0014	0.470
	40	688.0	165.5	123209.9	297.70	0.8259	0.0019	0.532
	50	688.0	165.5	124690.7	297.76	0.8226	0.0024	0.568
	60	688.0	165.5	125571.4	297.82	0.8207	0.0029	0.625
	70	688.0	165.5	127063.3	297.86	0.8279	0.0033	0.627
	80	688.0	165.5	128139.7	297.91	0.8223	0.0038	0.655
	90	688.0	165.5	129198.0	298.00	0.8290	0.0042	0.667
	100	688.0	165.5	130744.0	298.05	0.8269	0.0047	0.688
Rotameter 2	20	688.0	165.5	140113.4	298.04	0.8227	0.0083	0.776
	30	688.0	165.5	150019.6	298.02	0.8276	0.0123	0.813
	40	688.0	165.5	157669.6	297.95	0.8311	0.0164	0.837
	50	688.0	165.5	166302.2	297.94	0.8255	0.0206	0.849
	60	688.0	165.5	179000.1	297.89	0.8247	0.0247	0.864
	70							
	80							
	90							
	100							

Table B.13: Void fraction in the minimum gap between the tubes (to the east of central tube)

Air Rotameter	Air flow rate (%)	Mass flux based on min area (kg/m^{2}s)	Mass flux (kg/m^{2}s)	Two-phase flow pressure (Pa)	Two-phase flow temperature (K)	Total mass flow rate (kg/s)	Quality (-)	Void fraction at the gap to the east of central tube (min gap)(-)
Rotameter 1	10	25.0	6.1	110100.1	294.18	0.0301	0.0129	0.340
	20	25.0	6.1	108519.5	294.12	0.0304	0.0257	0.439
	30	25.0	6.1	108076.8	294.03	0.0305	0.0384	0.489
	40	25.0	6.1	108034.5	294.06	0.0303	0.0516	0.530
	50	25.0	6.1	107846.7	293.96	0.0300	0.0650	0.597
	60	25.0	6.1	107030.3	293.92	0.0304	0.0770	0.645
	70	25.0	6.1	107328.9	293.91	0.0305	0.0894	0.661
	80	25.0	6.1	107350.0	293.97	0.0306	0.1021	0.676
	90	25.0	6.1	107585.7	293.97	0.0299	0.1174	0.702
	100	25.0	6.1	107314.4	293.92	0.0299	0.1302	0.718
Rotameter 2	20	25.0	6.1	106301.3	293.49	0.0305	0.2233	0.778
	30	25.0	6.1	106420.4	293.08	0.0300	0.3398	0.771
	40	25.0	6.1	105977.4	291.46	0.0301	0.4517	0.871
	50	25.0	6.1	105864.0	289.84	0.0322	0.5284	0.904
	60							
	70							
	80							
	90							
	100							
Rotameter 1	10	65.0	15.6	111599.8	295.99	0.0783	0.0050	0.363
	20	65.0	15.6	110216.2	296.16	0.0782	0.0100	0.471
	30	65.0	15.6	109665.5	296.16	0.0779	0.0150	0.518
	40	65.0	15.6	109587.3	296.16	0.0779	0.0200	0.583
	50	65.0	15.6	108951.7	296.18	0.0782	0.0249	0.645
	60	65.0	15.6	108891.4	296.18	0.0783	0.0299	0.677
	70	65.0	15.6	109071.5	296.23	0.0785	0.0348	0.700
	80	65.0	15.6	108926.5	296.38	0.0782	0.0399	0.722
	90	65.0	15.6	108838.5	296.30	0.0790	0.0444	0.744
	100	65.0	15.6	108627.9	296.25	0.0784	0.0497	0.765
Rotameter 2	20	65.0	15.6	108909.7	295.93	0.0783	0.0869	0.850
	30	65.0	15.6	109085.0	295.46	0.0784	0.1301	0.907
	40	65.0	15.6	110453.6	295.21	0.0793	0.1714	0.934
	50	65.0	15.6	110432.8	295.03	0.0771	0.2205	0.936
	60	65.0	15.6	109123.4	295.06	0.0782	0.2609	0.910
	70	65.0	15.6	108086.7	295.29	0.0781	0.3046	0.889
	80							
	90							
	100							

-continued-

Rotameter 1	10	105.0	25.2	112639.4	294.60	0.1264	0.0031	0.344
	20	105.0	25.2	111254.8	294.72	0.1261	0.0062	0.453
	30	105.0	25.2	110388.8	294.82	0.1270	0.0092	0.491
	40	105.0	25.2	110374.3	294.90	0.1274	0.0122	0.553
	50	105.0	25.2	109983.7	294.97	0.1261	0.0155	0.609
	60	105.0	25.2	109768.7	295.06	0.1262	0.0185	0.642
	70	105.0	25.2	109971.8	295.14	0.1264	0.0216	0.666
	80	105.0	25.2	109870.9	295.18	0.1260	0.0248	0.698
	90	105.0	25.2	109871.5	295.24	0.1263	0.0278	0.712
	100	105.0	25.2	109905.7	295.27	0.1263	0.0309	0.743
Rotameter 2	20	105.0	25.2	110401.0	295.11	0.1270	0.0535	0.816
	30	105.0	25.2	111336.0	295.01	0.1260	0.0810	0.845
	40	105.0	25.2	112068.8	294.81	0.1269	0.1072	0.884
	50	105.0	25.2	114221.7	294.64	0.1271	0.1337	0.904
	60	105.0	25.2	116555.0	294.47	0.1263	0.1615	0.917
	70	105.0	25.2	119327.0	294.19	0.1266	0.1880	0.927
	80							
	90							
	100							
Rotameter 1	10	156.0	37.4	113207.0	295.20	0.1862	0.0021	0.339
	20	156.0	37.4	111993.8	295.26	0.1865	0.0042	0.433
	30	156.0	37.4	111371.7	295.31	0.1860	0.0063	0.479
	40	156.0	37.4	111096.3	295.37	0.1877	0.0083	0.530
	50	156.0	37.4	111040.0	295.43	0.1879	0.0104	0.571
	60	156.0	37.4	111275.5	295.88	0.1865	0.0125	0.618
	70	156.0	37.4	111283.0	295.94	0.1858	0.0147	0.643
	80	156.0	37.4	111385.8	295.98	0.1852	0.0168	0.660
	90	156.0	37.4	110952.3	297.46	0.1889	0.0186	0.685
	100	156.0	37.4	111263.2	297.50	0.1856	0.0210	0.709
Rotameter 2	20	156.0	37.4	112046.1	297.38	0.1877	0.0362	0.785
	30	156.0	37.4	114482.9	297.27	0.1874	0.0544	0.827
	40	156.0	37.4	114874.6	295.53	0.1872	0.0727	0.862
	50	156.0	37.4	117758.5	295.40	0.1898	0.0896	0.881
	60	156.0	37.4	120710.9	295.29	0.1872	0.1090	0.896
	70							
	80							
	90							
	100							
Rotameter 1	10	208.0	49.9	114553.5	296.56	0.2492	0.0016	0.326
	20	208.0	49.9	113283.5	296.50	0.2500	0.0031	0.401
	30	208.0	49.9	112759.2	296.55	0.2490	0.0047	0.464
	40	208.0	49.9	112150.9	296.59	0.2489	0.0063	0.541
	50	208.0	49.9	112316.4	296.71	0.2479	0.0079	0.569
	60	208.0	49.9	112438.7	296.71	0.2497	0.0094	0.654
	70	208.0	49.9	113178.9	296.85	0.2503	0.0109	0.624
	80	208.0	49.9	113050.8	296.82	0.2500	0.0125	0.661
	90	208.0	49.9	113283.0	296.81	0.2468	0.0142	0.668
	100	208.0	49.9	113028.1	296.82	0.2488	0.0157	0.691

-continued-

Rotameter 2	20	208.0	49.9	114350.1	296.75	0.2488	0.0273	0.770
	30	208.0	49.9	116530.7	296.95	0.2505	0.0407	0.809
	40	208.0	49.9	118915.3	296.88	0.2445	0.0556	0.837
	50	208.0	49.9	120960.1	296.79	0.2374	0.0716	0.858
	60	208.0	49.9	125778.3	296.64	0.2508	0.0813	0.863
	70	208.0	49.9	129125.4	296.83	0.2359	0.1009	0.871
	80	208.0	49.9	133869.2	296.76	0.2462	0.1105	0.880
	90	208.0	49.9	135765.5	296.71	0.2440	0.1254	0.893
	100							
Rotameter 1	10	312.0	74.8	116563.7	297.62	0.3739	0.0010	0.291
	20	312.0	74.8	115379.3	297.75	0.3740	0.0021	0.387
	30	312.0	74.8	114917.4	297.92	0.3749	0.0031	0.446
	40	312.0	74.8	114634.7	297.97	0.3733	0.0042	0.505
	50	312.0	74.8	114760.0	298.03	0.3738	0.0052	0.550
	60	312.0	74.8	114976.3	298.09	0.3739	0.0063	0.569
	70	312.0	74.8	115724.9	298.16	0.3719	0.0073	0.607
	80	312.0	74.8	115281.5	298.17	0.3744	0.0083	0.644
	90	312.0	74.8	116294.5	298.24	0.3721	0.0094	0.657
	100	312.0	74.8	115941.4	298.27	0.3729	0.0105	0.679
Rotameter 2	20	312.0	74.8	119554.4	299.65	0.3698	0.0184	0.764
	30	312.0	74.8	122661.4	299.52	0.3664	0.0278	0.809
	40	312.0	74.8	125915.7	299.48	0.3731	0.0365	0.833
	50	312.0	74.8	130969.6	299.42	0.3673	0.0463	0.853
	60	312.0	74.8	134388.0	299.31	0.3707	0.0550	0.865
	70	312.0	74.8	138068.8	299.10	0.3735	0.0637	0.875
	80	312.0	74.8	144348.3	298.91	0.3673	0.0740	0.883
	90	312.0	74.8	150821.0	298.91	0.3771	0.0811	0.889
	100	312.0	74.8	157952.9	298.76	0.3769	0.0902	0.896
Rotameter 1	10	416.0	99.8	118179.1	299.35	0.4984	0.0008	0.248
	20	416.0	99.8	117187.0	299.34	0.4976	0.0016	0.360
	30	416.0	99.8	116915.5	299.40	0.4989	0.0023	0.445
	40	416.0	99.8	117030.9	299.43	0.4994	0.0031	0.492
	50	416.0	99.8	117274.9	299.48	0.4981	0.0039	0.529
	60	416.0	99.8	118053.8	299.53	0.4978	0.0047	0.568
	70	416.0	99.8	118257.5	299.58	0.4976	0.0055	0.596
	80	416.0	99.8	119282.8	299.62	0.4981	0.0063	0.617
	90	416.0	99.8	119496.3	299.64	0.4973	0.0071	0.639
	100	416.0	99.8	119162.5	299.67	0.4989	0.0078	0.655
Rotameter 2	20	416.0	99.8	124150.6	299.65	0.4978	0.0137	0.755
	30	416.0	99.8	129413.5	299.61	0.5005	0.0204	0.795
	40	416.0	99.8	135126.4	299.56	0.4951	0.0275	0.820
	50	416.0	99.8	139165.7	299.54	0.4959	0.0343	0.839
	60	416.0	99.8	145566.2	299.53	0.4998	0.0408	0.852
	70	416.0	99.8	150921.4	299.27	0.4967	0.0479	0.863
	80	416.0	99.8	158623.9	299.10	0.4973	0.0547	0.870
	90	416.0	99.8	164854.5	298.99	0.4983	0.0614	0.878
	100							

-continued-

Rotameter 1	10	541.0	129.6	120132.4	295.78	0.6484	0.0006	0.256
	20	541.0	129.6	119589.7	295.89	0.6489	0.0012	0.369
	30	541.0	129.6	119563.8	296.06	0.6481	0.0018	0.407
	40	541.0	129.6	119852.3	296.13	0.6480	0.0024	0.458
	50	541.0	129.6	120303.1	296.19	0.6488	0.0030	0.508
	60	541.0	129.6	121206.8	296.23	0.6486	0.0036	0.542
	70	541.0	129.6	121762.5	296.30	0.6484	0.0042	0.572
	80	541.0	129.6	122621.5	296.35	0.6475	0.0048	0.590
	90	541.0	129.6	123278.3	296.39	0.6503	0.0054	0.601
	100	541.0	129.6	124978.2	296.45	0.6479	0.0060	0.634
Rotameter 2	20	541.0	129.6	131727.6	296.46	0.6473	0.0105	0.739
	30	541.0	129.6	137455.0	296.46	0.6472	0.0158	0.771
	40	541.0	129.6	143930.0	296.45	0.6495	0.0209	0.798
	50	541.0	129.6	150187.5	296.46	0.6478	0.0262	0.815
	60							
	70							
	80							
	90							
	100							
Rotameter 1	10	688.0	165.5	122836.6	299.62	0.8279	0.0005	0.176
	20	688.0	165.5	122836.6	299.71	0.8283	0.0009	0.284
	30	688.0	165.5	122900.0	299.78	0.8264	0.0014	0.357
	40	688.0	165.5	123209.9	299.83	0.8298	0.0019	0.395
	50	688.0	165.5	124690.7	299.94	0.8275	0.0024	0.445
	60	688.0	165.5	125571.4	300.00	0.8216	0.0028	0.479
	70	688.0	165.5	127063.3	300.10	0.8270	0.0033	0.514
	80	688.0	165.5	128139.7	300.14	0.8204	0.0038	0.537
	90	688.0	165.5	129198.0	300.19	0.8258	0.0043	0.551
	100	688.0	165.5	130744.0	300.25	0.8225	0.0047	0.571
Rotameter 2	20	688.0	165.5	140113.4	300.34	0.8277	0.0082	0.675
	30	688.0	165.5	150019.6	300.35	0.8279	0.0123	0.730
	40	688.0	165.5	157669.6	300.31	0.8244	0.0165	0.759
	50	688.0	165.5	166302.2	300.29	0.8211	0.0207	0.780
	60	688.0	165.5	179000.1	300.26	0.8271	0.0247	0.802
	70							
	80							
	90							
	100							

Table B.14: Pitch void fraction

Air Rotameter	Air flow rate (%)	Mass flux based on min area (kg/m^{2}s)	Mass flux (kg/m^{2}s)	Two-phase flow pressure (Pa)	Two-phase flow temperature (K)	Total mass flow rate (kg/s)	Quality (-)	Void fraction pitch (-)
Rotameter 1	10	25.0	6.1	109968.4	296.05	0.0302	0.0129	0.373
	20	25.0	6.1	108603.0	295.98	0.0301	0.0259	0.472
	30	25.0	6.1	108434.1	295.91	0.0302	0.0388	0.514
	40	25.0	6.1	108033.6	295.88	0.0302	0.0517	0.576
	50	25.0	6.1	107828.8	295.79	0.0300	0.0651	0.631
	60	25.0	6.1	107454.3	295.73	0.0302	0.0776	0.673
	70	25.0	6.1	107477.8	295.69	0.0304	0.0898	0.696
	80	25.0	6.1	107332.2	295.70	0.0303	0.1028	0.710
	90	25.0	6.1	107584.9	295.64	0.0300	0.1168	0.737
	100	25.0	6.1	107342.9	295.62	0.0299	0.1306	0.754
Rotameter 2	20	25.0	6.1	106358.8	294.84	0.0302	0.2251	0.814
	30	25.0	6.1	106436.5	294.07	0.0300	0.3403	0.820
	40	25.0	6.1	105843.0	291.48	0.0300	0.4539	0.887
	50	25.0	6.1	105557.4	289.60	0.0325	0.5228	0.934
	60							
	70							
	80							
	90							
	100							
Rotameter 1	10	65.0	15.6	111725.9	296.05	0.0782	0.0050	0.365
	20	65.0	15.6	110284.4	296.17	0.0781	0.0100	0.480
	30	65.0	15.6	109762.3	296.23	0.0780	0.0150	0.537
	40	65.0	15.6	109349.9	296.26	0.0780	0.0200	0.595
	50	65.0	15.6	109029.4	296.30	0.0782	0.0249	0.647
	60	65.0	15.6	108883.7	296.34	0.0783	0.0299	0.688
	70	65.0	15.6	109025.1	296.39	0.0782	0.0349	0.713
	80	65.0	15.6	108868.4	296.50	0.0781	0.0399	0.738
	90	65.0	15.6	108767.0	296.49	0.0786	0.0447	0.757
	100	65.0	15.6	108729.5	296.48	0.0782	0.0499	0.780
Rotameter 2	20	65.0	15.6	108829.4	296.15	0.0783	0.0869	0.859
	30	65.0	15.6	108931.8	295.76	0.0782	0.1305	0.899
	40	65.0	15.6	110435.6	295.49	0.0789	0.1724	0.922
	50	65.0	15.6	110982.4	295.26	0.0776	0.2191	0.926
	60	65.0	15.6	110688.8	294.98	0.0780	0.2615	0.918
	70	65.0	15.6	110538.7	294.93	0.0781	0.3048	0.911
	80							
	90							
	100							

-continued-

Rotameter 1	10	105.0	25.2	112353.3	294.67	0.1264	0.0031	0.356
	20	105.0	25.2	110758.2	294.81	0.1261	0.0062	0.474
	30	105.0	25.2	109966.5	294.89	0.1264	0.0093	0.526
	40	105.0	25.2	110018.9	294.99	0.1267	0.0123	0.580
	50	105.0	25.2	109878.5	295.07	0.1262	0.0154	0.637
	60	105.0	25.2	109645.6	295.16	0.1262	0.0185	0.672
	70	105.0	25.2	109788.3	295.21	0.1264	0.0216	0.694
	80	105.0	25.2	110063.1	295.28	0.1261	0.0247	0.721
	90	105.0	25.2	109832.2	295.33	0.1263	0.0278	0.740
	100	105.0	25.2	109771.4	295.37	0.1261	0.0309	0.758
Rotameter 2	20	105.0	25.2	110463.2	295.23	0.1265	0.0537	0.838
	30	105.0	25.2	111264.3	295.11	0.1261	0.0809	0.866
	40	105.0	25.2	112399.8	294.92	0.1264	0.1076	0.895
	50	105.0	25.2	114129.1	294.75	0.1270	0.1339	0.909
	60	105.0	25.2	116414.0	294.63	0.1263	0.1615	0.919
	70	105.0	25.2	118965.2	294.43	0.1265	0.1881	0.927
	80							
	90							
	100							
Rotameter 1	10	156.0	37.4	113207.0	294.59	0.1865	0.0021	0.350
	20	156.0	37.4	111993.8	294.68	0.1869	0.0042	0.446
	30	156.0	37.4	111371.7	294.72	0.1866	0.0063	0.500
	40	156.0	37.4	111096.3	294.76	0.1876	0.0083	0.555
	50	156.0	37.4	111040.0	294.84	0.1873	0.0104	0.596
	60	156.0	37.4	111275.5	295.13	0.1869	0.0125	0.639
	70	156.0	37.4	111283.0	295.14	0.1862	0.0147	0.665
	80	156.0	37.4	111385.8	295.18	0.1861	0.0168	0.684
	90	156.0	37.4	110952.3	296.02	0.1881	0.0187	0.708
	100	156.0	37.4	111263.2	296.02	0.1865	0.0209	0.729
Rotameter 2	20	156.0	37.4	112046.1	296.01	0.1878	0.0362	0.805
	30	156.0	37.4	114482.9	295.82	0.1873	0.0545	0.841
	40	156.0	37.4	114874.6	294.92	0.1874	0.0726	0.864
	50	156.0	37.4	117758.5	294.81	0.1888	0.0900	0.877
	60	156.0	37.4	120710.9	294.73	0.1875	0.1088	0.888
	70							
	80							
	90							
	100							
Rotameter 1	10	208.0	49.9	114553.5	295.85	0.2494	0.0016	0.338
	20	208.0	49.9	113283.5	295.86	0.2499	0.0031	0.436
	30	208.0	49.9	112759.2	295.94	0.2493	0.0047	0.500
	40	208.0	49.9	112150.9	296.01	0.2493	0.0063	0.568
	50	208.0	49.9	112316.4	296.13	0.2485	0.0078	0.607
	60	208.0	49.9	112438.7	296.18	0.2498	0.0094	0.672
	70	208.0	49.9	113178.9	296.29	0.2500	0.0109	0.670
	80	208.0	49.9	113050.8	296.30	0.2495	0.0125	0.702
	90	208.0	49.9	113283.0	296.32	0.2482	0.0141	0.712
	100	208.0	49.9	113028.1	296.43	0.2492	0.0156	0.739

-continued-

Rotameter 2	20	208.0	49.9	114350.1	296.31	0.2493	0.0273	0.817
	30	208.0	49.9	116530.7	296.37	0.2500	0.0408	0.848
	40	208.0	49.9	118915.3	296.28	0.2470	0.0551	0.869
	50	208.0	49.9	120960.1	296.25	0.2431	0.0700	0.883
	60	208.0	49.9	125778.3	296.09	0.2498	0.0817	0.891
	70	208.0	49.9	129125.4	296.17	0.2429	0.0981	0.898
	80	208.0	49.9	133869.2	296.07	0.2475	0.1099	0.906
	90	208.0	49.9	135765.5	296.04	0.2470	0.1239	0.915
	100							
Rotameter 1	10	312.0	74.8	116563.7	296.03	0.3742	0.0010	0.317
	20	312.0	74.8	115379.3	296.12	0.3739	0.0021	0.425
	30	312.0	74.8	114917.4	296.21	0.3739	0.0031	0.487
	40	312.0	74.8	114634.7	296.26	0.3737	0.0042	0.548
	50	312.0	74.8	114760.0	296.32	0.3739	0.0052	0.592
	60	312.0	74.8	114976.3	296.39	0.3741	0.0063	0.621
	70	312.0	74.8	115724.9	296.45	0.3731	0.0073	0.648
	80	312.0	74.8	115281.5	296.50	0.3741	0.0083	0.684
	90	312.0	74.8	116294.5	296.55	0.3731	0.0094	0.697
	100	312.0	74.8	115941.4	296.57	0.3736	0.0104	0.725
Rotameter 2	20	312.0	74.8	119554.4	297.28	0.3724	0.0183	0.806
	30	312.0	74.8	122661.4	297.19	0.3693	0.0276	0.837
	40	312.0	74.8	125915.7	297.23	0.3743	0.0363	0.855
	50	312.0	74.8	130969.6	297.12	0.3701	0.0459	0.873
	60	312.0	74.8	134388.0	297.01	0.3724	0.0548	0.883
	70	312.0	74.8	138068.8	296.97	0.3734	0.0637	0.891
	80	312.0	74.8	144348.3	296.78	0.3692	0.0737	0.898
	90	312.0	74.8	150821.0	296.76	0.3768	0.0812	0.906
	100	312.0	74.8	157952.9	296.63	0.3774	0.0901	0.911
Rotameter 1	10	416.0	99.8	118179.1	297.35	0.4991	0.0008	0.282
	20	416.0	99.8	117187.0	297.38	0.4980	0.0016	0.404
	30	416.0	99.8	116915.5	297.37	0.4987	0.0023	0.478
	40	416.0	99.8	117030.9	297.41	0.4995	0.0031	0.532
	50	416.0	99.8	117274.9	297.46	0.4982	0.0039	0.579
	60	416.0	99.8	118053.8	297.53	0.4980	0.0047	0.609
	70	416.0	99.8	118257.5	297.58	0.4982	0.0055	0.633
	80	416.0	99.8	119282.8	297.62	0.4985	0.0063	0.661
	90	416.0	99.8	119496.3	297.65	0.4978	0.0071	0.679
	100	416.0	99.8	119162.5	297.70	0.4990	0.0078	0.695
Rotameter 2	20	416.0	99.8	124150.6	297.70	0.4984	0.0136	0.792
	30	416.0	99.8	129413.5	297.69	0.4993	0.0204	0.825
	40	416.0	99.8	135126.4	297.66	0.4965	0.0274	0.846
	50	416.0	99.8	139165.7	297.64	0.4969	0.0342	0.862
	60	416.0	99.8	145566.2	297.61	0.4996	0.0408	0.873
	70	416.0	99.8	150921.4	297.48	0.4984	0.0478	0.883
	80	416.0	99.8	158623.9	297.40	0.4978	0.0546	0.890
	90	416.0	99.8	164854.5	297.28	0.4988	0.0613	0.895
	100							

-continued-

Rotameter 1	10	541.0	129.6	120132.4	295.94	0.6486	0.0006	0.274
	20	541.0	129.6	119589.7	296.11	0.6487	0.0012	0.387
	30	541.0	129.6	119563.8	296.26	0.6483	0.0018	0.449
	40	541.0	129.6	119852.3	296.37	0.6479	0.0024	0.515
	50	541.0	129.6	120303.1	296.38	0.6487	0.0030	0.549
	60	541.0	129.6	121206.8	296.44	0.6479	0.0036	0.587
	70	541.0	129.6	121762.5	296.57	0.6475	0.0042	0.615
	80	541.0	129.6	122621.5	296.64	0.6478	0.0048	0.641
	90	541.0	129.6	123278.3	296.74	0.6498	0.0054	0.651
	100	541.0	129.6	124978.2	296.81	0.6486	0.0060	0.675
Rotameter 2	20	541.0	129.6	131727.6	296.88	0.6481	0.0105	0.774
	30	541.0	129.6	137455.0	296.80	0.6484	0.0157	0.806
	40	541.0	129.6	143930.0	296.85	0.6492	0.0209	0.826
	50	541.0	129.6	150187.5	296.82	0.6487	0.0262	0.842
	60							
	70							
	80							
	90							
	100							
Rotameter 1	10	688.0	165.5	122836.6	298.66	0.8287	0.0005	0.214
	20	688.0	165.5	122836.6	298.68	0.8280	0.0009	0.337
	30	688.0	165.5	122900.0	298.74	0.8281	0.0014	0.413
	40	688.0	165.5	123209.9	298.77	0.8279	0.0019	0.463
	50	688.0	165.5	124690.7	298.85	0.8251	0.0024	0.507
	60	688.0	165.5	125571.4	298.91	0.8212	0.0028	0.552
	70	688.0	165.5	127063.3	298.98	0.8275	0.0033	0.571
	80	688.0	165.5	128139.7	299.03	0.8214	0.0038	0.596
	90	688.0	165.5	129198.0	299.10	0.8274	0.0042	0.609
	100	688.0	165.5	130744.0	299.15	0.8247	0.0047	0.629
Rotameter 2	20	688.0	165.5	140113.4	299.19	0.8252	0.0082	0.725
	30	688.0	165.5	150019.6	299.18	0.8277	0.0123	0.772
	40	688.0	165.5	157669.6	299.13	0.8277	0.0164	0.798
	50	688.0	165.5	166302.2	299.12	0.8233	0.0206	0.814
	60	688.0	165.5	179000.1	299.07	0.8259	0.0247	0.833
	70							
	80							
	90							
	100							

B.3.1 Predicted void fractions [1,2,3,70]for 19 mm staggered bundle

Table B.15: Predictions of void fraction

Air flow rate (%)	Mass flux based on min area (kg/m^2s)	Mass flux (kg/m^2s)	Void fraction pitch (-) (present study)	Void fraction (-) prediction by Schrage et al [1]	Void fraction (-) prediction by Feenstra et al [3]	Void fraction (-) prediction by Dowlati et al [2]	Maximum slip model by Chisholm [70]	Homogenous model by Chisholm [70]
10	25	6.07	0.373	0.091	0.333	0.245	0.266	0.910
20	25	6.07	0.472	0.216	0.460	0.375	0.426	0.954
30	25	6.07	0.514	0.303	0.535	0.459	0.530	0.969
40	25	6.07	0.576	0.364	0.586	0.519	0.605	0.977
50	25	6.07	0.631	0.413	0.624	0.564	0.661	0.982
60	25	6.07	0.673	0.452	0.655	0.600	0.703	0.985
70	25	6.07	0.696	0.484	0.679	0.629	0.735	0.987
80	25	6.07	0.710	0.513	0.700	0.654	0.763	0.989
90	25	6.07	0.737	0.540	0.718	0.675	0.788	0.991
100	25	6.07	0.754	0.564	0.734	0.694	0.809	0.992
20	25	6.07	0.814	0.681	0.813	0.781	0.891	0.996
30	25	6.07	0.820	0.770	0.866	0.833	0.936	0.998
40	25	6.07	0.887	0.831	0.902	0.864	0.959	0.998
50	25	6.07	0.934	0.864	0.922	0.885	0.969	0.999
10	65	15.63	0.365	0.079	0.305	0.244	0.122	0.793
20	65	15.63	0.480	0.166	0.432	0.374	0.219	0.886
30	65	15.63	0.537	0.238	0.507	0.458	0.298	0.922
40	65	15.63	0.595	0.291	0.558	0.517	0.363	0.941
50	65	15.63	0.647	0.332	0.596	0.563	0.416	0.952
60	65	15.63	0.688	0.365	0.627	0.599	0.463	0.960
70	65	15.63	0.713	0.394	0.651	0.628	0.503	0.966
80	65	15.63	0.738	0.418	0.671	0.653	0.537	0.970
90	65	15.63	0.757	0.440	0.689	0.675	0.567	0.973
100	65	15.63	0.780	0.460	0.704	0.693	0.595	0.976
20	65	15.63	0.859	0.561	0.776	0.780	0.727	0.987
30	65	15.63	0.899	0.635	0.822	0.832	0.807	0.992
40	65	15.63	0.922	0.686	0.850	0.863	0.852	0.994
50	65	15.63	0.926	0.728	0.872	0.884	0.886	0.995
60	65	15.63	0.918	0.760	0.889	0.899	0.907	0.996
70	65	15.63	0.911	0.788	0.903	0.911	0.924	0.997
10	105	25.22	0.356	0.070	0.283	0.244	0.079	0.701
20	105	25.22	0.474	0.150	0.410	0.374	0.147	0.827
30	105	25.22	0.526	0.217	0.488	0.458	0.207	0.878
40	105	25.22	0.580	0.264	0.539	0.516	0.257	0.906
50	105	25.22	0.637	0.303	0.578	0.561	0.303	0.923
60	105	25.22	0.672	0.334	0.609	0.598	0.344	0.936
70	105	25.22	0.694	0.361	0.634	0.627	0.380	0.945
80	105	25.22	0.721	0.384	0.655	0.652	0.413	0.951
90	105	25.22	0.740	0.405	0.673	0.673	0.443	0.957
100	105	25.22	0.758	0.423	0.689	0.692	0.470	0.961
20	105	25.22	0.838	0.517	0.761	0.778	0.611	0.978
30	105	25.22	0.866	0.586	0.807	0.831	0.708	0.985
40	105	25.22	0.895	0.634	0.835	0.862	0.768	0.989
50	105	25.22	0.909	0.671	0.855	0.882	0.808	0.991
60	105	25.22	0.919	0.701	0.870	0.897	0.838	0.993
70	105	25.22	0.927	0.727	0.881	0.908	0.861	0.994
10	156	37.44	0.350	0.061	0.260	0.243	0.054	0.611
20	156	37.44	0.446	0.139	0.387	0.373	0.104	0.761
30	156	37.44	0.500	0.201	0.465	0.457	0.149	0.828
40	156	37.44	0.555	0.246	0.518	0.515	0.188	0.864
50	156	37.44	0.596	0.283	0.559	0.560	0.225	0.889
60	156	37.44	0.639	0.313	0.591	0.596	0.259	0.906
70	156	37.44	0.665	0.339	0.618	0.627	0.292	0.919
80	156	37.44	0.684	0.361	0.639	0.651	0.320	0.929
90	156	37.44	0.708	0.380	0.658	0.673	0.345	0.936
100	156	37.44	0.729	0.397	0.674	0.691	0.371	0.942
20	156	37.44	0.805	0.487	0.749	0.777	0.508	0.966
30	156	37.44	0.841	0.552	0.794	0.829	0.611	0.977
40	156	37.44	0.864	0.598	0.823	0.861	0.680	0.983
50	156	37.44	0.877	0.632	0.842	0.881	0.726	0.986
60	156	37.44	0.888	0.661	0.857	0.896	0.764	0.988
10	208	49.92	0.338	0.054	0.243	0.245	0.042	0.543
20	208	49.92	0.436	0.128	0.363	0.370	0.078	0.700
30	208	49.92	0.500	0.189	0.444	0.455	0.115	0.781
40	208	49.92	0.568	0.234	0.501	0.516	0.149	0.828
50	208	49.92	0.607	0.268	0.541	0.559	0.178	0.856
60	208	49.92	0.672	0.299	0.575	0.597	0.207	0.878
70	208	49.92	0.670	0.322	0.600	0.624	0.232	0.892
80	208	49.92	0.702	0.344	0.623	0.650	0.258	0.905
90	208	49.92	0.712	0.363	0.642	0.670	0.282	0.915

-continued-

100	208	49.92	0.739	0.380	0.659	0.689	0.303	0.923
20	208	49.92	0.817	0.468	0.738	0.776	0.434	0.954
30	208	49.92	0.848	0.531	0.784	0.828	0.535	0.969
40	208	49.92	0.869	0.575	0.813	0.859	0.609	0.977
50	208	49.92	0.883	0.611	0.834	0.880	0.666	0.981
60	208	49.92	0.891	0.635	0.847	0.894	0.698	0.984
70	208	49.92	0.898	0.661	0.859	0.906	0.736	0.986
80	208	49.92	0.906	0.679	0.867	0.914	0.757	0.987
90	208	49.92	0.915	0.696	0.876	0.921	0.780	0.989
10	312	74.8	0.317	0.042	0.201	0.233	0.026	0.422
20	312	74.8	0.425	0.117	0.328	0.371	0.054	0.608
30	312	74.8	0.487	0.170	0.405	0.451	0.078	0.697
40	312	74.8	0.548	0.215	0.466	0.514	0.103	0.758
50	312	74.8	0.592	0.248	0.508	0.557	0.125	0.795
60	312	74.8	0.621	0.278	0.544	0.595	0.147	0.824
70	312	74.8	0.648	0.300	0.571	0.622	0.166	0.844
80	312	74.8	0.684	0.321	0.595	0.647	0.185	0.861
90	312	74.8	0.697	0.340	0.615	0.668	0.204	0.874
100	312	74.8	0.725	0.356	0.633	0.687	0.222	0.885
20	312	74.8	0.806	0.443	0.716	0.773	0.332	0.930
30	312	74.8	0.837	0.503	0.766	0.825	0.428	0.952
40	312	74.8	0.855	0.545	0.796	0.856	0.495	0.962
50	312	74.8	0.873	0.577	0.816	0.876	0.551	0.969
60	312	74.8	0.883	0.603	0.831	0.892	0.594	0.974
70	312	74.8	0.891	0.625	0.843	0.903	0.628	0.977
80	312	74.8	0.898	0.644	0.852	0.911	0.659	0.979
90	312	74.8	0.906	0.659	0.858	0.918	0.677	0.980
100	312	74.8	0.911	0.673	0.863	0.923	0.697	0.982
10	416	99.84	0.282	0.043	0.186	0.243	0.021	0.366
20	416	99.84	0.404	0.109	0.302	0.373	0.041	0.539
30	416	99.84	0.478	0.155	0.372	0.447	0.059	0.627
40	416	99.84	0.532	0.197	0.432	0.509	0.077	0.694
50	416	99.84	0.579	0.231	0.478	0.555	0.096	0.740
60	416	99.84	0.609	0.260	0.514	0.592	0.113	0.774
70	416	99.84	0.633	0.284	0.545	0.622	0.129	0.800
80	416	99.84	0.661	0.305	0.569	0.646	0.145	0.819
90	416	99.84	0.679	0.324	0.591	0.668	0.161	0.836
100	416	99.84	0.695	0.339	0.609	0.685	0.174	0.849
20	416	99.84	0.792	0.423	0.694	0.770	0.266	0.905
30	416	99.84	0.825	0.483	0.746	0.822	0.349	0.932
40	416	99.84	0.846	0.524	0.778	0.852	0.415	0.947
50	416	99.84	0.862	0.556	0.800	0.874	0.467	0.956
60	416	99.84	0.873	0.581	0.814	0.888	0.507	0.961
70	416	99.84	0.883	0.602	0.827	0.900	0.544	0.966
80	416	99.84	0.890	0.620	0.835	0.908	0.573	0.969
90	416	99.84	0.895	0.635	0.843	0.915	0.598	0.971
10	541	129.6	0.274	0.038	0.159	0.237	0.016	0.298
20	541	129.6	0.387	0.096	0.266	0.365	0.031	0.461
30	541	129.6	0.449	0.143	0.342	0.448	0.046	0.562
40	541	129.6	0.515	0.182	0.399	0.507	0.060	0.631
50	541	129.6	0.549	0.215	0.445	0.553	0.074	0.680
60	541	129.6	0.587	0.242	0.481	0.588	0.087	0.717
70	541	129.6	0.615	0.265	0.511	0.617	0.100	0.747
80	541	129.6	0.641	0.285	0.537	0.642	0.113	0.770
90	541	129.6	0.651	0.304	0.559	0.663	0.125	0.790
100	541	129.6	0.675	0.320	0.577	0.680	0.136	0.804
20	541	129.6	0.774	0.404	0.667	0.766	0.213	0.873
30	541	129.6	0.806	0.464	0.723	0.818	0.284	0.908
40	541	129.6	0.826	0.504	0.757	0.849	0.342	0.927
50	541	129.6	0.842	0.536	0.780	0.870	0.391	0.939
10	688	165.5	0.214	0.038	0.146	0.247	0.013	0.259
20	688	165.5	0.337	0.082	0.229	0.355	0.023	0.386
30	688	165.5	0.413	0.129	0.308	0.445	0.036	0.494
40	688	165.5	0.463	0.168	0.368	0.508	0.048	0.570
50	688	165.5	0.507	0.200	0.414	0.553	0.059	0.623
60	688	165.5	0.552	0.222	0.444	0.583	0.068	0.657
70	688	165.5	0.571	0.247	0.477	0.615	0.079	0.691
80	688	165.5	0.596	0.268	0.504	0.639	0.090	0.719
90	688	165.5	0.609	0.283	0.523	0.658	0.098	0.737
100	688	165.5	0.629	0.300	0.544	0.677	0.108	0.756
20	688	165.5	0.725	0.384	0.637	0.761	0.170	0.835
30	688	165.5	0.772	0.443	0.694	0.813	0.230	0.877
40	688	165.5	0.798	0.484	0.731	0.844	0.280	0.901
50	688	165.5	0.814	0.515	0.755	0.865	0.323	0.916
60	688	165.5	0.833	0.539	0.770	0.879	0.357	0.924

APPENDIX C

C.1 Measured and predicted pressure drop in 38 mm in-line bundle

Table C.1: Measured and predicted pressure drop at 25 – 688 kg/m^{2}s in 38 mm in-line bundle

Air mass flow rate kg/s	Water mass flow rate kg/s	Mass flux min area kg/m^{2}s	Measured pressure drop			Predicted friction pressure drop		Predicted gravity pressure drop kPa	Total predicted pressure drop (gravity and [5]) kPa	Total predicted pressure drop (gravity and [4]) kPa	Inlet pressure kPa	Quality (-)	Inlet temperature °C
			Friction kPa	Gravity kPa	Total kPa	Xu et al [5] kPa	Ishihara et al [4] kPa						
0.00039	0.02961	25	0.125	2.404	2.530	0.029	0.003	2.779	2.809	2.783	110.19	0.01300	21.2
0.00078	0.02922	25	0.232	2.147	2.379	0.043	0.006	2.381	2.424	2.386	108.86	0.02600	21.2
0.00117	0.02883	25	0.354	1.950	2.305	0.055	0.008	2.107	2.161	2.115	108.39	0.03900	21.1
0.00156	0.02844	25	0.439	1.747	2.187	0.065	0.011	1.903	1.968	1.914	108.09	0.05200	21.1
0.00195	0.02805	25	0.357	1.674	2.032	0.075	0.014	1.744	1.819	1.757	107.74	0.06500	20.9
0.00234	0.02766	25	0.398	1.517	1.914	0.080	0.015	1.614	1.694	1.630	107.43	0.07800	20.9
0.00273	0.02727	25	0.453	1.419	1.872	0.091	0.019	1.507	1.598	1.526	107.22	0.09100	20.9
0.00312	0.02688	25	0.501	1.334	1.836	0.099	0.022	1.416	1.515	1.437	106.92	0.10400	20.7
0.00351	0.02649	25	0.503	1.257	1.760	0.107	0.025	1.337	1.444	1.362	106.92	0.11700	20.6
0.00390	0.02610	25	0.592	1.149	1.740	0.113	0.028	1.269	1.382	1.296	106.82	0.13000	20.6
0.00680	0.02320	25	0.619	0.708	1.327	0.147	0.047	0.933	1.081	0.980	105.01	0.22667	19.1
0.01020	0.01980	25	0.652	0.486	1.138	0.189	0.075	0.725	0.913	0.800	103.92	0.34000	18.6
0.01360	0.01640	25	0.700	0.333	1.033	0.289	0.148	0.528	0.817	0.676	103.75	0.45333	17.0
0.01700	0.01300	25	0.787	0.226	1.013	0.272	0.141	0.528	0.800	0.669	112.05	0.56667	14.7

-continued-

0.00039	0.07761	65	-0.15	2.482	2.330	0.073	0.015	2.784	2.858	2.799	112.357	0.00500	20.8
0.00078	0.07722	65	0.03	2.165	2.198	0.105	0.022	2.387	2.492	2.408	110.763	0.01000	20.7
0.00117	0.07683	65	0.04	2.009	2.048	0.128	0.028	2.112	2.240	2.140	110.034	0.01500	20.7
0.00156	0.07644	65	0.30	1.817	2.114	0.160	0.038	1.908	2.068	1.946	109.472	0.02000	20.7
0.00195	0.07605	65	0.25	1.674	1.924	0.175	0.043	1.749	1.924	1.792	109.362	0.02500	20.7
0.00234	0.07566	65	0.37	1.593	1.960	0.196	0.050	1.619	1.815	1.670	108.838	0.03000	20.7
0.00273	0.07527	65	0.41	1.469	1.877	0.216	0.058	1.511	1.727	1.570	108.512	0.03500	20.7
0.00312	0.07488	65	0.46	1.389	1.851	0.228	0.064	1.420	1.648	1.484	108.283	0.04000	20.6
0.00351	0.07449	65	0.40	1.350	1.749	0.247	0.072	1.341	1.588	1.413	108.209	0.04500	20.6
0.00390	0.07410	65	0.47	1.266	1.736	0.262	0.079	1.272	1.535	1.351	107.954	0.05000	20.6
0.00680	0.07120	65	0.79	0.858	1.650	0.353	0.128	0.938	1.291	1.065	107.242	0.08718	20.5
0.01020	0.06780	65	0.73	0.641	1.371	0.445	0.187	0.731	1.175	0.918	107.100	0.13077	20.0
0.01360	0.06440	65	0.77	0.493	1.262	0.540	0.255	0.605	1.145	0.860	107.806	0.17436	19.6
0.01700	0.06100	65	0.86	0.367	1.224	0.650	0.337	0.519	1.169	0.856	108.553	0.21795	19.4
0.02040	0.05760	65	0.89	0.300	1.189	0.701	0.388	0.457	1.158	0.844	109.975	0.26154	19.0
0.02380	0.05420	65	0.97	0.251	1.219	0.768	0.450	0.408	1.176	0.858	110.590	0.30513	18.8
0.00039	0.12561	105	-0.14	2.536	2.393	0.119	0.033	2.788	2.908	2.821	114.186	0.00310	20.9
0.00078	0.12522	105	0.05	2.231	2.278	0.168	0.045	2.392	2.560	2.437	112.744	0.00619	21.0
0.00117	0.12483	105	0.20	2.014	2.211	0.208	0.057	2.118	2.326	2.175	111.919	0.00929	21.1
0.00156	0.12444	105	0.27	1.863	2.137	0.244	0.070	1.915	2.159	1.985	111.266	0.01238	20.0
0.00195	0.12405	105	0.36	1.709	2.071	0.275	0.082	1.754	2.029	1.836	111.091	0.01548	21.1
0.00234	0.12366	105	0.42	1.577	1.995	0.300	0.092	1.626	1.926	1.717	110.965	0.01857	21.0
0.00273	0.12327	105	0.40	1.510	1.906	0.330	0.105	1.518	1.848	1.623	110.650	0.02167	21.0
0.00312	0.12288	105	0.39	1.460	1.851	0.362	0.119	1.426	1.788	1.546	110.435	0.02476	21.1
0.00351	0.12249	105	0.47	1.379	1.850	0.384	0.130	1.347	1.730	1.477	110.146	0.02786	21.1
0.00390	0.12210	105	0.53	1.264	1.796	0.403	0.140	1.279	1.682	1.419	110.192	0.03095	20.0
0.00680	0.11920	105	0.61	0.915	1.527	0.552	0.225	0.942	1.494	1.167	109.130	0.05397	20.9
0.01020	0.11580	105	0.73	0.728	1.456	0.698	0.324	0.736	1.434	1.060	109.630	0.08095	20.7
0.01360	0.11240	105	0.80	0.581	1.386	0.848	0.434	0.611	1.460	1.045	111.230	0.10794	20.5
0.01700	0.10900	105	0.97	0.484	1.450	0.968	0.531	0.526	1.494	1.057	112.845	0.13492	20.4
0.02040	0.10560	105	1.16	0.407	1.567	1.078	0.625	0.464	1.542	1.089	115.003	0.16190	20.1
0.02380	0.10220	105	1.17	0.330	1.501	1.191	0.724	0.416	1.607	1.140	117.165	0.18889	20.0

-continued-

0.00039	0.18681	156	-0.07	2.542	2.474	0.179	0.063	2.791	2.970	2.854	114.860	0.00208	19.1
0.00078	0.18642	156	0.13	2.240	2.371	0.248	0.083	2.395	2.643	2.478	113.074	0.00417	19.1
0.00117	0.18603	156	0.25	2.094	2.340	0.305	0.102	2.122	2.427	2.224	112.447	0.00625	19.1
0.00156	0.18564	156	0.32	1.950	2.272	0.355	0.122	1.918	2.274	2.041	112.021	0.00833	19.0
0.00195	0.18525	156	0.41	1.805	2.212	0.398	0.140	1.758	2.156	1.898	111.396	0.01042	19.1
0.00234	0.18486	156	0.46	1.651	2.109	0.441	0.160	1.629	2.070	1.789	111.327	0.01250	19.0
0.00273	0.18447	156	0.53	1.559	2.092	0.482	0.180	1.521	2.003	1.701	111.048	0.01458	19.0
0.00312	0.18408	156	0.61	1.452	2.064	0.509	0.194	1.430	1.939	1.623	110.854	0.01667	19.0
0.00351	0.18369	156	0.57	1.444	2.018	0.547	0.213	1.350	1.897	1.564	110.580	0.01875	19.1
0.00390	0.18330	156	0.56	1.393	1.954	0.579	0.231	1.282	1.860	1.513	110.625	0.02083	19.1
0.00680	0.18040	156	0.76	0.973	1.736	0.805	0.373	0.943	1.749	1.316	108.938	0.03632	19.0
0.01020	0.17700	156	0.90	0.747	1.650	1.017	0.527	0.737	1.753	1.264	109.293	0.05449	18.9
0.01360	0.17360	156	1.02	0.628	1.646	1.174	0.655	0.612	1.786	1.267	110.956	0.07265	18.6
0.01700	0.17020	156	1.19	0.508	1.699	1.353	0.805	0.528	1.881	1.333	113.252	0.09081	18.4
0.02040	0.16680	156	1.30	0.432	1.733	1.534	0.964	0.465	1.999	1.429	115.458	0.10897	18.4
0.00039	0.24921	208	-0.06	2.599	2.542	0.248	0.104	2.793	3.041	2.897	115.938	0.00156	19.5
0.00078	0.24882	208	0.16	2.275	2.436	0.335	0.132	2.398	2.734	2.530	114.324	0.00312	19.5
0.00117	0.24843	208	0.27	2.124	2.397	0.405	0.158	2.126	2.531	2.284	113.746	0.00469	19.4
0.00156	0.24804	208	0.39	1.971	2.357	0.464	0.183	1.922	2.386	2.104	113.248	0.00625	19.4
0.00195	0.24765	208	0.46	1.822	2.285	0.521	0.209	1.763	2.285	1.972	113.168	0.00781	19.4
0.00234	0.24726	208	0.57	1.662	2.227	0.575	0.236	1.634	2.208	1.870	112.978	0.00937	19.4
0.00273	0.24687	208	0.60	1.589	2.184	0.621	0.259	1.526	2.147	1.786	112.809	0.01094	19.5
0.00312	0.24648	208	0.67	1.509	2.179	0.666	0.285	1.435	2.101	1.720	112.809	0.01250	19.6
0.00351	0.24609	208	0.73	1.416	2.146	0.700	0.303	1.356	2.056	1.659	112.751	0.01406	19.5
0.00390	0.24570	208	0.77	1.333	2.101	0.747	0.331	1.287	2.034	1.618	112.643	0.01562	19.5
0.00680	0.24280	208	0.98	0.918	1.898	1.015	0.509	0.954	1.969	1.463	113.211	0.02724	19.4
0.01020	0.23940	208	1.14	0.724	1.861	1.270	0.704	0.746	2.016	1.450	113.980	0.04087	19.4
0.01360	0.23600	208	1.29	0.615	1.904	1.512	0.905	0.622	2.134	1.527	116.574	0.05449	19.3
0.01700	0.23260	208	1.47	0.519	1.985	1.761	1.123	0.538	2.299	1.661	119.774	0.06811	19.2
0.02040	0.22920	208	1.58	0.435	2.013	1.923	1.274	0.475	2.398	1.750	122.394	0.08173	19.1
0.02380	0.22580	208	1.68	0.372	2.053	2.056	1.401	0.429	2.485	1.830	126.383	0.09535	19.1
0.02720	0.22240	208	1.78	0.321	2.098	2.304	1.634	0.391	2.696	2.025	129.470	0.10897	19.1
0.03060	0.21900	208	1.86	0.262	2.120	2.403	1.731	0.362	2.766	2.093	133.723	0.12260	19.0

-continued-

0.00039	0.37401	312	0.06	2.617	2.679	0.396	0.209	2.801	3.198	3.011	120.155	0.00104	19.8
0.00078	0.37362	312	0.28	2.304	2.580	0.515	0.253	2.410	2.925	2.662	118.694	0.00208	19.8
0.00117	0.37323	312	0.40	2.126	2.530	0.606	0.290	2.138	2.744	2.428	118.127	0.00312	19.8
0.00156	0.37284	312	0.56	1.979	2.535	0.689	0.330	1.936	2.625	2.265	117.916	0.00417	19.9
0.00195	0.37245	312	0.63	1.866	2.501	0.761	0.367	1.777	2.539	2.144	117.906	0.00521	19.8
0.00234	0.37206	312	0.79	1.673	2.463	0.830	0.405	1.648	2.478	2.053	117.908	0.00625	19.9
0.00273	0.37167	312	0.77	1.647	2.421	0.889	0.438	1.542	2.431	1.980	118.075	0.00729	19.8
0.00312	0.37128	312	0.87	1.531	2.402	0.949	0.475	1.450	2.400	1.925	118.075	0.00833	19.8
0.00351	0.37089	312	0.95	1.441	2.392	1.011	0.514	1.371	2.382	1.885	117.840	0.00938	19.8
0.00390	0.37050	312	1.06	1.307	2.366	1.065	0.549	1.302	2.367	1.851	118.062	0.01042	19.9
0.00680	0.36760	312	1.37	0.891	2.261	1.410	0.800	0.969	2.379	1.769	119.655	0.01816	19.8
0.01020	0.36420	312	1.53	0.671	2.200	1.775	1.105	0.762	2.537	1.867	121.802	0.02724	19.8
0.01360	0.36080	312	1.70	0.544	2.248	2.046	1.348	0.638	2.684	1.986	125.796	0.03632	19.8
0.01700	0.35740	312	1.92	0.479	2.397	2.338	1.624	0.554	2.892	2.178	130.020	0.04541	19.7
0.02040	0.35400	312	1.95	0.413	2.367	2.621	1.900	0.492	3.113	2.392	134.677	0.05449	19.7
0.02380	0.35060	312	2.24	0.368	2.610	2.828	2.110	0.443	3.272	2.553	137.873	0.06357	19.7
0.02720	0.34720	312	2.31	0.337	2.648	3.047	2.331	0.406	3.453	2.737	142.566	0.07265	19.8
0.03060	0.34380	312	2.43	0.310	2.738	3.317	2.616	0.374	3.691	2.990	145.411	0.08173	19.7
0.03400	0.34040	312	2.58	0.286	2.865	3.515	2.806	0.353	3.868	3.159	154.183	0.09081	19.6
0.00039	0.49881	416	0.17	2.678	2.851	0.558	0.340	2.812	3.370	3.152	125.787	0.00078	20.3
0.00078	0.49842	416	0.36	2.372	2.734	0.699	0.395	2.425	3.123	2.820	124.607	0.00156	20.3
0.00117	0.49803	416	0.55	2.159	2.704	0.810	0.446	2.155	2.965	2.601	124.252	0.00234	20.3
0.00156	0.49764	416	0.66	2.009	2.667	0.906	0.494	1.953	2.859	2.447	123.953	0.00312	20.3
0.00195	0.49725	416	0.77	1.888	2.660	0.994	0.543	1.795	2.789	2.338	124.265	0.00391	20.3
0.00234	0.49686	416	0.97	1.699	2.669	1.071	0.588	1.667	2.738	2.255	124.454	0.00469	20.4
0.00273	0.49647	416	1.07	1.622	2.695	1.148	0.636	1.560	2.708	2.196	124.546	0.00547	20.4
0.00312	0.49608	416	1.13	1.556	2.682	1.220	0.684	1.468	2.688	2.151	124.546	0.00625	20.4
0.00351	0.49569	416	1.19	1.448	2.640	1.288	0.730	1.390	2.679	2.120	125.218	0.00703	20.4
0.00390	0.49530	416	1.27	1.395	2.663	1.351	0.773	1.321	2.672	2.094	125.340	0.00781	20.4
0.00680	0.49240	416	1.55	0.935	2.481	1.780	1.112	0.982	2.762	2.093	125.340	0.01362	20.4
0.01020	0.48900	416	1.75	0.710	2.464	2.173	1.455	0.781	2.953	2.235	131.535	0.02043	20.4
0.01360	0.48560	416	1.98	0.604	2.582	2.523	1.789	0.654	3.178	2.444	135.755	0.02724	20.3
0.01700	0.48220	416	2.17	0.532	2.704	2.847	2.115	0.568	3.416	2.683	140.090	0.03405	20.3
0.02040	0.47880	416	2.38	0.461	2.845	3.157	2.441	0.504	3.661	2.944	143.514	0.04087	20.3
0.02380	0.47540	416	2.56	0.425	2.983	3.427	2.721	0.457	3.884	3.179	149.845	0.04768	20.3
0.02720	0.47200	416	2.71	0.395	3.107	3.674	2.982	0.420	4.094	3.402	155.872	0.05449	20.2
0.03060	0.46860	416	2.92	0.363	3.282	3.935	3.266	0.389	4.324	3.655	160.797	0.06130	20.2

-continued-

0.00039	0.64881	541	0.28	2.763	3.040	0.770	0.524	2.808	3.577	3.331	119.587	0.00060	24.4
0.00078	0.64842	541	0.39	2.409	2.798	0.930	0.590	2.420	3.349	3.010	118.469	0.00120	24.5
0.00117	0.64803	541	0.46	2.223	2.681	1.061	0.657	2.150	3.211	2.807	118.174	0.00180	24.6
0.00156	0.64764	541	0.58	2.043	2.623	1.175	0.721	1.949	3.124	2.670	118.219	0.00240	24.9
0.00195	0.64725	541	0.66	1.929	2.585	1.274	0.780	1.792	3.066	2.572	118.463	0.00300	24.9
0.00234	0.64686	541	0.87	1.743	2.615	1.367	0.839	1.665	3.031	2.504	118.913	0.00360	25.0
0.00273	0.64647	541	0.97	1.664	2.636	1.453	0.898	1.558	3.011	2.456	119.174	0.00421	25.0
0.00312	0.64608	541	1.09	1.569	2.663	1.533	0.954	1.467	3.000	2.421	119.411	0.00481	25.2
0.00351	0.64569	541	1.20	1.512	2.710	1.613	1.013	1.390	3.003	2.403	119.909	0.00541	25.3
0.00390	0.64530	541	1.32	1.400	2.721	1.688	1.070	1.322	3.010	2.392	120.494	0.00601	25.4
0.00680	0.64240	541	1.96	0.949	2.908	2.159	1.463	0.990	3.149	2.454	123.866	0.01047	25.4
0.01020	0.63900	541	2.19	0.740	2.925	2.621	1.900	0.786	3.407	2.686	128.428	0.01571	25.3
0.01360	0.63560	541	2.43	0.634	3.062	3.030	2.319	0.660	3.689	2.979	133.520	0.02095	25.3
0.01700	0.63220	541	2.57	0.555	3.122	3.388	2.700	0.575	3.963	3.275	139.153	0.02619	25.4
0.00039	0.82521	688	0.44	2.954	3.397	1.044	0.774	2.823	3.867	3.597	122.369	0.00047	24.1
0.00078	0.82482	688	0.53	2.595	3.129	1.221	0.852	2.441	3.662	3.293	121.707	0.00094	24.3
0.00117	0.82443	688	0.67	2.375	3.045	1.361	0.924	2.174	3.536	3.099	121.679	0.00142	24.4
0.00156	0.82404	688	0.86	2.142	2.998	1.494	1.005	1.975	3.469	2.980	122.054	0.00189	24.6
0.00195	0.82365	688	0.93	2.010	2.944	1.604	1.074	1.819	3.422	2.893	122.624	0.00236	24.8
0.00234	0.82326	688	1.09	1.888	2.979	1.711	1.148	1.692	3.402	2.839	123.179	0.00283	24.9
0.00273	0.82287	688	1.27	1.755	3.021	1.808	1.217	1.587	3.395	2.804	124.409	0.00331	24.9
0.00312	0.82248	688	1.36	1.697	3.053	1.887	1.273	1.496	3.383	2.769	125.120	0.00378	25.0
0.00351	0.82209	688	1.53	1.594	3.127	1.980	1.347	1.417	3.397	2.764	125.679	0.00425	28.2
0.00390	0.82170	688	1.67	1.485	3.157	2.057	1.406	1.350	3.406	2.756	126.568	0.00472	28.2
0.00680	0.81880	688	2.58	1.050	3.629	2.584	1.869	1.017	3.602	2.886	132.011	0.00824	28.2
0.01020	0.81540	688	2.91	0.830	3.743	3.089	2.367	0.810	3.899	3.178	137.403	0.01235	28.1
0.01360	0.81200	688	3.10	0.707	3.807	3.538	2.843	0.685	4.223	3.528	144.911	0.01647	28.0
0.01700	0.80860	688	3.16	0.638	3.801	3.927	3.283	0.596	4.523	3.879	150.276	0.02059	28.0
0.020400	0.80520	688	3.30	0.571	3.874	4.284	3.698	0.531	4.816	4.229	155.817	0.02471	28.0

C.2 Measured and predicted pressure drop in 19 mm in-line bundle

Table C.2: Measured and predicted pressure drop at 25 - 688 kg/m^{2}s in 19mm in-line bundle

Air mass flow rate	Water mass flow rate	Mass flux min area	Measured pressure drop			Predicted friction pressure drop		Predicted gravity pressure drop	Total predicted pressure drop (gravity and [4])	Total predicted pressure drop (gravity and [4])	Inlet pressure	Quality (-)	Inlet temperature
			Friction	Gravity	Total	Xu et al [5]	Ishihara et al [4]						
kg/s	kg/s	kg/m^{2}s	kPa	kPa	kPa	kPa	kPa	kPa	kPa	kPa	kPa		°C
0.00039	0.02961	25	0.16	2.179	2.335	0.050	0.007	2.412	2.462	2.419	110.240	0.01303	19.0
0.00078	0.02922	25	0.25	1.988	2.242	0.075	0.013	1.998	2.073	2.011	108.660	0.02571	19.1
0.00117	0.02883	25	0.43	1.814	2.248	0.094	0.018	1.731	1.825	1.749	108.170	0.03867	19.1
0.00156	0.02844	25	0.57	1.640	2.215	0.111	0.023	1.541	1.653	1.565	107.980	0.05134	19.2
0.00195	0.02805	25	0.61	1.553	2.163	0.128	0.029	1.396	1.524	1.425	107.890	0.06443	19.5
0.00234	0.02766	25	0.72	1.419	2.144	0.143	0.034	1.281	1.424	1.315	107.600	0.07836	19.5
0.00273	0.02727	25	0.76	1.329	2.084	0.157	0.040	1.187	1.344	1.227	107.220	0.08967	19.5
0.00312	0.02688	25	0.78	1.294	2.069	0.171	0.046	1.108	1.278	1.154	107.080	0.10205	19.6
0.00351	0.02649	25	0.79	1.268	2.058	0.184	0.052	1.040	1.224	1.092	107.000	0.11602	19.5
0.00390	0.02610	25	0.79	1.178	1.964	0.197	0.059	0.980	1.177	1.039	106.470	0.12782	19.5
0.00680	0.02320	25	0.82	0.970	1.788	0.293	0.113	0.702	0.995	0.815	105.380	0.22391	18.8
0.01020	0.01980	25	1.01	0.738	1.745	0.416	0.195	0.537	0.953	0.732	105.790	0.34054	18.5
0.01360	0.01640	25	1.00	0.597	1.597	0.570	0.311	0.437	1.007	0.747	105.460	0.44620	16.9
0.01700	0.01300	25	3.32	0.285	3.608	0.778	0.475	0.370	1.148	0.845	105.430	0.57045	14.6
0.00039	0.07761	65	0.43	2.195	2.629	0.102	0.025	2.414	2.515	2.439	112.030	0.00500	22.9
0.00078	0.07722	65	0.45	1.974	2.428	0.147	0.038	2.000	2.146	2.038	110.200	0.01001	22.9
0.00117	0.07683	65	0.49	1.853	2.344	0.183	0.050	1.733	1.916	1.783	109.780	0.01496	23.1
0.00156	0.07644	65	0.59	1.685	2.271	0.215	0.062	1.544	1.759	1.606	109.670	0.01992	23.2
0.00195	0.07605	65	0.68	1.530	2.212	0.243	0.074	1.398	1.641	1.472	109.000	0.02501	23.4
0.00234	0.07566	65	0.82	1.426	2.246	0.269	0.086	1.283	1.552	1.369	108.910	0.02991	23.4
0.00273	0.07527	65	0.86	1.390	2.254	0.294	0.098	1.188	1.483	1.286	108.670	0.03494	23.5
0.00312	0.07488	65	0.86	1.323	2.184	0.317	0.110	1.109	1.427	1.219	108.520	0.04001	23.5
0.00351	0.07449	65	0.92	1.272	2.194	0.340	0.122	1.041	1.382	1.163	108.340	0.04486	23.5
0.00390	0.07410	65	0.90	1.192	2.092	0.361	0.133	0.982	1.343	1.116	107.980	0.05010	23.5
0.00680	0.07120	65	1.05	0.926	1.980	0.501	0.223	0.704	1.205	0.927	107.440	0.08769	23.3
0.01020	0.06780	65	1.15	0.727	1.872	0.647	0.332	0.538	1.185	0.870	107.550	0.13029	22.9
0.01360	0.06440	65	1.25	0.586	1.841	0.783	0.445	0.439	1.222	0.884	108.160	0.17253	22.4
0.01700	0.06100	65	1.36	0.472	1.836	0.904	0.553	0.373	1.277	0.926	109.490	0.21823	22.0
0.02040	0.05760	65	1.42	0.421	1.845	1.024	0.664	0.326	1.350	0.990	111.290	0.26128	21.6
0.02380	0.05420	65	1.50	0.389	1.885	1.144	0.779	0.289	1.434	1.068	111.700	0.30396	21.1

-continued-

0.00039	0.24921	208	0.47	2.309	2.774	0.379	0.186	2.424	2.803	2.610	115.300	0.00157	20.5
0.00078	0.24882	208	0.63	1.988	2.620	0.504	0.235	2.011	2.515	2.247	113.740	0.00313	21.0
0.00117	0.24843	208	0.73	1.867	2.593	0.604	0.283	1.744	2.348	2.027	113.160	0.00469	21.5
0.00156	0.24804	208	0.88	1.758	2.639	0.689	0.328	1.553	2.242	1.881	112.770	0.00627	21.9
0.00195	0.24765	208	1.02	1.610	2.632	0.767	0.372	1.408	2.175	1.781	112.560	0.00783	22.3
0.00234	0.24726	208	1.18	1.445	2.621	0.843	0.420	1.294	2.137	1.713	112.530	0.00936	22.6
0.00273	0.24687	208	1.31	1.322	2.634	0.912	0.464	1.198	2.110	1.662	112.440	0.01091	22.9
0.00312	0.24648	208	1.35	1.266	2.620	0.974	0.507	1.119	2.093	1.626	112.260	0.01248	23.1
0.00351	0.24609	208	1.37	1.192	2.560	1.040	0.554	1.051	2.091	1.605	112.120	0.01408	23.4
0.00390	0.24570	208	1.52	1.035	2.554	1.094	0.593	0.992	2.086	1.585	112.050	0.01569	23.6
0.00680	0.24280	208	2.05	0.746	2.795	1.490	0.916	0.715	2.205	1.631	112.820	0.02706	23.8
0.01020	0.23940	208	2.53	0.556	3.084	1.880	1.279	0.549	2.429	1.828	114.330	0.04035	23.8
0.01360	0.23600	208	2.80	0.440	3.238	2.219	1.621	0.451	2.670	2.071	115.960	0.05433	24.0
0.01700	0.23260	208	3.09	0.361	3.450	2.539	1.958	0.384	2.923	2.342	118.090	0.06815	23.9
0.02040	0.22920	208	3.16	0.318	3.482	2.835	2.273	0.338	3.173	2.611	121.230	0.08202	23.7
0.02380	0.22580	208	3.39	0.291	3.685	3.131	2.591	0.304	3.435	2.895	126.350	0.09524	23.5
0.02720	0.22240	208	3.59	0.281	3.875	3.397	2.883	0.275	3.672	3.159	128.170	0.10954	23.3
0.03060	0.21900	208	3.97	0.275	4.250	3.655	3.162	0.254	3.909	3.416	133.490	0.12276	23.2
0.00039	0.37401	312	0.65	2.383	3.037	0.648	0.389	2.431	3.079	2.820	117.060	0.00105	20.3
0.00078	0.37362	312	0.82	2.080	2.897	0.826	0.470	2.019	2.844	2.489	115.720	0.00208	20.6
0.00117	0.37323	312	0.90	1.960	2.860	0.962	0.542	1.752	2.715	2.295	115.110	0.00313	20.8
0.00156	0.37284	312	1.08	1.802	2.886	1.087	0.617	1.563	2.650	2.180	114.910	0.00415	21.0
0.00195	0.37245	312	1.32	1.669	2.990	1.195	0.687	1.418	2.613	2.104	114.810	0.00521	21.2
0.00234	0.37206	312	1.57	1.503	3.070	1.298	0.758	1.303	2.600	2.061	114.920	0.00624	21.6
0.00273	0.37167	312	1.79	1.429	3.220	1.393	0.828	1.208	2.601	2.035	114.930	0.00726	21.9
0.00312	0.37128	312	1.77	1.362	3.131	1.485	0.898	1.128	2.612	2.026	114.780	0.00830	22.4
0.00351	0.37089	312	1.90	1.224	3.128	1.565	0.961	1.060	2.625	2.021	114.940	0.00936	22.8
0.00390	0.37050	312	2.05	1.159	3.209	1.647	1.029	1.001	2.648	2.030	115.070	0.01044	22.9
0.00680	0.36760	312	2.64	0.817	3.456	2.186	1.518	0.724	2.910	2.242	116.890	0.01804	23.0
0.01020	0.36420	312	3.65	0.605	4.259	2.695	2.041	0.558	3.253	2.599	119.170	0.02740	23.0
0.01360	0.36080	312	4.46	0.475	4.938	3.154	2.544	0.461	3.615	3.005	123.580	0.03655	22.9
0.01700	0.35740	312	4.75	0.431	5.181	3.594	3.050	0.394	3.989	3.444	126.780	0.04550	22.9
0.02040	0.35400	312	4.79	0.380	5.174	4.015	3.550	0.346	4.361	3.896	129.510	0.05428	22.8
0.02380	0.35060	312	5.18	0.356	5.532	4.362	3.953	0.312	4.674	4.265	136.860	0.06390	22.7
0.02720	0.34720	312	5.55	0.341	5.886	4.729	4.390	0.285	5.014	4.675	140.960	0.07296	22.4
0.03060	0.34380	312	5.62	0.327	5.950	5.095	4.832	0.262	5.357	5.094	144.080	0.08155	22.1
0.03400	0.34040	312	5.77	0.301	6.070	5.346	5.110	0.246	5.592	5.356	151.540	0.09183	21.8

-continued-

0.00039	0.49881	416	0.72	2.453	3.171	0.977	0.662	2.431	3.408	3.094	118.380	0.00078	21.9
0.00078	0.49842	416	1.18	2.158	3.334	1.199	0.773	2.021	3.219	2.793	117.300	0.00156	22.9
0.00117	0.49803	416	1.21	2.008	3.214	1.372	0.873	1.754	3.125	2.627	116.810	0.00235	23.1
0.00156	0.49764	416	1.24	1.874	3.116	1.526	0.974	1.564	3.090	2.538	116.650	0.00313	23.3
0.00195	0.49725	416	1.45	1.667	3.118	1.663	1.071	1.420	3.083	2.491	116.800	0.00391	23.7
0.00234	0.49686	416	1.56	1.582	3.145	1.790	1.167	1.306	3.095	2.472	117.010	0.00468	23.4
0.00273	0.49647	416	1.74	1.436	3.180	1.906	1.259	1.211	3.117	2.470	117.330	0.00547	23.5
0.00312	0.49608	416	1.81	1.364	3.178	2.021	1.355	1.132	3.153	2.487	117.430	0.00625	23.7
0.00351	0.49569	416	1.86	1.282	3.144	2.127	1.446	1.065	3.191	2.510	117.580	0.00702	23.8
0.00390	0.49530	416	1.89	1.230	3.121	2.230	1.538	1.006	3.236	2.544	117.690	0.00781	23.9
0.00680	0.49240	416	2.74	0.823	3.561	2.885	2.182	0.730	3.615	2.911	120.400	0.01360	24.1
0.01020	0.48900	416	4.26	0.614	4.878	3.540	2.906	0.565	4.104	3.470	123.640	0.02034	24.7
0.01360	0.48560	416	4.38	0.527	4.907	4.099	3.573	0.466	4.565	4.039	127.410	0.02727	24.6
0.01700	0.48220	416	4.58	0.462	5.042	4.609	4.202	0.400	5.009	4.602	131.540	0.03414	24.5
0.02040	0.47880	416	4.85	0.410	5.260	5.095	4.816	0.353	5.448	5.169	136.660	0.04100	24.3
0.02380	0.47540	416	5.24	0.378	5.623	5.578	5.437	0.317	5.895	5.754	139.660	0.04773	24.2
0.02720	0.47200	416	5.36	0.362	5.725	6.011	5.994	0.289	6.300	6.284	145.660	0.05477	24.0
0.03060	0.46860	416	6.54	0.344	6.889	6.405	6.487	0.268	6.673	6.755	152.990	0.06132	23.6
0.00039	0.64881	541	1.09	2.455	3.544	1.439	1.070	2.437	3.875	3.507	120.280	0.00060	19.6
0.00078	0.64842	541	1.21	2.234	3.443	1.701	1.209	2.030	3.731	3.239	119.370	0.00121	19.9
0.00117	0.64803	541	1.34	2.084	3.420	1.920	1.349	1.764	3.684	3.113	119.150	0.00180	20.2
0.00156	0.64764	541	1.59	1.892	3.477	2.106	1.480	1.575	3.681	3.055	119.400	0.00240	20.3
0.00195	0.64725	541	1.82	1.784	3.600	2.268	1.603	1.429	3.697	3.032	119.560	0.00301	20.6
0.00234	0.64686	541	2.04	1.599	3.634	2.421	1.727	1.315	3.736	3.042	120.010	0.00361	20.8
0.00273	0.64647	541	2.17	1.508	3.676	2.562	1.848	1.221	3.784	3.069	120.400	0.00421	20.9
0.00312	0.64608	541	2.21	1.442	3.653	2.696	1.966	1.143	3.839	3.109	120.910	0.00482	21.4
0.00351	0.64569	541	2.32	1.351	3.674	2.825	2.086	1.075	3.900	3.161	121.240	0.00542	21.5
0.00390	0.64530	541	2.69	1.199	3.892	2.947	2.203	1.017	3.964	3.219	122.160	0.00602	21.8
0.00680	0.64240	541	3.29	0.858	4.147	3.740	3.038	0.739	4.479	3.778	124.680	0.01049	21.8
0.01020	0.63900	541	4.93	0.649	5.579	4.490	3.922	0.575	5.065	4.497	129.760	0.01582	22.0
0.01360	0.63560	541	4.27	0.550	4.824	5.188	4.802	0.477	5.665	5.279	134.880	0.02092	22.0
0.01700	0.63220	541	4.47	0.507	4.978	5.794	5.611	0.409	6.203	6.020	139.270	0.02629	22.0

-continued-

0.00039	0.82521	688	1.52	2.650	4.174	2.098	1.676	2.442	4.540	4.118	123.160	0.00047	19.5
0.00078	0.82482	688	1.72	2.374	4.089	2.389	1.836	2.041	4.430	3.877	122.630	0.00094	19.8
0.00117	0.82443	688	1.84	2.224	4.067	2.637	2.002	1.775	4.411	3.777	122.790	0.00141	19.9
0.00156	0.82404	688	2.01	2.082	4.096	2.856	2.168	1.590	4.445	3.757	123.040	0.00189	20.1
0.00195	0.82365	688	2.21	1.923	4.138	3.048	2.324	1.446	4.495	3.770	123.570	0.00235	20.3
0.00234	0.82326	688	2.55	1.805	4.354	3.229	2.479	1.333	4.562	3.812	124.770	0.00282	21.0
0.00273	0.82287	688	2.74	1.690	4.434	3.386	2.621	1.239	4.626	3.860	125.570	0.00329	21.1
0.00312	0.82248	688	2.85	1.555	4.405	3.522	2.747	1.161	4.682	3.908	126.300	0.00378	21.2
0.00351	0.82209	688	2.89	1.488	4.378	3.672	2.893	1.094	4.766	3.987	127.080	0.00425	21.4
0.00390	0.82170	688	3.00	1.407	4.406	3.802	3.023	1.036	4.837	4.059	127.680	0.00473	21.5
0.00680	0.81880	688	3.99	1.020	5.012	4.725	4.032	0.763	5.488	4.794	133.260	0.00822	21.7
0.01020	0.81540	688	6.17	0.803	6.970	5.596	5.107	0.596	6.192	5.703	138.050	0.01231	21.9
0.01360	0.81200	688	5.44	0.713	6.151	6.335	6.073	0.498	6.833	6.571	145.530	0.01645	22.0
0.01700	0.80860	688	5.44	0.625	6.061	6.995	6.977	0.431	7.426	7.408	151.010	0.02066	22.0
0.020400	0.80520	688	5.84	0.571	6.410	7.659	7.919	0.381	8.040	8.300	156.500	0.02481	22.0

C.3 Measured and predicted pressure drop in 19 mm staggered bundle

Table C.3: Measured and predicted pressure drop at 25 - 688 kg/m^{2}s in 19mm staggered bundle

Air mass flow rate	Water mass flow rate	Mass flux min area	Measured pressure drop			Predicted friction pressure drop		Predicted gravity pressure drop	Total predicted pressure drop (gravity and [5])	Total predicted pressure drop (gravity and [4])	Inlet pressure	Quality	Inlet temperature
			Friction	Gravity	Total	Xu et al [5]	Ishihara et al [4]						
kg/s	kg/s	kg/m^{2}s	kPa	kPa	kPa	kPa	kPa	kPa	kPa	kPa	kPa	(-)	^{o}C
0.00039	0.02961	25	0.49	1.646	2.137	0.291	0.043	1.981	2.273	2.024	108.510	0.01290	20.9
0.00078	0.02922	25	0.56	1.388	1.949	0.431	0.073	1.639	2.070	1.713	107.240	0.02620	21.1
0.00117	0.02883	25	0.63	1.277	1.906	0.545	0.104	1.420	1.965	1.524	106.440	0.03921	21.2
0.00156	0.02844	25	0.78	1.114	1.893	0.645	0.135	1.264	1.909	1.398	106.250	0.05206	21.4
0.00195	0.02805	25	0.84	0.971	1.811	0.734	0.166	1.144	1.878	1.310	105.360	0.06560	21.5
0.00234	0.02766	25	0.89	0.860	1.752	0.820	0.198	1.049	1.870	1.248	105.450	0.07882	21.6
0.00273	0.02727	25	0.92	0.800	1.719	0.903	0.232	0.972	1.875	1.204	105.440	0.09149	21.9
0.00312	0.02688	25	0.94	0.764	1.708	0.982	0.267	0.908	1.890	1.175	105.520	0.10296	21.9
0.00351	0.02649	25	0.94	0.691	1.634	1.053	0.300	0.853	1.906	1.153	105.470	0.11633	21.9
0.00390	0.02610	25	1.13	0.649	1.783	1.125	0.336	0.804	1.929	1.140	105.200	0.12927	22.1
0.00680	0.02320	25	1.10	0.491	1.592	1.635	0.632	0.576	2.211	1.208	104.180	0.22605	21.0
0.01020	0.01980	25	1.07	0.475	1.547	2.223	1.050	0.440	2.663	1.490	104.260	0.34025	20.8
0.01360	0.01640	25	1.07	0.299	1.368	2.886	1.578	0.358	3.244	1.936	104.310	0.45189	19.6
0.01700	0.01300	25	1.15	0.177	1.331	3.649	2.208	0.304	3.953	2.512	104.530	0.52020	16.6
0.00039	0.07761	65	0.66	1.667	2.329	0.495	0.123	1.986	2.480	2.109	111.450	0.00499	20.9
0.00078	0.07722	65	0.72	1.366	2.089	0.715	0.184	1.644	2.360	1.829	109.780	0.00999	21.2
0.00117	0.07683	65	0.82	1.218	2.043	0.893	0.244	1.425	2.319	1.670	109.330	0.01496	21.4
0.00156	0.07644	65	1.01	1.066	2.075	1.049	0.304	1.268	2.317	1.572	109.040	0.01996	21.7
0.00195	0.07605	65	1.05	0.928	1.976	1.193	0.364	1.149	2.341	1.513	108.470	0.02485	22.2
0.00234	0.07566	65	1.13	0.822	1.951	1.324	0.423	1.054	2.378	1.477	108.290	0.02991	22.3
0.00273	0.07527	65	1.12	0.757	1.876	1.448	0.483	0.976	2.425	1.459	107.840	0.03479	22.5
0.00312	0.07488	65	1.18	0.689	1.870	1.563	0.541	0.911	2.475	1.453	107.840	0.03992	22.6
0.00351	0.07449	65	1.26	0.641	1.902	1.679	0.603	0.856	2.535	1.458	107.740	0.04493	22.8
0.00390	0.07410	65	1.29	0.581	1.871	1.788	0.663	0.807	2.595	1.470	107.380	0.04973	22.8
0.00680	0.07120	65	1.54	0.374	1.913	2.519	1.123	0.580	3.098	1.702	106.890	0.08680	22.5

-continued-

0.01020	0.06780	65	1.74	0.267	2.010	3.292	1.691	0.443	3.734	2.134	107.050	0.13040	22.1
0.01360	0.06440	65	1.88	0.209	2.092	4.042	2.295	0.362	4.404	2.657	108.130	0.17255	21.9
0.01700	0.06100	65	2.02	0.197	2.216	4.747	2.902	0.307	5.054	3.209	109.140	0.21759	21.5
0.02040	0.05760	65	2.23	0.217	2.444	5.505	3.578	0.267	5.772	3.846	110.130	0.25994	21.2
0.02380	0.05420	65	2.42	0.237	2.659	6.266	4.276	0.237	6.504	4.513	111.790	0.30193	20.8
0.00078	0.12522	105	0.88	1.382	2.264	0.966	0.317	1.648	2.614	1.965	113.150	0.00308	19.7
0.00117	0.12483	105	0.97	1.247	2.219	1.193	0.405	1.428	2.622	1.833	110.960	0.00927	20.6
0.00156	0.12444	105	1.06	1.105	2.164	1.392	0.491	1.272	2.664	1.763	110.520	0.01235	20.9
0.00195	0.12405	105	1.26	0.956	2.218	1.570	0.575	1.153	2.723	1.728	110.150	0.01544	21.2
0.00234	0.12366	105	1.32	0.864	2.183	1.737	0.660	1.058	2.795	1.718	109.750	0.01850	21.4
0.00273	0.12327	105	1.38	0.805	2.185	1.892	0.743	0.980	2.872	1.723	109.650	0.02167	21.8
0.00312	0.12288	105	1.49	0.735	2.227	2.040	0.827	0.915	2.956	1.743	109.450	0.02468	21.9
0.00351	0.12249	105	1.49	0.686	2.180	2.181	0.910	0.859	3.040	1.770	109.370	0.02789	22.0
0.00390	0.12210	105	1.61	0.638	2.247	2.319	0.995	0.811	3.130	1.806	109.200	0.03090	22.5
0.00680	0.11920	105	1.95	0.428	2.383	3.233	1.623	0.583	3.816	2.206	109.040	0.05388	22.4
0.01020	0.11580	105	2.19	0.354	2.546	4.177	2.369	0.447	4.624	2.816	109.900	0.08069	22.2
0.01360	0.11240	105	2.65	0.279	2.930	5.063	3.130	0.365	5.429	3.496	111.270	0.10802	22.2
0.01700	0.10900	105	2.97	0.242	3.213	5.926	3.907	0.311	6.237	4.218	113.100	0.13499	22.1
0.02040	0.10560	105	3.23	0.215	3.443	6.745	4.665	0.273	7.017	4.937	115.340	0.16250	21.8
0.02380	0.10220	105	3.81	0.195	4.009	7.572	5.441	0.244	7.816	5.685	118.750	0.18757	21.6
0.00039	0.18681	156	0.95	1.707	2.656	0.922	0.387	1.986	2.908	2.372	115.210	0.00206	19.9
0.00078	0.18642	156	1.09	1.457	2.551	1.254	0.506	1.645	2.900	2.151	113.620	0.00419	20.2
0.00117	0.18603	156	1.21	1.314	2.528	1.523	0.622	1.427	2.950	2.049	113.170	0.00631	20.4
0.00156	0.18564	156	1.44	1.171	2.609	1.772	0.747	1.270	3.042	2.017	112.970	0.00827	20.6
0.00195	0.18525	156	1.61	1.062	2.675	1.985	0.859	1.151	3.136	2.011	112.750	0.01038	20.9
0.00234	0.18486	156	1.78	0.949	2.726	2.182	0.971	1.057	3.238	2.028	112.790	0.01247	21.2
0.00273	0.18447	156	2.03	0.882	2.911	2.361	1.077	0.979	3.341	2.057	112.760	0.01465	21.6
0.00312	0.18408	156	2.17	0.832	2.997	2.536	1.187	0.915	3.451	2.102	112.780	0.01678	21.7
0.00351	0.18369	156	2.17	0.768	2.939	2.716	1.307	0.858	3.574	2.165	112.540	0.01887	21.9
0.00390	0.18330	156	3.11	0.713	3.822	2.872	1.412	0.811	3.683	2.222	112.730	0.02094	22.0
0.00680	0.18040	156	3.27	0.515	3.785	3.967	2.241	0.584	4.551	2.825	114.110	0.03614	22.2
0.01020	0.17700	156	4.03	0.419	4.450	5.078	3.197	0.448	5.526	3.645	115.900	0.05398	22.3
0.01360	0.17360	156	5.00	0.361	5.363	6.082	4.126	0.368	6.450	4.494	119.730	0.07297	22.2
0.01700	0.17020	156	5.72	0.325	6.044	7.098	5.114	0.314	7.412	5.428	123.390	0.08924	22.1
0.02040	0.16680	156	6.42	0.297	6.718	8.004	6.007	0.275	8.279	6.282	127.140	0.10901	22.1

-continued-

0.00039	0.24921	208	0.48	1.738	2.222	1.151	0.566	1.986	3.138	2.552	115.660	0.00156	20.4
0.00078	0.24882	208	0.72	1.481	2.198	1.532	0.719	1.646	3.179	2.366	114.370	0.00312	20.6
0.00117	0.24843	208	0.92	1.313	2.235	1.834	0.862	1.427	3.261	2.289	113.910	0.00469	21.0
0.00156	0.24804	208	1.13	1.136	2.269	2.100	1.004	1.271	3.371	2.274	113.620	0.00627	21.2
0.00195	0.24765	208	1.34	1.033	2.376	2.347	1.148	1.152	3.499	2.300	113.480	0.00774	21.5
0.00234	0.24726	208	1.56	0.864	2.423	2.566	1.283	1.058	3.623	2.341	113.390	0.00939	21.6
0.00273	0.24687	208	1.68	0.867	2.547	2.776	1.421	0.981	3.757	2.401	113.420	0.01094	22.1
0.00312	0.24648	208	1.87	0.783	2.648	2.973	1.555	0.916	3.889	2.471	113.480	0.01250	22.2
0.00351	0.24609	208	1.91	0.757	2.666	3.158	1.686	0.860	4.018	2.546	113.510	0.01406	22.4
0.00390	0.24570	208	2.05	0.688	2.741	3.346	1.825	0.812	4.158	2.637	113.630	0.01559	22.5
0.00680	0.24280	208	2.90	0.484	3.386	4.552	2.811	0.585	5.137	3.396	114.760	0.02707	22.6
0.01020	0.23940	208	4.02	0.402	4.426	5.774	3.939	0.450	6.224	4.389	117.810	0.04065	22.7
0.01360	0.23600	208	4.71	0.348	5.061	6.877	5.032	0.369	7.246	5.401	120.800	0.05432	22.7
0.01700	0.23260	208	5.50	0.310	5.811	7.909	6.090	0.316	8.225	6.406	125.560	0.06784	22.5
0.02040	0.22920	208	6.07	0.289	6.363	8.979	7.240	0.276	9.256	7.517	127.640	0.08170	23.2
0.02380	0.22580	208	6.88	0.272	7.148	9.913	8.218	0.248	10.160	8.466	133.590	0.09502	23.0
0.02720	0.22240	208	7.03	0.249	7.281	10.928	9.332	0.225	11.152	9.557	136.740	0.10829	22.8
0.03060	0.21900	208	7.70	0.228	7.924	11.864	10.340	0.207	12.071	10.547	143.100	0.12177	22.6
0.00039	0.37401	312	0.54	1.793	2.331	1.591	0.957	1.987	3.579	2.944	115.860	0.00104	20.4
0.00078	0.37362	312	0.81	1.509	2.320	2.020	1.152	1.648	3.669	2.801	115.010	0.00209	20.6
0.00117	0.37323	312	1.01	1.348	2.353	2.366	1.340	1.430	3.796	2.769	114.680	0.00313	20.8
0.00156	0.37284	312	1.27	1.188	2.454	2.666	1.521	1.274	3.939	2.794	114.600	0.00417	21.1
0.00195	0.37245	312	1.48	1.073	2.554	2.940	1.701	1.155	4.095	2.856	114.600	0.00521	21.2
0.00234	0.37206	312	1.74	0.997	2.736	3.191	1.877	1.060	4.251	2.938	114.480	0.00625	21.7
0.00273	0.37167	312	1.92	0.925	2.849	3.423	2.047	0.983	4.406	3.030	114.670	0.00730	21.8
0.00312	0.37128	312	2.30	0.831	3.133	3.650	2.224	0.918	4.567	3.141	114.870	0.00834	23.8
0.00351	0.37089	312	2.27	0.797	3.068	3.859	2.390	0.863	4.722	3.253	115.130	0.00938	23.9
0.00390	0.37050	312	2.43	0.725	3.156	4.065	2.561	0.814	4.879	3.375	114.970	0.01044	24.0
0.00680	0.36760	312	3.80	0.511	4.309	5.398	3.777	0.589	5.987	4.366	117.660	0.01814	24.1
0.01020	0.36420	312	4.96	0.430	5.393	6.732	5.146	0.453	7.186	5.599	120.590	0.02726	24.1
0.01360	0.36080	312	5.89	0.383	6.274	7.967	6.514	0.373	8.340	6.887	125.120	0.03624	24.0
0.01700	0.35740	312	6.68	0.337	7.022	9.091	7.794	0.319	9.410	8.114	129.000	0.04533	23.9
0.02040	0.35400	312	7.44	0.310	7.746	10.191	9.093	0.281	10.471	9.373	133.320	0.05450	23.8
0.02380	0.35060	312	7.82	0.288	8.111	11.232	10.324	0.252	11.483	10.576	139.610	0.06359	23.7
0.02720	0.34720	312	8.12	0.270	8.389	12.269	11.572	0.228	12.497	11.800	140.890	0.07270	23.4
0.03060	0.34380	312	8.83	0.250	9.084	13.262	12.769	0.210	13.473	12.979	147.550	0.08184	23.3
0.03400	0.34040	312	9.06	0.237	9.298	14.212	13.896	0.196	14.408	14.092	153.310	0.09079	23.1

-continued-

0.00039	0.49881	416	0.67	1.885	2.551	2.003	1.359	1.990	3.993	3.349	117.990	0.00078	20.4
0.00078	0.49842	416	0.99	1.566	2.561	2.453	1.584	1.651	4.105	3.236	117.120	0.00156	20.6
0.00117	0.49803	416	1.28	1.373	2.649	2.815	1.799	1.433	4.248	3.232	116.980	0.00235	20.7
0.00156	0.49764	416	1.58	1.230	2.811	3.132	2.009	1.277	4.409	3.286	116.820	0.00313	21.0
0.00195	0.49725	416	1.81	1.107	2.921	3.413	2.209	1.159	4.572	3.367	117.000	0.00392	21.2
0.00234	0.49686	416	2.28	1.027	3.310	3.676	2.409	1.065	4.741	3.474	117.320	0.00469	21.9
0.00273	0.49647	416	2.35	0.966	3.321	3.921	2.606	0.987	4.909	3.593	117.530	0.00548	22.0
0.00312	0.49608	416	2.58	0.892	3.472	4.154	2.800	0.923	5.077	3.723	117.830	0.00626	22.1
0.00351	0.49569	416	2.93	0.844	3.772	4.375	2.992	0.868	5.243	3.860	118.210	0.00703	22.3
0.00390	0.49530	416	3.11	0.802	3.916	4.590	3.187	0.819	5.409	4.006	118.390	0.00782	22.6
0.00680	0.49240	416	4.82	0.548	5.366	5.968	4.545	0.595	6.563	5.140	122.090	0.01363	22.7
0.01020	0.48900	416	6.73	0.461	7.188	7.341	6.067	0.460	7.802	6.527	126.790	0.02046	22.8
0.01360	0.48560	416	7.20	0.408	7.604	8.563	7.508	0.380	8.944	7.888	132.580	0.02720	22.8
0.01700	0.48220	416	8.51	0.366	8.878	9.720	8.942	0.326	10.045	9.268	136.860	0.03405	22.9
0.02040	0.47880	416	8.55	0.337	8.888	10.781	10.265	0.288	11.069	10.553	144.490	0.04097	22.8
0.02380	0.47540	416	10.33	0.310	10.640	11.830	11.613	0.258	12.088	11.871	149.100	0.04764	22.7
0.02720	0.47200	416	11.11	0.293	11.398	12.807	12.852	0.236	13.043	13.088	155.420	0.05457	22.6
0.03060	0.46860	416	12.33	0.279	12.605	13.771	14.091	0.217	13.988	14.308	161.560	0.06141	22.4
0.00039	0.64881	541	1.04	1.905	2.944	2.451	1.825	1.992	4.444	3.817	120.260	0.00060	22.7
0.00078	0.64842	541	1.49	1.610	3.098	2.903	2.069	1.655	4.558	3.724	119.610	0.00120	22.9
0.00117	0.64803	541	1.86	1.448	3.306	3.266	2.301	1.437	4.703	3.739	119.680	0.00181	23.0
0.00156	0.64764	541	2.29	1.275	3.562	3.583	2.528	1.282	4.865	3.810	119.990	0.00241	23.2
0.00195	0.64725	541	2.56	1.185	3.742	3.868	2.749	1.164	5.032	3.913	120.450	0.00302	23.3
0.00234	0.64686	541	2.92	1.085	4.003	4.130	2.963	1.070	5.200	4.033	120.830	0.00362	23.5
0.00273	0.64647	541	3.26	1.012	4.273	4.376	3.176	0.994	5.370	4.169	121.580	0.00422	23.6
0.00312	0.64608	541	3.58	0.944	4.527	4.607	3.384	0.929	5.537	4.313	122.130	0.00482	23.7
0.00351	0.64569	541	3.77	0.919	4.685	4.834	3.598	0.874	5.708	4.473	122.820	0.00541	23.8
0.00390	0.64530	541	4.25	0.856	5.105	5.043	3.799	0.827	5.870	4.626	123.480	0.00600	23.9
0.00680	0.64240	541	6.73	0.595	7.326	6.408	5.239	0.603	7.010	5.841	128.360	0.01049	23.9
0.01020	0.63900	541	9.25	0.513	9.763	7.753	6.827	0.468	8.221	7.295	135.040	0.01581	23.9
0.01360	0.63560	541	9.38	0.459	9.844	8.952	8.342	0.388	9.340	8.730	142.430	0.02098	23.9
0.01700	0.63220	541	10.60	0.418	11.016	10.040	9.757	0.335	10.375	10.092	151.130	0.02619	23.2

-continued-

0.00039	0.82521	688	2.52	2.062	4.580	2.915	2.328	2.001	4.915	4.329	129.420	0.00047	23.4
0.00078	0.82482	688	3.26	1.742	4.997	3.345	2.574	1.667	5.012	4.242	130.280	0.00094	23.7
0.00117	0.82443	688	3.89	1.541	5.427	3.696	2.815	1.451	5.148	4.266	131.220	0.00141	23.8
0.00156	0.82404	688	4.87	1.410	6.275	4.009	3.057	1.297	5.306	4.354	133.190	0.00186	24.1
0.00195	0.82365	688	5.45	1.297	6.752	4.267	3.261	1.181	5.448	4.442	134.880	0.00236	24.4
0.00234	0.82326	688	6.37	1.179	7.553	4.512	3.469	1.089	5.600	4.557	137.340	0.00283	24.5
0.00273	0.82287	688	6.72	1.129	7.850	4.747	3.684	1.012	5.759	4.696	138.310	0.00333	24.8
0.00312	0.82248	688	7.39	1.063	8.449	4.965	3.887	0.949	5.914	4.836	140.790	0.00378	24.9
0.00351	0.82209	688	7.75	1.028	8.779	5.176	4.095	0.895	6.071	4.990	142.580	0.00426	25.2
0.00390	0.82170	688	8.51	0.975	9.487	5.373	4.292	0.848	6.221	5.139	144.090	0.00473	25.4
0.00680	0.81880	688	13.41	0.724	14.133	6.651	5.686	0.625	7.275	6.311	155.700	0.00827	25.5
0.01020	0.81540	688	17.65	0.603	18.252	7.906	7.230	0.490	8.396	7.719	166.470	0.01225	25.5
0.01360	0.81200	688	20.97	0.534	21.503	8.984	8.619	0.410	9.395	9.029	180.830	0.01638	25.5
0.01700	0.80860	688	22.07	0.491	22.560	9.994	9.995	0.354	10.348	10.349	188.440	0.02046	25.5
0.02040	0.80520	688	21.72	0.443	22.161	10.916	11.272	0.315	11.231	11.587	197.780	0.02451	25.3

REFERENCES

[1] Schrage D.S., Hsu J.T., Jensen M.K., 1988, *Two-phase pressure drop in vertical crossflow across a horizontal tube bundle*, AIChE Journal, **34**, 107-115.

[2] Dowlati R., Kawaji M., Chan A.M.C., 1990, *Pitch-to-diameter effect on two-phase flow across an in-line tube bundle*, AIChE Journal, **36**, 765-772.

[3] Feenstra P.A., Weaver D.S., Judd R.L., 2000, *An improved void fraction model for two-phase cross-flow in horizontal tube bundles*, International Journal of Multiphase Flow, **26**, 1851-1873.

[4] Ishihara K., Palen J.W., Taborek J., 1980, *Critical review of correlations for predicting two-phase flow pressure drops across utbe banks*, Heat Transfer Engineering 1(**3**), 23-32.

[5] Xu G.P., Tso C.P., Tou K.W., 1998, *Hydrodynamics of two-phase flow in vertical up and down-flow across a horizontal tube bundle*, International Journal of Multiphase Flow, **24**, 1317-1342.

[6] Rahman F.H., Gebbie J.G., Jensen M.K., *Interfacial friction correlation for shell-side vertical two-phase cross-flow past horizontal in-line and staggered tube bundles*, International Journal of Multiphase Flow, **22**(**4**)**,** 753-766.

[7] Simovic Z.R., Ocokoljic S., Stevanovic V.D., 2007, *Interfacial friction correlations for the two-phase flow across tube bundle*, International Journal of Multiphase Flow, **33**(**2**), 217-226.

[8] Pezo M., Stevanovic V.D., Stevanovic Z., 2006, *A two-dimensional model of the kettle reboiler shell side thermal-hydraulics*, International Journal of Heat and Mass Transfer, **7-8**, 1214-1224.

[9] Dowlati R., Kawaji M.D., Chisholm D., Chan A.M.C., 1992, *Void fraction prediction in two-phase flow across a tube bundle,* AIChE J, **38**, 619-622.

[10] Khusnood S., Khan Z.M., Malik M.A., Korashi C.U., Khan M.A., 2004, *A review of heat exchanger tube bundle vibrations in two-phase crossflow*, Nuclear Engineering and Design, **230**, 233-225.

[11] Xu G.P., Tou K.W., Tso C.P., 1998, *Two-phase void fraction and pressure drop in horizontal crossflow across a tube bundle*, Transaction of ASME, **120**, 140-145.

[12] Dowlati R., 1992, *Hydrodynamics of two-phase cross-flow and boiling heat transfer in horizontal tube bundles*, Ph.D. Thesis, Univ. of Toronto, Dept.of Chemical Engineering and Applied Chemistry, Toronto, Canada.

[13] Dowlati R., Kawaji M.K., Chan A.M.C., 1988, *Void fraction and friction pressure drop in two-phase flow across a horizontal tube bundle*, A.I.Ch.E. Symposium Series, **84**, 126-132.

[14] Wallis G.B., 1969, *One-dimensional two-phase flow*, McGraw-Hill Companies.

[15] Axisa F., Boheas M.A., Villard B., 1985, *Vibration of tube bundles subjected to steam water crossflow; a comparative study of square and triangular arrays*, 8th Int. Conference on S.M.R.T., Brussels.

[16] Noghrehkar G.R., 1996, *Investigation of local two-phase patameters in crossflow – induced vibration of tubes in tube bundles*, In Dept. of Chemical Engineering and Applied Chemistry, University of Toronto, Toronto, Canada.

[17] Chan A.M.C., Shoukri M., 1987, *Boiling characteristics of small multitube bundles*, Journal of Heat Transfer, **109**, 753-760.

[18] Kondo M., Nakajima K.I., 1980, *Experimental investigation of air-water two-phase upflow across horizontal tube bundles*, Bull. JSME, **23**, 385-393.

[19] Fair J.R., Klip A., 1983, *Thermal design of horizontal reboilers*, Chem. Eng. Prog **79**, 86-96.

[20] Palen J.W., Yang C.C., 1983, *Circulation boiling model for analysis of kettle and internal reboiler performance*, In: Kitto, J.B., Robertson, J.M. (Eds.), Heat Exchangers for Two-Phase Applications, HTD-Vol, **27**, ASME, New York, 55-61.

[21] Payvar P., 1983, *Analysis of performance of full bundle submerged boilers. In: Two-phase heat exchanger symposium*, HTD-Vol. **44**. ASME, New York, 11-18.

[22] Whalley P.B., Butterworth D., 1983, *A simple method for calculating the recirculation flow in vertical thermosyphon and kettle reboilers*, Heat exchanger for Two Phase Applicants, ASME HTD-Vol. **27**, 47-53.

[23] Leong L.S., Cornwell K., 1979, *Heat transfer coeffcients in a reboiler tube bundle*, The Chem. Engineer, **343**, 219-221.

[24] Brisbane T.W.C., Grant I.D.R., Whalley, P.B., 2000, *A prediction method for kettle reboiler performance*, ASME paper no., 80-HT-42. 10.

[25] Burnside B.M., Cuthbertson G., McNeil D.A., 2000, *Pressure drop in downward flow of condensing steam over a horizontal bundle of square pitched tubes*, Experimental Heat Transfer, **13**, 259–273.

[26] Burnside B.M., 1999, *2-D kettle reboiler circulation model*, Int. J. Heat Fluid Flow, **20** (**4**), 437–445.

[27] Kumar S., 2003, *Recirculation model of kettle reboiler*, International Journal of Heat and Mass Transfer, **46**(**15**), 2899-2909.

[28] Jensen M.K., 1998, *Model for the recirculating flow in a kettle reboiler*, in: Proceedings, Houston, TX, USA, Publ by AIChE, New York, NY, USA.

[29] Lockhart R.W., Martinelli R.C., 1948, *Proposed correlation of data for isothermal two-phase two-component flow in pipes*. Chemical Engineering Progress, **45**, 39-48.

[30] Bamardouf K.H., McNeil D.A., 2009, *Experimental and numerical investigation of two-phase pressure drop in vertical cross-flow over a horizontal tube bundle*, Journal of Applied Thermal Engineering, **29**, 1356-1365.

[31] Sadikin A., McNeil D.A., Bamardouf K.H., 2010, *Two-phase flow on the shell side of a shell and tube heat exchanger*, In: Proc. of the 14th Int. Heat Transfer Conference, August 8-13, Washington DC, USA.

[32] McNeil D.A., Bamardouf K.H., Burnside B.M., Almeshaal M., 2010, *Investigation of flow phenomena in a kettle reboiler*. International Journal of Heat and Mass Transfer, **53**, 836-848.

[33] Cornwell K., Duffin N.W., Schueller R.B., 1980, *Experimental study of the effects of fluid flow on boiling within a kette reboiler tube bundle*, American Society of Mechanical engineers, (**80**-HT-**45**), 619-622.

[34] Edwards D.P., Jensen M.K., 1991, *Two-dimensional numerical model of two-phase heat transfer and fluid flow in a kettle reboiler*. Proceedings. 1991, Minneapolis, MN, USA, Publ by ASME, New York, NY, USA.

[35] Stosic Z.V., Stevanovic V.D., 2002, *Advanced three-dimensional two-fluid porous media method for transient two-phase flow thermal-hydraulics in complex geometries*, Numerical Heat Transfer, Part B: Fundamentals, **41**(**3-4**),263-289.

[36] Stevanovic V.D., Stosic Z.V., Kiera M., Stoll U., 2002, *Horizontal steam generator yhermal-hydraulics at various steady-state power levels*, in: Proceedings of the tenth International Conference on Nuclear Engineering, Arlington, VA, United States, **3**, 767-779.

[37] Stevanovic V.D., Stosic Z.V., Kiera M., Stoll U., 2002, *Numerical simulation and analyses of the loss of feedwater transient at the unit 4 of kola npp*, in: Proceedings of the tenth International Conference on Nuclear Engineering, Arlington, VA, United States, **3**, 781-792.

[38] Ishii M., Zuber N., 1975, *Drag coefficient and relative velocity in bubbly, droplet or particulate flows*, AIChE Journal, **25**(**5**), 843-855.

[39] Dowlati R., Chan A.M.C., Kawaji M., 1992, *Hydrodynamics of two-phase flow across horizontal in-line and staggered rod bundles*, Journal of Fluids Engineering, Transactions of the ASME, **114** (**3**), 450-456.

[40] McNeil D.A., Bamardouf K.H., Burnside B.M., 2010, *A one-fluid, two-dimensional flow simulation model for a kettle reboiler*. International Journal of Heat and Mass Transfer, **53**, 825-835.

[41] Collier J.G., Thome J.R., 1999, *Convective Boiling and Condensation*, 3rd Ed. Oxford University Press, Oxford.

[42] Owens W.L., 1963, *Two-phase pressure gradient*, In: International Developments in Heat Transfer, ASME 363-368.

[43] Martinelli R.C., Nelson, D.B., 1948, *Prediction of pressure drop during forced circulation boiling of water*, Transaction of ASME, **64**, 193-200.

[44] Tong L.S., Tong T.S. Tang Y.S., 1997, *Boiling heat transfer and two-phase flow*, CRC Press.

[45] Grant I.D.R., Chisholm D., 1979, *Two-phase flow on the shell side of a segmentally baffled shell-and-tube heat exchanger*, Journal of heat transfer, Transaction ASME, **101**(**1**), 38-42.

[46] Ulbrich R., Mewes D., 1994, *Vertical, upward gas liquid two-phase flow across a tube bundle*, International Journal of Multiphase Flow, **20**(**2**), 249-272.

[47] Noghrehkar G.R., Kawaji M., Chan A.M.C., 1999, *Investigation of two-phase flow regimes in tube bundles under cross-flow conditions*, International Journal of Multiphase Flow, **25**(**5**), 857-874.

[48] Ribatski G., Thome J.R., 2005, *Dynamic of two-phase flow across horizontal tube bundle – a review*. Thermal Engineering, **4**(**2**), 122-131.

[49] Aprin L., Mercier P., Tadrist L., 2007, *Experimental analysis of local void fractions measurements for boiling hydrocarbons in complex geometry*, International Journal of Multiphase Flow, **33**(**4**), 371-393.

[50] McNeil D.A., Sadikin A., Bamardouf K.H., 2012, *A mechanistic analysis of shell-side two-phase flow in an idealized in-line tube bundle*, International Journal of Multiphase Flow, **45**, 53-69.

[51] Bamardouf K.H., 2008, *An experimental and numerical study of two-phase flow in a kettle reboiler*, Ph.D Thesis, Heriot-Watt University, School of Engineering and Phsical Sciences, Edinburgh, UK.

[52] ESDU, 1979, *Crossflow pressure loss over banks of plain tubes in square and triangular arrays including effects of flow direction*, Engineering Sciences Data Unit, **79034,** 17.

[53] Stuart A.D., 2005, *The effects of a highly viscous liquid phase on two-phase flow in a vertical pipe and pipeline components*, Ph.D Thesis, Heriot-Watt University, School of Engineering and Pyhsical Sciences, Edinburgh, UK.

[54] Patrick M. Swanson B.S., 1958, *Radiation attenuation method of measuring density of a two-phase fluid*, The Review of Scientific Instruments, **29**, 1079-1085.

[55] Hogsett S., Ishii, M., 1997, *Local two-phase flow measurements using sensor techniques*, Nuclear Engineering and Design, **175**, 15–24.

[56] Hibiki T., Hogsett S., Ishii M., 1998, *Local measurement of interfacial area, interfacial velocity and liquid turbulence in two-phase flow*, Nuclear Engineering and Design, **184**, 287–304.

[57] Wu Q., Ishii M., 1999, *Sensitivity study on double-sensor conductivity probe for the measurement of interfacial area concentration in bubbly flow*, International Journal of Multiphase Flow, **25**, 155-173.

[58] Kim S., Fu X.Y., Wang X., Ishii M., 2000, *Development of the miniaturized four-sensor conductivity probe and the signal processing scheme*, International Journal of Heat and Mass Transfer, **43**, 4101-4118.

[59] Zhao D., Guo L., Lin C., Zhang X., 2005, *An experimental study on local interfacial area concentration using a double-sensor probe*, International Journal of Heat and Mass Transfer, **48**, 1926-1935

[60] Leung W.H., Revankar S.T., Ishii Y., Ishii M., 1995, *Axial development of interfacial area and void concentration profiles measured by double-sensor probe method*, Int. J. Heat Mass Transfer, **38**, 45-453.

[61] Hibiki T., Ishii M., 1999, *Experimental study on interfacial area transport in bubbly two-phase flows*, International Journal of Heat and Mass Transfer, **42**, 3019-3035.

[62] Hibiki T., Ishi M., Takashi X.Z, 2001, *Axial interfacial area transport of vertical bubbly flows*, International Journal of Heat and Mass Transfer, **44**, 1869-1888.

[63] Hibiki T., Situ R., Mi Y., Ishii M., 2003, *Local flow measurements of vertical upward bubbly flow in an annulus*. International Journal of Heat and Mass Transfer, **46**, 1479–1496.

[64] Hibiki T., Situ R., Mi Y., Ishii M., 2003b, *Experimental study on interfacial area transport in vertical upward bubbly two-phase flow in an annulus*, International Journal of Heat and Mass Transfer, **46**, 427–441.

[65] Wu Q., Welter K., McCreary D., Reyes J.N., 2001, *Theoretical studies on the design criteria of double-sensor probe for the measurement of bubble velocity*, Flow Measurement and Instrumentation, **12**, 43–51.

[66] Muñoz-Cobo J.L., Peña J., Chiva S., Mendez S., 2007, *Monte-Carlo calculation of the calibration factors for the interfacial area concentration and the velocity of the bubbles for double sensor conductivity probe*, Nuclear Engineering and Design, **237**, 484–496.

[67] Chaumat H., Billet-Duquenne A.M., Augier F., Mathieu C., Delmas H., 2007, *On the reliability of an optical fibre probe in bubble column under industrial relevant operating conditions*, Experimental Thermal and Fluid Science, **31**, 495-504.

[68] Van Der Welle R., 1985, *Void fraction, bubble velocity and bubble size in two-phase flow*, International Journal Multiphase Flow, **11**, 317-345.

[69] Angeli P., Hewitt G.F., 2000, *Flow structure in horizontal oil-water flow*, International of Multiphase Flow, **26**, 1117-1140.

[70] Chisholm D., 1983, *Two-phase flow in pipelines and heat exchangers*, George Goodwin, London and New York.

[71] Dowlati R., Kawaji M., Chan A.M.C., 1996, *Two-phase crossflow and boiling heat transfer in horizontal tube bundles*, Journal of Heat Transfer, Transaction ASME, **118**(**1**), 124-131.

[72] Reinke M.J. Jensen M.K., 1987, *Comparison of boiling heat transfer and two-phase pressure drop between an in-line and staggered tube bundle*, ASME HTD- **85**, 41-50.